

europhysics
conference
abstracts

22nd European Physical Society Conference on

Controlled Fusion and Plasma Physics

Bournemouth, 3rd-7th July 1995

Editors: B E Keen, P E Stott and J Winter

Contributed Papers, Part II

blished by: The European Physical Society

ries Editor: Prof. R Pick, Paris

naging Editor: G Thomas, Geneva

Volume 19C

Part II

22nd European Physical Society Conference on

Controlled Fusion and Plasma Physics



Bournemouth International Centre, United Kingdom

3-7 July 1995

Editors: B.E. Keen, P.E. Stott and J. Winter

europhysics conference abstracts

22nd European Physical Society Conference on

Controlled Fusion and Plasma Physics

Bournemouth, 3rd-7th July 1995

Editors: B E Keen, P E Stott and J Winter

Max-Planck-Institut für Plasmaphysik
09. NOV. 1995
Bibliothek

Contributed Papers, Part II

Published by: The European Physical Society

Series Editor: Prof. R Pick, Paris

Managing Editor: G Thomas, Geneva

Volume 19C

Part II

95-0981

EUROPHYSICS CONFERENCE ABSTRACTS is published by the European Physical Society, © 1995.

Reproducing rights reserved.

This volume is published under copyright of the European Physical Society. We wish to inform authors that the transfer of the copyright to the EPS should not prevent an author from publishing an article in a journal quoting the original first publication or to use the same abstract for another conference. This copyright is just to protect EPS against using the same material in similar publications.

The Proceedings may be purchased from "The Publications Officer, The JET Joint Undertaking, Abingdon, Oxon, OX14 3EA, UK".

Preface

The 22nd European Physical Society Conference on Controlled Fusion and Plasma Physics, under the auspices of the Plasma Physics Division of the European Physical Society, was hosted by and local arrangements were made by the JET Joint Undertaking, Abingdon, UK. Following the guidelines of the Board of the EPS Plasma Physics Division, the 1995 Conference included topics from the areas of: Tokamaks; Stellarators; Alternative Magnetic Confinement Schemes; Magnetic Confinement Theory and Modelling; Plasma Edge Physics; Plasma Heating; Current Drive and Profile Control; Diagnostics; and Basic Collisionless Plasma Physics.

The scientific programme and paper selection was the responsibility of the International Programme Committee appointed by the Board of the EPS Plasma Physics Division. The Programme Committee selected 492 contributed papers (out of 600 submitted abstracts) for presentation as posters in four sessions at the meeting. In order to maintain participants interest throughout all four poster sessions, the sessions were not divided into topic groups, but a mixture of posters from all topic groups was arranged at each session. As a consequence, the Proceedings of the Conference are published in four volumes, which correspond to the four poster sessions (Sessions P, Q, R and S) rather than to the Topic Groups.

In 1994, for the 21st EPS Conference, the Board of the EPS Plasma Division agreed to an important change in the arrangements for contributed papers. The Proceedings were printed after the meeting, allowing a later submission date for abstracts and giving authors the opportunity to present latest results in the four-page papers. This arrangement was continued for the 22nd EPS Conference, in 1995. Consequently, authors of contributed papers handed in their four-page papers to the Scientific Secretary during the conference and these are reproduced in these volumes.

According to EPS Plasma Physics Division regulations, the Conference Proceedings contain the four-page papers of all those contributions for which at least one author was a registered participant at the Conference. There are 462 papers which satisfy this condition. The four volumes of the proceedings will be mailed to all registered participants of the Conference.

The papers of the nine Review Lectures and 18 Topical Lectures will be published in a Special Issue of the journal "Plasma Physics and Controlled Fusion", which will also be mailed to all registered participants.

B E Keen, P E Stott and J Winter

July 1995

Acknowledgements

The Conference Organisers gratefully acknowledge financial support from the following:

The European Commission
Holec Projects bv
Thomson Tubes Electroniques
Brush Wellman Inc
Institute of Physics Publishing
Ansaldo
Spinner GmBH
E Zanon Spa
Linde Cryogenics Ltd
JET Joint Undertaking

Programme Committee

J Winter	(KFA, Jülich, Germany - Chairman)
F Alladio	(ENEA Frascati, Italy)
A Bers	(MIT, Cambridge, USA)
A Bondeson	(Uppsala University, Sweden)
M Chatelier	(CEA, Cadarache, France)
R O Dendy	(UKAEA, Culham Laboratory, UK)
J R Drake	(RIT, Stockhom, Sweden)
V E Golant	(Ioffe Institute, St Petersburg, Russia)
O Gruber	(IPP, Garching, Germany)
N J Lopes-Cardozo	(FOM, Nieuwegein, The Netherlands)
J Sanchez	(CIEMAT, Madrid, Spain)
F Sluijter	(Eindhoven University, The Netherlands - Chairman, Plasma Physics Division EPS
P E Stott	(JET Joint Undertaking, Abingdon, UK)

Local Organising Committee

P E Stott	Chairman
B E Keen	Scientific Secretary
G Blankenback (Mrs)	Conference Secretary
J H C Maple	
K R Musgrave	
C Norris (Mrs)	Finance Officer

Contents

Part II: Poster Session Q

Title	Presenting Author	Page No:
• H-mode, ß-limit and Instability Studies on COMPASS-D	Morris AW	II-001
• Characteristics of Radiative Boundary Discharges with Different Impurity Injection Conditions	Kallenbach A	II-005
• Helium and Neon Transport Experiments at JET	von Hellerman M	II-009
• Strongly Inhomogeneous Electron Heat Diffusivity in RTP	Hogeweij D	II-013
• MHD Activity and Operational Limits on START	Gryaznevich M	II-017
• Instability Control on COMPASS-D	McArdle G	II-021
• H-Mode Thresholds and MHD Stability in COMPASS-D	Fielding S	II-025
• Estimate of Magnetic Reconnection Sawtoothing RTP Plasmas by means of Soft X-Ray Tomography	Tanzi C	II-029
• Modelling the Neutralisation and Energy Distribution Function of MeV Ions during Combined ICRF and NBI Heating in JET	Stuart A	II-033
• Runaway Electron Diffusion Measurements in the JET Tokamak	Esposito B	II-037
• New Insight into Runaway Electrons Production and Confinement	Martin G	II-041
• New TORE SUPRA Steady-state Operating Scenario	Martin G	II-045
• Current Carrying Regimes in a Tokamak with Additional Inclined Coils	Moroz P	II-049
• Evolution and Optimisation of Neutron Emissivity Profiles in JET	Marcus FB	II-053
• Measurement of Atomic Hydrogen Fluxes in MeV-energy Range on ICRF-heated JT-60U Plasmas	Afanassiev VI	II-057
• Triton Burnup Study in JT-60U	Nishitani T	II-061

Title	Presenting Author	Page No:
• Comparison of JET and DIII-D Temperature and Density Profile Shapes and their Parametric Dependence	Schissel DP	II-065
• Quasi Steady-state Advanced Tokamak Scenarios in JET	Challis CD	II-069
• Density Scaling of the H-mode Power Threshold in JET	Righi E	II-073
• The Optimisation of Recycling in High Performance Hot-Ion H-mode JET Discharges	Lawson KD	II-077
• Ohms Law for Tokamaks and Toroidal Current Drive by Radial Plasma Flow in Pellet Injection Experiments	Kalmykow S	II-081
• Electrons and Ions Heating and Improved Confinement Regime in Lower Hybrid Heating Experiments on FT-2 Tokamak	Lashkul S	II-085
• Microwave Backscattering Experiment in Ohmic H-Mode Discharge in TUMAN-3 Tokamak	Bulanin V	II-089
• Characteristics of Low q(a) Plasmas in the CDX-U Spherical Tokamak	Hwang YS	II-093
• H-mode Threshold for Ohmic Plasmas in TCV	Duval B	II-097
• Plasma Shape Control in TCV Using MGAMS	Hofmann F	II-101
• TF Ripple Loss of Alpha Particles in TFTR D-T Experiments	Redi M	II-105
• Improved Performance of DT Supershots in TFTR using New Techniques of Limiter Conditioning with Lithium	Mansfield D	II-109
• Supershot Performance with Reverse Magnetic Shear in TFTR	Batha S	II-113
• HIBP Diagnostics on TJ-I Tokamak and First Results of Plasma Parameters Measurements	Hidalgo C	II-117
• Effect of Active Pumping and Fuelling on Divertor Plasma Discharges in JET	Saibene G	II-121
• Characterisation of Long Pulse Steady-state H-modes in the JET Pumped Divertor Configuration	Stork D	II-125
• Non-Maxwellian Velocity Distributions and Spatial Structures in Electron Temperature Profiles of Ohmic and EC-Heated Discharges in RTP	Box FMA	II-129
• Toroidal and Poloidal Rotation in the COMPASS-D Tokamak	O'Connell R	II-133
• Quasi-Helical Symmetry of L=1 Torsatron	Shiina S	II-137

Title	Presenting Author	Page No:
• An Experimental Study of RF Produced Plasmas in the H-1 Toroidal Heliac	Borg G	II-141
• Global Internal Modes in the H1 Heliac	Cooper WA	II-145
• Investigations of Plasma Beta in TJ-IU Torsatron	Qin J	II-149
• Ion Confinement Studies in the TJ-IU Spanish Torsatron	Zurro B	II-153
• Recent Results in TJ-I U Torsatron	Ascasibar E	II-157
• Studies of Hot Spots and their Correlation with other Phenomena in PF-Type Discharges	Jakubowski L	II-161
• Magnetic Surfaces, Plasma Confinement and Heating in Tornado-X	Abramova KB	II-165
• Observations of a 7μm Carbon Fibre Z-Pinch	Beg F	II-169
• Mega-Ampere Carbon Fibre Z-Pinch Experiments	Mitchell IH	II-173
• Optimal Plasma Parameters in Mirror Based Neutron Source FEF-II	Tohrisawa K	II-177
• Plasma Equilibrium in Gas-Dynamic Trap at Intense Injection of Neutral Beams	Kotelnikov IA	II-181
• Applicability of the Rebut-Lallia-Watkins Model used for ASDEX Discharges	Woloch F	II-185
• Collisional Drift Fluids and Drift Waves	Pfirsch D	II-189
• Simulation of Transport in the Ignited ITER with Broad Density Profiles and High Radiative Fraction	Becker G	II-193
• Radiative Transport via Electron-Bernstein Waves	Puri S	II-197
• Limits of Radiative Edge Cooling by Impurities in a Fusion Reactor	Samm U	II-201
• Transport Modelling in Tight Aspect Ratio: Testing against START Ohmic Data and Predictions for MAST	Roach C	II-205
• ECRH-Assisted Start-up in ITER	Lloyd B	II-209
• Predictive Modelling of Energy Transport in JET Discharges	Erba M	II-213
• Numerical Studies of the Dynamics of MARFEs for a Deuterium-Carbon Plasma at ASDEX-Upgrade	Kastelewicz H	II-217
• Alpha-Particle Driven TAE Instability Suppression by the Resonant RF Field	Marchenko V	SII-221
• Energetic Ion Effects on the Propagation and Absorption of Kinetic Alfven Wave in Fusion Plasmas	Huang L	II-225

Title	Presenting Author	Page No:
• Interpretation of Ion Cyclotron Emission from Sub-Alfvénic Fusion Products in TFTR	Dendy R	II-229
• Modelling Collective Losses of Energetic Particles	Berk HL	II-233
• Kinetic Toroidicity Induced Alfven Eigenmodes in Toroidal Shaped Plasmas	Borba D	II-237
• Modelling the Expulsion of Helium Ash from Tokamaks at the Precessional Drift Resonance	Kam K	II-241
• Non-Perturbative Kinetic Effects on Alfven Eigenmodes in Tokamak Plasmas	Appert K	II-245
• Influence of Alpha-Particle Diffusion on Burn Dynamics in Tokamaks	Mantsinen M	II-249
• Topological Transitions of Fast Ion Orbits	Porcelli F	II-253
• Particle Simulations of Transport of High Energy Ions in Tokamak Plasmas	Kashiwagi M	II-257
• TAE-Induced Diffusion of Fast Particles in JET	Appel LC	II-261
• 3D Calculations of Fast Ion Distributions in Tokamaks	O'Brien M	II-265
• The Distribution Function of Fusion Products at Birth	Sadler G	II-269
• Impurity Production and Erosion/Redeposition at the JET MKI Divertor	Guo H	II-273
• Plasma Shield Formation and Divertor Plate Erosion for ITER Tokamak Plasma Disruptions	Piazza G	II-277
• In-situ Measurement of Erosion/Deposition in the DIII-D Divertor by Colorimetry	Weschen-felder F	II-281
• Disruption-Caused Wall Erosion and Vapor Shield Formatation	Lengyel L	II-285
• Boron Erosion and Transport in the ASDEX Upgrade Divertor	Krieger K	II-289
• Investigation of Target Plate Interaction and Impurity Radiation from the Divertor During High-Performance H-mode Discharges in ASDEX-Upgrade	Field AR	II-293
• Investigation of Chemical Sputtering at the Plasma/Generator PSI-1 - First Experimental Results and Modelling	Bohmeyer W	II-297
• Surface Layer Composition of the JET Vessel Walls, Material Transport and Hydrogen Trapping in the Vessel Walls	Mayer M	II-301

Title	Presenting Author	Page No:
• The Penetration of Impurity Atoms into the Plasma Boundary and its Impact on Central Impurity Concentration	Unterberg B	II-305
• Chemical Erosion Measurements from Various Carbon Based Limiters and Coatings in TEXTOR	Pospieszczyk A	II-309
• Impurity Screening in ALCATOR C-Mod	McCracken G	II-313
• Impurity Influxes and Production Mechanisms in RFX	Puiatti ME	II-317
• Studies of High-Z Wall Components in TEXTOR 94: Local Impurity Release and Impact on the Plasma Core	Philipps V	II-321
• Fundamental Deuterium, Second Harmonic Tritium and Alpha Particle Heating and Current Drive for Fusion Plasmas	Scharer J	II-325
• Physics Aspects of Coupling the ICRF A2 Antennae to JET Discharges	Lamalle P	II-329
• Three-Dimensional Antenna Coupling to Core Plasma in Fusion Devices	Carter M	II-333
• On a New Method to Compute RF Antenna Characteristics	Pecoul S	II-337
• ICRF Heating and Enhanced Confinement Modes in Alcator C-Mod	Takase Y	II-341
• On the Lower Hybrid Current Drive in HL-1 Tokamak	Pan YD	II-345
• Momentum and Energy Exchange Between LH Waves and MeV Alpha Particles	Sipila S	II-349
• Fast Wave Current Drive Experiments in JET Divertor Plasmas	Nguyen F	II-353
• Role of MHD Activity in LH-assisted Discharges in the PBX-M Tokamak	Talvard M	II-357
• Lower Hybrid Current Drive Experiments in the TdeV Tokamak	Cote A	II-361
• Absorption of Finite-Size LH Wave Beams in Tokamak Plasmas	Pereverzev G	II-365
• A Photoelectron Spectrometer with Magnetic Analyzer (Measurements on the T-10 Tokamak)	Shurygin VA	II-369
• Measurement of Line Radiance of Low-Z Impurity by USX and VUV Spectroscopy on CASTOR Tokamak	Badalec J	II-373

Title	Presenting Author	Page No:
• High Resolution Spectroscopic Measurements of Impurity Radiation Distributions and Neutral Deuterium Profiles in the JET Scrape-Off Layer	Breger P	II-377
• Combined Measurement of the Electric and Poloidal Magnetic Field in a Tokamak Device	Bertschinger G	II-381
• Determination of Absolute Metal Impurity Densitites in TORE SUPRA	Platz P	II-385
• Spectral and Angular Dependence of Photodiode Response to Soft X-Rays	Anton M	II-389
• Ultra-Soft X-Ray Spectroscopy using Multilayer Mirrors on TCV	Weisen H	II-393
• Interpretation of Charge Exchange Spectra emitted by Fast ^{3}He during Experiments on Transport Control by ICRH on TEXTOR	Van Wassenhove G	II-397
• Use of Heated, Diagnostic Optical Fiber for the Suppression of Transmission Loss during D-T TFTR Discharges	Tighe W	II-401
• Observations of Ion Cyclotron Emission from Charged Fusion Products in TFTR	Cauffman S	II-405
• Time and Space Resolved Soft X-Ray Spectroscopy on RTP	Meijer FG	II-413
• Spectroscopic Vector Tomography at RTP	Howard J	II-413
• An Investigation of a CV Line Ratio Variation in the TJ-I Tokamak and its Sensitivity to Neutral Concentration	McCarthy K	II-417
• The Vacuum Ultra Violet Spectrum of W VIII	Bakos JS	II-421
• Modulational Interaction of Short-Wavelength Ion Acoustic Oscillations in Dusty Plasmas	Popel SI	II-425
• Vlasov Eulerian Simulation in Two Dimensions - Phase Space Hole Deflation by a Static Magnetic Field	Fijalkow E	II-429
• A New Drift Wave Soliton in an Inhomogeneous Plasma	Nejoh Y	II-433
• The Effects of Sub-Alfvenic Shear Flow on the Resistive G-Mode	Paris RB	II-437
• On the Possibility of Measuring a Model of the L-H and ELM Dynamics	Bak P E	II-441
• First Observations of Collective Thomson Scattering from JET Plasmas	Hoekzemo JA	II-445

Title	Presenting Author	Page No:
• Pellet Refuelling of ELM-y H-mode Discharges beyond the Greenwald Limit in ASDEX Upgrade	Lang P T	II-449
• Toroidal Momentum Slowing Down and Replacement Times in JET Divertor Discharges	Zastrow KD	II-453

H-MODE, β-LIMIT AND INSTABILITY STUDIES ON COMPASS-D

A W Morris, L C Appel, J D Ashall, K B Axon, R A Bamford, R Barnsley[1] M G Booth, R J Buttery, P G Carolan, G G Castle, A Colton, N J Conway[2], T Edlington, A M Edwards, S J Fielding, D Gates, T C Hender, J Hugill, C Hunt, B Lloyd, G J McArdle, S J Manhood, I M Melnick[3], M R O'Brien, R O'Connell[2], M O'Mullane[4], N J Peacock, T Pinfold, D C Robinson, P R Simpson, M Singleton[4], K Stammers, J Tomas, T N Todd, M Valovič, P Vyas, J Waterhouse, G A Whitehurst, C D Warrick and the COMPASS-D and RF teams

UKAEA Government Division Fusion, Culham, Oxon OX14 3DB UK
(UKAEA/EURATOM Fusion Association)

[1] Leicester University, UK
[2] University College, Dublin, Rep of Ireland
[3] University College, London, UK
[4] University College, Cork, Rep of Ireland

1 Introduction

In order to be able to predict the performance of the next generation of tokamaks such as ITER, the scaling of the key parameters and operating regimes has to be established on the soundest basis possible. The modest size of COMPASS-D, combined with the ability to make ITER-like single-null divertor (SND) configurations with H-modes and strong additional heating will provide information on the size scaling, and the adaptable systems for instability control and error-field studies are used to address MHD stability issues, in particular the question of the effects of error-fields. The SND geometry allows edge physics models to be tested, such as for helium exhaust [1]. The device parameters (achieved) are: $I_p \leq 320$kA; $B_T \leq 2.0$T, $R = 0.56$m, $a \leq 0.21$m, $\kappa \simeq 1.6$ (SND). Nine 200kW, 60GHz gyrotrons are available for additional heating and up to 1.4MW has been injected into the plasma in a variety of combinations of $\omega_{ce}, 2\omega_{ce}$, X- and O-mode, low-field and high-field-side antennas. Two 300kW 1.3GHz klystrons are installed, and LHCD power levels approaching 200kW have been launched into COMPASS-D plasmas.

An overview of the results is presented here, with several other papers at this conference describing the data in more detail.

2 High-β_N experiments

The use of ECRH allows heating without significant momentum injection, and thus studies of the β-limit without strong rotation effects are possible. Injection of 700kW-1MW into low density ($\bar{n}_e \simeq 8 \times 10^{18}\mathrm{m}^{-3}$) discharges with $q_{95} = 4.0 - 4.5, I_p = 150$kA, $B_T \simeq 1.2$T leads to an experimental limit of $\beta_N \simeq 2.1$ where $\beta_N \equiv \beta(\%)/(I_p/aB_T)$ (MA,m,T). The limit is either hard (disruptive) or soft, but in both cases a large $m = 2, n = 1$ mode grows. A systematic scan of the launch angle of the ECRH waves has been performed [2], which shows that the best performance is obtained when the high field-side lines are orientated to provide counter-current drive on axis. Operating at low density means that these discharges have very high temperatures: the diamagnetic average temperature ($1.5\langle p_\perp \rangle / \bar{n}_e$) can exceed 5keV (the ions are cold, ≤ 250eV) and the central electron temperature is expected to be over 10keV (beyond the measurement range of the Thomson scattering system). As a consequence, the collisionality is very low ($\nu_{*,e} \sim 10^{-3}$), and a large bootstrap current flows ($\sim 70\% I_p$ from initial estimates based on a steady-state calculation with the SCENE code). The loop voltage is generally well

below 100mV and often below zero.

3 H-modes, thresholds and ELMs

H-modes have been produced routinely in Ohmic SND discharges over a wide range of parameters ($q_{95} = 2.7 - 5$) [3]. Both ELM-free and ELMy discharges are observed and show the normal characteristics of H-mode, with indications of impurity accumulation in ELM-free periods [4]. Examination of the H-mode threshold has been undertaken and it is found that while H-modes occur when the power exceeds the ASDEX scaling law ($P_{thresh} \propto \bar{n}_e B_T S$) at high densities, there is a sharp increase in power required for the transition at low density. Adding ECRH to low density plasmas leads to good confinement ($H \sim 2$ compared to ITER89-P L-mode scaling, but apparently with weaker power degradation), but not all the H-mode characteristics are then seen (for example no clear ELMs). The power required is very high confirming the failure of the threshold scaling law at low density. No H-modes have yet been observed with unfavourable ∇B direction in Ohmic or low density ECR heated plasmas. There is a threshold observed for the transition to ELM-free H-mode, which appears to be better represented by a threshold in β_N than in power [5], and can explain the hysteresis in power for H-L compared to L-H transitions. A pressure threshold may lend credence to the "peeling" mode as a cause of ELMs, as this edge-current-driven mode is stabilised by pressure between two limits. Some more direct evidence is provided by discharges where I_p is ramped up and down, and ELM-free H-mode is triggered on ramp-down and ELMs stimulated on ramp-up [3, 5].

Turning to the ELM itself - both type-III and type-I ELMs are seen, as defined by the behaviour of the repetition frequency with power (type-I having a frequency which increases with increasing power). The comprehensive magnetic diagnostics in close proximity to the plasma on COMPASS-D allow precursors to be clearly seen to both types of ELM. Rotating precursors ($v_\phi \sim 10^5 \mathrm{m.s^{-1}}$) with $n = 3 - 5$ are seen propagating normally to $\mathbf{B}$, with more than one component present in general. The energy loss at the ELM can be modelled assuming that the precursors correspond to magnetic islands close to the plasma edge [6]. Whether these modes are related to the peeling mode has yet to be determined (the present peeling-mode theory is for highly-localised mode structures).

4 Changes in plasma rotation in H-modes

Passive spectroscopy of CIII has been used to measure the rotation in the outer regions of COMPASS-D, with new results [7]. Previous data when BIV alone was used has been confirmed with improved resolution ($\Delta v \sim 0.5 \mathrm{km.s^{-1}}$) – very little change ($\sim 1 \mathrm{km.s^{-1}}$) in poloidal velocity is seen from BIV, which emits from $r \sim 0.75a$ according to impurity transport modelling. The new results come from the CIII emission (from $r \sim 0.9a$) viewed both poloidally and toroidally. The transition to ELM-free H-mode is marked by a sudden change in v_{pol} (2-3km.s^{-1}/ms, Δv_{pol} starting within 0.3ms of the final ELM) leading to velocities in the electron diamagnetic drift direction of up to $\sim 20 \mathrm{km.s^{-1}}$ corresponding to $\Delta E_r \sim -20 \mathrm{kVm^{-1}}$, i.e. directed inwards. The full change in v_{pol} takes 5-10ms. The reverse transition at the end of the ELM-free period is even faster, 10km.s^{-1}/ms. The change in mean velocity at the onset of ELMy H-mode (from L-mode) is small.

The toroidal velocity of BIV does show changes during ELM-free H-mode, but in general these are much slower. The central toroidal rotation as seen with X-ray spectrometry from core-resident ions also changes by a similar amount, and this change in bulk plasma rotation appears to play a vital role in the behaviour of the plasma in the presence of

error-fields in ELM-free H-mode (see below and [8]).

5 Error field studies and instability control

External saddle windings (poloidal extent $\sim 90°$) below the X-point have been used both to generate and correct error fields. Error-field islands have also been removed with localised ECRH [8]. These coils form part of the comprehensive array of saddle windings covering the whole COMPASS-D vessel. A campaign on the effect of plasma pressure has been conducted [8] for $q_{95} \sim 4.5$ and it is found that, at least up to $\beta_N \sim 1.0$ (produced by 1MW of ECRH), the critical error-field to produce an island is not influenced significantly by the pressure, and the general characteristics of the driven island are similar to those in Ohmic plasmas, e.g. sawteeth are removed after penetration of the error-field. The saddle windings have also been used to change the power flux to the divertor target – production of a magnetic island leads to movement and splitting of the strike-points, as modelled with field-line tracing and measured with infra-red thermography [9]

The situation in H-mode is very different: once the plasma enters ELM-free H-mode, it becomes much more sensitive to error-fields. For example, for an error-field level that will produce an island only for $\bar{n}_e \lesssim 1 - 1.5 \times 10^{19}\mathrm{m}^{-3}$ in L-mode Ohmic plasmas, in ELM-free H-mode it will lead to an island at densities an order of magnitude higher, $\bar{n}_e \sim 1 \times 10^{20}\mathrm{m}^{-3}$. This increase in sensitivity is correlated with the measured change in toroidal fluid rotation in the bulk plasma after transition to ELM-free H-mode in the absence of any error-field. The rotation change is in the direction (ion drift) to make penetration easier. However, the strong poloidal impurity (CIII) rotation in the electron drift direction at the plasma edge seems not to affect the penetration. Once the island appears, an ELM is triggered, and thus careful use of helical fields may provide a technique for controlling ELMs, as does localised ECRH [10].

6 Vertical instabilities and disruptions

The similarity of the plasma shape to that in ITER and the relative robustness of COMPASS-D make it well suited for disruption studies [11]. Disruptions are invariably accompanied by vertical displacement events (VDEs) in single null plasmas. ELM-free H-modes often terminate in disruptions either initiated by an ELM which triggers a VDE and a consequent current quench, or an m=2 mode grows triggering either an ELM or a quench directly. Halo current measurements show that, with the assumption of axisymmetry, the current flowing through the divertor tiles can exceed 40% of the flat-top plasma current. The thermal energy quenches occur in 20-300μs and peak current decay rates of 500MA/s are observed, with some indication of slower decays at higher densities [11].

7 Microwave heating and current drive

An 8-guide antenna is installed in COMPASS-D to launch 1.3GHz waves for LHCD [12]. Coupling studies have led to an optimum phasing of the antennae, and good coupling has been achieved which allows continuous injection through transitions into H-mode. At relatively modest powers (140kW, $\bar{n}_e = 7 - 8 \times 10^{18}\mathrm{m}^{-3}$, $B_T = 1.4\mathrm{T}$), the full plasma current (135kA) has been driven non-inductively. The efficiency is $\eta_{20} = 0.035 - 0.04$, in accord with theoretical predictions. This system has allowed 1 second discharges to be produced, corresponding to many thousands of seconds on ITER (scaling the resistive diffusion time), and initial data on sawtooth stabilisation has been obtained.

The highly adaptable ECRH system on COMPASS-D [13] has allowed routine injection of powers well in excess of 1MW, and both X-mode and O-mode heating at the first

harmonic have been demonstrated. Changes in antenna angle (i.e. $k_{||}$) have been used in the β-limit studies described above. After conditioning, injection into very low densities is possible without impurity influx or significant radiated power fraction ($P_{rad} \lesssim 15\%$), even at the very high power densities used ($> 10\text{MWm}^{-2}$ for 1cm deposition width on the tiles and small radiative losses). A system for modulating the gyrotron power (up to 25kHz, square wave) has allowed a programme of fast feedback control of the $m = 2$ tearing mode to start, and initial closed loop experiments have been performed.

8 Summary

A wide range of topics has been investigated experimentally in a single-null configuration on COMPASS-D which are briefly covered in this overview. An experimental beta limit ($\beta_N \sim 2.1$) has been found, significantly below the optimum ideal-MHD β-limit ($\beta_N \sim 3$), whose actual value depends on the direction of EC current drive (i.e. the details of $J(r)$). Electron temperatures in excess of 10keV are deduced for these low density low collisionality plasmas. H-mode studies continue to show that there is a lower density limit for H-mode access, contrary to the traditional scaling laws. The transition to ELM-free H-mode seems to depend on β_N rather than power, pointing to pressure-stabilisation of type-III ELMs. New data on edge-localised rapid poloidal velocity changes at the transition to ELM-free H-mode have been obtained, corresponding to a large inward-pointing radial electric field. Changes in toroidal velocity during ELM-free H-mode lead to much higher sensitivity to error-field-driven magnetic islands, indicating that there can be problems even at very high densities ($\bar{n}_e \sim 1 \times 10^{20}\text{m}^{-3}$ on COMPASS-D).

This work is jointly funded by the UK Department of Trade and Industry and EURATOM.

[1] G P Maddison and M Baelmans. Modelling of helium exhaust in COMPASS-D. *This conference.*

[2] D Gates et al. The effect of current profile control on the β-limit in the COMPASS-D tokamak. *ibid.*

[3] S J Fielding et al. H-mode thresholds and MHD stability in COMPASS-D. *ibid.*

[4] N J Peacock et al. Ion transport and impurity accumulation during Ohmic H-modes in the COMPASS-D tokamak. *ibid.*

[5] M Valovic et al. Comparison of transition to ELM-free H-mode regime on COMPASS-D and ASDEX-Upgrade. *ibid.*

[6] R J Buttery et al. ELM-related MHD activity on the COMPASS-D tokamak compared with ASDEX-Upgrade. *ibid.*

[7] P G Carolan et al. Toroidal and poloidal rotation in the COMPASS-D tokamak. *ibid.*

[8] G J McArdle et al. Instability control on COMPASS-D. *ibid.*

[9] R J Buttery et al. Effects of resonant magnetic perturbations on divertor target loads in COMPASS-D. *ibid.*

[10] A W Morris et al. Control of Error-field modes and ELMs in ITER-shaped plasmas on COMPASS-D. *Proc 15th IAEA conf. Seville* **A-2-IV-1** (1994).

[11] A W Morris et al. Disruptions, vertical instabilities and halo currents in COMPASS-D. *This conference*

[12] C D Warrick et al. First results from LHCD in COMPASS-D. *ibid.*

[13] G A Whitehurst et al. High power ECRH in COMPASS-D. *ibid.*

Characteristics of radiative boundary discharges with different impurity injection conditions

A. Kallenbach, R. Dux, G. Haas, A. Herrmann, S. Hirsch, V. Mertens, J. C. Fuchs, F. Mast, S. de Peña Hempel, F. Ryter, H. Zohm, ASDEX Upgrade- NI- and ICRH-Teams
MPI für Plasmaphysik, EURATOM Association, Garching & Berlin, Germany

1 Introduction

Although impurity-induced, improved L-modes exhibit quite high energy confinement[1,2], the H-mode ist still the first candidate as the reactor operational regime owing to the narrow confinement margin for the achievement of ignition and self-sustained burn. Therefore, indispensible measures to reduce the power load of the divertor have to be compatible with H-mode operation, though the intense power bursts connected to type-I ELM activity in the H-mode will not be acceptable at all in a reactor.

The Completely Detached High-Confinement (CDH-) mode recently discovered in ASDEX Upgrade[3] would meet the requirements for an operational mode of a reactor: radiative power removal closely inside the separatrix moderates the ELM activity from type-I to type-III enabling the divertor plasma to buffer the remaining small power bursts before reaching the target plates, while high H-mode energy confinement is preserved. However, the extrapolability of this regime to reactor conditions is still an open question, the answer to which mainly depends on the relative locations of the H→L and detachment power thresholds: the CDH mode in ASDEX Upgrade is obtained only in deuterium plasmas, where the H→L power threshold is low and subsequent detachment relatively easy to achieve. Since neither the H-mode- nor the detachment-thresholds in a reactor are precisely known so far, flexibility has to be demonstrated in present day experiments in order to develop different solution scenarios which can meet the various requirements.

2 Influence of the divertor neutral flux

An important experimental parameter is the neutral flux in the divertor. It is measured by ionization gauges and feedback-controlled by deuterium puffing in the main chamber. An increasing divertor neutral density has two beneficial effects on the performance of discharges with impurity injection[2,4]: Firstly, the divertor retention increases leading to better pumping of noble gases and faster feedback response on the request of radiation reduction. Secondly, and more important, the higher divertor neutral density creates a higher edge electron density in the main plasma[5] and increased ELM activity. These effects lead to a higher radiative capability at the edge and core screening of impurities[2]. The price for the improved radiative behaviour is a moderate degradation of the energy confinement of roughly $\tau_E \propto n_{0,div}^{-0.1}$. The discharges presented in this paper had the divertor neutral flux feedback-controlled to our 'standard' value corresponding to $n_0^{div} = 1.5 \cdot 10^{20}\ m^{-3}$.

3 Comparison of highly radiating discharges with Ne, Ar and N_2 injection

Fig. 1 compares 3 discharges with high radiation levels obtained by injection of Ne, Ar and N_2 under otherwise almost identical external parameters. Discharge # 6136 exhibits

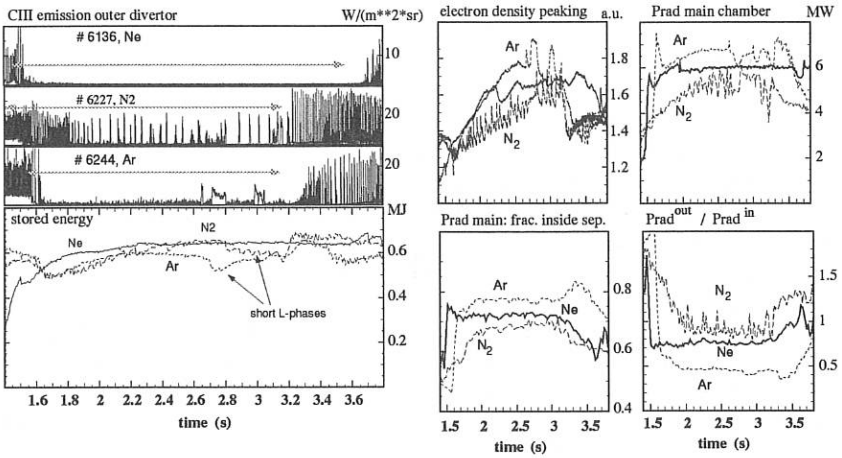


Figure 1: *Comparison of highly radiating discharges with Ne, Ar and N_2 injection in the main chamber. P_{heat}= 7.5 MW, $D^0 \rightarrow D^+$ NBI, I_p= 1 MA, q_{95}= 4.*

the CDH-mode with stored energy, radiation level (well feedback-controlled) and density peaking approaching stationary values. Using Argon, the electron density profile shows higher peaking factors and short L-phases are triggered by the high radiation level. With Nitrogen, compound-ELMs and L-phases appear even at a radiation level lower than that obtained with Neon.

The radiation fraction inside the separatrix is calculated with a special fitting procedure to bolometer line integrals in the upper halfplane under the assumption E= $f(\rho_{pol})$ prescribing the functional profile shape in accordance to impurity transport simulations. The emission function is then used to derive the total radiation P^{in}_{rad}= f_{in}·P^{main}_{rad} inside the separatrix using the total main chamber radiation taken from 30 line integrals of the horizontal bolometer camera. P^{out}_{rad}= (1-f_{in})·P^{main}_{rad} + P^{div}_{rad}, the total radiation outside the separatrix, is the sum of the SOL radiation in the main chamber and the divertor radiation, the latter taken from the deconvolution of all the 72 bolometer line integrals[6]. As shown in Fig. 1 the emissivity is shifted towards the interior plasma with increasing Z of the radiating species. Simultaneously, SOL and divertor radiation decrease leading to a reduction of the parameter $P^{out}_{rad}/P^{in}_{rad}$ by a factor of 2 from Nitrogen to Argon.

4 H-mode thresholds in radiative scenarios

The most important parameter for radiative H-mode scenarios is the value of the H→L threshold power. Taking intrinsic radiation into account, $P_{sep}^{L\rightarrow H} = 0.125 \cdot \overline{n}_e B_t$ is a good approximation for 'standard' conditions, the corresponding value for the H→L backtransition being about a factor of 2 lower.

Figure 2 shows P_{sep} versus $\overline{n}_e \cdot B_t$ for discharges with various radiation levels, the dashed line indicates the 'standard' L→H threshold. The factor (2.6 - $0.8A_{plasma}$) takes into account the isotope effect of hydrogen in comparison to deuterium (factor 1.8 from D to H). The analysis of a number of discharges with strong radiation reveals that the power

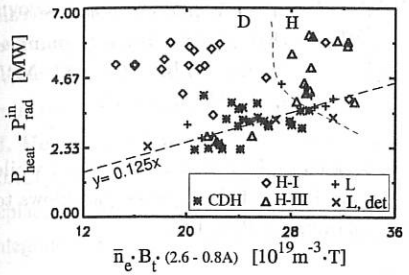


Figure 2: *Operational diagram of radiative discharges with respect to the standard L→H transition threshold for D and H plasmas. Ne, Ar and N_2 injection, P_{heat}= 5-8 MW, I_p= 0.8-1 MA, q_{95}= 2.8-4.*

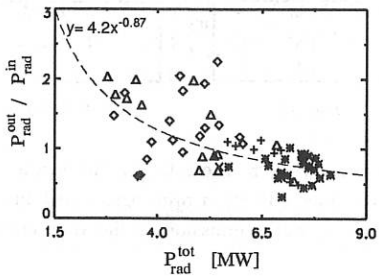


Figure 3: *Ratio of radiation inside and outside (SOL+divertor) the separatrix versus the total radiated power. Ar data points are systematically below, N_2 data slightly above the dashed curve*

flux over the separatrix, $P_{sep} = P_{heat} - P_{rad}^{in}$, is a useful parameter for the ELM-types and H-mode threshold, although the influence of radiation *outside* the separatrix cannot be ruled out completely so far. However, the hysteresis between the L→H and H→L transitions disappears in highly radiating scenarios. It may be speculated, that this behaviour is coupled to the overall alignment of improved L and H-mode in these scenarios.

An important parameter for the performance of radiative discharges is the ratio $P_{rad}^{out}/P_{rad}^{in}$, where P_{rad}^{in} is limited by the H→L separatrix threshold power. Fig. 3 shows $P_{rad}^{out}/P_{rad}^{in}$ as obtained for various experimental parameters versus the total radiated power: High values of P_{rad}^{tot} are closely connected to comparatively low radiation levels in the SOL and divertor. For reactor conditions with high H→L threshold, a high value of $P_{rad}^{out}/P_{rad}^{in}$ would be required simultaneously with a high level of the total radiated power.

5 Control of $P_{rad}^{out}/P_{rad}^{in}$

The feedback control of the total radiated power in the main chamber also allows to vary the radiated power fractions inside and outside the separatrix. Fig. 4 shows an

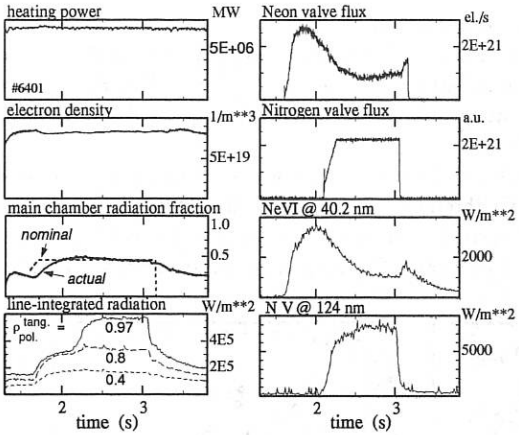


Figure 4: *Radiation feedback control with different impurities: Ne radiation is replaced by N_2 radiation, while the total main chamber radiation is kept constant. The parameter f_{in} decreases from 0.68 at t= 2 s to about 0.54 at t= 2.5 s (see bolometer line integrals for 3 tangency radii). Comparison of VUV line emsission reveals that N_2 is effectively pumped by the walls. $H^0 \rightarrow H^+$ NBI, I_p= 1 MA, q_{95}= 3.2*

experiment, where the total radiation was feedback-controlled by neon injection, while N_2 was injected with a preprogrammed flux. The variation of the injected gas allows to control the radial emission profile and hence the parameter $P_{rad}^{out}/P_{rad}^{in}$.

6 Conclusions

Stationary CDH-modes are routinely obtained with Neon injection in ASDEX Upgrade. In comparison to Neon, Argon shows higher radiation levels inside the separatrix and less SOL and divertor radiation. Owing to the stronger n_e peaking, it is unclear wether impurity accumulation in the center can be avoided and long and stationary CDH-modes can be achieved for ASDEX Upgrade conditions with Argon. Nitrogen exhibits the most favourable values of the parameter $P_{rad}^{out}/P_{rad}^{in}$, however, up to now no 'quiescent' CDH-mode could be obtained due to the disturbing appearance of large compound-ELMs and early H→L backtransition. For the experimental parameter space covered in ASDEX Upgrade so far, high total radiation levels are always connected to low radiation levels in the SOL and divertor. If this behaviour cannot be overcome by improved divertor concepts in the future, reduced target plate power load in a reactor can only be achieved under radiative H-mode conditions if $P_{sep}^{L \rightarrow H}$ is low.

References

[1] U. Samm et al., Plasma Phys. Contr. Fusion **35** (1993) B167.

[2] A. Kallenbach et al., Report IPP 1/284 (1995), Nuclear Fusion in press.

[3] O. Gruber et al., Phys. Rev. Lett. **74** (1995) 4217.

[4] R. Dux et al., this conference.

[5] J. Schweinzer et al., this conference.

[6] J. C. Fuchs et al., this conference.

'Helium and Neon Transport Experiments at JET'

M von Hellermann, K.Barth, A.J.Bickley, D.Campbell, U.Gerstel, J de Haas, D.Hillis*, L.Horton, A.Howman, R.König, L.Lauro-Taroni, C.Mayaux, P.Nielsen, W.Obert, G.Saibene, M.F.Stamp, D.Stork, M.Wade*, K-D Zastrow

JET Joint Undertaking, Abingdon, OX14 3EA, UK, *ORNL, Oak Ridge, Tennessee, USA

I. Introduction - In the pumped divertor phase of JET, dedicated helium transport experiments were carried out based on edge and central (beam) fuelling. Exhaust studies involve the use of argon frost on the divertor cryo-pump in order to achieve active pumping of helium. Charge exchange spectroscopy measurements are used to monitor the evolution of helium density profiles. Transport and exhaust of neon and nitrogen was investigated in radiative divertor experiments.

II. Helium Confinement and Exhaust Studies - The helium content added by the short (0.1s) gas-puffs is of the order 2 to $3 \cdot 10^{20}$ (or 5% of the total plasma particle content). Particle replacement times are experimentally determined by the measurement of the volume integrated impurity density profiles (He, Ne, N) and the temporal evolution of inward and outward radial particle flows:

$$\tau_p^* = \frac{\int dV \cdot n_Z(\rho)}{A \cdot (\Gamma_{out} - \Gamma_{in})}$$

pulse	comment	P_{NB} MW	I_p MA	$n_e(0)$ $10^{19}m^{-3}$	$n_\alpha(0)$ $10^{18}m^{-3}$	$T_e(0)$ keV	Ar-frost	τ_p^* (s)	τ_E (s)
33333	ELMy H-mode scan of x-point	10.5	2.0	5.0	2.1	5.0	yes	5-10	0.25
33476	L-mode	5.0	2.0	3.5	1.8	3.5	no	>11	0.24
33994	L-mode	13.0	2.0	3.5	4.2	4.0	yes	3.2 ± 0.3	0.25
33995	ELMy H-mode	4.0	2.0	4.0	3.4	3.0	yes	>12	0.45
34324	ELMy H-mode	4.0	2.0	4.0	1.5	3.0	no	>22	0.64

Table I *Overview of plasma data in representative helium edge puff experiments with active argon frost pumping (divertor target tiles are graphite).*

Typical τ_p^* values for helium are of the order 8 to 15s (H-mode) in the case of active argon-frost pumping, compared to 20 to 30s in the case of no argon-frost (Fig.1). Corresponding values for L-mode confinement are approximately half the values of the H-mode case. The observed alpha particle replacement times exceed energy confinement times τ_E, which are of the order 0.3 to 0.5s, by more than a factor of 20 (H-mode, argon-frost) and 5 to 10 (L-mode, argon-frost). Time dependent variations of the particle replacement time following the initial pump phase indicate saturation effects in argon frost pumping. Sweeping of the x-point and the location of the strike zone with respect to the pump duct leads to significant changes in deduced particle decay rates (Fig.2). The L-mode evolution of N_{He}^{tot} (no active helium

pumping) (Fig.1a) is decribed by a fast decrease (<30ms) following the initial peak induced by the gas puff and settling then to a steady level which is determined by the recycling level.

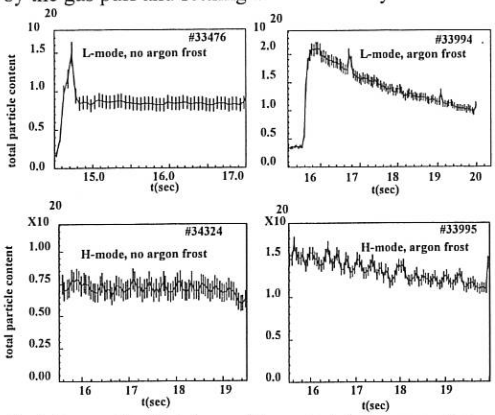


Fig.1 Decay of total alpha particle content in the case of no Ar-frost for a) H-mode, b) L-mode and active Ar frost pumping, c) H-mode d) L-mode.

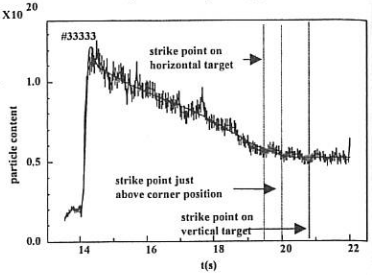


Fig.2 a) Particle content and variation of its decay rate in the case of sweeping of x-point and strike zone position. The decay rate reaches a maximum at a position close to the corner points of the divertor. Next to no pumping is observed when the strike zone is on the vertical target plates.

pulse	comment	P_{NBI} MW	I_p MA	$n_e(0)$ $10^{19}m^{-3}$	$n_{Ne}(0)$ $10^{17}m^{-3}$	$T_e(0$ keV	τ_p^* (sec)	τE (sec)
32778	ELMy-H-mode	18.0	3.0	5.0	1.1	5.0	5.5	0.38
33958	L-mode	10.0	2.0	3.0	2.0	4.5	1.8 ± 0.1	0.20
34372	L-mode	14.0	2.0	2.5	1.6	5.0	$1.3\pm.07$	0.26

Table II Overview of plasma data in neon edge fuelling and exhaust studies in L- and H-modes

III Neon exhaust in radiative divertor plasmas - Distinctively lower particle replacement times are observed in the case of neon gas-puff experiments (see table II), which were carried out as part of divertor radiative cooling studies. Similar to helium the H-mode particle confinement time τ_p^* is about 2 to 3 times the L-mode case. Fig.3 shows the rapid decay of the Ne^{10+} content following a puff of 200ms. Neon particle replacement times are about 5 to 10 times the energy confinement time.

IV.Experimental transport data (He gas-puff experiments) - Substantial progress has been achieved in the last experimental campaign at JET by a simultaneous measurement of carbon and helium CX spectra. By imposing the ion temperature deduced from CX CVI the uncertainties in the analysis of the HeII spectrum - in particular in erroneous profiles gradients induced by 'plume' effects etc. - can be much reduced. Diffusion coefficients and convective velocities are derived from particle flows Γ_z and gradients ∇n_z (i.e. $\frac{\Gamma_z}{n_z} = -D\frac{\nabla n_z}{n_z} + v_z$) measured during the period of density perturbation following the brief edge gas puff.

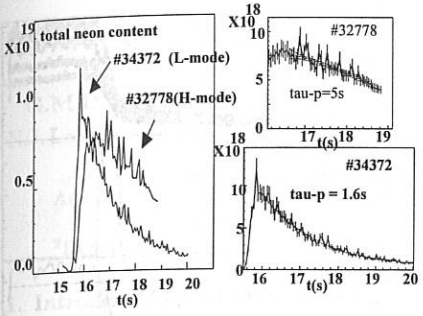


Fig.3 Total confined neon content and its decay in L-mode and H-mode

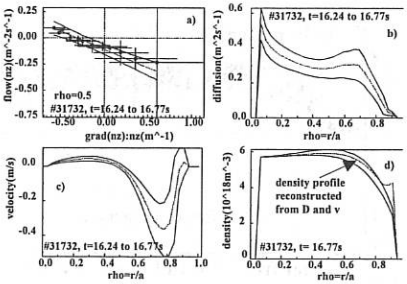


Fig.4a) Deduction of transport data from $\Gamma(n_Z)/n_Z$ *and* $\nabla(n_Z)/n_Z$, *b) D(ρ), c) v(ρ), d) steady state reconstruction of density profiles from v(r), D(r) and comparison with experimental upper and lower error bars.*

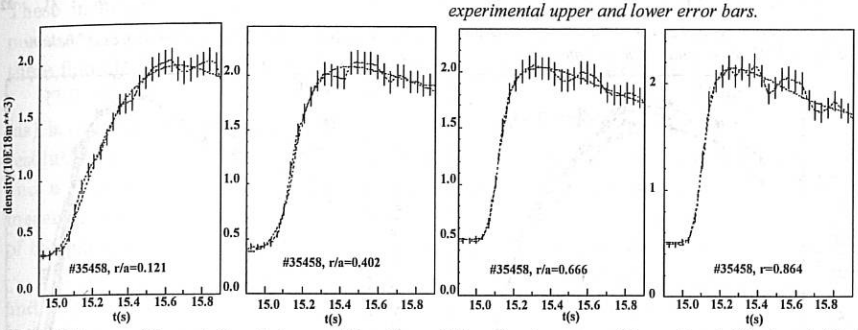


Fig.5 Helium profile evolution during an H-mode, radiative divertor, gas-puff experiment (Be target tiles) Experimental data and spline fit shown for 4 minor radii. Vertical bars indicate statistical errors.

B) Neon transport studies - Neon density profiles (similar to the intrinsic impurity carbon) remain even during substantial edge fuelling hollow (both in L- and H-mode) and convection velocities are directed outwards for the major part of the profiles.

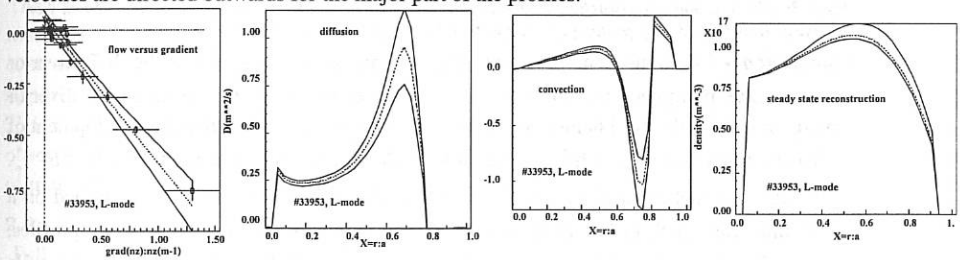


Fig.6 Deduction of neon transport data in L-mode confinement phase.

V. Beam fuelling experiments - A few experiments were performed with H- and L-mode helium core fuelling making use of the two neutral beam boxes at JET one acting as a source of high energy neutral helium and the second as diagnostic beam.

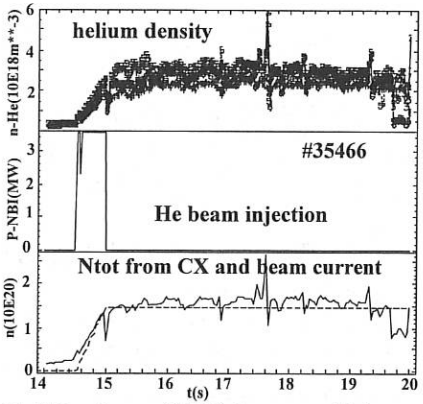


Fig.7 H-mode case, #35466, time traces of helium density, NBI power and particle content.

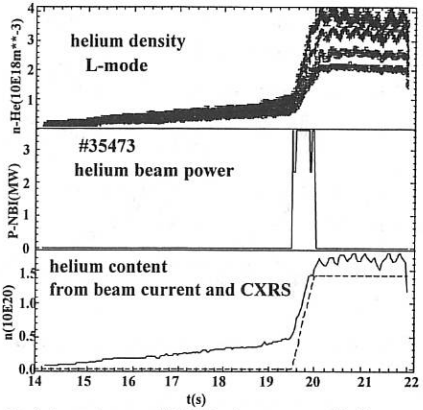


Fig.8 L-mode case, #35473, time traces of helium density, NBI power and particle content.

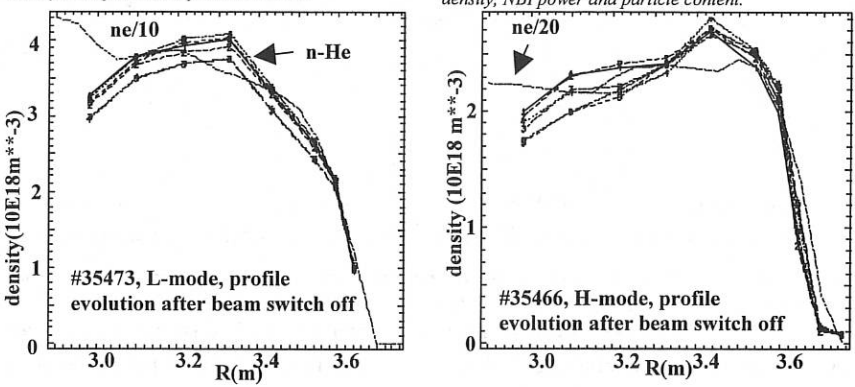


Fig.9 Profile evolution after switching-off the He fuelling beam a) L-mode #35473, b) H-mode #35466. For comparison electron density profile (divided by 10 and 20 respectively). Profiles at 20.1s and every 35ms.

Conclusion - Edge and central fuelling experiments were performed in the JET divertor phase. Active pumping was achieved by deposition of an argon frost layer on the divertor cryo-pumps. The observed helium replacement times $\tau_p^* >> \tau_E$ indicate that the development of efficient helium pumps will have to play a key role on the route to acceptable values of τ_p^*. Edge and core fuelling have demonstrated that steady state helium profiles are reached on a short time scale (both in H- and L-mode), and that in contrast to intrinsic impurity profiles, such as Be, Ne, or C, which are found to be consistently hollow, helium assumes profile shapes very similar to that of electron density profiles. No evidence at all is found of either helium accumulation on the magnetic axis or close to the separatrix. Core transport appears therefore not to be a limiting factor for projected next-step devices.

Strongly inhomogeneous electron heat diffusivity in RTP

G.M.D. Hogeweij, C.C. Chu, D.F. da Cruz, F. De Luca[1], G. Gorini[1], A. Jacchia[2], N.J. Lopes Cardozo, P. Mantica[2], A.A.M.Oomens, M. Peters, F.J. Pijper and R.W. Polman

FOM Instituut voor Plasmafysica 'Rijnhuizen',
Associatie EURATOM-FOM, P.O.Box 1207, 3430 BE Nieuwegein, The Netherlands
[1]Dipartimento di Fisica, Università degli Studi di Milano, Milano, Italy
[2]Istituto di Fisica del Plasma, Associazione EURATOM-ENEA-CNR, Milano, Italy

1. Introduction

The standard assumption that the radial electron thermal diffusivity χ_e is a smooth function of the radius, is challenged by recent experimental results in the RTP tokamak. These includes high resolution Thomson scattering data, pellet ablation experiments, perturbative transport studies, and steady state off-axis heating. This paper reports on these findings and relates them to observations made in other tokamaks.

RTP ($R_0 = 0.72$ m, $a = 0.164$ m, $B_T \leq 2.4$ T, $I_p \leq 150$ kA, pulse duration ≤ 600 ms) is equipped with a comprehensive set of diagnostics with high spatial and temporal resolution, including a 20-channel heterodyne ECE radiometer, a 19-chord interferometer and a 5-camera, 80-channel SXR tomography system. A Thomson scattering system measures electron temperature T_e and density n_e along a vertical chord through the centre of the plasma at 100 radial positions simultaneously, with a spatial resolution of 1.7 mm.

The plasma conditions can be manipulated with Electron Cyclotron Heating (ECH) and pellet injection. The ECH system consists of two 60 GHz, 200 kW, 100 ms gyrotrons, (LFS O-mode and HFS X-mode, respectively), plus a 110 GHz, 500 kW, 200 ms gyrotron (LFS X-mode).

2. Experimental evidence

2.1. Thomson scattering data

The most direct evidence for the existence of a transport barrier comes from T_e profiles measured with Thomson scattering. A salient feature common to many T_e profiles of centrally EC heated RTP plasmas, is a narrow steep gradient region, i.e. a step in T_e, apparently associated with the sawtooth inversion radius r_{inv} (Fig. 1) [1]. The step in T_e is most pronounced at high q_a. Temperature gradients of up to 1 MeV/m have been observed, corresponding to a drop of the electron thermal diffusivity χ_e with up to 2 orders of magnitude in this narrow region, i.e. down to the neoclassical level of $\simeq 0.01$ m^2/s.

2.2. Pellet ablation

Pellet ablation was studied by injecting a single pellet (velocity $\simeq 700$ m/s, $\simeq 5 \cdot 10^{18}$ atoms) into ohmic target plasmas ($q_a = 4.1 - 5.3$, $n_e(0) = 3.5 - 5.5 \cdot 10^{19}$ m^{-3}) and taking Thomson scattering profiles at various times during the ablation of the pellet [2].

Until the pellet reaches r_{inv}, the changes in both T_e and n_e are restricted to the area outside the pellet position, and here the decrease in T_e is nearly balanced by the increase in n_e, i.e. hardly affects the plasma pressure p_e; see Fig. 2a,b. When r_{inv} has been passed, a rapid collapse of the core pressure takes place, brought about by a collapse of

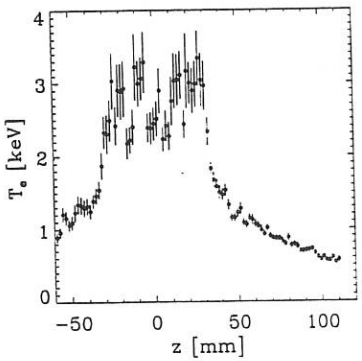


Figure 1: *Example of a T_e profile of an ECH heated RTP plasma with $q_a = 6.7$ and $n_e(0) \simeq 2.5 \cdot 10^{19} m^{-3}$. The sawtooth inversion radius for this discharge is near 2.5 cm, close to the location of the steep gradient.*

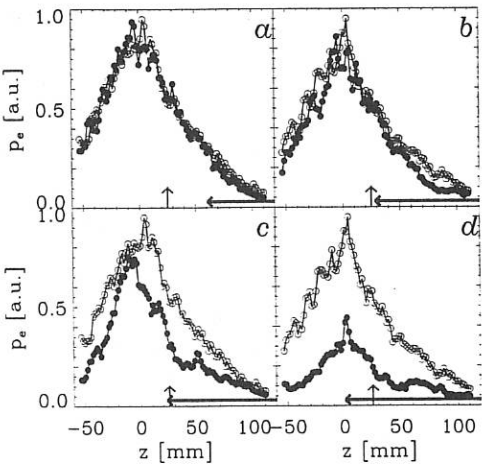


Figure 2: *p_e profiles of four RTP discharges during pellet ablation, all taken on the same day under the same plasma conditions (closed symbols). For comparison a pre-pellet profile in a similar discharge is plotted for each case (open symbols). The region passed by the pellet is indicated by a horizontal arrow; a vertical arrow indicates r_{inv}.*
Note the collapse of p_e ahead of the pellet in the two latter cases.

T_e without a compensating increase in n_e; see Fig. 2c,d. The ECE time traces show a behaviour consistent with the Thomson scattering profiles.

The rapid loss of energy within a few tens of μs once the pellet has crossed r_{inv}, corresponds to a temporary increase of χ_e to $\simeq$ 100 m^2/s over a large part of the plasma cross-section. Apparently the pellet crossing r_{inv} causes a temporary strong ergodization of the magnetic field. This is corroborated by the behaviour of runaway electrons during pellet ablation in TEXTOR [3]. These observations as such are no proof of the presence of a transport barrier, but show that r_{inv} plays a special role in thermal transport.

2.3. Perturbative transport studies

The shape of χ_e^{inc} near r_{inv} was probed in RTP in a series of off-axis modulated ECH (MECH) experiments, with $q_a = 3.2 - 5.0$. The ECH resonance was always r_{res} = -4 cm [4], which was outside r_{inv} except for the lowest q_a where $r_{res} \simeq r_{inv}$. For a resonance position outside r_{inv} the amplitude/phase data show a deep central hole/bump (Fig. 3a), which is flattened out when the resonance is inside r_{inv} (Fig. 3b).

The abrupt change of behaviour when the r_{inv} position is met by the resonance radius is an indication of the existence of a transport barrier located near r_{inv}. The different

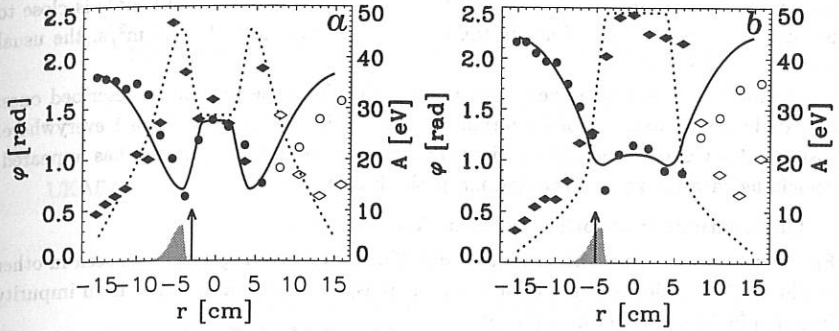


Figure 3: *Phases and amplitudes (circles and diamonds, respectively) of heat pulses induced by MECH as a function of radius. The first harmonic of the modulation frequency is shown for two RTP discharges with $q_a = 3.74$ (left) and 3.25 (right), both with $n_e(0) \simeq 3.0 \cdot 10^{19} m^{-3}$ and $r_{res} = 4$ cm at the HFS. An arrow indicates the position of r_{inv}; the power deposition is given by a shaded area.*
Also shown are the best fits of the phase (full lines) and amplitude (dotted lines) profiles, obtained with a transport barrier near r_{inv}. Only the HFS data and data in the central region (closed symbols) were fitted, since the LFS data (open symbols) suffer from suprathermal radiation.

behaviour of the discharge of Fig. 3b would then be due to power deposition inside rather than outside the barrier. The simulations shown in Fig. 3 correspond to the latter hypothesis, and have been obtained with a χ_e^{inc} profile characterized by a transport barrier at r_{inv} (with $\chi_e^{inc} \simeq 0.1$ m^2/s over a width of $\simeq 1$ cm) and a nearly constant value of χ_e^{inc} = 4-5 m^2/s elsewhere.

2.4. Off-axis ECH

In a series of off-axis heating experiments with the 110 GHz gyrotron, 350 kW was injected at $r_{res}/a \simeq 0.3$ into ohmic target plasmas ($q_a = 5.0$, $Z_{eff} \simeq 2 - 2.5$). Thomson scattering profiles of T_e and n_e were taken 30 ms after switch-on of ECH, i.e. when a steady state has been reached. At high densities hollow T_e profiles were obtained. For the discharge shown in Fig. 4 a local electron power balance analysis was performed. Assuming $\chi_i = \chi_{i,neoclass}$, one finds that $\chi_e^{pb} \simeq 0.02$ m^2/s $\ll \chi_e^{neo}$ inside r_{dep}. Even under

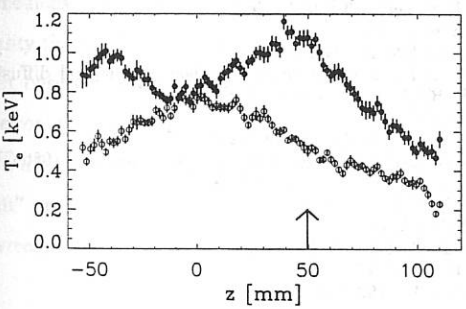


Figure 4: *T_e profile of RTP discharge r199\40701.034 during off-axis ECH, 30 ms ($\simeq 10\tau_E$) after switch-on (closed symbols), compared to the ohmic profile of a similar discharge (open symbols).*
The ECH resonance position is marked by an arrow.

the unrealistic assumption $T_i = 0$ everywhere, the calculated $\chi_e^{pb} \simeq 0.1$ m^2/s is close to neo-classical for $r < r_{dep}$. Outside the power deposition zone $\chi_e^{pb} \simeq 1$ m^2/s, the usual anomalous value for RTP.

It should be noted that these experiments differ from the previously described ones: off-axis heating creates a hollow current density profile, and q rises above 1 everywhere. Instead of a narrow transport barrier a broad region with low transport has appeared, coinciding with the zone of inverted magnetic shear s.

3. Observations from other experiments

Fine structures in T_e profiles measured with Thomson scattering have been seen in other machines [5]. Evidence of the existence of a transport barrier also comes from impurity injection [6, 7] and pellet ablation [8].

Examples of transient regimes of improved confinement due to negative magnetic shear s are the PEP-mode in JET [9], the regime achieved in DIII-D by rapid elongation ramping [10], and the Lower Hybrid Enhanced Performance regime in Tore Supra [11].

4. Discussion

The Thomson scattering data provide persuasive evidence for the existence of a strong transport barrier near r_{inv}. Off-axis MECH experiments showed that power modulation inside or outside r_{inv} yielded T_e perturbations with dramatically different phase and amplitude profiles, thus confirming the presence of a barrier near r_{inv}. The pellet ablation experiment highlights the special role of r_{inv} in radial thermal transport: as soon as the r_{inv} surface is hit by the pellet, transport increases dramatically, not only at this radius, but also in the outer region.

The creation and maintenance of a steady state hollow T_e profile is a unique observation, achieved in RTP because of the very good localization of the 110 GHz 2nd harmonic X-mode ECH, and the large ratio P_{ECH}/P_Ω. With off-axis ECH no peaking of T_e brought about by an inward heat pinch is observed, as in DIII-D [12].

Acknowledgements

This work was performed under the Euratom-FOM and the Euratom-ENEA-CNR association agreements, with financial support from NWO, CNR and Euratom.

References

[1] Lopes Cardozo, N.J., et al, Phys. Rev. Lett. **73** (1994) 256.
[2] Oomens, A.A.M., et al, *this conference.*
[3] Jaspers, R., et al, Phys. Rev. Lett. **72** (1994) 4093.
[4] Mantica, P., et al, 'Radial profile and q-dependence of the electron thermal diffusivity measured with ECH modulation in RTP', submitted to Nucl. Fusion.
[5] Nave, M.F., et al, Nucl. Fusion **32** (1992) 825.
[6] Giannella, R., et al, Plasma Phys. and Contr. Fusion **34** (1992) 687.
[7] Berlizov, A.V., et al, in Plasma Physics and Controlled Nuclear Fusion Research 1980 (Proc. 8th Int. Conf. Brussels, 1992), Vol. 1, IAEA, Vienna (1981) 23.
[8] TFR Group, Nucl. Fusion **27** (1987) 1975.
[9] Hugon, M., et al, Nucl. Fusion **32** (1992) 33.
[10] Lazarus, E.A., et al, Phys. Fluids (B) **3** (1991) 2220.
[11] Hoang, G.T., et al, Nucl. Fusion **34** (1994) 75.
[12] Petty, C.C., Luce, T.C., Nucl. Fusion **34** (1994) 121.

MHD activity and operational limits on START

M Gryaznevich, DJH Goodall, T.C.Hender, J Hugill, I Jenkins,

R Martin*, M.Price, C Ribeiro+, A Sykes, M J Walsh

UKAEA Government Division, Fusion, Culham, Abingdon, Oxon, OX14 4DB, UK

UKAEA/EURATOM Fusion Association

*UMIST, PO Box 88, Manchester, UK,

+CNPq/Universidade de São Paulo, Brazil

1. Introduction. MHD features of the low-aspect ratio tokamak plasma have been studied on the START tokamak [1] both in "natural" divertor and double-null (DND) configurations [2]. Although the operational limits diagram in $1/q_{cyl}$ vs $n_e R/B_\phi$ space, Fig.1, is similar to that for a conventional tokamak, no hard disruptions have been observed either at high density or low-q limits. The internal reconnection event (IRE), which limits the operational space on START is described and discussed.

2. Density limit study. The density limit has been studied using additional gas puffing during the discharge. The density rise was limited by internal reconnection events (IRE) [4], but these did not lead to a major disruption. Sometimes a spontaneous density rise ($\Delta\int n_e dl \sim 50\%$) has been observed in the "natural" divertor configuration. In this case the density rise features a "soft" saturation or is limited by sawteeth, but not by IREs, and is accompanied by a strong peaking of the SXR-profile, an

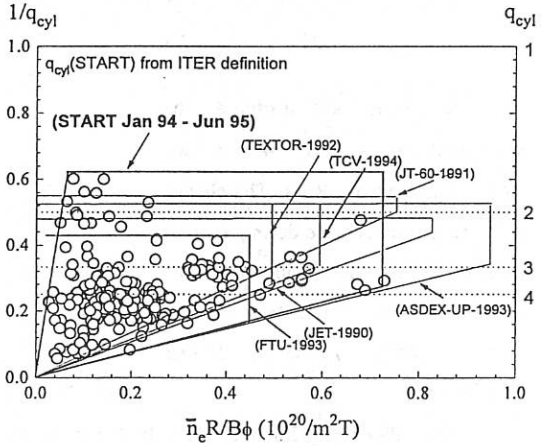


Fig.1. Operational limits (Hugill) diagram for START.

increase in MHD-activity level with a transition to a lower poloidal mode number, an increase in bolometer signal and the appearance of a "radiating core".

A spontaneous density rise has also been observed in the DND-configuration, accompanied by a decrease in the high-frequency $\tilde{B}_\theta$ fluctuations in the region of 0.6 - 1.4 MHz. At densities higher than $3\times10^{19}m^{-3}$ edge localised activity has been observed mainly seen near the X-point region, Fig.1. Irregular and regular (with frequency f ~ 3 - 12 kHz) spikes on the D_α signal are observed which are not correlated with sawteeth, central SXR or Mirnov oscillations (no magnetic precursor has been detected so far).

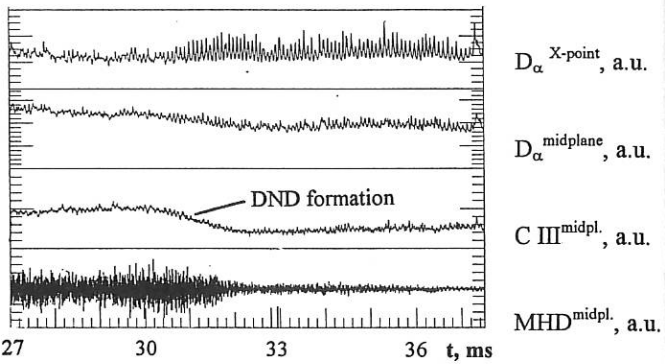


Fig.2. The edge localised activity on START in DND configuration.

3. Low-q limit study. At the low-q limit, values of $q_\psi \sim 4$ have been achieved, limited by IRE's. The change of the plasma inductance during the IRE leads to a loss of equilibrium in the absence of a horizontal position feedback system, preventing further reduction in q.

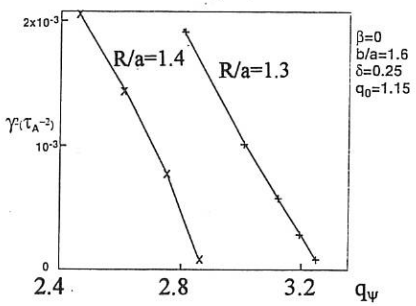


Fig.3. Increase in q_ψ critical for low A, ERATO

The sufficient condition for ideal MHD stability of a cylindrical plasma, $q_\psi - q_0 > 1$, [3] at low aspect ratio becomes more severe. According to Degtyarev [4], the critical q_ψ value for destabilization of small-scale ballooning and ideal modes for A = 1.3 is $q_\psi^{crit} \leq 3.5 - 5$ depending on the peakedness of the current density profile. ERATO code simulations for ideal

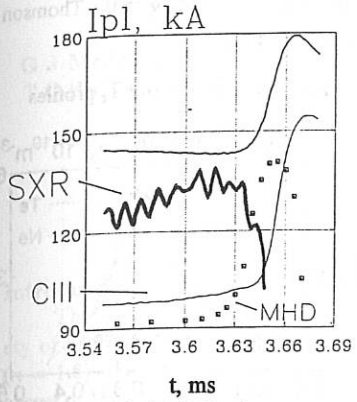


Fig.4. IRE in START: plasma current, central SXR, CIII, amplitude of MHD fluctuations with f >0.2 MHz.

n=1 kink modes for START show similar values of q_ψ^{crit}, Fig.3. The value of q_ψ less then 4 obtained on START is close to this ideal limit.

4. Internal Reconnections in START. The extension of the stable operation region in START both in the low-q and high density directions is limited by IREs. Improvement in the vacuum conditions and boronization help to expand the operational space. During the IRE a large positive current spike occurs, Fig.4, accompanied by an increase in radiation (CIII is shown as an example) and a decrease in the central SXR signal. Internal reconnections can happen any time during the discharge and can have different precursors and consequences. As discussed in [5], low-frequency (f < 200kHz) precursors to IREs are not always observed. However, the amplitude of high frequency magnetic fluctuations increases 10 - 20 μs before an IRE.

In regimes with sawteeth and "snakes" it has been determined that the inversion radius of the IRE is close to the q = 1 radius. The possible stabilization of sawteeth and other low-*m* modes in the low-aspect ratio configuration is predicted by theory [1], but START appears to be more stable than predicted, for example, by the criterion for collisionless reconnection of the *m=1* mode, [6]. However, the stability diagram plotting shear at the q = 1 surface along the vertical axis, and density and temperature gradients along the horizontal axis, Fig.5, shows some agreement with the trends predicted in [6]. Here all parameters are calculated with the ASTRA code [7], using the experimental T_e and n_e profiles and assuming neoclassical conductivity.

The density profiles in START often feature the broad shoulders with a peaked central part, Fig.6. This peaking may be connected with the neoclassical particle pinch or with the accumulation of impurities. If, as suggested by theory, the existence of a high density gradient near the q = 1 resonance surface can stabilize the internal reconnection, then both flattening of the density profile (caused by sawteeth or a reduction in the pinch) near the q = 1 surface

or peaking of the profile inside q = 1 surface could cause the IRE. According to the Thomson scattering data, the first case seems to be more plausible on START.

Fig.5. IRE stability diagram on START

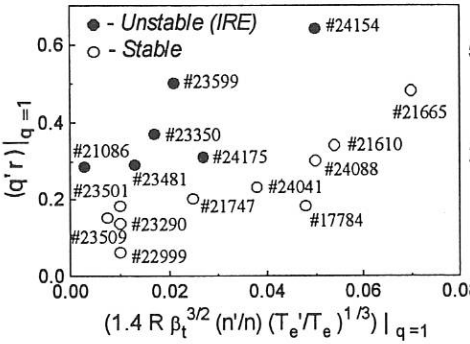
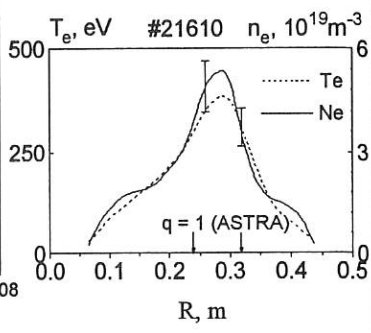


Fig.6. Typical n_e and T_e profiles



5.Conclusions. The operational regime space on START without auxiliary heating is similar to that for a conventional tokamak, but is limited by internal reconnections (IRE) and not by hard disruptions. Decrease in the density gradient near the q = 1 resonance surface may be a possible cause of the internal reconnection.

A spontaneous density rise and edge localised activity seen in the D_α signal have been observed in the Double-Null Divertor configuration. An increase in visible light radiation at the magnetic axis, accompanied with spontaneous density rise and an increase in the low-*m* MHD activity has been observed in several regimes.

Acknowledgement. This work is funded jointly by the UK Department of Trade and Industry, and EURATOM.

References.

1. A.Sykes, et al., *Nuclear Fusion*, **32(6)**, 694 (1992)
2. A.Sykes, at al., this conference.
3. L.Zakharov, *Sov. J. Plasma Phys.*, 7, 714, (1981)
4. L.Degtyarev, et al., *Sov. J. Pl. Phys.*, **12(7)**, 441, (1986)
5. M.Gryaznevich, et al., *Proc. 20th EPS, Lisboa, 1993,* **vol.17C Part 1,** 231 (1993)
6. F.M.Levinton, L.Zakharov, et al., *Phys. Rev.Let.*,**72,** 2895, (1994)
7. C.Roach, et al., this conference.

INSTABILITY CONTROL ON COMPASS-D

G J McArdle, P G Carolan, A L Colton, N J Conway*, A M Edwards, D A Gates, T C Hender, B Lloyd, A W Morris, R O'Connell* and the COMPASS-D and ECRH teams.

UKAEA Government Division Fusion, Culham, Oxon OX14 3DB UK (UKAEA/EURATOM Fusion Association)

* *University College, Dublin, Republic of Ireland*

Introduction

The COMPASS-D tokamak ($R = 0.56$m, $a \leq 0.22$m) is equipped with a variety of tools for study and control of low-m instabilities in single null divertor plasmas ($\kappa = 1.6$) similar to those proposed for ITER and used on JET. High power ECRH (in excess of 1MW at 60GHz) is used to approach the β-limit and for control of both rotating $m = 2, n = 1$ instabilities and error-field-driven magnetic islands. Current-carrying saddle coils outside the vacuum vessel allow error-field studies in H-modes and at high-β_N, including effects on ELMs. Key diagnostics for the error-field studies include fast Doppler spectrometers [1] for measurements of the impurity-ion flow.

Error-field penetration in H-modes and at high β_N

The model for penetration of helical field perturbations into rotating tokamaks developed by Fitzpatrick and Hender leads to a scaling with density in agreement with the general observation that error-field-driven islands occur most readily at low $\bar{n}_e$. It has been found on COMPASS-D, however, that error-fields can penetrate very easily into ELM-free H-modes [2] at very high densities ($\bar{n}_e$ up to $1.2 \times 10^{20}\mathrm{m}^{-3}$). This has both beneficial and troublesome consequences: generation of islands with small external fields can help to spread the power striking the divertor target plates [3], and ELMs are triggered by $m = 2$ modes, driven or natural, leading to a possible control method; on the other hand the ELMs tend to be large and lead to disruptions [4]. It is notable that the ELMs triggered by a stationary error-field island have rotating precursors, and the prompt effect of the ELM can extend further into the plasma than the error-field island itself [2].

Fig. 1 shows the evolution of impurity toroidal velocity [1] as a helical field is applied during an ELM-free H-mode. The field is provided by four saddle coils below the X-point, of about 90° poloidal extent, similar to the lower saddle coils in JET. 1kA in all 4 coils provides $B_n^{m=2,n=1} = 2.30$G on a surface with $R = 0.557$m, $r = 0.127$m, $\kappa = 1.4$. Examination of a sequence of shots, with $q_{95} = 3.3 - 3.9$, shows that longer delays between application of the error-field and penetration are associated with the plasma velocity taking longer to drop sufficiently. The velocity shift before penetration seems to be about 75% of the final value after penetration for these cases. The theoretical scaling of penetration threshold is $B_r^{m=2,n=1}/B_\phi \propto (\Delta f_{m=2})^{4/3} n_e^{2/3}$, where $\Delta f_{m=2}$ is the frequency change to bring the $m = 2$ frame to rest. Therefore, with the assumption that the $m = 2$ frame is shifted by a constant frequency with respect to the measured BIV velocity, $\Delta f_{m=2}$ is reduced by a factor 4 and hence the critical density is increased by a factor 16 for the same error field. The observed $\bar{n}_e$ at penetration is indeed increased by about an order of magnitude (scaling experiments remain to be done). The large change in poloidal velocity, as measured from CIII emission [1], seems to play no major role; this may be understood

in terms of its being localised well outside $q = 2$ in the H-mode transport barrier.

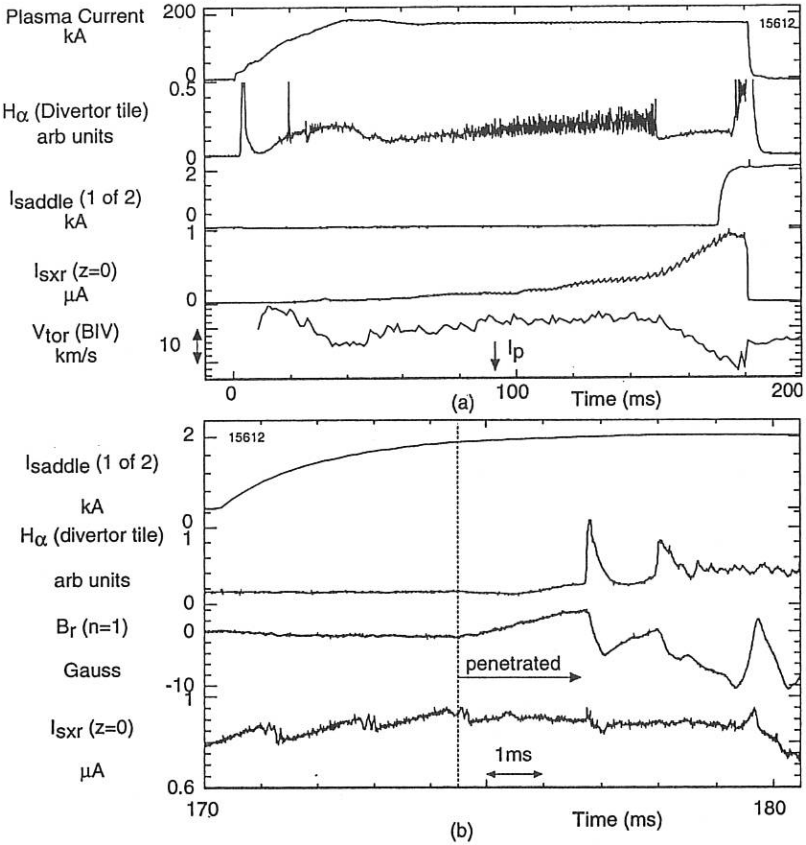


Fig. 1: *Penetration of error-fields at high density in an Ohmic ELM-free H-mode. Note how the toroidal velocity drifts in the direction to make penetration easier (a). The penetration, removal of sawteeth and subsequent ELM and disruption are seen in the enlargement (b).* $q_{95} = 3.6, B_T = 1.21\,T, I_p = 170kA, \bar{n}_e(t = 170ms) \simeq 1.0 \times 10^{20} m^{-3}$.

Fig. 2 shows a pair of L-mode shots with and without ECRH, showing that the error-field threshold is not substantially affected by the change in β_N (β_N reaches ~ 1.0 with ECRH) and the normal spin-up of the mode is seen after the error-field is removed (cf. DIII-D, [5]). ECRH does however change the plasma rotation in a stabilising sense - it increases $v_{tor}(BIV)$ in the electon drift direction, and in many cases the locked mode starts to rotate while the error field is still present, the rotation slowing if the ECRH power is reduced. Initial data at higher β_N indicates a modest increase in error-field sensitivity.

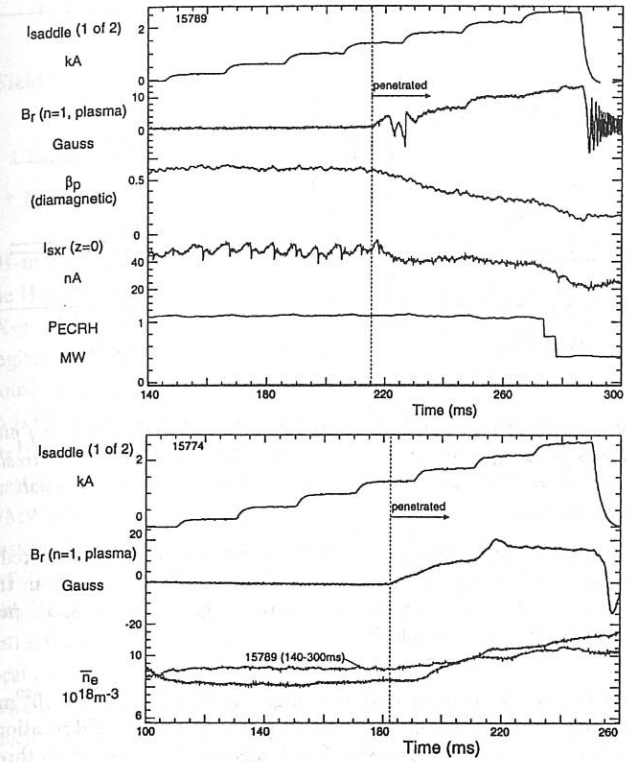


Fig. 2: *Penetration of error-fields into a high power ECRH discharge, compared to a similar OH shot. $I_p = 160kA$, $B_T = 1.16T$, $q_{95} = 4.5 - 4.7$. The critical I_{saddle} is seen to be the same ($\beta_N \sim 1$ for the ECRH case) and the sawteeth are removed at penetration. Both density traces are overlaid in the lower figure.*

Modelling of ECRH for removal of error-field-driven islands

It has been shown [2] that ECRH localised close to the $q = 2$ surface can be used to remove error-field-driven modes in COMPASS-D. As with rotating modes, it is expected that depositing the power at the O-point should be much more effective than X-point or average heating. However, experiments showed that there was little sensitivity to the phase of the locked island with respect to the ECRH/ECCD antenna position (the error-field was slowly rotated toroidally), and thus another mechanism for the stabilisation is needed. It has been shown [6] that changes in Δ' occur quickly enough to influence the stability as rapidly as observed, but the robustness of the technique and the fact that the error-field mode is removed and stays absent suggests that more is involved. A non-linear reduced-MHD code with plasma rotation included has now been used. An error-field is applied to a stable, rotating plasma at a level to cause slowing, penetration and a steady island. Axisymmetric heating is then added, and if the power is located sufficiently close

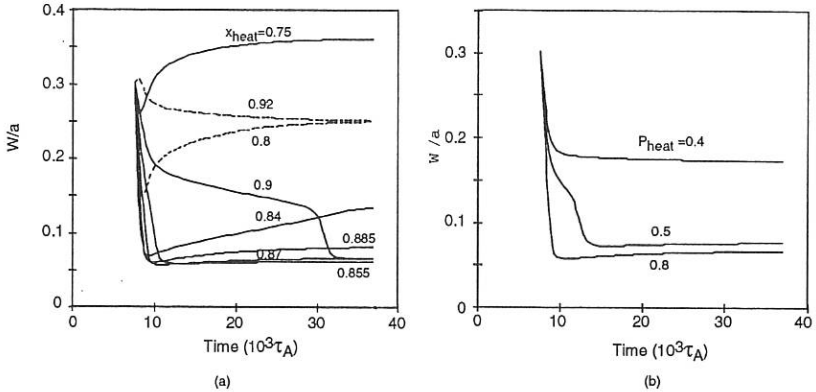


Fig. 3: *Modelling removal of error-field island with localised ECRH in rotating plasmas. (a) the island unlocks for $x_{heat} = 0.84 - 0.90$ ($x_{q=2} = 0.82, x = r/a$), (b) a threshold in power, P_{heat}, is seen. $S = 10^5$, and the 5% island remaining is due to the relatively low value of S in the simulation.*

to q=2 ($r_{heat} - r_{q=2} \lesssim 0.1a$, $P(r) = P_{heat} e^{-200(x-x_{heat})^2}$) it is found that the initial reduction in the island size due to Δ' changes is sufficient to allow the viscous drag from the rest of the plasma to spin up the island which then decays (Fig. 3). A threshold power is required (Fig. 3(b)) for the island to unlock.

Summary

Error fields are shown to penetrate at very high densities ($\bar{n}_e \sim 1 \times 10^{20} \mathrm{m}^{-3}$) in ELM-free H-mode, and this is attributed to the slowing of the electron fluid rotation. The H-mode transport barrier seems to have no significant effect on the penetration threshold. No strong dependence of the error-field threshold on β_N is seen in ECRH-heated, L-mode plasmas at $\beta_N \leq 1$, the limit of the data set. Earlier results showing removal of error-field-driven islands by ECRH localised to $q = 2$ are consistent with resistive MHD calculations when the effect of the bulk plasma flow is included.

This work is jointly funded by the UK Department of Trade and Industry and EURATOM.

[1] P G Carolan et al. Toroidal and poloidal rotation in the COMPASS-D tokamak. *This conference.*

[2] A W Morris et al. Control of Error-field modes and ELMs in ITER-shaped plasmas on COMPASS-D. *Proc 15th IAEA conf. Seville* **A-2-IV-1** (1994).

[3] R J Buttery et al. Effects of resonant magnetic perturbations on divertor target loads in COMPASS-D. *This conference.*

[4] A W Morris et al. Disruptions, vertical instabilities and halo currents in COMPASS-D. *ibid.*

[5] R J La Haye, et al. Non-linear instability to low $m, n = 1$ error fields in DIII-D as a function of plasma fluid rotation and beta. *Nuclear Fusion* **32** (1992) 2119.

[6] P G Carolan et al. Correction of error field locked modes in COMPASS-D. *in Proc 21st EPS Conf., Montpellier,* **1** 214, (1994).

H-mode thresholds and MHD stability in COMPASS-D

S.J.Fielding, J.Ashall, A.Colton, D.A.Gates, J.Hugill, A.W.Morris, F.Ryter*, M.Valovic
and the COMPASS-D and Microwave Heating Teams

UKAEA Government Division, Fusion, Abingdon,OXON OX14 3DB, UK
(UKAEA/EURATOM Association)
* Max-Planck-Institut fur Plasmaphysik, EURATOM-Association D-85740, Garching

1. H-mode thresholds

The H-mode threshold has been studied on COMPASS-D (R=0.557m, a=0.17m, single-null X-point divertor configuration, κ~1.6) with emphasis on H-mode access at low density, the regime proposed for ITER to minimise additional heating power. It has been reported previously [1] that H-mode occurrence on COMPASS-D at line-average densities above $\overline{n}_e$~$2.5\times10^{19}m^{-3}$ is not inconsistent with the ASDEX-Upgrade power scaling $P_{thresh}/S(MW/m^2) = 4.4\times10^{-3}B_T\,\overline{n}_eB_T$ ($10^{20}m^{-3}T$) [2], although sharp L-H transitions are not normally seen in Ohmically heated discharges. Below $\overline{n}_e$~$2.5\times10^{19}m^{-3}$ the H-mode was not observed, with up to 0.7MW of ECRH. In this paper we report observation of improved confinement transitions at considerably lower line-average densities, ~$7\times10^{18}m^{-3}$, using two different ECR (60 GHz, $\leq$1.4MW) heating configurations.

With $2\omega_{ce}$ X-mode ECRH (B_T=1.1T, nominal resonance R=0.54m, I_p=155kA, q_{95}~4, $P_{ECRH}\leq$1MW) efficient absorption is obtained at line-average densities substantially lower than the local cut-off value, $2.2\times10^{19}m^{-3}$. Fig 1 shows data from one such discharge ($\overline{n}_e$~$8\times10^{18}m^{-3}$) where the ECRH power is increased in steps to identify the threshold. Substantial electron heating is produced: the loop voltage falls from ~1V to $\leq$0.1V and volume-averaged electron temperatures exceeding 6keV can be inferred from the measured diamagnetic energy. When the RF input power exceeds ~0.6MW a sharp, ~factor 2, reduction is seen on the D_α signal accompanied by a marked increase in $d\overline{n}_e/dt$ (from ~0 to ~$5\times10^{20}m^{-3}/s$). If it is assumed that the density increase corresponds to a transition to infinite particle confinement time, then the required particle influx to give the measured density rise rate, scaled to the D_α level, gives a particle confinement time of 5ms prior

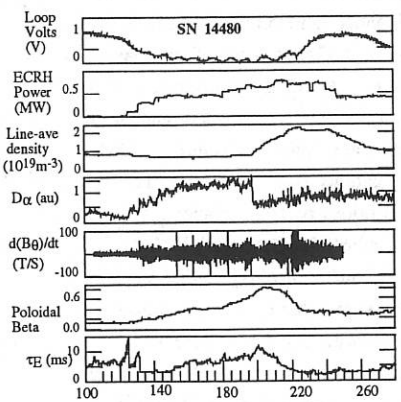


Fig 1: Parameters for $2\omega_{ce}$ ECR heated deuterium discharge, Ip=150kA, B_T=1.1T. The H-mode transition is at ~197ms. The value of τ_E after ~210ms is unreliable due to RF cut-off.

to the confinement enhancement. This, when compared with the measured energy confinement time of 8ms prior to the transition, is not an unreasonable value and suggests that particle retention is indeed very high after the transition. The total radiation rises from 35kW to 165kW (~1/4 of the total input power), whereas the density increases by a factor 2.5, indicating no increase in relative impurity density. Diamagnetic measurements show only a modest rise in energy confinement time at the transition, from 8 to 10 ms. The transient nature of this increase is a direct result of the particle confinement enhancement - as the density rises the coupling of the RF into the plasma is reduced, the electron temperature falls (loop voltage rises) and τ_E (calculated with reference to the incident ECRH power) decreases to ~3ms. The peak measured τ_E of 10ms corresponds to an H-factor of ~2 (cf ITER89P), with H~1.6 prior to the transition. No clear ELMs are seen in these discharges but the reduction in D_α, increase in $\overline{n}_e$ and decrease in magnetic edge activity suggest that this is an H-mode which is self-terminating, but not abruptly so, due to the degradation in RF heating efficiency as the density rises. Low density $2\omega_{ce}$ ECR heated discharges can be sustained for longer periods, and attain H-factors close to 2, provided that the H-mode transition is avoided [3].

ECRH has also been applied in low density discharges using a combination of low-field-side O-mode and high-field-side X-mode launch with fundamental absorption at higher toroidal field (B_T=1.9T, I_p=200kA, q_{95}~5). The cut-off density (O-mode) is a factor 2 higher than for the $2\omega_{ce}$ experiments ($4.4\times10^{19}m^{-3}$ at the resonance field value of 2.14T, which occurs 0.07m inboard of the plasma centre; off-radial propagation and refraction effects broaden and shift the absorption zone). Code calculations [4] show that the RF absorption is less efficient at ω_{ce}, particularly for O-mode. Fig 2 shows data from a discharge with stepped RF power, which exhibits a transition event, with a sudden decrease in D_α and increase in n_e. The density increase saturates at $\overline{n}_e$~$2.5\times10^{19}m^{-3}$ as a regular near-sinusoidal H-L-H oscillation, or dithering transition, develops (see D_α trace) indicating threshold behaviour. The L-H transition occurs at about the maximum available heating power and higher power behaviour cannot presently be explored. β_p values (~0.55) are less than those reached with $2\omega_{ce}$ heating (~0.75), despite nearly twice the input power, and the lower loop voltage drop also

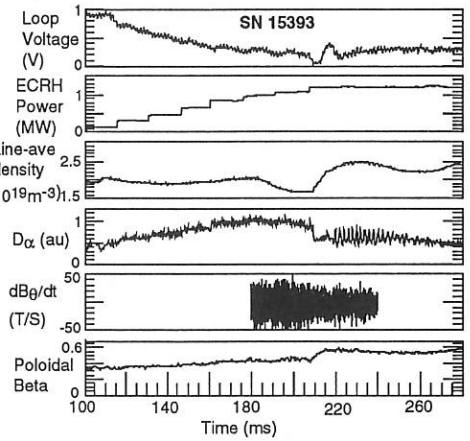


Fig 2: Parameters for $2\omega_{ce}$ ECR heated deuterium discharge, I_p=200kA, B_T=1.9T. The H-mode transition is at ~192ms. Dithering H-mode occurs at ~220ms.

indicates less efficient heating. Estimated energy confinement times (~3ms) and H-factors (~1), computed using the incident rather than absorbed power, are low in these discharges. Again, no ELMs are observed in these low density H-modes.

Fig 3 shows these ECRH discharges on a P/S vs $\overline{n}_e B_T$ diagram, together with data from Ohmic discharges. It is clear that at low densities on COMPASS-D the H-mode power threshold increases as the density is reduced, in contrast to the usual $P_{thresh} \propto n_e$ or $n_e^{0.75}$ scalings. At $\overline{n}_e = 7 \times 10^{18} m^{-3}$, the lowest density at which an H-mode transition has been obtained, the measured P_{thresh} of 0.65MW is a factor ~40x that predicted by the ASDEX-Upgrade scaling. Reversal of the ion ∇B drift direction has given only L-mode plasmas, although not all scenarios have been investigated for this field direction. DIII-D have also observed a power threshold minimum at intermediate densities, Alcator C-Mod and JFT-2M report low-density limits [5]. A possible cause for these observations is discussed in the next section.

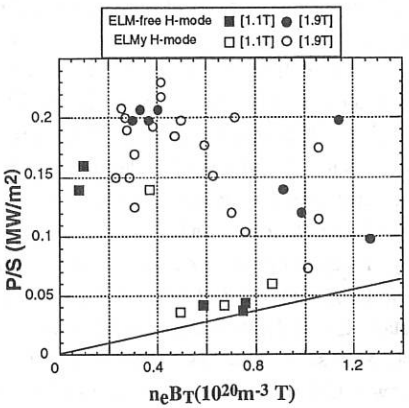


Fig 3: H-mode threshold diagram for Ohmic and ECRH discharges. The line shown corresponds to the ASDEX-Upgrade scaling:
$P_{thresh}/S(MW/m^2) = 4.4 \times 10^{-3} n_e B_T (10^{20} m^{-3}\ T)$.

2. MHD stability of ELMs

At higher densities the transition to and from ELM-free H-mode in COMPASS-D is better correlated with β_N [$\equiv \beta(\%) a B_T / I_p(MA)$] than with power alone [6], suggesting that pressure stabilisation of the instabilities responsible for Type III ELMs plays a role. Current ramp-down, where the edge current density is reduced, stimulates a transition to ELM-free H-mode see fig 4. Also shown is the opposite effect, where a programmed rise in surface voltage is applied in order to increase the edge

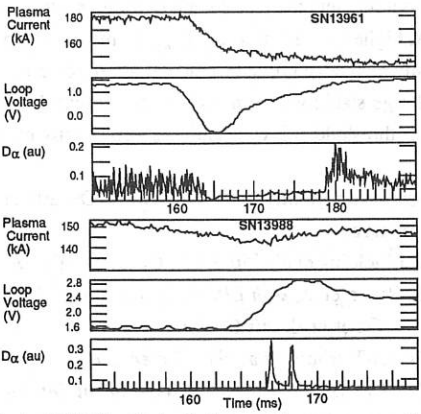


Fig 4: SN 13961: Ohmic discharge with current ramp-down to reduce edge current. This results in production of ELM -free H-mode. SN13988: Discharge with programmed surface voltage rise to increase edge current. This results in the production of type-III ELMs in an ELM-free ohmic discharge.

current. In this case Type III ELMs are produced in an ELM-free part of the discharge. Both of these observations suggest that edge current is destabilising. In these particular examples the effect is transient, limited by current diffusion times (~15ms for Δr~0.08m at 100eV) and is only reliably produced in discharges close to ELM-free and ELMing behaviour respectively. Edge-localised ECRH reduces the frequency of type III ELMs [7], consistent with improvement in H-mode stability due to increased edge pressure or pressure gradient.

The current-driven peeling mode [8] which is an ideal-mhd mode localised near the surface of the plasma, driven by finite edge current and stabilised by increased pressure gradient, has many of the right properties to explain these phenomena. The criterion that β_N exceed some critical value (~1) for ELM-free H-mode may also explain the low density observations. At constant I_p and B_T, the criterion implies that the plasma energy must exceed some threshold value. At these low densities on COMPASS-D $\tau_E \propto n_e$ [8] and hence $P_{thresh} \propto 1/n_e$. In addition the low collisionality associated with high T_e means that the bootstrap curent becomes more significant, increasing the edge current density and so increasing further the power threshold, according to peeling mode theory. This is consistent with the observation in high temperature $2\omega_{ce}$ heated discharges at the ELM-free H-mode transition of experimental β_N values greater than those at higher densities [6].

3. Summary

A significant increase in H-mode power threshold is observed on COMPASS-D in low density ECR heated discharges. H-factors as high as 2 are observed High particle confinement after the L-H transition and the absence of ELMs leads to a fast rise in density, degrading the RF coupling into the plasma and limiting the duration of the H-mode.

At higher densities, where P_{thresh} increases with n_e, experiments which change edge current density and edge pressure gradient are observed to influence ELM behaviour, consistent with discharge stability determined by the current-driven peeling mode. The observed increase in power threshold at low densities is also consistent with this theory.

This work was jointly funded by the UK Department of Trade and Industry and Euratom.

References

[1] S.J.Fielding et al, *15th IAEA Conf*, Seville, IAEA-CN-60/A2/4-P-4 (1994)
[2] F. Ryter et al, *20th EPS Conf*, Lisbon **1** (1993) 23
[3] D.A.Gates et al, *this Conference*
[4] G.A.Whitehurst et al, *this Conference*
[5] *ITER Physics Performance Assessment, Interim Design Report*, June (1995)
[6] M. Valovic et al, *this Conference*
[7] A.W.Morris et al *15th IAEA Conf, Seville*, IAEA-CN-60/A-2-IV-1 (1994)
[8] J.W.Connor, R.J.Hastie and H.Wilson *private communication,* 1995
[9] S.J.Fielding et al, *21st EPS Conference*, Montpelier **1** (1994) 322

Estimate of magnetic reconnection in sawtoothing RTP plasmas by means of soft x-ray tomography

C.P. Tanzi, H.J. de Blank*, and the RTP team

FOM-Instituut voor Plasmafysica 'Rijnhuizen', Association Euratom-FOM, P.O.Box 1207, 3430 BE Nieuwegein, The Netherlands

* Max-Planck Institut für Plasmaphysik, EURATOM Association, Garching, Germany

Introduction, motivation

Sawtooth instabilities are in general clearly visible on soft x-ray (sxr) diagnostics, and their $m = 1$ poloidal mode structure is often well reconstructed by means of multiple camera tomography. On RTP, five cameras covering the whole plasma cross section allow to reconstruct the 2-D emissivity profile [1] and to study the spatial structure of the $m = 1$ instability during sawtooth oscillations.

Various theoretical models proposed for the sawtooth collapse have attributed different importance to the processes of *(i)* ideal MHD convection, *(ii)* resistive MHD reconnection, and *(iii)* enhanced cross-field transport. The presence of either processes *(i)* or *(ii)* is well established, because of the clearly observed $m = 1$ displacement of the hot core. It has long been hoped that process *(ii)* could be distinguished by sxr tomography because changes in magnetic topology cause changes in the topology of emissivity contours in tomograms. However, even with the increasing numbers of poloidal views of present day sxr systems, the determination of changes in magnetic topology has remained ambiguous.

The purpose of the present paper is to show that quantitative estimates of the amount of reconnection and/or radial transport during the $m = 1$ precursor phase can be given, hence discriminating between the ideal $m = 1$ displacement *(i)* and the non-ideal processes *(ii)* and *(iii)*. The method, first presented in Refs. [2,3], is to compute from the sxr tomograms several ideal MHD invariants that systematically decrease when non-ideal relaxation processes (reconnection, transport) are present. These decrements are then compared with the values obtained from a model (phantom) of the emissivity during $m = 1$ reconnection.

In contrast with Refs. [2,3], now definite quantitative results can be given. We now provide proof that the changes in measured ideal MHD invariants cannot be caused by the finite spatial resolution of the sxr diagnostic in combination with the tomographic method. For this we have used phantoms that represent purely convective (ideal MHD) $m = 1$ displacements, and have verified that for $m = 1$ amplitudes that match the observed ones, the MHD invariants derived from the tomograms do not change significantly. The case of one sawtooth precursor during intense ECR heating of RTP plasmas is presented, with an $m = 1$ precursor which is consistent with an ideal $m = 1$ displacement. By contrast, precursors during ohmic heating, a few sawtooth periods later in the same discharge, are shown to involve reconnection.

Description of experiment

Two sawteeth during the same discharge are presented, as they allow comparison of ECR heating and ohmic heating. The target plasma has a central density $n_e \approx 1 \times 10^{20}\,\mathrm{m}^{-3}$,

$q(a) = 3.1$ and T_e varying between $T_e = 1\,\mathrm{keV}$ during the 340 kW off-axis heating phase with the 110 GHz ECRH system [4] and an estimated $\approx 800\,\mathrm{eV}$ in the Ohmic phase. The $q = 1$ radius is estimated from the Thomson scattering T_e profile following neoclassical conductivity at $r/a \approx 0.3$ (5 cm)[5]. ECRH power is deposited off-axis at about $r/a \approx 0.5$, determining a low shear and $q(0) \approx 1$. We first concentrate on a sawtooth with large precursor during the heating phase, which we compare to another sawtooth 4 ms after ECRH was switched off. The latter emissivity profile is broader and the emissivity in the centre increases by 30%. The sxr tomograms of the precursors of both sawteeth show a displacement of the hot core and a flat region in the emissivity. During the rotation of thsee $m = 1$ structures, the flat region continuously changes shape, with the result that visual inspection of the tomograms cannot distinguish an $m = 1$ island from an ideal MHD perturbation. We therefore in the next section use the method of Refs. [2,3].

Analysis method

Two alternative models ('phantoms') are used to simulate the measurements of the $m = 1$ redistribution of soft x-ray emissivity prior to the sawtooth crash.

One model for the emissivity profile is based on the magnetic reconnection model of Kadomtsev [6] and is described in Ref. [3]. To ensure that the emissivity in the growing island is exactly constant, the emissivity profile is chosen as in Ref. [3]: $e(r) \sim (r_{\mathrm{width}}^2 - r^2)^2$. The height and width of $e(r)$ to fit the experimental profile are obtained by matching the two values $\int e\, d^2x$ and $\int e\, r^2\, d^2x$. The sawtooth mixing radius r_{mix} in the model is chosen consistent with the measurement. In the model, $r_{\mathrm{mix}} = \sqrt{2}\, r_{q=1}$.

The other, newly developed, model involves ideal MHD motion only. We assume incompressible flow in the poloidal (x, y) plane given by the stream function $y\xi$, with $\xi(r) \sim (1 - r^2)^2(1 + 2r^2)$, and where r is normalized to r_{mix}. Line integrals over the emissivity profile $e(x, y)$ ('pseudo-measurements'), deformed by this flow pattern, are computed by tracing back a sufficient number of points on these lines according to the repeated steps $\Delta x = -\Delta t \times (\xi + y^2\xi'/r)$, $\Delta y = \Delta t \times xy\xi'/r$. For comparison with the measurements, the local emissivity is calculated by tomographic inversion. The same emissivity profile as for the reconnective phantom is used.

As mentioned before, it is inadequate to directly compare the tomograms $e(x, y)$ of the phantoms with tomograms of the measured data. Instead, we employ suitably chosen ideal MHD invariants. They are integrals over parts of the tomographic domain, bounded by given values of $e(x, y)$. The present definition differs from the one in Refs. [2,3] by employing $\sqrt{e}$ instead of e. This choice is based on the dependence of e on density and temperature as $e \propto n^2 T^\alpha$, so that $\sqrt{e}$ is approximately conserved. Exact conservation is assumed in the reconnection model for the emissivity. In the absence of sources and sinks, the conservation is exact if $\alpha = 0$ (mass conservation) and if $\alpha = 2$ (energy conservation). The invariants are of the form

$$H(e_-, e_+) \equiv \int\limits_{e>e_-} d^2x\, (\sqrt{e} - \sqrt{e}_-)^2 - \int\limits_{e>e_+} d^2x\, (\sqrt{e} - \sqrt{e}_+)^2.$$

This quantity decreases whenever reconnection, or particle and energy transport, takes place in the domain defined by $e_- < e < e_+$. In the case of island growth, the decrease

is quadratically proportional to the reconnected area. On the longer time scale of the sawtooth rise, H increases due to heating. In our analyses, the full range in e is subdivided into 14 intervals $[e_-, e_+]$, equally spaced in $\sqrt{e}$.

Results

Fig. 1a shows the invariants H calculated from the tomograms of one sawtooth during the ECRH phase, together with e_{max} and its displacement $\langle x \rangle$ as in Refs. [2,3]. We concentrate on the behaviour close to the crash time, comparing its slope with the slopes in Fig. 1b and Fig. 1c, which show H computed from the reconstruction of pseudo-measurements for the Kadomtsev and the ideal MHD model, respectively. Fig. 1c shows that H is indeed an MHD invariant, even after the spatial resolution of the system is taken into account. The comparison of the slope of H in Fig. 1a before the crash with Fig 1c shows that the sawtooth of Fig. 1a is consistent with an ideal displacement $\geq$ 5cm ($r/a = 0.3$) (for which a similar slope is seen). It can be seen that the reconnection model (Fig. 1b) with an island width of less than 3 cm (corresponding to 30% reconnection) exhibits such small decrease of H that it is also consistent with the measured values (Fig. 1a). However, the displacement $\langle x \rangle$ of the hot core (also shown in Fig. 1b) is too small to be consistent with the measurements. We conclude that in this case the process is driven by ideal MHD.

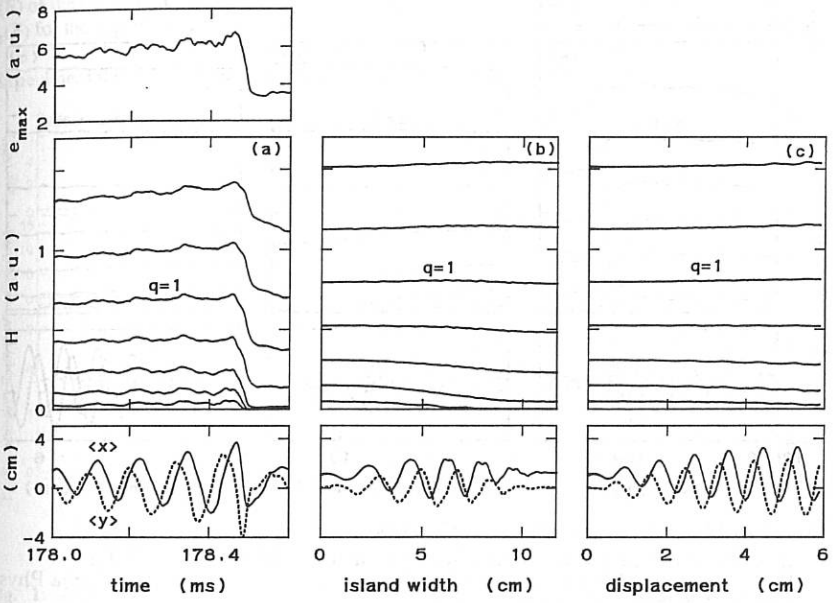


Fig. 1 *The MHD invariant H as given in this paper, shown for 7 of 14 equispaced intervals in $\sqrt{e}$. The line corresponding to the $q = 1$ surface is marked; surfaces inside the $q = 1$ are lines below it. e_{max} and its average $\langle x \rangle$ displacement are also given. (a) From tomograms of a sawtooth during ECR heating. From tomograms calculated from the pseudo-measurements of a model following Kadomtsev (b), and following ideal MHD displacement (c).*

For comparison, we show a sawtooth during the ohmic phase, for which it will be shown that reconnection does take place. Measurements are shown in Fig. 2a and the decrease of H is visible from $t = 199.1$ ms. Fig. 2b shows that, before the sawtooth crash, at 199.2 ms, this is consistent with an island width of about 5 cm, corresponding to about 50% reconnection. Fig. 2c shows the ideal MHD evolution of a phantom with $r_{\mathrm{mix}} = \sqrt{2}\, r_{q=1}$, in which there is no comparable decrease of H. It can be argued that, due to loss of resolution, H is not always constant for ideal MHD displacements, as Fig. 1c in particular shows. However, to obtain a decrease of H comparable to the one in Fig. 2a, a r_{mix} too large to be consistent with the measurements would be needed. This is consistent with a decrease of the magnetic Reynolds number of at least 30% from the previous case. Summarizing, the analysis shows that a sawtooth in the ECRH-free phase (though probably not fully relaxed to an ohmic steady state) shows at least 50% reconnection before the crash, so that the $m = 1$ precursor is not ideal MHD. Sawtooth precursors during off-axis ECRH on the other hand are determined by ideal MHD processes.

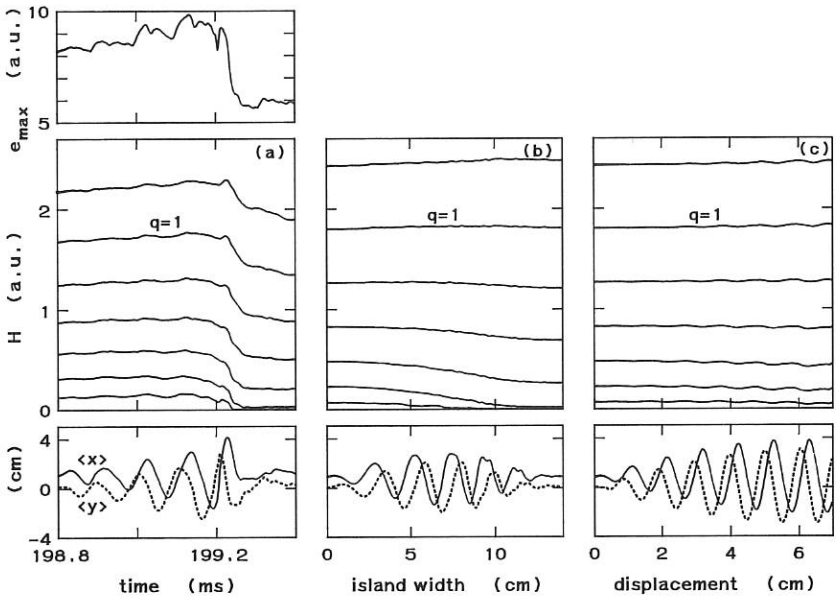


Fig. 2 *As Fig. 1, for a sawtooth during the ohmic phase.*

[1] D.F. da Cruz and A.J.H. Donné, Rev. Sci. Instrum. **65 (7)**, 2295 (1994)
E.S. Lyadina *et.al.*,Proc. of the 20th EPS Conf. on Contr. Fusion and Plasma Phys., Lisbon (1993),Vol. III, p.1151.
[2] C.P. Tanzi and H.J. de Blank, Proc. of the 21st EPS Conf. on Contr. Fusion and Plasma Phys., Montpellier (1994), Vol. I, p. 226.
[3] C.P. Tanzi, H.J. de Blank and A.J.H. Donné, Rev. Sci. Instrum. **66**(1) (1995) 537.
[4] N. Oomens et al., EC9 Workshop, 1995, Borrego Springs, California.
[5] B. de Groot, priv. comm.
[6] B.B. Kadomtsev, Sov. J. Plasma Phys. **1**, 389 (1975)

MODELLING THE NEUTRALISATION AND ENERGY DISTRIBUTION FUNCTION OF MeV IONS DURING COMBINED ICRF AND NBI HEATING IN JET

A.J.G.Stuart, S.C.Dalla, L-G.Eriksson, A.Gondhalekar
JET Joint Undertaking, Abingdon, OX14 3EA, England

Introduction: Impurity Induced Neutralisation (IIN) of hydrogenic ions [1] is applied to analyse the flux of MeV energy atoms during combined hydrogen minority ion cyclotron resonance frequency heating (D(H) ICRF heating) and deuterium neutral beam injection (NBI) heating in JET. When NBI was applied during ICRF heating simultaneously (i) the ICRF driven proton tail temperature T_p was observed to decrease slowly, (ii) a reduction in the proton density n_p in the tail took place, and (iii) a deuteron distribution was created with energy $0.25 \leq E(MeV) \leq 1.1$. These measurements suggest that during NBI the RF power available for fundamental frequency heating of proton minority decreases, that part of the ICRF power goes to second harmonic heating of the high energy deuteron species and that n_H/n_D decreases due to beam-induced dilution and/or transport.
To test this hypothesis we present (i) measurements of hydrogen and deuterium fluxes, using a high energy neutral particle analyser (NPA), showing the behaviour mentioned above, (ii) an outline of the IIN model and its application to the above data in order to deduce the energy distribution function f(E) of the ICRF driven protons and deuterons, (iii) modelling of the Stix energy distribution function $f_s(E)$ for the experimental conditions.

Experimental setup and measurement of evolution of hydrogen flux, $\Gamma_H(E)$:

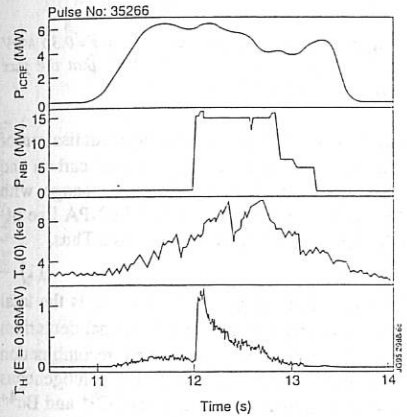


Fig. 1: *Deuterium plasma with B_ϕ =3.2T, I_ϕ =4.7MA, n_e (0)=3-6x10^{19} m^{-3} , and Z_{eff} ≈2. RF power at f=51.4 MHz, in dipole antenna configuration, was applied for D(H) ICRF heating at the plasma centre. NBI deuterium was applied at 80 kV in oct.4 and at 140 kV in oct.8. The last trace shows evolution of 0.36 MeV hydrogen flux received by the NPA from the plasma.*

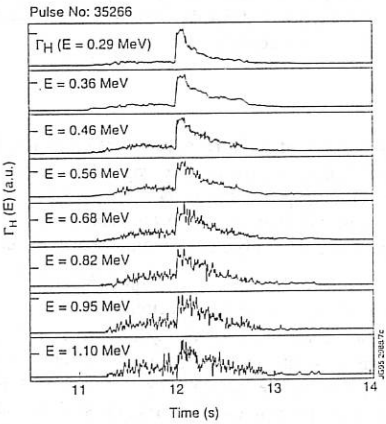


Fig. 2: *Hydrogen flux received in the eight channels of the NPA spanning $0.29 \leq E(MeV) \leq 1.1$. The increase at t=12 s is due to NBI raising the density of electron donors which are either [H] ions or the beam atoms themselves.*

Measurements were made with the NPA located at the top of the torus with its vertical line-of-sight intersecting the ICRF resonance and the oct.4 NB at the plasma centre. The measured hydrogen flux $\Gamma_H(E)$ is due to neutralisation of ICRF driven protons with $v_z/v_\phi \geq 2x10^2$, their banana tips lying on the line-of-sight and within the ICRF power deposition region. Thus $\Gamma_H(E)$ and inferred $f_p(E)$ are representative of the plasma core region.

Fig.1 shows evolution of ICRF power, total NBI power, $T_e(0)$ and $\Gamma_H(E)$ in one NPA channel. As expected, $\Gamma_H(E)$ arises with application of ICRF and is amplified due to NBI raising the density of electron donors at t=12s. However $\Gamma_H(E)$ decays to zero at t=13s whilst ICRF and NBI are still applied. Fig.2 shows that such evolution of $\Gamma_H(E)$ occurs at all energies. This is due to a combination of reduced plasma transparency for the exiting high energy hydrogen atoms, increased attenuation of the NBs, and reduced n_H/n_D due to NBI induced dilution and/or transport. Fig.3 shows deuterium flux, $\Gamma_D(E)$, which arises when NBI is applied. Thermal deuterons are unaffected by the ICRF; only beam deuterons are heated.

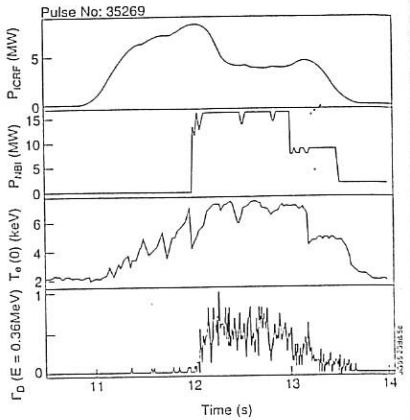


Fig. 3: *Evolution of deuterium flux at E=0.36 MeV in a similar plasma to #35266. Note that the flux arises only when NBI is applied.*

Deduction of $f_p(E)$ from measured flux $\Gamma_H(E)$ using IIN modelling: Agents for neutralisation of MeV energy protons are hydrogen-like [H] ions of the main impurities in JET plasmas, carbon and beryllium[1]. Significant populations of such [H] ions are maintained by charge exchange with deuterium atoms present in the plasma due to recycling, NBI, and NB halo. When the NPA line-of-sight intersects a NB contributions due to direct CX with beam and halo atoms also arise. Thus,

$$f_p(E) = \Gamma_H(E) / \{ P_v(E) \times \varepsilon(E) \} \quad (1)$$

where $\varepsilon(E)$ is plasma transparency for the exiting high energy hydrogen atoms and $P_v(E)$ is the total proton neutralisation rate. $P_v(E)$ is the sum of rates due to: charge exchange with thermal deuterium atoms, beam atoms, halo atoms, different species of [H] impurity ions q; and recombination respectively. Densities n_q for C^{5+} and Be^{3+} are computed in a steady state, infinite, homogeneous plasma with characteristic parameters of the plasma centre using measured densities of C^{6+} and Be^{4+} and using a statistical balance formalism for ionisation equilibrium between impurity nuclei and [H] ions. Only collisions with electrons and neutral deuterium are considered; minority species are assumed to have no effect on the ionisation balance. Hydrogenic impurity ions created in octant 8, 9 metres around the torus, may migrate to octant 4 and, in a similar way, those created in octant 4 by cx from NBI may leave the region viewed by the NPA: we denote the coupling coefficients by $\gamma_{4,8}$. The background thermal deuterium atom density n_d is the only free parameter in this model which is determined over a controlled change of beam neutrals.

In figure 4 we show the deduced experimental proton distribution function integrated along the NPA line-of sight; in fig. 5 we show the deduced deuterium distribution function.

Table I:

Plasma parameters:	t=11.9s	t=12.15s	t=12.5s	t=12.8s
electron density, $n_e(0)$ [10^{19} m^{-3}]	2.8	3.0	3.9	6.3
electron temperature, $T_e(0)$[keV]	5.5	7.8	8.7	7.8
average plasma ion charge, Z_{eff}	1.8	1.7	2.2	2.0
best fitted thermal deuterium density n_d (0) (m^{-3})	10^{12}	10^{12}	10^{12}	10^{12}
neutral density from octant 4 NBI (10^{13} m^{-3})	0	22.7	11.6	1.5
neutral density from octant 8 NBI (10^{13} m^{-3})	0	10.2	5.2	1.4
density of beryllium nuclei (10^{17} m^{-3})	5.4	5.2	12.	14.
coupling coefficient from octant 4 NBI: γ_4	n/a	0.037	0.038	0.045
coupling coefficient from octant 8 NBI: γ_8	n/a	0.026	0.026	0.025
density of hydrogen-like beryllium (10^{13} m^{-3})	3.1	16.	21.	5.7
density of carbon nuclei (10^{17} m^{-3})	5.4	5.2	12.	14.
coupling coefficient from octant 4 NBI: γ_4	n/a	0.030	0.031	0.033
coupling coefficient from octant 8 NBI: γ_8	n/a	0.026	0.026	0.026
density of hydrogen-like carbon (10^{14} m^{-3})	2.0	8.8	12.	3.7
P_γ(E=0.36 MeV) (10^{-3} s^{-1})	7.1	41.	48.	13.
ε(E=0.36 MeV)	0.47	0.43	0.26	0.18
measured Γ_H(E=0.36 MeV) (10^{11} $m^{-2}keV^{-1}st^{-1}s^{-1}$)	1.1	5.5	2.5	0.61
deduced f_n(E=0.36MeV) (10^{13} $m^{-2}keV^{-1}st^{-1}$)	3.3	3.1	2.0	2.6

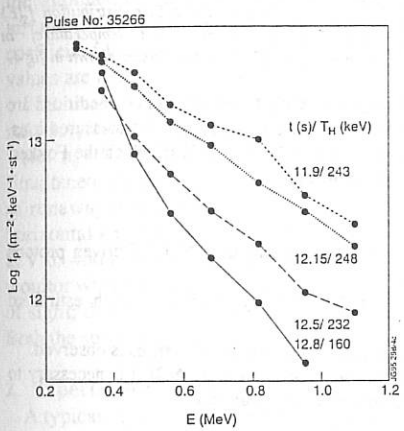


Fig. 4: *Deduced ICRF driven proton energy distribution function $f_p(E)$, integrated along the NPA line-of-sight. $f_p(E)$ at t=12.15s has been matched to that at 11.9s by adjusting the thermal deuterium density in the plasma whilst assuming the proton distribution function is unchanged: n_d = 10^{12} m^{-3} is deduced. The tail temperature of the distribution function reduces slowly and the hydrogen minority density in the tail above 0.3 MeV continuously decreases after NBI is introduced.*

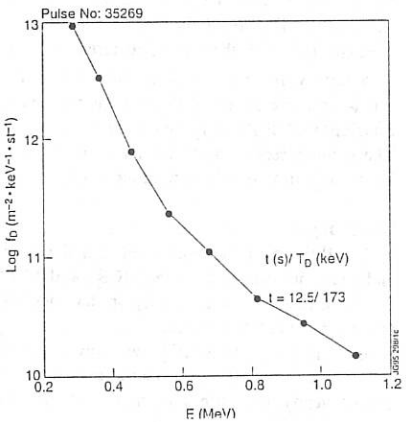


Fig. 5: *Experimental energy distribution function of second harmonic ICRF driven deuterons, $f_d(E)$. This is deduced taking n_d the same as in #35266 and is averaged over the period 12.0≤t(s)≤12.5.*

Modelling of ICRF-driven proton distribution function using Stix's analytic theory:

The energy distribution function was modelled for the experimental conditions using the Stix theory [3] which determines a flux surface, pitch angle averaged distribution $f_s(E)$ in the zero-banana-width approximation. The line-integrated $f_s(E)$ was calculated at several time points close to those of the measurements shown in fig.4. The ICRF power deposition profile $P_H(r)$ required as input for the Stix calculation was computed using the PION-T code [4] in which the effect of NBI was simulated by rapidly increasing the deuteron majority temperature from measured $T_i \approx 4$ keV before NBI to 30 keV during NB heating. This caused reduction of ICRF power available for hydrogen minority heating due to increased absorption at second harmonic of deuteron ion cyclotron frequency.

Using $P_H(r)$ computed with constant $n_H/n_D = 0.1$ during NBI, the modelled $f_s(E)$ gives tail temperatures strongly decreasing with time, shown in fig.6. This is contrary to the measurement of nearly constant T_p until 12.5s and then a slow decline. A better correspondence of modelled $f_s(E)$ with measurements was obtained when n_H/n_D was allowed to linearly decline from 0.1 to 0.03 during $12 \le t(s) \le 13$. This result is only of qualitative value because: (i) while the NPA measures $f_p(E)$ for ions in a narrow pitch-angle range around $\pi/2$, $f_s(E)$ is pitch-angle averaged, (ii) the Stix model is valid in steady-state while the experimental conditions are transient with $P_H(r)$ varying on a time-scale shorter than the slowing-down time of the measured ions. These weaknesses may be overcome by using the time-dependent PION-T code in which the Fokker-Planck equation is solved without using the approximations of Stix.

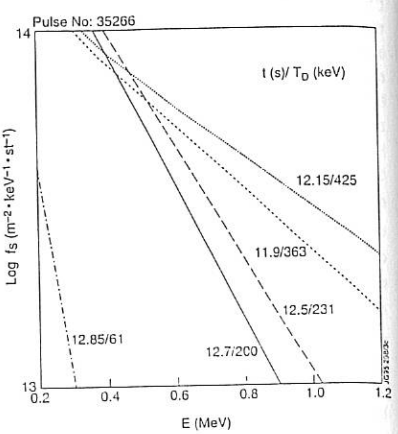


Fig. 6: *Result of simulation using Stix's model. The required input of radial profile of ICRF heating power density available to hydrogen minority, $P_H(r)$, was computed using the PION-T code with $n_H/n_D = 0.1$. The resulting Stix distribution $f_s(E)$ shows rapidly declining tail temperature, in disagreement with the measurement shown in fig 4.*

Summary:

1. The IIN model has been used to deduce the energy distribution function of ICRF driven protons and deuterons during combined ICRF and NBI heating.
2. Thermal deuterium density in the plasma centre of 10^{12} m^{-3} is determined with estimated uncertainty a factor of three.
3. Sharing of applied ICRF power between proton minority and NB injected deuterons is observed.
4. In order to model the measured evolution of proton tail temperature during NBI it is necessary to invoke steady reduction in n_H/n_D due to beam induced dilution and/or transport.

Acknowledgements:

We would like to thank J. de Haas and D. Muir for providing electron density data.

References:

[1] A.Korotkov and A.Gondhalekar, Europhysics Conference Abstracts 18B(1994)pt. I - 266
[2] N. N. Ljepojevic, *et al.*, J.Phys B., 17(1984)3057
[3] T. H. Stix, Nuclear Fusion 15(1975)737.
[4] L.-G. Eriksson, *et al.*, Nuclear Fusion 33(1993)1037

Runaway Electron Diffusion Measurements in the JET Tokamak

B Esposito[1], M Adams[3], E Cecil[4], B Fischer, P Froissard, O N Jarvis, F B Marcus, R Martin Solis[2], G Sadler, P van Belle and N Watkins[3]
JET Joint Undertaking, Abingdon, Oxon, OX14 3EA, UK.
[1]Associazione Euratom-ENEA CRE, 00044-Frascati, Italy.
[2]Universidad Carlos III de Madrid, C/Butarque 15, Leganes, 28911-Madrid, Spain.
[3]AEA Industrial Technology, Harwell Laboratory, Oxon OX11 0RA, UK.
[4]Colorado School of Mines, Golden CO 80401, US.

Abstract

Runaway electrons up to few MeV energy have been detected in the plasma current ramp-up of JET low density ohmic discharges, by measuring the emitted perpendicular hard X-ray bremsstrahlung radiation. A diffusion model, simulating the temporal evolution of the line integrated hard X-ray signals, has been used to obtain the runaway radial transport coefficient in the central region of the plasma ($r/a<0.5$): $D_r \sim 0.2$ m^2/s. The data allow to set a lower limit on the level of radial magnetic field fluctuations in the plasma core.

1. Introduction

The diffusion of runaway electrons in tokamak plasmas provides useful information for understanding the mechanisms involved in anomalous particle transport.

Both electrostatic and magnetic turbulence theories have been considered in order to explain the anomalous transport; runaway electrons are particularly suited to testing magnetic turbulence as they closely follow the magnetic field lines. So far, the runaway diffusion coefficient has been measured in several tokamaks by using different methods and typical values are in the range $D_r = 0.05\text{-}1$ m^2/s (see [1] for a review).

The runaway electron measurements described in this paper have been performed during the start up phase of JET ohmic discharges in the 1994 campaign. Typical discharge parameters were: $n_e \sim 0.5\text{-}1.5 \times 10^{19}$ m^{-3}, $I_p = 1\text{-}1.6$ MA and $B_t \sim 2.75$ T. Three sets of instruments have simultaneously detected the x-ray bremsstrahlung emission (perpendicular to the magnetic field) of runaway electrons: the collimated fast electron bremsstrahlung (FEB) monitor, with 10 horizontal and 9 vertical channels [2], sensitive to x-rays in four energy windows from 133 keV to 400 keV (such cameras replace the neutron detection cameras in the neutron profile monitor when LHCD studies are in progress); the γ-ray spectrometer, with a vertical central line of sight; the hard x-ray monitor scintillators, viewing at the plasma on the equatorial plane. Both the spectrometer and the scintillators are sensitive to photons above 200 keV.

2. Experimental Data

A typical time trace of the line integrated x-ray emission ("photon brightness") from the FEB central vertical detector (channel 15, energy window = 133-200 keV), is shown in Fig.1 for shot 29586, together with the LIDAR electron density, the plasma current, the loop voltage, the hard X-ray and neutron emission. The signal starts at $t \sim 0.2$ s after the beginning of the discharge, it increases up to a maximum at $t_{peak} \sim 1$ s (t_{peak}=time of maximum signal in the central chord) and then it decays to almost zero level at $t \sim 4$ s. The same behaviour is shown by the γ-ray spectrometer, whose spectra also indicate an average electron energy of roughly 2 MeV.

The most interesting feature of the FEB data is the different time evolution of the line integrated signals in different chords (Fig.2). The maximum in the measured x-ray emission is

reached progressively at later times in the edge chords than in the central ones: the effect is present on both cameras and is symmetric with respect to the plasma magnetic axis (vertical camera) and the z=0 cm plane (horizontal camera).

The brightness data are converted to the local x-ray emissivity through a 1-D inversion algorithm. The code (ORION) uses a minimisation procedure which fits a trial FEB emissivity radial profile. It is found that the emissivity radial profiles, initially peaked, tend to flatten with time. The local x-ray emissivity dI/dVdtdhν (in W/m^3keV) can be expressed by the approximate relation:

$$\frac{dI}{dVdtdh\nu} = C n_e n_r Z_{eff} \exp\left(-\frac{h\nu}{T_{ph}}\right) \qquad (1)$$

where hν is the photon energy, n_r the runaway electron density, Z_{eff} the effective ion charge and C a constant. T_{ph} is the "photon temperature", a parameter related to the energy distribution function of the electrons and also depending on the photon energy interval in which is evaluated [3]. T_{ph}, as obtained both from FEB and γ-ray spectrometer data, shows an initial increase, but after t_{peak} it remains constant at ~160 keV (Fig.2).

The values of the toroidal electric field, responsible for the electron acceleration, obtained from the experimental V_{loop} are in accordance with those calculated by means of the transport code JETTO: from initial values at the edge of the plasma of ~0.25 V/m, E_t decreases to 0.04 V/m at t_{peak} (the Dreicer field at this time is: E_D~1V/m); E_t at the centre is a factor of 2 lower. The main production and acceleration of runaways takes place in the interval 0.2-1.0 s, as is also indicated by the rise of T_{ph}.

These results suggest the following picture: a beam of fast electrons may be produced in the plasma central region during the initial low density ($\sim 10^{19}$ m^{-3}) phase of a JET ohmic discharge. The electrons are accelerated by the electric field above the critical energy and enter the runaway regime. As the runaway production stops (a t_{peak} when $V_{loop} < 1.5$ V), the radial X-ray emission profile broadens, indicating an outward diffusion of the electrons which finally hit the vessel walls (note the peaking in the signal of the x-ray monitors at t ~ 5 s in Fig.1).

3. Diffusion Model

A diffusion model in cylindrical geometry has been used to simulate the time evolution of the X-ray bremsstrahlung brightness. The equation governing the process is the following:

$$\frac{\partial n_r(r,t)}{\partial t} = \frac{1}{r}\frac{\partial}{\partial r}\left(r D_r(r)\frac{\partial n_r(r,t)}{\partial r}\right) + S_r \qquad (2)$$

The simulation starts at t_{peak} and the subsequent electron dynamics has been assumed to be only determined by diffusion. Moreover, as the runaway production strongly decreases after t_{peak}, the source term S_r has been set equal to zero. The critical energy is increasing after t_{peak}, therefore a low energy fraction of the fast electron distribution is progressively slowed down and no longer contributes to the x-ray emission. As this collisional slowing down effect is neglected in the model (i.e. the observed decay of the FEB signal is assumed to be due to diffusion only), the determination of the diffusion coefficient using eq. (2) is an upper limit.

The code uses the time traces of Z_{eff} and n_e to calculate, for each FEB line of sight, the photon brightness to be compared with the experimental one. The initial n_r used in eq. (2) has been determined by means of eq. (1). The Z_{eff} (whose radial profile is assumed constant with radius) has been taken from the visual bremsstrahlung diagnostics and the n_e from LIDAR. The analysis has been restricted to r/a < 0.5, where T_{ph} is almost flat and constant in time (the exponential factor in eq. (1) can be set equal to a constant). At the edge, where E_t is higher, we

should have an increased electron acceleration which, in turn, should produce higher x-ray emission and T_{ph}; however, this effect on T_{ph} is not apparent due to the large error bars.

The diffusion equation has been solved using a flat D_r. The best agreement between the predicted and experimental photon brightness is found with $D_r \sim 0.2$ m^2/s (fig.3), for discharge 29586. Depending on the discharge, D_r can vary in the range 0.14-0.21 m^2/s. This diffusion coefficient refers to electrons having energies in the range 0.2-2 MeV and is consistent with results from other tokamaks [1].

4. Discussion

The determined radial transport coefficient D_r can be used to set a lower limit on the level of fluctuating radial magnetic field (b_r) in the plasma core. Using the relation [4] $D_r \leq \pi q R u (b_r/B_t)^2$, in which q is the safety factor, R the major radius and u the electron velocity, it is found that $(b_r/B_t) > 6*10^{-6}$ (discharge 29586). This is only true if the runaway electron diffusion is due to magnetic turbulence. Under such assumption, it also follows that magnetic turbulence cannot be the main cause of thermal electron transport in the plasma centre, as (with χ_e evaluated for discharge 29586 by means of power balance calculations) we get $D_r/\chi_e = 0.07$-1, while the theory predicts a much lower χ_e (according to [5] we should have $D_r/\chi_e \sim u/v_{\|th} \sim 13$).

On the other hand, electrostatic turbulence might reconcile both thermal and runaway experimental diffusion coefficients: the predicted ratio of D_r to χ_e (given in this case by $D_r/\chi_e \sim v_{\|th}/u$) is marginally consistent with the measured value, but at the same time a high value of the electric field fluctuation is needed: ~5 KV/m.

References

[1] A.J. Wootton, FRCR #437, University of Texas (1993)

[2] P. Froissard, PhD Thesis, Universite de Provence Aix-Marseille I (1992)

[3] S.von Goeler et al., *Rev. Sci. Instrum.*, **57** (8), 2130 (1986)

[4] J.R. Myra et al., *Phys. Fluids* B **4**(7), 2092 (1992)

[5] H.E.Mynick and J.D.Strachan, *Phys. Fluids* **24**(4), 695 (1981)

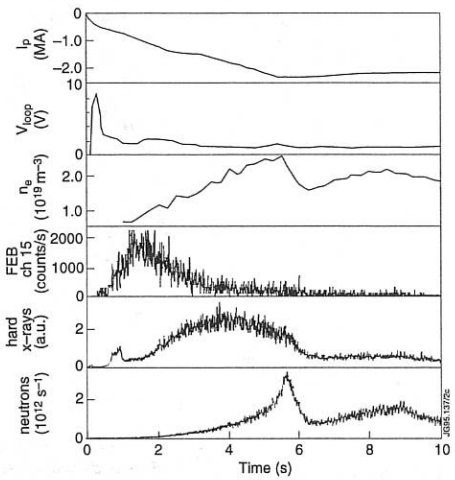


Fig.1: Time traces of I_p, V_{loop}, n_e, FEB channel 15, hard x-rays and neutrons (discharge 29586).

Max Planck Institut für Plasmaphysik

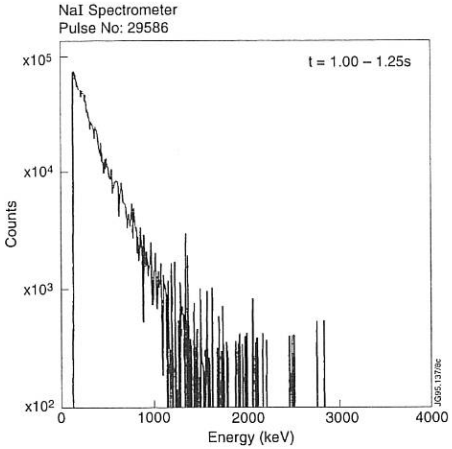


Fig.2: Bremsstrahlung spectrum measured by γ-ray spectrometer at t_{peak}.

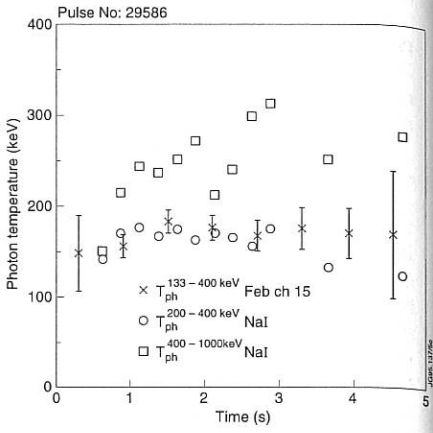


Fig.3: Photon temperature vs time.

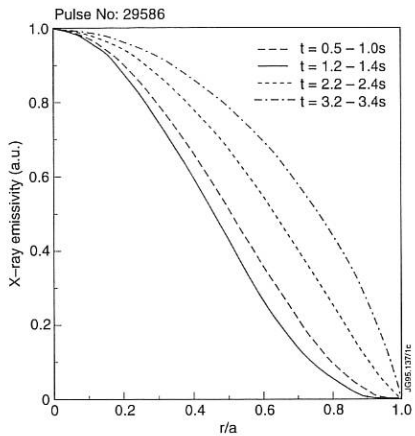


Fig.4: Time sequence of normalized inverted FEB emissivity profiles.

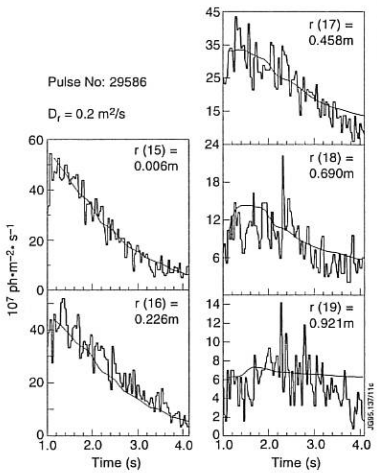


Fig. 5: Comparison between measured and simulated (smooth curves) time traces of photon brightness for FEB channels no. 15, 16, 17, 18, 19 in discharge 29586: D_r=0.2 m^2/s is used.

New Insight into Runaway Electrons Production and Confinement

G. Martin, M. Chatelier and C. Doloc
Association Euratom-CEA, CEN Cadarache, 13108 Saint-Paul-lez-Durance, FRANCE

1. Introduction

Runaway Electron avoidance and control are both important issues for future large Tokamaks like ITER. Runaway Electrons have been observed on toroidal devices since their very beginning, that is for more than 40 years. On small machines they were produced primarily during the "break-down" or "current plateau" phase of plasma pulses and could be avoided after some operation time or by working at sufficiently high density or in clean machines. On present large devices like JET, JT60U, TFTR or Tore Supra, they are produced in large amounts during disruptions, with the noticeable exception of DIII-D where none have been detected [1]. They might prove detrimental for first wall components, especially in actively cooled devices. Reliable models, for both creation, energy limit, confinement and loss are still needed to explain or predict the behaviour of these electrons. Important features that a model should accommodate are discussed on the grounds of several years of observations on Tore-Supra and other devices. A code has been developed to show easily where damages are to be expected.

2. Classical Runaway Electron Creation Rates

The runaway electron creation process during the current plateau of tokamak discharges has been well understood on small tokamaks [3]. The plateau production depends strongly on plasma density and much more weakly on other parameters like e.g. the toroïdal field. Extrapolations to future devices can be made with some confidence, although they are not very useful since this source of electrons is generally weak enough to be ignored.

The large amounts of runaway electrons produced during plasma current disruptions on present days large tokamaks seem to follow quite different rules as observed on Tore Supra. On figure 1, the number of photo-neutrons detected during disruptions for a variety of pre-disruptive conditions is plotted (this number can give a good estimate of the number of electrons accelerated to energies well above 10 MeV). While photo-neutron production does not seem to depend on the pre-disruptive plasma density over a broad range (1-5 $10^{19}m^{-3}$), it increases significantly with the value of the toroidal magnetic field. Below 2T, photo-neutrons are only rarely detected (coherently with DIIID results which always works below 2T?). At 3.8T, the value for present experiments, systematic photo-neutron production is observed.

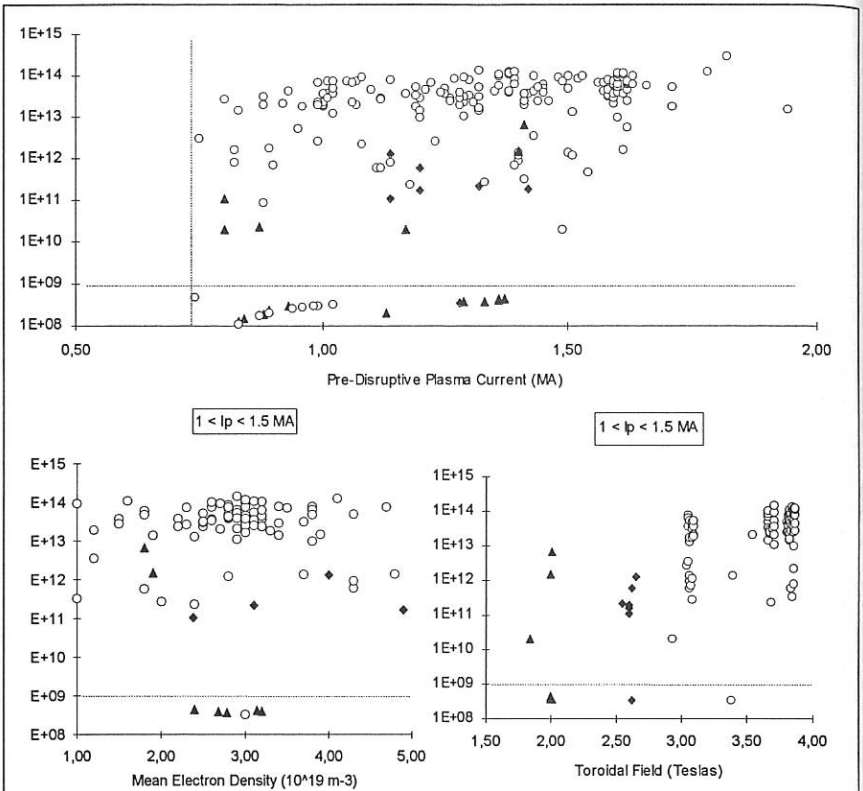


Fig. 1: Photo-neutron production due to disruption induced runaway electrons on TORE-SUPRA

(The 10^9 line shows the detection limit: points below this limit are for neutron free disruptions)

3. Model for runaway electron creation

In classical models, plasma parameters evolve slowly compared to collision time scales, typical for electrons to cross the Dreicer limit. In disruptions this is no longer true: the thermal quench duration τ_{qE} is much shorter than the mean collision time τ_{coll} for fast electrons. One of the most striking feature of disruptions is the fact that this duration is more or less the same on all tokamaks, irrespective of their size. On figure 2, τ_{coll} (α v^3/n_e) has been plotted for supra-thermal electrons in a typical plasma at $4.10^{19}m^{-3}$. It can be seen that 6-10 keV electrons loose only a small fraction of their energy by collision during the typical 0.5 ms duration of the thermal quench.

During the thermal quench, the stored energy is lost through two channels: radiation, enhanced by impurity influx and lower temperature, and transport due to a partial ergodisation of the magnetic structure. This suggests a natural model in which the fate of the electrons depends on their initial energy:

↳ The colder bulk experiences a high collision rate and strong interaction with impurities. Electrons lose their energy mainly through radiation on a time scale dominated by atomic physics: the observed "collapse duration", which does not change from one tokamak to the other, being due to local phenomena.

↳ The hotter tail is more sensitive to field ergodisation. These electrons are less collisional and travel more rapidly along the field lines. They are lost in a diffusive process, which means that their number decreases exponentially with time. At the end of the quench, when the magnetic track restores, some of these fast electrons are still there. Due to the low temperature of the bulk, the Dreicer limit is then very low, and all these residual electrons "run away".

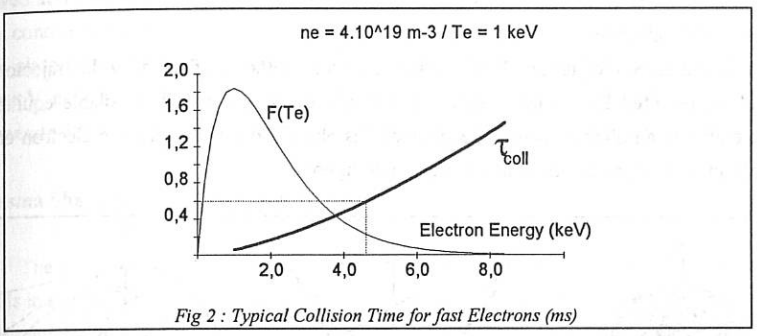


Fig 2 : Typical Collision Time for fast Electrons (ms)

In this model, the density does not play a dominant role, but the magnetic field and the size of the device do. It has been observed that runaway electrons confinement is better for stronger field during plateau conditions [3]. The diffusion process of fast electrons is greatly enhanced in low field plasma ($D \alpha v.(\delta B/B)^2$), and the number of electron still there at the end of the quench depends exponentially on the field strength, as well as on the small radius of the plasma.

This model is still qualitative: we lack the precise measurements needed during the quench phase to put real numbers on the phenomena. It is anyhow possible to check that the order of magnitude and tendencies are correct. In particular, the number of runaways is always a small fraction of the number of the electrons initially carrying the plasma current, and this fraction varies from one disruption to the other, as expected from a diffusive loss mechanisms.

Runaway Electron Trajectography

To follow electron trajectories after their creation, with the main goal of determining possible impact location, a new method has been developed. Initially conceived for fusion products [4], the code uses adiabatic theory. Collisionless fast particles are followed in the magnetic topology aid of the conservation of three invariant:

- Their energy, which change very slowly on the cyclotron characteristic time.
- The magnetic momentum, which is supposed to be equal to zero for runaways.
- The toroidal momentum: $L \equiv 2\pi.m.\vec{v}_{//}.R + q.\vec{A}_{\varphi}(R,Z).R$

The magnetic potential A_φ is related to the vertical flux function Ψ_p. The poloïdal projection of the trajectory can then be represented by equation {I}: $\varphi_p(R,Z) = \frac{\rho_{lp}}{a}.\frac{R}{R_0} + \varphi_0$

where the function $\varphi_p(R,Z)$ is the flux function Ψ_p, normalised to $\mu_0.R.I_p$, ρ_{lp} is the poloïdal Larmor radius of the electron $\frac{2\pi.m_e.c.\gamma}{e.\mu_0.I_P}a \cong 0.0166\frac{E(MeV)}{I_{P(MA)}}a$ and φ_0 is defined by the initial position of the electron.

The structure of equation {I} suggests a graphical method to find easily the trajectory : it will be represented by the intersection of the flux function, a usually available equilibrium parameter, and an oblique plane. The slope of this plane is determined by the electron energy and plasma current ratio. An example is given on figure 3.

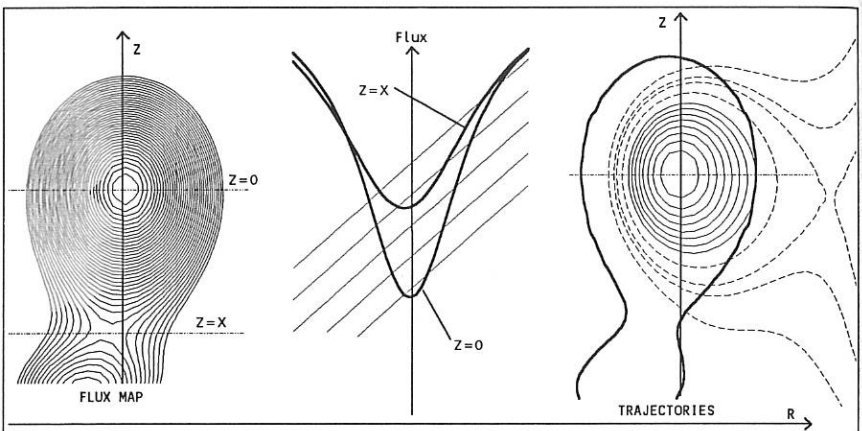


Fig 3: Graphical determination of Runaway Trajectories.

[1] Proceedings from the IAEA TCM on Tokamak Disruption, Culham Laboratory, 10-12 Sep. 1991.

[2] J.W. Connor and R.J.Hastie, Nuclear Fusion 15 p415, 1975

[3] M. Altman et al., Nuc. Inst. and Meth. 215 p453, 1983

[4] C. Doloc et al, accepted to be published in Physic of Plasma, Princeton, 1995

New TORE SUPRA steady state operating scenario

G. Martin, F.Parlange, D. van Houtte and T. Wijnands
Association Euratom-CEA, CEN Cadarache,
13108 Saint-Paul-lez-Durance, FRANCE

1. Introduction

Operation for times larger than the time required to reach full equilibrium conditions in plasma wall interaction (several minutes) is one of the main goals of TORE SUPRA. This operational regime can only be achieved with a non inductive plasma current. Lower Hybrid Waves (LHW) are used for this purpose. Steady state plasma control has been successfully achieved at TORE SUPRA by developing a new plasma control system which not only allows a better control of the plasma shape and position, but is also able of feedback control on some global plasma equilibrium parameters like the safety factor at the plasma edge $q_\Psi(a)$, the loop voltage V_l and the plasma current ramp rate dI_p/dt. Its capability to control the current drive and operate TORE SUPRA plasma discharge in steady state regime has been demonstrated.

2. Plasma Shape and Position Control

The design of the poloidal field system of TORE SUPRA [1] is particular in the sense that it fulfils in a single set of coils ohmic heating, radial and vertical position control of the plasma. In this way, the total installed power and the total weight of the conductors is minimised. The poloidal field system is constituted of 9 coils, associated with 9 power generators, allowing the control of the plasma boundary at 9 points. They are located on 9 axis directed towards the coils, the eigen axis of the system (see figure 1). The plasma control system makes use of the magnetic measurements of the poloidal field B_θ and the vertical flux on the vacuum vessel. The position of the plasma is identified through the isoflux method along the 9 axis. Differences between the measured points and programmed ones are then converted into generator voltages aid of a 9X9 transfer matrix.

During plasma operation, the required plasma shape and position are parametrised by 4 parameters: major radius R, vertical position Z, elongation ε and small radius a, obtained consistently with the contact between the plasma and one of the movable limiters or the inner wall. At each step of the control algorithm, the required plasma shape $\{R,Z,a,\varepsilon\}$ is translated into 9 control points $\{\rho_i\}$ along the 9 eigen axis, by using simple trigonometric formulas.

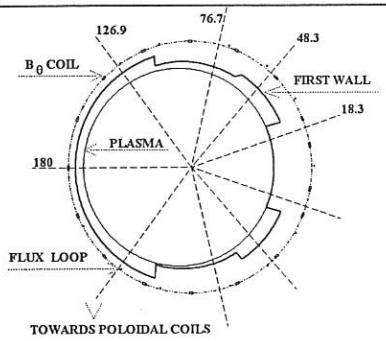


Fig 1: Geometry for Position Control

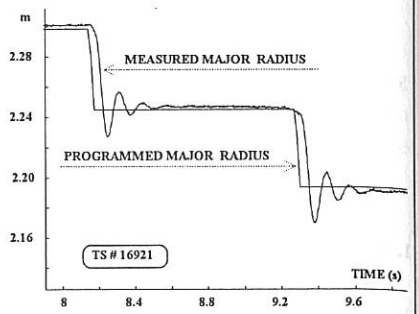


Fig 2: Plasma Position Control

3. Real-Time Determination of Equilibrium Parameters

If the forward mapping, from {R,Z,a,ε} to $\{\rho_i\}$, is straightforward, the inverse mapping is more difficult to perform in real time. Due to its non-linearity, it requires the use of a Multi Layer Perceptron Neural Network [2]. This network fits an ellipse characterised by its central position {R,Z} and its two axis {a,b} on the 9 plasma positions $\{\rho_i'\}$, determined for the generators voltage control. A typical result for the major radius R has been plotted on figure 2, along with the programmed value. The small oscillation around 11 Hz shows the characteristic time response of the feed-back loop.

More sophisticated parameters are then calculated:

↳ The safety factor at the edge: $q_\Psi \equiv \frac{1}{2\pi}\int_0^{2\pi}\frac{\partial\varphi}{\partial\theta}d\theta = B_{T0}R_0\sum_{i=1}^{9}\frac{\rho_i\Delta\theta_i}{R_i\Psi_i'}$ Preliminary tests have been performed to control its value, either by varying the plasma current or the plasma position. An example is plotted on figure 3: the plasma current has been modified by the pilot, and the feed-back system has changed the major radius to keep the safety factor close to a constant value (6.5).

↳ The two first Shafranov momentum [3], which are integrals of the poloidal field on the measurement surface, i.e. the vacuum vessel. They allow the determination of the stored energy in the plasma via the equilibrium field: $\beta+l_i/2$

↳ The kinetic energy (β) can then be separated from the magnetic energy (l_i) with the use of a diamagnetic loop surrounding the plasma. This second parameter will be used in a near future for current profile control algorithms, in particular during current ramp-up.

4. Feed-back Control during L.H.W. Current Drive

The new plasma control system has the capability to control the iron core flux evolution, by modulating the main poloidal generator. It allows in particular to run constant flux plasmas, a necessity for very long discharge (true steady-state), provided that some non-inductive current drive is used (L.H.W on TORE-SUPRA). In contrast with constant current mode operation for which the typical decay time of the iron core transformer system is very long, this zero loop voltage (constant flux) operating mode allows OH current to decrease with a time constant of about 4 sec.

In this kind of scenario, the plasma current is able to take any arbitrary value, depending on plasmas parameters and the LHW current drive efficiency. As the plasma current intensity has a large effect on the current profile and plasma performances it cannot be allowed to vary outside a limited range and one must control precisely its value. Therefore, a second proportional feedback algorithm was install to control the pulse amplitude of the injected LHW power to keep the plasma current constant rather than the usual opposite (i.e. constant rf power but varying current) (see figure 4).

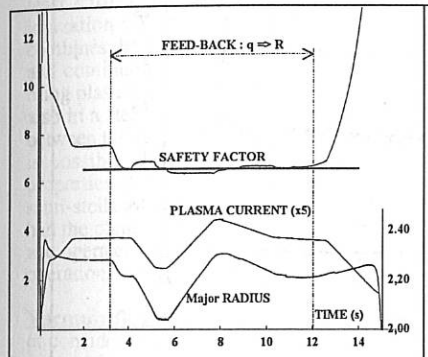


Fig 3: Control of the Safety Factor

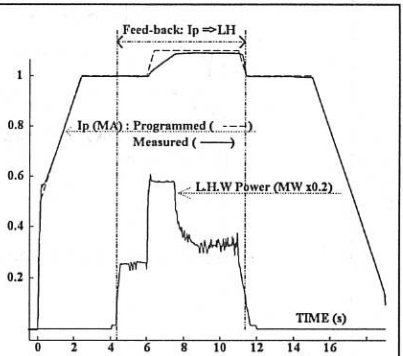


Fig 4: Control of Ip with LHW Power

Thanks to this new plasma control system which has proven a versatile tool, fully non inductive steady state regimes for the first time in a large tokamak could be maintained for up to 15 seconds without indicating any operational limit [4].

We have put in evidence during these experiments the need for an extra margin in the available LHW power to cope with temporary losses of current drive efficiency and/or plasma confinement. On the other hand during full Lower Hybrid Current Drive (LHCD), after the few seconds needed by the profile to evolve from its ohmic to LHCD shape, a strong MHD activity arises very often and degrades subsequently plasma performances. For some LHW spectra, however, no MHD activity appears, indicating potential stable LHCD current profile (figure 5).

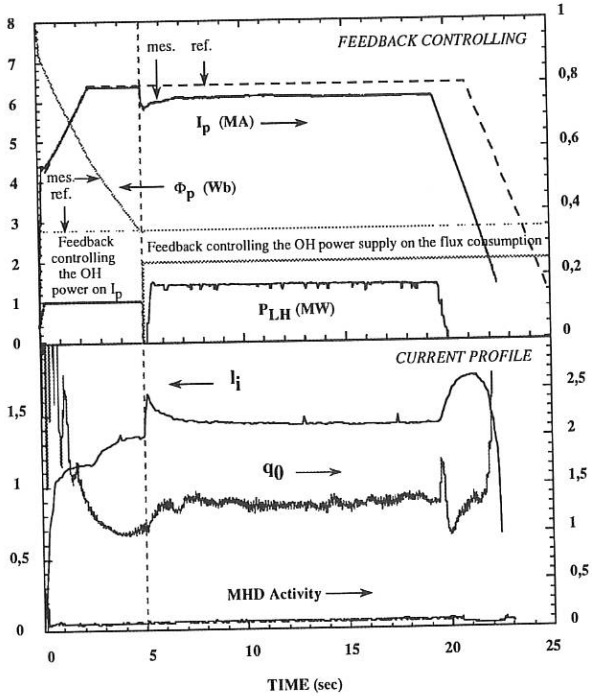


Fig 5: Full Lower Hybrid Current Drive Plasma

[1] ANE, J.M.et al., XVth SOFT Conference, Utrecht, Holland, 1988.

[2] WIJNANDS, T.J. et al., XXIth EPS Conference, Montpellier, France, 1994.

[3] SHAFRANOV, V.D.,Plasma Physics, vol. 13 pp757, Pergamon Press 1971.

[4] KAZARIAN-VIBERT, F. et al, This EPS Conference.

CURRENT CARRYING REGIMES IN A TOKAMAK WITH ADDITIONAL INCLINED COILS.

Paul E. Moroz
University of Wisconsin, Madison, WI 53706, USA
and Lodestar Research Corporation, Boulder, CO 80301, USA

Abstract. A device of a new type, stellamak [1], that can be ascribed to the stellarator-tokamak hybrids is discussed. This device features two systems of coils: the standard toroidal field (TF) coils of a tokamak and an additional system of simple coils to produce the stellarator-like effects. As an example, a system of additional vertically inclined planar coils is used in the otherwise standard tokamak configuration. The present paper is focused on the regimes with the plasma current. It is demonstrated that smooth transition from the pure stellarator mode to the pure tokamak mode, or operation in the alternating current (AC) regime are feasible, thus making possible the continuous operation of a stellamak.

Introduction. Continuous operation of a future thermonuclear reactor is, probably, absolutely necessary to make the electricity production cost comparable with the other non-fusion methods [2]. However, the main type of fusion devices, tokamaks, are principally pulsed devices. Various current drive schemes are intensively analyzed, theoretically and experimentally, to convert a tokamak into the steady operated device. However, there is no solution so far fully acceptable for the reactor parameters. Second main type of devices for magnetic plasma confinement are stellarators, which are intrinsically the steady devices. However, stellarators have there own drawbacks. There is one more approach to a continuous operation: AC regime in tokamaks [3-6]. However, this regime can be beneficial only if the plasma is not lost at current reversal. Although the experiments on a small tokamak, STOR-1M [3], have been encouraging and demonstrated an electron density of at least $2\ 10^{12}\ cm^{-3}$, the similar experiments on a large tokamak, JET [4], stated that the plasma ionization was fully lost during the dwell time at current reversal. Stellamak conception combines the best properties of both, tokamaks and stellarators, to make the ohmically heated and continuously operated device. Ohmic heating is efficient and, in principle, can alone bring plasma to ignition [7,8]. Good plasma confinement properties of tokamaks can be used also in a stellamak. Continuous operation of a stellamak comes from successive switching between the stellarator and tokamak modes without plasma loss. The AC stellamak operation is possible, and the plasma can be confined during the dwell time via the stellarator properties. A few stellarator-tokamak hybrids have been considered in literature in the past: semi-stellarator [9], tokatron [10], or a tokamak with tilted coils [11]. Many early stellarators had the ohmic heating possibility as well. However all these devices have not been designed and operated as a stellamak, which permit the fully featured tokamak and stellarator modes of operation, as well as smooth transition between them.

Vacuum flux surfaces produced by the planar inclined coils. The principal scheme of considered configuration of a stellamak is presented in Figs. 1 and 2. Fig. 1 gives the 3D perspective view of the coil system together with the last closed vacuum flux surface, while Fig. 2 shows the poloidal view of the coils and two sets of closed vacuum flux surfaces (internal and external sets [12]) in two cross-sections: at the toroidal location of the inclined coils (solid curves), and between the inclined coils (dashed). Shown are the rectangular TF coils used for a pure tokamak operation, inclined circular coils used for a pure stellarator operation, and a few poloidal field (PF) rings necessary for compensation of the vertical magnetic field produced by the inclined coils. The shapes of the rectangular TF coils and the circular inclined coils shown have been chosen only because we are proposing to use this system for the modernization of the Phaedrus-T tokamak, which presently has the rectangular TF coils and a circular plasma cross-section. In principle, some other simple coils can produce

the stellarator effects (see, for example, [12]), and thus can be used as a basis for a stellamak. For simplicity, the magnitude of all currents in the PF rings was chosen to be the same. However, to make the PF system compensated, the direction of the currents in the PF rings at R = 0.4 m is opposite to the direction of currents in other PF rings, thus making the total current to be zero. Compensation of the PF system is not necessary for the pure stellarator regime, but it is important during transition from the stellarator to tokamak regime with the ohmic current when the net current in the PF system might interfere with the performance of the ohmic current transformer. Dependence of the produced rotational transform on the average minor radius is shown in Fig. 3. The internal and external sets of flux surfaces are not equal due to toroidicity [12]. While the external set is featuring the strong magnetic well (and, hence, good plasma stability properties), the internal set has a magnetic hill. However, the finite plasma pressure improves the situation. In particular, for the internal set, the magnetic well appears for the significant part of the plasma already at $\beta \sim 0.5$ %.

Transition between the stellarator and tokamak modes. The three-dimensional equilibrium code, VMEC [13-15], in its free-boundary mode, is used in these calculations. Our main requirements for the configuration of flux surfaces during the transition process were the sufficiently large rotational transform ($\iota > 0.1$ everywhere in plasma) and a magnetic well, which ensure good stability properties of the configuration at all stages of transition. The starting flux surface configuration corresponds to the pure stellarator mode, and is similar to the vacuum one presented in Figs. 1, 2. The main visible difference for the plasma with finite β=0.5% is a further shift of the magnetic axis to the low-field side. For the external set, other effects are: rotational transform at the magnetic axis has increased to $\iota(0) = 0.29$, and the magnetic well has increased to $|W| = 30$ %, in comparison with $|W| = 21$ % for the vacuum case. Detailed calculations [16] have been carried out for many intermediate steps of the transition. Here we present results for a half transition when a relatively small plasma current of 16 kA is induced in the plasma (for comparison, the nominal plasma current in the device considered with the parameters of the Phaedrus-T tokamak is 70-90 kA). In this case, half of the toroidal magnetic field is due to inclined coils and half is due to the standard TF coils of a tokamak. Fig. 4 shows the equilibrium flux surfaces in two cross-sections, under the inclined coils (solid curves) and between them (dashed). With the current, the flux surface shape became closer to the circular one, typical for the Phaedrus-T tokamak. The total rotational transform in the center became $\iota(0)=0.36$, and at the plasma edge, $\iota(a)=0.11$. Further increase of the ohmic current, turning off the power in inclined coils, and doubling the current in the TF coils brings the configuration to the standard pure tokamak mode.

AC regime of operation. AC operation, in general, has a lot of advantages over the pulsed operation [5,6]. The magnetic energy stored after the first half of a discharge can be utilized for the subsequent discharge without need for additional power for the ohmic transformer recharging. Regarding the future reactor, the continuous electrical energy output can be obtained with minimum-cost energy storage unit. Stellarator properties of a stellamak used during the dwell time can make AC operation especially beneficial. Availability of two sets of closed flux surfaces with opposite helicity is an important feature for AC operation of a stellamak. Each helicity supports the ohmic current of definite direction, and two available sets will support the configuration near the current reversal phase. To demonstrate this effect, we present results of calculations for two cases with the low plasma current, $I_p = 12$ kA, and opposite current directions. The plasma with β=0.5% is considered. Fig. 5 shows two sets of flux surfaces in the cross-section under the inclined coil. The external set corresponds to the case with the positive plasma current, while the internal set - with the negative current. Significant intersecting region is seen, although each set is shifted, relative to the inclined coil center, to the side corresponding to its location in the pure stellarator mode. The total

rotational transform for these two sets has opposite sign, and shown in Fig. 6 together with the ohmic current contribution. The rotational transform is above 0.1 everywhere in the plasma while the contribution coming from the plasma current at the edge is only $\iota_{oh}(a)=0.045$. One can see that the stellarator rotational transform produced by inclined coils and the ohmic rotational transform add constructively for plasma currents of both directions. This improves plasma stability near the current reversal phase when currents are small and cannot support the stable plasma by themselves. It is important to note that the total rotational transform is not equal to the sum of the stellarator and ohmic contributions. This is because of the location of flux surfaces is different from that in the pure stellarator mode. For the internal set, for example, the magnetic axis has a large shift in comparison with the pure stellarator mode and the stellarator rotational transform does not contribute near the center. Only when there is good correspondence between the shape and location of flux surfaces the total rotational transform becomes close to the sum of the stellarator and ohmic contributions.

Discussion. The properties of a new type of device, stellamak, are analyzed. The system with the additional planar inclined coils is used as an example. In Ref. [12] it was clarified that there are two main current filaments of the inclined coils responsible for the stellarator-like properties and existence of two sets of closed flux surfaces with opposite helicity: the external current filament (at the large major radius) and the internal filament (at small major radius). Different engineering solutions can be found that conserve the external and/or internal current filaments but change the overall inclined coil geometry. In fact, there were a few proposals for tokamak modernization in the past to use the coils of different geometry [9,17,18] not encircling the plasma in the poloidal direction. Although the particular stellamak configuration presented in this paper is simple, effective, and fully suitable for the proof-of-principle experiment, in our future studies we are planning to search for even more efficient and simple stellamak configuration, with the good plasma confinement, stability, and accessibility properties.

Acknowledgment. Cooperation of Steve Hirshman in making the VMEC code available and his help and valuable instructions are greatly appreciated. The work was supported by the U.S. DOE Grants DE-FG02-88ER53264 and DE-FG02-88ER53263.

References.

[1] P. E. Moroz, submitted to *Fusion Technology* ; UW Report PLR-95-05 (April 1995).
[2] W. M. Nevins, Proc. 11th Int. Conf. on RF Power in Plasmas, Palm Springs (May 1995).
[3] O. Mitarai, et al., *Nuclear Fusion* **27**, 604 (1987).
[4] B. Tubbing et al., Bull. Am. Phys. Soc. **36**, 2365 (1991).
[5] O. Mitarai, et al., *Fusion Technology* **15**, 204 (1989).
[6] O. Mitarai, et al., *Fusion Technology* **20**, 285 (1991).
[7] D. R. Cohn, et al., *Nuclear Fusion* **16**, 31 (1976).
[8] B. Coppi, et al., *Physica Scripta* **45**, 112 (1992).
[9] H. Ikezi, K. F. Schwarzenegger, C. Ludescher, *Phys. Fluids* **22**, 2009 (1979).
[10] A. H. Boozer, et al., Proc. 9th IAEA Conf. on Plasma Phys. and Contr. Nucl. Fus. Res., Baltimore 1982, Vienna, **Vol. 3**, p. 129 (1983).
[11] A. V. Georgievskij, et al., Proc. IAEA Tech. Comm. Meet. on Stellarators and Other Helical Conf. Systems, Garching, 1993, Vienna, p. 480 (1993).
[12] P. E. Moroz, submitted to *Physics of Plasmas* ; UW Report PLR-95-03 (March 1995).
[13] S. P. Hirshman, J. C. Whitson, *Phys. Fluids* **26**, 3553 (1983).
[14] S. P. Hirshman, H. K. Meier, *Phys. Fluids* **28**, 1387 (1985).
[15] S. P. Hirshman, D. K. Lee, *Comp. Phys. Comm.* **39**, 161 (1986).
[16] P. E. Moroz, UW Report PLR-95-06 (May 1995), prepared for submission.
[17] H. P. Furth, C. W. Hartman, *Phys. Fluids* **11**, 408 (1968).
[18] G. V. Sheffield, H. P. Furth, Princeton University, Report PPPL-1827 (1981).

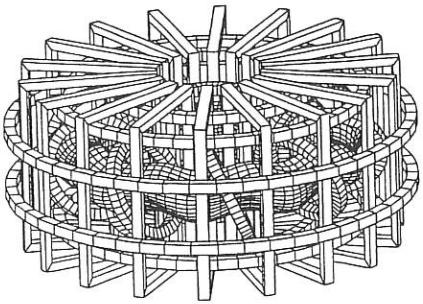


Fig. 1. Principal scheme of a stellamak.

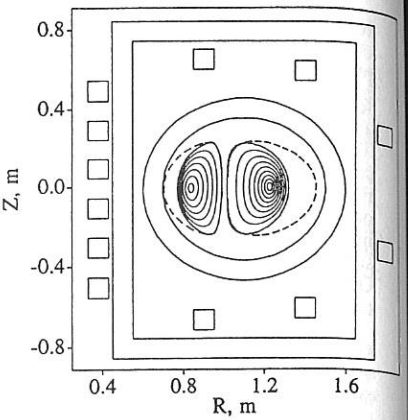


Fig. 2. Two sets of vacuum flux surfaces.

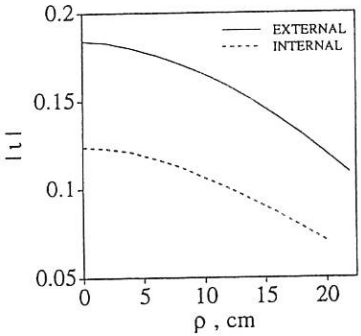


Fig. 3. Radial dependence of vacuum rotational transform.

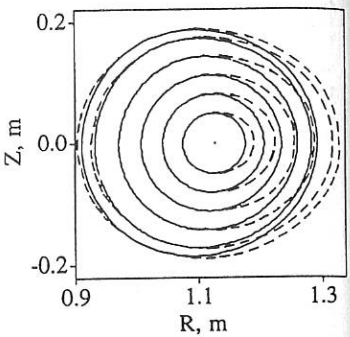


Fig. 4. Flux surfaces at half transition.

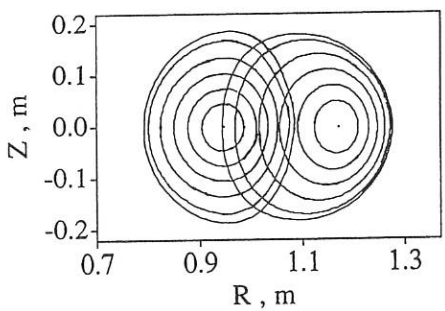


Fig. 5. Two sets with opposite plasma currents.

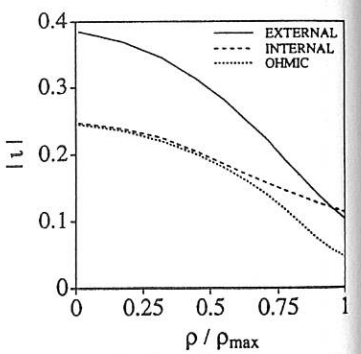


Fig. 6. Rotational transform corresponding to two sets in Fig. 5.

Evolution and Optimisation of Neutron Emissivity Profiles in JET

F B Marcus, J M Adams*, D S Bond*, M A Hone, O N Jarvis, T T C Jones, R Koenig, M J Loughlin, M F F Nave, G Sadler, B Schunke, P Smeulders, N Watkins*

JET Joint Undertaking, Abingdon OX14 3EA, and *AEA Technology Harwell, U. K.

1. Introduction

The goals of the JET program include maximising d-d (and d-t) neutron production and fusion Q. Several operational parameters are involved in this optimisation: neutral beam trajectory (by choice of Positive Ion Neutral Injectors, PINIs), beam energy and particle current; beam power waveform; MHD equilibrium; particle density and profile. The JET neutron emission profile monitor (Fig. 1) is used to observe the effects of these parameters.

2. Beam Deposition

To investigate the extremes of beam trajectory, two plasma discharges were compared, both with the same MHD equilibrium, with the magnetic axis at 0.3 m above the machine mid-plane. In #33398, PINIs are chosen preferentially near, and in #33420, far from the plasma axis. The line-integral neutron rates measured by the horizontal camera at 12.6 s are shown for both discharges in Fig. 2. The channels measuring off-axis neutron emission show similar rates, but the profile is slightly broader for #33420, and the chords passing through the axis are significantly lower. The vertical camera channels show a similar pattern. Tomographic inversion of the data from both cameras shows that the axial neutron emissivity is a factor of two lower in #33420 with off axis injection. However, the global properties of the two discharges are similar in stored energy, MHD activity and ELM-free period. The global neutron rates after 1.1 s of beam heating are 1.9×10^{16} n/s in #33398 compared to 1.6×10^{16} n/s in #33420, i.e. only a weak dependence on beam trajectory.

3. Density Profiles

Two 4 MA plasmas, #31893 and #32798, with similar MHD configuration and stored energy (~ 9 MJ), are compared to study the effect of different electron density profiles. In Fig. 3, these profiles for the two discharges are shown at times corresponding to 1 s after the start of high power beam heating at 18.2 MW. Due to a higher recycling level in #31893, the density is higher and hollow, compared to the peaked profile in #32798. The line integral neutron emissivities from the vertical camera are compared at this time. In #31893, the Full Width Half Maximum (FWHM) is 1.1 m versus 0.8 m in #32798, indicating that the beam is being trapped away from the plasma axis, as is indicated by beam deposition calculations. The total neutron rate in #31893 is lower (as is the peak line integral) at 1.4×10^{16}n/s compared to 2.3×10^{16}n/s. Since the thermal emission is a feature of the plasma core, beam ions deposited near the edge do not contribute to raising the axial ion temperature. Furthermore, beam ions trapped near the edge where the electron temperature is 1-2 keV contribute a lower beam-thermal neutron emission per ion than those trapped near the axis.

The initial rate of rise in #31893 of the neutron emission rate is about half that in #32798. Modelling of the initial rate of rise of the neutron yield in #31893 indicates an initial deuterium fraction n_d/n_e of 0.5, contributing to a reduced rate of neutron production despite beam fuelling with pure deuterium. Contamination is more deleterious at high plasma target density, since the fraction of contamination compared to beam deposited deuterium is greater.

4. High Neutron Rate

Discharges in JET have produced high global neutron rates, up to 4.8×10^{16}n/s in #33643, a 4 MA plasma with 18.5 MW of beam heating.. The neutron rate, stored energy, and plasma density all increase continuously until 1.3 sec after the beginning of full power beam heating. The neutron emissivity profile at this time is shown in Fig. 4, as determined by tomography from the neutron profile monitor. The peak emissivity of 3×10^{15}n/m^{3}s is within 15% of that calculated from Charge Exchange Recombination Spectroscopy (CXRS) measurements. The global yield seems to be predominantly from thermal fusion. The implication is that optimisation of the fusion output is strongly related to optimisation of the thermal fusion yield. This hot-ion ELM-free H-mode discharge was terminated by a sawtooth crash, accompanied by an inversion in the neutron emissivity profile at intermediate radius, and a giant ELM.

5. Beam Power Step Down

In order to avoid or delay MHD events and maintain a discharge at a high performance level in a quasi steady state condition, the plasma density and stored energy need to approach steady state conditions while maintaining a high rate of neutron production. One method of achieving this is to reduce the beam power and its associated fuelling rate. The best results were obtained using a power step down by eliminating 80 keV beams and predominantly retaining 140 keV beams, which have a low particle fuelling rate per MW delivered (and a high beam-thermal fusion rate per ion). With low wall recycling and the in-vessel cryopump, the plasma volumetric density increase is reduced to the beam fuelling rate, both before and after power step-down.

In the 3.5 MA, 3.4T plasma #34236, high-performance, quasi-steady state operation was achieved, with an equivalent d-t fusion Q maintained above 0.5 for 1 s, approximately the energy confinement time, as shown in Fig. 5 (using an approximation of the equivalent d-t fusion Q $\sim 2.5 \times 10^{-10}$[NeutRate/BeamPower(W)]). (If corrections for alpha heating and beam shinethrough were included, Q would reach 0.8, and exceed 0.7 for 1 s.) The rate of density rise is slower after step down, and the neutron rate and stored energy are nearly constant. Nevertheless, the slow increase of energy and density finally lead to a discharge terminating ELM. The ion temperature is also approaching the electron temperature. The discharge remains ELM-free during this time. In Fig. 6, the count rates from horizontal neutron camera channels 5-9 are shown for #34236. At power step down, the outer channels are unchanged, but the central channels show a drop before reaching a new steady state.

In Fig. 7, the measured global neutron yield is shown, together with calculated global yields based on CXRS measurements of ion temperature and density, including the 80 and 140 keV beam contributions separately, the thermal d-d contribution, and their total, which agrees (except at maximum density) with the measured neutron rate evolution. Most of the neutrons are produced by thermal fusion. At step down, when the 6 of the 8 high current 80 keV PINIs are turned off, their beam-thermal contribution becomes negligible. The neutron rate is then constant for 0.2 s, and afterwards there is a decrease in the neutron emissivity on axis, corresponding to a decrease in the thermal fusion yield.

The fusion Q during the step down is more representative of steady state Q values for d-t extrapolation, since the energy and confinement times are nearly in steady state. At 13.15 s, the time of maximum fusion Q, tomographic inversion of the neutron camera data has been used to calculate the local 2-D neutron emissivity profile, for which the maximum emissivity is 1.7×10^{15}n/m^{3}s. The calculated CXRS axial value is similar, and the integral totals are the same. The emissivity is dominated by thermal fusion.

In Fig. 8, the results of step down from 16.4 MW to 4.5 MW are shown for the 4 MA plasma #33106. The stored energy stayed nearly constant for 0.5 s, and the plasma was ELM free. The energy confinement time increased from about 1 s before to 1.6 s after the step down, with 10 - 11 MJ of stored energy. The plasma loss power was only 6 MW, compared to the beam power of 4.5 MW. The fusion Q was 0.7 - 1.0 . The rate of density increase was slowed. It is encouraging that ELM free H-modes can be maintained with a low loss power.

6. Conclusions and Discussion

Neutron production is relatively insensitive to (possible) variations of beam trajectory. The altered neutron emissivity profiles within the plasma correspond to only a 16% reduction in the integrated total emission in the two discharges compared with different PINI choices.

Hollow and high density profiles reduce the plasma ion temperature and broaden the neutron emissivity profile. The global emission was reduced by 40% in this comparison, due to reduced temperatures, beam trapping at the edge, and an initially low deuterium fraction.

In hot-ion ELM-free H-modes with the highest neutron production, in the present JET configuration, and especially with beam power step down experiments, the d-d neutron production by thermal fusion significantly exceeds the beam thermal contribution. The plasma stored energy and neutron rate are limited by MHD instabilities (Hender et al; Smeulders et al, this EPS conference), not by maximum power. Once the plasma enters the H-mode via high power beam heating (to rapidly increase the density and ion temperature), this mode can be maintained with a step down to low input power at the plasma loss power level, near the L-H transition threshold of about 5-10 MW at a medium plasma density of 4-6x$10^{19}$$m^{-3}$. Enhanced fusion Q can be obtained at low beam power in quasi-steady state. Plasmas with beam power step down still have a residual density increase, approximately equal to the reduced beam fuelling rate. The problems associated with this density increase are: beam trapping near the plasma edge; ion temperature reduction and instability or H to L transition.

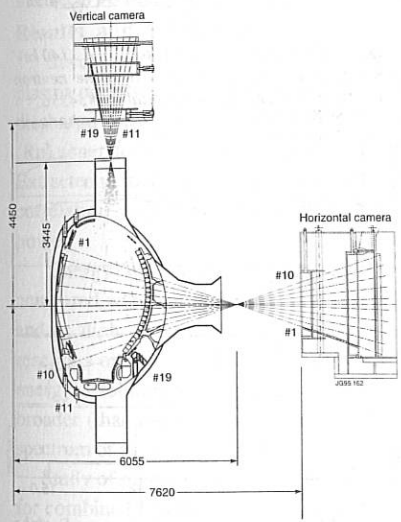


Fig. 1. JET Neutron Emission Profile Monitor-Upgrade Version, with channel numbers.

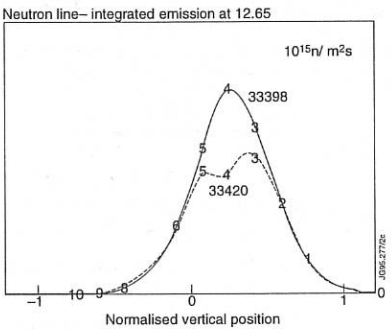


Fig. 2. The line-integral neutron rates in channels 1-10, measured by the horizontal camera at 12.6 s for #33398 and #33420.

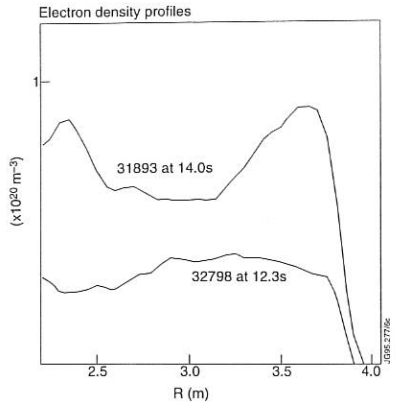


Fig. 3. The electron density profiles for #31893 and #32798 after 1 sec of18.2 MW beam heating.

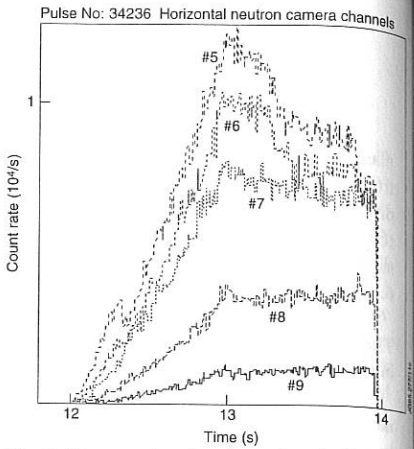


Fig. 6. The count rates from the horizontal neutron camera channels 5-9 for #34236.

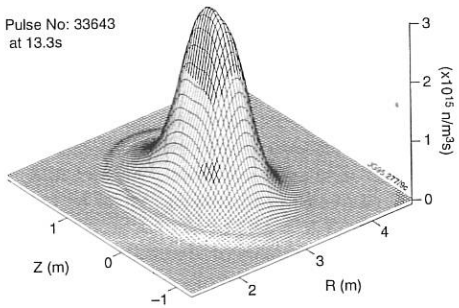


Fig. 4. The 2-D neutron emissivity profile in #33643 after 1.3 sec of full power beam heating.

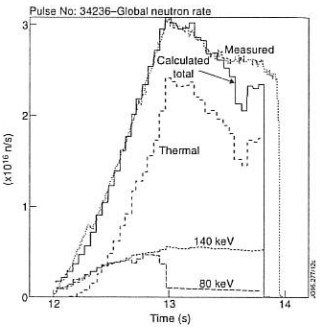


Fig. 7. Contributions of 80 keV and 140 keV beam-thermal and thermal fusion to the neutron rate, their total and measured total for #34236.

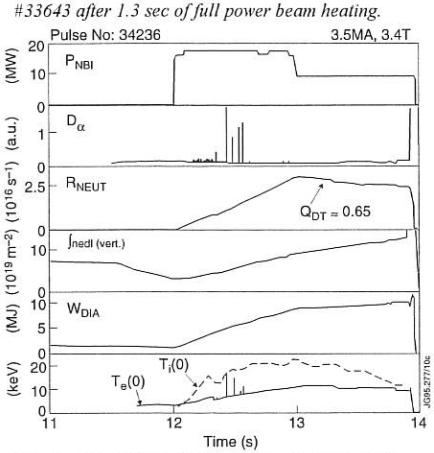


Fig. 5. The neutral beam power, D-alpha light, neutron rate, line-average electron density, stored energy, and centralTi and Te vs time for #34236.

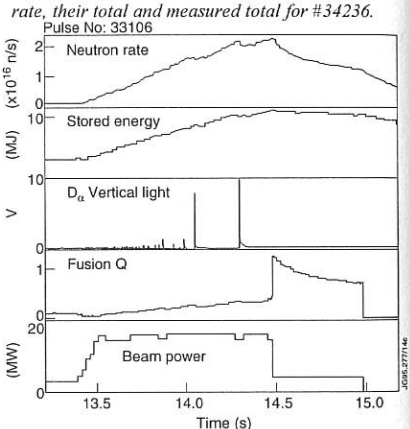


Fig. 8. The neutron rate, stored energy, D-alpha light, fusion Q, and neutral beam injected power vs time for #33106.

Measurement of Atomic Hydrogen Fluxes in MeV-Energy Range in ICRF-heated JT-60U plasmas

V.I.Afanassiev*, Y.Kusama, M.Nemoto, T.Nishitani, S.Ya.Petrov*, S.S.Kozlovskij**, M.Satoh, A.Morioka, Y.Tsukahara, T.Kondoh, H.Kimura, K.Hamamatsu, S.Moriyama, M.Saigusa and T.Fujii

Japan Atomic Energy Research Institute, Naka Fusion Research Establishment, Naka-machi, Naka-gun, Ibaraki-ken, 311-01, Japan

*A.F.Ioffe Physical-Technical Institute, Politechnicheskaya 26, St.Petersburg, 194021, Russia

**State Technical University, Politechnicheskaya 29, St.Petersburg, 195251, Russia

Introduction

In a collaboration between Japan Atomic Energy Research Institute and A.F.Ioffe Physical-Technical Institute, a high energy neutral particle analyzer (NPA) has been installed on JT-60U tokamak to clarify the alpha-particle physics for future tokamak reactors [1]. This paper presents the measurements of fast atomic hydrogen fluxes using the NPA in ICRF-heated discharges.

Neutral Particle Analyzer

The NPA is an E||B type analyzer and has eight energy channels. The main parameters are as follows: energy range 0.5-4.0 MeV for alphas and 0.2-2.0 MeV for protons, energy resolution is 6-11%, detection efficiency is 0.05-0.4 for helium atoms and 0.2-0.4 for hydrogen isotopes. In comparison with similar devices [2,3], this instrument is first equiped with 16-channel pulse height analysis system for all the NPA detectors. Using the different pulse height response of detector, this system provides reliable distinguishing the particle signal from a noise even under intense neutron and γ-rays radiation. The NPA is located on the top of torus and its line of sight intersects vertically the plasma center and allows to detect the banana particles.

Results and Discussion

Successful application of this new data acquisition system is illustrated in Fig.1 for DD-plasma operation. Typical pulse height distributions are shown in Fig.2 for NBI and NBI+ICRH discharge phases where appeared particle peak is clearly seen. Neutron and γ-ray background (Rn) separated by the NPA detectors is rather similar to detected by neutron diagnostics (Sn). Extracted particle signal (Ro) is coincided with ICRF power timing. There are also observed the correlation with sawtooth activity and slowing down process after switching off the ICRF power.

Energy dependences of neutron sensitivity and energy resolution of the NPA detectors are compared with calibrated data in Fig.3 and Fig.4 respectively. Enhancement of the sensitivity and its slight rise tendency with channel number are due to an additional contribution of n(p)-reactions on detector chamber wall which is opposite to detector row. Small reduction of the energy resolution properties is explained by inhomogeneity of photocathode surface and its broader (than under monoenergetic cyclotron beam) illumination because of the wide energy spectrum of detected particles.

Study of higher harmonic beam ion acceleration (from 2nd to 5th harmonic) was carried out for combined ICRF+NBI(Ho) heating by scanning the toroidal magnetic field (1.6-3.8T) with fixed antenna frequency (116MHz). In contrast with the previous result below 200 keV [4], effective tail temperature (Teff) evaluated within 0.32-0.86 MeV energy range is found to be

increased with harmonic number (except for 5th harmonic case, see Fig.5) and decreasing tendency is observed for tail ion stored energy defined as $Wtail=2/3(\Delta Wdia-\Delta Wth)$. Energy spectra of hydrogen atoms for central position of all the resonance layers are presented in Fig.6. Both tendencies are consistent with calculation of a 1-D full wave code incorporating a Fokker-Planck equation [5] and explained by dependence of RF diffusion coefficient on harmonic number and particle velocity $D_{\perp}(v)\sim J_{n-1}^{2}(v)$. It is considered that in 5th harmonic case protons may be intercepted by 6th harmonic resonance layer (simultaneously existed in plasma from low field side). Since this layer is near to tokamak wall (r/a=0.85) these intercepted particles are fast lost (see Wtail).

Parametric study of dependences on launched IC power and on plasma density were investigated in 2nd harmonic H-minority ICRF-heated discharges without a beam injection.

Independence of tail temperature (Teff) on IC power and saturation in atomic fluxes for the power grater than ~5MW are measured (see Fig.7). The typical energy spectra are shown in Fig.8. It should be noted that charge-exchange process on H-like light impurity ions (C^{+5}, B^{+4}, Be^{+3}) is considered as a main neutralization mechanism of fast protons at present time [2] and the similar saturation effect measured on JET was explained by a reduction in H-like impurity (target) concentration [6]. In our case, however, this explanation is not suitable because of extremely the same plasma parameters and influx of neutrals from the wall. Besides the saturation is also observed in tail ion stored energy. This tendency is considered to be caused by enhancement of the part of IC power absorbed by very high energy particles which are not confined in plasma and lead to increasing the power losses.

On the contrary, the changes in target should be taken into account for density scan experiment. As opposed to measurements on JET [7] for fundamental harmonic heating, a slight rise tendency of effective tail temperature caused by increasing the more energetic atomic flux with plasma density has been found (see Fig.9). On the other hand, significant reducing the tail ion stored energy confirmed by γ-spectroscopy data is observed as well. The degradation of ion energy spectrum is compensated in atomic fluxes by rather substantial gain of the target density owing to charge exchange of light impurity nuclei on a neutral influx from the wall (see H_{α}-emission). It should be noted that Fokker-Planck simulation finds more strong dependence of tail temperature with density for fundamental than for 2nd harmonic case and explains the same reduction in fast ion population for lower particle energy: 0.5MeV (fundamental harmonic, JET case) in comparison with 2.5MeV (2nd harmonic, JT-60U case).

Decay time of effective tail temperature of hydrogen atoms ($dT/T=-t/2\tau_S$) is plotted in Fig.10 against classical slowing down time within wide variation of electron temperature and density. Notice that significant reduction in plasma current does not change this dependence, but low current discharges are corresponded to low effective tail temperatures. So the relaxation time of fast particle population with mean energy equal to Teff is comparable with slowing down time.

Summary

First applied pulse height distribution system provides reliable distinguishing the particle signal from neutron and γ-ray background noise in DD-plasma operation. Sensitivity to neutron and γ-ray radiation and energy resolution of the NPA detectors are found as comparable with calibrated data. Enhanced sensitivity is due to additional contribution of n(p)-reactions on

detector chamber walls. Reduction of resolution properties is caused by more broad illumination of detector window because of wide energy spectra of detected particles.

Observed tendency of increasing the tail temperature with harmonic number (2nd-4th) is consistent with Fokker-Planck code simulation. Reduction for 5th harmonic is probable deal with the interception of higher energy protons by 6th harmonic resonance layer. Saturation of both CX-fluxes in MeV-range and Wtail is observed for ICRF power above 4-5MW. This phenomena is probably explained by absorption of IC power by more energetic particles which are not confined in plasma. Absence of degradation tendency in CX-fluxes and Teff with increasing the plasma density is opposite to γ-rays and Wtail measurements and may be explained by significant changes in CX-target. The relaxation time of fast particle population with mean energy equal to Teff is comparable with classical slowing down time.

References

[1] Y.Kusama et al, *Rev. Sci. Insrum.* **66** 339 (1995).

[2] M.P.Petrov et al, *19th EPS Conf. on Contr. Fusion and Pl.Physics* **16C(II)** 1031 (1992).

[3] S.S.Medley et al, *20th EPS Conf.on Contr. Fusion and Pl.Physics* **17C(III)** 1183 (1993).

[4] H.Kimura et al, *Plasma Physics and Controlled Fusion* **35** 845 (1993).

[5] K.Hamamatsu et al, *Nucl. Fusion* **29** 147 (1989).

[6] A.A.Korotkov et al, *21th EPS Conf.on Contr. Fusion and Pl.Physics* **18B(I)** 266 (1994).

[7] A.V.Khudoleev et al, *Tech. Rep. JET-P(92)* **31** (1992).

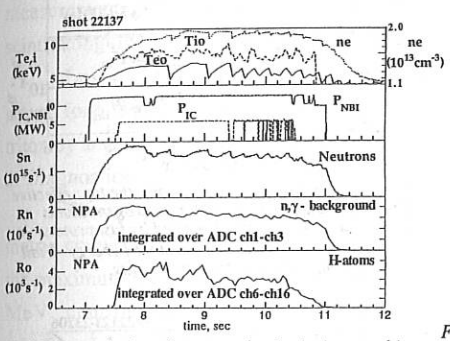


Fig.1 Time evolution of average density (ne), central ion and electron temperatures (Tio,Teo), neutron emission rate (Sn), neutron/gamma background (Rn) and 1MeV hydrogen counting rate (Ro) detected in ch8 of the NPA.

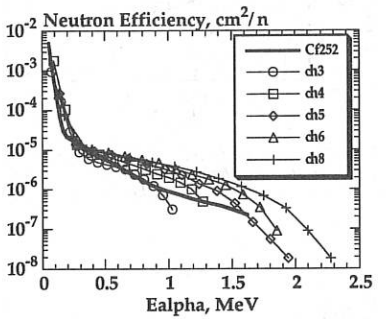


Fig.3 Neutron sensitivity of NPA detectors measured in DD-plasma discharges in comparison with calibrated data (Cf252 radiative source).

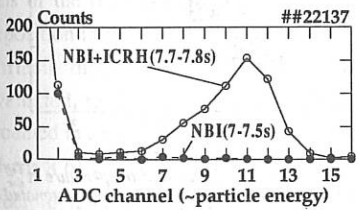


Fig.2 Pulse height distribution of ch8 (Ep=1MeV) at NBI alone and NBI+ICRH phases.

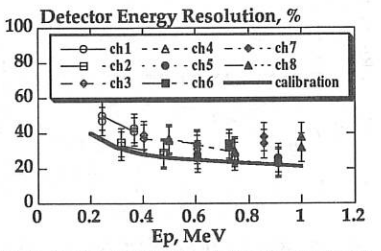


Fig.4 Energy resolution of the NPA detectors measured in plasma experiment as compared to calibrated data (cyclotron accelerator).

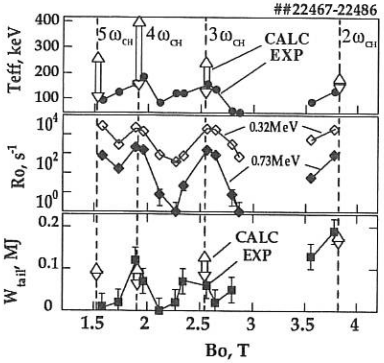


Fig.5 Bt-scan experiment. From the top: effective tail temperature Teff and flux of hydrogen atoms Ro, and tail ion stored energy Wtail versus toroidal magnetic field Bo.

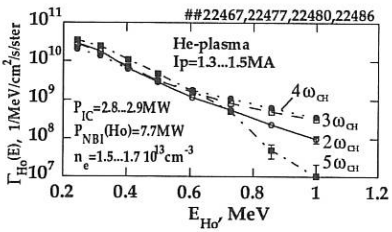


Fig.6 Bt-scan experiment. Energy spectra of hydrogen atoms for Bo when resonance layer position of n-th harmonic coincides with the plasma center.

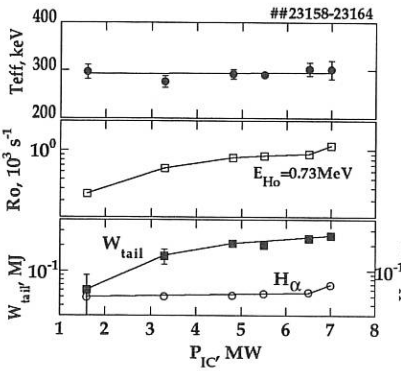


Fig.7 P_{IC}-scan experiment. From the top: effective tail temperature Teff, atomic flux Ro , tail ion stored energy Wtail and H_α-emission versus IC power P_{IC}.

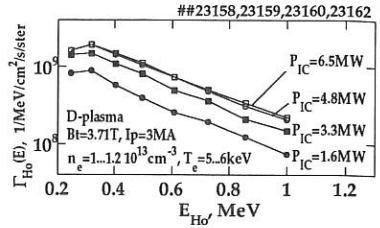


Fig.8 P_{IC}-scan experiment. Energy spectra of hydrogen atoms for different values of IC power P_{IC}.

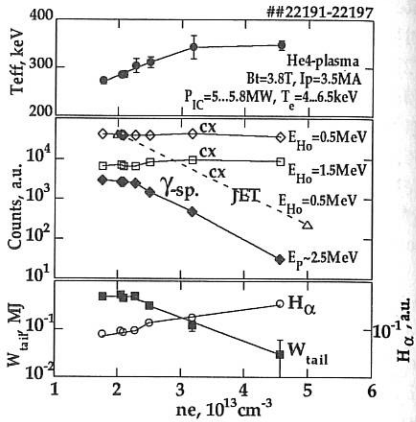


Fig.9 n_e - scan experiment. From the top: effective tail temperature Teff, fluxes of hydrogen atoms cx and gamma rays γ-sp. produced by fast protons in reaction with B^{11}, and tail ion stored energy Wtail and H_α-emission versus plasma density.

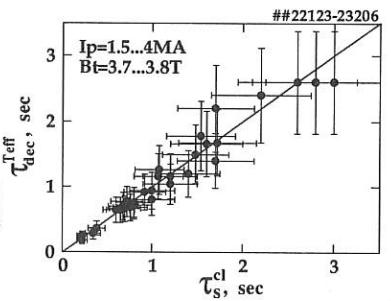


Fig.10 Decay time of effective tail temperature τ_{dec}^{Teff} against to classical slowing down time τ_s^{cl} estimated from the values of central temperature and average density of electrons.

Triton Burnup Study in JT-60U

T. Nishitani, M. Hoek[1], H. Harano[2], G.A. Wurden[3], R.E. Chrien[3], M. Isobe, K. Tobita and Y. Kusama

Naka Fusion Research Establishment, Japan Atomic Energy Research Institute, Naka-machi, Naka-gun, Ibaraki-ken 311-01, JAPAN

[1]Present address: Max-Planck Institute für Plasmaphysik, D-85748 Garching, GERMANY

[2]Department of Engineering, Univ. of Tokyo, Bunkyo-ku, Tokyo 113, JAPAN

[3]Los Alamos National Laboratory, New Mexico 87544, USA

1. Introduction

The behavior of 1 MeV tritons produced in the d(d,p)t reaction is important to predict the properties of D-T produced 3.5 MeV alphas because 1 MeV tritons and 3.5 MeV alphas have similar kinematic properties, such as Larmor radius and precession frequency. The confinement and slowing down of the fast tritons were investigated by measuring the 14 MeV and the 2.5 MeV neutron production rates. Here the time resolved triton burnup measurements have been performed using a new type 14 MeV neutron detector based on scintillating fibers[1], as part of a US-Japan tokamak collaboration.

Loss of alpha particles due to toroidal ripple is one of the most important issues to be solved for a fusion reactor such as ITER. We investigated the toroidal ripple effect on the fast triton by analyzing the time history of the 14 MeV emission after NB turn-off.

2. Diagnostics

The detector consists of an array of scintillation fibers embedded in an aluminum matrix coupled to a magnetic resistant photo tube with a high current-capable base. Because the maximum recoil-proton range for a 14 MeV neutron is 2.2 mm in plastic scintillator, we chose to use either 1 mm or 0.5 mm diameter scintillation fiber optics. Because only the neutron coming on the axis of the fiber gives the highest energy deposition in the fiber, this detector has an intrinsic directionality, which has been evaluated to be ±30°. The detector is mounted in a small collimator box, 40 cm × 61 cm × 61 cm of borated polyethylene, in order to improve the directionality. The

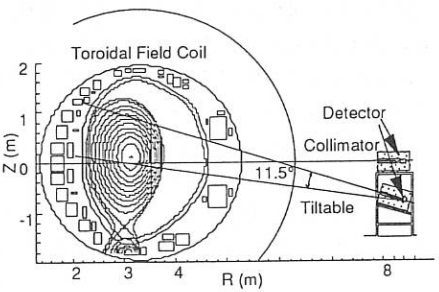


Fig.1 Schematic of sightlines of JT-60U, for the horizontal and tiltable detectors.

full-width half maximum of the viewing angle with the collimator box was measured to be 15° using a 14 MeV neutron generator.

Two sets of detectors have been installed near the midplane of the vessel, just outside the toroidal field coil position as shown in Fig.1. The scintillating fiber detectors have been calibrated by the shot-integrated 14 MeV neutron yield measured with the neutron activation technique using a pneumatic foil transfer system[2]. The foils are irradiated at 20~30 cm outside of the plasma. The counts of the scintillating fiber detectors and the 14 MeV neutron yield measured with the neutron activation technique have a good linearity in the range of 14 MeV neutron yield 10^{12}- 10^{15} /shot.

Figure 2 shows the typical wave forms of total and 14 MeV neutron emission in the neutral beam (NB) heated discharge. Here total neutron emission is measured with neutron monitors using ^{235}U fission chamber[3]. The scintillating fiber detector system operates in a background of DD neutrons which are ~100 times brighter than the DT neutron signal, at the counting rate up to 100 MHz. The peak DT neutron rate at the time of neutral beam(NB) turn-off is as high as 2% of the total neutron emission. After NB turn-off, 14 MeV neutron emission decays exponentially with time constant of 435 ms. The total neutron emission decays exponentially with faster time constant of 121 ms just after NB turn-off. After 8.3 s, total and 14 MeV neutron emissions coincide each other, which means that 14 MeV neutron emission is dominant because the neutron monitor is designed to has almost same detection efficiency in the range of energy 5 eV-14 MeV.

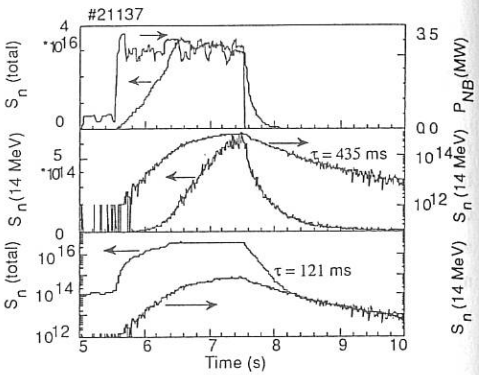


Fig.2 Typical wave forms of total and 14 MeV neutron emissions in the neutral beam heated discharge.

3. Time Dependent Analysis

We measured and analyzed the time histories of the 14 MeV emission after turn-off of the 1.5-2 second NB injection. Table 1 shows plasma parameters for three discharges analyzed here, where r_{eff} is an averaged radius weighted by the triton birth profile as

$$r_{eff} = \frac{\int r \cdot 2\pi r F_{triton}(r) dt}{\int 2\pi r F_{triton}(r) dt} \quad (1)$$

where F_{triton} is the triton birth profile calculated by the steady state version of the 1.5D tokamak code TOPICS[4] .

Table. 1 Shot list of time dependent analysis

Shot number	21137	23664	23663
Plasma current (MA)	2.2	1.5	1.5
Major radius (m)	3.13	3.19	3.46
Volume (m^3)	49	69	67
q_{eff}	4.5	6.5	5.6
r_{eff}/a	0.36	0.37	0.47
Ripple rate at r_{eff} (%)	0.02	0.06	0.2

The time-dependent 14 MeV neutron emissivity was simulated by a simple classical slowing down model. The plasma was divided into 51 annular shells in the calculation. In each shell, the tritons were divided into 500 groups according to their birth time, with 10 ms time bins. The number of tritons in a group is proportional to the 2.5 MeV neutron emissivity at the birth time of the tritons. Tritons were allowed to slow down in each shell according to the classical energy loss represented by following formula:

$$\left(\frac{dE}{dt}\right)_{classical} = -\frac{\alpha}{\sqrt{E}} - \beta E \qquad (2)$$

$$\alpha = 1.81 \times 10^{-13} \ln \Lambda_{ii} A^{1/2} Z^2 \sum_j \frac{n_j Z_j}{A_j}$$

$$\beta = 3.18 \times 10^{-15} \ln \Lambda_{ei} \frac{Z^2}{A} \frac{n_e}{(T_e)^{1.5}}$$

where E is the triton energy , T_e is the electron temperature both in eV, n_e is the electron density in m^{-3} and $ln\Lambda$ is the Coulomb logarithm. A and Z are the triton mass and charge number; n_j, A_j, and Z_j are the hydrogen and impurity density in m^{-3}, mass and charge numbers, respectively. First term of R.H.S. of the Eq(1) is the slowing down on electrons and second on is on ions.

The loss of confined tritons was taken into account assuming an exponential decay of the number of tritons of the form $e^{-t/\tau}$ where t

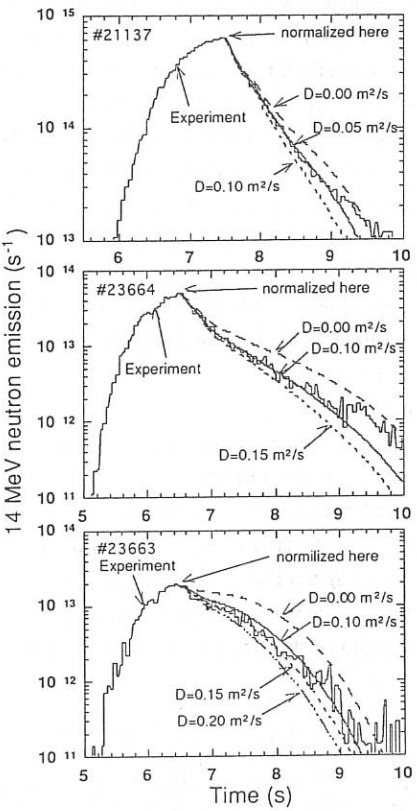


Fig.3 Experimetal and calculated 14 MeV neutron emissions for #21137,#23664 and #23663.

and τ are the time since the birth and the confinement time of the tritons, respectively. The diffusivity of fast triton, D_{triton}, was estimated by using the relation for the confinement time $\tau = a_p^2 / 5.8 D_{triton}$, to reproduce the experimental triton burnup ratio. The time history of the 14 MeV neutron emission rate was calculated by using the electron temperature profile from ECE measurement, the ion temperature profile from charge exchange recombination spectroscopy, and the electron density profile from the FIR and CO_2 interferometers as the time dependent plasma parameters. The triton birth profile was calculated using the TOPICS code for a typical time and the shape of the profile was assumed to be constant during the period of the triton burnup. The angular distribution of the tritons was assumed to be isotropic. First orbit losses were taken into account.

Figure 3 shows the experimental and calculated 14 MeV neutron emissions for three discharges listed in Table 1. Calculated curves are normalized to the experimental data at the time of NB turn-off to reject any systematic error of detection efficiencies for the total and 14 MeV neutron emissions. The fast triton diffusivity, D_{triton}, of 0.05, 0.1 and 0.15 m^2/s give a good agreement with the experimental date in shot #21137, #23664 and #23663, respectively, which indicate that D_{triton} increases with the toroidal ripple rate as shown in Fig.4.

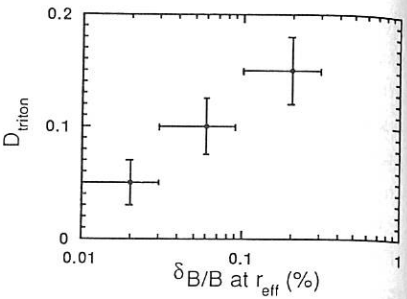


Fig. 4 Fast triton diffusivity plotted against the toroidal ripple rate at the effective minor radius of the triton birth profile.

4. Summary

The time resolved triton burnup measurements have been performed using a new type 14 MeV neutron detector based on scintillating fibers. Time histories of 14 MeV emission after NB turn-off have been analyzed based on the classical slowing down theory. Assuming the loss of fast tritons can be represented as a diffusivity, then values increasing with increasing toroidal ripple were determined between 0.05-0.15 m^2/s, form the modeling of the time histories of the 14 MeV emission after the NB turn-off. We have a plan to evaluate the fast triton diffusivity due the toroidal ripple losses using the OFMC code[5].

References

[1] G.A. Wurden, R.E/ Chrien, et al., Rev. Sci. Instrum. **66** 901 (1995)
[2] M. Hoek, T. Nishitani, Y. Ikeda, A. Morioka, Rev. Sci. Instrum. **66** 885 (1995)
[3] T. Nishitani, H. Takeuchi, et al., Rev. Sci. Instrum. **63** 5270 (1992)
[4] NAKA FUSION RESEARCH ESTABLISHMENT, Japan Atomic Energy Research Institute Report JAERI-M 91-159 (1991)
[5] K. Tani, et al., J. Phys. Soc. Jpn. **50** 1726 (1981)

COMPARISON OF JET AND DIII–D TEMPERATURE AND DENSITY PROFILE SHAPES AND THEIR PARAMETRIC DEPENDENCIES

D.P. Schissel

General Atomics, P.O. Box 85608, San Diego, CA 92186-9784

B. Schunke

Joint Undertaking, Abingdon, Oxon, OX14 3 EA, UK

Kaya Imre and K.S. Riedel

New York University, 251 Mercer Street, New York, New York 10012-1185

In the absence of a first principles understanding of the physics that governs plasma energy transport, empirical scaling relationships have been developed that describe global energy confinement. These expressions have been developed from single machine databases (with no size scaling) and in large multi-machine databases (where a size scaling can be addressed). In general, these expressions have been developed assuming a power law fit of the form

$$\tau = C_0 I_p^{\alpha 1} P_L^{\alpha P} R^{\alpha R} \ldots \quad (1)$$

Unfortunately, these expressions do not describe the radial variation of the plasma profiles and therefore neither ignition nor local transport issues can be addressed.

The goal of our work was to develop a scaling expression which adequately describes profiles in existing tokamaks and which could be used to predict plasma profile shapes and magnitudes for future devices, such as ITER and TPX, without the need for a plasma transport model. This paper presents a multi-machine feasibility study of this goal. Specifically, we present an initial assessment of an effort to derive an empirical expression for the normalized plasma electron temperature and electron density profile in terms of global quantities. We chose a form

$$T_e(\rho)/\overline{T}_e \text{ or } n_e(\rho)/\overline{n}_e = \mu(\rho) I_p^{f_I(\rho)} P_L^{f_P(\rho)} R^{f_R(\rho)} \ldots \quad (2)$$

where $\mu(\rho)$ is a fitting constant similar to C_0 in Eq. (1) but here is a function of the normalized toroidal flux (ρ). Global instead of local variables were chosen since they allowed a large enough database to be assembled for this statistical study. If this general approach appears fruitful a more detailed analysis in terms of local variables may be warranted. In Eq. (2) the exponents, $f_\ell(\rho)$, are functions of ρ in contrast to the α's in Eq. (1) which represent a constant value.

ANALYSIS

Data from both JET and DIII–D were obtained in a single-null configuration with an expanded boundary divertor. The JET H–mode data used in this study consists of 48 ELM-free discharges heated with neutral beams (NB) and combined NB and ICRH from the

1990–1991 time period. The JET experiments were carried out between 1.4 T and 2.9 T, with an I_p range of 2.0–3.0 MA, q_{95} from 3.0 to 7.0, P_{aux} from 1 to 13 MW, and an $\bar{n}_e$ of $(1.3\text{–}5.2) \times 10^{19}$ m^{-3}. The 63 ELMing H–mode discharges from DIII–D all have NB heating and a B_T parameter range of 1–2 T, I_p from 0.8–2.0 MA, q_{95} from 3.0–9.7, P_{aux} from 1–15 MW, and $\bar{n}_e$ from $(3.0\text{–}10.7) \times 10^{19}$ m^{-3}.

The unknown functions, $f\ell(\rho)$, of Eq. (2) are estimated using smoothing splines and linear regression [1]. This profile parameterization methodology has most recently been applied to JET data [2]. We consider for each machine the parameters I_p, P_L, $\bar{n}_e$, P_{RF}/P_{aux}, B_T, Z_{eff}, q_{95}, and V_L and retain only those that improved the quality of the fit as determined by the sequential selection procedure described in Ref. [1]. Our analysis indicates that for both JET and DIII–D the n_e shape is described by I_p and the T_e shape by q_{95}, P_{aux}, and P_{RF}/P_{aux}. Since our dataset contains a sufficient variation in I_p and B_T, we can contrast the q_{95} dependence with the separate I_p and B_T dependencies. Furthermore, the n_e and T_e profiles have similar $f\ell(\rho)$ dependencies in both machines. Figure 1 displays, as an example, $f\mathrm{I}(\rho)$ for DIII–D and JET n_e data. The $\mu(\rho)$ curve represents each machine's average n_e profile.

Since the same global quantities are required to describe JET and DIII–D profiles separately and the exponents $[f\ell(\rho)]$ are similar it makes sense to combine the data and determine a size scaling for the profile expressions. However, since the aspect ratio is similar for both machines an individual R and a scaling can not be determined. Instead, a general size scaling has been used and will be written in terms of R. Our analysis indicates that the n_e and T_e profiles in the combined database are well described by the same variables as in the individual fits with the addition of the size R. The variables B_T, Z_{eff}, and V_L are not important parameters for modeling our dataset. Both κ and R/a had too small a variation to be studied. Figures 2(a) and 2(b) show the $f\ell(\rho)$ and $\mu(\rho)$ dependencies for the n_e and T_e profiles respectively.

Figure 3 uses the T_e fit to give the reader a feeling for the quality of our analysis. Figures 3(a,b) show the measured T_e and the predicted profiles from our scaling expression for DIII–D and JET respectively. We evaluate the average relative error (similar to reduced χ^2) for each profile and the histogram displays [Fig. 3(c)] these values for the combined T_e fit. The location on the histogram of the two temperature profiles shown in Figs. 3(a,b) is marked by vertical arrows. More than 50% of the T_e profiles are predicted more accurately than those shown in Figs. 3(a,b). For the entire database the average relative error for the

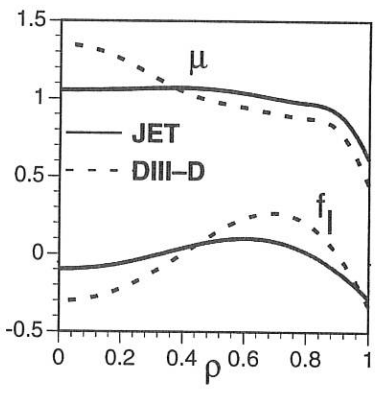


Fig. 1. JET and DIII–D n_e profiles are described in a similar way by I_p.

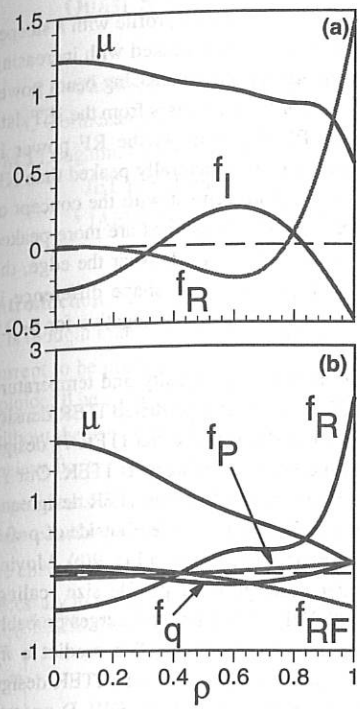


Fig. 2. (a) Density profile broadens with I_p and R. (b) Temperature profile broadens with R and becomes more peaked with I_p and P_{RF}/P_{aux}.

normalized electron density fit is 8% and is 16% for the electron temperature. Relative error tends to weight the edge more, so our predictions are significantly better than this in the core of the profile.

DISCUSSION

Our density profile parameterization [Fig. 2(a)] indicates that as the plasma current is increased, the n_e profile broadens and the edge gradient increases. This is entirely consistent with what is observed during operation of either JET or DIII–D.

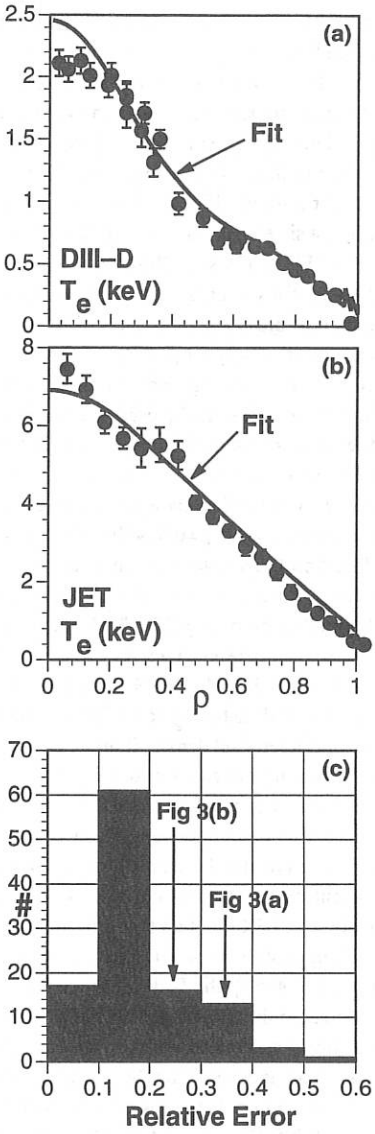


Fig. 3. (a) Sample DIII–D T_e data with our predicted value. (b) Sample JET T_e data with our predicted value. (c) Combined dataset histogram of relative error for the T_e profile fit.

With higher current comes not only more density but a broader density profile with a steeper edge gradient. In contrast the temperature [Fig. 2(b)] becomes more peaked with increasing q_{95} and RF power fraction and the T_e shape broadens slightly with increasing beam power (f_P is almost constant in ρ). The importance of the RF power fraction arises from the JET data where their experiments have shown that the T_e profile broadens as the RF power is deposited farther off-axis. In general RF power deposition is more centrally peaked than NB power deposition. The T_e profile dependence on q_{95} is in agreement with the concept of profile consistency. For both the T_e and n_e profiles, the DIII–D profiles are more peaked than the JET profiles as illustrated by the average profile (μ) in Fig. 1. Near the edge, the DIII–D profiles decrease much more than do the JET profiles. This shape difference is attributed to plasma size in our scaling expression. As a result, $f_R(\rho)$ is negative for $\rho<0.5$ and increases rapidly for $\rho>0.8$.

Similar to a scaling expression that predicts confinement, our density and temperature scaling expressions can be used to extrapolate to ITER profiles. Our predicted ITER density profile is hollow and our temperature profile has a similar shape to the flat ITER T_e design profile. We do not believe that a hollow density profile correctly represents ITER. Our T_e profile flattens (hollow by about 20%) at $\rho=0.5$ compared to $\rho=0.4$ for the ITER design and then decreases out to $\rho=0.8$ with a similar slope of the ITER design profile. Outside of $\rho=0.8$ our ITER profile substantially increases due to the increasing $f_R(\rho)$ seen in Fig. 2(b). Moving to a local variable representation may allow a better description of profile size scaling. Additionally, combining JET ELM-free discharges with DIII–D ELMing discharges probably enhances the difference in profile shape between the two machines. We predict a $\bar{n}_e$ substantially below the ITER design value and a $\bar{T}_e$ substantially above the ITER design value. Our optimistic $\bar{T}_e$ for ITER is understandable since both JET and DIII–D operate below the Greenwald density limit while ITER is designed about a factor of 2 above the limit. If we arbitrarily increase our density to the ITER design value and reduce our $\bar{T}_e$ by $1/\bar{n}_e$, as seen in DIII–D experiments, our ITER prediction is similar to their design value.

Since this technique can (1) adequately describe JET and DIII–D profiles with each machine requiring the same global parameters, (2) produce scaling behaviors that are consistent with experimental results, and (3) produce a reasonable core T_e profile shape estimate for ITER, we feel that this analysis method can be a fruitful avenue of research for describing profile behavior. Expanding to local variable analysis could begin with the n_e profile by replacing the I_p dependence with B_p or J. Additionally a specific set of discharges, for example only NBI-heated ELMing H–modes, could be gathered to eliminate some of the uncertainties associated with profile broadening in the larger machine. Future work should also focus on understanding the predicted magnitude of n_e and T_e for ITER.

This is a report of work supported by the U.S. Department of Energy under Contract No. DE-AC03-89ER51114 and Grant No. DE-FG02-86ER53223.

[1] Imre K, Riedel K S, and Schunke B (1995) *Phys. Plasmas* **2** 1614 (1995)

[2] Schunke B, Imre K, Riedel K S (1994) in Proc. 21st EPS Conf. on Contr. Fusion and Plasma Phys, Montpellier, France (European Physical Society, Petit-Lancy) Vol. 18B, p. 668.

Quasi Steady State Advanced Tokamak Scenarios in JET

C D Challis, B Balet, V P Bhatnagar, J C M de Haas, L-G I Eriksson, M Gadeberg, C Gormezano, C W Gowers, J A How, G T A Huysmans, S Ishida*, W O K Kerner, M J Loughlin, F G Rimini, G J Sadler, A C C Sips, A Tanga, B J D Tubbing and D J Ward
JET Joint Undertaking, Abingdon, Oxon, OX14 3EA, United Kingdom
* JAERI, Naka Fusion Research Establishment, Ibaraki-ken, Japan 311-01

Introduction

It is thought that a steady state tokamak reactor will need a substantial fraction of the plasma current to be provided by the neoclassical bootstrap effect. To achieve this requires that the poloidal β be significantly greater than unity which, in turn, requires good energy confinement without the use of very high plasma currents. It is likely that such a plasma would also have to achieve $\beta_N \geq 3$ ($\beta_N = \beta_T aB_T/I_p$ in %mT/MA) if very high toroidal fields are to be avoided. Experiments have been performed in JET with the demanding aim of simultaneously achieving these conditions, high β_p, high confinement and high β_N, in steady state. The investigation of the characteristics of plasmas in this domain, the so-called 'Advanced Tokamak Scenario', is necessary to assess the prospects for steady state reactor concepts.

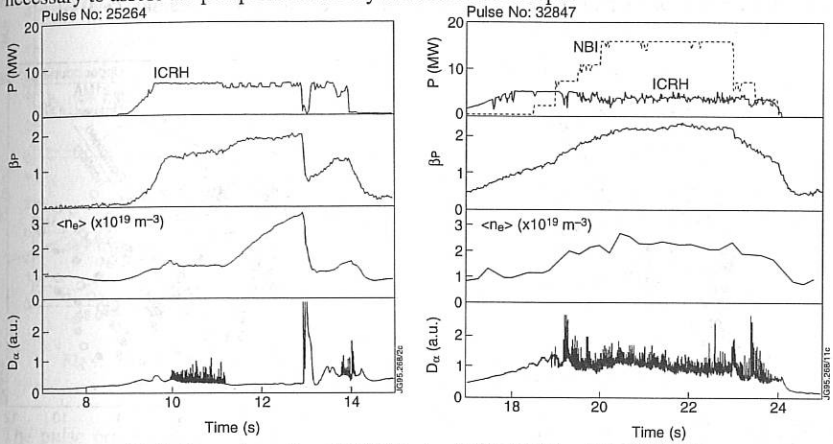


Fig 1: Comparison of two 1MA/2.8T pulses #25264(1991) and #32847(1994)

Quasi Steady State

Improved power handling has been achieved in the new JET pumped divertor configuration and has allowed long pulse high power heating of ELMy (Edge Localised Mode) H mode plasmas which reach quasi steady conditions with respect to density and plasma stored energy. Figure 1 shows the comparison between a recent high β_p plasma (#32847) and a discharge obtained

before the installation of the JET pumped divertor (#25264). Stationary conditions have been achieved in pulse 32847, whereas in pulse 25264 the density rises in the ELM free H mode until a collapse of the plasma stored energy occurs during which the density falls. The cause of this collapse has not been unambiguously identified [1], but similar values of β_p have now been achieved without either the density rise or the collapse phenomena. However, significantly higher additional heating power is required to reach the same value of β_p in the ELMy regime. This, together with the more modest plasma density in these plasmas, results in a significant fraction (≈ 30%) of the plasma stored energy being due to fast particles. The fraction of the plasma current driven by the bootstrap effect is estimated (using only the thermal pressure) to be ≈50% in the ELMy regime compared with about 70% in the ELM free experiments.

High β_p Plasmas

Figure 2 shows the achieved values of β_p plotted against q_{95}. The plasma currents were in the range I_p≈1.0-1.75MA. Approximate lines of constant β_N are shown for the JET pumped divertor configuration. A notional 'Advanced Tokamak Domain', typical of reactor concepts such as SSTR [2], is indicated. The optimum value of q_{95} depends mainly on the achievable β_N. Plasmas have been obtained approaching the overall conditions required for a steady state reactor although the bootstrap current in these plasmas is probably insufficient to provide the necessary fraction of the plasma current required for a true 'Advanced Tokamak' (>70%).

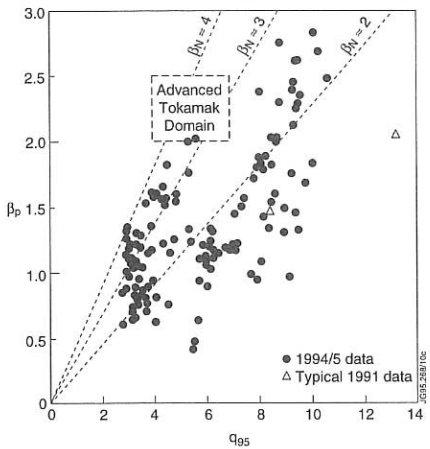


Fig 2: β_p(diamagnetic) plotted against q95

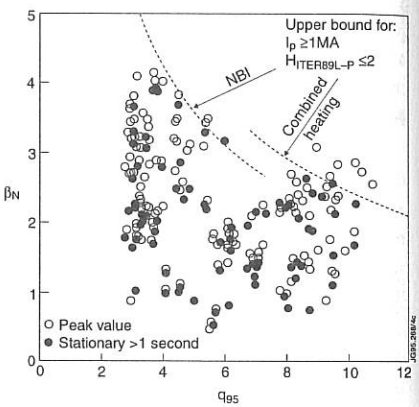


Fig 3: β_N(diamagnetic) plotted against q95

High β_N Plasmas

Figure 3 shows the values of β_N achieved in 1994/5 with I_p≈1.0-1.75MA. The curves indicate the power limit at $H_{ITER89L-P}$=2 (typical for this dataset [3]) for plasmas with I_p=1MA in both

the high and low q_{95} domains. The ITER89L-P scaling is given in ref [4]. The curves differ in the two regions since at low q_{95} the high values of β_N have been achieved with predominantly neutral beam heating (up to 20MW), whereas combined neutral beam and radio frequency heating up to 28MW has been employed at high q_{95} ($B_T > 2.6T$ at 1MA).

At high values of q_{95} the plasma performance, and hence the value of β_N, has been limited by the plasma confinement and available additional heating power. At $q_{95} < 4$, however, the plasma stored energy can exhibit confinement degradation at high heating power levels which is suggestive that a global β limit may have been reached.

Figure 4 shows the time evolution of a pulse at $q_{95} \approx 3.1$ with a plasma current of 1MA and a toroidal field of 1T where the neutral beam heating power is increased in three steps to 17.5MW. The total plasma stored energy increases at the first two power steps, but at the third step no significant further increase is observed. The maximum value of β_N is about 3.8. The frequency of the ELMs in this discharge increases at the final power step, and this may be the cause of the reduced confinement. The calculated fast ion stored energy for this plasma represents about 40% of the plasma stored energy during the high power heating phase. This results in a more modest value for β_N when only the thermal plasma energy is considered.

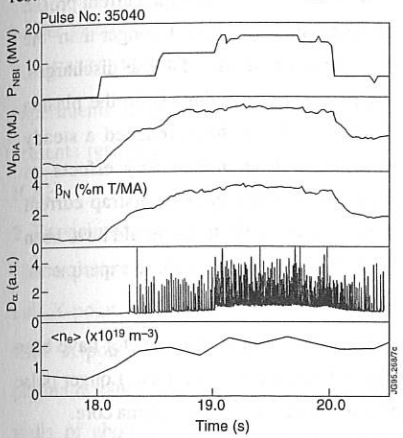


Fig 4: Time evolution of a plasma at 1MA/1T ($q_{95} \approx 3.1$)

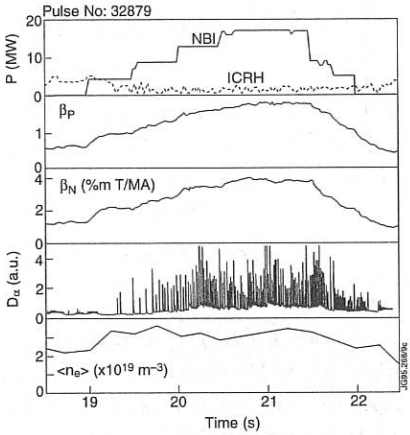


Fig 5: Time evolution of a plasma at 1MA/1.4T ($q_{95} \approx 4.7$)

The pulse presented in Fig 4 is representative of a conventional 'ITER-like' configuration ($q_{95} \approx 3.1$, elongation ≈ 1.65, triangularity ≈ 0.2). In Fig 5 is shown the time evolution of a plasma more representative of the steady state tokamak domain. In this case the plasma current is 1MA and the toroidal field is 1.4T giving $q_{95} \approx 4.7$, and a more shaped equilibrium is used (elongation ≈ 1.7, triangularity ≈ 0.4). This discharge combines high β_p (≈ 1.8) and high β_N (≈ 3.8) with $H_{ITER89L\text{-}P} \approx 2.2$ in an ELMy H mode plasma with steady density.

The pulse shown in Fig 5 achieves a similar value of β_N to that in Fig 4 despite the higher toroidal field strength and almost identical neutral beam heating power. This is due to the degraded confinement in the lower field discharge at high power. Since the high value of β_N was only just attainable at the highest power in the high field case, it is not known whether there would be degradation of confinement at still higher powers. It should be noted that the fast ion stored energy represents a smaller fraction of the total plasma stored energy in the case shown in Fig 5 ($\approx 30\%$) resulting in a higher achieved thermal β_N.

Long Pulse Experiments

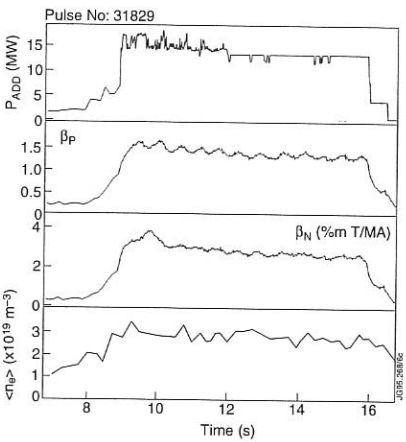


Fig 6: Long pulse plasma at 1MA/1.4T

Long pulse heating has been applied to plasmas at high β_p to assess the long timescale effects. Figure 6 shows the time evolution of a plasma with $\beta_p \approx 1.5$ and $\beta_N \approx 3.0$ maintained during a 7 second heating pulse.

Although the timescale for redistribution of the plasma current profile in the plasma core is still longer than the heating pulse length of these discharges, the plasma current density in the plasma periphery should have reached a steady value in 2-3 seconds. Any effects on stability from the edge bootstrap current density in these plasmas should have been seen on the timescale of these experiments.

Conclusion

Quasi steady state conditions approaching those required for a steady state reactor have been achieved in ELMy H mode plasmas for pulse lengths in the range 1–7 seconds. Longer pulse experiments are required to assess the effects of current redistribution in the plasma core.

An apparent global β limit has been observed at $\beta_N \approx 3.8$ with $q_{95} \approx 3.1$. Similar values of β_N were obtained at $q_{95} \approx 4.7$ but it is not possible to establish whether a β limit has yet been reached with the available heating power.

References

[1] C D Challis, et al, Nucl Fusion **33** (1993) 1097.

[2] M Kikuchi, Nucl Fusion **30**(1990) 265.

[3] A C C Sips, et al, this conference.

[4] P N Yushmanov, et al, Nucl Fusion **30** (1990) 1999.

Density Scaling of the H-Mode Power Threshold in JET

E Righi, DJ Campbell, JG Cordey, J Ehrenberg, R Giannella, J de Haas, P Harbour, N Hawkes, P Nielsen, L Porte, G Saibene, DFH Start, K Thomsen, M von Hellermann
JET Joint Undertaking, Abingdon, OXON, OX14 3EA, UK

1. Introduction

Analysis of the ITER Threshold Database revealed a linear dependence of the H-mode power threshold on the plasma density [1]. However the JET database has never been conclusive on the subject, although there was the indication of a density dependence of the H-mode power threshold, as well as of the lower threshold of H-modes produced by Ion Cyclotron Resonance Heating (ICRH) in single null X-point configuration on beryllium target plates. Since one of the crucial issues for the design of ITER is to establish field, size and density scaling of the power threshold, the ITER Confinement and Transport Expert Group has asked JET, DIII-D, ASDEX-U, JT60-U, COMPASS, C-MOD, JFT-2M, and PBX-M to carry out a series of experiments in a given ITER-like configuration with $q_{95} \cong 3$ at the transition. This paper presents results obtained on the JET tokamak using both Neutral Beam Injection (NBI) and ICRH.

2. Experimental parameters

The experiment was carried out in a single null X-point JET standard fat configuration, with X-point height of about 25cm and plasma distance from both the inner and outer walls of about 8cm. The ion ∇B drift was towards the target plates, while triangularity was kept constant at $\delta \cong 0.15$. At the transition the edge safety factor was $q_{95} \cong 3$, which allowed us to work at different combinations of toroidal field and plasma current, namely 1MA/1T, 2MA/2T, 3MA/3T. Density was increased by both gas puffing and controlled

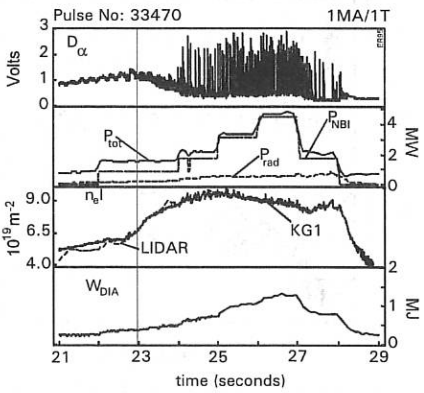


Fig.1 Transition into H-mode for a discharge in the database. KG1 here indicates the FIR interferometer.

NBI fuelling, with the cryopump at the LHe temperature. Two heating schemes were used, namely D^0 NBI and H minority ICRH in D plasmas. The present paper is focussed on the results obtained with CFC divertor target tiles and NBI. However, preliminary analysis of experiments using a Be target are reported, as well as very recent ICRH-only H-modes on Be at 3MA/2.9T. All data were taken about 30msec before the L-H transition and were validated against a dataset of L-modes.

3. Density scaling of the power threshold

The power threshold P_{th} was determined at the L-H transition as total power coupled to the plasma,

$$P_{TOT} = P_{AUX} + P_{OHM} \ , \qquad (1)$$

where P_{AUX} is the power of the auxiliary system used (ICRH or NBI), while P_{OHM} is the Ohmic power input; or as power flux through the separatrix,

$$Q_{NET} = (P_{TOT} - P_{RAD}^{bulk} - dW_{DIA} / dt) / S \ , \qquad (2)$$

with P_{RAD}^{bulk} total radiation emitted by the bulk plasma, while dW_{DIA} / dt is the slope of the diamagnetic energy, and $S \cong 140\ m^2$ is the plasma surface area. As shown in Fig.2, the threshold has an approximately linear dependence on $< n_e >$. Departure from the linear scaling is evident for the 3MA/3T data at low and high densities (Figs.2,3). Analysis is in progress to estimate in the low density range the amount of NBI shine through, which could reduce P_{TOT} by up to 20%. Note also that the ICRH data indicate a power threshold somewhat lower, in agreement with results from the 1991-92 database [2]. Also,

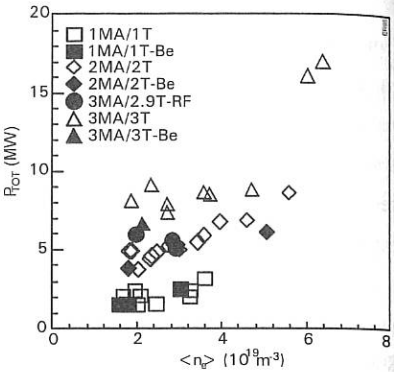


Fig 2 H-mode power threshold scaling with volume averaged density. Data have been obtained with NBI and CFC target (open symbols), Be target (filled symbols), and ICRH on Be (filled circles).

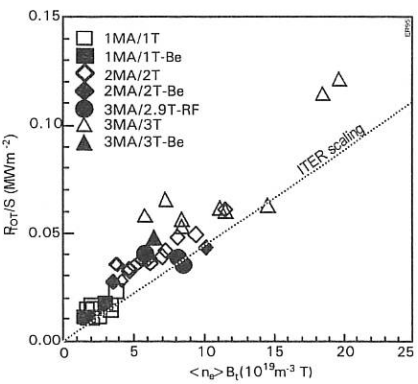


Fig.3 The data roughly agree with the ITER scaling [1], with the exception of some of the 3MA/3T data.

there is no appreciable difference in P_{th} with either Be or CFC tiles and NBI heating, although at high $<n_e>$ no data exist. The dependence of P_{th} on B_t and $<n_e>$ has been determined through nonlinear regression analysis:

$$P_{TOT} \propto B_t^{1.19} <n_e>^{0.74}, \quad (3)$$

$$Q_{NET} \propto B_t^{0.63} <n_e>^{0.88}, \quad (4)$$

similar to dimensionally correct forms of the H-mode power threshold [3,4].

4. Edge measurements

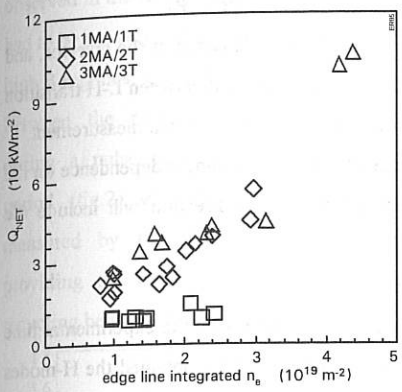


Fig.4 Net power flux through the separatrix as a function of edge line integrated density (CFC data).

In this section are summarised the first partial results obtained from the measurement of edge electron density and temperature, and neutral flux at the divertor, thought to be relevant to the understanding of H-mode transition physics. Line integrated electron density at the plasma edge (R=3.75m) was obtained and cross-checked using both the LIDAR Thomson scattering diagnostic and the Far Infra Red (FIR) interferometer. These measurements show that the power flux Q_{NET} depends roughly linearly on the edge density n_{ea} for the 2MA/2T and 3MA/3T data, while the 1MA/1T series shows a much weaker dependence (Fig.4). Moreover, the B_t scaling at the plasma edge is not so clear-cut as in Fig.2: in particular, there is no clear distinction between the 2MA/2T and 3MA/3T data. On the other hand the dependence of Q_{NET} on the neutral flux, obtained with pressure gauges in the divertor [5,6], is weaker than that with n_{ea}, while that on B_t is clear.

The electron temperature was measured at R=3.6m, for B_t=2,3T with the heterodyne radiometer, and at R=3.75m, for B_t=1,2,3 T with LIDAR. T_{ea} shows a nonlinear dependence on both n_{ea}, and B_t, the latter indicating the importance of Larmor radius.

5. Conclusions and future analysis

The power threshold, expressed both as P_{TOT} and Q_{NET}, depends roughly linearly on $<n_e>$ and on n_{ea}, although there are deviations from linearity at low and high densities. Scaling with B_t is

evident with P_{TOT}, not so much with Q_{NET}. The database is roughly in agreement with the ITER scaling, although deviations exist for low and high densities (Fig.3).

Results of regression analysis are similar to dimensionally correct forms of P_{th} [3,4].

Similar discharges carried out on CFC and Be divertor target plates show no significant difference in the power threshold. No data however were obtained at high densities ($< n_e > \geq 6 \times 10^{19}$ m^{-3}) with Be.

ICRF-only H-modes on Be target show a lower power threshold. Future analysis will compare ICRH and NBI produced H-modes to clarify the reasons for the different P_{th}.

Q_{NET} shows a mildly nonlinear dependence on the neutral flux as measured at the divertor, and a roughly linear scaling with B_t. However a link needs to be established between L-H transition and recycling conditions at the edge, of which the particle flux is only a partial measurement.

Measurements of electron temperature at the plasma edge show a nonlinear dependence on the the edge density and the magnetic field. Further analysis in this direction will include the scaling of T_{ea} with B_t at the plasma edge.

Acknowledgements

The authors acknowledge the collaboration of Task Force D, who gave the experimental time and expertise to carry out the experiments, and of Task Force T, who obtained the H-modes with ICRH-only.

References

[1] R Ryter and the H-mode Database Working Group, Proc. 20th EPS Conference on Controlled Fusion and Plasma Physics, Lisbon, Vol.17C, part I,15 (1992).

[2] DFH Start *et al.*, Proc. 21st EPS Conference on Controlled Fusion and Plasma Physics, Montpellier, France, Vol.18B, part I, 314 (1994).

[3]W Kerner, JG Cordey, O Pogutse, E Righi, These Proceedings.

[4] F Ryter and the H-mode Database Working Group, to be submitted to Nuclear Fusion.

[5] G Saibene *et al.*, These Proceedings.

[6] J Ehrenberg *et al.*, These Proceedings.

The Optimization of Recycling in High Performance Hot-Ion H-Mode JET Discharges

K D Lawson*, N Deliyanakis, N C Hawkes, M G von Hellermann, T T C Jones,
R W T König, P J Lomas, A C Maas, F B Marcus, R Sartori, B Schunke,
P Smeulders, M F Stamp and P R Thomas

JET Joint Undertaking, Abingdon, OX14 3EA, UK
*UKAEA Government Division, Fusion, Culham, Abingdon, OX14 3DB, UK
(UKAEA/Euratom Fusion Association)

Introduction In hot-ion H-mode high performance discharges an immediate difference was observed in the frequent ELM behaviour compared with earlier operations in which the ELMs had to be actively induced through strong gas-puffing, the use of hydrogen fuel or operation in high β regimes. Correlations have been found between the peak reaction rate achieved during a pulse (fig.1) and the ELM free period (fig.2) with the particle influx as measured by the D_α line intensity, this providing the impetus for a study of the recycling behaviour in these discharges.

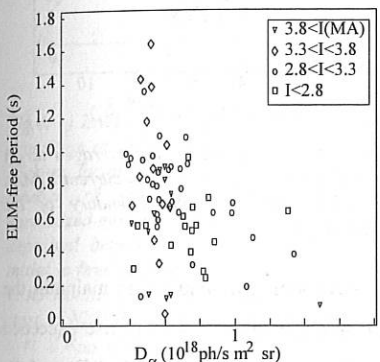


Fig.2: ELM free period vs vertical D_α intensity sorted by plasma currrent I (MA)

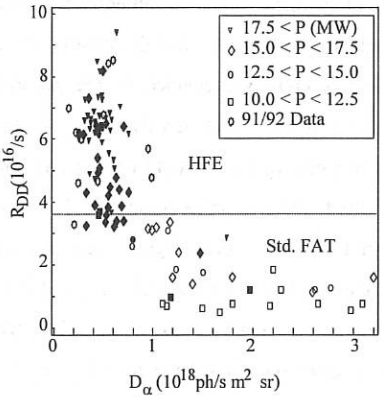


Fig.1: DD reaction rate vs vertical D_α intensity sorted by neutral beam input power P (MW) for High Flux Expansion (HFE) and standard FAT configurations. Filled symbols refer to pulses with cryopump.

Detailed modelling of the recycling can be found in [1]. Conditioning has been achieved by D and He GDC and the use of 2 or 4 Be evaporators. The divertor cryopump became available in August 94 and the improvement in pumping is evident from fig.1 which includes pulses with and without cryopump. A clear reduction in the particle influx is normally observed when the cryopump is used (see also [2]). Fig.1 also has data from some of the best high performance discharges run during the 1991/92 operations. The D_α line intensity is comparable with measurements for the best pulses in the 1994/95 campaign.

Configuration In the 1994/95 campaign, even when low recycling was achieved, only a change of the magnetic configuration from the 'Standard FAT' to a 'High Flux Expansion' (HFE) configuration allowed access to a high performance regime with reaction rates $> 3.5\times10^{16}$ s^{-1}. This change was due to improved stability against ELMs as evidenced by an increase in the ELM-free period, this hardly exceeding 0.5 s in the 'standard FAT' configuration. Higher triangularities and elongations were achieved in the HFE configuration which have a stabilizing effect on edge pressure gradient driven modes due to the higher edge shear. Although the optimization of these parameters was found necessary for the achievement of long ELM-free periods, other parameters must be considered to explain the wide range of performance subsequently achieved.

Beam deposition Of crucial importance in achieving high performance in the hot-ion regime is a low target density, which in the present campaign, is limited by the maximum permitted beam shine-through. This is illustrated in fig.3, this diagram including all of the best 30 pulses of the current operations. A low target density requires a sufficiently low level of recycling. In pulses having the best conditioning, the increase in the total D count corresponded to or could even fall below the beam fuelling rate. In the highest performance pulse 33643, the pumping is so strong that the beam fuelling is insufficient and D gas fuelling is required to maintain the plasma density. More usually in these hot-ion H-mode discharges the density rise exceeded the beam fuelling rate by ~3-4$\times10^{20}$ particles/s. An extensive investigation of the effect of the particle influx on the beam deposition and n_e profiles showed no marked dependence, fig.4. The effect of beam deposition on the neutron emission profiles is discussed in [3]. A clear effect is seen on the neutron emission profile but not on the total neutron yield. The evolution of the n_e and beam deposition profiles are illustrated for the highest performance pulse 33643. This is a 3.7 MA discharge, with D fuel and 18.5 MW of D NBI. An overview of the plasma parameters is shown in fig.5. In fig.6, it can be seen that, as n_e rises, the beam particles are

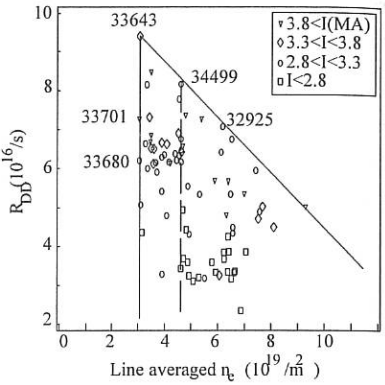


Fig.3: DD reaction rate vs line averaged target electron density sorted by plasma current I (MA). The solid lines mark the boundary of the operational space

deposited increasingly towards the plasma edge. The same behaviour is found for the power deposition profiles. This effect is summarized in the deposition profile ratios shown in fig.7 for the pulses along the sloped boundary marked in fig.3. It is observed that the turnover in R_{DD} occurs at a ratio of ~2-3. The edge pressure gradients are determined from LIDAR n_e and T_e measurements and charge exchange spectroscopy n_i and T_i data which come from a new high resolution edge diagnostic. When data from reflectometry and hetrodyne ECE radiometry are available these are included in the calculation of the pressure profile. The best available edge pressure gradients are shown for the same pulses in fig.7. A correlation is observed between the duration of the threshold ELMs and the delay in the rise of the beam deposition ratios. The longer

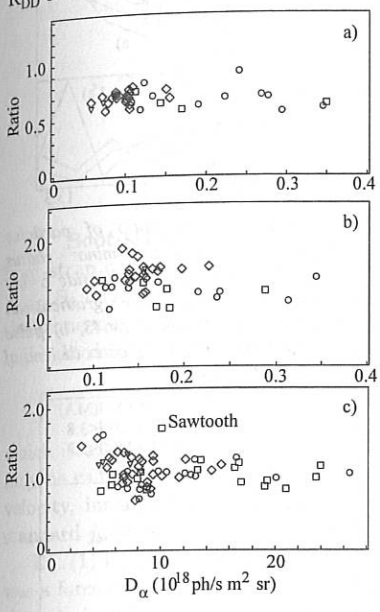


Fig.4: a) Inverse peaking factor of beam particle deposition at start of NBI vs horizontal D_α. The peaking factor is defined as the ratio of the number of particles deposited between a normalized minor radius of 0.0 and 0.55 to those deposited between 0.55 and 0.85. b) Ratio of initial to final peaking factors of beam deposition vs horizontal D_α. The initial value is taken at the start of NBI; the final value is taken at the roll-over of R_{DD}. c) Ratio of initial to final n_e peaking factors vs divertor D_α. The peaking factor of n_e is defined as the ratio of electron density integrated between a major radius of 3.25 m and 3.35 m to the electron density integrated between a major radius of 3.65 m and 3.8 m.
Figures sorted by peak R_{DD}, ▽ $8\times10^{16}\leq R_{DD}$, ◇ $6\times10^{16}\leq R_{DD}<8\times10^{16}$, ○ $4\times10^{16}\leq R_{DD}<6\times10^{16}$, □ $R_{DD}<4\times10^{16}$.

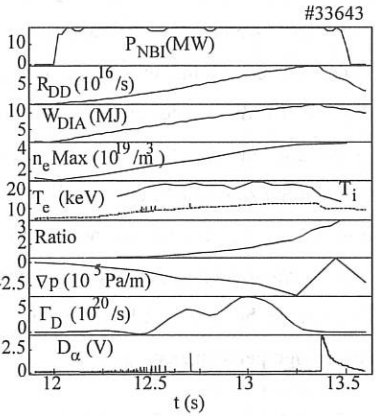


Fig.5: Overview of plasma parameters for pulse #33643, neutral beam power, DD reaction rate, total stored energy from the diamagnetic loop, maximum electron density from LIDAR, electron and ion temperature, ratio of particles deposited between normalized minor radius ρ=0.7 and ρ=1 to those deposited inside ρ=0.3, electron + ion pressure gradient at R=3.77 m, deuterium gas influx rate, vertical D_α intensity.

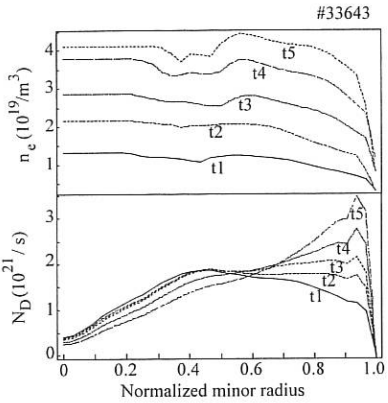


Fig.6: Electron density and calculated neutral beam particle deposition (integrated over flux surface) profile evolution vs normalized minor radius at t1=12.0 s, t2=12.4 s, t3=12.8 s, t4=13.1 s, t5=13.3 s.

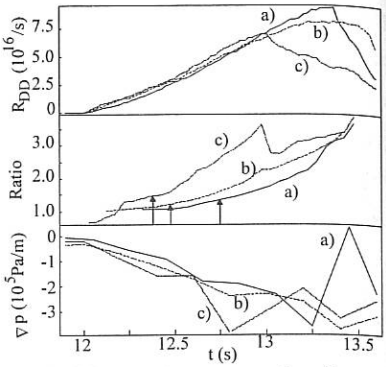


Fig.7: DD reaction rate, ratio of particles deposited between normalized minor radius ρ=0.7 and ρ=1 to those deposited inside ρ=0.3 and electron + ion pressure gradient at R=3.77 m vs time for a) pulse 33643, b) pulse 34499, c) pulse 32925. The ↑ indicates the end of the threshold ELM period.

this delay the more the terminating instabilities are postponed and the higher the neutron yield. Among such instabilities, of particular concern in the present discharges are the giant ELMs [4] and the slow rollovers [5]. Choosing pulses at a constant target density, the threshold ELM duration shows a relation to the particle influx as measured by D_α, fig.8, this being a possible additional explanation for the benefit of low recycling in achieving high performance.

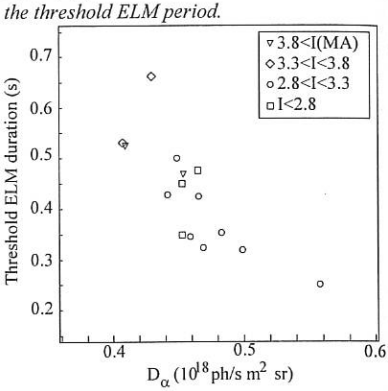


Fig.8: Duration of threshold ELMs vs vertical D_α sorted by plasma current I (MA), at constant target density for pulses along dashed line of fig.3.

Conclusions The performance of hot-ion H-mode discharges depends crucially on the lowest target densities being achieved, this requiring low recycling. Although no correlation has been found between the deposition of neutral beams and recycling, a tentative relation is suggested between recycling and the duration of the threshold ELMs. These delay the unfavourable build-up of beam deposition in the plasma edge, which leads to the onset of the terminating instabilities.

[1] K McCormick et al., [2] G Saibene et al., [3] F Marcus et al., [4] T Hender et al., [5] P Smeulders et al., 1995, all this conference

Ohm's Law For Tokamaks and Toroidal Current Drive by Radial Plasma Flow in Pellet Injection Experiments

S.G. Kalmykov, A.F.Ioffe Physical-Technical Institute
V.Yu. Sergeev, State Technical University
St.Petersburg, Russia

1. **Boot-strap current and the radial plasma flux.** The fact that the boot-strap current is related to the radial velocity of the neoclassical diffusion, $j_{bs} \sim V_{r,diff} B_\theta / c$ (B_θ is the poloidal magnetic field component), might be deduced even from the pioneering works of A.A.Galeev and R.Z.Sagdeev [1]. In [2,3] this relation is more highlighted by means of another formulation of Ohm's law for the toroidal current

$$j_z = \sigma_{\parallel Sp}(E_z + V_r B_\theta / c), \; j_{pfd} = \sigma_{\parallel Sp} V_r B_\theta / c, \tag{1}$$

which is entirely equivalent to the "standard" form $j_z = \sigma_{neo} E_z + j_{bs}$. In Eq. (1) j_{pfd} may be called "plasma flux driven current" because it is proportional to the net radial velocity, including both the neoclassical diffusion and the Ware pinch, whereas the standard j_{bs} is only the "diffusion driven current".

Eq. (1) looks like as if the toroidal component of the Lorentz electric field, $V_r B_\theta / c$, was a force driving the current j_{pfd}. This may be explained in a simplified way [4] with the aid of a poloidal sign dependent force, $F_\theta = -\nabla_\theta p_i - en\,\partial\phi/\partial\theta + ...$ (ϕ is the plasma potential). It originates from induced by the $gradB$ drift poloidal variations of plasma pressure and potential. Then, in the frames of the MHD approximation, F_θ projection onto the magnetic field line will maintain j_{pfd}: $R_{pfd} = -nej_{pfd}/\sigma_{\parallel Sp} = -F_{\theta\parallel}$ (R_{pfd} is the ion-electron friction force), but the transverse component induces the radial particle flux: $\Gamma_r = nV_r = cF_{\theta\perp}/eB$. Eliminating F_θ from the both latters, obtain $R_{pfd} = -neV_r B_\theta / c$.

However, actually the transport in tokamaks is very far from to be neoclassical. Thus, under quasi-stationary OH conditions in the tokamak T-10 (see Part 2) the velocities at $r/a = 0.5$ are: $V^{neo}_{r,diff} \approx 3$cm/s, $V^{neo}_{r,pinch} \approx -16$cm/s (!) whereas experimentally $V^{exp}_{r,total} \approx 3-10$cm/s. In such "distorted" situation j^{neo}_{bs} calculations, performed for many tokamak experiments and using neoclassical formulae [5], seem to be rather doubtful.

The Ohm's law formulation of Eq. (1), where V_r was *the velocity of actual plasma flux deduced from the experimental data*, has been successfully applied to explain "anomalies" in the loop voltage behaviour in experiments on off-central pellet injection in the tokamak T-10 [6].

2. **Experimental evidences.** In the experiments mentioned in [6] (Sh. 49961, $R_0 = 150$cm, $a = 28$cm, $B_t = 30$kG, $I_{pl} = 200$kA, D_2), small pellets of LiD and of H_2 evaporated somewhere half way towards the center of the discharge. They weakly

disturbed the plasma and caused by them large increase in the loop voltage could be explained neither by the weak and transient electron temperature decrease nor by the vanishing variation in effective ionic charge (Fig. 1). In Fig. 2 results of loop voltage simulations are shown together with supposed boundary temperature variations, $T_e(a,t)$, which were not measured experimentally. The simulation took into account variations of plasma conductivity, induced by the change in T_e, n and Z_{eff}, and inductive effects due to the accompanying modification of current density radial profile but assumed no plasma motion. From the above it is clear that the plasma voltage behaviour required a nontrivial explanation.

In contrast to the temperature, the profile of plasma density exhibited stronger variations (Fig. 3). Such an evolution suggested that a plasma influx arose, at least, in an inner part of the discharge where the ionization rate $S_i \ll \partial n/\partial t$. Two velocity profiles for such an influx taken at $t = 567$ms are presented in Fig. 4. They were derived as $V_r(r) = -(\int_0^r \partial n/\partial t\, r dr)/(nr)$ at different assumptions about boundary of the area where S_i might be neglected: $r/a \leq 0.55$ (curve 1) and $r/a \leq 0.67$ (curve 2). These velocities have been used in Ohm's law (Eq. (1)) which was incorporated into the loop voltage simulation model. The results of the simulation are displayed by dashed curves in Fig. 5. The current, driven by the actual plasma flux, is very likely to be the explanation required. Velocities obtained by taking into account the ionization rate contribution (see [6]), $V_r(r) = (\int_0^r (S_i - \partial n/\partial t) r dr)/(nr)$ (in Fig. 4 curve 3 for $t = 567$ms and curve 4 for the quasi-stationary OH stage at $t = 560$ms, and the time evolution $V_r(r = 12\text{cm},t)$), have provided the good agreement between simulated (Fig. 5 , black dots) and experimental (solid line) loop voltage waveforms.

The currents j_{pfd} were calculated for the both quasi-stationary and dynamic phases. In Fig. 6 they are compared with the net plasma current density, j_{pl}, and with neoclassical j_{bs}^{neo} estimated by using formulae [5]. At the steady state j_{pfd} is distributed more peripherically than j_{bs}^{neo} but its total value is three times as much as the latter.

The "anomalous" loop voltage behaviour suggesting the influence of the current, driven by the actual plasma flux, has also been observed in other dynamic experiments: in the off-central injections of small pellets in T-10 [6] and in TUMAN-3 tokamak [7], and in pre-programmed current ramp-down in T-10 (not yet published).

3. **Is the current driven by the actual plasma flux compatible with the neoclassical physics?** The question arises if such substantially modified j_{pfd} (Fig. 6) is compatible with the neoclassical mechanisms. The response may be positive because j_{pfd} is defined, in addition to the magnetic configuration, by the plasma potential space variations (see Part 1). As soon as the potential is distorted, both the radial flux and the boot-strap current will vary proportionally keeping to be quite neoclassical. A little change in relative velocity of electrons and ions in their ambipolar flow seems to be sufficient to produce a significant plasma potential variation. Such a change might be provoked by some non-stationary intervention into the discharge or/and by a relatively weak turbulence which played then role of a "trigger". Thus, to explain both V_r and j_{pfd} in the experiments above described, the equivalent poloidal electric field, $E_\theta = F_\theta/ne$, should be about -13mV/cm ($\phi_{top-bottom} \sim 0.5$V) at $r/a = 0.5$ for the dynamic phase when the particle flux flowed inwards. At the plasma column periphery, where $V_r \approx 100 - 150$cm/s, $E_\theta \sim 40$mV/cm and $\phi_{top-bottom} \sim -3.5$V. Of course, a direct

influence on the transport accompanied no contribution to the boot-strap current may not be excluded for the case of a strong turbulence.

4. **Plasma flux driven current in the $L \rightarrow H$ transition.** The chain of events occurring at the $L \rightarrow H$ transition [8] suggests noticeable variations in j_{pfd} as well. It starts with a dramatic alteration in the plasma potential value and even in the sign, what reveals itself through the change in the poloidal plasma rotation. Then the plasma outflux drops; in [7] even the inversion of the radial particle flux has been observed. The loop voltage increase happened there also. It might be related to the j_{pfd} inversion but the authors of [7] have explained it by a hypothetical boundary temperature depression ($T_e(a)$ was not measured in the experiment).

References

[1] A.A.Galeev, R.Z.Sagdeev. In: Rev. of Plasma Phys., edited by M.A.Leontovich (Consultant Bureau, N.-Y., 1979), v.7, p.257.

[2] J.-S.Kim, J.M.Green. Plasma Phys. Control. Fusion **31** (1989) 1069.

[3] S.E.Segre, V.Zanza. Nucl. Fusion **31** (1991) 819; **32** (1992) 1005.

[4] V.A.Rozhanskii. State Tech. Univ., St.-Petersburg, Russia. Personal comm., 1995.

[5] F.L.Hinton, R.D.Hazeltine. Rev. Mod. Phys. **48** (1976) 239.

[6] S.G.Kalmykov et al.. To be published in Nucl. Fusion **35** (1995) No.7.

[7] M.V.Andrejko et al.. Plasma Phys. Control. Fusion Research 1992 (14th IAEA Conf. Proc., Würzburg, 1992), Vienna, 1993, v.1, p.485.

[8] R.J.Groebner. Phys. Fluids B **5** (1993) 2343.

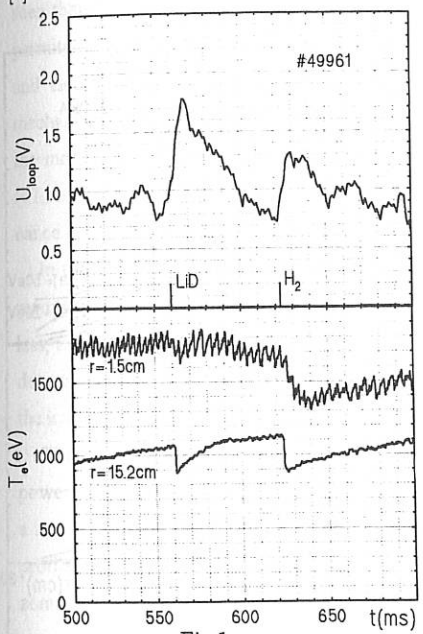


Fig.1

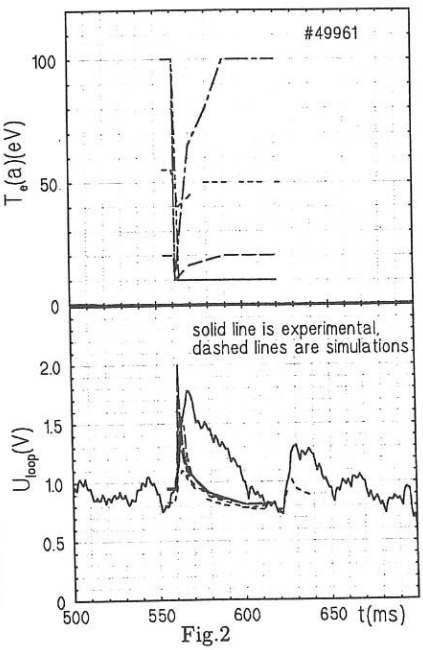


Fig.2

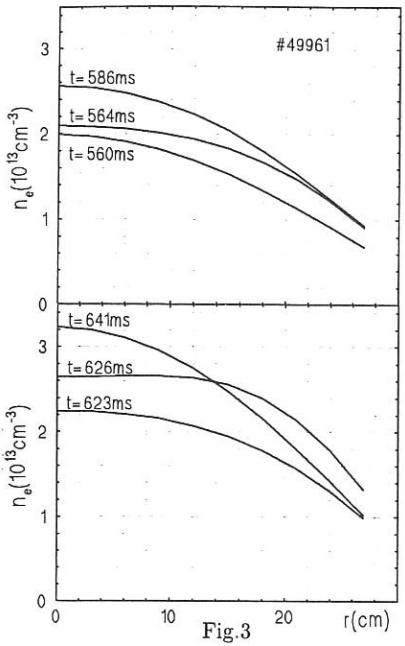


Fig.3

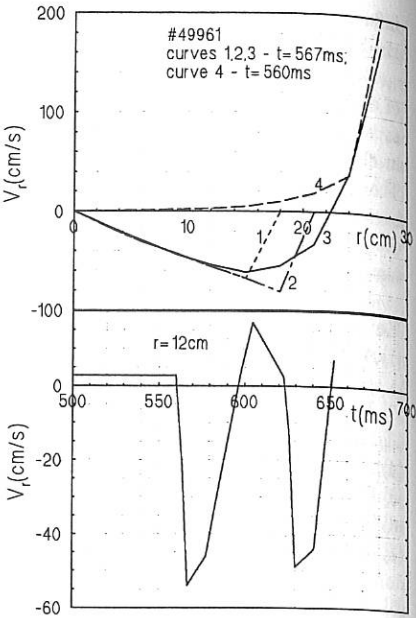


Fig.4

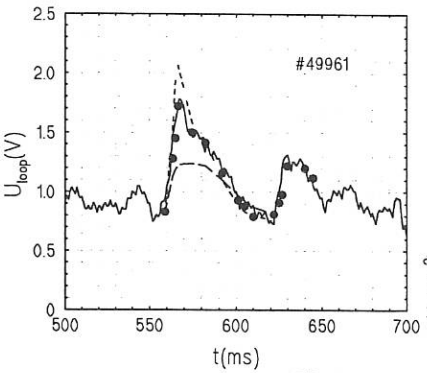


Fig.5

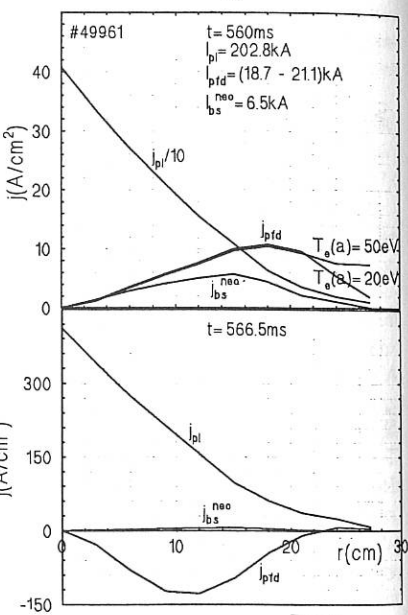


Fig.6

Electrons and Ions Heating and Improved Confinement Regime in Lower Hybrid Heating Experiments on FT-2 Tokamak.

V.N.Budnikov, G.I.Chashchina, V.V.Dyachenko, L.A.Esipov, M.A.Irzak, E.R.Its, **S.I.Lashkul**, A.D.Lebedev, K.A.Podushnikova, O.N.Shcherbinin, V.Yu.Shorikov, A.Yu.Stepanov.

A.F.Ioffe Physico-Technical Institute, 194021, St.Petersburg, Russia.

In the previous lower hybrid (LH) heating experiments on FT-2 tokamak the effective heating of electrons and ions has been observed [1]. The general scheme of the plasma-wave interaction is shown in Fig.1. The loop voltage drop $\Delta U_L/U_L$ — (1), charge exchange fluxes at energies 1.5 — (2) and 3.7 keV — (3), the derivative dT_e/dt — (4) for the moment of LH pulse switch on, electron and ion temperature increase ΔT_e — (5) and ΔT_i — (6) with respect to the end of LH pulse are presented here as a function of current density. $\Delta U_L/U_L$ represents the current drive efficiency and dT_e/dt — the power transfer to the bulk electrons. For these characteristics n_0 is the central plasma density at the moment of LH pulse switch on. It can be seen that the electron heating and the fast ion generation begin at the same density. This fact permits us to make the conclusion about the same mechanism of wave interaction with ions and electrons for the densities $n_0 > n_d$. According to our previous investigations [2] this mechanism is associated with the parametric decay of the pump wave f_0. The ion heating with the most efficiency occurs for the densities, when the energy input to the electrons vanishes ($dT_e/dt = 0$) and can be explained by the classical mechanism due to the fulfillment of LH resonance condition in plasma center.

In the experiments described below we planned to confirm and to investigate in detail the regime of the effective plasma heating, but, unfortunately, we failed to reproduce it. Nevertheless, the data obtained in these experiments seems to be very useful for heating mechanism understanding and, as we hope, permit us to find that "latent" parameter, which is responsible for the irreproducibility of the LH heating experiments [1].

The experiment's conditions are described in rep. EPS 22/329, this conference. The RF power 100 kW at a frequency 920 MHz was launched from the outer side of the torus through a two-waveguides grill and exceeded the ohmic heating power (60–80 kW). Ion temperature profiles and fast ion fluxes were registered by two movable charge exchange analyzers in horizontal and vertical directions. The measurements in all directions gave the coinciding results.

The main result of these experiments is the observation of the influence of the electron temperature upon the wave absorption process. Electron temperature depended upon the quality of the chamber wall cleaning during the set of experiments. Fig.2, 3 and 4 show three different T_i profiles at RF heating, obtained by chord scanning of CX analyzer. Fig.3 and Fig.4 referred to the described set of experiments. For the same values of n_e, B_t, I_p and P_{RF} = 100 kW $Ti(r)$ profile in Fig.4 is considerably broader than in Fig.3. The narrow $T_i(r)$ profile (Fig.2) have been obtained in the previous set of experiments [1], characterized by high electron temperature $T_e \approx 700$ eV, high value of $Z_{eff} \approx 3$, but low radiation losses. The common discharge (Fig.3) had high radiation losses, $T_e \approx 500$ eV and $Z_{eff} \approx 3$. The lowest value of the electron temperature was observed in the "clean" discharge: $T_e \approx 350$ eV, $Z_{eff} \approx 1.8$, Fig.4. For this case the ion temperature had been also checked by the Doppler broadening of OV line (278,1 nm), Fig.6. It should be noted that during RF heating the emissivity position of this line change phase due to the electron temperature increase. Time behavior of $T_e(r)$ for the described discharge types is presented in Fig.5. Thus, when the central electron temperature is rather high, the pump wave reaches the center yielding the high heating efficiency. The curves marked in Fig.5 by I, II and III correspond to experimental conditions of Fig.2, 3 and 4, respectively. The modification of the discharge type influence also upon the **characteristic** density n_d. In the experiments [1] the threshold density n_d was $2.9 \cdot 10^{13}$ cm^{-3} (Fig.1). While the transition from "dirty" to "clean" discharge happens, n_d decreases from $1.8 \cdot 10^{13}$ cm^{-3} to $1.3 \cdot 10^{13}$ cm^{-3}.

We associated the fast ion generation with the parametric decay instabilities [2]. A necessary condition for developing these instabilities is the exceeding of the threshold for the wave power $P_{th} \approx T^{\alpha}/n^{\beta}$ [3], where α, β = 1–1.5 depend upon the type of instability. When the electron temperature decreases the pump wave decay region shifts to the lower density, which is reflected in the broader Ti profile and lower n_d. **Thus, the sought-for "latent" parameter, responsible for the irreproducibility of LH experiments seems to be the electron temperature.**

We have reported earlier about the observation of the transition to an improved confinement regime in LH heating experiments [4]. In the post-heating stage MHD activity and H_β line emission decreased, while total diamagnetic signal rose. The energy confinement time increased by the factor of 2–3. We have observed also the ELMs (edge-localized relaxation modes), which often arise in the improved confinement regime and reveal themselves as outbursts on H_β line emission and SXR signal, Fig.7a. H_β radial profiles, registered by the rapid scanning optical system, also modified during transition to the improved confinement regime,

Fig.7b, where 1, 2, 3 point to the moments of H_β profile scanning. The above mentioned modification of $H_\beta(r)$ are more distinct in the electron drift direction.

Cross-correlation analysis of magnetic probes signals indicates to the decrease of the electron poloidal rotation velocity at the plasma periphery in LH heating regime: $V_\vartheta^e(\mathrm{OH}) \approx 7\cdot10^5$ cm/s, $V_\vartheta^e(\mathrm{LH}) \approx 5\cdot10^5$ cm/s. In the post-heating phase, when the improved confinement regime is observed, poloidal velocity has the same value. It should be noted, that both magnetic probes signals and microwave reflectometry data show that electrons poloidal rotation velocity $V_\vartheta^e = V_E + V_{dr}^e$ increases from the center to the periphery and for the radii $r > 4$ cm exceeds the electron diamagnetic velocity, $V_{dr}^e(4\text{ cm}) = 3\cdot10^5$ cm/s. It testifies to the significance of the radial electric field at the plasma periphery. During LH pulse V_{dr}^e also rises up to the value $5\cdot10^5$ cm/s on the radius 4 cm. Unfortunately, up to now we have no data concerning V_ϑ^e for $r < 4$ cm. But the estimations of the impurity rotation velocity, obtained by the Doppler shift of OV line, indicate at the absence of noticeable influence of the radial electric field on plasma rotation in the center of the discharge. During LH heating the poloidal rotation velocity in $r < 4$ cm region rises due to the increased diamagnetic velocity and for $r > 4$ cm decreases due to the damping in the radial electric field. The poloidal rotation shear at the plasma periphery can be responsible for the appearance of the characteristic indicator of the improved confinement regime — the suppression of MHD oscillations on the frequencies up to 500 kHz. Such suppression have been observed by magnetic probes, enhanced scattering of microwave radiation method and reflectometry technique.

The research described in this publication was made possible in part by Grant #23000 from the ISF and by Grant #95-02-04072-a from Russia FS.

References

[1] V.N.Budnikov, V.V.Dyachenko, L.A.Esipov et al. Proc. of the 21st Europ. Conf. on Controlled Fusion and Plasma Physics, Montpellier, **18B**, part II, EPS, 1028, (1994).

[2] V.N.Budnikov. Nuclear Fusion, **31**, 611, (1991).

[3] M.Porkolab. Phys. Fluids, **17**, 1432, (1974); Phys. Fluids, **20**, 2058, (1978).

[4] V.N.Budnikov, V.V.Dyachenko, L.A.Esipov et al. Pis'ma v ZhETF, **59**, #10, p.651–654, (1994).

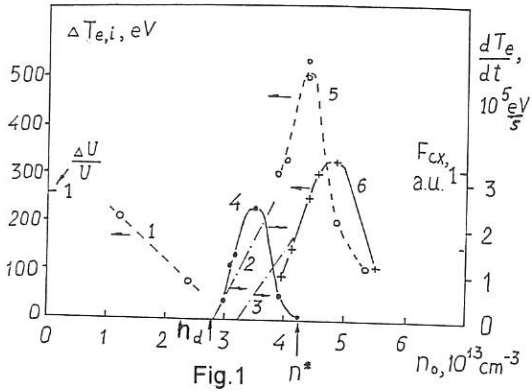


Fig.1

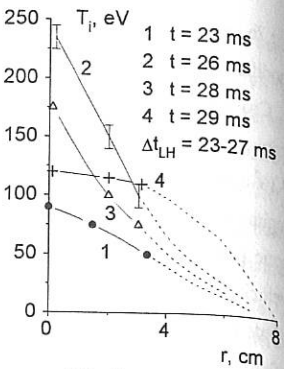


Fig.2

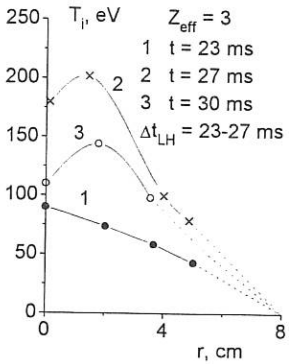


Fig.3

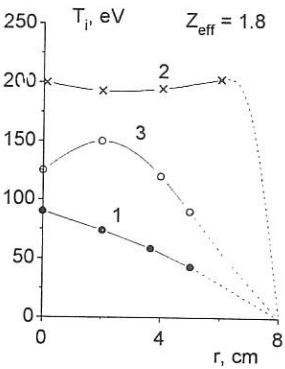
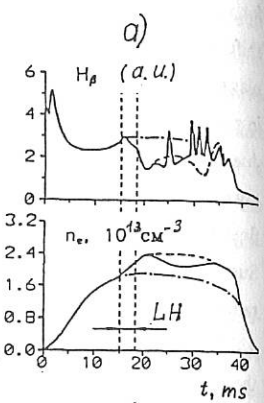


Fig.4



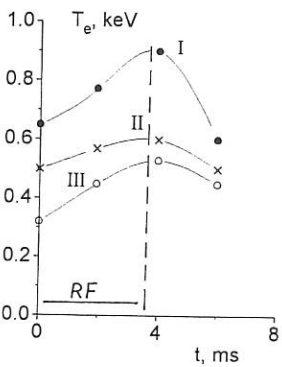


Fig.5

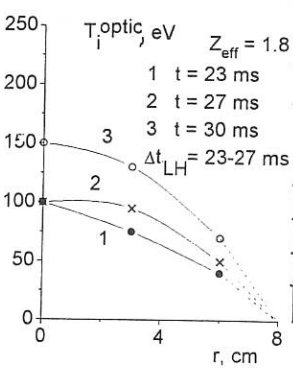


Fig.6

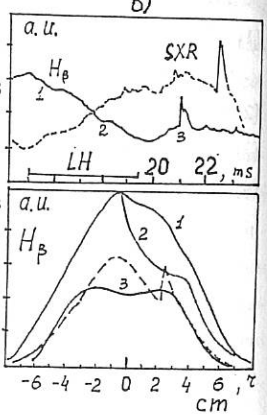


Fig.7

Microwave Backscattering Experiment in Ohmic H-Mode Discharge in Tuman-3 Tokamak

V.Bulanin, D.Korneev, V.Rozhansky, M.Tendler*
State Technical University, St. Petersburg, Russia
*Fusion Plasma Physics, EURATOM-NFR Association,Alfven Laboratory,Royal Institute of Technology, Stockholm, Sweden

1. Introduction.

The collective scattering of electromagnetic waves has been employed by many research groups in order to address the issue of plasma turbulence resulting in anomalous transport in a tokamak. Yet, investigations were primarily focused on intensities of plasma fluctuations versus values of local transport coefficients. The novel approach based upon collective scattering method has been put forward in [1] thereby offering to measure a diffusion coefficient directly from the shape of the scattering spectrum. The method has been successfully employed on Tore - Supra tokamak using the CO_2 - laser scattering. Here, the similar approach has been used in order to unravel the backscattering spectra resulting from the tangential microwave probing during the L - H transition, carried out on the TUMAN 3 tokamak.

2. Collective scattering from turbulent plasma

Along the lines of the new approach [1] in a case where the plasma turbulent motion is statistically independent of the electron density fluctuations, the scattering spectrum is directly proportional to the Fourier transform $P(\boldsymbol{K},\omega)$ of the probability distribution $P(\Delta,\tau)$ (Here Δ is the plasma displacement-in- time τ, the scattering wavevector is defined by the Bragg condition- $\boldsymbol{K}=\boldsymbol{K}_S-\boldsymbol{K}_i$). When the observation wavelength $\lambda=2\pi/K$ is larger than the turbulent motion correlation length, a brownian-type diffusive plasma motion with a variance $\langle\Delta^2\rangle = 2D\tau$ determines the probability distribution. Here D is the turbulent diffusion coefficient. The scattering spectrum has to be a Lorentzian profile, centred at the mean plasma motion Doppler frequency - $\boldsymbol{KU}$:

$$S(\omega)=\frac{2K^2D}{(\omega-\boldsymbol{KU})^2+(K^2D)^2} \qquad (1)$$

According to Eq.(1) the frequency spectrum width is directly connected with the cross-diffusion coefficient. So the plasma mean motion velocity and diffusion coefficient could be recovered from the relative measurements of spectrum shape.

In the specific conditions of the strong shear of plasma rotation during the L-H transition the additional mechanism of spectrum broadening takes place. The shear of poloidal velocity is followed by another dependence of the mean square displacement in time τ along the poloidal direction: $\Delta_\theta=\int (dV_\theta/dr)\Delta_r\tau$; $\langle\Delta_\theta^2\rangle=(1/3)D(dV_\theta/dr)^2\tau^3$. The scattering spectrum now is defined as:

$$S(\omega) = \int (4\pi D\tau)^{-1} \exp\left(-\left(\frac{\Delta_r^2 + \Delta_\theta^2}{4D\tau}\right) + iK_\theta\left(\Delta_r \frac{dV_\theta}{dr}\tau + \Delta_\theta\right) + i\omega\tau\right) d\Delta_r d\Delta_\theta d\tau \quad (2)$$

The associated estimate of the spectrum width for the strong shear of rotation is $D\left(dV_\theta / dr\right)^2 K^2\Big)^{1/3}$. The spectrum becomes similar to the Gaussian-like profile. It is true only for the scattering wavevector directed towards the poloidal velocity (K_r=0). That is just the case of the backscattering under the tangential probing in tokamak. Note that this effect of spectrum broadening does not appear under the probing beam directed transversely to the flux surface (K_θ=0) because of the microwaves are scattered mainly from the radial moved fluctuations.

3. Experimental results

To study the backscattering spectrum evolution during the transition to the H-mode two similar tangential probing schemes have been implemented in Tuman-3 for the simultaneous measurements of signals reflected from the both high and low magnetic field sides [2].Two antennae horns were used to transmit the O-mode microwaves under the angle of 50^0 with respect to the last closed flux surface (LCFS) and to receive the backscattering signals. The Fig 1 shows schematically the ray tracings for different incident beam frequency. The presented trajectories have been obtained neglecting the antenna directivity width for the electron density profile measured before the transition. Two typical spectra obtained in the both upper and lower frequency sidebands just before and after the transition are shown in Fig 2.a,b. The spectra have been computed using the output signals of dual homodyne receiver [2] in a time frame of 0.5 or 1.0 ms The spectrum profiles are found to be basically of Lorentzian shape. The best fit Lorentzian curves are presented in Fig 2 as well. The difference between spectrum widths before and after the transition is evident. The calculated spectra are happened to be shifted towards the electron or ion diamagnetic drift directions. The poloidal velocity recovered from the frequency shift ($V_\theta = \delta\omega/K$) is depicted in Fig 3 in relation to the distance between the microwave trajectory turn point and the LCFS. Here K has been estimated for the turn point space position. The data have been obtained while using the different incident beam frequencies at two moments of time - before and just after the transition. It is quite clear that the presented data are averaged over the whole scattering volume. Nevertheless , the velocity pattern is in qualitative agreement with that obtained by other methods in the divertor tokamaks.

The Lorentzian-type spectrum width has been calculated over the whole period of a discharge. As an example Fig 4c shows the temporal behaviour of the spectrum width under the inside probing at incident frequency 21.5 GHz. The set of curves illustrating the transition is presented here as well. One can see the drastic drop of the width Δf during the transition. Note that the level of fluctuations is kept constant or even increased for the same period of time (See Fig.4d). Under the assumption, that the spectrum broadening is determined by the cross-diffusion (see (1)), one can estimate the diffusion coefficient values. The D-scale in Fig 4c corresponds to K-value at the trajectory turn point. The estimated coefficients are the right order of magnitude for the diffusion process in plasma edge obtained from the balance discharge analysis [3]. So this result can be treated as an evidence of the turbulent diffusion suppression during the ohmic H-mode appearance that is in line with theory of the transition [4].

As for the low magnetic field side probing there is no strong evidence of the spectrum narrowing during the transition. At some incident frequencies even the increasing of the spectrum width has been observed (see Fig 4e). The different behaviour of the spectrum width for the low and high magnetic field sides has been accounted for the particular space positions of the scattering regions regards to the LCFS. Under the outside probing with 22 GHz frequency the microwave trajectories are coming just near the LCFS where the shear of rotation is significant. So it is believed that the spectrum width could be determined mainly by the shear of rotation. In such a case the diffusion coefficient estimate seems to be problematic for the accurate velocity shear value is required to be known. Using the theoretically predicted value ~ 10^5 cm/s at the moment of transition [5] the diffusion suppression can be recovered from the outside probing data as well as from the inside ones. However another indirect evidence of the diffusion reduction at low magnetic field side is connected with the reflectometry data obtained under the probing directed transversely to the magnetic flux surfaces. If this is the case the shear of rotation influence on the spectrum shape is disappeared thus the spectrum narrowing is expected to occur along with the diffusion suppression during the transition. The Fig 2c,d shows two typical spectra of reflectometry output signals. The both spectrum widths are drastically decreased as compared with the tangential backscattering ones. In accordance to the formula (1) the spectrum narrowing could be due to the incident beam wavenumber decrease near the cut-off layer. The difference between the widths of spectra derived before and after the transition is seen as well. The Fig 5 presents as an example the temporal dependence of the output spectrum width in a discharge with ohmic H-mode. One can see the drop of the spectrum width which could be associated with the cross-diffusion suppression in the low magnetic field side. The accurate estimation of the diffusion coefficient from reflectometry data seems however to be impossible due to the pronounced uncertainty of K-value in the scattering region.

4. Conclusions.

The impact of the rotational shear and the resulting from it suppression of the anomalous cross - field diffusion has been addressed by the microwave backscattering diagnostics. The shape of the backscattering spectrum has been demonstrated to yield the dramatic dependence on the shear of rotation. The reduction of the anomalous diffusion during the transition has been demonstrated to be maintained at both the low and high field sides of the tokamak.Our measurements yield the absolute value of the diffusion coefficient consistent by order of magnitude with the value obtained from the particle balance.

Acknowledgements.

The Tuman-3 team assistance in experiments is gratefully appreciated. The authors greatly benefited from stimulating discussions with D.Gresillon. This work was performed under the grant of the Russian Fond of Fundamental Researches No 94-02-04759a and supported in part by the Swedish Institute.

References.

[1] Gervais F et al, 21st EPS Conf. on Contr. Fusion and Pl. Phys., V18B, 118 (1994)
[2] Bulanin V.et al, 20th EPS Conf. on Cont. Fusion and Pl. Phys.,V17B, 1117 (1993)
[3] Andrejko M et al 14th Int. Conf on Plasma Phys. V1, 485 (1993)
[4] Kim Y.B et al Phys. Fluids B2(9), 2143 (1990)
[5] Rozhansky V.,Tendler M, Phys Fluids, 4(7), 1877 (1992)

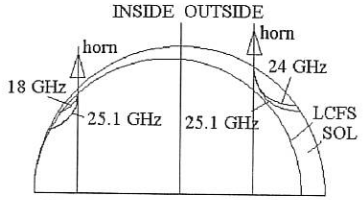


Fig. 1. Diagnostic layout in TUMAN 3

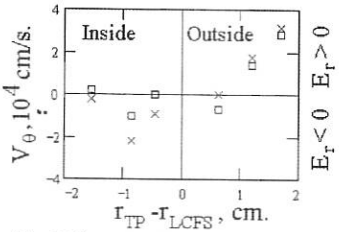


Fig. 3. Plasma oscillatory mode poloidal velocity V_θ in relation to the distance between the trajectory turn point and LCFS. E_r - radial electric field, × - before and □ - after the transition

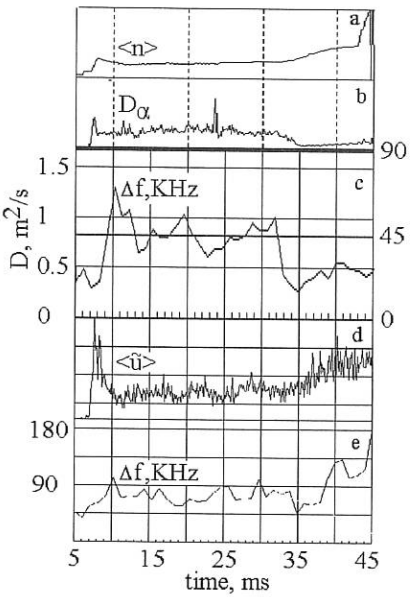


Fig. 4. Temporal behaviour of spectrum width Δf obtained from the inside (c) and the outside (e) probing, (a) - D_α-emission, (b)-averaged density.

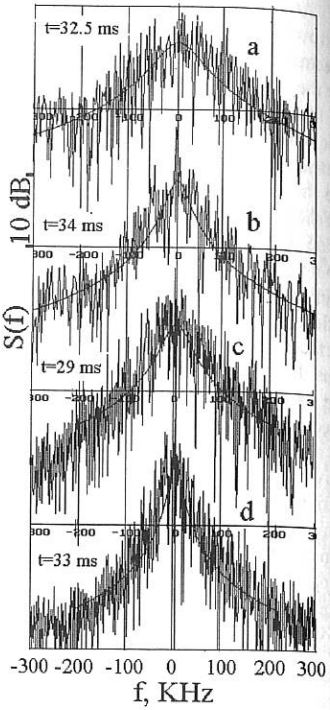


Fig. 2. Backscattering spectra and the best fit Lorentzian profiles in dB scale obtained from the tangential probing data at 18 GHz (O-mode) - (a), (b) and from the reflectometry ones at 17 GHz (X-mode) - (c),(d).Transition time moment- 33 ms for (a), (b) and 30 ms for (c), (d).

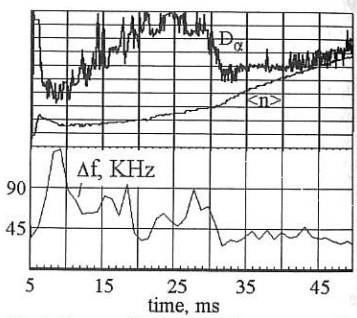


Fig. 5. Temporal behaviour of spectrum width Δf computed from the reflectometry data. (18 GHz, X-mode)

Characteristics of Low q(a) Plasmas in the CDX-U Spherical Tokamak*

Y.S. Hwang, T.G. Jones, D. Stutman, W Choe, E. Lo, J. Menard and M. Ono
Princeton Plasma Physics Laboratory, Princeton, NJ,08543, USA,

1. Introduction

The spherical tokamak (ST) or low-aspect-ratio tokamak (LART) configuration offers promising possibilities for a cost-effective, high-performance (high beta, high bootstrap fraction) plasma regime which lends itself naturally to a compact volumetric neutron source as well as a high beta advanced fuel reactor [1]. The recent results from START have been encouraging [2]. To test the viability of the LART configuration at MA-level plasma currents, the National Spherical Tokamak Experiment (NSTX) [3] is being proposed. The CDX-U tokamak at Princeton [4] with the recent installation of an ohmic heating (OH) solenoid can be used to proto-type LARTs such as NSTX. In a typical LART design, space for a central OH solenoid and for central toroidal field (TF) conductors is very limited. This means that ohmic current drive efficiency is of major concern in addition to the development of effective, non-inductive current drive methods. Non-inductive current drive results using internally generated bootstrap currents and helicity injection current drive in a low-aspect-ratio configuration have been reported previously [5]. Present research on CDX-U (a LART with $R \approx 35$ cm, $A \geq 1.4$, and $I_{tf} \leq 250$ kA) has focused on issues that are relevant for NSTX, in particular, efficient tokamak start-up and the MHD I_{tf}/I_p, or q(a) limit.

In this paper, we report the recent LART experimental investigations in two important areas; I. tokamak start-up experiments in CDX-U using ECH break-down to minimize the volt-second consumption as well as the induced wall eddy currents, and II. investigation of a low q(a) regime [$q(a) \leq 5$ for $A \approx 1.5$] in CDX-U.

2. Experimental Set-up

CDX-U is a low-aspect-ratio tokamak facility with $R \approx 35$ cm , $A \geq 1.4$ and with $I_{tf} \leq 250$ kA (steady-state or pulsed). Presently, an OH power supply with a 40 mV-s flux swing capability (OH solenoid capability is 150 mV-s) is operational on CDX-U. Four pairs of PF coils are used to control the plasma shape and position. One 2.45 GHz, 4 kW ECH source provides initial plasma break-down for the start-up. The device cross-sectional view is shown in Fig. 1. The inner wall containing TF and OH coils, is made of a 4 in. O.D. Inconel tube with 1/8 in. thickness wall. Top and bottom vessel walls are 5/8 in. thick stainless steel. The outer wall is made of 1.5 in. thick Aluminum with a toroidal electrical break. A low base pressure, $P \leq 1\text{-}2 \times 10^{-7}$ Torr is maintained with the combination of cryo-pumping and

* This work was supported by DoE contract No. DE-AC02-76-CHO-3073.

Ti-gettering. The experiment was conducted mostly with hydrogen gas puffing. Diagnostics include a 2-D scanning microwave interferometer, a poloidal array of magnetic pick-up coils, and a 2-D scannable magnetic probe. Recently, various spectroscopic/soft X-ray diagnostics have been added and a multi-pass Thomson scattering system is being installed in collaboration with the Ioffe Institute.

3. Low-Aspect-Ratio Tokamak Start-up and Volt-second Consumption

Since the CDX-U vacuum vessel, like that of NSTX, is relatively close to the plasma and has a toroidally continuous vessel wall, OH start-up techniques in the presence of significant wall eddy currents must be investigated. Using ECH preionization, it is possible to initiate low-aspect-ratio tokamak plasmas with a wide range of TF current [I_{tf} = 70 kA - 180 kA with R(ECH) = 16 cm - 40 cm]. Plasma initiation is also possible with an almost arbitrarily low loop voltage of $V_{loop} \leq 1V$, though we have typically operated with a peak voltage of $V_{loop} \approx$ 1 - 8 V, depending on the desired current ramp-up rate. Plasma current generating efficiency of 1.7 kA / mV-s was obtained up to I_p = 60 kA. Figure 2 shows the maximum plasma current obtained thus far in CDX-U ohmic discharges as a function of volt-second expenditure for various discharges. An Ejima coefficient C_E [6], a measure of ohmic current drive efficiency, has been obtained down to 0.3 which is quite low compared to that of typical large tokamaks. An average current ramp-up rate of 6 kA / ms for C_E=0.3 has been obtained in these efficient ohmic current drive. When I_{tf} was reduced by a factor of 2.3 (from I_{tf} = 160 kA to 70 kA), the observed current generating efficiency and the ramp-up rate only dropped by 10% unless plasma current or q(a) limits are reached..

4. Lower q(a) Discharge Characteristics

A typical plasma equilibrium in this low-aspect-ratio geometry, shown in Fig. 3, has been reconstructed with the EFIT equilibrium code [7], from magnetic measurements, and has plasma parameters of : R = 0.34 m, a = 0.22 m, line integrated density, $n_eL \approx (0.3 - 2.0) \times 10^{18}$ m^{-2}, and estimated T_e in the range of 100 - 200 eV from both VUV spectrometer and soft X-ray measurements. These parameters indicate that the plasma is already in the low collisionality regime with $\nu^*_e \approx 0.1 - 0.3$, where trapped particle effects become important. Maintenance of a 5-10 ms flat-top discharge at $I_p \approx 35$ kA, with an average loop voltage $\approx$ 1 - 3 V also indicates that the plasma has entered a relatively hot, collisionless regime. We typically observe an increase in the central plasma density and density gradient with the toroidal magnetic field, suggesting an improvement of plasma confinement.

Taking advantage of the relative insensitivity of ECH plasma start-up to the toroidal magnetic field (B_T), it is possible to attain q(a) < 5 tokamak discharges for a wide range of B_T. Maximum plasma current obtained thus far in CDX-U ohmic plasmas, as a function of

toroidal field, is shown in Fig. 4. The maximum plasma current at a given B_T appears to be limited to $q(a) \geq 3.5$ ($q_{cyl} \approx 1$) and $q(0) \approx 1$ as shown in Fig. 4.

As the q(a) is decreased, internal reconnection events (IRE) similar to those observed in START [2] have been observed more often with relatively smaller plasma current spikes. With close fitting top and bottom graphite limiters, vertically stretched plasmas hit limiters with relatively hot temperature particles, resulting in strong carbon impurity influx, which in turn causes a large density increase and rapid cool down of the plasma. By changing limiter materials from graphite to Molybdenum, carbon impurities have been reduced significantly (total radiated power loss is less than 20 % of OH heating power) and abrupt plasma terminations have also been reduced. However, lower q(a) plasmas still show abrupt termination due to plasma-limiter interactions and strong MHD activity even without strong impurity influxes. Also, a significant enhancement of m=1-3/n=1 internal MHD modes in the 10-15 kHz range, as shown in Fig. 5(a), was observed with lower q(a). Fluctuations are stronger at the low field side than the high field side, and strong inside the plasma than outside the plasma. The radial structure of these modes shows a dip in the $\delta B_Z/B_Z$ signal but not in the $\delta B_R/B_Z$ signal as shown in Fig. 5(b), which suggests the possible existence of large magnetic islands at the low field side. As the central safety factor q(0) goes down to less than one, these islands can couple with m=1/n=1 sawteeth which can lead to disruption. The q(0) of maximum plasma current discharges for various toroidal magnetic fields were estimated to be near one, which supports the above conjecture. Detailed MHD studies of possible sawtooth activity are ongoing.

5. Conclusion and Future Plans

In the CDX-U low-aspect-ratio tokamak, a lower q(a) regime (i.e. $q(a) \leq 5$, $A = R/a \approx 1.5$) has been explored for $I_p \leq 65$ kA, and $q(a) \geq 3.5$ [$q_{cyl}(a) \geq 1$]. The MHD activity shows an increase as the edge safety factor is reduced, which could lead to some abrupt plasma terminations due to the MHD induced plasma-limiter interactions. More detailed study of these modes and possible stabilization schemes will be continued. Also, high-harmonic fast wave heating and current drive experiments are under preparation. Fast wave heating and current drive will be an essential tool for achieving NSTX missions such as a long pulse discharge, and high beta, advanced ST regimes.

References

[1] Y-K. M. Peng, J. D. Galambos, and P.C. Shipe, Fusion Technology **21**, 1729 (1992).

[2] A. Sykes et al., Plasma Physics and Controlled Fusion **35**, 1051 (1993).

[3] J. Robinson et al., Bull. Am. Phys. Soc. **38**, 2005 (1993).

[4] Y.S. Hwang, et al., IAEA-CN-60/A5-II-6-2 (1994)

[5] M. Ono et al., Plasma Physics and Controlled Nuclear Fusion Research 1992, Vol. 1, 693 (IAEA, Vienna, 1993).
[6] S. Ejima, et al., Nucl. Fusion **22**, 1313(1982)
[7] L. Lao, et al., Nucl. Fusion **30**, 1035(1990)

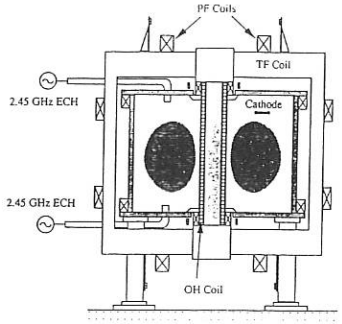


Fig.1. Schematic of CDX-U device

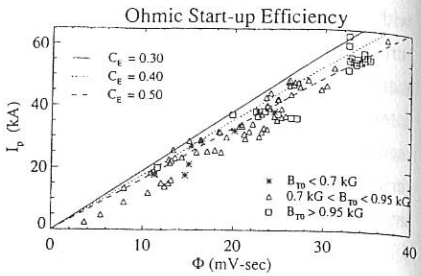


Fig.2. Ohmic efficiency during CDX-U start-up

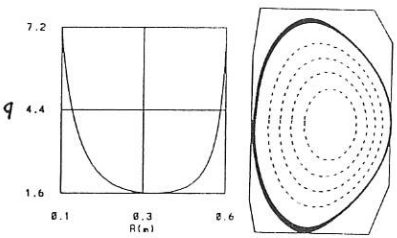


Fig. 3. Reconstructed plasma equilibrium

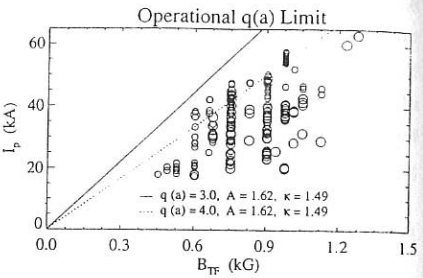


Fig.4 Operational q(a) limit.

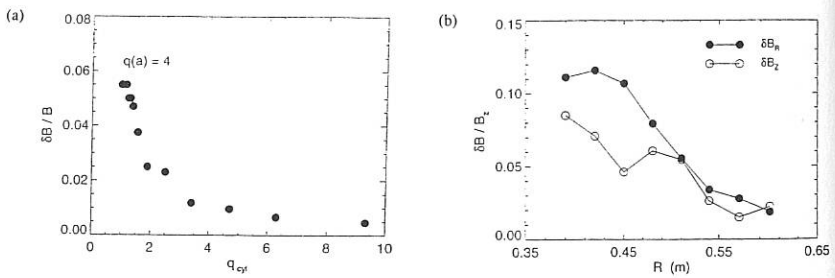


Fig. 5. MHD fluctuations. (a) Poloidal magnetic fluctuation amplitude dependence on q_{cyl}. The discharge of $q_{cyl} \approx 1$ is equivalent to that of $q(a) = 4$. (b) Radial and vertical magnetic fluctuation variations with major radius at the midplane.

H-mode Threshold for Ohmic Plasmas in TCV

B.P. Duval, Y. Martin, M.J. Dutch, F. Hofmann, J.B. Lister, J.-M. Moret, Ch. Nieswand, R.A. Pitts, Z.A. Pietrzyk, A. Pochelon, G. Tonetti, H. Weisen

Centre de Recherches en Physique des Plasmas
École Polytechnique Fédérale de Lausanne
Association EURATOM - Confédération Suisse
21 Avenue des Bains, CH-1007 Lausanne, Switzerland

1. Introduction

Following the first boronisation of the TCV vacuum vessel, a clear H-mode transition has been observed with Single-Null (SN), Double-Null (DN) and highly elongated Limited magnetic configurations using ohmic heating only [1,2]. Figure 1 shows the reconstructed magnetic equilibria at the time of the L-H transition for a variety of plasma shapes for which a transition has been observed. For SN equilibria (Fig. 1a -b), H-mode is obtained only when the ion ∇B drift is directed towards the X-point. In DN configurations, H-mode transitions are equally observed independently of which of the X-points (upper Fig. 1d or lower Fig. 1e), lies on the separatrix. For most of these discharges, a clear density threshold is observed, in that, once the full magnetic configuration is established, as the density rises, H-mode is achieved at a density value that is often well reproduced by subsequent similar discharges.

Following a brief description of the general character of the H-mode transition in TCV, this paper reports on the behaviour of the density threshold for this transition. Whilst there is some early evidence for a dependence of the transition threshold on magnetic configuration, notably the plasma triangularity, there are strong indications that the threshold density is dominated by local recycling conditions.

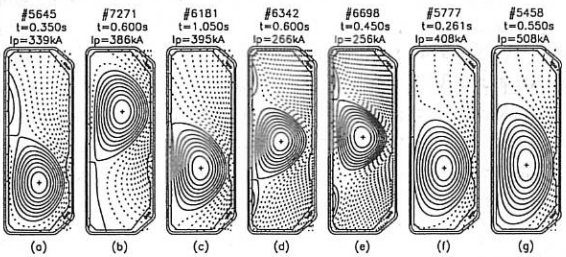


Figure 1. A selection of plasma equilibria at the time of the L-H transtion

2. H-mode Characteristics

The essential features of the ohmic H-mode transition in TCV are illustrated in Figure 2, where the time variation of the Dα emission integrated along a vertical chord through the plasma is

shown for four different discharges, reasonably typical of the observed behaviour. In general, the transition is marked by a sharp reduction (20 - 70% in less than 0.5ms) in the Dα intensity. It may be preceeded by a relatively calm phase marked by small fluctuations in the Dα intensity (Fig 2a), or by large amplitude oscillations ("dithering" phases) together with smaller fluctuations due to the effect of sawtooth activity on the edge plasma (Fig 2b-d). Indeed, many of the transitions are observed to be provoked by a sawtooth crash. The transition is most often followed by a quiescent "ELM-free" phase of at least 20ms, and later by small ("mossy") or large, probably type I, ELMs [3].

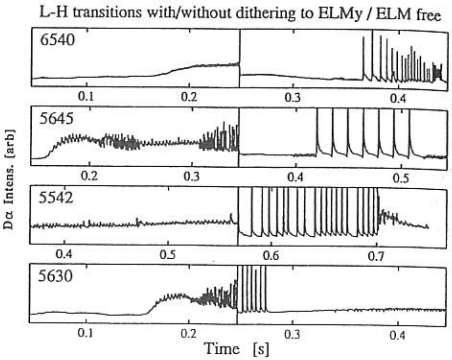


Figure 2:
Examples of different Dα intensity behaviour across the H-mode transition

3. Transition Threshold

3.1 Comparison with Power Threshold Scaling

With ohmic heating only, the existence of a power threshold (as proposed in [4] as a scaling of the power per unit surface crossing the last closed flux surface (P/S) with the product Bn_e) is not easily determined. Each configuration requires a certain minimum current in order to enter H-mode which limits operation to $2.1 \leq q_{95} \leq 3$. Following the L-H transition, the loop voltage often decreases by ~30% and the plasma density rises due to the improved particle confinement. The loop voltage is also observed to increase with plasma density both before and during the H-mode.

Thus, in a discharge with constant shape and plasma current, P/S is a fairly linear function of density. Figure 3 illustrates a TCV discharge in which the locus of P/S Bn_e follows the power scaling law until the discharge passes into H-mode. Although, in general, the plasma parameters at the transition are in agreement with the proposed power scaling [1], the subsequent decrease in the heating power and the concurrent density rise imply that the neutral particle beam power determined P/S, Bn_e law is less relevant as a description of the ohmic H-mode transition.

3.2 Behaviour with Density

The wide flexibility of TCV for the generation of varied plasma shapes and the easy access to the ohmic H-mode permit an examination of the density threshold as an independent function of a number of parameters, such as elongation, triangularity, wall separation, wall conditioning etc. In TCV, H-modes have been observed with a line averaged threshold plasma density in the range 1.7 to 7.1 x 10^{19} m^{-3}.

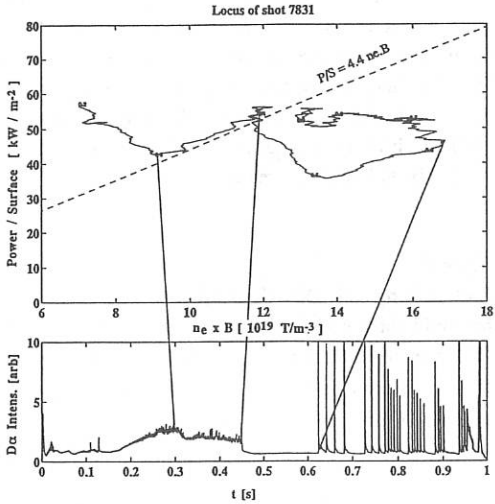


Figure 3:
The locus of the P/S against Bn_e for a SNU discharge. The Dα trace as a function of time is shown together with lines indicating the pre-H-L, H-L and post-H-L periods

Effect of wall conditioning: At present, graphite protection tiles cover ~64% of the vessel surface including, the entire central column and the top and bottom divertor target zones. The well known tendency for uncontrolled gas release from carbon surfaces coupled with the open divertor configurations of TCV, mean that the local recycling effects and wall conditioning may be expected, and are in fact observed, to have a strong influence on the transition threshold. For the SNU configuration of Fig1a, with Ip parallel to Bϕ (both ACW looking from the top of the machine), fresh boronisation and prolonged helium glow results in ELMing H-mode plasmas, with the ELMs becoming rarer with successive discharges and with the density threshold for the transition generally increasing. The consequent ELM-free H-modes often terminate in high density disruptions and further periods of He glow are required both to recover the ELMs and reduce the density threshold. Eventually, only ELM free H-modes are possible and a further boronisation is necessary to restore the initial conditions. Interestingly, inverting the direction of Bϕ appears to change the character of the H-mode in SNL discharges (ion ∇B drift again directed towards the X-point). Dithering phases and large ELMs are virtually absent and the discharges show a significant number of H-L-H transitions despite repetitive He glows and further boronisation. This is in contrast to the SNU (Bϕ ACW) where repeated H-L-H transitions are observed only in discharges following a long post-boronisation period. The reasons for the differences are as yet unknown and are under further investigation.

Effect of plasma shape: Results of a series of SNL experiments in which the density threshold is measured as separate functions of plasma elongation, plasma triangularity and wall separation are inconclusive. The density threshold is, for example, observed to rise by 100% as the plasma elongation is increased from 1.5 to 1.65, whereas a different series of similar discharges

showed less than 30% change. Varying these parameters changes the position of the divertor strike points and is therefore also likely to influence the local recycling. Figure 4 shows the variation of the density threshold as a function of the upper triangularity, δ_u for SNL discharges (Fig 1b). Here the divertor magnetic geometry and the lower triangularity remain virtually unchanged with δ_u varying from 0.14 to 0.26 (elongation varied only slightly from 1.58 to 1.60). A clear and reproducible scaling is observed in which the density threshold increases linearly by 80% as δ_u increases.

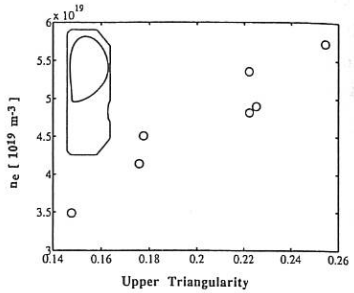


Figure 4:
The scaling of the density threshold for the H-L transition with upper triangularity

5. Conclusion

Under boronised wall conditions, ohmic H-mode transitions in TCV are observed in a variety of SN, DN and limited equilibria provided that in the SN configurations the ion ∇B drift be directed towards the X-point. With ohmic heating alone, since the heating power depends on the density via the loop voltage, it is difficult to determine a power threshold for the transition. A clear density threshold is, however, observed for configurations with easy access to the H-mode. This threshold can vary strongly with time and appears to be strongly influenced by wall recycling, leading to poor reproducibility in experiments designed to quantify the threshold dependence on plasma shape parameters. For a series of discharges in which recycling effects were minimised, an increase in the density threshold of 80% was observed as the upper triangularity of a SNL configuration was increased from 0.14 to 0.26.

Acknowledgements: This Work was partially supported by the Fonds National Suisse de la Recherche

References

[1] F. Hofmann et al. Plasma Phys. Control Fusion **36** B277, 1994

[2] J.-M. Moret et al. *Ohmic H-mode and confinement in TCV*, at this conference (invited)

[3] H. Weisen et al, *Edge Localised Modes in the TCV Tokamak*, at this conference.

[4] Ryter et al., 20th EPS Conference, Lisbon, 1993, ECA Vol 17C, I-23.

Plasma Shape Control in TCV using MGAMS

F. Hofmann, M.J. Dutch, J.-M. Moret
Centre de Recherches en Physique des Plasmas, EPFL
Association EURATOM - Confédération Suisse,
21 Avenue des Bains, CH-1007 Lausanne, Switzerland

1. Introduction

TCV is a rather unusual tokamak since it allows the creation of an extreme variety of plasma shapes and magnetic configurations. The MGAMS shape and position control algorithm [1] has been developed specifically for TCV with the aims of versatility, accuracy and ease of operation. The basic idea is that the operator only specifies the plasma shape and plasma current evolution and everything else is done automatically by the MGAMS software. This concept has proven very efficient in TCV since it allows us to create completely new plasma shapes in a single discharge, without using any information from previous discharges.

Plasma shape control in tokamaks involves basically four steps: (a) Identification of the plasma shape in real time, (b) Comparison of the real plasma shape with a preprogrammed shape, (c) Evaluation of coil current corrections such as to bring the real shape as close as possible to the preprogrammed shape, (d) Evaluation of coil voltages to produce the desired coil current corrections. In the following sections, we will show how each of these four steps is implemented in the MGAMS algorithm.

2. Shape Identification

In MGAMS, the plasma current distribution is reconstructed, in real time, in the form of a finite element matrix [2]. The current elements are fixed in space, and their amplitudes are determined such as to produce the best fit to the magnetic measurements (magnetic field probes, flux loops, coil currents and vessel currents). It should be noted that in TCV, it is essential to include the effects of vessel currents in the shape identification procedure, since the vacuum vessel has very low toroidal resistance (55 $\mu\Omega$). Once the plasma current distribution is known, shape parameters can be derived in various ways. The standard method in MGAMS consists of defining a number of moments of the plasma current distribution,

$\Sigma I_i (Z_i - Z_o)$	vertical position
$\Sigma I_i (R_i - R_o)$	radial position
$\Sigma I_i (Z_i - Z_o)^2$	elongation
$\Sigma I_i (Z_i - Z_o) (R_i - R_o)$	tilt
$\Sigma I_i (Z_i - Z_o)^2 (R_o - R_i)$	triangularity

where I_i is the total current in the i-th element, (R_i , Z_i) are the coordinates of the current centroid of the i-th element and (R_o, Z_o) are the coordinates of an arbitrary reference position, usually taken as the expected initial position of the magnetic axis.

Alternatively, the plasma shape can be defined in terms of flux errors at the plasma boundary [1] or, equivalently, in terms of gaps between plasma surface and vessel wall.

3. Reference Shape

The time evolution of the reference plasma shape must be specified by the operator, either in analytic form, $R(t) = R_o + a \cos(\theta + \delta\sin\theta + \lambda\sin2\theta)$ and $Z(t) = Z_o + a\,\kappa\,\sin\theta$, where θ is the poloidal angle and the parameters R_o, Z_o, a, κ, δ, λ are functions of time, or in the form of discrete boundary points, $R_i(t)$, $Z_i(t)$. The number of boundary points specified at each time slice is typically between 4 and 20. In addition, coordinates of X-points and separatrix strike points can be prescribed as functions of time. Using this information, MGAMS starts the shot preparation by computing a number of free-boundary equilibria [3]. This gives us a first estimate of the coil currents as functions of time. From these equilibria we also compute the various moments of the plasma current distribution, as defined in section 2. They serve as reference waveforms for those shape parameters which are feedback controlled. The final step in the shot preparation is the calculation of feed-forward coil voltages. This is achieved by solving the circuit equations for the complete tokamak discharge, including plasma and vessel currents.

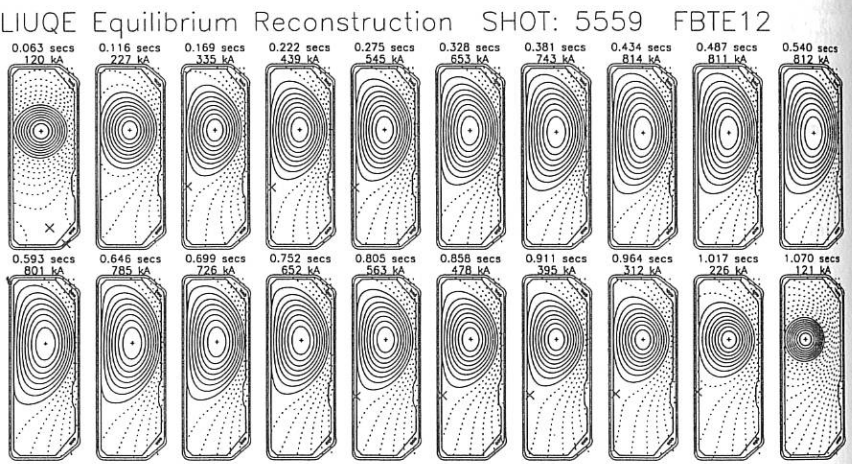


Fig.1. Typical plasma evolution in TCV discharge ($I_{p,\,max}$ = 810 kA, κ_{max} = 2.0)

4. Coil Current Corrections and Coil Voltages

Coil current corrections are computed in real time by the TCV hybrid matrix multiplier [4]. In MGAMS, these corrections are usually applied in the form of moments (vertical field, radial field, quadrupole field, hexapole field, etc.). Each moment is defined by a particular coil current distribution and, ideally, controls only one shape parameter. The moments are constructed as an orthogonal set. The amplitude of each moment, in real time, depends on the deviation of the measured shape parameter from its preprogrammed value. If the plasma shape is expressed in terms of flux errrors at the plasma boundary, the coil current corrections are evaluated in such a way as to minimize the flux errors [1]. The computation of instantaneous coil voltages which are required to produce the desired coil current corrections is basically straightforward, but it is complicated by the perturbing effect of the vessel currents.

5. User Interface

A graphical user interface has been developed for MGAMS, based on MATLAB software. The operator first specifies all input parameters: The plasma current must be given as a function of time (rampup phase, flattop and rampdown phase). The shape evolution must be specified, as explained in section 3, above. The rampdown phase is usually assumed to be the exact inverse of the rampup phase. However, in many cases, it is advantageous to program the rampdown phase slightly differently in order to avoid disruptions during rampdown. Finally the proportional, differential and integral gains have to be specified for the various feedback loops (plasma current, vertical position, radial position, plasma density, shape parameters, etc.). Once the operator has set the various parameters described above, the MGAMS shot preparation is launched. Coil currents and voltages are computed as functions of time, and the control matrices and reference waveforms are generated. Matrices and waveforms are then loaded into the TCV hybrid computer and the machine is ready for triggering a discharge.

6. Results

The MGAMS algorithm has allowed the creation of many different plasma shapes in TCV. A typical plasma evolution is shown in Fig.1. The equilibrium reconstructions shown here were performed after the discharge, using the LIUQE code [5]. The plasma current is ramped up to 810kA in 0.43 sec and the maximum elongation is 2.0. The accuracy of the shape control algorithm can be verified by comparing the preprogrammed shape with the shape obtained from full equilibrium reconstructions. It can also be tested by making use of other diagnostics, such as soft X-ray and visible imaging cameras. It is found that, for vertically elongated plasmas, the radial accuracy is

Max-Planck-Institut für Plasmaphysik
- Bibliothek -

generally better than 5 mm and the vertical accuracy is of the order of 1 cm. Fig.2. shows a number of plasma shapes that were produced in TCV, using MGAMS. Each image is taken from a different shot, and in each case, the shape is shown at the time when the plasma current has reached its maximum value. Some of the shapes shown here were generated for testing the algorithm, but in most cases, the particular shape was a necessary condition for reaching a certain physics goal.

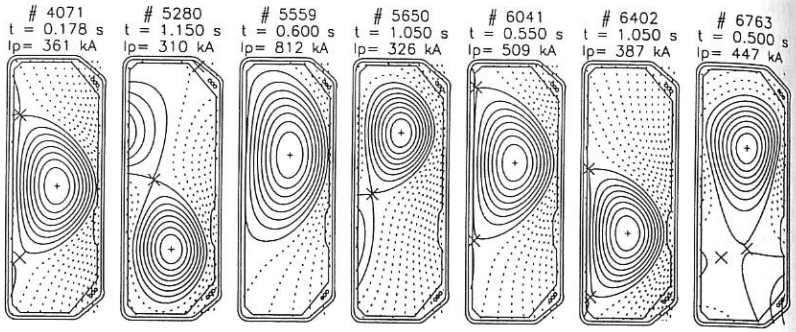


Fig.2. Selection of equilibrium reconstructions of plasmas produced in TCV using the MGAMS algorithm

7. Conclusion

MGAMS has proven to be an extremely versatile tool. It can generate any arbitrary plasma shape, subject to obvious physical constraints, without reference to a data base of precalculated equilibria or previous discharges. The shape accuracy depends on the precision of the magnetic measurements and is typically between 5 mm and 1 cm. Thanks to a graphical user interface, the algorithm is very easy to use. The original goal, i.e., that the operator only specifies the evolution of plasma current and shape and the algorithm does the rest, has been fully attained.

Acknowledgements: It is a pleasure to acknowledge the support of the entire TCV team. This work was partly supported by the Swiss National Science Foundation.

References:

[1] F. Hofmann, S.C. Jardin, Nuclear Fusion 30 (1990) 2013.

[2] F. Hofmann, G. Tonetti, Nuclear Fusion 28 (1988) 519.

[3] F. Hofmann, Computer Physics Communications 48 (1988) 207.

[4] P.F. Isoz, J.B. Lister, Ph. Marmillod, Proc. 16th Symp. on Fusion Technology, 1264 Oxford, 1990 (1991).

[5] F. Hofmann, G. Tonetti, Nuclear Fusion 28 (1988) 1871.

TF Ripple Loss of Alpha Particles in TFTR DT Experiments

M. H. Redi, R. V. Budny, D. S. Darrow, A. C. Janos, D. C. McCune, **S. S. Medley**, J. Schivell,S. D. Scott, R. B. White, M. C. Zarnstorff, S. J. Zweben and the TFTR group
Princeton Plasma Physics Laboratory,
P. O. Box 451, Princeton, NJ 08543

1. Introduction

Quantitative evaluation of TF ripple loss of DT alpha particles is a central issue for reactor design because of potentially severe first wall heat load problems. DT experiments on TFTR [1] allow experimental measurements to be compared to modelling of the underlying alpha physics, with code validation an important goal. Modelling of TF ripple loss of alphas in TFTR now includes neoclassical calculations of alpha losses arising from first orbit loss, stochastic ripple diffusion, ripple trapping and collisional effects. Recent Hamiltonian coordinate guiding center code (ORBIT) [2] simulations for TFTR have shown that collisions enhance the stochastic TF ripple losses at TFTR [3]. A faster way to simulate experiment has been developed which uses a simple stochastic domain model for TF ripple loss within the TRANSP analysis code [4].

2. ORBIT/TRANSP Renormalization of the Stochastic Domain Model

TRANSP, the primary PPPL time-dependent analysis code, has been upgraded with a simple model of fast ion ripple loss, renormalized by guiding center code simulations [3]. A simple criterion was obtained by Goldston, White and Boozer (GWB) for fast ion particle loss due to the TF ripple of tokamaks, which lack perfect axisymmetry due to a finite number of toroidal field coils [5]. The criterion, derived with a zero banana width, collisionless approximation in simplified geometry, compares the TF ripple $\delta = (B_{MAX}-B_{MIN})/(B_{MAX}+B_{MIN})$ to a stochastic ripple loss threshold $\delta_{GWB} = (\varepsilon/N\pi q)^{3/2}(1/\rho q')$. Here B_{MAX} and B_{MIN} are the maximum and minimum field magnitudes at constant major radius and elevation, ε= inverse aspect ratio, N = number of coils, q is the plasma safety factor, $q' = dq/dr$ and ρ is the ion Larmor radius. Trapped ions whose turning point lies in a region where δ exceeds the threshold, δ_{GWB}, are subject to stochastic ripple diffusion.

The ripple loss model in TRANSP is based on the above criterion. For both neutral beam ions and fusion products such as alpha particles, Monte Carlo ions are followed so that at each bounce point the TF ripple is compared to a threshold δ_S proportional to δ_{GWB}. The ratio δ_S/δ_{GWB} is evaluated by comparing particle and energy loss fractions to those found from ORBIT simulations for the same equilibrium geometry and source profile [4].

The total alpha energy which was ripple lost in each TRANSP and ORBIT simulation was used to renormalize the stochastic threshold for alphas. The $\delta_S = 0.6\ \delta_{GWB}$ threshold for alphas is reduced compared to the GWB model estimate, possibly due to the large banana width of the alpha particles. Eriksson and Helander [6] have examined semi-analytically, the stochastic ripple loss of RF heated ions at JET. They find that finite banana width causes the stochastic threshold to be decreased by as much as an order of magnitude.

For neutral beam ions, evaluating the stochastic threshold is complicated by the effects of charge exchange which are significant for these ions in the plasma. TRANSP follows beam and fusion product ions with an algorithm for artificial acceleration of pitch angle collisions (AAPAC) relative to the banana bounce time, to minimize computational time. The stochastic threshold for neutral beam ions is very sensitive to the AAPAC level. $\delta_S = 2\ \delta_{GWB}$ is practical at the default level used for routine transport analysis at TFTR, but $\delta_S = 4\ \delta_{GWB}$ corresponds to minimal AAPAC. For 100 keV beam ions, this high threshold, compared to δ_{GWB}, may arise from collisional stochastization of the resonant contribution to banana ripple diffusion or from present oversimplifications: the finite ripple diffusion time for neutral beam ions is not modelled, requiring an effectively higher threshold to match ORBIT code losses.

These code comparisons indicate that analysis codes, such as MAPLOS and SNAP, which set $\delta_S = 0.5\ \delta_{GWB}$ for all fast ions and which do not include effects of pitch angle scattering on the loss fractions, will underestimate alpha particle ripple losses by about a factor of 2 and will overestimate neutral beam ion ripple losses by about the same factor. The TRANSP code calculates the selfconsistent evolution of the plasma equilibrium along with ripple loss, collisional effects, beam driven and bootstrap current, *etc.* As a result, a new stochastic loss region develops near the magnetic axis when ripple losses are calculated [4]. The appearance of this region may be an artifact of modelling the diffusion process too simplistically.

3. Comparison with Experimental Measurements

The renormalized stochastic domain ripple model has been used for analysis of current TFTR DT experiments. Ripple loss energy fractions range from 2-15% for alpha particles and from 2-20% for neutral beam ions. The effects of pitch angle scattering accummulate over τ^{α}_{s} so that losses increase as Ip increases, as was also found in ORBIT simulations [3].

General Atomics, the Princeton Plasma Physics Laboratory and the Ioffe Physical-Technical Institute have developed a pellet charge exchange diagnostic (PCX) [7] to observe the confined alpha particle distribution function. For a sawtooth free experiment (#84550), good agreement with the ORBIT/TRANSP renormalized stochastic domain model [8] is found. This is an important validation of the ripple model, unaffected by unresolved questions about sawtooth modelling.

Limiter heating found with DT experiments agrees within a factor of 2 with estimates from alpha heating based on 6.2 MW maximum fusion power [9].

Lost alpha measurements [10] are difficult to compare quantitatively with the TRANSP modelling, which does not follow the entire ripple lost ion orbit. Figure 1 shows (a) the Ip dependence of alphas measured on TFTR at about 20 degrees below the midplane and 1.7 cm behind the limiter shadow, as well as (b) the TRANSP global loss rates for the alpha particle stochastic ripple and first orbit losses. TRANSP error bars are due to Monte Carlo noise for simulations with 2000 particles. Both measurements and calculations of global stochastic ripple losses show increased loss with increasing Ip at low current. At high Ip, the current dependent behavior of midplane alpha data [11] and its time dependence after neutral beam turnoff are similar to the TRANSP global first orbit loss, with no increase in alpha loss per DT neutron nor decreased average lost alpha energy after beam turnoff, unlike global stochastic ripple loss calculations. The predicted increase in stochastic ripple loss after NBI, strongest at zero degrees, might not be observable with the probe. Differences between the observed and predicted current and time dependence of alpha losses after beam turnoff, may be due to the midplane probe collecting significant first orbit and "fattest banana" orbit losses. Further work is in progress to resolve understanding of the data.

Work supported by the U. S. Department of Energy Contract No. DE-AC02-76-CHO-3073.

References

[1] Hawryluk, R., *et al* ., Phys. Rev. Lett., **72** 3530 (1994).

[2] White, R. B. and Chance, M. S., Phys. Fluids **27** 2455 (1984) .

[3] Redi, M. H., *et al*, "Collisional Stochastic Ripple Diffusion of Alpha Particles and Beam Ions on TFTR", Nuclear Fusion, in press.

[4] Redi, M. H., *et al*, "Modelling TF Ripple Loss of Alpha Particles in DT Experiments", submitted to Nuclear Fusion.

[5] Goldston, R. J., *et al*, Phys. Rev. Lett. **47** 647 (1981) .

[6] Eriksson, L.-G. and Helander, P., Nucl. Fusion, **33** 767 (1994) .

[7] Fisher, R. K., *et al* , "Measurements of Fast Confined Alphas on TFTR", Phys. Rev. Lett, in press.

[8] Petrov, M. P., *et al*, "Studies of Energetic Confined Alphas with the Use of Pellet Charge Exchange Diagnostic on TFTR", submitted to Nuclear Fusion.

[9] Janos, A. C.,*et al*, Rev. Sci. Instrum. **66**, 1 (1995) 354.

[10] Zweben, S. J., *et al.*, "Alpha Particle Loss in the TFTR DT Experiments", Nuclear Fusion, in press.

[11] Zweben, S. J., *et al.*, "Measurements of DT Alpha Particle Loss near the Outer Midplane of TFTR", submitted to Nuclear Fusion.

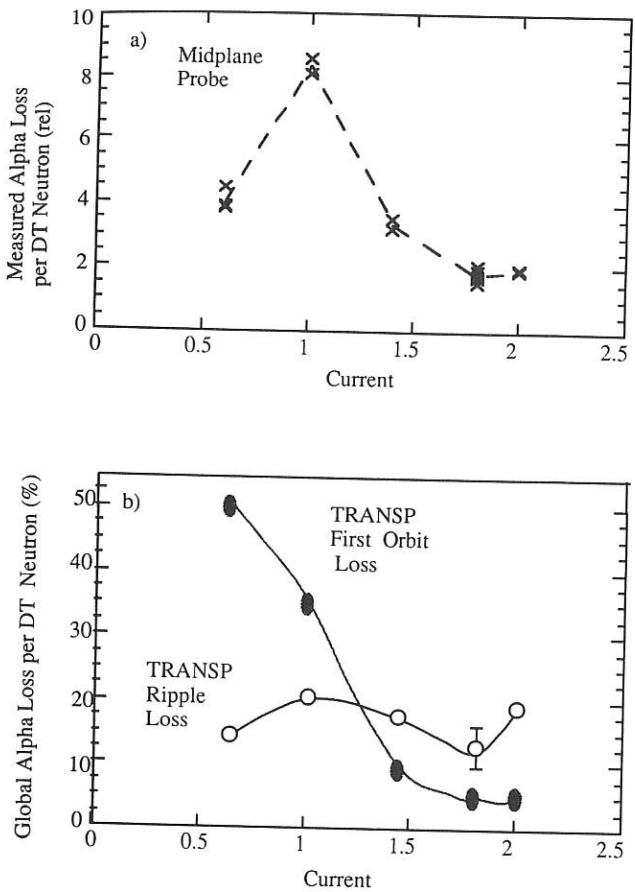


Fig. 1: Ip dependence of alpha ripple losses for R=2.52m plasmas from a) midplane probe measurements and b) TRANSP calculations of global first orbit and stochastic ripple loss.

Improved Performance of DT Supershots in TFTR Using New Techniques of Limiter Conditioning with Lithium

D. K. Mansfield, J. D. Strachan, M. G. Bell, S. Scott, R. Budny, C. E. Bush
and the TFTR Group
Princeton University, Plasma Physics Laboratory
P.O. Box, 451, Princeton, NJ 08543&
J. Terry, E. Marmar and J. Snipes
Massachusetts Institute of Technology, Cambridge, MA 02139

Improved performance of tritium-fueled supershots has been achieved in the Tokamak Fusion Test Reactor (TFTR) by using improved techniques to cover the limiter surface with lithium (Li). These techniques include increasing the number of Li pellets injected prior to plasma heating with neutral beam injection and depositing additional Li on the limiter surface by injecting multiple pellets into three Ohmic pre-conditioning discharges. This sequence of discharges was designed to "paint" the limiter surface with Li just prior to attempting the supershot of interest. These techniques have led to supershots with enhanced core confinement properties as well as with extremely peaked density and pressure profiles. Indeed, because of this peakedness, several of these Li-assisted supershots have reached central ratios of fusion output power to input power approaching unity ($\equiv Q_{DT}(r=0) = 0.6$ - 0.8) even though the global Q_{DT} of these discharges remained at the more modest value of 0.27. Moreover, experiments employing these techniques of limiter conditioning have culminated in a tritium-fueled discharge which reached a Lawson triple product of $n_e\tau_E{}^*T_i \approx 9 \times 10^{20}$ m^{-3} s keV. This discharge exhibited both the highest energy confinement time ($\tau_E \approx$ 330 ms) and the highest ion temperature ($T_i \approx 45$ keV) attained to date in TFTR .

In Fig. 1 is shown the time evolution of the Lawson triple product for shot #83546. This quantity is compared against several similar discharges fueled only by deuterium and which did not have the advantage of Li conditioning. It should also be noted that shot #83546 was carried out at the highest toroidal field and plasma current which were consistent with the injection of the maximal number of Li pellets (4 pellets, 5.5 T, 2.3 MA). Clearly, the combined effects of tritium fueling, Li conditioning and operation at high plasma current and high toroidal field have led to enhanced particle and energy confinement in shot # 83546. This, in turn, has led to a dramatic increase in the attainable Lawson triple product.

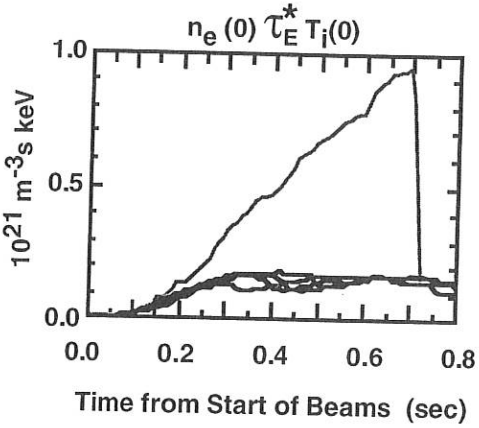


Fig. 1 The Lawson triple product of this discharge (shot #83546) is seen to increase dramatically when compared to D-only supershots at the same beam power. This discharge had 17 MW of T-only neutral beam injection.

Additionally, an unexpected phenomenon has been seen in the behavior of the electron temperature in these discharges. In several of the D-T fueled supershots studied in these experiments, the electron temperature was seen to rise dramatically *after* the termination of beam heating. Shown in Fig. 2 are two traces of electron temperature taken for discharges which were each heated with 16 MW of NBI power. In one case D and T beams at roughly equal powers were injected into a discharge with a plasma current of 2.3 MA and a toroidal field of 5.5 T. In the other case, beams were injected into a 2.1 MA, 5.1 T discharge fueled with D only. In both discharges, four Li pellets were injected just prior to the start of NBI. In both cases the electron temperature is seen to rise after the termination of neutral beam heating. However, in the D-T fueled discharge this rise is much more pronounced. This dramatic rise in Te is finally terminated by an MHD event just before the start of the ramp down phase of the discharge. This particular discharge, shot # 83545, exhibited the highest electron temperature (Te $\approx$ 15 keV) of any TFTR discharge to date.

Because neutral beams are a source of cold electrons, some modest rise in Te is to be expected when beam heating is terminated. Indeed, this rise is often seen in TFTR supershots and is represented by the comparison shot in Fig. 2. However, the anomalously large rise in Te seen in D-T supershots with maximal lithium conditioning suggests that additional physics is contributing to this phenomenon. While it is still under study, this phenomenon is considered to be a consequence of improved core confinement and *may* be associated with residual alpha particle heating of electrons.

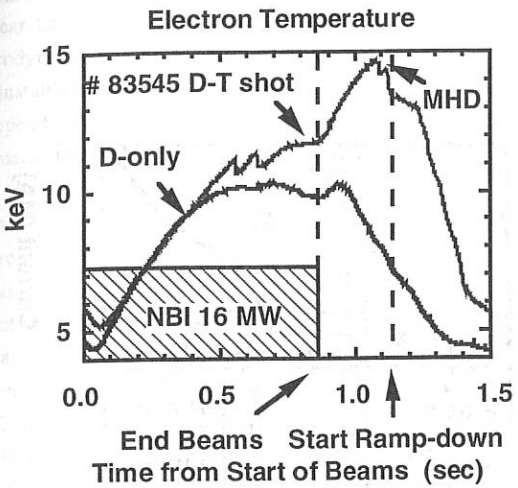


Fig 2 The electron temperature is seen to rise dramatically after the termination of D-T neutral beam injection. A much smaller rise is seen in the case of a D-only discharge.

The improvement in fusion performance outlined in this work is a result of the conditioning effects of Li and *may* also be a consequence of the manner in which Li was introduced onto the inner wall in the discharges preceding the supershot of interest. Generally, before attempting a tritium-fueled supershot, the graphite limiter surface of TFTR was pre-conditioned by a series of three D-only Ohmic discharges. These pre-conditioning discharges were initiated on the outboard limiter of TFTR. After establishing plasma breakdown on the

outboard limiter and waiting until the early MHD activity had dissipated, the plasma column was moved inward to engage the inboard limiter just long enough to accomplish the injection and subsequent pump-out of four Li pellets. The plasma column was then moved back onto the outboard limiter and allowed to terminate. This outboard-inboard-outboard procedure was undertaken to minimize the amount of Li eroded from the inboard limiter by the MHD activity excited during plasma breakdown and termination. As is shown in Fig. 3, each of the three pre-conditioning discharges was carried out at a different major radius; the first discharge was carried out at R = 245 cm, the next at R = 252 cm and the third at R = 257 cm. This increasing sequence of major radii was undertaken in an effort to "paint" the limiter with Li.

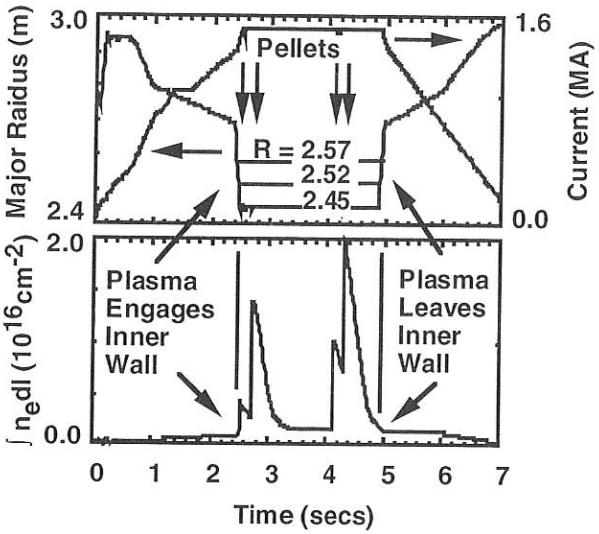


Fig. 3 The scenario employed to pre-condition the TFTR graphite limiter in these experiments is summarized in this figure. Three discharges with sequentially increasing major radii are each injected with four Li pellets. Each of these low current, Ohmic discharges is initiated and terminated on the outboard limiter. The Plasma column is allowed to engage the inner limiter just long enough to accommodate the injection and subsequent pump-out of four pellets. These tactics were used in an effort to cover as much of the limiter surface as possible while avoiding erosion of the Li during breakdown and termination of the discharge.

Supershot Performance with Reverse Magnetic Shear in TFTR

S. H. Batha,[a] F. M. Levinton,[a] M. C. Zarnstorff,[b] and G. L. Schmidt[b]
[a]Fusion Physics and Technology, Inc., Torrance, CA USA 90503
[b]Princeton Plasma Physics Laboratory, P.O. Box 451, Princeton, NJ USA 08543

1. Introduction

Discharges with large regions of reversed magnetic shear and good energy and particle confinement have been produced in the Tokamak Fusion Test Reactor (TFTR).[1] Negative magnetic shear has been predicted to improve transport by stabilizing some classes of magnetohydrodynamic instabilities such as ballooning and resistive tearing modes, and also some microinstabilities. It is also desirable for good bootstrap current alignment. The stability is dependent upon q(0), the minimum value of q (q_{min}), and the location of the q_{min} surface [normalized minor radius $(r/a)_{qmin}$ or major radius R_{qmin}], as well other parameters which are as yet unknown. Several techniques have been developed to control the q profile on TFTR and are described in section 2. High-performance discharges are created by injecting more than 18 to 25 MW of neutral beam power into a reversed-shear target plasma. Such a discharge is described in section 3.

Heating of the plasma during a rapid plasma current increase is necessary to produce a reversed-shear current profile. Heating raises the plasma temperature which increases the current diffusion time and slows penetration of the plasma current to the center of the plasma. The most efficient method is to start the heating as early as possible during a "prelude" phase during the initial current ramp. The current ramp alone is insufficient, as shown in Fig. 1.

The prelude heating can be from tangential neutral beams (NB), as shown in Fig. 2(c), or from ICRF. The preferred "prelude" phase of the discharge has P_{nb} = 5 MW beginning at about 0.55 sec and increasing to 8 MW at 1.0 sec with P_{co} = 6 MW and P_{ctr} = 2 MW. The plasma current rises at a rate of 1.6 MA/sec for the first half second. The ramp rate is then decreased to 0.4 MA/sec until the desired plasma current of 1.6 MA is reached at 2.0 sec. The plasma major radius is approximately the final value of 2.60 m at 0.1 sec. The toroidal field reaches its full value of 4.6 T at 2.60 m at 0.0 sec.

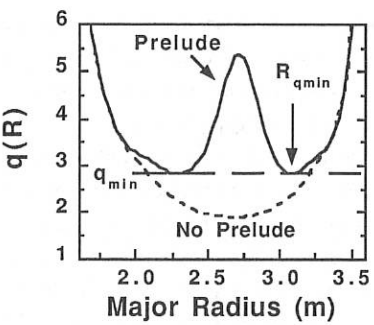


Fig. 1: The measured q profile at 2.55 sec for discharges with and without prelude heating.

Profiles of the magnetic-field pitch angles in

TFTR are measured by a motional-Stark-effect polarimeter with good spatial and temporal resolution.[2] The equilibria are then reconstructed with the VMEC free-boundary equilibrium code[3] which determines the values of q_{min} and $(r/a)_{qmin}$ with accuracies of 10% and 5%, respectively.

2. q-Profile Control

Control of the q profile has been achieved by optimizing the plasma startup, prelude start time, the NB directionality during the prelude heating phase, and the plasma current ramp rate. It has been observed that high levels of MHD activity during the prelude phase can lead to very rapid current penetration even with early neutral-beam injection. The resulting plasmas have lower values of q(0) and no regions of reverse shear. Details of the plasma startup such as current ramp rate, time at which the current ramp rate changes, major radius evolution, and value of q(a), have been optimized to avoid such MHD.

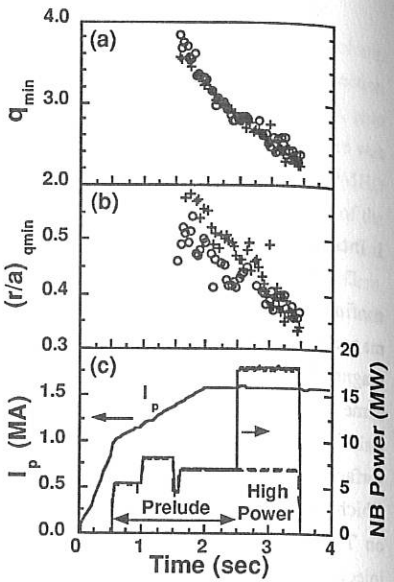


Fig. 2: qmin (a) and $(r/a)_{qmin}$ (b) for discharges with (o) and without (+) a high-power phase starting at 2.5 sec. The plasma current and neutral-beam heating waveforms are shown in (c).

Shear reversal over half the plasma minor radius at the start of the heating phase has been obtained by very early beam injection as shown in Fig. 3. Delaying the prelude heating decreases the size of the reverse shear region. The value of q_{min} also decreases at 2.55 sec (the start of the high-power phase) from q_{min} = 2.8 to 2.0 as the prelude start time is delayed from 0.55 to 1.5 sec. Also, q(0) decreases from about 6 to about 2. The prelude start time has little affect on the rate at which the shear reversal region shrinks or q_{min} decreases. Further control of $(r/a)_{qmin}$ and q_{min} can be achieved by varying the start time of the high-power heating phase, as shown in Fig. 2.

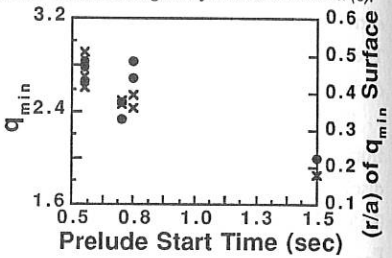


Fig. 3: Delaying the prelude heating start time decreases q_{min} (•) and the size of the region with reverse shear (X) at the start of the high-power heating phase.

The q profile is also affected by the direction of the injected neutral-beam power during the prelude. For example, unidirectional NB injection would lead to strong beam-driven

currents while injection with equal amounts of power in the direction of the plasma current (co-injection) and counter to the plasma current (ctr-injection) would minimize the beam-driven current. Experiments which varied the amount of co- and ctr-injected power during the prelude phase are shown in Fig. 4. The largest values of $(r/a)_{qmin}$ are created by predominantly co-injection. However, co-only injection of 8 MW during the prelude caused the discharge to disrupt. It is not yet clear whether pure co-injection of less than 8 MW raises q_{min} more than does a co-fraction of ≈ 0.5.

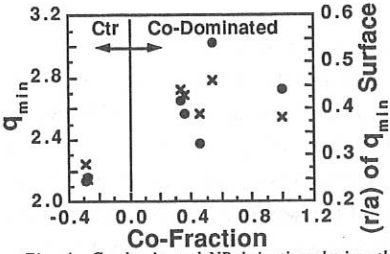


Fig. 4: Co-dominated NB injection during the prelude phase increases q_{min} (•) and the region of reverse shear (x). Co-Fraction is defined as $(P_{co} - P_{ctr})/P_{nb}$.

Increasing the current ramp rate from the nominal 0.4 MA/sec after 0.5 sec modified the q profile and its evolution. Discharges with faster ramp rates reached the final current earlier in time than 2.0 sec. Comparisons at 0.16 sec after a plasma current of 1.6 MA was reached showed that a 20% faster ramp rate increased both the size of the reverse shear region and q_{min}. Both quantities were reduced at the fixed time of 2.55 sec, however. Because q_{min} and $(r/a)_{qmin}$ decrease at a predictable and reproducible rate during the discharge, a range of values can be accessed by varying the time of high-power injection.

Figure 5 displays the wide range of q profiles, as parameterized by q_{min} and $(r/a)_{qmin}$, produced during the high-power phase of reversed-shear discharges through the techniques described here. Modest independent control of $(r/a)_{qmin}$ and of q_{min} has been demonstrated. During the discharge, lower values of q_{min} and $(r/a)_{qmin}$ are reached since both quantities continue to fall during a discharge. Future experiments are intended to develop methods that change the relationship between these quantities and to create larger regions of reversed shear with controlled values of q_{min}. Raising the plasma current from 1.6 MA, increasing the plasma current ramp rate, and beginning beam injection as early as 0.3 sec will be explored. It will also be important to develop techniques such as mode-conversion current drive (MCCD)[4] or lower-hybrid current drive (LHCD) to hold q_{min} and $(r/a)_{qmin}$ constant during a discharge.

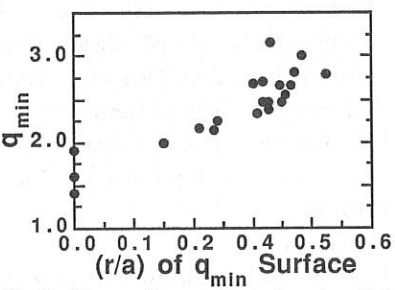


Fig. 5: The q profile control techniques described in this paper have accessed these q profiles. Data is shown at the start of the high-power phase.

3. High Performance

High performance discharges were created by injecting up to 25 MW of NB power when the values of q_{min} and $(r/a)_{qmin}$ reached the desired values, typically at 2.5 sec. The values of q(0), q_{min} and $(r/a)_{qmin}$ decreased during the discharge at a predictable rate, Fig. 2. High-power injection did not strongly affect the evolution of any of these quantities.

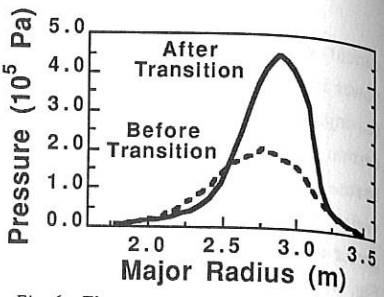


Fig. 6: The pressure at the center of the plasma is greatly increased when the discharge enters the R/S mode.

When an observed P_{nb} threshold of 18 to 25 MW was surpassed, the discharge entered the reversed shear confinement mode (R/S mode) with drastically reduced particle and energy transport in the core of the plasma.[1] Figure 6 shows that the pressure in the center of the plasma was like that of a typical TFTR supershot before the R/S transition occurred during the high-power phase. After the transition, the pressure and pressure peaking factor [p(0)/<p>] increased greatly. The increased central pressure reflects an increased central particle density caused by a dramatic decrease in both the electron and ion particle diffusivity. The global energy confinement time also increased

The plasma performance of the reverse shear plasma during the prelude phase was already similar to that of the supershot mode. Both have high electron and ion temperatures, high ratio of T_i/T_e, peaked density profiles, and energy confinement enhancement greater than 2 compared to L-mode scaling. When the plasma made the transition into the R/S mode, performance was further improved.

Most of the discharges reaching the R/S mode have disrupted due to MHD instabilities. The driving mechanism has not yet been determined unequivocally. However, the MHD activity was only observed outside $(r/a)_{qmin}$ which is significantly outside the location of the peak pressure gradient. There was no activity observed in the core of the plasma. In contrast, the disruption stability of standard TFTR supershots is limited by MHD instabilities in the plasma core at the peak of the pressure gradient.

This work was supported by the U. S. Department of Energy Contract No. DE-AC02-76-CHO-3073.

References

1. F. M. Levinton *et al.*, *submitted to Phys. Rev. Lett.* (1995).
2. F. M. Levinton *et al.*, *Phys. Fluids B* **5**, 2554 (1993).
3. S. P. Hirshman *et al.*, *Phys. Plasmas* **1**, 2277 (1994).
4. R. Majeski *et al.*, *to be published in Phys. Rev. Lett.* (1995).

HIBP diagnostics on TJ-1 tokamak and first results of plasma parameters measurements

I S Bondarenko, S M Khrebtov, L I Krupnik, I S Nedzelskij,
Institute of Plasma Physics, National Scientific Centre "KhIPT", Kharkov, Ukraine.
N K Kharchev, A V Melnikov, L G Zimeleva,
Institute of Nuclear Fusion, Russian Research Centre "Kurchatov Institute", Moscow, Russia
C Hidalgo, I Garcia-Cortes, Ciemat, Madrid, Spain.

1. Introduction

The essential role of the electric field on the fusion plasma confinement and equilibrium is well recognized [1]. The effect of the electric field on the behavior of toroidal plasmas is twofold. The first is the control of some confinement processes by static electric field. The effect of the intrinsic electric field on the plasma confinement through the **E*B** drift was discussed both in the bumpy torus [2] and stellarators [3]. After discovering of the H-regimes the significance of the static radial electric field in tokamaks was recognized also [4]. The second is the effect of the electrostatic fluctuations on the transport processes [5]. The Heavy Ion Beam Probing (HIBP) is the only method allowing to investigate both sides of the phenomenon of the plasma electric field. HIBP is able to measure as the potential time evolution (oscillations) in each selected point, as the radial electric field profiles in different time interval of discharges. The measurements are possible both in the plasma edge and in the plasma core [6]. In this report we describe the basic properties of HIBP on TJ-1 tokamak, and some results of the plasma potential and density investigation.

2. HIBP Diagnostic Set-Up

To study the TJ-1 plasma a system for probing by Cs^+ beam with the energy up to 100keV was developed (Fig.1). There was installed the toroidal steering electrostatic plates before the energy analyzer to correct the toroidal displacement of the secondary ions. The detector grid in the midplane of the plasma for the toroidal magnetic field B=1.5T, with corresponding values of beam energies and injection angles is placed also in Fig.1. It shows that the total plasma cross section can be observed with the energies 6-62keV and injection angles $27^o \pm 12^o$. The most of the measurements were carried out along the detector line passing through the center of the discharge chamber (bold line in Fig.1). The spatial resolution was L=2-5mm, temporal resolution was limited by the data acquisition system (the bandwidth 20kHz).

3. Experimental Results

The measurements were performed in the regime with the magnetic field B=1.1-1.4T, and current I=26-32kA, pulse duration 25ms. The energy analyzer is schematically shown in Fig.2(a,b). Fig.2 also presents the typical traces of the secondary beam currents I_1 - I_4 coming from the plasma centre to four detector collecting plates (1-4 in Fig.2 (b)). Here also the total

secondary current $I_{tot} = I_1 + I_2 + I_3 + I_4$ is presented, which is connected with the plasma density n as follows: $I_{tot} \propto n L$. Plasma potential φ and toroidal displacement Z_{tor}, produced by the poloidal magnetic field, are calculated from these currents by:

$$\varphi \propto (I_2 + I_3 - I_1 - I_4)/I_{tot} \qquad Z_{tor} \propto (I_1 + I_2 - I_3 - I_4)/I_{tot}$$

Plasma potential is presented in absolute values, toroidal displacement in arbitrary units. Fluctuations of the density and potential during the short time interval are shown in more details. The typical oscillation frequency is 10 kHz, the phase difference the density and potential oscillations is 180°. The level of fluctuations is changed in different discharges from 5% up to 25%. Fig.3 presents the example of the absolute plasma potential and relative density profiles, obtained by scanning of the injector angle three times during one discharge. The scanning time was less than 2ms. The solid lines were obtained during one shot by scanning along the central detector line. The dashed line was obtained in another shot along the outer detector line. The absolute potential reference was made by absolute calibration of analyzer on the He gas target. It is in agreement with the Langmuir probe potential measurements. The shift of the plasma column along the detector line (down and outward), is in accordance generally with SXR emission measurements. The spatial structures on the density profiles could be connected with magnetic islands near the rational q surfaces.

4. Conclusions

1 HIBP on TJ-1 demonstrated the possibility of measurements of the plasma parameters (electric potential, density) with a good time and spatial resolution. Shot by shot measurements allow to obtain the time evolution of the plasma parameters in every desired point of the detector grid. Used bandwidth of the system allows to see slow oscillations. Scanning along the detector line in the single shot allows to get a few profiles.

2. During flat-top phase of discharge the density profile is symmetrical and the plasma column is generally centered. In the current ramp down phase the density profile becomes non symmetrical and moves generally outward.

3. There are space nonregularities on the density profiles, their presence may be connected with MHD structure near the rational q surfaces.

4. During the discharge the plasma potential change its sign from negative values in flat top phase to positive one in the current ramp down phase. The potential and the electric field change the sign very rapidly. This evidence is reproduced in H and D discharges with toroidal fields B=1.1-1.4T.

5. The absolute values of the plasma potential are changing, in general, from -50V to +300V.

6. There are the 10kHz oscillations on the density and potential profiles. The phase difference the density and potential fluctuations is 180°.

References.

[1] K.Ida, Y.Muira, S-I Itoh et al." Physical Mechanism Determining the Radial Electric Field and its Radial Structure in a Toroidal Plasma". NIFS-313, Oct.1994, Nagoya, Japan

[2] F.M.Bieniosek, K.A.Connor "Space potential profile in ELM bumpy Torus (EBT) experiment". Phys. Fluids, vol. **26,** p.2256, 1983.

[3] L.M.Kovrizhnykh " The energy confinement time in stellarator". Nucl. Fusion, vol. **24**, p 435, 1984.

[4] S-I Itoh, K. Itoh "Model of L to H-mode transition in tokamaks" Phys.Rev.Lett., vol. 60, p2276, 1988.

[5] B.B. Kadomtsev, Plasma Turbulence. London-New York. Academic press, 1965.

[6] Yu. N. Dnestrovskij, A.V.Melnikov, L.I.Krupnik, I.S Nedzelskij, "Development of Heavy Ion Beam Probe Diagnostics", IEEE Transactions in Plasma Science vol.**22,** N4, p 310, 1994.

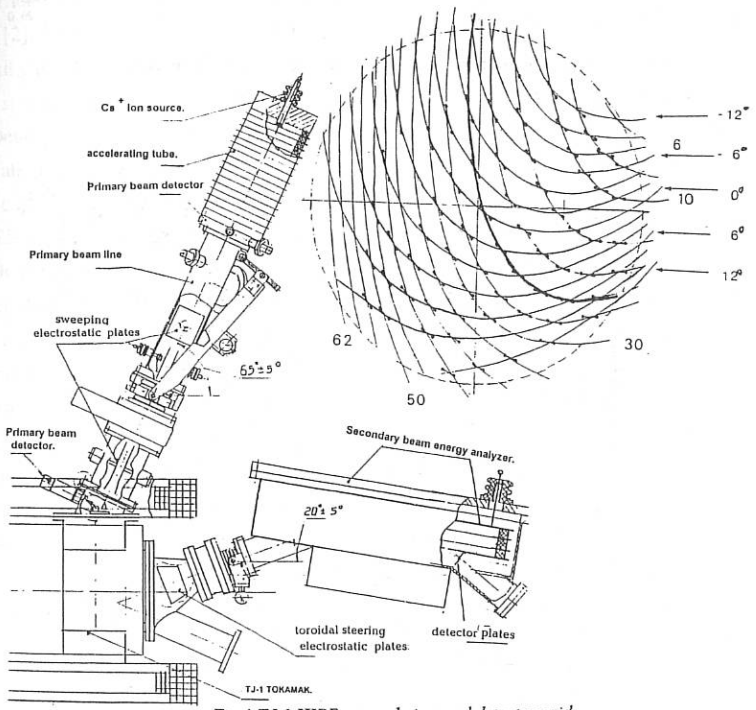


Fig.1 TJ-1 HIBP general view and detector grid

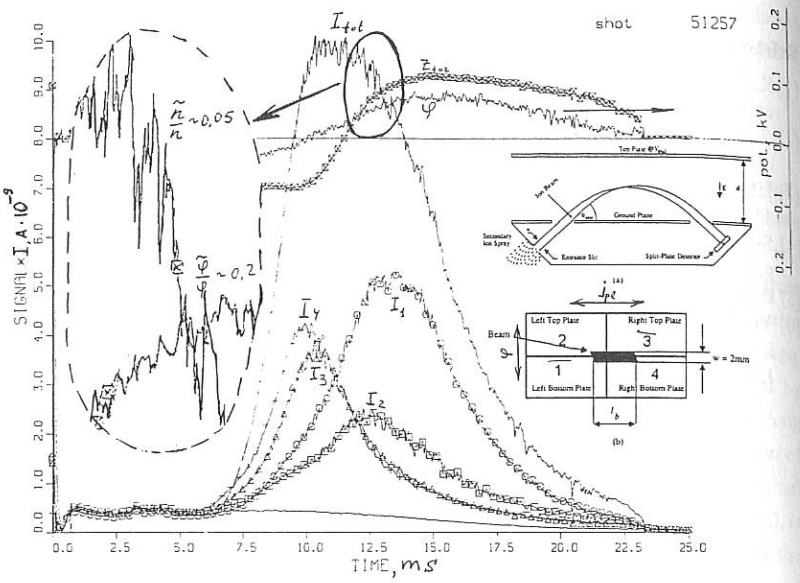


Fig.2 Energy analyzer and the typical signal from the collecting plates.

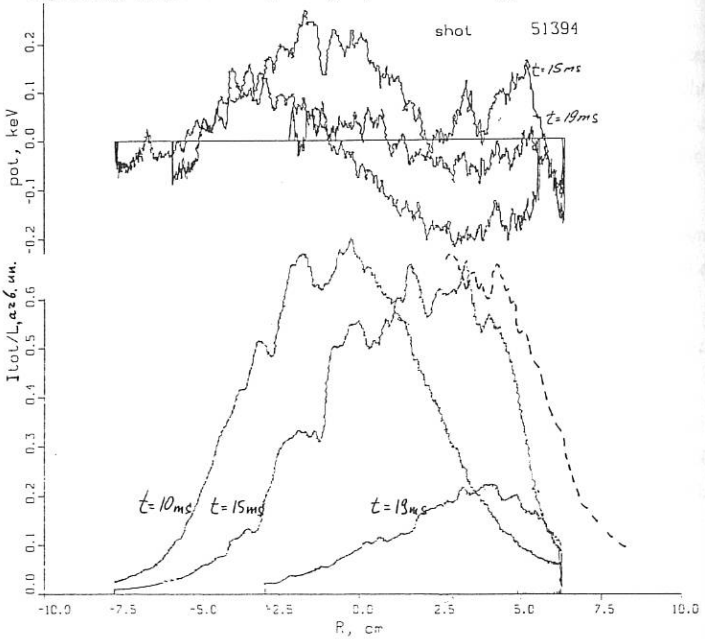


Fig.3 The plasma electric potential and density profiles.

EFFECTS OF ACTIVE PUMPING AND FUELLING ON DIVERTOR PLASMA DISCHARGES IN JET

G Saibene, M L Apicella[1], K Bart, D J Campbell, J K Ehrenberg, P J Harbour, L D Horton, C G Lowry, A Loarte, R D Monk[2], W Obert, A Rossi, R Sartori, D Stork and E Thompson.
JET Joint Undertaking, Abingdon, Oxon, OX14 3EA, UK
[1]Associazione Euratom-ENEA sulla Fusione, CRE Frascati, 00044 Frascati (Roma), Italy
[2]and Dept of Physics, Royal Holloway College, University of London, Surrey, TW20 0EX, UK

Abstract: This paper presents an overview of the experiments carried out to study and characterise the influence of active pumping on the main plasma and divertor parameters during the JET MkI 1994-95 experimental campaign. Results are presented for pure Deuterium plasmas; for a study of impurity retention and flows effects see [1].

1. NEW FEATURES OF THE FUELLING AND PUMPING SYSTEMS OF JET

Gas can be introduced into the vessel from 10 individually controllable modules, which provide a distributed source for the plasma, with up to $5x10^{22}$ D^o s^{-1} steady state fuelling capability. Six modules provide fuelling in the main SOL, and the remaining four modules, located in the divertor, fuel gas into the private flux region.

Active particle removal during plasma discharges is provided by a toroidally continuous cryopump [2], located below the divertor plates (figure 1). The cryopump operates at 4.6 K, therefore all gases but H_2 and He are pumped by cryosorption. The pump is equipped with an in-situ Ar spray system, to allow pumping of He and H_2 by cryotrapping (Ar frosting). The effective Deuterium pumping speed of the cryopump on the vacuum vessel is about 160 m^3s^{-1}, while it is about 240 m^3s^{-1}, or $\approx 1x10^{25}$ atoms $mbar^{-1}s^{-1}$ at the LN shields (gauge 5, figure 1). The pump capacity is $\approx$ 300 discharges.

2. DEUTERIUM PUMPING DURING PLASMA DISCHARGES

2a. Particle removal in Ω, L and H mode regimes - Due to the toroidal gaps between tiles in the MkI divertor target, particles are pumped for all separatrix positions on both the horizontal and vertical divertor target plates. The particle removal rate varies only by a factor of two, for any separatrix position (figure 2).

The removal rate is directly proportional to the neutral pressure in front of the cryopump, which in turn, depends on the plasma density and confinement regime.

In Ohmic and L mode discharges, the pressure in the divertor increases with the plasma density whilst, in Elm-free H modes, both the D_α and the pressure in front of the pump are low (typically $\approx 5x10^{-4}$ mbar), due to the improved particle confinement, and decoupled from the main plasma density. However, higher particle pumping is observed during ELMy H modes, when pressure bursts in the divertor are measured $\approx$ 10ms after the D_α spikes. The integral particle removal associated with isolated giant ELMs can be of about 30% of the typical plasma particle content. For normal type I ELMy discharges, the integral particle removal associated to one ELM varies, up to approximately twice the net plasma inventory loss. This

indicates that some of the particles removed by the pump are originated by plasma induced desorption from material surfaces [3]. The particle removal rate also depends on the type and duration of the ELMs and on the "baseline" recycling level (i.e. on the discharge configuration, density and fuelling). Hence, either an equilibrium between particle input and removal or net wall depletion is achieved. In the case of short, high power and low recycling discharges, net wall depletion is generally not observed.

2b. Neutral pressure in the divertor and fuelling effects (see also [4]) - The plasma configuration sketched in figure 2 was used to carry out detailed comparison between pump on and off, and to assess the effects of the gas inlet location (#31584, pump off, top fuelling; #31585, pump off, divertor fuelling; #31725, pump on, top fuelling). These discharges had volume average density of $3x10^{19}m^{-3}$. In figure 3, the neutral pressure profiles (gauge 4, figure 1) are compared to those of the ion flux J_{sat}, measured with a triple Langmuir probe sitting at the same poloidal location in the outer strike zone. The characteristic decay length of the ion flux λ_{Jsat} is $\approx$ 2.5cm, while λ_o for the sub-divertor neutral flux is approximately 15cm, for both the pump on and off cases. This result is consistent with neutral recirculation playing an important role in determining the neutral distribution. The broad pressure profiles explain the good pumping obtained in every magnetic configuration. For #31584, we compared the integrated ion and D_α fluxes at the outer strike zone to the neutral flux as measured by the ionisation gauges below the divertor target: these are about $4.6x10^{22}s^{-1}$, and all agree to within 25%. When the plasma detaches [5,6], the equivalence between ion flux and neutral pressure in the divertor no longer holds. Therefore, active particle exhaust is maintained also for detached plasmas. The location of the gas inlets (top or divertor, pump on or off) does not strongly affect either J_{sat} at the target or the neutral pressure (with the exception of the private flux region). The integrated fuelling efficiency decreased with the pump on from $\approx$ 10% to 2%.

2c. Effects of active pumping on plasma parameters - H-mode discharges with active pumping are characterised by a reduction of the D_α intensity both in the main chamber and in the divertor and by an increase in the plasma stored energy, central ion temperature T_i and neutron rate R_{DD}.[7, 8 and 9]. These changes are more pronounced in plasma configurations with a medium-high "intrinsic" level of recycling. The improved performance can be correlated with the changes in the density profiles, in particular for ELMy H modes, the edge density (inside the separatrix) is generally reduced, and more peaked temperature profiles are measured. This is consistent with reduced recycling from the wall, and an improved neutral beam penetration. Changes are also observed in the divertor parameters (J_{sat}, n_e and T_e) with the pump on: target profiles become steeper by approximately 20% in-between ELMs, while during ELMs, the n_e profiles become steeper and T_e profiles are broader. The *integrated* ion flux to the target decreases by a factor of $\approx$ 2, the *peak* electron temperature T_e in both strike zones increases by approximately the same amount, whereas the *peak* density n_e is down by a factor of 2 at the inner target and is a factor of 3 to 4 at the outer target.

2d . Density control during H modes - With the pump on, density control in steady state is achieved during ELMy H modes, both for neutral beam only and neutral beam+gas fuelled discharges. In contrast to pump off cases, where the steady state plasma density is determined by the beam fuelling and the ELM characteristics, the combination of fuelling and pumping allows the steady state density of H-mode discharges to be varied by a factor of two (figure 4).

3. He PUMPING

The Ar frost technique, used in He transport and exhaust experiments, has proven to be difficult, and this has limited the amount of useful data obtained. In contrast to DIII-D [10], we find that the Ar spray contaminates the plasma facing surfaces, leading to Ar contamination of the discharges and disruptions. Two to three pulses are required to recover normal divertor plasma operation. The He pumping speed S_{He} depends on the D^o load on the Ar layer (figure 5) and also on the flow rate of D^o. In particular we have evidence of "recovery" of pumping speed between plasma pulses. This would indicate that D^o and He diffuse into the 10μm thick Ar layer in the time between discharges (≈ 30min).

Even before the He is injected ($1x10^{20}$ He atoms), the amount of Deuterium used to fuel is typically around $5x10^{22}$ D^o, corresponding to an Ar/(D^o+He) of about 20. Around this ratio and below, S_{He} starts to decrease exponentially, with loss of effective pumping.

4. SUMMARY

The JET divertor cryopump has been routinely used during the 1994-95 campaign.

The plasma parameters and confinement regime both affect the pressure in the divertor, and therefore the particle removal rate. The strongest pumping is observed during ELMy H modes. Depending on the nature of the ELM and fuelling, true steady state or net wall depletion can be achieved. Broad neutral pressure profiles are measured in the sub-divertor region, consistent with the high transparency of the MkI target, and explain the weak dependence of the particle removal rate on separatrix position.

Plasma performance is improved with active pumping. The reduction of the main chamber recycling and of the edge density are correlated to the peaking of the temperature profiles and increased fusion reactivity. With the pump on, the combination of fuelling and pumping allows density control during steady state ELMy H modes.

Ar frost is very effective in pumping He, but only at low D^o and He loads. Ar contamination of the vessel and saturation of the layer have limited so far its application for He exhaust experiments.

5. REFERENCES

[1] P J Harbour et al, these Proceedings
[2] W Obert et al, 16th SOFT, Fus Tech 1990, p 488
[3] J Lingertat et al, these Proceedings
[4] J K Ehrenberg et al, as above
[5] A Loarte et al, as above
[6] R D Monk et al, as above
[7] K Lawson et al, as above
[8] K McCormick et al, as above
[9] D Stork et al, as above
[10] D H Hillis et al, IAEA-CN-60/A2/4-P-11, 1994

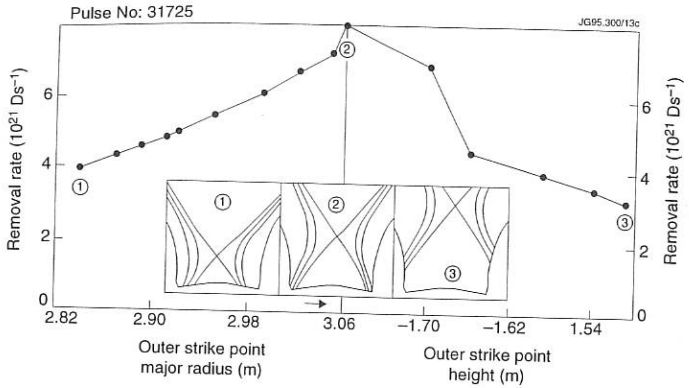


Figure 2: particle removal rate in atoms per second as function of the separatrix position, on the horizontal (a) and vertical plates (b). Pulse # 31725, 2MA/2T. The sweep of the separatrix is carried out over 10s. Maximum pumping is obtained with the divertor strike point located in the outer corner of the target.

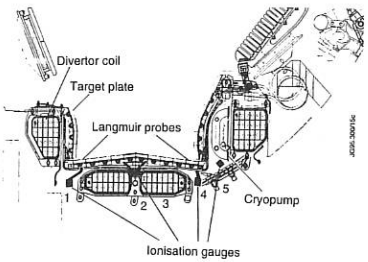


Figure 1 : location of the cryopump and of the fast ionisation gauges in the sub-divertor region. The rows of tiles in the Mark I divertor are separated by gaps, accounting for approximately 10% of the total area.

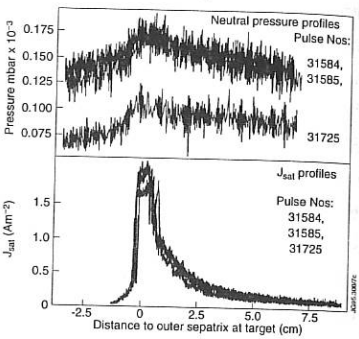


Figure 3: neutral pressure profiles and ion flux profiles for pulses 31584, 31585 and 31725, 2MA/ 2.8T. The profiles are mapped to the sweeping of the outer separatrix.

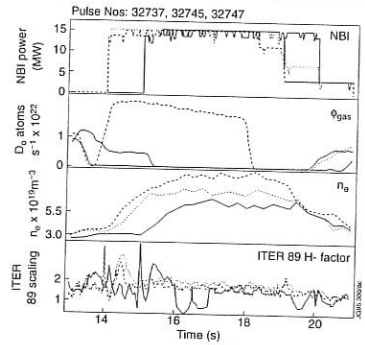


Figure 4: NBI power, D° fuelling rate, plasma density and H factor (ITER89P L mode) for pulses #32737 (corner eq. no gas), #32745 (centred eq., no gas) and #32747 (centred eq, gas fuelled) , all at 3MA/2.8T.

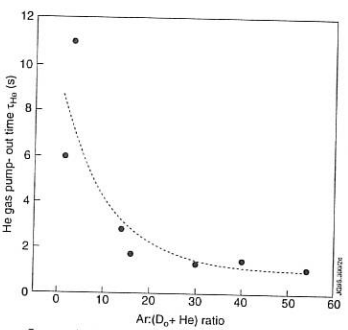


Figure 5: variation in He gas pump-out time τ_{He} as function of (D°+He) load on the Ar layer. Note : $S_{He}=V_{Torus}/\tau_{He}$

Characterisation of Long Pulse Steady-State H-modes in the JET Pumped Divertor Configuration

D Stork, A J Bickley, D J Campbell, S Clement, S Davies, K Erents[1], M Garribba, N Hawkes[1], L D Horton, A Howman, R Konig, H Lingertat, A Loarte, C Maggi, R Monk[2], R Reichle, E Righi, G Saibene and M von Hellerman
JET Joint Undertaking, Abingdon, Oxon, OX14 3EA, United Kingdom
[1] UKAEA Fusion, Culham, Abingdon, Oxon OX14 3DB, United Kingdom
[2] Dept of Physics, Royal Holloway College, Univ of London, Surrey TW20 0EX, UK

1. Introduction

ELMy H-modes with *'giant'* (type I) ELMs have been identified as a regime of interest to Next Step Devices (eg: ITER-EDA [1]) in the route to ignition phase. It is also important to establish *steady-state* behaviour where the H-mode period (t_H) is much longer than the energy and particle confinement times (τ_E, τ_p) and also long compared to the resistive diffusion time (τ_R).

For ignition, ITER requires an energy confinement enhancement (H) over L-mode (ITER89-P) of ~ 1.6-2.0 [1], with operation at q_{95} ~ 3.and $Z_{eff} < 1.8$. Hence H/q_{95} ~ 0.53-0.67 is relevant.

In this paper, we report a study of such H-modes in the JET Pumped Divertor configuration with the *'Mark I'* divertor target ('**JET-PD(I)**'). Achieving these H-modes in the JET-PD(I) configuration is helped by the engineering capabilities of the machine [2] notably:

- the excellent power handling capabilities of the Mark I divertor CFC target;
- the ability to sweep the divertor strike zones to spread the power load on the target;
- the in-vessel divertor cryopump to provide non-saturable (on the timescale of a pulse) pumping for particle control [3].

2. Steady-state H-mode overview

The Mark I divertor configuration routinely produces ELMy H-modes with type I ELMs. The mechanisms for this are not fully understood but the ELM-free period has been shown clearly to depend on the edge shear and triangularity [4] and also the recycling level. The plasma configuration used for the long-pulse Steady-State H-mode (SSHm) development has low triangularity ($\delta \leq 0.2$) and edge shear (S_{95} ~ 3) and so is a *naturally ELMy* configuration. The plasmas were also well separated from the vessel inner and outer wall structures (> 10cm distance). The recycling conditions are discussed below.

ELM production generally helps to spread the power over a larger area than the ELM-free H-mode and ELMs contribute to the ability to give steady-state plasmas in which impurity ingress is kept at bay.

Figure 1 shows the longest duration ELMy H-mode achieved in the JET-PD(I) machine. The discharge length is limited only by the machine engineering constraints. This discharge (at 2MA/2.1T) has: an H-mode duration $t_H \sim 50*\tau_E$ (τ_E ~ 0.4s) and $t_H \sim 0.85*\tau_R$, where the resistive diffusion time is evaluated at mid-radius. The internal inductance ℓ_i is constant indicating that the discharge current profile has reached steady state (the incidence of sawteeth

brings the relevant time down below the calculated τ_R). The energy confinement time, close to the ITER93H-P scale value for *ELM-free* H-modes; Z_{eff}, recycling conditions and radiated power fraction all in steady-state. In addition, the divertor tile temperatures are constant and well below the design value (1500°C). The control of density and recycling indicates that the pumping has not saturated within the pulse, unlike previous JET campaigns [5] where only wall-pumping was available.

The regime in which SSHm discharges have been achieved with $t_H \geq 10*\tau_E$ covers $1 \leq I_p \leq 3MA$; $2.2 \leq q_{95} \leq 4.7$; input power up to 20MW and discharges with normalised $\beta_N > 3$ (the last are considered in a separate paper [6]). The density range over which the regular type I ELMs exist in Steady-State is $3.5\ 10^{19}m^{-3} < \langle n_e \rangle \leq 9{\cdot}10^{19}m^{-3}$ for power levels up to 18-20MW.

At the upper end of the density range, strong deuterium puffing establishes small (*'type III'* or *'grassy'*) ELM behaviour. In these discharges (see Fig 2), the confinement enhancement relative to L-mode has dropped to ~ 1.2-1.3, a factor ~ 0.6-0.7 of the ITER93-HP confinement.

3. Power balance and energy confinement

Radiated power levels in the SSHm regime are found to be ~ 25-40% of the input power. The radiation is split in the ratio ~ 2:1 between the X-point region and the bulk plasma. The power conducted across the separatrix (P_{in}-P_{rad}(bulk)) is typically in the range ~ 1.1-1.5 times the L-H transition threshold, which is found in JET discharges to be approximated by the ITER scaling $P_{L\text{-}H} \sim 0.004 \simeq \langle n_e \rangle B_T S$ [7]. The radiated power in both regions does *not* show a monotonic dependence on either $\langle n_e \rangle$ or $\langle n_e \rangle^2$.

The energy confinement enhancement (H) relative to L-mode is found to be:

- in the range $H_{ITER89P} \sim 1.6\text{-}2.2$;
- independent of density, ie, the density form of ITER89P seems to hold;
- independent of q_{95} down to $q_{95} \sim 2.2$;
- declining as the normalised main chamber recycling increases (see Fig 3).

Examination of individual discharges shows that the effect of high recycling may be important in influencing the early ELM behaviour so that edge pedestals for ion and electron temperatures cannot build up. Lower recycling can increase the central T_i by as much as 30-40% in otherwise similar discharges.

4. Impurity Behaviour

The intrinsic impurity concentrations in SSHm discharges remain low and constant throughout the evolution of the discharge. ELMs are beneficial in keeping target-generated impurities from entering the plasma. The Z_{eff} profiles for a typical 3MA/2.8T SSHm are shown in Fig 4.

4.1 Use of different target materials

SSHm's have been generated using both the CFC and beryllium target plates in the JET-PD(I) configuration. To first order, there is very little difference between the H-modes generated on the two targets. The only differences are that plasma oxygen levels are much higher with the CFC target (factor ~ 5). In all cases, Z_{eff} remains low (~ 1.5).

5. Divertor and edge characteristics

ELMs significantly disturb the edge recycling, impurity radiation and probe signals in SSHm's but approximately constant 'base' levels exist between ELMs.

ELM frequency increases with input power, but the variable behaviour with density and added gas puffs make scaling studies difficult. ***Between ELMs***, the scrape-off layer (SOL) parameters measured by target Langmuir probes show a more dense (by ~ 2-3:1) and colder (by ~ 2:1) plasma at the inner strike zone than at the outer strike zone. The SOL thicknesses are in the range of 1-1.5cm at the target with the outer zone density scrape off length being somewhat larger. ***During ELMs*** the SOL thicknesses increase up to 3-fold (Fig 5).

The inner strike zone density is much larger than the midplane separatrix density (~ 8 $10^{19}m^{-3}$ compared to ~ $10^{19}m^{-3}$ from the reflectometer) but high recycling conditions are marginal at the outer zone between ELMs. However, a basic analysis shows that *between ELMs* the target fluxes at each zone are ~ 6-9 $10^{22}s^{-1}$ (roughly balanced inner and outer) whilst ***during ELMs*** the fluxes rise to ~ 8 10^{23}-1.5 $10^{24}s^{-1}$ (outer-inner). These fluxes are much higher (by an order of magnitude) than those which can be inferred from the flux across the separatrix ($\Gamma_D^{sep} \simeq \dot{N}_D + N_D / \tau_p - \Gamma_{NBI}$ where τ_p is assumed $\geq$ 1 sec ie. $\geq 2*\tau_E$). Thus high recycling conditions even between ELMs seem plausible. The electron temperature at the target is ~ 20-50 eV.

6. Conclusions

The successful generation of Steady-State ELMy H-modes in the JET-PD(I) with duration up to 50 energy confinement times; confinement enhancement equivalent to *ELM-free* H-mode scalings under the best recycling conditions; adequate plasma Z_{eff}; H/q_{95} in the ITER relevant range of 0.53-0.67, and demonstrated impurity control, is an important step in the development towards ITER. The giant ELMs accompanying these discharges exist at plasma density levels up to ~ $10^{20}m^{-3}$ for power conducted across the separatrix at 10-50% above the L-H transition threshold. It is likely that high recycling conditions exist in the divertor region throughout these H-mode periods.

References

[1] F N Perkins et al, contrib paper 15th Int Conf on Plasma Phys and Contr Nucl Fus Res (IAEA, Seville 1994), paper IAEA-CN-60/E-1-I-3.

[2] The JET Team (presented by D Stork), ibid [1], paper IAEA-CN-60/A-1-I-3.

[3] G Saibene et al, these proceedings.

[4] The JET Team (presented by T T C Jones), these proceedings.

[5] P R Thomas et al, Europhys Conf Abstracts **16C**(I) (1992) 239.

[6] C D Challis et al, these proceedings.

[7] E Righi et al, these proceedings.

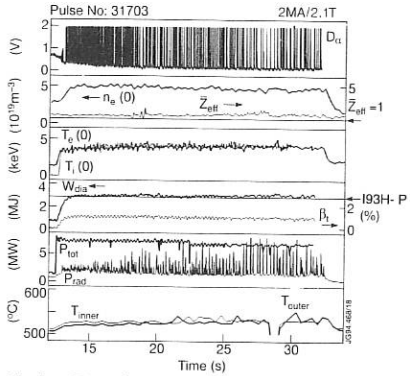


Fig 1: Time development of a long pulse steady state ELMy H-mode at 2MA/2.1T (the 'I93H-P' label indicates the stored energy level corresponding to the ITER93H-P scaling).

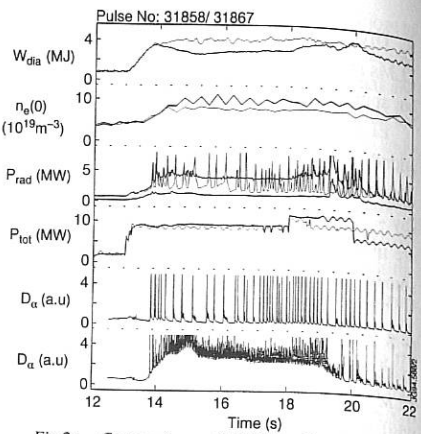


Fig 2: Comparison of SSHm with giant ELMs (#31858) with a discharge subjected to strong D2 puffing (#31867) where the occurrence of 'type III' or 'grassy' ELMs is seen at densities ~ 10 20 m -3 with consequent decline in the H factor.

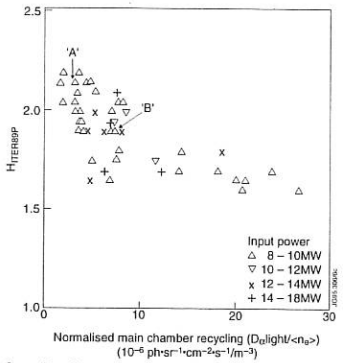


Fig 3: Decline of confinement enhancement with increase in normalised main chamber recycling for 2-3MA SSHm with $tH \geq 10\tau E$.

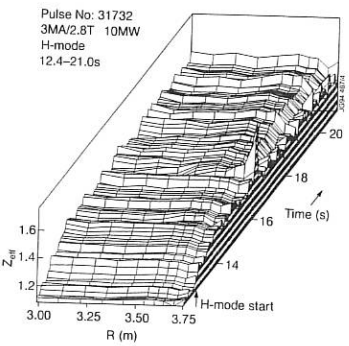


Fig 4: Zeff profiles as a function of time for a 3MA/2.8T 9s ELMy H-mode with 10MW input power.

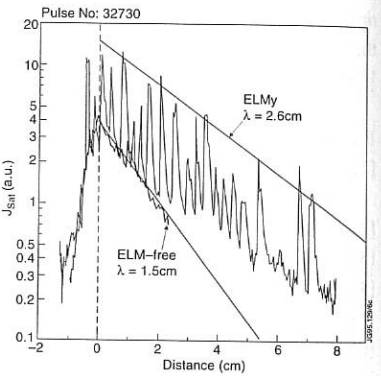


Fig 5: Comparison of profile of ion saturation current (J_{sat}) at outer target for ELM-free and ELMy periods in a 3MA/2.8T SSHmode.

Non-Maxwellian velocity distributions and spatial structures in electron temperature profiles of ohmic and EC-heated discharges in RTP

F.M.A. Box, M.N.A. Beurskens, M.F.M. Steenbakkers, C.J. Barth, C. C. Chu, N.J. Lopes Cardozo, F.J. Pijper, E. Westerhof and the RTP-team

FOM-Instituut voor Plasmafysica 'Rijnhuizen', Associatie Euratom-FOM, P.O. Box 1207, 3430 BE Nieuwegein, The Netherlands

Abstract

Multiposition Thomson scattering measurements in the Rijnhuizen tokamak experiment RTP are presented. Electron temperature profiles measured with a spatial resolution of 1.7 mm show structures with a typical size of 1 cm. Statistical tests are presented showing that these structures are significant and no artifacts are introduced by the diagnostic. Individual spectra, resolved in 57 wavelength channels with a spectral resolution of 3.9 nm, show a two-temperature character. This is especially pronounced at high gradients, and depends on the phase of the sawtooth cycle.

Introduction

Detailed measurements of the electron temperature (T_e) profile in RTP (R/a = 0.72/0.16 m) have shown a variety of small scale structures [1]. These include hot filaments in the centre of the plasma and steep gradients (T_e jumps of 1 keV over 2 mm) near the sawtooth inversion radius under intense electron cyclotron (EC) heating. Also ohmic discharges show bumps with a typical scale of 1 cm. The measurements were done with a multi position Thomson scattering (TS) set up, which measures along a vertical cord through the plasma with a resolution of $\Delta z = 1.7$ mm and $\Delta\lambda = 3.9$ nm covering -53< z< 110 mm and $580 < \lambda < 800$ nm.

These measurements challenge the conventional picture that the magnetic field in a tokamak is formed by a nest of perfect, nested flux surfaces. In this paper we present an extended data set T_e profiles of both ohmic and EC-heated discharges, and statistical analyses aimed at assessing the statistical significance of the measured structures. The high resolution also allows an assessment of the Maxwellian character of the individual spectra.

Although a Maxwellian velocity distribution is assumed for the T_e determination, the TS spectra sometimes show significant distortions from this ideal spectrum. A mixing between high and low temperatures is seen as a function of the temperature gradient and the phase of the sawtooth cycle. Furthermore, we will discuss random structures in the spectra with variable extend in wavelength combined with spatial extension of up to 10 mm in the plasma.

Testing the significance of structures on the T_e profiles.

A series of 8 ohmic discharges were selected in which the discharge conditions were kept nearly constant ($n_e(0) = 7.2 \cdot 10^{19} m^{-3}$, $q_a = 7$). The average squared Fourier spectrum (power spectrum) of these profiles is shown in Fig. 1, where it is compared with the power spectrum of artificial data. The latter is obtained by taking a smooth fit of the T_e profile and generating simulated measurements of this fit with added random noise. The simulation mimicks the entire diagnostic. The noise introduced is tested separately and is in agreement with the error bars determined independently [2]. Clearly, there are significant structures in the real data of size down to a few mm. Also note that the spectrum of the simulated data is very flat, and approaches the measured spectrum at

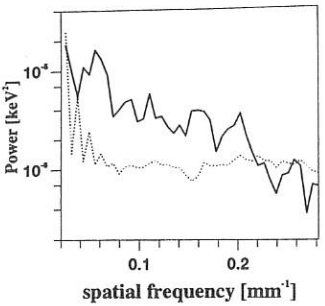


Figure 1: *Averaged PS of 8 ohmic discharges (solid line) compared to the noise level (dotted line).*

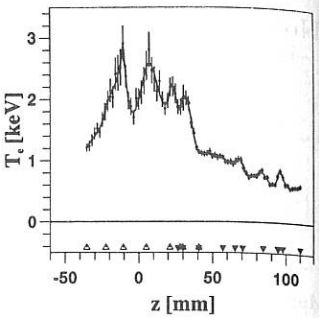


Figure 2: *FK fit of the T_e profile of an EC-heated discharge. The triangles indicate the knot-position.*

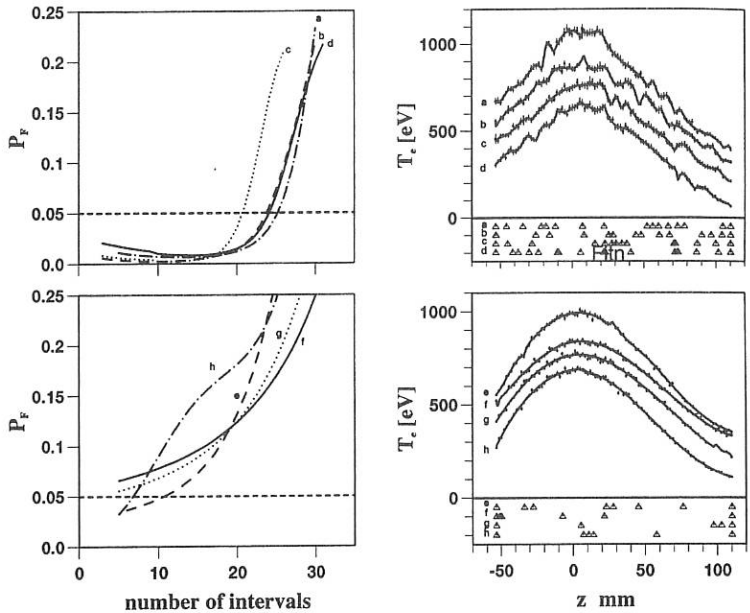


Figure 3: *FK fits of ohmic (top) and simulated (bottom) T_e profiles. P_F is the probability of no improvement.*

very short wavelength (indicating that the errors are not underestimated). The same analysis is applied to a larger data set (79 similar discharges) gave the same result.

To study the significance of the structures in more detail in the real space domain, a method based on free knot cubic spline (FK) fits is used. In this test, a cubic spline with N free knot is fitted to the T_e profile and the χ^2 value of the fit computed. Next, the same is done with a cubic spline fit with N+1 knots. An F-test is used to determine whether the improvement of χ^2 is sufficient to warrant the additional knot. An FK fit

through an EC-heated T_e profile, Fig. 2, $n_e(0) = 1.7 \cdot 10^{19} m^{-3}$, $q_a = 7$, needs 20 knots. The figure shows that edge structures down to 1 cm, the filaments as well as the steep T_e gradients are significant. The top of Fig. 3 shows the fits of T_e profiles of 4 ohmic discharges from the above data set. To test the method, also the fits of 4 simulated T_e profiles were carried out (Fig. 3, bottom). 20 to 24 knots are needed to fit the measurements, whereas 1 to 10 knots suffice to get a good fit of the simulations. The fits of the measurements clearly indicate bumps of size down to 1 cm.

Non-Maxwellian shape as a function of the temperature gradient.
For Ohmic and EC-heated plasmas the ratio between the temperatures derived from a fitting of the wings and of the central part of the Thomson spectrum are investigated as a function of the temperature gradient. The division between the wing and central region is chosen on the place where the velocity of the electrons corresponds to the thermal energy. The fit to the central region leads to a 'center-temperature'. The blue and red wings are fitted together which leads to a 'wing-temperature'. It appears that the ratio $T_{wing}/T_{central}$ is increasing with the gradient steepness. This effect seems most pronounced in EC-heated plasmas just after the sawtooth crash (see Fig. 4). For longer times after the crash the ratio decreases at the highest values of ∇T_e as shown in fig. 4.

After the sawtooth crash there are steep gradients outside the mixing radius and it is in this region where the highest ratio is found. This can probably be understood by the fact that the collision times are of the same order of magnitude as the local transport times in these steep gradient regions. The high and low temperatures are mixed and this effect is affected by the sawtooth crash.

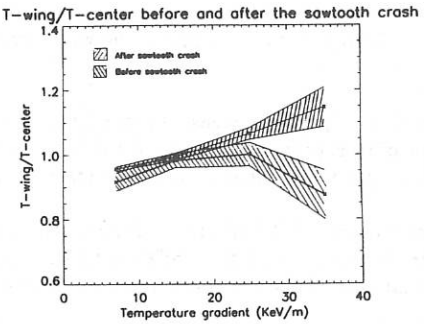


Figure 4: *$T_{wing}/T_{central}$ as function of the gradient steepness. Note that various values are put together in 4 bins with increasing gradient.*

Other non-Maxwellian features of the Thomson spectrum.
Visual inspection of the measured wavelgth spectra gives often the impression that some structures exist superinposed on the Maxwellian spectra. The verification if these structures are significantly above the statistical noise level, has been done on two ways. First the FK analysis as described before indicated that 12 knots were significant whilst from simulated data 3-4 knots would be significant. This suggests that indeed some structures could be real.

The second method has been used to see if a deviation at a selected wavelength extended also in real space, i.e. on neighbouring spectra. For every camera pixel in the

λ_i, z_j domain the errorfunction was calculated.
$P(\lambda_i, z_j) = Erf[(I_{mean}(\lambda_i, z_j) - I_{fit}(\lambda_i, z_j)\ /\sigma(\lambda_i, z_j)]$,
in which I_{mean} is the measured intensity, I_{fit} the intensity as follows from the Maxwellian fit and σ the statistical standard deviation at the pixel λ_i, z_j.

In Fig. 5 a contourplot of $P(\lambda_i, z_i)$ is given for P=-0.68,-0.85,-0.95, 0.68,0.85,0.95 indicating deviations more than 1, 1.5 and 2 σ. For comparison the same is shown for simulated data. From this it can be concluded that some structures of about 10 nm in wavelength and up to 1 cm in real space might be real, but if so coming only barely above the statistical noise level. It should be investigated if these structures are of instrumental nature. More analysis is needed.

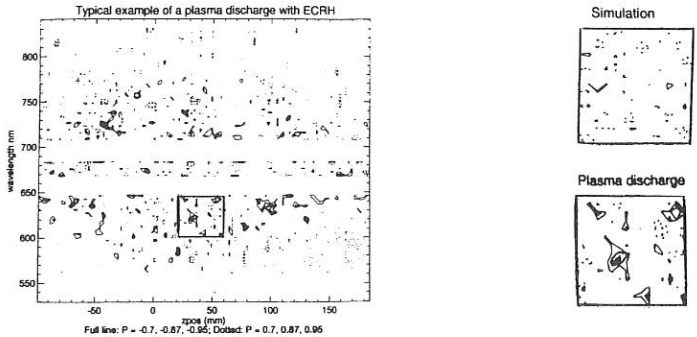


Figure 5: *Contour plot of the structures.*

Conclusions

The statistical tests of the T_e profiles measured with the high resolution TS diagnostic, show the significance of structures in both ohmic and EC-heated plasmas of sizes down to 1 cm. In addition, these tests showed that the structures are not caused by any instrumental effect.

Furthermore, analysis of the TS spectra indicated that the ratio T_{wing}/T_{center} is a function of the T_e gradient and seems to be affected by the phase in the sawtooth cycle. Finally, it appears that the TS spectra contain random structures which extend in real space.

Acknowledgements

Many thanks to the technical staff of RTP for very efficient operation of the machine, and to Tim Luce who introduced us to the technique of cubic spline fitting. This work was performed under the Euratom-FOM association agreement, with financial support from NWO and Euratom.

[1] N.J. Lopes Cardozo et al, 1994, *Phys Rev Lett* **73**, 256.
[2] C.C. Chu et al, 1994, *EPS94, Europhysics conference Abstract, 1248.*

Toroidal and poloidal rotation in the COMPASS-D tokamak

P G Carolan, R O'Connell[#], N J Conway[#], R A Bamford, J Hugill and I M Melnick[+]

UKAEA Government Division, Fusion, Culham Laboratory, Abingdon, Oxon OX14 3DB, UK

(UKAEA/EURATOM Association)

[#]Dept. of Exp. Physics, University College Dublin, Ireland; [+]University College London, UK.

1 Introduction

The COMPASS-D device can provide a variety of plasma conditions that alter the fluid velocity, often within a single discharge. These include Ohmic L- to H-mode transitions[1],[2], mode locking, either naturally occurring[3] or due to applied resonant magnetic perturbations, RMPs, [4]. Multichord Doppler spectrometers are used to examine the behaviour of boron and carbon impurity fluid rotation at the edge regions, both toroidal and poloidal. Core Doppler measurements of chlorine and aluminium are obtained from an X-ray spectrometer. The fast time resolution available allows the investigation of synchronism down to ~0.15-0.3 msec time resolution. We concentrate primarily on the ELM-free periods.

2 Experimental arrangements

Our earlier attempts[1] at observing poloidal velocities were restricted to a single chord at a time and using a BIV line (282nm). We have since looked further out in the plasma, using a CIII line (465nm), and upgraded to a multichord system, incorporating an 8x8 multi-anodal photomultiplier (MAP)[5]. An order of magnitude higher improvement in photo-electron statistics is also available from another spectrometer with a UV CCD detector array. The viewing geometry is shown in Fig.1. Each chord is about 30mm wide in the equatorial plane. Also shown are typical magnetic reconstructions. Statistical errors of typically ~2km.s^{-1} are obtained for the chord integrated Doppler spectra at a 0.3msec time interval. Up to 4 chords are observed simultaneously. The CCD spectrometer provides the high velocity resolution (~0.2km.s^{-1}) at a time resolution of ~1msec. Estimates of the regions of maximum line emissivity place CIII and BIV at ~20mm and ~40mm from the separatrix, respectively. Absolute velocities are obtained using a nickel spectral lamp and radial views.

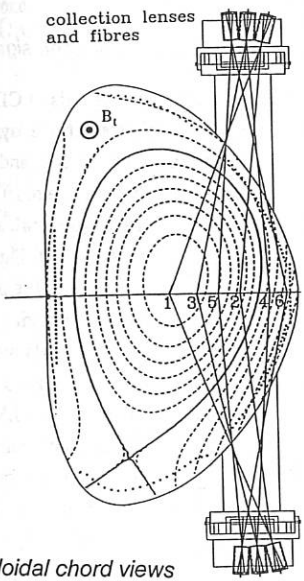


Fig.1 Poloidal chord views

3 H-mode plasmas

In Fig. 2 are shown typical temporal behaviours of chord-integrated poloidal velocities (CIII), during an Ohmic H-mode discharge. The quality of H-mode improves gradually with decreasing ELM frequency followed by the appearance of ELM-free periods interspersed with ELM bursts. The upper graph compares the D-alpha signal and the CIII velocity obtained from

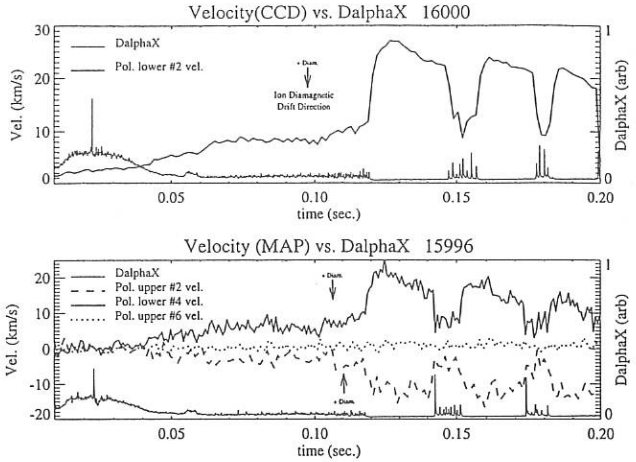


Fig.2 Several poloidal views (CIII) compared with D-alpha signals

the CCD spectrometer measurements and the lower graph shows three chords of CIII velocities (the arrow shows the ion diamagnetic direction) derived from the photomultiplier system; the middle trace is from the outermost chord (#6), showing little change in velocity, and the other two from almost opposing views (upper#2 and lower#4 - cf. Fig.1). Changes to the poloidal velocity entering ELMy H-mode are relatively gradual and up to 5km.s^{-1}. On entering the ELM-free period, high poloidal and toroidal accelerations are seen from CIII, approx 7km.s^{-1}.ms^{-1};3km.s^{-1}.ms^{-1}, respectively. During the ELM bursts the velocity drops again, even more rapidly. In the case of BIV the changes in poloidal

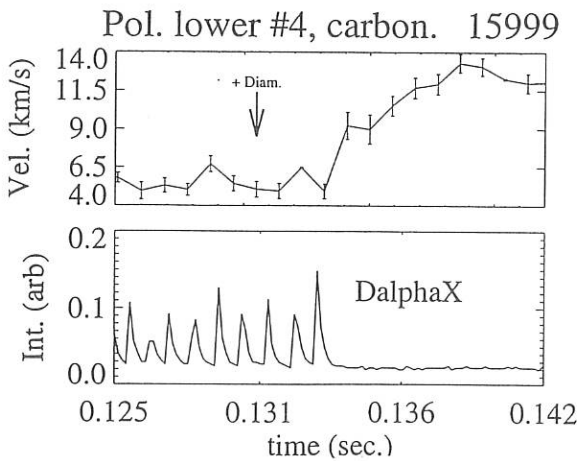


Fig.3 Poloidal velocity (CIII)at beginning of ELM-free period

velocity, albeit smaller, follow the CIII but the toroidal accelerates ~2-3 times slower and is in the ion diamagnetic direction i.e. opposite to CIII. (Core impurities, AlXII and ClXVI, show similar toroidal velocity behaviour to BIV.) The velocity shifts, particularly for CIII, are generally much larger than the impurity diamagnetic velocity, estimated to be ~3km.s^{-1} from Doppler temperatures and modelled impurity-density scale-lengths (30eV and 10mm, respectively). Therefore, a simple radial force balance indicates that these changes in the poloidal velocity are associated with a radial electric field. The outermost poloidal view sees little or no velocity change (<0.5km.s^{-1}), while the peak velocity change is ~20km.s^{-1} for CIII and up to ~10km.s^{-1} for BIV. The peak of the derived electric field ΔE_r ~ -20kV.m^{-1}, i.e. pointing inwards. Figure 3 shows synchronous changes to the poloidal velocity and the shift to ELM-free behaviour. During the ELM-free periods there is a reduction in the poloidal velocity (cf. Fig. 2) with a decay time of ~30msec. ELM bursts, or single ELMs, following ELM-free periods produce the fastest poloidal, ~20km.s^{-1}.ms^{-1}, as seen in Fig.4. The effect on the poloidal velocity is synchronous with the start of an ELM, within the sampling time of 0.15msec.

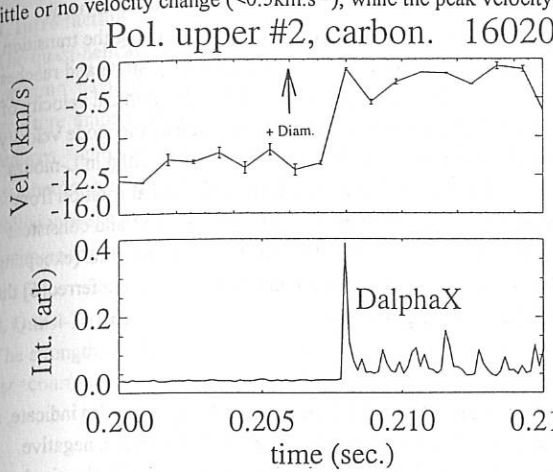


Fig.4 Poloidal velocity (CIII)at end of ELM-free period

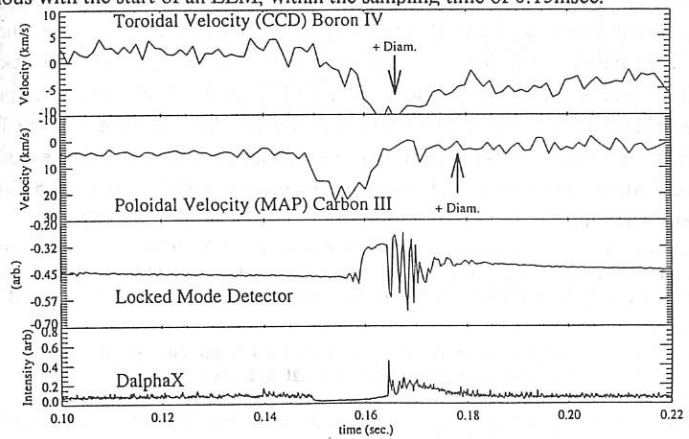


Fig.5 Toroidal and poloidal velocities at locked-mode termination of ELM-free period

4 Rotation and mode-locking

Impurity velocity behaviour during mode-locking in L-mode discharges in both COMPASS-C and COMPASS-D has been reported elsewhere[3]. Here we deal with ELM-free periods during Ohmic H-mode discharges. An example of a naturally occurring locked mode is shown in Fig. 5. Also displayed are the changes to the toroidal velocity of BIV and the CIII poloidal velocity (generally similar to its toroidal component). The poloidal velocity (in the electron diamagnetic direction) decreases as the mode locks. The drop in poloidal velocity, together with the appearance of the locked mode, is rapidly followed by a reversion to an L-mode plasma. The toroidal velocity (BIV), still accelerating in the usual way following the transition to ELM-free H-mode, is ~5km.s^{-1} (ion diamagnetic direction) when locking starts and reaches ~10km.s^{-1} when the ELM-free period terminates. It may be noted that the poloidal velocity of CIII is observed remote from the q=2 surface and is in the same direction as the mode velocity. The shift in BIV toroidal velocity is in the same direction as during mode-locking in L-modes. In RMP locked mode studies[4], the BIV ions are observed to shift in toroidal rotation from weakly in the electron direction (~5km.s^{-1}) to 10-20km.s^{-1} in the ion direction and consistent with the acceleration of the electron fluid rotation. In ELM-free H-modes such ions (excepting the CIII ions) are observed to be moving in the ion direction naturally. It can be inferred[6] that the electron fluid is more susceptible to locking.

5 Discussion and Conclusions

The high values of poloidal rotation observed from CIII lines in ELM-free H-modes indicate, as on other devices, the presence of a transport barrier with a width of ~20mm and a negative (inwards) radial electric field up to ~20kV.m^{-1}. The timescale for formation of the barrier is a few msec and it is abruptly reduced by ELMs in <0.2ms. The effect of transitions to and from ELM-free H-mode transitions on the BIV ions, which radiate ~20mm further into the plasma, is smaller (~10kV.m^{-1}). In ELM-free H-modes there is a gradual increase in the toroidal velocity, in the ion drift direction, seen from BIV to the core ClXVI and AlXIII ions, which indicates an increase in the radial electric field. The application of RMPs, which can slow and lock MHD modes at resonances such as the q=2 surface in both L-mode and H-mode plasmas, produces the expected increase in ion toroidal rotation in the ion drift direction. The locking effect occurs more easily in an ELM-free H-mode plasma, (sometimes with an unstable mode in the absence of RMPs), whilst the bulk of the plasma is already rotating in the ion drift direction.

Acknowledgements

We are grateful for diagnostic assistance from C A Bunting and P N Stubbington, for discussions with J V Hofmann on the ASDEX-Upgrade experiment and for magnetic reconstruction from L Appel. This work was jointly funded by the UK Department of Trade and Industry and EURATOM.

References

[1] P G Carolan, S J Fielding, S Gerasimov et al, Plasma Phys. and Contr. Fus. **36**, (1994), A111
[2] S J Fielding, J D Ashall, K B Axon et al., J Nucl. Mat. **220-222**, (1995) 284-287
[3] D A Gates and T C Hender, Culham Laboratory Internal Report UKAEA-FUS-284 (1995)
[4] A W Morris, P G Carolan, R Fitzpatrick et al, 20th Conf. Contr. Fus. Plasma Phys, (1993) **I**, 227.
[5] P G Carolan and R O'Connell Rev. Sci. Instrum. **66**, (1995), 609
[6] G J McArdle, P G Carolan, A L Colton et al. this conference.

Quasi-Helical Symmetry of L=1 Torsatron

M. Aizawa, K.H. Saito, K.N. Saito, I. Kawakami and **S. Shiina**
Atomic Energy Research Institute, College of Science and Technology,
Nihon University, Surugadai 1-8, Chiyoda-ku, Tokyo, Japan

1. Introduction

The quasi-helically symmetric configuration and attractive transport features of compact L=1 torsatron having a spatial magnetic axis are described. In addition to the simplest coil structure among other helical systems, the negative pitch modulation of coil winding law reduces significantly the effective toroidal curvature and gives rise to the quasi-helically symmetric configuration. This novel feature is really confirmed by the particle orbit and collisionless particle confinement calculations. There is the pitch modulation parameter to optimize the confinement.

2. Quasi-Helical Symmetry of L=1 Torsatron

The strength of the magnetic field in magnetic coordinates (ψ,θ,ϕ) on a given flux surface (ψ=constant) is represented by its Fourier components $A_{n,m}(\psi)$ as follows,

$$B(\psi,\theta,\phi) = A_{0,0}(\psi) + 2\sum{}' A_{n,m}(\psi)\cos(n\phi - m\theta) \qquad (1)$$

where the prime indicates that the uniform term n=0, m=0 is excluded from the sum. The each term $A_{n,m}$ can be determined numerically in an automatic manner by following the field line. The relatively large inhomogeneous components correspond to $(n,m) = (N,0)$, $(0,1)$, and $(N,1)$, where N is the field period number. The $A_{N,0}$ component corresponds to the field ripple on the magnetic axis, the $A_{0,1}$ term is due to the toroidal curvature and the helical curvature term $A_{N,1}$ leads to the helical symmetry axis of the system. In the case of spatial magnetic axis configuration, the rotational transform N associated with the twisting of the surface about the major axis must be added to the usual rotational transform in stellarators with planar axes $\iota(\psi)$, so that

$$\theta \sim \iota(\psi)\phi + \omega, \quad \omega = N\phi \qquad (2)$$

where the relation of $\omega = N\phi$ is exact near the magnetic axis[1]. With $\iota(\psi) \sim 1.0$, $N = 17$ in present case, equation (2) gives $\theta \sim N\phi$ and an expression for B,

$$\begin{aligned} B(\psi,\theta,\phi) &\sim A_{0,0}(\psi) + 2\left(A_{0,1}(\psi) + A_{17,0}(\psi)\right)\cos\theta + 2A_{17,1}(\psi)\cos(17\phi - \theta) \\ &\sim A_{0,0}(\psi)\left(1 - \varepsilon_t(\psi)\cos\theta - \varepsilon_h(\psi)\cos(17\phi - \theta)\right) \end{aligned} \qquad (3)$$

where we define $\varepsilon_t(\psi) \equiv -2\left(A_{0,1}(\psi) + A_{17,0}(\psi)\right) / A_{0,0}(\psi)$ and $\varepsilon_h(\psi) \equiv -2A_{17,1}(\psi) / A_{0,0}(\psi)$. Accordingly, the toroidal curvature term proportional to $\cos\theta$ is given by the effective toroidal curvature term ε_t rather than the original toroidal curvature term $-2A_{0,1} / A_{0,0}$, and

the helical curvature term by ε_h. These three Fourier components are compared between the different values of coil pitch modulation parameter α^*; the coil winding law is $\theta = N\phi + \alpha^* \sin N\phi$. The negative pitch modulation ($\alpha^*<0$), in which the coil pitch angle is larger inside than outside the torus, strengthens the good local curvature of the magnetic lines of force and makes the local magnetic well[2]. As shown in Fig.1, the helical curvature term $A_{17,1}$ is the largest compared with other inhomogeneous components except around the magnetic axis region, depending on α^* so that it decreases in association with the pitch modulation. It is noteworthy that two symmetry-breaking components of $A_{0,1}$ and $A_{17,0}$ have each other same sign for $\alpha^*>0$, on contrary, opposite sign for $\alpha^*<0$. Hence, the effective toroidal curvature term ε_t is increased for $\alpha^*>0$ and decreased for $\alpha^*<0$. The profile of ε_t is nearly flat and $\varepsilon_t(\psi) \sim 0$ at $\psi \sim 0.35$, $\psi \sim 1.0$ for $\alpha^* = -0.2$. The significant reduction of the effective toroidal curvature (especially for $\alpha^* = -0.2$) gives rise to the quasi-helically symmetric configuration with $\varepsilon_h >> \varepsilon_t$. The novel features of reducing the effective toroidal curvature and quasi-helically symmetrizing the configuration are really confirmed by collisionless particle confinement calculation in next section.

3. Collisionless Particle Confinement in L=1 torsatron

In order to confirm the quasi-helical symmetry of L=1 torsatron mentioned above, collisionless particle drift motion is investigated. If the confinement system has a symmetrical configuration, collisionless particles are completely confined. The guiding center drift orbits are calculated by solving the drift Hamilton's equations in Boozer's magnetic coordinates since they only depend on B in magnetic coordinates $B(\psi, \theta, \phi)$, and its derivatives[3]. The particles are started at a given magnetic flux surface ψ with random values in the pitch angle $\eta \equiv v_{//} / v$ (v is absolute value of velocity, $v_{//}$ parallel velocity to magnetic line of force) and with the particle energy E_K up to 100keV. The trajectories are followed until $\omega_{ct} t = 10^5$. Fig.2 shows the loss cones in the configurations with $\alpha^* = -0.2$ and $\alpha^* = -0.4$ for the particles starting at different positions of θ but for $\phi = 0, \psi = 0.5$. The most part of loss particles can be seen for the starting position of $\theta = \phi = 0$ where B is minimum. The average over θ and ϕ enhances the confined particle number fraction. The averaged fraction over θ for $\alpha^* = -0.2$ case is 95%(156/164)for E_K=25keV and 94%(154/164)for E_K=100keV, and for $\alpha^* = -0.4$ case is 86%(141/164) for =25kev, which is smaller than that for $\alpha^* = -0.2$ case as a result of the larger ε_t. For the particles starting at the inner flux surface $\psi = 0.3$($r = 0.55a$ or aspect ratio 15.3)and $\phi = 0$, the loss cone region becomes narrower and the averaged confinement fraction for $\alpha^* = -0.2$ case is 97.5%(160/164) for =100keV, which is larger than that for the starting position of $\psi = 0.5$.

4. Comparison with Banana Center Orbit Theory

In the stellarator regime with $1 >> \varepsilon_h >> \varepsilon_t$, the banana center drifts along trapped(super) banana orbit with the excursion width $\Delta_{SB} \sim r\sqrt{\varepsilon_t / \varepsilon_h}$ or untrapped(transit) banana orbit with the excursion width $\Delta_{TB} \sim r(\varepsilon_t / \varepsilon_h)$[4]. Actually the super-banana orbit is observed only in negatively pitch-modulated configuration with $\varepsilon_h >> \varepsilon_t$. The observed excursion width of the super-banana orbit is $\sim 1.8 \times 10^{-2}$m in the configuration with $\alpha^*=-0.2$ and larger with $\alpha^*=-0.4$, for the particle starting $\psi=0.5$ and $E_K=100$keV, being quantitatively consistent with the predicted at $\psi=0.5$(or $r=0.7a$) although it is independent of E_K. Decreasing particle energy to $E_K=25$keV from 100keV makes its excursion width smaller by a factor of about a half, as shown in Fig.3. The value of Δ_{SB} for =10keV is $\sim 6 \times 10^{-3}$m, value of which is comparable to the banana width $\sim 5 \times 10^{-3}$m in tokamak plasma with reactor grade parameters (T_i=10keV, B=10T, safety factor/$\sqrt{\varepsilon_t}$ ~5) and means the same order of magnitude as the tokamak diffusion coefficient in low(banana) collisional regime. The observed excursion width of Δ_{SB} depends on not only ε_t but also the other higher harmonic field components. The effect of the higher harmonics on Δ_{SB} is nearly equal to that due to ε_t. This result gives an indication that the higher harmonics indeed break the helical symmetry of configuration in conjunction with ε_t. The fraction of the super-banana particles is predicted to be, which is $\sim 1 \times 10^{-1}$ at $\psi=0.5$ for $\alpha^*=-0.2$ case. This value is compared with the averaged fraction of the observed loss particle number for the particles starting at $\psi=0.5$ and $\psi=0$, which is ~6% for $E_K=100$keV and less than or comparable to the predicted value of $\sqrt{\varepsilon_t}$ depending on E_K. As mentioned above, the consistency between the predictions and the observations for collisionless particle orbits indicates the real contribution of ε_t to the confinement and suggests a great improvement of diffusion coefficient, which is the same order of magnitude as that for tokamak reactor plasma. The energy dependent excursion and fraction of super-banana particles would be explained by solving exactly the drift equations of banana center with the inclusion of higher harmonic field components.

5. Conclusion

In the conjunction with the torsion and curvature of helical magnetic axis, the negative pitch modulation of L=1 torsatron coil winding reduces significantly the effective toroidal curvature proportional to $\cos\theta$, ε_t, as the result, leads to quasi-helically symmetrical configuration. These novel features are really supported by collisionless particle confinement calculation, indicating a great improvement of diffusion coefficient which is comparable to that in tokamak reactor plasma.

References

[1] Reiman A. H. and Boozer A. H., Phys. Fluids **27** 2446(1984)

[2] Aizawa M. et al, Proc. 14th IAEA Conf. on Plasma Phys. and Controlled Nucl. Fusion

Research (Würzburg, 1992) **2** 439 (1993)
[3] Boozer A. H., Phys. Fluids **24** 1999(1981)
[4] Furth H. P. et al, Plasma Phys. and Controlled Nucl. Fusion Research (Conf. Proceedings Novosibirsk in 1968) **1** 821(1969)

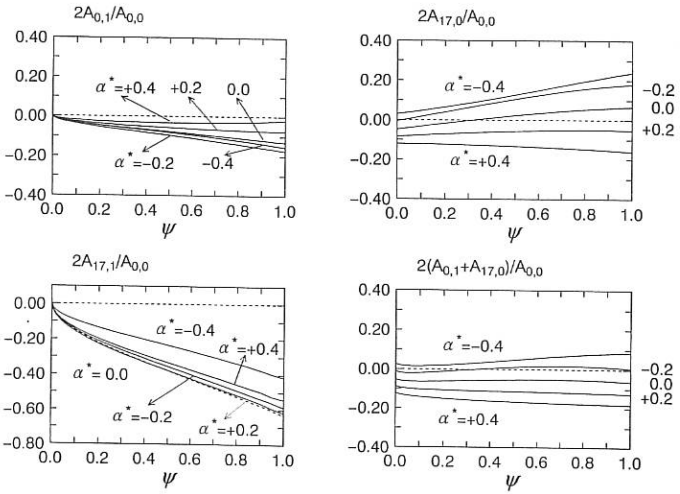


Fig.1: Fourier components $A_{n,m}$ of B in magnetic coordinates for $L=1$ torsatron with 17 periods, aspect ratio R/a~7.5, $\beta=0$ (B_0=4.4T), as function of ψ and α^*, and note $-\varepsilon_h \equiv 2A_{17,1}/A_{0,0}$, $-\varepsilon_t \equiv 2(A_{0,1}+A_{17,0})/A_{0,0}$.

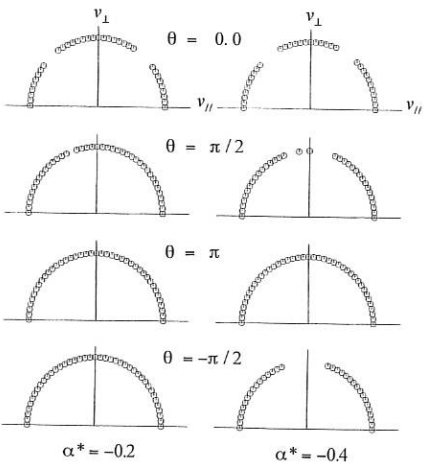


Fig.2: Loss-cones for different starting positions of θ but $\phi=0$, $\psi=0.5(E_K=25keV)$: for $\alpha^*=-0.2,-0.4$.

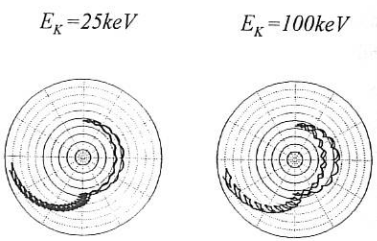


Fig.3: Super-banana orbits in the configuration with $\alpha^*=-0.2$ for the particles starting at $\psi=0.5$, $\theta=\phi=0$, with $E_K=25keV$ and 100keV(pitch angle $\eta=v_{//}/v=0.76041$).

AN EXPERIMENTAL STUDY OF RF PRODUCED PLASMAS IN THE H-1 TOROIDAL HELIAC

G.G.Borg, B.D.Blackwell, D.L.Rudakov, M.G.Shats, L.E.Sharp and G.B. Warr

Plasma Research Laboratory
Research School of Physical Sciences and Engineering
Australian National University
Canberra 0200 ACT
Australia

I. INTRODUCTION

H-1 is a toroidal helical axis stellarator of major radius 1.0 m, mean minor radius 0.20 m, 3 field periods and a variable rotational transform in the range $0.6 < \iota < 2.0$ [1]. In quasi-continuous mode, plasmas are formed using 60 kW Ion Cyclotron Range plasma formation at 7.0 MHz with very low magnetic fields, B_0 (< 1200 G). The RF power is coupled to the plasma by a phased pair of earthed saddle coil antennas [2]. Improved plasma formation has been obtained using a 300 Torr.liter/second neutral gas injector based on a VEECO-PV10 piezoelectric valve with orifice bored from 0.5 to 1.3 mm. The gas injector has been installed directly in the vacuum with a 1.2 liter plenum chamber. A 0.70 mm ID, 100 mm long capillary tube directs the gas towards the RF antennas.

The main diagnostics employed in the following experiments are a pair of diamagnetic loops located at toroidal locations, ϕ=335° and 225° which measure $< \beta >$, a RF Rogowski coil installed on one of the antennas at $o = 135°$ to monitor the RF sheath current for breakdown detection and a ceramically shielded ($\phi = 3mm$) Langmuir probe at toroidal location $\phi = 0$ [2].

II. EXPERIMENTAL RESULTS AND DISCUSSION

Fig. 1 shows the final pressure rise in the H-1 tank and the instantaneous flow rate of the gas injector as a function of the applied puff time width for a bias voltage of 180 V. Note that for short times the flow rate is highest and settles to a constant value for long pulse widths. The minimum number of injected particles is about $1. \times 10^{18}$ at 30 μseconds.

Plasmas were produced in both helium and hydrogen with maximum achievable on-axis densities of $\sim 2 \times 10^{12}$ and $7 \times 10^{11} cm^{-3}$ respectively. In this paper we only present hydrogen results. Since the low density, quiescent plasma of the heliac in quasi-continuous mode is amenable to probe techniques, we have begun an investigation of the decay of I_{sat} and $< \beta >$. These results were taken in the decay of the discharge

after the termination of the RF pulse to eliminate RF effects on confinement and the probe.

Characteristic of both types of plasma is that termination of the RF pulse produces a decay of the ion saturation current I_{sat} and $< \beta >$ in the range 0.4 - 2 msecs which is much longer than expected from energy or particle confinement. If one unrealistically assumes that all the RF power is effectively coupled into the bulk plasma energy at $T_e \approx 30$ eV, then the global energy confinement for a hydrogen plasma is only about 50 $\mu secs$ (lower limit) at $B_0 \approx 560$ G. Fig. 2 shows the dependence of the RF sheath current, central I_{sat} and the scaling of the decay time of I_{sat} on B_0 for the standard magnetic configuration [1]. Note that I_{sat} falls sharply above 700 G without any effect on the decay time. Both a waveguide cutoff and interference by the probe are responsible for the reduction in plasma density at high field. For hydrogen plasmas, the $< \beta >$ measurement was not sufficiently sensitive to confirm this time decay scaling at high fields but at low fields the $< \beta >$ decay time was about half the I_{sat} decay time. The I_{sat} decay time is observed to increase linearly with magnetic field as shown in Fig. 2c. Note that the horizontal lines in the I_{sat} time decay plots are the instrumental baselines for a fast rise-time square wave pulse.

Further investigations of the decay indicated a detectable dependence on radial location, the confinement tending to be better at inner radii as shown in Fig. 3a for the standard configuration. This dependence on radius is inconsistent with a simple low order diffusive mode. Radial profiles of the probe floating potential are also shown in Fig. 3a for the same conditions. The probe floating potential is -200 volts in the centre of the plasma implying a negative plasma potential. If one assumes a plasma potential of -200 V then the resultant plasma rotation velocity of $\sim$ 20 km/sec is comparable to the Bohm velocity, $\sim$ 30 km/sec for $T_e \approx$ 15-30 eV. The decay of the probe floating potential however is much more rapid than that of I_{sat} and implies that the decay of the plasma density and temperature is not influenced by the plasma potential or by the decay of any plasma rotation. Moreover the plasma potential observed would be positive if it were determined by an earthed RF antenna. It has been observed for helium that the strongly negative floating potentials can be made smaller or even positive by gas puffing after the plasma has been established. In the absence of puffing the probe floating potential regains its large negative value in the centre on a time scale of about 10 msecs. Gas puffing during the plasma decay had no observable effect on the decay time constant.

For comparison with the standard configuration. Fig. 3b shows the same results close to the 1:1 resonance where the plasma is divided between two islands [3]. Although a double peaked structure corresponding to the stationary plasma density profiles for each island are not evident in Fig. 3b, it is clear that the plasma density and the plasma decay time have both decreased significantly. We may conclude that both the global confinement and the plasma decay are adversely affected by the presence of islands.

The probe bias voltage was typically set to around -400 volts due to the high negative plasma potential. The possibility that the plasma was maintained by the probe was excluded by examination of the plasma dynamic response to small signal RF power modulation and by delaying the probe negative bias until the plasma afterglow.

Finally Fig. 4 shows the dependence of the $< \beta >$ decay time on the instantaneous

hydrogen filling pressure read from a fast ion gauge. The non-reproducibility in the $< \beta >$ data is due to a density transition resulting from the proximity of a waveguide cut-off. This is a common observation in plasma formation experiments in the helicon wave range of frequencies. The $< \beta >$ decay time however decreases quite uniformly with filling pressure, consistent with degraded energy confinement at higher electron-neutral collisionality.

We conclude that measurements of the I_{sat} decay time may be used for local transport analysis for a range of magnetic fields and configurations in H-1.

[1] HAMBERGER S.M. et. al. Fusion Technology **17**, (1990) 123.
[2] BLACKWELL et. al. accepted for publication in Fus. Eng. and Design.
[3] SHATS M.G. et. al. Nuc. Fus. **34**. (1994) 1653.

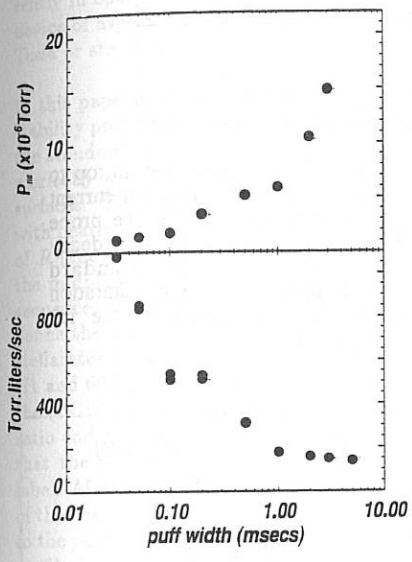


Figure 1. Final tank pressure and instantaneous flow rate for hydrogen produced by the H-1 neutral gas injector as a function of voltage pulse width.

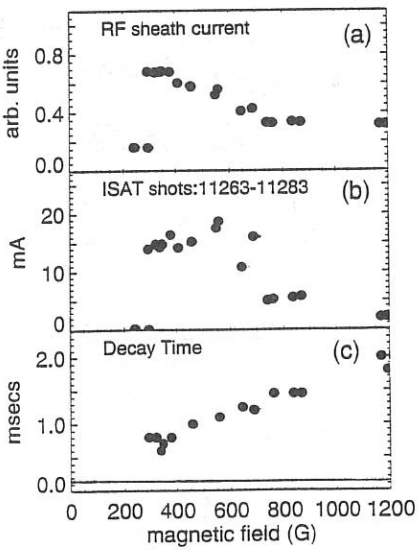


Figure 2. Magnetic field scalings of (a) The RF sheath current. (b) the ion saturation current near the magnetic axis and (c) the decay time of the ion saturation current.

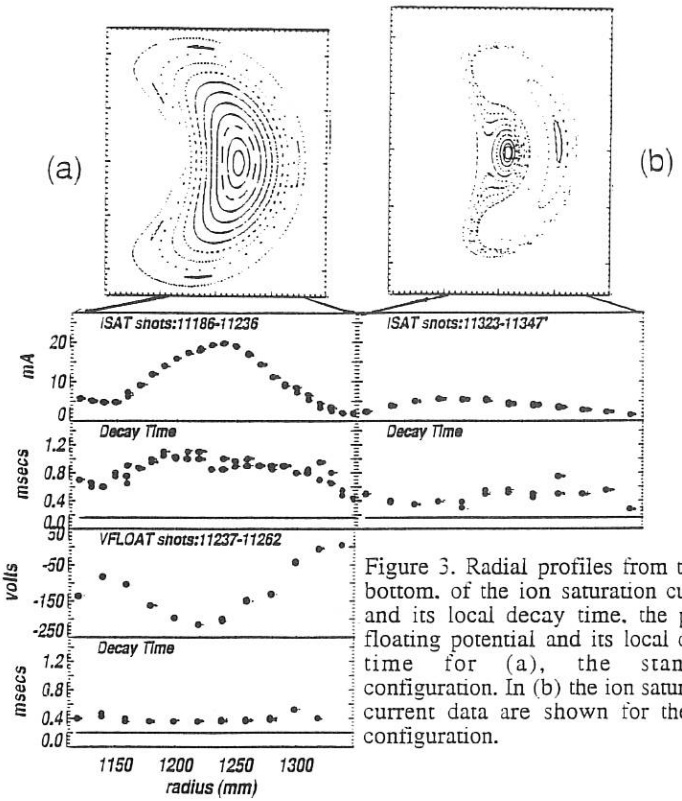


Figure 3. Radial profiles from top to bottom. of the ion saturation current and its local decay time. the probe floating potential and its local decay time for (a), the standard configuration. In (b) the ion saturation current data are shown for the 1:1 configuration.

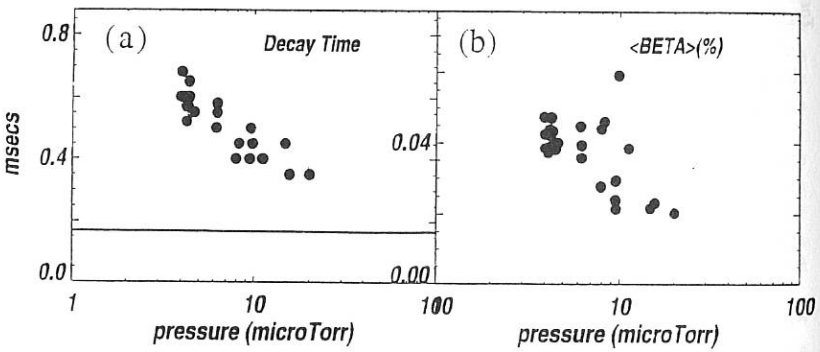


Figure 4. The dependence of (a), the time decay of <β>(%) and (b), the magnitude <β>(%) on the instantaneous filling pressure.

Global Internal Modes in the H1 Heliac

W. A. Cooper
CRPP/EPFL, Association Euratom/Confederation Suisse,
Lausanne, Switzerland
and
H. J. Gardner
Plasma Research Laboratory and Department of Theoretical Physics,
Research School of Physical Sciences and Engineering,
The Australian National University,
Canberra, Australia

Heliac devices are three dimensional (3D) stellarator configurations with relatively large rotational transform per field period and relatively weak magnetic shear. They are realised with toroidal coils appropriately displaced about a central conductor to produce bean shaped plasmas that rotate around this conductor. The H1 heliac is currently in operation at the Australian National University [1]. It is a $L = 3$ field period device of aspect ratio $A \simeq 5$ that can operate in either a $1s$ pulsed mode at a field of 1 Tesla or steady state at a field of 0.25 Tesla.

In this paper we examine the global internal ideal 3D magnetohydrodynamic (MHD) stability properties of a sequence of configurations with 3 field periods that encompasses the standard configuration of the H1 heliac. The 3D equilibria have been obtained numerically with the VMEC code [2] and are constrained to have nested magnetic flux surfaces. The starting point of the sequence corresponds to a helical axis stellarator with nearly circular cross section and we linearly change the $M \neq 0$ Fourier components of R (the horizontal distance from the major axis) and Z (the vertical distance from the midplane) that describe the plasma-vacuum interface so that the end point of the sequence corresponds to the H1 heliac in its standard configuration. This allows us to define the continuous parameter f as a measure of the transition from the helical axis stellarator to the H1. Hence, $f = 0.4$ corresponds to the configuration that is 40% the H1 and 60% the helical axis stellarator. In this procedure, however, we have also fixed the $(M = 1, N = 0)$ and $(M = 1, N = 1)$ components to roughly conserve the aspect ratio and we have altered the $(M = 0, N = -1)$ component independently to guarantee that the edge rotational transform remains approximately constant. We employ the labels M and N for the poloidal and toroidal mode numbers of a Fourier decomposition of the equilibrium state. These are to be distinguished from m and n which correspond to the poloidal and toroidal mode numbers of an instability structure. The plasma mass profile is prescribed as

$$M(s) = M(0)(1 - s), \tag{1}$$

with an adiabatic index $\Gamma = 2$ used to evaluate the corresponding pressure profile [2]. The radial variable $0 \leq s \leq 1$ is proportional to the toroidal magnetic flux and the volume enclosed. We vary $M(0)$ to fix the volume averaged β to 1.65%. The entire sequence, including the H1, is unstable to Mercier [3] and to ballooning modes [4] at this value of β. We also prescribe zero net toroidal plasma current within each flux surface in the computation of the equilibria. The rotational transform ι profiles for configurations with $f = 0.4$ (solid dots), $f = 0.5$ (dashed curve), $f = 0.6$ (dot-dash curve), $f = 0.7$ (dotted curve) and $f = 0.75$ (solid curve) are shown in Fig. 1a.

The 3D TERPSICHORE code [5] is used to investigate the global internal modes of the sequence of equilibria calculated with VMEC. An initial test of stability was carried out with a set of Fourier modes to describe the instability structure limited to the $m = 7, n = 8$ component and its three closest poloidal sidebands. The configurations with a boundary description less than 40% of the H1 have nonmonotonic ι profiles (see Fig. 1a) and in particular have the $\iota = 8/7$ rational surface near the centre of the plasma and near the edge. This initial test demonstrated a dominant core localised $m = 7, n = 8$ mode that became marginal as the $\iota = 8/7$ surface near the centre vanished into the magnetic axis as the plasma shaping was increased to a $3/8$ fraction of the standard H1. The family of Fourier components that have toroidal mode numbers that are a multiple of 3 (the number of field periods) constitute the modes of the equilibrium. Those that are not a multiple of 3 constitute a single family that describe the structure of an instability [6,7]. It has been our experience, however, that an arbitrary selection of toroidal sidebands in helical axis stellarators yields very ill conditioned matrices. The selection of toroidal sidebands of the main instability structure, therefore, requires a careful evaluation of the dominating Fourier components of the equilibrium state. The most relevant components of the equilibrium for the sequence we have investigated are:

M	NL
$0-4$	0
$1,2$	-3
$0-5$	3
$1,2$	-6
$0-3$	6
$0-3$	9
$2-5$	12

where NL denotes the product of N times L. We have found that the $m = 5, n = 5$ component becomes more important than the $m = 7, n = 8$ component as the plasma shaping increases because as shown in Fig. 1a the value of ι on axis decreases to almost unity for the configurations that are $70\% - 75\%$ of the H1 before starting to increase again. Considering the $m = 5, n = 5$ as the dominant component of the instability, we obtain that it couples with 48 additional sidebands of significance through beatings with the equilibrium components we have identified (eg.,$m - 5 = M, n - 5 = NL; m + 5 = M, n + 5 = NL$) [6,7]. The eigenvalues as a function of the square of the inverse of the number of radial intervals (which were varied from 48 to 108) for the configurations with $f = 0.5$, $f = 0.6$, $f = 0.7$ and $f = 0.75$ are shown in Fig. 1b. In Fig. 2a, the converged eigenvalues extrapolated to infinitesimal mesh in Fig. 1b are plotted with respect to the shaping parameter f which reveals that the configuration that is 78% the H1 heliac and 22% the helical axis stellarator becomes marginal to the $m = 5, n = 5$ mode. This stabilisation is mostly due to the deepening of the magnetic well with f, but also the increase of ι on axis for $f > 0.7$ that displaces the $\iota = 1$ resonant surface further away plays a rôle. The five dominant Fourier components of the radial component of the perturbed displacement vector as a function of the radial variable s are shown in Fig. 2b for the configuration with $f = 0.75$ and the corresponding profile of the potential energy perturbation is shown in Fig. 3a.

The $M = 8, N = 3$ component of the equilibrium state constitutes another potentially important contribution to the stability picture because it corresponds to a resonance condition within the plasma where the parallel current density can diverge. We have

thus included two additional sidebands, the $m = 3, n = 4$ and the $m = 13, n = 14$ components, which couple with the main $m = 5, n = 5$ component to beat with the equilibrium $M = 8, NL = 9$ term. We obtain eigenvalues that are more unstable, but a convergence study in the radial mesh size shows that the perturbed potential energy becomes a δ function about the $\iota = 9/8$ resonant surface as shown in Fig. 3b. The mode structures that are excited all localise about the 9/8 rational surface and the magnitude of the eigenvalues depend sensitively on how close the mesh point is located with respect to the 9/8 surface as we change the number of radial intervals. Therefore, this type of instability appears to be a manifestation of a shortcoming of the equilibrium description. The extreme localisation of the perturbed energy suggests that the model may be inadequate. Magnetic islands and finite Larmor radius effects should resolve the narrow unstable layer.

In conclusion, we have analysed a sequence of equilibria that lead to the standard H1 configuration with respect to global ideal MHD internal modes. This study suggests that the H1 should be stable to global structures well beyond the β limits imposed by local Mercier and ballooning modes.

References

[1] Hamberger S M et al, *Fusion Technol.* **17** 123 (1990)
[2] Hirshman S P and Betancourt O, *J. Comput. Phys.* **96** 99 (1991)
[3] Gardner H J and Blackwell B D, *Nucl. Fusion* **32** 2009 (1992)
[4] Cooper W A and Gardner H J, *Nucl. Fusion* **34** 729 (1994)
[5] Anderson D V et al, *Int. J. Supercomp. Appl.* **4** 34 (1990)
[6] Cooper W A et al, *Proc. Joint Varenna – Lausanne Int. Workshop on Theory of Fusion Plasmas* (Editrice Compositori, Bologna 1990) p.655
[7] Schwab C, *Phys. Fluids* **5** 3195 (1993)

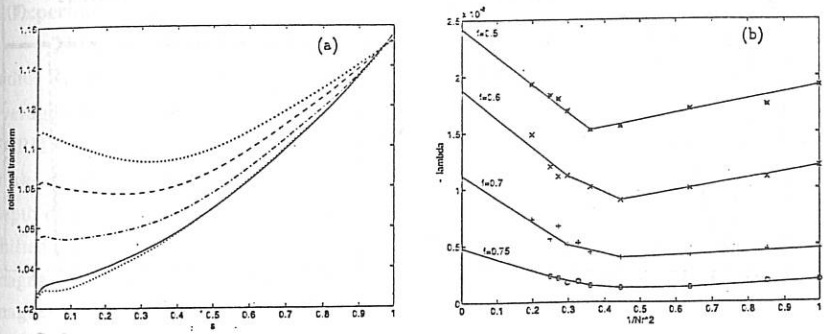


Figure 1: (a) The rotational transform ι profiles for the configurations with $f = 0.4$ (top dotted curve), $f = 0.5$ (dashed curve), $f = 0.6$ (dot-dashed curve), $f = 0.7$ (lower dotted curve) and $f = 0.75$ (solid curve); (b) Radial convergence of eigenvalues for configurations ranging from 50% to 75% of the standard H1

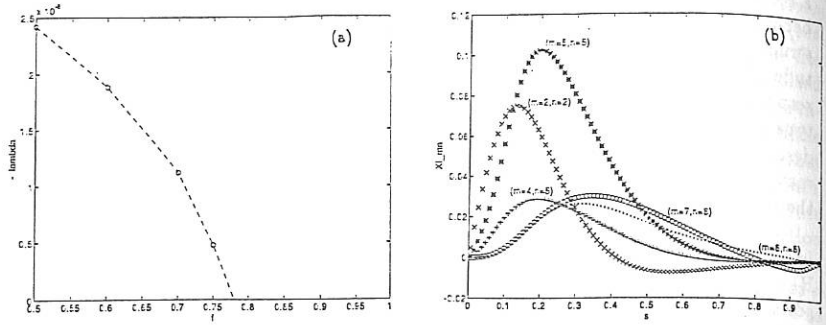


Figure 2: (a) The converged eigenvalue dominated by the $m = 5, n = 5$ component with 49 mode pairs as a function of the heliac shaping parameter f; (b) The Fourier mode structure of the radial component of the perturbed displacement vector with 49 mode pairs for the configuration with $f = 0.75$

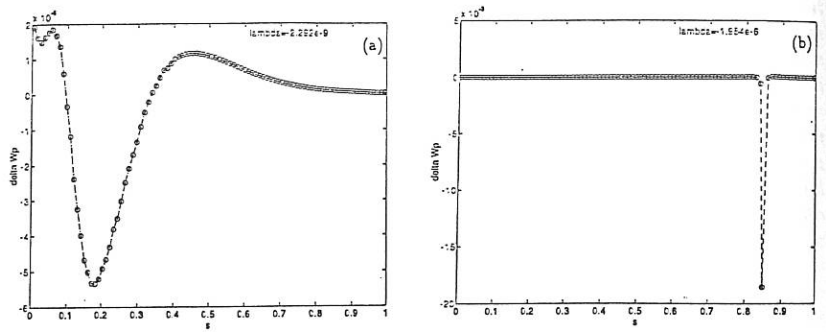


Figure 3: The perturbed potential energy profile for the configuration corresponding to $f = 0.75$ with (a) 49 mode pairs which is dominated by the $m = 5, n = 5$ component and with (b) 51 mode pairs which is dominated by the $m = 13, n = 14$ component

Investigations of Plasma Beta in TJ-IU Torsatron

J. Qin, E. Ascasíbar, C. Alejaldre, T. Estrada, O. Fedyanin*, J. Herranz, J.A. Jiménez, A. López-Fraguas, F. Medina, M.A. Ochando, I. Pastor, M.A. Pedrosa, J. Sánchez, F. Tabarés, D. Tafalla, B. Zurro, ECH Group* and TJ-IU Team

Asociación EURATOM-CIEMAT para Fusión, Av. Complutense 22, 28040 Madrid, Spain

**General Physics Institute, Russian Academy of Sciences, Moscow, Russia*

1. Introduction

Preliminary experiments to study the plasma beta behaviour were performed on ECRH plasmas in TJ-IU torsatron. So far, all the beta data obtained show a similar behaviour versus the electron density, that is, the plasma beta increases with the electron density in the low density region and becomes saturated in the high density region. However, those improved beta data obtained with an inward shifted magnetic configuration form a different branch from the normal one, as a function of the electron density. Their beta values are almost twice the normal beta values obtained with the standard magnetic configuration. The magnetic configuration seems to be important to achieve these higher beta values. Careful control of gas puffing is also needed in order to control the special time evolution of electron density which can jump suddenly at some critical density up to the value close to the cut-off density. In this paper some preliminary analyses of experimental data are presented. Further analyses and more experiments are under way.

2. Experimental set-up

TJ-IU[1] is a ℓ=1/m=6 (one helical field coil with six periods) torsatron with a major radius R_0=60cm and an average plasma radius $\bar{a}$=10cm. The device can be operated with average magnetic field at the magnetic axis B(0)=0.5T/0.67T for the 28GHz/37.5GHz ECRH (2nd harmonic heating) plasma experiments, respectively. The rotational transform ι in the standard magnetic configuration is above 0.2 with almost negligible shear, and the depth of magnetic well is about 6.9%, reaching up to the plasma boundary. For an inward shifted configuration, ι-value decreases and the shear increases to be positive. The depth of magnetic well decreases for both inward and outward shifted configurations. The shape of magnetic surface cross-sections varies toroidally: it is elliptical at $\phi=0^0$ and triangular at $\phi=30^0$ (half period). The magnetic axis has a slight helicity with $\pm$2.5cm elongation.

Figure 1 shows the vacuum magnetic surfaces measured at $\phi=10^0$ in TJ-IU for two magnetic configurations used for plasma beta experiments: (a) the standard (R_{ax}=59cm) and (b) the inward shifted (R_{ax}=58.5cm) configurations. With this 0.5cm inward shift of

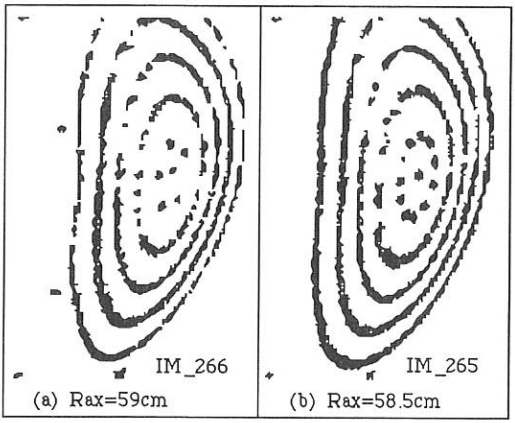


Fig.1 Two magnetic configurations used for plasma beta experiments: (a) the standard and (b) the inward shifted configurations.

magnetic axis, the properties of magnetic configuration change slightly: ι-value decreases about 5%, the depth of magnetic well decreases by 7.3% and the magnetic shear increases to 4%, respectively.

3. Analyses and results

Plasma beta experiments are carried out in TJ-IU at a low magnetic field B(0)=0.5T, and ECRH plasmas are produced by one 28GHz gyrotron with 200kW input power (25ms duration) launched perpendicularly at $\phi=30^0$. Those improved beta discharges are all obtained with the inward shifted magnetic configuration as shown in Fig.1b.

Figure 2 shows the time behaviour of two kinds of discharges: shot #767 represents improved beta discharges and shot #710 is one of normal discharges obtained with the standard configuration (Fig.1a). Signals displayed from top to bottom are: plasma beta $\beta(0)$ ($\beta(0)\equiv 3<\beta>$) from magnetic measurements, line average electron density $\bar{n}_e$ and gas puffing, thin ECE signal, OV line emission, H_α signal (180^0 away from gas-puffing port), plasma current I_p, microwave transmission signal ECA (free microwave power in the chamber, 180^0 away from ECRH injection port), and the central plasma temperature T(0) estimated from signals of plasma beta and electron density with assumed profiles of $T(\rho)=T(0)*(1-\rho^2)^{1.5}$ and $n_e(\rho)=n_e(0)*(1-\rho^2)^{0.5}$, where ρ is the normalized minor radius of plasma. As it can be seen, an increase of about 80% in the peak value of plasma beta has been obtained for improved beta discharges. The highest values of plasma beta correspond to the highest electron density before reaching the cut-off density. However, even if the electron density in shot #767 is similar to or even lower than that in shot #710 during the time interval of 15-21ms, the plasma beta is already much higher in the former than in the later, and it increases rapidly. This is probably due to the more effective heating and the increase in plasma temperature, as indicated by some relevant signals in Fig.2. Such kind of beta increase behaviour has been found for all improved beta discharges.

In addition to the above mentioned differences between these two kinds of discharges, a big jump in the $\bar{n}_e$ signal of #767 can be seen. However, there are no corresponding changes in H_α signal and OV emission. This fact means that the profile of electron

density might have changed suddenly. This kind of jump in the electron density is a common characteristic of improved beta discharges. The jump can occur earlier or later, depending on the gas puffing. In fact, there exists a critical density for the density jump, the value of which is $(2.0\text{-}2.4)\times10^{12}\text{cm}^{-3}$. The reason for this phenomenon is not clear yet, probably the magnetic configuration plays an important role here.

The rise of plasma beta can be divided into two phases, as seen clearly in Fig.3 which shows the plasma beta plotted versus the electron density for three improved beta shots (#763, 767 and 776) and one normal shot (#710). Generally, the plasma beta increases with the electron density in the low density region and becomes saturated in the high density region. For those improved beta shots however, the increment of plasma beta within the density range of $(1.4\text{-}2.4)\times10^{12}$ cm^{-3} is very sharp (fourfold). By applying the curve-fit $\beta(0)\sim\bar{n}_e^{\alpha}$ to the experimental data, we find that the exponent α=2.8-4.0 (increasing phase) and $\alpha\approx0.1$ (saturated phase) for improved beta shots, while for normal shots α=0.5-0.7 (increasing phase) and $\alpha\approx0.35$ (saturated phase). The later cases follow roughly the LHD scaling[2], but not the former cases which have very large α values. One possible explanation is that for these improved beta shots, the absorption of ECRH power by plasmas has improved significantly. The electron

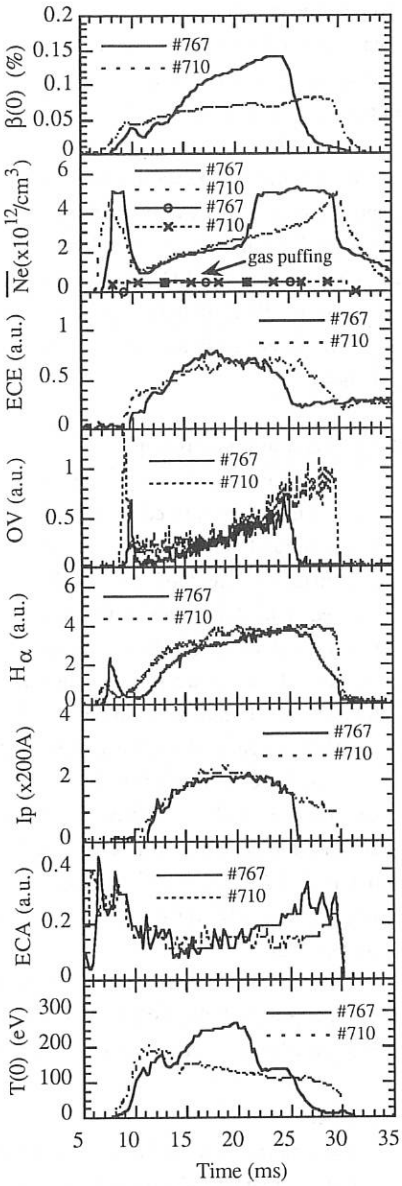


Fig.2 Time behaviour of two kinds of discharges: #767 is a high beta shot and #710 a normal shot.

temperature estimated from soft X-ray data is about 250eV for improved beta shots, against the value of 150eV obtained for normal shots. Other experimental evidences of the better absorption of ECRH power during these improved beta shots are also found from the signal reduction in microwave transmission monitor ECA, the signal increase in ECE detector and the enhanced plasma radiation measured by bolometry.

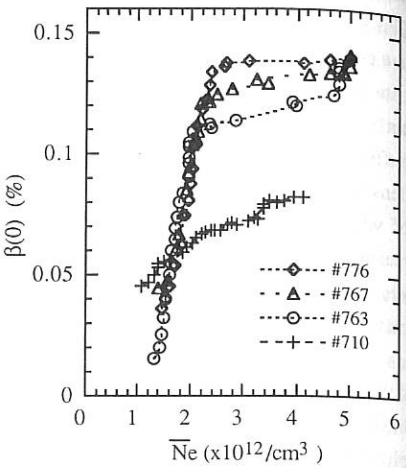


Fig.3 Plasma beta versus electron density: #763, #767 and #776 are high beta shots and #710 is a normal shot.

4. Summary and discussion

Experimental investigations of plasma beta are performed on ECRH plasmas in TJ-IU torsatron operated at a low magnetic field of B(0)=0.5T. Improved beta discharges with peak values of beta about 0.15% have been obtained with an inward shifted magnetic configuration. The achieved higher plasma beta values are mainly due to the more effective absorption of ECRH power by plasmas during these shots, which results in the increase of plasma temperature.

For those improved beta discharges, a big jump in the time-evolution of line average electron density is always observed. The reason for this is not clear yet, so more experimental efforts need to be done. There exists a critical density to start the density jump, the value of which is (2.0-2.4)x10^{12} cm^{-3}. It seems that the density profile might have changed suddenly after the jump. It is probable that the magnetic configuration used for those shots plays an important role.

Plasma beta experiments in TJ-IU are going on, more data will be available from some new installed diagnostics. Also, new experimental programs will be carried out soon with scans of magnetic configuration, electron density, ECRH input power, etc.

References

[1] Ascasíbar E., et al., in Plasma Physics and Controlled Nuclear Fusion Research (Proc. 15th International Conference, Sevilla, 1994), IAEA-CN-60/A6-I-1.

[2] Sudo S., et al., Nuclear Fusion **30** 11 (1990).

ION CONFINEMENT STUDIES IN THE TJ-IU SPANISH TORSATRON

B. Zurro, E. Ascasibar, J. Qin, B. P. Van Milligen, T. Estrada, C. Burgos, K. J. McCarthy, F. Tabarés, D. Tafalla and J. Vega. Asociación EURATOM/CIEMAT para Fusión. E-28040 Madrid. Spain

Introduction. Initial spectroscopic studies have been carried out on ion heating, rotation and impurity emission asymmetries in the TJ-IU spanish torsatron. In this l/m = 1, 6 torsatron (R=60 cm, a = 10 cm), the plasma is created and heated by injecting 200 kW of ECRH at 37.5 GHz through a quartz window, the microwaves are guided from the Gyrotron to the plasma by a cuasi-optical system. The magnetic field coils are powered by capacitor banks and the discharge lasts around 30 ms. The generation of runaway electrons during the fields build-up is avoided by a pre-programmed gas pulse, two other additional piezoelectric valves are used to obtain the desired density. The gyrotron is turned on when a hydrogen base pressure of around $4x10^{-5}$ Torr is achieved.

Preliminary results of parallel proton and impurity temperatures and relative toroidal rotation of O V as a function of plasma density are reported, as well as the observation of O V emission asymmetry and its temporal evolution along a standard discharge.

Experimental. High resolution spectroscopic studies have been performed using a 1 m high resolution spectrometer. In addition, a 1/4 m monochromator has been used to systematically monitor the time evolution of the 2271 Å C V line used as a basic electron temperature monitor. The first apparatus has two kinds of detectors in its double focal plane: a photomultiplier and an intensified multichannel detector. By the use of a folding mirror either of them can be used in a particular discharge. The plasma was observed through the same quartz window used to inject the microwave heating power. The plasma radiation was relayed to the spectrometer by means of an optical head made up of a quartz lens and a 1 mm diameter and 25 m long fibre. The optical head can be moved up and down in a shot to shot basis to scan 10 cm of the plasma cross-section along a toroidal line-of-sight.

The bulk electron temperature has been determined by fitting the time evolution of the C V line (2271 Å) by iteratively solving the carbon ionisation equilibrium. The estimated electron temperature values in this campaign are similar to those measured by ECE in the previous campaign at 28 GHz, for standard densities ranging between 150 - 250 eV.

Density scan of temperatures and rotation. The proton temperature has been deduced from analysis of the $H\alpha$ line wings. Its behaviour with plasma density is shown in Fig. 1 (a). A similar plot for O V temperature is depicted in Fig. 1 (b). Because of fiber transmission limitations the hottest impurity ion available to Doppler studies, with an unambiguously identified spectral line, was O V (2781 Å); its line-integrated emission peaking at a radius of 4 cm. The observations were made almost tangential, therefore, the rotation and ion temperature to which we refer here are parallel to the toroidal field. The O V ion temperatures, plotted in the figure, were determined using the spectral line shape averaged along the line-of-sight while assuming that the whole width, after correction by the instrumental function, was due to Doppler broadening. The quasi-static Stark effect produced by the heating wave electric field was ignored, but perhaps its effect at the ECRH injection port in particular might not be negligible.

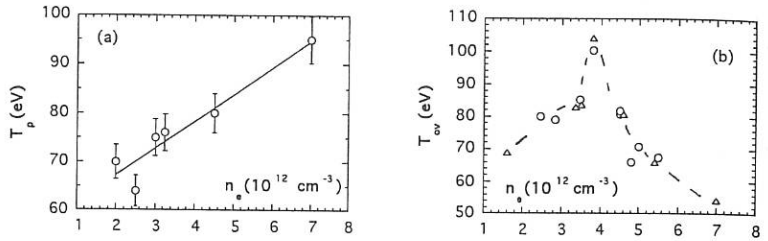


Fig. 1. (a) Plot of the proton temperature against electron density; (b) Plot of chord-averaged O V ion "temperature" versus electron density for a constant ECRH injection power of 200 kW.

Two features must be highlighted in the temperature trends shown in Fig. 1. Firstly, the central proton temperature is higher than expected and secondly the apparent O V temperature, averaged along the line-of-sight, is higher than for the former and exhibits a different behaviour with density. The expected kinetic temperature behaviour with density has been estimated using a zero-dimensional model (1). The results obtained, for the highest density case and for three different values of neutral concentration, are plotted in Fig. 2 (a) as a function of the enhancement factor in the electron-ion heat transfer term. These results suggest that in order to understand the central proton temperatures obtained some anomalous ion heating mechanism providing a power input to ions of around a factor three the classical collisional term is needed. The different behaviour of proton and impurity temperatures can be understood by considering the existence of nonthermal velocity fluctuations whose influence in the latter is more dramatic due to their higher mass.

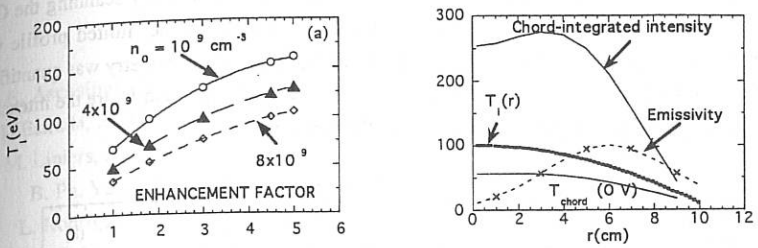


Fig. 2. (a) Theoretical ion temperatures in TJ-IU, for different assumed neutral densities, as a function of enhancement factor in the electron-ion heat transfer; (b) Simulation of O V chord-averaged intensities and temperatures and their comparison with local magnitudes.

The O V apparent temperature behaviour can be understood to be caused by the presence of nonthermal velocities. They have been analysed using a method, borrowed from astrophysics, and already used in the TJ-I tokamak (2). In Fig. 2 (b), the relationships between O V chord-averaged data (intensity and temperature) and local one are shown.They have been obtained using a code explained in Ref. (3). From the relation between the apparent impurity temperature and the kinetic one, $T_{app} = T_i + A_{OV} T_{turb}$, where A is the atomic mass of the impurity ion and T_{turb} the energy of the turbulence causing the nonthermal velocities, we can deduce the required level of nonthermal velocities in the plasma bulk. This is plotted as a function of the electron density in Fig. 3 (a). Notice the qualitative correlation between these turbulent velocities and the relative toroidal rotation of O V which is depicted in the accompanying plot of Fig. 3 (b).

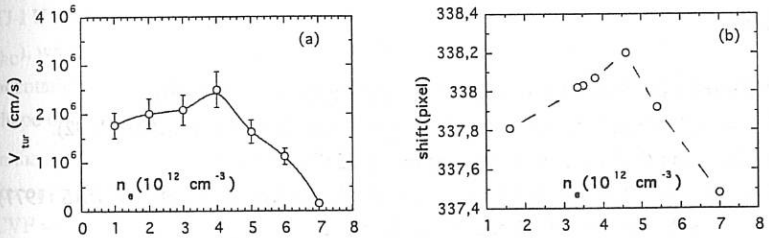


Fig. 3. a) Level of nonthermal velocities as a function of electron density, deduced from the difference between proton and O V apparent temperatures ; b) Similar plot for the toroidal shift of O V 2781 Å line; the maximum relative rotation change shown in this figure is ≈ 6 km/s.

O V up/down emission asymmetry. We have determined, by spatially scanning the OV 2781 Å line, that an up/down radiation asymmetry is evident in the limited profile we obtained. A slice profile is shown in Fig. 3 (a). The strength of the asymmetry was quantified by the asymmetry parameter defined by $\xi = (I_1-I_2)/(I_1+I_2)$, where I_1 and I_2 are the intensity of emission peaks at the upper and lower part of the vertical scan.

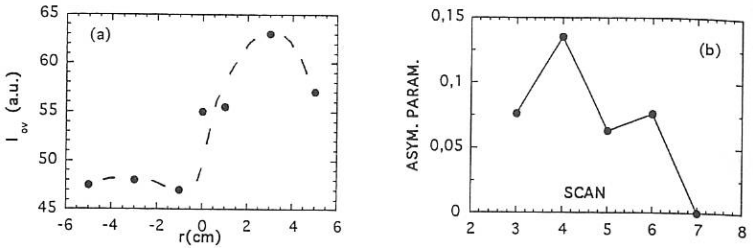


Fig. 4. (a) Plot of O V most asymmetric line-averaged emission profile; (b) Temporal evolution of the asymmetry parameter, the elapsed time between scans is 6 ms.

The asymmetry parameter evolves along a discharge as shown in the plot of Fig. 3 (b). Here the asymmetry parameter is plotted as a function of the multichannel detector scan, the time between successive scans is 6 ms. Although these kinds of asymmetries are extensively reported in tokamaks experiments, see Ref. (3) and references therein, we have found only one report of similar asymmetries in stellarators (4). In the latter no systematic behaviour was found when studied at different toroidal positions, in contrast to tokamaks where interpretations based on physical principles have been advanced.

References

(1) B. Zurro et al., Plasma Physics and Controlled Fusion **32**, 565 (1990).

(2) B. Zurro, J. Vega, F. Castejón and C. Burgos, Phys. Rev. Lett. **69**, 2919 (1992).

(3) B. Zurro and C. Burgos, Rev. Sci. Instrum. **63**, 5196 (1992).

(4) J.L. Terry, E.S. Marmar, K.I. Chen and H.W. Moos, Phys. Rev. Lett. **39**, 1615 (1977); K. Brau, S. Sukewer and S.K. Wong, Nucl. Fusion **23**, 1657 (1983)

(5) H. Hacker and W-VII-a Team, Proc. European Conference on Plasma Physics and Controlled Fusion (1986).

Recent results in TJ-I U Torsatron

E. Ascasíbar, C. Alejaldre, J. Alonso, R. Balbín, B. Brañas, E. de la Cal, F. Castejón, T. Estrada, M. Francés, I. García-Cortés, J. Guasp, J. Herranz, C. Hidalgo, J.A. Jiménez, M. Liniers, A. López-Fraguas, A. López-Sánchez, E. De La Luna, R. Martín, F. Medina, B. Ph. Van Milligen, M. A. Ochando, L. Pacios, I. Pastor, M. A. Pedrosa, J. Qin, L. Rodríguez-Rodrigo, A. Salas, E. Sánchez-González, J. Sánchez-Sanz, F. Tabarés, D. Tafalla, V. Tribaldos, A. Varias, J. Vega, B. Zurro and ECH and TJ-I U Teams

Asociación EURATOM-CIEMAT para Fusión, Av. Complutense 2228040 Madrid, Spain

L.M.Kovrizhnykh, D. C. Akulina, O. F. Fedyanin, S. Grebenshchikov, N. Kharchev, L.V.Kolik, K.M.Likin, N.V. Matveev *, Yu.I.Netchaev, A.Ye.Petrov, K.A.Sarksyan, I. Sbitnikova

General Physics Institute, Russian Academy of Sciences, Moscow, Russia

** Electrotechnical Center, Istra of Moscow Region, Russia*

1. Introduction

TJ-I Upgrade is a l =1, m=6 torsatron in operation at CIEMAT, Madrid since April 1994 [1]. It has a major radius of 0.6 m, average plasma radius of 0.1 m and average magnetic field, B = 0.5÷0.7 T, and magnetic ripple of 7.6 %, on axis. In the standard configuration the rotational transform, ι, is above 0.2 with negligible shear, and magnetic well of 6.9%. ECRH plasmas (X-mode, 2nd harmonic, P = 190÷250 kW, pulse length ≈ 25 ms) have been produced at 28 and 37 5 GHz. TJ-I U coils are powered by capacitor banks, producing a useful "plateau" of up to 30 ms. Within it the maximum variation of magnetic field never exceeds 1%.

2. Control of the magnetic configuration

TJ-I U magnetic configuration is determined by two relevant current parameters: CVF (= I_{evf} / I_{hc}), which controls the inward/outward shift of the magnetic axis and, consequently, the value of rotational transform and magnetic well depth, and α (= I_{ivf} /I_{evf}), which can change the shape of magnetic surfaces and modify the ι-profile, where I_{hc}, I_{evf} and I_{ivf} are the currents in the helical, external vertical and internal vertical field coils, respectively.

Recently, vacuum magnetic configurations [2] have been intensively measured in the range CVF = 0.35 - 0.52, $\alpha = \pm 0.8$, corresponding to a rotational transform variation, $\iota(0) = 0.1$-0.6 (horizontal magnetic axis shift of 15 cm). The shape of the magnetic surfaces can be changed dramatically with α, from bean-shaped (elongation, $\kappa \approx 3.4$) for $\alpha = -0.8$ ($\alpha < 0$ meaning that the direction of current I_{ivf} is reversed) to almost circular ($\kappa \approx 1.3$) for $\alpha = 0.8$. Internal and external sources of field errors have been identified studying the effect of changing the magnetic field intensity and reversing its direction on the measured magnetic surfaces. As a

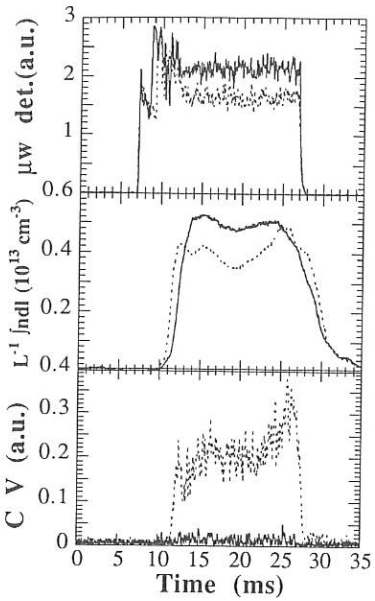


Fig. 1: Plasma traces from discharges #1830 (dashed line) and #1831 (solid line). Top to bottom: microwave monitor signal, line electron density and C V line emission

final result a theoretical model has been elaborated which can reproduce very accurately the measured surfaces and can be used confidently to simulate the real magnetic configurations in full field operation.

3. Heating. Power modulation

ECRH plasmas are produced using second harmonic extraordinary waves, launched perpendicularly to the magnetic field. Microwave power (Gaussian beams with almost linear polarisation) is transmitted by means of a quasi-optical transmission line (four cylindrical mirrors coupled in pairs so that the curvature radii of each couple lie in perpendicular planes) and injected through a quartz window located at an external equatorial port ($\phi = 30°$).

Recently, a power modulation system has been developed. It allows to modulate the gyrotron output power in the drift frequency range (4-40 kHz), by means of the modulation of the output voltage of the gyrotron power supply. With the help of this system, experiments aiming to detect non-linear interactions between the plasma turbulence and externally excited waves are about to start.

4. Experimental results and discussion

4.1 Wall conditioning and fueling

In TJ-I U the non-bakeable stainless steel chamber acts as a limiter. Incomplete wall conditioning typically leads to strong impurity desorption during the microwave power injection [3]. Wall conditioning by means of He DC glow discharge (2 anodes, $p \approx 7 \times 10^{-3}$ torr, $I \approx 20\ \mu A\ cm^{-2}$) has been used in order to minimise the impurities contribution (<10%) as compared with the injected working gas one.

A critical problem was found when trying to control the density ramp-up after the plasma formation. There were two almost antagonistic requirements to satisfy: on one hand the neutral pressure just before the microwave pulse should be low enough ($< 5 \times 10^{-5}$ torr) to allow plasma start-up; otherwise only cold plasmas were obtained. This fact is illustrated in figure 1, which displays two consecutive shots with the same magnetic configuration. The only difference between them is that in the second one, #1831, the initial neutral pressure was

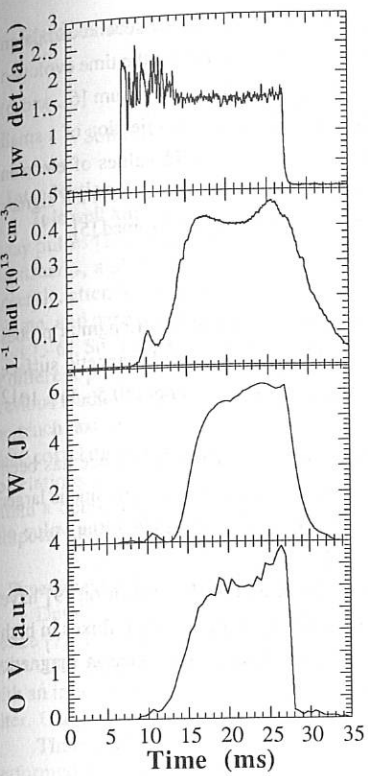


Fig.2: Plasma traces from discharge #1321. Top to bottom: microwave monitor signal, line electron density, energy content and O V line emission

slightly increased, in an attempt to raise the electron density, still under the cut-off level. The result is a cold plasma discharge (no power absorption at all, although electron density is similar) because preionization failed, as can be deduced from the C V line emission. On the other hand, X ray supression during and after the discharge required high enough neutral pressures during the ramp-up of the magnetic fields (mainly the vertical one) to avoid the presence of high energy electrons. To face this problem a gas injection system based on two fast (rise time ≈ 1 ms) piezoelectric valves that can be supplied with up to four short gas pulses has been designed and constructed. Even with such a complex puffing system the operational window for plasma start-up is extremely narrow, so that an additional ultraviolet source for preionization [4] is being constructed and will be installed in the next experimental campaign.

4.2 Confinement

Radiative electron temperature, as deduced from ECE measurements during the 28 GHz campaign was $T_r(0) \approx 140 \div 200$ eV, in plasmas with line average electron densities, $\langle n_e \rangle \approx 0.3 \times 10^{13}$ cm^{-3}. Typical shots in this campaign had stored energy of about 5 J, although "improved" beta discharges were obtained for inward shifted configurations [5] in which peak beta-values reached up 0.15%, corresponding to stored plasma energies about 10 J. During the 37.5 GHz series of experiments, higher electron densities have been attained, $\langle n_e \rangle \approx 0.6 \times 10^{13}$ cm^{-3}, with plasma energy values up to 10 J. Figure 2 shows a typical 37.5 GHz shot, displaying the temporal evolution of several traces: microwave detector signal (measuring the free microwave power inside the vacuum vessel), line averaged electron density, energy content (from magnetic flux loops) and O V line emission.

In some shots, the fraction of absorbed power may be estimated from the microwave detector (diode) signal, as shown in figure 1. The difference between the two microwave signals gives an estimate of the absorbed power fraction in the first discharge; it is about 20%, corresponding

to an energy confinement time of about 0.2 ms. Electron temperature in the second campaign (37.5 GHz) has been estimated by means of two different methods: a) Fitting the time evolution of the C V line (2271 Å) by iteratively solving the carbon ionisation equilibrium [6], and b) Measuring the intensity of two He emission lines (706 and 728 nm) after injection of a small amount of helium into the H plasma discharge [3]. Both methods yield values of electron temperature ranging between 150 - 200 eV. Similar values are also estimated from the signals of plasma beta and electron density if temperature and density profiles are assumed [5].

4.3 Turbulence

Radial fluctuations profiles have been measured by means of an array of four Langmuir probes in the plasma edge [7]. The edge electron temperature, near the last closed magnetic surface (LCMS), is about 15 eV, and the electron density, in the same position, about (0.5 - 1) x 10^{12} cm^{-3}.

A comparison of TJ-I U with other stellarators in terms of edge plasma turbulence has been done ([8]. While the estimated plasma density fluctuations level in the bulk plasma side is larger in TJ-I U (low shear) than in W7-AS (low shear) and ATF (moderate shear), the value of bicoherence in TJ-I U is similar to the one observed in ATF.

Comparative studies of the edge turbulence in TJ-I tokamak and TJ-I U torsatron [9] have shown that there is a strong similarity in the statistical properties of the turbulent fluxes in both machines, supporting the idea of the universal character of plasma turbulence in magnetic devices.

References

[1] Ascasíbar E et al, *Transactions of Fusion Technology*, **27**, 198, (1995).

[2] Qin J et al, *Proc. 10th Int. Conf. on Stellarators* , Madrid, 1995 (to be published)

[3] Tabarés F et al, *Proc. 10th Int. Conf. on Stellarators* , Madrid, 1995 (to be published)

[4] Smeulders P, *Rev. Sci. Instrum.*, **46** (7), 909, (1975)

[5] Qin J et al, in *these Proceedings*

[6] Zurro B et al, *Proc. 10th Int. Conf. on Stellarators* , Madrid, 1995 (to be published)

[7] Pedrosa M A et al, *Proc. 10th Int. Conf. on Stellarators* , Madrid, 1995 (to be published)

[8] Sánchez E et al, *Proc. 10th Int. Conf. on Stellarators* , Madrid, 1995 (to be published)

[9] Hidalgo C et al, *Proc. 10th Int. Conf. on Stellarators* , Madrid, 1995 (to be published)

Studies of Hot-Spots and Their Correlation with Other Phenomena in PF-Type Discharges

L. Jakubowski and M. Sadowski
Soltan Institute for Nuclear Studies, 05-400 Świerk n. Warsaw, Poland

1. Introduction

It is well known that high-current carrying discharges of the PF type are sources of intense X-ray pulses [1-2]. Such a radiation is usually accompanied by the emission of fast electron and ion streams, and in the case of deuterium discharges - by the emission of neutron pulses [3-4]. Recently, attention has been paid to various non-linear phenomena which appear within a pinch column, and particularly to miniature regions with increased X-ray emission which are called hot-spots [5-6]. Such phenomena have also been investigated at SINS in Świerk, Poland, by means of different plasma facilities, and in particular with the MAJA-PF and PF 360 devices [7-8]. The previous studies have revealed the correlation between the spatial distribution of hot-spots along the pinch axis and a temporal sequence of their appearance [9]. There have also been observed some correlations with other phenomena, e.g., with corpuscular emission pulses. Studies of such correlations are of particular importance for the understanding of physical processes occurring within a dense magnetized plasma. The main aim of this work has been a detailed spatial - and temporal study of the hot-spots and their correlations with other kinds of the radiation.

2. Experimental Facilities and Diagnostic Equipment

Detailed measurements of X-rays and e-beams have been carried out with the MAJA-PF device [7]. The system was powered by a condenser bank which was usually charged to 44 kJ at 35 kV. The integral x-ray emission has been registered by means of a pinhole camera equipped with an input diaphragm of about 100 μm in diam., which was covered with a 10μm-thick Be-foil filter. Use has also been made of a standard ionization chamber of the VAJ type.

Time-resolved measurements of the X-ray emission from the whole pinch region have been performed by means absorption filters and scintillation detectors coupled through optical cables with fast photomultipliers Philips XP2020 type. The first detection system was adjusted at the angle of 45° to the z-axis and it made possible the registration of a relatively soft radiation of energy ranging from 1 to 8 keV, and a harder X-rays of energy 15-40 keV. The hard X-rays (above 100 keV) were registered with a scintillation probe which was placed at a distance of about 5 m from the electrode ends, and used also for neutron measurements.

Time-integrated X-ray pinhole pictures made possible an analysis of a spatial distribution of hot-spots. A comparison of those pictures with time-resolved X-ray signals has shown that the formation of a distinct hot-spot depends on a distance from the electrode ends [9]. In order to investigate this dependance there was designed a special measuring system made possible to register the X-ray emission from two selected regions of 8 mm in diameter, which were situated at the pinch axis at distances of about 10 mm and 30 mm, respectively. X-ray pulses, as emitted from these two regions, have been measured by means of scintillator-photomultiplier detectors. The waveforms were registered with a multi-channel 250 MHz digital oscilloscope of the HP-16500 type, and compared with other diagnostics signals (up to 12 traces).

3. Experimental Results

3.1. Studies of hot-spots. An analysis of x-ray pinhole camera pictures, as taken under different initial gas conditions, has shown that an admixture of a small amount of a noble gas to

the working medium (deuterium) can induce the formation of small bright (strongly emitting) regions, i.e. distinct hot-spots. Within the MAJA-PF device a small argon admixture can cause a considerable increase in the number of the hot-spots observed. It has, however, been found that for the argon admixture within 5-35% range there appears the saturation effect, and an average number of hot spots per shot is about 5. The maximum hot-spots number amounts to 12.

Measurements of the X-ray emission from the small regions placed at the axis of the pinch column have enabled to discern pulses originating from individual hot-spots, which accidentally appeared within the field of observation. In Fig.1 there are presented some pulses emitted by separate hot-spots formed close to the electrode end (at z=12 mm, trace X_{SN}) and at a larger distance (at z=28mm, trace X_{SF}). They can be compared with a soft and hard X-rays emitted from whole FP-region (traces X_S, X_H) as well as with a spatial X-ray picture taken with the pinhole camera.

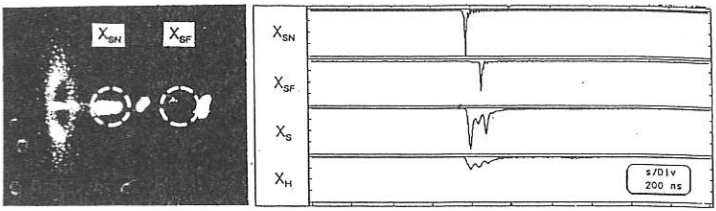


Fig.1. Comparison of space-resolved hot-spots and time-resolved X_{SN} and X_{SF} signals corresponding to the soft and hard X-rays, emitted from the whole pinch region (X_S,X_H).

Life-times individual hot-spots, as characterized by FWHM values of X-ray pulses emitted from the hot-spots, have been estimated to be about 7-10 ns. These values have evidently been overestimated because of the limited frequency band of the detection system.

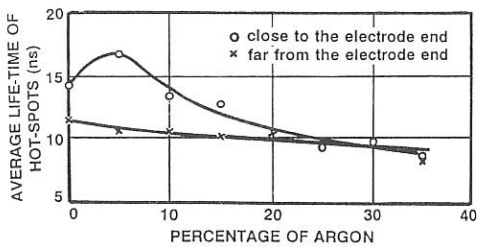


Fig.2. Average life-time of hot-spots within two different regions as a function of the argon admixture

Average values of the measured hot-spots life times vs the percentage admixture of argon have been presented in Fig.2. The longest life-time has been observed for a 5% argon admixture, but in general the hot-spot life-time decreases with an increase in the Ar amount. It should, however, be noted that for a low argon concentration life-time of the hot-spots formed at a larger distance from the electrode front plate is about half of that observed for the hot-spots situated near the electrode end. For higher argon concentrations (above 25%) the average life-times of all the hot-spots are comparable. An analysis of the X-ray pinhole pictures has shown that linear dimensions of the considered hot spots are usually below 100 μm

An average amplitude (intensity) of X-ray pulses emitted from individual hot-spots has the maximum value when the percentage of the argon admixture is about 20-25%. This dependance has been observed for the hot-spots formed close to the electrode front plate as well as for those generated at a larger distance, as shown in Fig.3. A comparison of the both curves shows that intensity of the hot-spots near the electrode end is several times higher than that for more distant

ones. It means that hot-spots emission intensity decreases with an increase in the distance from the electrode outlet.

Within about 300 investigated discharges the X-ray pulses from the hot-spots formed near the electrode front plate have appeared earlier than those from more distant region. Time differences between those pulses have been 45-85 ns. Considering that the current sheath collapses on the z-axis first at the electrode end-plate, during later phases other parts of the current sheath are compressed, and a region of the maximum plasma concentration can propagate along the axis. Under this assumption one can estimate a phase velocity of such a region. It has been calculated, that an average value of this velocity is (1.5-3.5) x 10^7 cm/s. The maximum velocity of the collapse region (along the z-axis) has been observed for a 10-15% argon admixture.

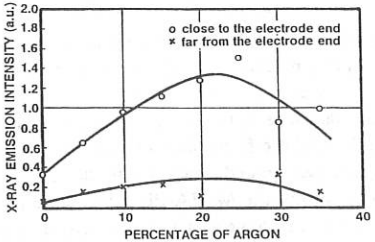


Fig.3 Amplitude of X-ray pulses from the hot-spots formed within two different pinch region, as measured for various argon admixtures

3.2. Correlations with other phenomena. It has been found that soft X-ray pulses, which are registered from the whole pinch region depend strongly on dynamics and microstructure of the pinch column. Therefore, these pulses characterize the positioning and appearance of individual hot-spots (vide the X_S - trace in Fig.1). The emission of such a radiation lasts usually about 150 ns.

Harder X-rays (X_H), as measured within energy range from 15 keV to 40 keV, are well correlated with voltage- and current-peculiarities, and they are usually emitted during 300-400 ns. On contrary, the emission of very hard X-rays (above 100 keV), as registered with the scintillation probe placed far from the stainless steel experimental chamber, lasts about 100 ns only. Hard X-rays have also been registered with the VAJ-type ionization radiometer during experiments carried out with different argon admixtures. An analysis of about 250 discharges has shown that with an increase of the argon concentration in the working deuterium gas, intensity of the hard X-ray emission decreases even by an order of magnitude and the steepest decrease is delivered for admixture up to about 15%, as demonstrated in Fig.4.

In addition to neutron time-resolved measurements with the scintillation probe, there have also been performed time-integrated measurements of the neutron emission by means of silver activation counters placed perpendicular and at 45° to the z-axis. It has been observed that the side-on counter indicates usually the neutron yield about 3 times lower that registered by the second counter. It says about a relatively large anisotropy of the neutron emission. An analysis of about 220 discharges, as performed with the D_2 filling and different argon admixtures, has confirmed that the neutron yield decreases considerably

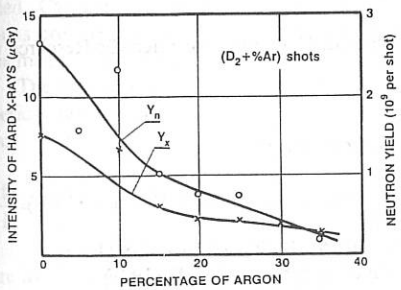


Fig.4. Intensity of the hard X-ray emission (Y_n) and the fusion neutron yield (Y_n) as a function of the argon admixture percentage)

with an increase in the argon admixture. The Y_n characteristics are similar to these of the X-ray emission (Y_X). It suggests that analogous physical processes are responsible for the generation of the two kinds of the emission under consideration. It should be noted, however, that for lower (5-10%) argon admixtures there is observed relatively large jitter in the experimental data.

In order to measure electron beams emitted in the upstream direction through a central 10-mm-dia. channel, the use has been made of a Cerenkov-type detector placed at a distance of 40 cm behind the front plate of the inner electrode. To register electrons of energy down to 50 keV there was applied a radiator made of a diamond plate. Measurements of an electron energy spectrum within the MAJA-PF device have proved that it ranges up to about 500 keV.

Time-resolved electron measurements have shown that electron signals appear in the close correlation with the voltage spikes which are coupled with current peculiarities and hard X-ray pulses. The electron signals last usually 30-50 ns and it is possible to discern spikes with FWHM equal to about 8 ns. An analysis of numerous oscillograms has not however demonstrated any distinct correlation of the investigated electron beams with the appearance of individual hot-spots.

4. Summary and conclusions

The most important results of the recent studies performed with the MAJA-PF device can be summarized as follows:

1. Miniature regions of a dense high-temperature plasma (hot-spots) which are formed within the pinch column, in particular within discharges with small admixture of argon, emit strong X-ray pulses with FWHM of 5-10 ns. Their linear dimensions, as determined on the basis of X-ray pinhole pictures, are well below 100 μm.
2. During PF-type discharges the hot-spots are formed at the z-axis successively, starting from the end of the inner electrode. This effect can be explained by the propagation of the current-sheath collapse region along the axis. An axial velocity of this propagation has been found to be $(1.5\text{-}3.5)\times10^7$cm/s.
3. An admixture of argon (added to deuterium) induces an increase in the hot-spots population, but simultaneously it reduces the hard X-ray emission and the neutron yield.
4. Fast electron beams, emitted in the upstream direction through the inner electrode, are well correlated with voltage spikes occurring simultaneously with current peculiarities, but they are not correlated with the number and appearance of hot-spots observed in the X-ray pinhole pictures.

Acknowledgement

This work has been partly supported by the State Committee for Scientific Research under a contract No. 2-P302-058-06.

References.

[1] N.V.Filippov, et al.: *Nucl. Fusion,* Suppl. Pt.2, 577 (1962)
[2] J.W.Mather: *Phys. Fluids* **8** 366 (1965)
[3] L.Jakubowski, et al.: *Workshop Phys. of Altern.Magn.Conf.Schemes,* Varenna (1990)
[4] Y.Kondoh, et al.: *Jap. J.Appl.Phys.* **20** 393 (1981)
[5] M.Sadowski, et al.: *Proc. 12th Europ. Conf. CF&RP* (Budapest) Pt.1, 538 (1985)
[6] P.Antsiferov, et al.: *Proc. 18th EPS Conf. CF&PF* (Berlin) Pt.2, 221 (1991)
[7] M.Sadowski, et al.: *EPS Conf. CF&PL* (Lisboa), Pt.2, 537 (1993)
[8] L.Jakubowski, et al.: Soltan Institute for Nuclear Studies, *Annual Report* (1992)
[9] M.Sadowski, et al.: *Proc. 21th. EPS Conf. CF&PP* (Montpellier) Pt.3, 1320 (1994)

Magnetic surfaces, plasma confinement and heating in Tornado-X

K.B.Abramova, G.A.Galetchyan, M.L.Lev, A.A.Semenov, E.M.Sklyarova, **A.V.Voronin**
Ioffe Physico-Technical Institute, 194021, St Petersburg, Russia

A numerical calculation of magnetic field lines in a separatrix-bounded volume has been carried out. The field of the trap has been shown to possess a regular structure consisting of nesting toroidal surfaces. Studies of the decaying plasma permit a conclusion that plasma losses are governed by classical diffusion. Plasma heating by charged-particle drift in crossed magnetic and electric fields has been achieved. The rotating-plasma parameters obtained in Tornado-650 have been reproduced.

1. Introduction

The magnetic field of the trap for plasma thermal insulation, proposed in 1970 by Peregood and Semenov [1], is generated by two oppositely directed currents, I_{in} and I_{out}, flowing through spherically-arranged concentric helical conductors with radii r_{in} and r_{out}. The spherical separatrix of radius $r_S = \sqrt{r_{in} r_{out}}$, separating the closed magnetic field of the trap, exists if the condition $I_{out}/I_{in} = \sqrt{r_{in} / r_{out}}$ is met. The central region of the trap with a lower magnetic field is surrounded by a magnetic barrier located near the separatrix. Since the magnetic field is primarily poloidal, there is no toroidal drift. The closed poloidal trap Tornado has an improved field structure and, thus, permits achieving larger plasma-to-magnetic field pressure ratios. In an experiment performed on Tornado-650 with stored capacitor bank energy of 100 kJ, barrier magnetic field of 0.15 T, plasma density of 10^{13} cm^{-3}, ion temperature of 200 eV, and proton rotation energy of 1 keV, the Alfven limit of plasma rotation velocity was exceeded by a factor ten (3×10^7 cm/s) [2]. These results provide a basis for plasma production with a density of 10^{14} cm^{-3}, ion temperature of 1.5 keV, and directed proton-motion energy of 8 keV in the Tornado-X trap with a barrier magnetic field of up to 1 T.

2. Method

Numerical calculation of magnetic field lines in the separatrix-bounded volume has been performed. Calculations of sufficiently long field-line sections provide a basis for deriving the structure of the magnetic surfaces.

The magnetic field lines were obtained by numerical integration of coupled differential equations:

$$\frac{d\eta}{H_\eta} = \frac{\eta d\theta}{H_\theta} = \frac{\eta \cos\theta d\varphi}{H_\varphi} = \frac{ds}{H}$$

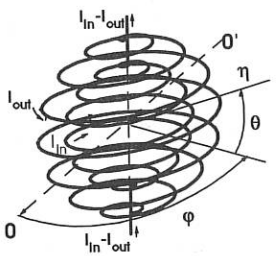


Fig. 1 Scheme of two spiral Tornado trap

where ds is the differential of the field line arc length, H is the magnetic field strength calculated from the Biot-Savart law, and η, θ, and φ are the spherical coordinates (Fig. 1). This system was integrated by the fourth-order Runge-Kutta method.

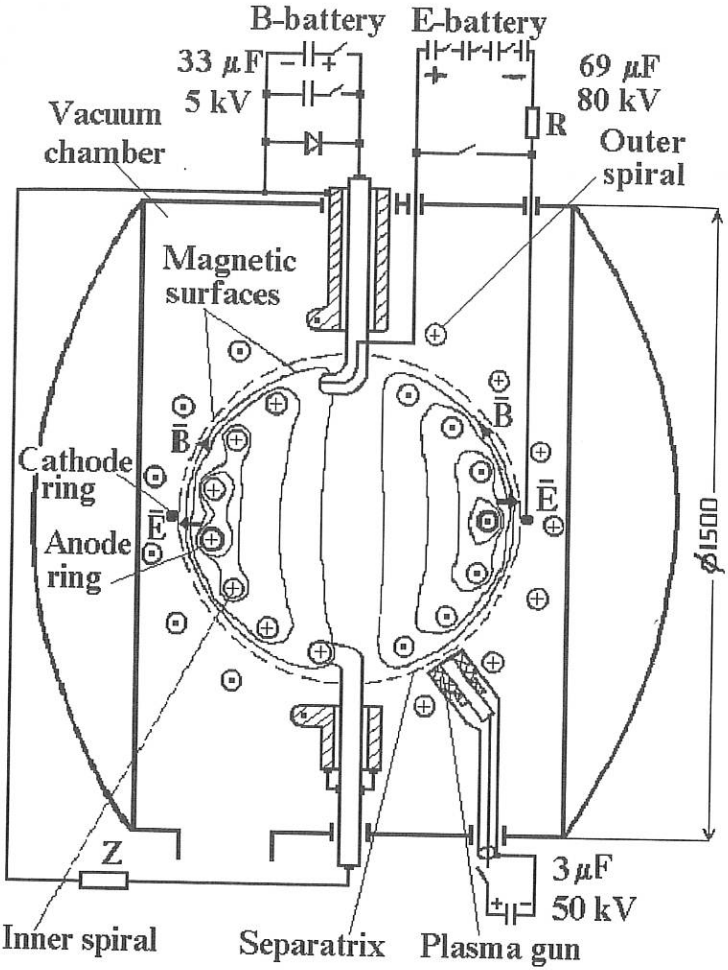


Fig. 2: Scheme of Tornado-X experiment

A mechanically rigid Tornado-X trap, capable of passing the required electric current through the helical conductors and using high-strength materials, has been developed and manufactured [3]. Final projection, selection of the material and manufacturing of spirals had been carried out by scientific, engineering an technical staff of the Division of Fusion Plasma Physics, Alfven Laboratory in Stockholm.

The trap confinement has been studied from the decay of the electronic plasma component density, which is measured along the trap diameter in the equatorial region with an HCN-laser interferometer at 337 μm. Plasma rotation and heating produced in collisions of charged particles as they drift in crossed magnetic and electric fields were achieved with the trap filled by the plasma generated by an erosion-type injector, and an electric field applied between electrodes perpendicular to the magnetic field of the trap (Fig. 2). The plasma rotated around the axis passing through the helix poles.

3. Results

The calculations yielded two types of field lines, individual and generalized. Individual field lines always encircle the conductor of one turn (Fig. 3), and do not encircle those of adjacent turns. Generalized field lines encircle two or more adjacent turns of the inner helix. Individual field lines in the pole region enter the helix gap and pass near the inner side of the separatrix, thus forming in repeated passes the toroidal surfaces predicted in Ref. [4]. It turns out that the generalized field lines form toroidal surfaces with holes, out of which emerge helical conductors encircled by individual field lines. A typical feature of the trap in question are surfaces which in the $\varphi = 0$ and $\varphi = \pi$ regions encircle, accordingly, one-two, three-four, five-six, and seven-eight conductors. One of such surfaces is shown in Fig. 4.

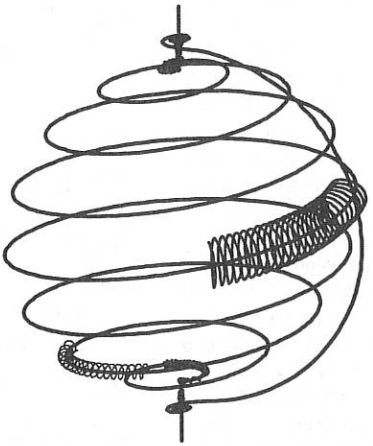


Fig. 3: Fragments of individual magnetic strength line

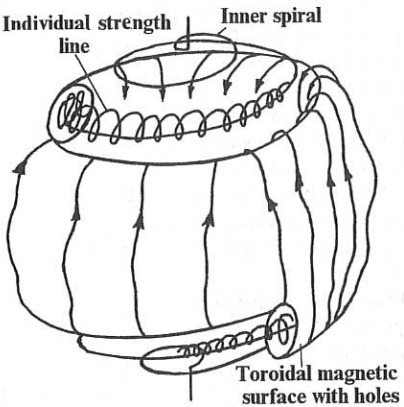


Fig. 4: A generalizing magnetic surface with conductor of inner spiral surrounded by individual magnetic strength line

Studies of the decaying plasma permit to get the charged particle confinement time. It depends upon the magnetic field. As the magnetic induction increases, the charged-particle confinement time grows by a quadratic law up to $B = 0.13$ T and reaches 950 μs. Further increase of the magnetic field does not affect the lifetime of the plasma because of its decay through volume electron-ion recombination. Recombination during the existence of magnetic field can be suppressed by increasing the injector current with simultaneous reduction of injector operation time.

Rotating plasma experiments have been carried out. Estimates based on the measurements (Fig. 5) suggest that the plasma is fully ionized, rotates with velocities of up to 5×10^7 cm/s, and its ion temperature can reach 0.5 keV.

4. **Conclusions**

The magnetic field of the trap has a regular structure and consists of nesting toroidal surfaces of two types. The Tornado-X device has been established to be closed, the plasma losses from it being governed by classical diffusion. An analysis of the measured parameters suggests that the plasma is fully ionized and rotates, and its rotation velocity is considerably in excess of the Alfven limit, the ion temperature reaching a few hundred electron volts.

This work was partially supported by the Soros Foundation under recommendation of the American Physical Society (February 17, 1993) and by the Russian Ministry of Sciences.

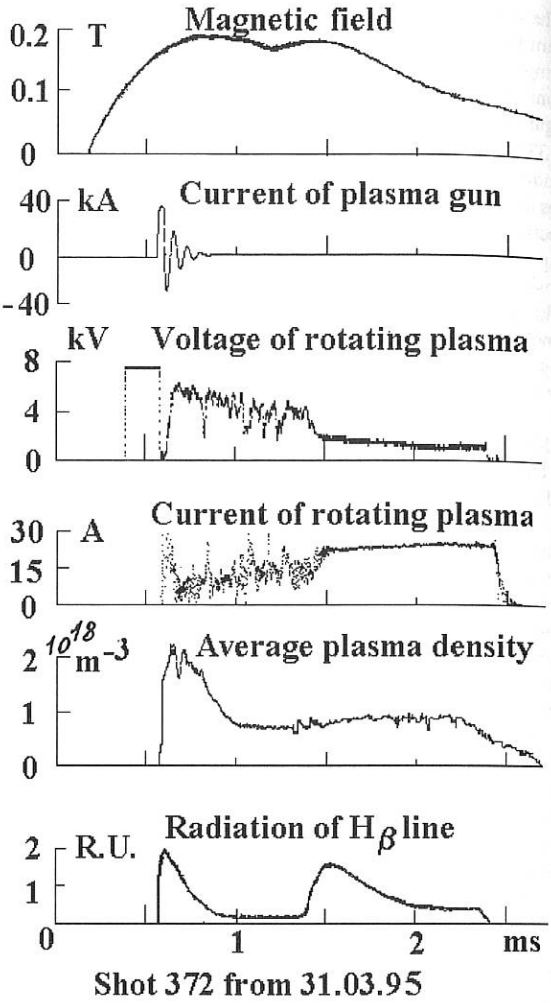


Fig. 5: Measured parameters

REFERENCES

[1] B. P. Peregood, A. A. Semenov, Zh. Tekh. Fiz., **61**(**11**) 2297 (1971).

[2] B. P. Peregood et al., *Voprosy Atomnoj Nauky i Techniky "Termoyadernyj Sintez"*, **3**(**16**) 46 (1984).

[3] A. V. Voronin at al., Zh. Tekh. Fiz., **57**(**3**) 469 (1987).

[4] G. V. Skornyakov, Zh. Tekh. Fiz., **32**(**3**) 261 (1962).

Observations of a 7μm Carbon Fibre Z-pinch

F. N. Beg, P. Lee, M. Tatarakis and A. E. Dangor
The Blackett Laboratory, Imperial College
London SW7 2BZ, UK.

I. Introduction

There has been much interest in the dense Z-pinch due to nuclear fusion [1] and radiative collapse [2]. For these applications the plasma must be both dense and stable for a long time. Further, for radiative collapse to occur the current must exceed the Pease-Braginskii value [3]. It is thus important that there is little expansion of the pinch and that instabilities do not develop. It has been suggested that it is possible to generate a Z-pinch in a plasma parameter range where ideal magnetohydrodynamics (MHD) does not apply. Indeed , Sethian *et al.* [4] reported two experiments on a Z-pinch where the pinch was seen to be free from gross instabilities up to current maximum and coincident with this was a large neutron pulse. Similar results were reported by Hammel and Scudder [5], in a Z–pinch produced in a frozen deuterium fibre, though here instabilities were reported to occur earlier in some shots.

Deuterated polythene fibres have been used by Kies *et al.* [6] on the KALIF pulsed power generator. An inhomogeneous plasma was seen to develop along with a string of axially located x-ray bright spots. An isotropic neutron flux was also seen. Figura *et.al.* [7] investigated a quartz fibre Z-pinch with diameters that ranged from 10 to 125 μm driven by a current of 150 kA with a 50 ns rise time. The pinch was seen to develop m=0 instabilities early in the discharge. It was inferred that these instabilities developed in a coronal plasma and that the whole fibre had not been converted into plasma by the end of the current rise. No enhanced stability was seen.

The work presented in this paper investigates the dynamics of a 7 μm carbon fibre pinch. A current generator that gives current of 100 kA in 60 ns ($dI/dt = 1.66 \times 10^{12}$ As^{-1}) was used. The details of the current generator and the electrical signals can be found in ref. [8]. The Z-pinch plasma was formed from commercially available 7 μm diameter carbon fibre, 20 mm in length having line density of 4.6×10^{18} m^{-1}.

II. Experimental Results

1. Optical Emission

An optical streak camera was used to monitor the optical emission from the plasma. Figure 1(a) shows an optical radial streak photograph. The light appears at t = 0 (start of the current). The pinch expands radially with a velocity of 1.2×10^4 ms^{-1}. The modulated optical emission is due to the axial motion of bright spots across the streak camera slit. The pinch expands to maximum diameter of about 500 μm.

Figure 1(b) is an axial streak photograph which shows that the breakdown starts from the cathode at t=0 and light appears at the anode after 4 ns. There are two sets of bright spots. First

set appears at about 7-8 ns and second set appears at about 18 ns. These bright spots move axially in either direction with a velocity of 3 x 10^5 ms^{-1}. The emission from the electrodes is also observed. The optical emission lasts for 65 ns.

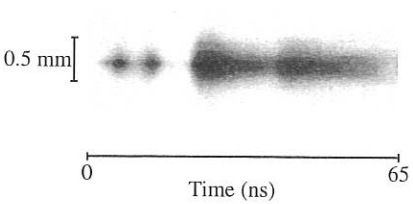


Figure 1(a). An optical radial streak photograph showing modulated emission due to motion of the bright spots.

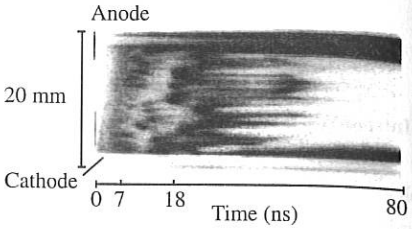


Figure 1(b). An optical axial streak photograph showing non-uniform breakdown and axial motion of the bright spots.

2. X-ray Observations

Figure 2 shows four time integrated x-ray pinhole images recorded on Kodak DEF-59 film. A set of the pinhole diameters and x-ray filters was used. These images show a series of bright spots non-uniformly distributed along the fibre axis. The filter used in Fig.2(a) transmits the line radiation (characteristic and recombination) above 200 eV. The other three images are pinhole limited. It can be concluded that the bulk of soft x-radiation was in the form of line radiation. On average ten bright spots were observed in every discharge. The total x-ray flux above 200 eV estimated to be 6 Joule, about 0.6 J per bright spot. The anode emission is visible and so is the capillary used to guide the fibre between the electrodes. The bright spot temperature in range of 80-135 eV was obtained from the time integrated x-ray pinhole photographs. The Bennett temperature at the time of appearance of the bright spots assuming fully ionised plasma with 36 kA current is 21 eV.

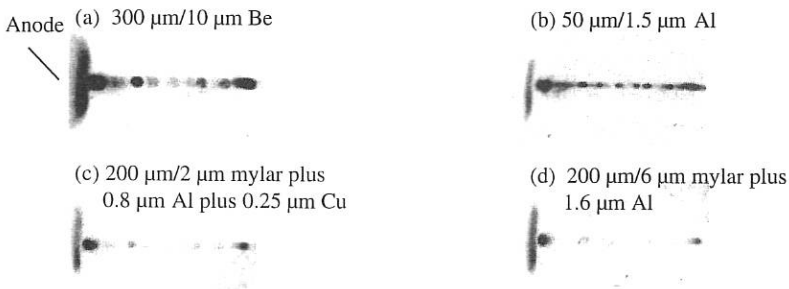


Figure 2. A set of time integrated x-ray pinhole photographs. Pinhole diameters and x-ray filters used to record the images are mentioned above each image.

Figure 3 shows an x-ray streak photograph. The x-ray bright spots appear at about 7 ns of the current start. The anode emission occurrs about 5 ns before the intense bright spots. These bright spots were seen to occur only when the anode emission was largest. These bright spots

were also observed to bifurcate and move axially with a velocity of 3×10^5 ms^{-1}. The duration of x-ray emission from the plasma was 20 ns. The x-ray emission from the anode was in the form of pulses each of duration 20 ns. X-ray pinhole images were streaked with several filters but good image were obtained with the filters which transmit the line radiation (characteristic and recombination).

The temporal and spectral information of the hard x-rays from the anode was obtained with the scintillator/photomultiplier setup. These give 4 kA electron beam > 50 keV at the start of current. Second electron beam which is associated with the plasma was detected by a filtered time integrated x-ray pinhole camera and uncollimated filtered PIN diodes. An electron beam of 16 keV and 20 kA was inferred from the x-ray emission from the anode using two filter method.

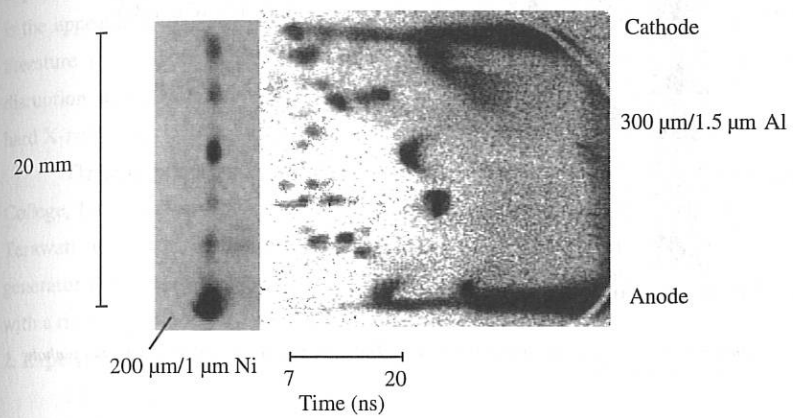


Figure 3. An x-ray streak photograph showing emission from the plasma and the electrodes simultaneously. The time integrated x-ray pinhole photograph is shown on the left.

3. The Simultaneous Observations

Figure 4 show simultaneous optical and x-ray observations of the pinch. The results are described below:-

(a) The bright spots do not occur simultaneously and they appear at different axial locations along the fibre.
(b) The optical and x-ray bright spots were coincident in time and space.
(c) The life time of the x-ray bright spots was shorter than 1 ns
(d) The x-ray bright spots bifurcated like optical bright spots and after bifurcation x-ray bright spot emitted less intense x-rays.

III. CONCLUSIONS

The two observations, i) optical emission begins at the cathode and propagates towards the anode, ii) there is a large high energy electron beam, clearly indicate that the breakdown is due to the electrons presumably produced by the field emission from the cathode. Some of these electrons impact the fibre closest to the cathode first producing secondary electrons and by this means the

Max-Planck-Institut für Plasmaphysik
- Bibliothek -

breakdown propagates along the fibre to the anode.

The rapid expansion is followed by the instability growth in form of bright spots. The supersonic axial motion of bright spots is attributed to $\mathbf{J}_r$ x **B** force in the constricted regions [9]. An electron beam of longer duration is observed 5 ns before the bright spots and these bright spots emit intense x-rays whenever there is electron beam suggesting that an electron beam plays an important role in the dynamics of the pinch.

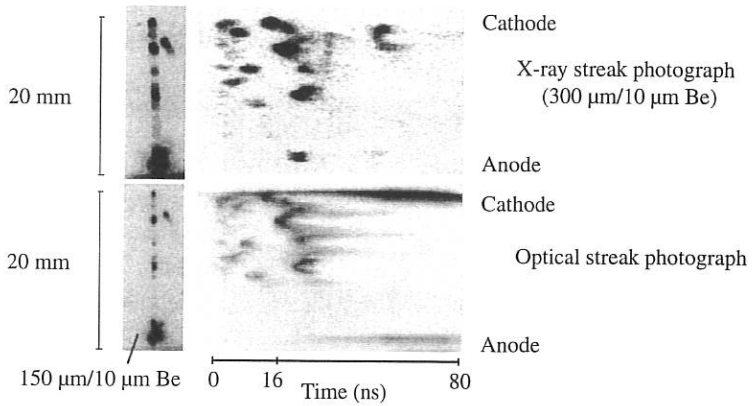


Figure 4. A simultaneous optical and x-ray streak photograph. The corresponding time integrated x-ray pinhole photographs are shown on the left.

References:

[1] Haines M. G. et al., In Plasma Physics and Controlled Nuclear Fusion Research, IAEA , pp 287 (1987).

[2] Shrearer J. W., Phys. Fluids **B19**, 1426 (1976).

[3] Pease R. S., Proc. Phys. Soc. Lon. Ser. **B70** (1957); Braginskii S. I., Sov. JETP **6**, 494 (1958).

[4] Sethian J. D. et al., Phys. Rev. Lett. **59**, 892 (1987); Sethian J. D et al., In Proceedings of alternative magnetic confinement schemes, Varena, Italy (1990).

[5] Hammel J., Scudder D. W., In Proceedings of the Fourteenth European Conference on Controlled Fusion and Plasma Physics, European Physical Society, Petit-Lancy, **pt 2**, pp. 450 (1987)

[6] Kies W. et al., J. Appl. Phys. **70**, 7261 (1991).

[7] Figura E. S., McCall G. H., Dangor A. E., Phys. Fluids **B3**, 2835 (1991).

[8] Niffikeer S.L., Beg F. N., Dangor A. E., Haines M. G. and McCall G. H., Proceedings of the Third International Conference on Dense Z-pinches **299** (edited by M. G. Haines and A. Knight), 495 (1993).

[9] Chittenden J. P. , Private Communication.

Mega Ampere Carbon Fibre Z-pinch Experiments

IH Mitchell, R Aliaga Rossel, JM Bayley, JP Chittenden, A Lorenz, M Tatarakis, K Wilson, AE Dangor and MG Haines

Imperial College of Science, Technology and Medicine,London SW7 2BZ, UK

1. Introduction

This paper investigates two particular phenomena common to dense Z-pinch experiments, the hot spots and the disruption. A feature observed in dense Z-pinch experiments is the appearance of highly localised, short lived, bright regions. These are referred to in the literature as hot spots, bright spots or micropinches. The second feature, referred to as the disruption generally occurs at late time. One of the signatures of the disruption is a pulse of hard X-rays which signifies de-coupling of the current from the plasma into electron beams.

The experiments described here were carried out on the MAGPIE generator at Imperial College, London using 25mm long, 33μm diameter carbon fibres as the load. MAGPIE is a Terawatt generator designed specifically for dense fibre Z-pinch experiments [1]. The generator was used at 60% of it's maximum charge resulting in a load current peaking at 1MA with a risetime of 150ns.

2. Experimental Results

2.1 Hot Spots

Optical streak photographs of the pinch axis have been discussed elsewhere [2]. The emission is seen to become non-uniform within the first few nanoseconds suggesting the presence of the m=0 instability. This early evolution of the m=0 instability is also seen in the nanosecond frames of the X-ray emission and as early as 5ns after the start of current. During the first 50ns of the current pulse, several groups of hot spots are seen to form. Shadowgrams from the laser diagnostics show that the m=0 instability is indeed present throughout the hot spot formation time. The actual formation of the hot spot is not resolved by the present diagnostics but the emission from the small dense regions is the dominant feature in both the X-ray and visible regimes at early times. Immediately after formation both emitting regions are seen to move axially with supersonic velocities of $3x10^5 ms^{-1}$. A typical X-ray streak of the early discharge can be seen in figure 1, taken with a 300μm diameter pinhole and a 10μm Be filter. The X-ray streak indicates that the lifetime of the hot spot is about two nanoseconds. It can be seen from the streak and also from time integrated X-ray pinhole pictures that the X-ray emission is dominated by the short lived hot spots. With 50μm diameter pinholes the image of

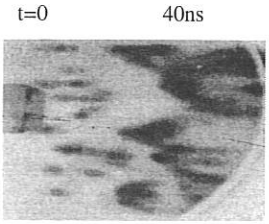


Figure 1: X-ray streak of Z-pinch axis showing formation of localised hot spots and consequent axial motion.

the hot spots are pinhole limited in the radial direction but can be longer in the axial direction due to the integration of the emission throughout the period of axial motion. The pinhole camera used produces six differently filtered images on Kodak DEF film. Using cross filtering techniques, and by assuming the radiation is recombination and bremmsstrahlung only with fully stripped carbon ions, the temperature of the hot spots have been measured as 250±50eV.

An estimation of the radiated power from a single hot spot has been obtained from the experimental data. Using the calibrations of DEF, the energy incident on the film of the time integrated pinhole camera can be calculated. By deconvolving the filter transmission, the hot spot spectrum can be obtained. An integration of the spectrum then leads to the radiated energy from the hot spot. Using 2ns as the hot spot lifetime, as shown by the X-ray streak photograph, a radiated power of 1MW per hot spot is obtained.

2.2 Hard X-ray Emission

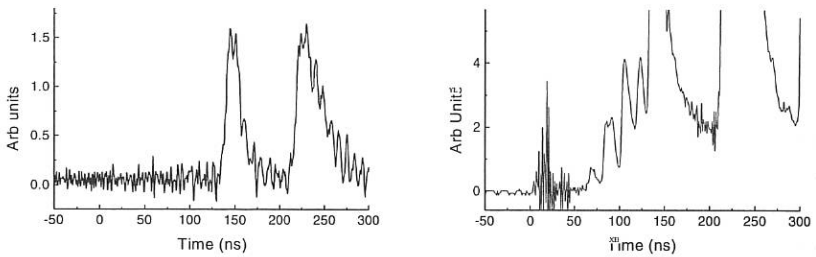


Figure 2: Hard X-ray emission during the discharge. a) Energy >100keV, b) Anode emission >10keV

The hard X-ray emission from a typical plasma shot is determined from the output of the scintillator hard X-ray detectors[3] and is shown shown in figure 2a). The detectors are situated outside the vacuum chamber and are filtered with 6mm stainless steel and several miliimetres of lead. Typically one or two hard X-ray pulses are seen between 150 and 250 ns into the current pulse. The energies of these X-rays have been measured by cross filtering

techniques and lie between 350 and 500keV. Such high energy X-rays can only feasibly be produced by electron beams striking the electrodes.

The X-ray emission from the anode is monitored using a collimated PIN diode filtered to look at energies from 10keV upwards. An output trace is shown in figure 2b). It can be seen that between 60 and 120ns, a series of short pulses of X-rays are emitted from the anode until at t=130ns, coincident with the first signal on the hard X-ray detectors, the diodes are saturated with a large X-ray flux. The PIN diode is again saturated when the second hard X-ray pulse is recorded. An optical streak photograph with the slit of the camera aligned with the pinch axis is shown in figure 3. The optical output from one of the hard X-ray scintillators is coupled to the streak camera and appears as the two short signals at the bottom of the signal. This gives accurate timing between the streak camera and the hard X-ray emission. It can be seen that at around 80ns, gaps start to appear in the axial emission. This is also around the time when the lower energy X-ray pulses are emitted from the anode. The large voltages likely to exist across these gaps will form E-beams which could be responsible for the anode emission. These gaps remain fairly constant as time progresses until at t=120ns the gap close to the anode is seen to widen more rapidly. One half of the gap is accelerated towards the anode at which time the first hard X-ray pulse is detected. After this the optical emission from the plasma is dramatically reduced and comes mainly from one axial location. Emission from the anode is also evident from this time onwards. The remaining bright region can then be seen to accelerate towards the anode. Again a hard X-ray pulse is observed coincident with the bright region striking the anode. After this second hard X-ray pulse, the remaining optical emission is dominated by that from the electrodes. Shadowgrams at late time show a single or a few islands of plasma, several millimetres in diameter, surrounded by tenuous plasma.

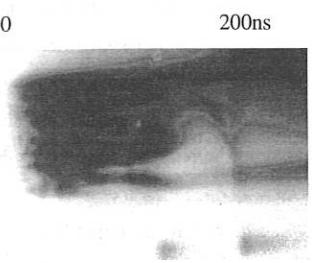


Figure 3: An optical streak of the pinch axis and, underneath, the output of the hard X-ray scintillator

3.Summary and Discussion

From the data obtained in these experiments, it is possible to estimate the density of the hot spots using the photon flux measured from the pinhole camera photograph. From the X-ray streak camera, it can be seen that the lifetime of the hot spot is of the order of 2ns, the

resolution of the streak. An upper limit on the volume of the hot spot, V_{hs}, can be obtained from the fact that the pinhole images are pinhole limited, implying that the hot spot is significantly less than 50μm in diameter. If we use the conservative assumptions that the lifetime is a few nanoseconds and the diameter is 25μm then the ion density required to generate the measured photon flux is ~10^{27} m^{-3}, approximately 1% of solid density. This is to be compared with densities of 10^{24} to $10^{25}m^{-3}$ measured in the corona using interferometry.

The current in the pinch at the time of hot spot formation is of the order of 100kA which gives a Bennet temperature of approximately 6eV, assuming a fully ionised pinch column. The hot spot temperature measured from the X-ray images is well above this value. This can be accounted for by considering the ion line density in the hot spot. Assuming the density and radius mentioned above, the line density in the hot spot is in fact reduced relative to that of the solid fibre. The axial motion observed on the streaks could be an indication of the ejection of the material from the central region as the m=0 neck forms. Both the aspects of axial motion and of a decrease in the line density in the neck of have been observed in recent 2D simulations of the m=0.[4].

The hard X-rays emitted during the discharge are found to come from the anode. Pulses of tens of keV are detected coincident with gaps in the optical emmission, forming along the axis. It is reasonable to assume that these gaps are regions of low plasma density which could be responsible for the production of runaway electrons. The interaction of these electrons with the plasma and the anode would be responsible for the hard X-ray emission. The X-ray pulses at late time have energies of several hundred kilovolts, greater than the anode-cathode voltage expected for a benign inductive load. This implies a large d(LI)/dt in the load. At these times the anode cathode gap is filled mainly by tenuous plasma with only a few islands of denser plasma. This may account for a dramatic drop in the load current and hence the generation of the high anode cathode voltage.

References

[1] I.H. Mitchell et al, "Proceedings of the 3rd International Conference on Dense Z-pinches", AIP Conf. Proc 299, Ed. M.G.Haines and A.Knight, 486, (1993)

[2] J.P. Chittenden et al, *Proc. 10th Int. Conf. on High Power Particle Beams, San-Diego, USA,* 756 (1994)

[3] P Choi and R Aliaga-Rossel, *Rev. Sci. Instrum.***65(9)** 3034 (1994)

[4] JP Chittenden to be published

OPTIMAL PLASMA PARAMETERS IN MIRROR BASED NEUTRON SOURCE FEF-II

K.Tohrisawa[1)], H.Yamaguchi[1)], T.Kawabe[1)], N.Mizuno[2)], S.Hirayama[3)]

1) Institute of Physics, University of Tsukuba, Tsukuba, Ibaraki, 305 Japan
2) Department of Physics. College of Humanities and Sciences. Nihon University, Sakurajousui, Setagaya-ku, Tokyo, 156 Japan
3) Department of Mechanical Engineering, Kanagawa Institute of Technology, Atsugi, Kanagawa, 243-02 Japan

1.Introduction

It has been recognized by the fusion community the importance and necessity of the neutron sources of the energy of 14MeV for the developments of the fusion reactor materials and also fusion nuclear engineering. We have been engaged in the conceptual design works on the mirror based neutron source, "FEF", since 1980[1]. We have completed this design study in 1990. and feasibility and issues have been published[2]. Recently, the emphasis of the research work on the neutron source is the early construction of the irradiation facility for the materials testing. For this purpose, we have started "FEF-II" project. FEF-II is two-component plasma system (target plasma and high energy fast ions), and has multi-pole field (Version 1) or RF plugged cusp (Version 2) for MHD stability. Configuration of magnetic field is formed basically by long solenoid with mirror field at both end. The fast ions are produced by oblique injection of NBI in mirror. These fast ions play important roles in two-component DT plasma. These fast ions produce intense neutron flux by fusion reaction between the fast ions and target plasma ions. We have developed the computer simulation code to study the behavior of the fast ions in the mirror confined target plasma. This code has been formed by combination of the Fokker-Planck code for the fast ions and the rate equations for the plasma parameters of the target plasma. In this way, we are able to obtain the optimal conditions for the plasma parameters both of the fast component and of the target plasma, as the intense 14MeV neutron source, which meet the requirements as the irradiation facility.

2.Simulation model

In the present simulation. we assume that the target plasma is isotropic and Maxwellian, and that mean free path of target ions for scattering into loss cone is larger than the mirror length. These two assumptions contradict each other. however, if the mirror ratio is large and the loss cone angle is small, then the results obtained in the present simulation. The velocity distribution of the fast ions is calculated by use of following Fokker-Planck equation:

$$\frac{\partial f}{\partial t} = \frac{1}{v^2}\frac{\partial}{\partial v}\left[v^2\left(Af + D_{/\!/}\frac{\partial f}{\partial v}\right)\right] + \frac{1}{v^2}D_{\perp}\frac{\partial}{\partial \zeta}\left[\left(1-\zeta^2\right)\frac{\partial f}{\partial \zeta}\right] - \frac{f}{\tau_{cx}} + S \qquad (1)$$

where f is the distribution function of the fast ions, S is the production term of the fast ions by NBI, τ_{cx} is the charge-exchange loss time, ζ is the cosine of the pitch angle. The Fokker-Planck coefficients A, $D_{/\!/}$, $D_{\perp}$ represent the slowing down, the energy diffusion and the pitch angle scattering, respectively[3]. the injected particles and ζ_0 is cosine of the injection angle. We set $1/2m_f(\Delta v)^2 = 1\text{keV}$ (m_f : mass of the fast ion), $\Delta\zeta = 0.01$, $\zeta_c = 0.82$ (cosine of the loss-cone angle).

We consider a model for the plasma including the temporal time variation of the parameters of the target plasma[4]. The particle and energy balance equations for target plasma are expressed as follows[5]:

particle balance

$$\left(\frac{dn_a}{dt}\right)_{loss} = -\frac{4}{\pi} Z_a \frac{n_a}{\tau_a} \frac{T_a}{e\phi} \frac{\exp\left(-\frac{e\phi}{T_a}\right)}{G(RZ_a)} I\left(\frac{T_a}{e\phi}\right) \tag{2}$$

energy balance(ion)

$$\frac{3}{2}\left(\frac{d(n_iT_i)}{dt}\right) = e\phi\left[\frac{1}{I(T_i/e\phi)} + \frac{3}{2}\frac{T_i}{e\phi}\right]\left(\frac{dn_i}{dt}\right)_{loss} + Q_{ie} + Q_{if} + Q_{sup} - Q_{cx} \tag{3}$$

energy balance(electron)

$$\frac{3}{2}\left(\frac{d(n_eT_e)}{dt}\right) = e\phi\left[\frac{1}{I(T_e/e\phi)} + \frac{3}{2}\frac{T_e}{e\phi}\right]\left(\frac{dn_e}{dt}\right)_{loss} \times \eta + Q_{ei} + Q_{ef} + Q_{sup} \tag{4}$$

where a is plasma species (ion, electron), ϕ is ambipolar potential, Z_a is 1/2 (ion), 1 (electron), R is mirror ratio, η is effective loss coefficient, Q_{ab} is energy flow from b-species to a-species, Q_{sup} and Q_{cx} represent energy flow by particle supply and charge-exchange, respectively. $I(x)$ and $G(x)$ are error functions.

In the calculation, we assume that the ion density of the target is kept constant by supplying particles. By using of Fokker-Planck equation and temporal varying model for the target plasma, the velocity distribution function of the fast ions was obtained. From this velocity distribution, axial distribution of the fast ions and the 14MeV neutron emission are deduced. The axial of neutron flux at the test section is obtained by using the neutron emission. In the simulation, we use the following parameters for initial value:

$T_{i0} = 15\text{keV}$ $T_{e0} = 300\text{eV}$ $E_{NBI} = 100\text{keV}$ $I_{NBI} = 100\text{A}$ $n_{e0} = n_{i0} = 4 \times 10^{14}\text{cm}^{-3}$

3.Results

When the density of fast ion become on steady state (~30msec), we obtained dependence of the neutron flux on various plasma parameters. As a result, dependencies of neutron flux on initial electron and target ion temperature were found to be small (see Fig.1,2). This due to the fact that electron temperature of steady state goes up to constant independent the initial temperature by heating from target ions, and similarly that

target ions are heated by fast ions. Furthermore we found that neutron flux is almost proportional to NBI trapped current (see Fig.3), and neutron flux strongly depend on NBI energy and on initial ions density of target plasma (see Fig.4,5). We have more detailed studies on these subject, and we found that there is a trade off between NBI energy and plasma density of the target plasma, for the fixed 14MeV neutron flux. We have studied for the following two cases for the neutron flux:

(a) $0.5MW/m^2$ (preliminary irradiation test)

(b) $2MW/m^2$ (main irradiation test)

The results are shown in Fig.6. From this figure, we are able to find the optimal conditions for the plasma parameters for each cases, The obtained parameters are listed in the Table 1. In the case(a), the plasma parameters are almost same as the ones obtained in the 2XIIB experiments in 1975. From this result, we may be able to say that the physics base for the mirror based neutron source for the preliminary irradiation testing is exist already. The physics base for the one for the main irradiation testing is also within our reach. This will be also confirmed from the operation of the neutron source for the preliminary irradiation testing.

4.Conclusion

To obtained the optimal conditions for the plasma parameters of the mirror based 14MeV neutron sources, the simulation code has been developed by combination of the Fokker-Planck code with the rate equations for the plasma parameters of the target plasma. Among the parametric dependence of the neutron flux on the plasma parameters, a trade off curves is obtained between the NBI energy and the density of the target plasma. By choosing a set of the plasma parameters, we found that physics base for the neutron source for the preliminary irradiation testing was quite realistic

References

[1] T.Kawabe, S.Hirayama, et al. : Fusion Technology, Nov./Dec. Vol.10, part 2B, (1986) 1102

[2] T.Kawabe and S.Hirayama : Proc. International School of Plasma Physics, Piero Caldirola, Physics of Alternative Magnetic Confinement Schemes, SIF, Bologna, (1991) 459-476

[3] N.Mizuno, H.Yamaguchi, T.Kawabe, A.A.Ivanov, Yu.A.Tsidulko and S.Hirayama : Proc. 20th EPS Conference on Controlled Fusion and Plasma Physics, (1993) II-549

[4] N.Mizuno, K.Tohrisawa, H.Yamaguchi, T.Kawabe, A.A.Ivanov and Yu.Tsidulko : Proc. 1994 International Conference on Plasma Physics, Vol.1 (1994) 193

[5] R.H.Cohen, M.E.Rensink, T.A.Cutler and A.A.Mirin : Nucl. Fusion 18 (1978) 1229

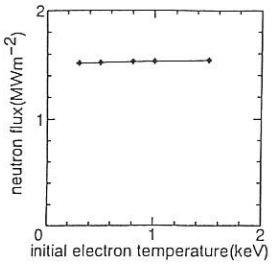


Fig.1 dependence on initial electron temperature

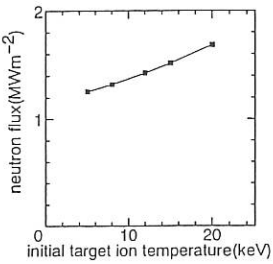


Fig.2 dependence on initial target ion temperature

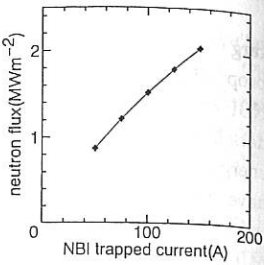


Fig.3 dependence on NBI trapped current

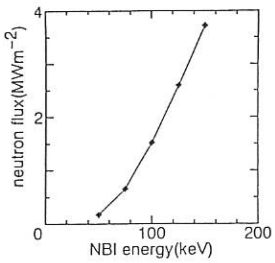


Fig.4 dependence on NBI energy

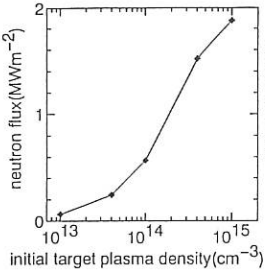


Fig.5 dependence on initial target plasma density

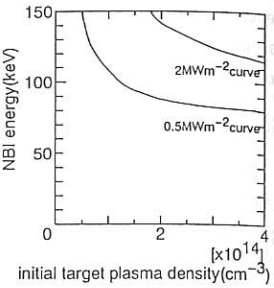


Fig.6 trade off curves

	0.5MWm^{-2}	2MWm^{-2}
initial electron temperature (keV)	0.3	0.3
initial target ion temperature (keV)	3	10
NBI trapped current (A)	80	100
NBI energy (keV)	120	150
initial target plasma density (cm^{-3})	6×10^{13}	1.8×10^{14}

table.1 optimal plasma parameters

Plasma Equilibrium in Gas-Dynamic Trap at Intense Injection of Neutral Beams

TD Akhmetov and **IA Kotelnikov**
Budker INP, Novosibirsk, 630090, Russian Federation

The injection of atomic beams into relatively cold target plasma may under certain circumstances affect the plasma equilibrium. The source of this effect is non-potential part of the force arising when neutral atoms (trapped by ionization and charge exchange) transfer their mechanical momentum to the plasma. This additional force $\boldsymbol{f}$ is very small in comparison with the pressure gradient. That is why it is usually neglected in the problem of plasma equilibrium though can play significant role in the problem of plasma stability as it has been known for a long time [1].

When the force is neglected, the effect of the neutral injection on the plasma equilibrium is reduced to slow reconstruction of magnetic surfaces in accordance with the balance between trapping of the atoms into the plasma and losses of the plasma. Such reconstruction takes approximately lifetime τ of plasma ions. For such time scales, stationary solution may not exist since the plasma tends to spread out in radial direction [2, 3]. However equilibrium still exists on a shorter time interval. In mirror confinement systems, equilibrium state is achieved in the time of order $\Gamma^{-1} \ll \tau$ with Γ the growth rate of flute perturbations. As it was shown in ref. [4], the additional force $\boldsymbol{f}$ considerably affects the shape of equilibrium magnetic surfaces if non-potential part $\boldsymbol{f}^t$ of the force is as small as p/R where p is the plasma pressure and R is the curvature radius of magnetic field line. Similar condition $f \gtrsim p/R$ (with the total additional force $\boldsymbol{f}$ instead of $\boldsymbol{f}^t$) assures that the effect of injection on flute stability prevails over the curvature effect [5].

If the magnetic field and the injection system were strictly axisymmetric (and, hence, the target plasma too) then the effect of the injection on the plasma equilibrium would be negligible since $\boldsymbol{f}^t = 0$. However a real injection system is not strictly axisymmetric since total symmetry formally requires infinite number of injector units to be installed.

Assuming the plasma velocity $\boldsymbol{v}$ to be zero, we start with the equation of ideal MHD

$$\frac{\partial}{\partial x_\beta}\left[p_\perp \delta_{\alpha\beta} + (p_\parallel - p_\perp)\tau_\alpha \tau_\beta\right] = \frac{1}{c}[\boldsymbol{j}, \boldsymbol{B}]_\alpha + f_\alpha$$

where the force $\boldsymbol{f}$ is calculated in [5, 4], and $\boldsymbol{\tau} = \boldsymbol{B}/B$. Applying a routine procedure described in [6] to the above equation we obtain

$$\int \frac{ds\,\kappa_n}{B^2}\frac{\partial}{\partial b}(p_\perp + p_\parallel) = -\int \frac{ds}{B^2}[\nabla, \boldsymbol{f}]_\tau \qquad (1)$$

where $\boldsymbol{\kappa} = \kappa_n \boldsymbol{n}$ is the curvature, the symbols n, b, and τ denote vector's components along the normal $\boldsymbol{n}$, binormal $\boldsymbol{b}$, and $\boldsymbol{\tau}$ respectively. The integration in (1) goes along a field line between two points (outside the central cell) where plasma density drops to a value, small enough for the plasma to be treated as detached from any conducting walls. According to the isorrhopicity hypothesis [7] $p_\perp$ and $p_\parallel$ are functions of the magnetic field B and of a magnetic flux ψ which is constant along magnetic field lines.

Arbitrary magnetic surface $\psi = \text{const}$ is comprehensively determined by its leading contour which is the intersection of the surface $\psi = \text{const}$ with a predefined surface $B = \text{const}$, e.g., with the midplane of the device (in the long-thin limit). Introducing the polar coordinates r_0, φ_0 in the midplane and using the Eq. (1) we can find the shape $r_0 = r_0(\varphi_0)$ of the leading contour for the equilibrium magnetic surface. In [4], leading contour is found analytically for the case where few injectors are equidistantly spaced over the azimuthal angle. Here we present the results of numerical simulation for the Gas-Dynamic Trap (GDT) [8].

To appreciate how large can the distortion of the magnetic surfaces be under the action of the neutral injection we estimate the force exerted on the plasma by single neutral beam. Typically, mirror system consists of a section of a uniform magnetic field of length L (where the injection is aimed to) and two mirror sections of length L_m; the radius a of the system is small as compared to L_m. We assume that the attenuation factor of the beam $\varkappa$ is optimal, i.e., comparable with the inverse plasma radius, $\varkappa \sim a^{-1}$. Since the beam width D, as a rule, is also about the plasma radius, the total number of hot ions produced in the plasma body per unit of time can be estimated just as the total equivalent current of the beam $\mathcal{I}_n$. Lifetime of fast ions is equal to the electron drag time τ_drag. Hence, the density n_h of fast ions can be estimated from the material balance relation $\mathcal{I}_n \sim a^2 L n_\mathrm{h}/\tau_\mathrm{drag}$. Then the force $f_n \sim \varkappa M v_n \mathcal{I}_n / D^2$ acting on the plasma from

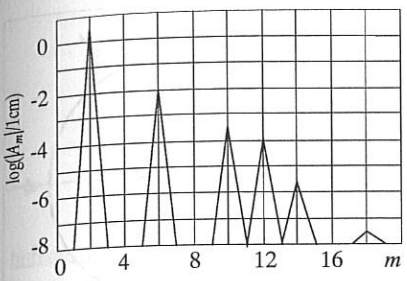


Fig. 1: GDT

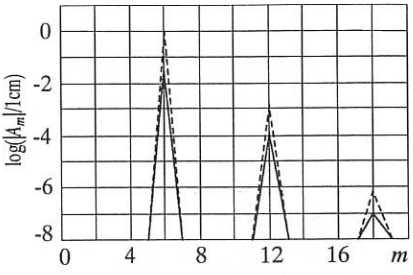


Fig. 2: 6 equidistant injectors

the side of single neutral beam can be expressed through the pressure $p_\mathrm{h} \sim M v_n^2 n_\mathrm{h}$ of the hot plasma component: $f_n \sim (L/L_\mathrm{inj})(p_\mathrm{h}/v_n \tau_\mathrm{drag})$. Bearing in mind that the curvature of a field line is of order of a/L_m^2, from Eq. (1) we evaluate the magnitude of radial distortion of the magnetic surface with mean radius (in the equatorial plane) $\langle r_0 \rangle = a$:

$$\frac{\Delta r}{a} \sim \frac{L L_\mathrm{m}}{v_n \tau_\mathrm{drag} a} \frac{p_\mathrm{h}}{p_\mathrm{c} + p_\mathrm{h}}.$$

Here p_c is the pressure of cold target plasma. For the following set of parameters $a = 10\mathrm{cm}$, $L = 2L_\mathrm{m} = 10^3\mathrm{cm}$, $v_n = 10^8\mathrm{cm/s}$, $\tau_\mathrm{drag} = 1\mathrm{msec}$, $p_\mathrm{h} \gg p_\mathrm{c}$ relevant to the Gas-Dynamic Trap (see [8]) the above estimation yields $\Delta r/a \sim 1$. Symmetrization of the atomic injection around plasma axes as the number of injectors is increased efficiently promotes reduction of the distortions.

When making numerical simulation, we assumed that the attenuation factor $\varkappa$ has diffuse profile, i.e., $\varkappa = \varkappa_0 \exp(-r^2/a^2)$. We also assumed diffuse profile for neutral beams. As a basic variant we adopted that $\varkappa_0 = 1/a$, $D = a = 8\mathrm{cm}$, injection energy $W_\mathrm{inj} = 20\mathrm{keV}$, density of target plasma $n = 5{\cdot}10^{13}\mathrm{cm}^{-3}$, temperature $T_e = T_i = 50\mathrm{eV}$ (the higher the temperature the smaller the distortions), equivalent injector's current $\mathcal{I}_n = 40\mathrm{A}$. GDT has 6 injectors by 3 units in two packages on opposite sides of the plasma column. In a package, the units are separated azimuthally by 30°. Using Eq. (1) we calculated the amplitude $A_m = \int_0^{2\pi} \frac{d\varphi}{2\pi} \frac{dr_0}{d\varphi} \mathrm{e}^{-im\varphi}$ of azimuthal harmonics in the equilibrium magnetic surface with the unperturbed radius $r_0 = 7\mathrm{cm}$. The results are shown on Fig. 1 (only integer values m have a sense). For comparison Fig. 2 shows these dependences for the case of 6 injectors, equidistantly spaced on azimuthal angle. Solid line corresponds to the above mentioned basic variant while dashed stands for $D = 5\mathrm{cm}$.

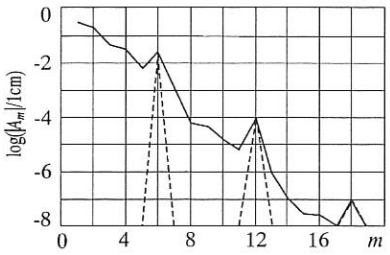


Fig. 3a

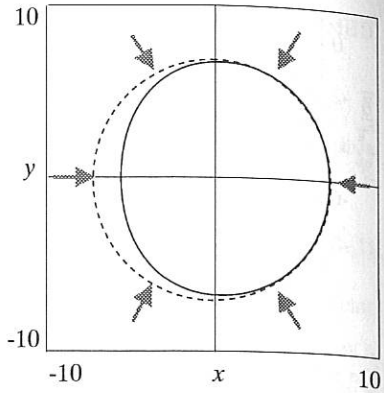


Fig. 3b

Magnetic surfaces in the system of 6 equidistant injectors: dashed lined—all units are switched on, solid line—1 unit produces current reduced by 20%.

Figs. 3 and 4 demonstrate that distortions of magnetic surfaces drastically increase if one of the injectors does not properly operate.

References

[1] Ryutov D D, *Proc. of the 1983 Varenna School on Mirror-Based and Field-Reversed Approaches to Fusion. CEC, Brussels* **16** 173 (1984).

[2] Woo J T, *Nucl. Fusion*, **17(6)** 1373 (1977)

[3] Mirnov V V, *In: Theory of Fusion Plasmas 1988, Proc. of the Joint Varenna-Lausanne Int. Workshop (Chexbres, Switzerland)* 41 (Editrice Compositori, Bologna, 1989)

[4] Kotelnikov I A, *Report BudkerINP 95-33* (Novosibirsk, Russian Federation, 1995)

[5] Kotelnikov I A et al. Sov. J. Plasma Physics 1990, Vol. 16(10), p. 669.

[6] Ryutov D D and Stupakov G V, *In: Reviews of Plasma Physics* **13** (Consultant Bureau, New York, 1984)

[7] Newcomb W A, *J. Plasma Physics* **23(3)** 529 (1981)

[8] Ivanov A A et al, *Phys. Plasmas* **1(5)** 1529 (1994)

Applicability of the Rebut-Lallia-Watkins-Model used for ASDEX discharges

F. Woloch, G. Kamelander
Austrian Research Center Seibersdorf, Austria
O. Gruber
Max Planck Institut für Plasmaphysik, Garching

Introduction

For the JET-tokamak the scaling of the heat transport coefficient and the critical electron temperature gradient of the semiempirical transport model of Rebut-Lallia-Watkins seemed to describe a broad variety of discharge regimes. As proposed in [Ref. 1] prefactors for the smaller ASDEX have been searched for to fit the model to L-mode discharges. One Ohmic phase and five neutral beam injection heating phases have been studied. The power of the hydrogen beam ranged from 0.8 MW to 1.5 MW having distinct energies of 40, 20 and 13.3 keV.

The study presented was performed not with an enhanced transport-coefficient to represent sawtooth effects but the Kadomtsev model for sawtooth oscillations was added to the plasma transport code JETTO [Ref. 2]. The temperature and density profile development was followed through the oscillations in the plasma centre. To find the fast particle deposition profiles from the neutral beam injection the SINBAD code [Ref. 3] was provided and incorporated into the JETTO version. Using the formula of Stix [Ref. 4] the energy deposition was then obtained.

The resulting energy deposition profiles for electrons and ions compare well with predictions from the Monte Carlo calculations with FREYA. JETTO contains the FRANTIC [Ref. 5] package to deal with ionisation and recombination effects in cylindrical geometry.

The impurity isotopes carbon and iron were used in a fixed density ration of 10:1 in connection with measured Zeff-profiles to calculate the ion density distribution, whereas the the impurity radiation losses measured by bolometry are used as input.

The Rebut-Lallia-Watkins Model [Ref 6]

Following the idea of turbulence in hydrodynamics to occur above a threshold of the fluid flow speed this model postulates a critical electron temperature gradient. Above it the magnetic turbulence occurs and the anomalous heat transport coefficient of the model is used. Below it neoclassical values are applied. This hard onset of turbulence is alleviated by using a ramp between 20 % below and 20 % above the critical gradient. In any case even for the

---

This work has been supported by the federal Ministry of Science and Research and the Austrian Academy of Sciences as the project Energietransport in Tokamaks numbered GZ 77.825/2-II/5/93

Ohmic shots a region of full turbulence should occur. The particle diffusion coefficient is set proportional to the electron heat transport coefficient. A convective heat flux was added to the anomalous heat flux definition of the model to get the total heat flux.

To put the model to work five prefactors have to be defined

1) Creb, a prefactor for the anomalous contribution to the electron energy transport coefficient (a fixed value of 200 m^2/s was used as neoclassical part)
2) Ceqei, a prefactor for the anomalous contribution to the ion energy transport coefficient (the Chang and Hinton formula is used for the neoclassical part)
3) a prefactor for the critical electron temperature gradient
4) Alfp, a prefactor to find the hydrogen diffusion coefficient from the energy transport coefficient for electrons
5) Alfinw, a prefactor to define the particle pinch contribution to the particle flux (this contribution is assumed proportional to the plasma radius. The Ware pinch flux is also always included)

Selected procedure

The main plasma parameters of the discharges studied are summarized in the Table 1.

Table 1: Asdex Shots

Shot	Mode	ne($10^{13}/cm^3$)	Te (keV)	P_{NBI} (MW)	Zeff
17529	Ohmic	6.71	0.88	-	1.5
17529	L	6.27	1.52	1.35	1.3
31440	L	5.24	1.17	0.85	1.8
31433	L	3.98	1.40	1.02	2.4
32993	L	3.33	1.52	1.46	2.3
32987	L	2.71	1.68	1.36	3.2

For all but the two last shots the selected procedure gave results as shown in Table 2

Table 2: Resulting Prefactors

Shot	Creb	Ceqei	Alfp	Alfinw
Ohmi	0.06	0.9	0.17	0.2
17529	0.14	0.4	0.33	0.2
31440	0.18	0.5	0.09	0.6
31433	0.21	0.3	0.12	0.1

The Ohmic shot was used to fix the prefactor for the critical electron temperature since the lowest electron temperatures and gradients occur there. The value found was 0.3. It is interesting to note that this prefactor is 6 for the JET tokamak.

The general procedure selected was to start from the experimental profiles as initial distributions keeping watch that the particle replacement time be comparable to the energy confinement time; the necessary neutral flux accross the plasma surface was provided by the puffing rate. After an initial transient steady conditions of maximal and spatially averaged values of densities and temperatures for electrons and ions equal to the measured ones were searched for by varying the input transport prefactor. For the electric conductivity the neoclassical formula of Hirshman was used. The safety factors needed to initiate the reconnection in the plasma centre were near 0.96 to get the measured sawteeth oscillation period near 10 milliseconds. The running times for the transients were up to 0.2 seconds. The allowed error of the solution vector for the system of equations is between 3 and 5 %.

For the L-mode of shot 17529 some results are compared with experimental data in Fig. 1-4.

Results and Conclusions (see Table 2)

1) Besides the different critical temperature gradient also the prefactors to the anomalous electron energy transport coefficient have to be reduced compared with JET results and range between 0.1 und 0.2 for the L-mode discharges.
2) The prefactor for the anomalous ion heat transport is only half of the electron heat transport.
3) Particle diffusivities are well below heat diffusivities.
4) It cannot be excluded that a smoother onset of turbulence controlling the electron energy transport or other smoothing procedures as for instance used in ASTRA [Ref. 7] may lead to a smaller scatter of prefactors. No regression analysis was done so far.

References

[1] O. Gruber et al., Energy transport in ASDEX in Relation to Theoretical and Semiempirical Transport Coefficients, IPP 5/29, September 1989

[2] G. Cenacchi, A. Taroni, JETTO: A free boundary plasma transport code (basic version), JET-IR (88) 03

[3] Y. Feng, Formulation and Application of the Neutral Particle Beam Deposition Code SINBAD, IPP III/190, January 1993

[4] T.H. Stix, Fast-Wave Heating of a two-component plasma, Nuclear Fusion 15, 7373, (1975)

[5] S. Tamor, SAI-Report 023-79-1056LJ

[6] D. Boucher, P.H. Rebut, JET-P (92) 23

[7] G.V. Pereverzev et al, ASTRA, An Automatic System for Transport Analysis in a Tokamak, IPP 5/42, August 1991

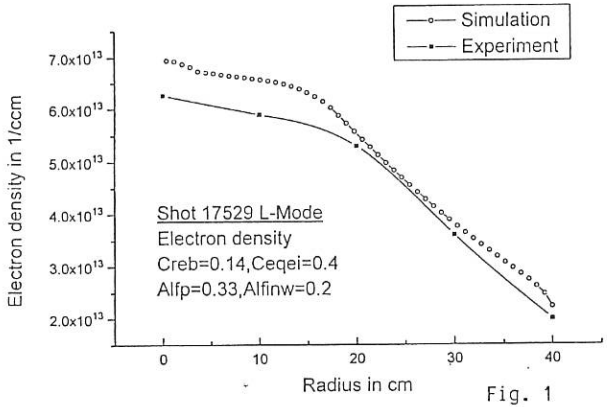


Fig. 1

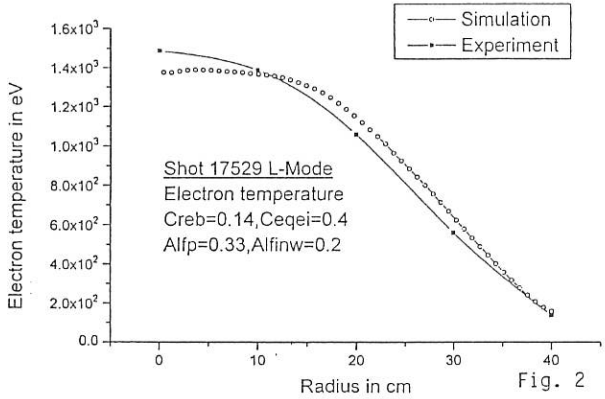


Fig. 2

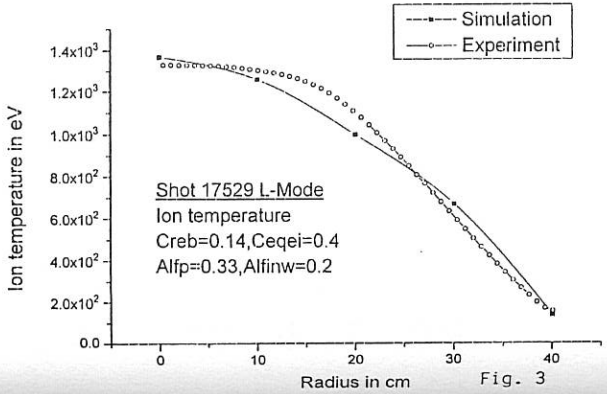


Fig. 3

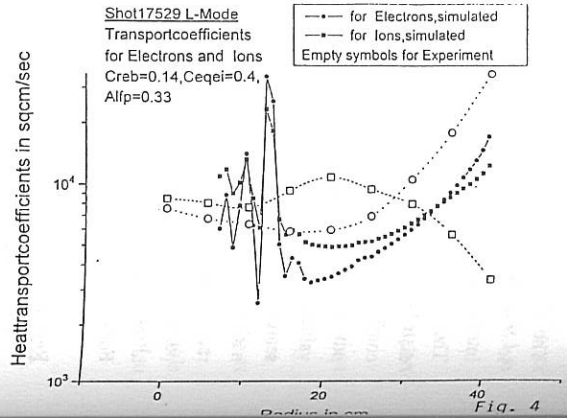


Fig. 4

Collisional Drift Fluids and Drift Waves

D. Pfirsch and D. Correa-Restrepo
Max-Planck-Institut für Plasmaphysik
EURATOM Association, D-85748 Garching, Germany

I. INTRODUCTION

Drift-wave turbulence is considered to be one of the possible causes of anomalous transport in a plasma. An exact theory describing these phenomena would be extremely complicated. It is therefore desirable to simplify the theoretical description. An attempt in this direction is the widely used theory of Hasegawa and Wakatani [1]. While the steps leading from a two-fluid theory to this approximate theory appear plausible to a certain extent, there may be problems, as can be illustrated by considering the relation interpreted as the time derivative of the energy. In dimensionless variables the Hasegawa-Wakatani equations, describing quasi-neutral two-fluid plasmas with massless electrons of constant temperature, cold ions, constant magnetic field in the z-direction, unperturbed density gradients in the x-direction and electrostatic perturbations, have the form $\partial_t\omega + \mathbf{v}\cdot\nabla\omega = (1/\nu)\nabla_\parallel^2(\delta n - \varphi)$, $\partial_t\delta n + \partial_y\varphi + \mathbf{v}\cdot\nabla\delta n = (1/\nu)\nabla_\parallel^2(\delta n - \varphi)$ with $\mathbf{v} = \hat{\mathbf{z}}\times\nabla\varphi$, $\omega = \nabla_\perp^2\varphi$. Here we have introduced a dimensionless collision frequency ν in order to indicate which terms relate to dissipation. The right hand sides of the first two equations result from Ohm's law for the parallel current density $j_\parallel = (1/\nu)\nabla_\parallel(\delta n - \varphi)$. These equations yield the relation $\frac{d}{dt}\int(1/2)\left((\nabla_\perp\varphi)^2 + (\delta n)^2\right)dV = -\int\delta n\partial_y\varphi dV - (1/\nu)\int\left(\nabla_\parallel(\delta n - \varphi)\right)^2 dV$. The second term on the RHS is ohmic dissipation. The first term on the RHS is nonzero for $\nu \neq 0$. It is the driving term for turbulence. Since it is proportional to the momentum of the plasma in the x-direction, it should be a constant of motion for the system considered, i.e. $\int\delta n\hat{\mathbf{z}}\times\nabla\varphi\ dV = const.$ If this vanishes initially, the above driving term would be zero for all times contrary to numerical solutions.

The main part of this paper presents a **derivation of collisional drift-fluid equations by a new method** allowing one to prove in a concise and consistent way **conservation laws, such as for energy and total angular momentum**, and obtain the **law for energy dissipation**. Energy conservation is of relevance to stability, in particular nonlinear instabilities relating to negative-energy perturbations [2, 3, 4]. Momentum conservation is of relevance to charge separation, generation of electric fields, and the L-H transition. The method consists of three steps:

1. Consideration of **single particle motion in drift approximation**; description in terms of Littlejohn's Lagrangian for particles in drift approximation [5] in the form given by Wimmel [6];
2. Obtaining, from the single particle Lagrangian, the **Lagrangian for (in particular quasi-neutral) dissipationless fluids in drift approximation with isotropic pressures**;
3. **Introduction of dissipative terms** such as resistivity, thermal forces, viscosity, heat conductivity and energy transfer between the different particle species.

Both **electrostatic** and **electromagnetic** perturbations are allowed. The **dissipative terms** are introduced by adding corresponding terms to the ideal equations of motion and of the pressures. **These equations, of course, no longer result from a Lagrangian via Hamilton's principle. Their relation to the ideal equations implies, however, also a relation to the ideal Lagrangian of which one can take advantage.** Instead of introducing heat conduction one can also prescribe $T(\mathbf{x}) = const$ or $\mathbf{B}\cdot\nabla T = 0$ initially and take the adiabatic coefficients $\gamma = 1$. This preserves then the initial property of $T(\mathbf{x})$ for all times. Assumptions of this kind are often made in the literature (Hasegawa et al.[1] and related papers). In this case the dissipated energy is not retained in the plasma as thermal energy, which means that the time derivative of the energy does not vanish and is negative.

The **variation of the Lagrangian**, when expressed in terms of **displacements, vanishes also for the nonideal equations**, if these displacements describe a **symmetry operation**, and leads to the correct **energy dissipation** for displacements discribing the time evolution of the system.

This **new method is not restricted** to the present kind of theories. It can equally well be applied to theories such as **multi-fluid theories without using the drift approximation**.

In order to be flexible in introducing **approximations** relating to the **masses without loosing the Lagrangian properties** we replace the masses by **mass tensors** which distinguish between masses for **motions parallel and perpendicular to the magnetic field**. This allows **different approximations for the parallel and perpendicular motions**.

II. LAGRANGIAN FOR FLUIDS IN DRIFT APPROXIMATION

Littlejohn's Lagrangian for particles in drift approximation [5] in the form given by Wimmel [6] is $L_p = (e/c)\dot{\mathbf{x}}\cdot\mathbf{A}^* - e\Phi^*$ with $\mathbf{A}^* = \mathbf{A} + (mc/e)(q_4\mathbf{b} + \mathbf{v}_E)$, $e\Phi^* = e\Phi + \mu B + \frac{m}{2}(q_4^2 + \mathbf{v}_E^2)$, $\mathbf{v}_E = c\frac{\mathbf{E}\times\mathbf{B}}{B^2}$, $\mathbf{E} = -\nabla\Phi - \frac{1}{c}\frac{\partial\mathbf{A}}{\partial t}$, $\mathbf{B} = \nabla\times\mathbf{A}$, $\mathbf{b} = \frac{\mathbf{B}}{B}$, μ = magnetic moment. q_4 is an additional variable to be varied indepently of $\mathbf{x}$. With indices for particle species suppressed, the following expression, as explained below, should be the **Lagrangian of a multi-fluid plasma in drift approximation**:

$L = \sum_{particle\ species}\int\left[n(\mathbf{x},t)\hat{L}_\mathrm{p} - \frac{p}{\gamma-1} - \frac{1}{8\pi N_s}\left[\mathbf{B}^2 - \mathbf{E}^2\right]\right]d^3x \equiv \sum\int\mathcal{L}\,d^3x$, N_s: number of species .

$n(\mathbf{x},t)$ is the density of "quasiparticles" , $\hat{L}_\mathrm{p} = \frac{e}{c}\mathbf{v}(\mathbf{x},t)\cdot\hat{\mathbf{A}} - e\hat{\Phi}$, $\mathbf{v}(\mathbf{x},t)$ the velocity of the quasiparticles, $\hat{\mathbf{A}} = \mathbf{A}^* = \mathbf{A} + \frac{c}{e}\underline{\underline{m}}\cdot(q_4(\mathbf{x},t)\mathbf{b} + \mathbf{v}_E)$, $e\hat{\Phi} = e\Phi^* - \mu B = e\Phi + \frac{1}{2}(m_\parallel q_4^2 + m_\perp\mathbf{v}_E^2)$, $\underline{\underline{m}} = m_\perp\underline{\underline{I}} + (m_\parallel - m_\perp)\mathbf{bb}$,

$I_{ik} = \delta_{ik}$. The isotropic pressure $p(\mathbf{x},t)$ replaces the adiabatically constant magnetic moment μ and the "thermal" part of the parallel particle energy. This form of the Lagrangian refers to adiabatic systems. Isothermal systems have a different pressure term, namely $-p\ln(p/p_c)$, with p_c an arbitrary reference pressure. When the **quasi-neutral approximation** is used, **no electric field energy term** $\mathbf{E}^2/8\pi$ appears in L.

The notion "quasiparticle" is introduced for entities which perform motions parallel to $\mathbf{B}$ with the velocity $v_\parallel(\mathbf{x},t)$, and perpendicular to $\mathbf{B}$ with the velocity $\mathbf{v}_\perp$ in the form of drift motions consisting of $\mathbf{E}\times\mathbf{B}$, polarization and centrifugal drifts, the usual additional drifts related to the variation of the direction of $\mathbf{B}$, and a diamagnetic drift. This is in contrast to guiding center motion as concerns the diamagnetic drift, which replaces the ∇B drift resulting from the Lorentz force.

Quantities to be varied are $n(\mathbf{x},t)$, $p(\mathbf{x},t)$, $\mathbf{v}(\mathbf{x},t)$, and in addition independently $q_4(\mathbf{x},t)$, $\Phi(\mathbf{x},t)$ and $\mathbf{A}(\mathbf{x},t)$.

III. VARIATION OF THE LAGRANGIAN

Since $\mathcal{L} = \mathcal{L}(q_4, n, p, \mathbf{v}, \Phi, \mathbf{A}, \mathbf{E}(\Phi,\mathbf{A}), \mathbf{B}(\mathbf{A}))$, the total variation $\delta\mathcal{L}$ of the Langrangian density $\mathcal{L}$ is given by $\delta\mathcal{L} = \delta q_4 \frac{\partial\mathcal{L}}{\partial q_4} + \delta n \frac{\partial\mathcal{L}}{\partial n} + \delta p \frac{\partial\mathcal{L}}{\partial p} + \delta\mathbf{v}\cdot\frac{\partial\mathcal{L}}{\partial\mathbf{v}} + \delta\Phi\frac{\partial\mathcal{L}}{\partial\Phi} + \delta\mathbf{A}\cdot\frac{\partial\mathcal{L}}{\partial\mathbf{A}} + \delta\mathbf{E}\cdot\frac{\partial\mathcal{L}}{\partial\mathbf{E}} + \delta\mathbf{B}\cdot\frac{\partial\mathcal{L}}{\partial\mathbf{B}}$. Here, all the variations are not completely arbitrary but have to fulfill the following constraints: $\delta n = -\nabla\cdot(n\zeta)$, $\delta p = -\zeta\cdot\nabla p - \gamma p\nabla\cdot\zeta$ (adiabatic systems), $\delta p = -\nabla\cdot(p\zeta)$, (isothermal systems), $\delta\mathbf{v} = \dot{\zeta} + (\mathbf{v}\cdot\nabla)\zeta - (\zeta\cdot\nabla)\mathbf{v}$, with ζ an arbitrary virtual displacement for each particle species and $\delta\mathbf{E} = -\nabla\delta\Phi - \frac{1}{c}\delta\dot{\mathbf{A}}$, $\delta\mathbf{B} = \nabla\times\delta\mathbf{A}$. For a prescribed magnetic field $\mathbf{B} = \mathbf{B}(\mathbf{x},t)$, i.e. electrostatic perturbations, one has $\delta\mathbf{A} = 0$. In this case, $\mathbf{A}(\mathbf{x},t)$ and related quantities entering $\mathcal{L}$ mean an explicit dependence of this quantity on $\mathbf{x}$ and t. Usually, there is no time dependence of the prescribed magnetic field, which then allows to have energy conservation. An $\mathbf{x}$-dependence will influence momentum or angular momentum conservation. In the following $\delta\mathbf{A}$ will be considered arbitrary. For given magnetic field, however, the Euler-Lagrange equation corresponding to $\delta\mathbf{A}$, which is Ampère's law, need not be satisfied.

Insertion of the constraints in $\delta\mathcal{L}$ results in the **basic relation**

$$\delta\mathcal{L} = \frac{\partial}{\partial t}\left\{\zeta\cdot\frac{\partial\mathcal{L}}{\partial\mathbf{v}} - \frac{1}{c}\delta\mathbf{A}\cdot\frac{\partial\mathcal{L}}{\partial\mathbf{E}}\right\} + \nabla\cdot\left\{-n\zeta\frac{\partial\mathcal{L}}{\partial n} - \gamma p\zeta\frac{\partial\mathcal{L}}{\partial p} + \left[\zeta\cdot\frac{\partial\mathcal{L}}{\partial\mathbf{v}}\right]\mathbf{v} - \delta\Phi\frac{\partial\mathcal{L}}{\partial\mathbf{E}} + \delta\mathbf{A}\times\frac{\partial\mathcal{L}}{\partial\mathbf{B}}\right\} + \delta q_4\frac{\partial\mathcal{L}}{\partial q_4} + \zeta\cdot$$
$$\left\{n\nabla\left[\frac{\partial\mathcal{L}}{\partial n}\right] + (\gamma-1)\frac{\partial\mathcal{L}}{\partial p}\nabla p + \gamma p\nabla\left[\frac{\partial\mathcal{L}}{\partial p}\right] + \mathbf{v}\times\left[\nabla\times\frac{\partial\mathcal{L}}{\partial\mathbf{v}}\right] - (\nabla\cdot\mathbf{v})\frac{\partial\mathcal{L}}{\partial\mathbf{v}} - \nabla\left[\mathbf{v}\cdot\frac{\partial\mathcal{L}}{\partial\mathbf{v}}\right] - \frac{\partial}{\partial t}\left[\frac{\partial\mathcal{L}}{\partial\mathbf{v}}\right]\right\}$$
$$+\delta\Phi\left\{\frac{\partial\mathcal{L}}{\partial\Phi} + \nabla\cdot\left[\frac{\partial\mathcal{L}}{\partial\mathbf{E}}\right]\right\} + \delta\mathbf{A}\cdot\left\{\frac{\partial\mathcal{L}}{\partial\mathbf{A}} + \frac{\partial}{\partial t}\left[\frac{1}{c}\frac{\partial\mathcal{L}}{\partial\mathbf{E}}\right] + \nabla\times\frac{\partial\mathcal{L}}{\partial\mathbf{B}}\right\}.$$

Hamilton's principle, $\delta\int_{t_0}^{t_1} L dt = 0$, yields the Euler-Lagrange equations, which result from the vanishing of the factors of δq_4 and ζ in $\delta\mathcal{L}$, and of $\delta\Phi$ and $\delta\mathbf{A}$ in $\delta\mathcal{L}_\Sigma = \sum\delta\mathcal{L}$. In the following, the **quasi-neutral approximation** is used. One obtains an **equation for the additional variable** q_4 of each species, $\frac{\partial\mathcal{L}}{\partial q_4} = 0$, the **equations of motion** $n\nabla\left[\frac{\partial\mathcal{L}}{\partial n}\right] + (\gamma-1)\frac{\partial\mathcal{L}}{\partial p}\nabla p + \gamma p\nabla\left[\frac{\partial\mathcal{L}}{\partial p}\right] + \mathbf{v}\times\left[\nabla\times\frac{\partial\mathcal{L}}{\partial\mathbf{v}}\right] - (\nabla\cdot\mathbf{v})\frac{\partial\mathcal{L}}{\partial\mathbf{v}} - \nabla\left[\mathbf{v}\cdot\frac{\partial\mathcal{L}}{\partial\mathbf{v}}\right] - \frac{\partial}{\partial t}\left[\frac{\partial\mathcal{L}}{\partial\mathbf{v}}\right] = 0$, the **quasi-neutrality condition** $\sum\left\{\frac{\partial\mathcal{L}}{\partial\Phi} + \nabla\cdot\frac{\partial\mathcal{L}}{\partial\mathbf{E}}\right\} = \frac{\partial\mathcal{L}_\Sigma}{\partial\Phi} + \nabla\cdot\frac{\partial\mathcal{L}_\Sigma}{\partial\mathbf{E}} = 0$ and **Ampère's law** $\sum\left\{c\frac{\partial\mathcal{L}}{\partial\mathbf{A}} + \frac{\partial}{\partial t}\left[\frac{\partial\mathcal{L}}{\partial\mathbf{E}}\right] + c\nabla\times\frac{\partial\mathcal{L}}{\partial\mathbf{B}}\right\} = c\frac{\partial\mathcal{L}_\Sigma}{\partial\mathbf{A}} + \frac{\partial}{\partial t}\left[\frac{\partial\mathcal{L}_\Sigma}{\partial\mathbf{E}}\right] + c\nabla\times\frac{\partial\mathcal{L}_\Sigma}{\partial\mathbf{B}} = 0$. When these relations are taken into account, one is left with

$$\delta\mathcal{L}_\Sigma = \sum\delta\mathcal{L} = \sum\left\{\frac{\partial}{\partial t}\left[\zeta\cdot\frac{\partial\mathcal{L}}{\partial\mathbf{v}} - \frac{1}{c}\delta\mathbf{A}\cdot\frac{\partial\mathcal{L}}{\partial\mathbf{E}}\right] + \nabla\cdot\left[-n\zeta\frac{\partial\mathcal{L}}{\partial n} - \gamma p\zeta\frac{\partial\mathcal{L}}{\partial p} + \left[\zeta\cdot\frac{\partial\mathcal{L}}{\partial\mathbf{v}}\right]\mathbf{v} - \delta\Phi\frac{\partial\mathcal{L}}{\partial\mathbf{E}} + \delta\mathbf{A}\times\frac{\partial\mathcal{L}}{\partial\mathbf{B}}\right]\right\},$$

valid for all ζ, $\delta\Phi$, $\delta\mathbf{A}$. Explicit equations are obtained when the explicit expressions for the derivatives are inserted. The relation for $\delta\mathcal{L}_\Sigma$ is used to obtain conservation laws. It is useful not only for conservative systems, but even when **dissipative effects** are introduced. For the **non-dissipative theory** the method is **Noether's** formalism.

IV. CONSERVATIVE SYSTEMS

The derivation of the **conservation laws for energy and momentum** are based, in the sense of **Noether's formalism**, on the total variations of the Lagrangian density $\delta\mathcal{L}_\Sigma$, a method which proves advantageous also when dissipative effects are introduced. The **local and global energy conservation laws** are obtained by considering $\delta\zeta$, $\delta\Phi$ and $\delta\mathbf{A}$ as resulting from the dynamic evolution of the system, and *not* as virtual displacements , i.e. $\zeta = \mathbf{v}\delta t$, $\delta\Phi = \dot{\Phi}\delta t$, $\delta\mathbf{A} = \dot{\mathbf{A}}\delta t$. Since $\delta\mathcal{L}_\Sigma$ represents the variation of $\mathcal{L}_\Sigma$ owing to the variations of $n(\mathbf{x},t)$, $p(\mathbf{x},t)$, etc..., it holds that $\delta\mathcal{L}_\Sigma = \delta t\frac{\partial\mathcal{L}_\Sigma}{\partial t}$, where the partial derivative is to be understood at constant $\mathbf{x}$. The equality of $\frac{\delta\mathcal{L}_\Sigma}{\delta t}$ and $\frac{\partial\mathcal{L}_\Sigma}{\partial t}$ is the **local energy conservation law**. If there are no contributions from the boundaries, space integration yields the following **global energy conservation law**

$$\frac{d\mathcal{E}}{dt} = 0 \quad , \quad \mathcal{E} = \int\left\{\sum\left[\frac{n}{2}\left(m_\parallel v_\parallel^2 + m_\perp\mathbf{v}_\perp^2 - m_\perp(\mathbf{v}_\perp - \mathbf{v}_E)^2\right) + \frac{p}{\gamma-1}\right] + \frac{1}{8\pi}\mathbf{B}^2\right\} d^3x \ .$$

This is the correct expression for the energy in **adiabatic systems**. In the case of **isothermal systems** the term $p/(\gamma-1)$ has to be replaced by $p\ln(p/p_c)$, with p_c an arbitrary constant.

Momentum conservation laws are derived by considering the change in $\mathcal{L}_\Sigma$ caused by a symmetry displacement of the whole system $\zeta = \zeta_s$, $\dot{\zeta}_s = 0$, $\nabla\cdot\zeta_s = 0$, with the corresponding changes $\delta\Phi = -\zeta_s\cdot\nabla\Phi$, $\delta\mathbf{A} = -\nabla[\zeta_s\cdot\mathbf{A}] + \zeta_s\times(\nabla\times\mathbf{A})$. Proceeding in a similar way as for the energy, one obtains the **local momentum conservation law**. The cases in which the magnetic field is considered

as given (electrostatic perturbations) and in which it is a dynamical quantity (electromagnetic perturbations) have to be treated separately. However, assuming vanishing density on the plasma surface, which is surrounded by a vacuum and superconducting coils of some symmetry (plane or axial), both cases yield the same **global momentum conservation law**

$$\frac{d}{dt}\int_{V_p(t)} d^3x \left\{\sum \zeta_s \cdot n \left[m_\parallel v_\parallel \mathbf{b} + m_\perp \mathbf{v}_\perp\right]\right\} = 0.$$

For plane symmetry (x-dependence only), $\zeta_s = const.\mathbf{e}_y$, $\zeta_s = const.\mathbf{e}_z$. For axial symmetry, $\zeta_s = const.Re_\varphi$.

V. DISSIPATIVE SYSTEMS

The starting point is again the basic relation for $\delta\mathcal{L}$. In this relation, the **dissipative equations** (dissipative equations of motion and time evolution $p\dot{\delta}t$) and the variations are inserted. The **conservation laws for local and global momentum remain unchanged by collisions**. As concerns the energy balance equations, adiabatic and isothermal systems have to be considered separately. While **the same total energy expression as in the ideal case** is conserved **in the adiabatic case**, the **global energy dissipation law of isothermal systems** is

$$\frac{d\mathcal{E}}{dt} = -\int \left[\mathbf{j}_\rho \cdot \underline{\underline{\eta}} \cdot \mathbf{j}_\rho + \sum \left(\mathbf{v} \cdot \underline{\underline{\Pi}} + \mathbf{v} \cdot \mathbf{R}_2\right)\right] d^3x \ ,$$

with $\mathcal{E}$ given above. Here $\mathbf{j}_\rho$ is the **v**-related quasi-particle current density $\mathbf{j}_\rho = \sum \rho \mathbf{v}$, with ρ the total charge density (including polarization charges). $\underline{\underline{\eta}}$ is the resistivity tensor, $\underline{\underline{\Pi}}$ is the stress tensor and $\mathbf{R}_2$ is the thermal friction. The dissipated energy has to be absorbed by the **heat reservoir** which is necessary to keep $dT/dt = 0$.

VI. CONSISTENCY PROBLEMS-COUPLING TO EXTERNAL CIRCUITS-STABILITY

The results obtained in the preceding sections are also valid for systems which are coupled to an external circuit, e.g. via an electric field driving the equilibrium current in a resistive plasma. As concerns the stability properties of such systems there is a problem that energy could be fed into the perturbations or removed from them by this coupling. In an isolated resistive plasma the driving electric field is generated by the decaying corresponding flux, which does not eliminate the problem. This means that the investigation of the stability properties of resistive plasmas must take into account these circumstances.

Another point concerns the electrostatic approximation. This approximation also implies coupling to an - artificial - external circuit: $\delta\mathbf{B} \equiv 0$ requires, strictly speaking, that at least the currents corresponding to the perturbations be compensated locally by currents flowing in an artificial medium. Since there are also electric fields with components parallel to these currents, the currents in the artificial medium must be driven against these fields, and this means that energy is fed into the plasma or removed from it. In order to find out whether this process could be relevant, let us look into some details of the nonlinear energy dissipation relation above. For small perturbations the r.h.s. of this equation is

$$-\int \left[\mathbf{j}_{\rho 0} \cdot \underline{\underline{\eta}} \cdot \mathbf{j}_{\rho 0} + 2\mathbf{j}_{\rho 1} \cdot \underline{\underline{\eta}} \cdot \mathbf{j}_{\rho 0} + 2\mathbf{j}_{\rho 2} \cdot \underline{\underline{\eta}} \cdot \mathbf{j}_{\rho 0} + \mathbf{j}_{\rho 1} \cdot \underline{\underline{\eta}} \cdot \mathbf{j}_{\rho 1} + \cdots\right] d^3x \ .$$

For discussion of the stability properties the second-order quantities are of interest. The term which is bilinear in the first-order perturbation $\mathbf{j}_{\rho 1}$ is negative, whereas the term linear in the second-order perturbation $\mathbf{j}_{\rho 2}$ is not. This latter term contributes, however, only if $\mathbf{j}_{\rho 2}$ possesses a nonvanishing average - say in a straight tokamak with $\mathbf{j}_{\rho 0} = const$ - parallel to $\mathbf{j}_{\rho 0}$. Since for such an average current there is a corresponding global perturbation of the magnetic field, the magnitude of this average current depends on boundary conditions determining the inductance of the system. In a straight tokamak with walls only at infinity the average of $\mathbf{j}_{\rho 2}$ must vanish and the second-order dissipative term is negative. If one neglected the magnetic field perturbation, the term with $\mathbf{j}_{\rho 2}$ could become an instability driving term overcompensating the damping term bilinear in $\mathbf{j}_{\rho 1}$.

A second point where neglect of the magnetic perturbation can lead to wrong results - independently of the strength of the unperturbed magnetic field - is in the energy expression itself: For an illustration let us assume, as often done, $m_e = 0$, $T_e = const$, $m_{i\parallel} = \infty$, $T_i = 0$, $\mathbf{E}_0 \propto \underline{\underline{\eta}}$. In this case the kinetic energy is the ion kinetic energy of the motion perpendicular to B only. Its zero-order contribution is proportional to $\underline{\underline{\eta}}^2$. The potential energy is the thermal energy of the electrons and the magnetic energy. Their second-order expressions in terms of displacements ξ_e for the electrons can be obtained with the help of one of the methods introduced by Pfirsch and Sudan [7]. The general expression for the second-order thermal energy of the electrons is therefore

$$W_e^{(2)} = \int \frac{T_e}{2}\left\{\frac{(\delta^{(1)}n_e)^2}{n_{e0}} + \xi_e\xi_e : n_{e0}\nabla\nabla \ln n_{e0}\right\} d^3x \ .$$

The second-order magnetic energy can easily be obtained for the limit $\underline{\underline{\eta}} \to 0$. In this case the magnetic field is frozen into the electrons. One can then again apply the method of Pfirsch and Sudan, which yields for the second-order magnetic energy

$$W_B^{(2)} = \int \left\{ \frac{1}{8\pi} \left(\delta^{(1)}\mathbf{B}\right)^2 + (\xi_e \cdot \nabla \xi_e) \cdot \nabla p + \frac{1}{c} (\xi_e \times \mathbf{j}) \cdot \delta^{(1)}\mathbf{B} \right\} d^3x \ .$$

It is important to note that this relation obtaines only when the equilibrium equations are satisfied exactly. The interesting point with this result is the term with ∇p. It is independent of the strength of the unperturbed magnetic field and combines directly with the thermal energy of the electrons. This "combined" thermal energy $W_c^{(2)}$ is

$$W_c^{(2)} = \int \frac{T_e}{2n_{e0}} \left\{ \left[n_{e0} \nabla \cdot \xi_e + \frac{1}{2} (\xi_e \cdot \nabla n_{e0}) \right]^2 - \frac{1}{4} (\xi_e \cdot \nabla n_{e0})^2 \right\} d^3x \ .$$

It is noteworthy that the term resulting from the magnetic field perturbation canceled the term with the second derivative of the density profile. Only first derivatives are left.

The total second-order potential energy is $W_c^{(2)} + \int \left\{ \frac{1}{8\pi} \left(\delta^{(1)}\mathbf{B}\right)^2 + \frac{1}{c} (\xi_e \times \mathbf{j}) \cdot \delta^{(1)}\mathbf{B} \right\} d^3x$. The residual magnetic terms with $\delta^{(1)}\mathrm{B}$ are the same ones as in ideal MHD, with ξ replaced by ξ_e. It is again emphasized that this relation for the potential energy is valid only for small resistivity.

For $\underline{\underline{\eta}} = 0$ the electrons behave "adiabatically" if in addition the effect of the the electric field corresponding to the magnetic field perturbation is neglected. This has the consequence that for modes one has $\xi_e \cdot \nabla n_{e0} = 0$ and the "thermal" term resulting from the magnetic perturbation does not enter. The kinetic energy is now directly of second order and the potential energy is positive semi-definite and in fact positive for drift waves for which $\delta^{(1)} n_e \not\equiv 0$. For $\underline{\underline{\eta}} \neq 0$ the electron displacements can possess components in the direction of the density gradient and therefore allow expansion with corresponding lowering of the thermal energy. The total second-order energy to become negative requires, however, a minimum resistivity. This would be necessary for instability if the average of $\mathrm{j}_{\rho 2}$ vanishes, a result which contradicts the Hasegawa-Wakatani theory.

VII. SUMMARY

Ideal and collisional drift-fluid theories were obtained starting with a Lagrangian for the drift motion of particles. The adiabatic invariant magnetic moment and the "thermal" parallel energy are incorporated in a pressure for which an adiabatic law combined with dissipative terms or an isothermal law can be prescribed. Resistivity and thermal forces can be added in a transparent way such that energy laws and conservation laws for momenta are immediately obtained. The final equations for quasi-neutral electrostatic perturbations are similar to those of, for instance, the Hasegawa-Wakatani theory and numerically tractable like these. Also electromagnetic perturbations are possible. The only restriction involved is the validity of the drift approximation. That the new theory avoids problems relating to conservation laws and boundary conditions is of importance in several respects: energy conservation for stability, in particular nonlinear instabilities relating to negative-energy perturbations. Momentum conservation is important in discussing the generation of radial electric fields, which are presently considered to be relevant for the L-H transition. Boundary conditions which do not introduce unclear "external" influences can be imposed only when treating a complete system without approximating unperturbed density profiles and density gradients as contants. The latter is dangerous also, because it can create artificial non-Hermitian parts of an in reality Hermitian operator. Although such a non-Hermitian part is possibly small compared with the correct Hermitian operator, it can lead to artificial instabilities.

References

[1] A. Hasegawa and M.Wakatani, Phys. Rev. Lett. 50, 682 (1983) and Phys. Fluids 27, 611 (1984).

[2] D. Pfirsch and D. Correa-Restrepo, Phys. Rev. E 47, 1947 (1993).

[3] J. Weiland and H. Wilhelmson, *Coherent Nonlinear Interaction of Waves in Plasmas* (Pergamon, New York, 1977).

[4] H. Nordman, V. P. Pavlenko and J. Weiland, Phys. Fluids B 5, 402 (1993).

[5] R. G. Littlejohn, J. Plasma Physics 29, 111 (1983).

[6] H. K. Wimmel, Z. Naturforsch. 38a, 601 (1983).

[7] D. Pfirsch and R. N. Sudan, Phys. Fluids B 5, 2052 (1993).

SIMULATION OF TRANSPORT IN THE IGNITED ITER WITH BROAD DENSITY PROFILES AND HIGH RADIATIVE FRACTION

G. BECKER
Max-Planck-Institut für Plasmaphysik,
Euratom-IPP Association, Garching
Germany

ABSTRACT. The confinement in ITER EDA is explored by special versions of the 1.5-D BALDUR predictive transport code applying empirical transport coefficients. The emphasis is on scenarios with flat density profiles and high radiative cooling in the main chamber due to argon and neon puffing. It is shown that self-sustained steady state thermonuclear burn is reached. The required radiation corrected energy confinement times are 4.1 s for argon and 3.5 s for neon, which are achievable according to the 1992 ITER ELMy H-mode scaling. Neon is superior due to its smaller radiative loss within the separatrix. In steady state, a helium fraction of 5 % is obtained. The concentrations of helium, argon and neon and the resulting fuel dilution are considerably lower than with peaked density profiles.

The purpose of this work is to study scenarios of the International Thermonuclear Experimental Reactor (ITER) |1| with flat density profiles and a high radiative power loss in the main chamber caused by argon and neon |2| and to compare the results with modellings for peaked density profiles |3|. The simulations are carried out with specially developed versions of the 1.5-D BALDUR predictive transport code which include a SOL model.

Transport Model

The computer experiments apply empirical relations for the electron and ion heat diffusivities χ_e and χ_i, the diffusion coefficient D and the inward drift velocity v_{in} in the confinement zone of ELMy H-mode plasmas |2|. Helium and the seeded impurities are treated by an impurity radiation model that solves rate equations for all ionization stages |4| and takes into account an impurity transport with the anomalous coefficients $D_I = D$ and $v_{in,I} = v_{in}$. The SOL model applies a Mach number for hydrogen M_{DT} of 0.02. For helium and the seeded impurities Mach numbers more than an order of magnitude smaller than M_{DT} are taken.

The simulations use feedback control of the neutral beam heating power as a fast burn control scheme with the fusion neutrons providing the sensor signal. An equilibrium moments code is applied which self-consistently computes 2-D fixed boundary equilibria with up-down symmetry. The calculations are performed until 400 s, where the profiles are found to be in steady state.

Results and Discussion

The parameters in the simulations of the EDA device are given in Table I. In the computations, the wall contour has a half-width in the midplane $a_w = 3.09$ m, an elongation $\kappa = 1.6$ and a triangularity $\delta = 0.3$. The computer experiments in the

argon and neon scenarios were conducted with a fixed radiative fraction $f_{rad,tot} = P_{rad,tot}/P_{\alpha} = 0.72$ corresponding to a total radiative power loss in the main chamber $P_{rad,tot} = 220$ MW. Prescription of the total heating then yields the same power exhaust to the divertor for both impurities.

TABLE I. Plasma parameters at 400 s in the simulations of ITER EDA with argon and neon radiation.

	argon	neon
$I_p\ (MA)$	24	24
$B_t\ (T)$	5.7	5.7
$R\ (m)$	8.1	8.1
$a\ (m)$	3.0	3.0
$< n_e >\ (10^{20}\ m^{-3})$	1.00	1.00
$< n_i >\ (10^{20}\ m^{-3})$	0.93	0.91
$< T_e >\ (keV)$	9.0	9.3
$< T_i >\ (keV)$	8.6	8.9
$W_{th}\ (MJ)$	872	894
$< \beta_t >\ (\%)$	2.3	2.4
$\tau_E\ (s)\ (required)$	4.1	3.5
$P_{\alpha}\ (MW)$	300	306
$P_{rad}(x_s)\ (MW)$	132	82
$P_{rad}(x_s)/P_{rad,tot}\ (\%)$	60	37
$N_{He}/N_e\ (\%)$	4.9	4.8
$N_{Ar}/N_e\ (\%)$	0.14	-
$N_{Ne}/N_e\ (\%)$	-	0.51
$Z_{eff}\ (0)$	1.54	1.57
$I_{bs}\ (MA)$	1.9	1.9

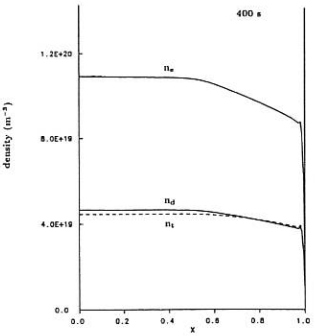


Fig. 1

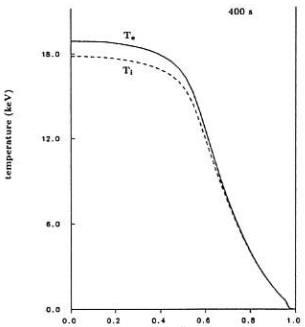


Fig. 2

Simulation of the neon scenario with broad density profiles

The modelling requires careful adjustments of the transport coefficients, neon influx rate, helium Mach number and $< n_e >$ value by computer experiments. The main results are presented in Table I and in Figs 1 to 8. A self-sustained steady state thermonuclear burn is achieved with $< T_i > = 8.9$ keV. Computed density and temperature profiles at 400 s are plotted in Figs 1 and 2. The x coordinate is the effective radius of a flux surface ρ normalised to the effective radius of the wall contour ρ_w and $x_s = \rho_s/\rho_w$ denotes the separatrix. The dilution of the fuel ion density is evident. At the separatrix (x_s=0.97), the electron density and temperature are found to be 8.7×10^{19} m^{-3} and 122 eV, respectively. Other results obtained at 400 s are the thermal energy content W_{th}, $< \beta_t >$ and the bootstrap current I_{bs}. In Figs 3 and 4, the required transport coefficients χ_e, χ_i, D and v_{in} are depicted.

The power balance is plotted in Figs 5 and 6. It is obvious from the P_{rad} contribution that a considerable radiative power is emitted from the confinement zone, primarily due to bremsstrahlung. But the radiative loss is clearly reduced in relation to the argon case especially when the edge is approached (see Table I). At the separatrix, the heating and loss powers are P_α = 306 MW, P_b = 35.3 MW, P_{OH} = 2.6 MW, P^e_{cond} = 146 MW, P^i_{cond} = 112 MW, P_{rad} = 81.6 MW and P_{cx} = 0.3 MW. The total radiative power loss is 219 MW, i.e. 37 % of $P_{rad,tot}$ is emitted from closed flux surfaces and 63% from the SOL. The resulting heat flux into the divertor is 118 MW. As the radiation profile of neon is more peripheral than that of argon, the requirements for the energy confinement time are somewhat reduced. After correction for P_{rad} (x_s), one obtains τ_E (x_s, 400 s) = 3.5 s which makes neon preferable to argon (see Fig. 7). Especially at high radiative fractions one has to pay a lower price for divertor heat load reduction by using neon instead of argon. The 1992 ITER ELMy H-mode scaling predicts $\tau_E^H \approx 4.1$ s and after correcting for the radiation 5.0 s. According to this scaling, the energy confinement time required in the neon scenario can be easily reached. Figure 8 shows the neon density profile at 400 s which is rather flat. The corresponding neon fraction and central Z_{eff} value are given in Table I. The helium density profile is clearly more peaked than the neon profile because of the central helium source due to DT fusion. The helium fraction is also given in Table I. In the present flat density scenarios, the concentrations of helium, argon and neon and the fuel dilution are much lower than with peaked density profiles |3|.

References

|1| ITER Outline Design Report, For the Fourth Meeting of the Technical Advisory Committee, San Diego, January 1994.

|2| Becker,G., 'Transport simulations of ITER with broad density profiles and high radiative fraction', to be published in Nuclear Fusion.

|3| Becker, G., Nucl. Fusion **35** (1995) 39.

|4| Lackner, K., et al., Z. Naturforsch., A: Phys. Sci. **37a** (1982) 931.

Figure Captions

Fig.1. Profiles of electron, deuteron and triton densities in the simulation of ITER EDA with neon radiation.

Fig.2. Profiles of electron and ion temperatures.

Fig.3. Profiles of electron and ion heat diffusivities and diffusion coefficient.

Fig.4. Profile of inward drift velocity.

Fig.5. Contributions of the cumulative heating powers to the total power balance.

Fig.6. Contributions of the cumulative loss powers to the total power balance.

Fig.7. Energy confinement time versus radiative fraction for the argon and neon cases.

Fig.8. Profiles of helium and neon densities.

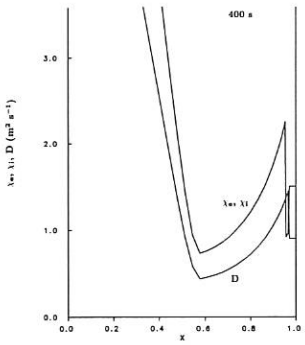


Fig. 3

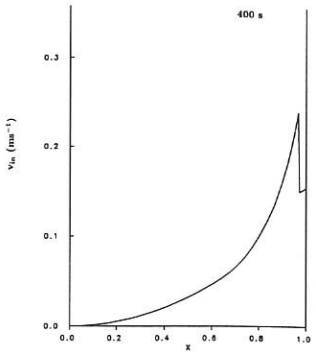


Fig. 4

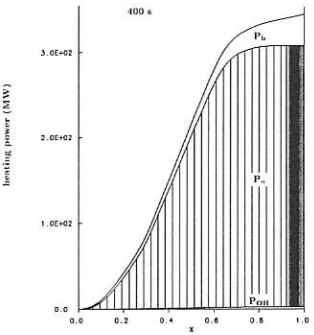


Fig. 5

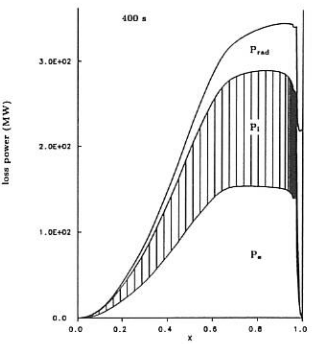


Fig. 6

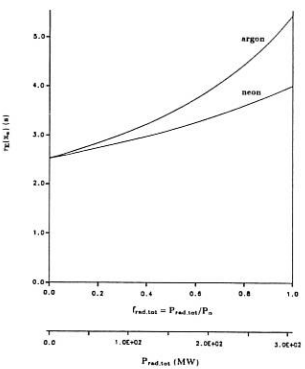


Fig. 7

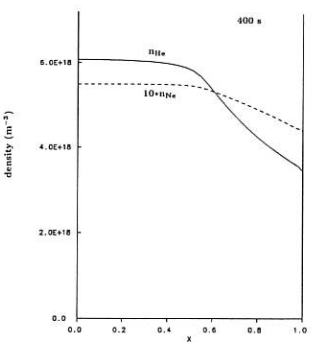


Fig. 8

RADIATIVE TRANSPORT VIA ELECTRON-BERNSTEIN WAVES

Satish Puri
Max-Planck-Institut für Plasmaphysik, EURATOM Association,
85748 Garching bei München, Germany

The importance of electron-Bernstein-wave induced radial electron thermal (as well as particle) transport in a tokamak plasma is examined. Since, instead of being concentrated near the local resonance, the cyclotron absorption/emission in a torus is spread over a wide region sorrounding the local resonance zone, transport via the electron-Bernstein waves could become significant in toroidal geometry.

1. INTRODUCTION

Electron thermal and particle transport processes across a magnetic field continue to be persistent enigmas. In Ref.[1], it was pointed out that the short-wavelength electron-Bernstein wave radiation can, under certain conditions, cause substantial thermal diffusivity in a magnetized plasma. In this paper the concept of Bernstein-wave induced diffusivity is extended to include toroidal effects.

Electrons in a magnetized plasma are profuse sources of synchrotron radiation. The collective effects in the plasma channel this radiation into fast (ordinary) cyclotron and slow (extraordinary) electrostatic cyclotron-harmonic (Bernstein) modes. Since the total radiated power scales as the k-space volume, radiation in a plasma is dominated by the small-wavelength (of the order of electron gyroradius) electron-Bernstein waves [1]. Using the Rayleigh-Jeans approximation of Planck's formula, Kirchhoff's law generalized to anisotropic media gives the total radiated power density as [1 – 3]

$$\eta_T = \frac{1}{(2\pi)^3} \int_{\mathbf{k}} \eta(\mathbf{k})\, d\mathbf{k} = \frac{2}{(2\pi)^3}\, T \int_{\mathbf{k}} \mathbf{k}_i(\mathbf{k}) \cdot \mathbf{v}_g(\mathbf{k})\, d\mathbf{k}\ , \tag{1}$$

where $\mathbf{k}$ is the propagation vector, $\mathbf{k}_i = \Im|\mathbf{k}|$ and $\mathbf{v}_g$ is the group velocity. The integration extends over all propagating waves that satisfy the dispersion relation

$$D(\omega, \mathbf{k}, \mathbf{r}) = 0\ . \tag{2}$$

In cylindrical geometry, the electron-Bernstein-wave radiation at the fundamental cyclotron-harmonic frequency is typically in excess of $1\,MW\,m^{-3}$. In Ref.[1], it was shown that for low temperatures, this emision gives rise to **electron thermal diffusivity $\chi \sim \mathcal{O}(0.5\,m^2 s^{-1})$, which greatly exceeds that due any other known classical mechanism**. The thermal diffusivity due to electron Bernstein waves decreases rapidly, however, for higher temperatures due to the decreasing k-space volume with increasing gyroradius. The normalized emissivity $\eta_\mathcal{E} = \eta_T/\mathcal{E}$, normalized with respect to the thermal energy density $\mathcal{E} = (3/2)nT$, as well as diffusivity χ found in Ref.[1] are reproduced in Figs.1 and 2, using the cylindrical-geometry value of ϵ in a tokamak with $R_0 = 3\,m$, $a = 1\,m$, $n_e = n_0(1-\rho^2)$, $T_e = T_0(1-\rho^2)$, $n_0 = 10^{21}\,m^{-3}$, $B_0 = 10\,T$.

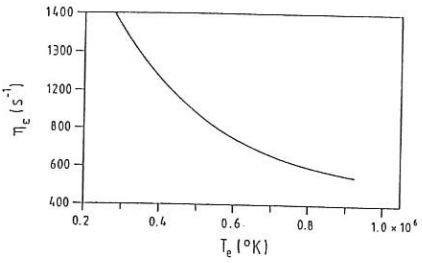


Fig.1
Normalized emissivity versus temperature

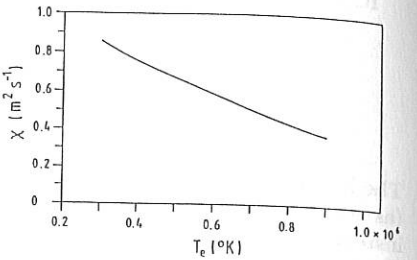


Fig.2
Diffusivity versus temperature

2. PARTICLE TRANSPORT

Absorption/emission of waves is inextricably bound with exchange of momentum between the particles and the waves. Thus an energy exchange ΔE would be accompanied by a significant momentum exchange $\Delta \mathbf{p} = (\mathbf{k}/\omega)\Delta E$ because of the large $\mathbf{k}$ associated with the small wavelength Bernstein modes. The parallel component of this momentum will directly contribute to the radial electron diffusivity.

3. TOROIDAL EFFECTS

The cylindrical geometry absorption/emission profile is related to the imaginary part of the plasma dispersion function $\Im[Z(\zeta)] \sim \exp(-\zeta^2)$. The width of the Gaussian equals $k_z v_t$ where $\zeta = (\omega - n\omega_c)/(k_z v_t)$. Although, the wave emission is strongest near the resonance $\omega = n\omega_c$, the contribution to the thermal transport is small because the emitted radiation is immediately absorbed before it can cover a significant radial distance. Further away from the resonance, the weaker emission is carried farther away and is the principal contributer to radiative transport. **Thus, for effective radiative transport one needs an extended region of weaker emission.**

An extended region of weaker emission is precisely the contribution of the toroidal geometry. In Ref.[4], it is shown how the fine splitting of the cylindrical-geometry resonance, as well as the interplay between the reactive and resistive effects in a torus combine to produce broad absorption/emission profiles.

Preliminary numerical results abtained by the method outlined in Ref.[4] for the plasma dielectric tensor component ϵ_{xx}^{tor} in a tokamak are given in Figs.3 and 4. The parameters used are $\omega R_0/\sqrt{2}v_t = 3300$, $n = 300$, and $h = 1$. Fig.3 shows that the imaginary part of ϵ_{xx}^{tor} is significantly broadened compared to its cylindrical geometry counterpart (computed for the local ζ value existing at the given ε and θ). Fig.4, which compares the imaginary parts of ϵ_{xx} in the toroidal and cylindrical geometries, shows that this broadening effect reflects a general trend. The horizontal axis in Fig.4 corresponds to $\omega/\omega_c(0)$, where $\omega_c(0)$ is the value of the cyclotron frequency at the plasma axis. It would appear that cyclotron waves absorption/emission originates from a large region sorrounding the resonance and is not sharply confined to a narrow Gaussian shape.

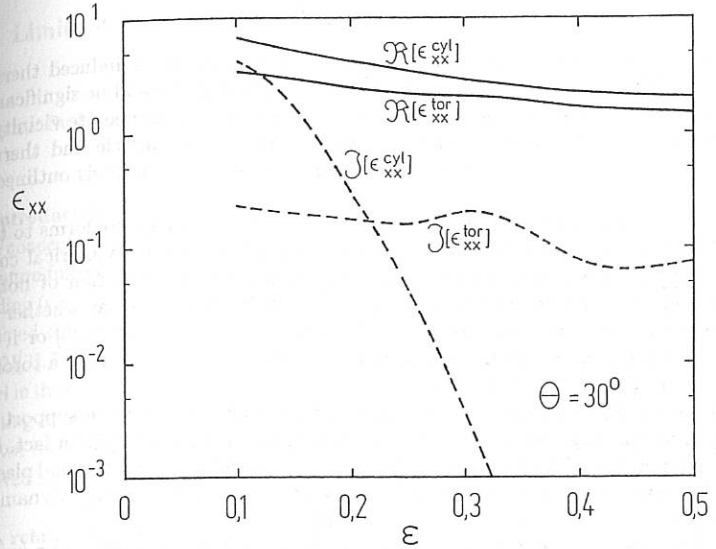


Fig.3 ϵ_{xx}^{tor} as a function of ε for $\theta = 30°$. ϵ_{xx}^{cyl} is estimated assuming the local ζ value.

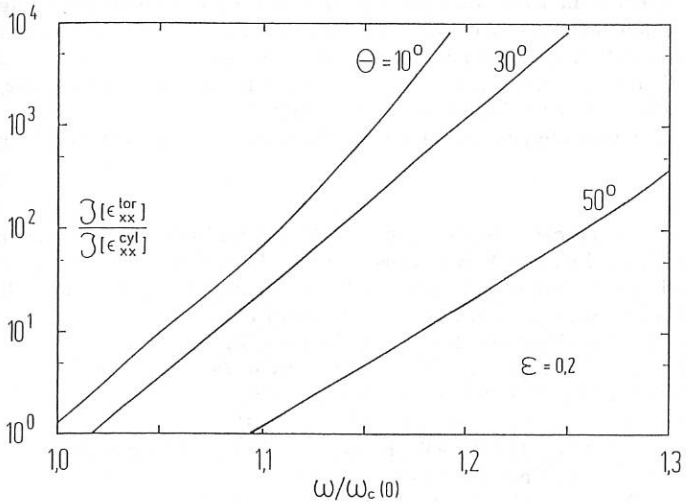


Fig.4 $\Im[\epsilon_{xx}^{tor}]/\Im[\epsilon_{xx}^{cyl}]$ versus $\omega/\omega_c(0)$ as a function of poloidal angle θ.

4. DISCUSSION

In this paper we have shown how the electron-Bernstein-wave induced thermal (and particle) diffusivity in a cylindrical geometry found in Ref.[1] could be significantly enhanced due to the spreading of the resonance zone beyond the immediate vicinity of the cyclotron resonance. A quantitative determination of the particle and thermal diffusivities D and χ is being pursued using accurate ray-tracing methods outlined in [1].

From Fig.3 one observes that the real part of ϵ_{xx}^{tor} substantially conforms to that of ϵ_{xx}^{cyl}. The imaginary part, however, departs significantly from its cylindrical counterpart. $\Im[\epsilon_{xx}^{tor}]$ exhibits a somewhat undulatory behaviour as a function of both ε and θ; however, these preliminary results are not conclusive enough to say whether the undulatory behaviour arises from the *echo like* phenomenon described in [5] or if the spreading of the absorption profile can indeed be approximated by asuming a toroidal modification of k_z in the manner of [6].

Still, it should be stressed that the present results do not appear to support the possibility of alternating absorption and emission regions as implied in [7]. In fact, it is difficult to see how negative absorption could ever occur in a Maxwellian, thermal plasma which could make a ray traversing through it grow instead of decay. Thermodynamical arguments should suffice to rule out such a possibility.

Further extensive computaitons are currently undertaken to enlarge our understanding of ϵ^{tor} and thereby extract acceptable approximations for ray-tracing studies.

We have employed the Grishanov-Nekrasov [8] derivation of the toroidal dielectric tensor in preference to more general and powerful approaches [9 – 11] because of its relative simplicity and transparency.

Some of the provocative features of electron-Bernstein-wave radiative transport pertinent to an understanding of toroidal transport include:

1. Since the ion emissivity is at least m/M times smaller than the electron emissivity, only electron and electron-thermal transport are modified.
2. Both D and χ would rapidly increase towards the plasma edge because of the increased emissivity at the higher values of $k \sim \mathcal{O}(r_c^{-1})$.
3. D and χ are intimately related because of the close connection between E and $\mathbf{p}$.

[1] PURI, S., Europhysics Topical Conference Report on Radiofrequency Heating and Current Drive of Fusion Devices, Brussels **14B** (1990) 1770.
[2] BEKEFI, G., in *Radiation Processes in Plasmas*, John Wesley, New York (1966).
[3] BORNATICI, M., et al., Nuclear Fusion **9** (1983) 1153.
[4] PURI, S., Plasma Dielectric Tensor in a Tokamak (this conference).
[5] FAULCONER, D. W., Plasma Phys. Contr. Fusion **29** (1987) 433.
[6] BRAMBILLA, M., Phys. Letters **A188** (1994) 376.
[7] SMITHE, D., et al., Phys. Rev. Lett. **60** (1988) 801.
[8] GRISHANOV, N. I., NEKRASOV, F. M., Fiz. Plasmy **16** (1990) 230.
[9] KAUFMAN, A. N., Phys. Rev. Lett. **15** (1972) 1063.
[10] GAMBIER, D. J., SAMAIN, A., Nuclear Fusion **25** (1985) 283.
[11] LAMALLE, P. U., Phys. Lett. **A175** (1993) 45.

Limits of Radiative Edge Cooling by Impurities in a Fusion Reactor

U. Samm, M.Z. Tokar', B. Unterberg
Institut für Plasmaphysik, Forschungszentrum Jülich GmbH, Association KFA-EURATOM
D-52425 Jülich, Germany

1. Introduction

The concept of a cold radiative plasma edge might be a solution for the power exhaust problem of future fusion devices like ITER. In previous experiments it has been shown that by impurity seeding (e.g. neon) about 90% of the total power (on a high power level, quasi-stationary) can be radiated from the plasma boundary without loosing the good energy confinement properties [1][2][3]. However, in a fusion reactor a burning plasma can only be maintained if the impurity level in the centre is sufficiently low. In this respect the injected impurities necessary for radiation cooling as well as the unavoidable helium ash have to be considered. In this paper it will be shown how the maximum radiation level is linked to the maximum impurity concentration derived from the conditions for a stationary burning plasma.

2. A relation for the maximum radiation

For the purpose of this paper a simple expression for the radiation level $\gamma=P_{rad}/P_{heat}$ is formulated using a parametrization for helium exhaust, impurity confinement and the radiation characteristics. He-exhaust can be described by the effective confinement time τ^*_{He}, which is determined by the particle confinement time τ_{He} and the recycling coefficient R according to $\tau^*_{He}=\tau_{He}/(1-R)$. The helium density in the plasma core for steady state is given by the product of the deuterium/tritium densities, the fusion rate coefficient and the effective confinement time as $n_{He} = n_D\, n_T <\sigma v>_{fus} \tau^*_{He}$. The concentration $c_{DT} = n_{DT}/n_e$ of deuterium/tritium is then $c_{DT} = 1 - 2c_{He} - Zc_i$, where Z is the charge number of the radiating impurity and c_{He} and c_i are the helium and impurity concentrations respectively.

Impurity transport is parametrized by the particle confinement time τ_i. Together with the radiation potential E_{rad} [1] the radiated power can be linked to the total impurity flux via $P_{rad}=E_{rad}\, N_i/\tau_i$. N_i is the total impurity content, which we also can write as $N_i=n_i\, V_i$ by introducing an effective volume V_i over which the impurities are distributed (normally the whole plasma volume). Many experimental data on the radiation potential of various impurities (mainly low Z) [4] and corresponding model calculations performed with the code RITM [5] are available. In steady state the total heating power is given via the energy confinement time τ_E by $P_{heat}=E/\tau_E$. The effective volume V_E to calculate the energy content $E = V_E\, 3\, n_e T\, \eta$ is normally significantly smaller then V_i (factor 2-4). Here $\eta = 1 - ½c_{He} - ½(Z-1)c_i$ represents a dilution factor due to the impurities and T is the central plasma temperature.

The solutions for ignition are found similar to the calculations in a previous paper [6], where the ratio $\rho^*_{He} = \tau^*_{He}/\tau_E$ has been identified as a crucial parameter. The acceptable level of impurities increases with decreasing ρ^*_{He}. In this paper a further constraint is added to the calculations by using a fixed $n_e\tau_E T$ value with the consequence that T is not anymore a free parameter. Assuming

$n_e\tau_E T=10^{22}$keVs/m^3 - a reasonable value expected for ITER - we obtain the maximum impurity level $c_{i,max}$ for a burning plasma as a function of ρ^*_{He} as shown in fig.1. It is evident from this figure that $c_{i,max}$ decreases with increasing Z. Furthermore, we can derive a scaling for the range of Z and ρ^*_{He} ≈5-10 finding $c_{i,max} \sim Z^{-\alpha}$, where $\alpha \approx -2.3$. Note that $c_{i,max}$ changes only moderately with small variations of the fusion triple product according to $\sim(n_e\tau_E T)^{0.4}$. These results will now serve as a basis for calculating the maximum radiation level possible with $c_{i,max}$. The radiation level is given by

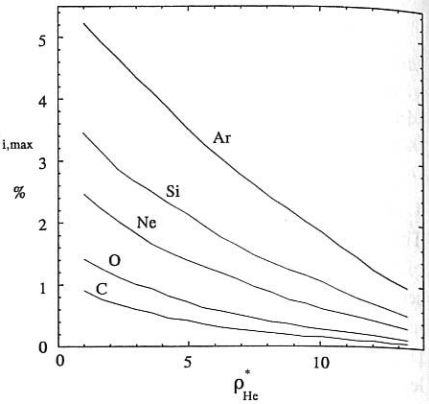


Figure 1 *Maximum impurity concentration (normalized to electron density as a function of the helium exhaust parameter* $\rho^*_{He}=\tau_{He}/\tau_E$ *for* $n_e\tau_E T_e=10^{22}$*keVs/m*^{3}

$$\gamma = \frac{P_{rad}}{P_{heat}} = \frac{E_{rad} n_i V_i/\tau_i}{3 n_e T \eta V_E/\tau_E} \quad , \quad (1)$$

or with $\rho_i = \tau_i / \tau_E$ and $c_i = n_i / n_e$

$$\gamma = \frac{E_{rad}}{3T\eta} \frac{c_i(\rho^*_{He})}{\rho_i} \frac{V_i}{V_E} \quad (2)$$

This relation describes the link between atomic physics, energy transport, He-exhaust, and impurity transport. The quality of predictions obtained from this equation depends of course on the quality of the input data. These may be obtained by model calculations or from experimental data.

3. Applications, predictions and scalings

We will apply equation 2 first to the experimental conditions found on TEXTOR for the case of 90% radiation (about 3 MW) by neon-feedback [7]. The typical figures are E_{rad}=30 keV, T_e=1 keV, ρ_i=0.2 and V_i/V_E=2. For c_i we use the impurity concentration of neon measured in the centre (≈1%). With η=1 we obtain $\gamma \approx$ 1, thus a high radiation level, indeed consistent with the experimental findings.

For the application to ITER conditions we have to extrapolate some parameters. For ρ^*_{He}=5 a maximum neon concentration of c_i=1.5% is obtained (fig.1). This implies a dilution factor of η=0.7. The central temperature will be T=15 keV and the profile factor is assumed to be also V_i/V_E=2. With respect to TEXTOR we expect an increase of τ_E by at least a factor of 60. Taking into account geometry effects (V/O) and higher plasma edge densities we estimate that τ_i will increase by a factor of 1.5-8. Using the more pessimistic figure (larger τ_i) we obtain ρ_i=0.03. With the same E_{rad} for neon as in TEXTOR equation 2 then gives $\gamma \approx$ 1, thus a cold radiative edge with a burning plasma in ITER would be possible. This result is critical in view of the

uncertainties: a) The variation of ρ^*_{He} is one of the crucial parameters. If we double the value to ρ^*_{He}=10 then the maximum neon density and proportional to it also the radiation level drop to 0.45 % of their previous values. b) τ_i is mainly determined by edge parameters, whereas τ_E is dominated by bulk properties giving rise to significant uncertainties for the $\rho^*_{He,i}$ scaling. c) Using the same radiation potential E_{rad} for ITER and TEXTOR is only justified if the edge temperature at the separatrix $T_e(a)$ lies below a certain value. According to our model calculations for neon we conclude that this assumption is valid for $T_e(a) \lesssim 150$ eV; i.e. a value close to half the ionization energy of the Li-like ion. In case of higher $T_e(a)$ values E_{rad} drops significantly. This problem can be overcome by choosing an element with higher Z (e.g. Si: $T_e(a) \lesssim 300$ eV or Ar: $T_e(a) \lesssim 600$ eV). However, $T_e(a)$ is not a free parameter. It depends largely on the radiation level itself. Thus a self-consistent treatment of the problem is required (see RITM code [5][8]).

For more accurate predictions about γ much more effort is needed for calculating the parameters discussed above. Nevertheless, the estimates presented can be helpful to make a guess at the feasibility of a cold radiative edge. Equation 2 may also serve as a tool to derive some *scalings* which may be useful for a further optimization. For this purpose we apply a simple particle transport model. This has to be seen in contrast to a complicated full transport modelling in other papers (e.g.[9]). Already such a simple model gives in a good approximation some valuable scalings. Particle transport is described only by diffusion. The particle source is determined by the ionization length of the neutrals entering the plasma boundary. Inside the source free zone the impurity profile (summed over all charge states) is flat [10]. The particle confinement time is given by $\tau_i = (\lambda/D)\,(V/O)$, where V and O depict vessel volume and surface respectively and D is the diffusion coefficient . In this simple picture we can derive an expression for the total radiation per particle by integrating over the radiation from the different ionization shells z of impurities, the width of which is given by $\sqrt{D\,\tau}$, where τ is the ionization time. The radiation potential then becomes [11]

$$E_{rad} = \frac{\lambda}{\sqrt{D}}\,S \qquad \textit{with} \qquad S = \sum_z \xi_z \sqrt{n_e^z}\,\frac{L_z(T_e)}{\sqrt{\langle\sigma v\rangle_i^z}} \quad . \tag{3}$$

The sum S over the different charge states z represents the atomic physics including the local values for the ionization rate coefficient $\langle\sigma v\rangle_i$, the radiation function $L(T_e)$ and the density n_e within the radiating shell. The factors ξ_z reflect the transport dominated ionization distribution. Following similar calculations for non-coronal radiation from low Z impurities [12] we may use the scaling $S \sim Z^3$. Inserting expression 3 into equation 2 and using $P_{rad} = E_{rad}\,\Gamma_i$ with $\Gamma_i = n_i\,V_i\,/\,\tau_i$ and $P_{heat}=3nT\eta V_E/\tau_E$ we obtain for the radiation level

$$\gamma = \sqrt{D}\;c_i\;S\;n_e\;/\;P_{surf} \quad . \tag{4}$$

P_{surf} is the power flow density onto the wall surface ($=P_{heat}/O$). The first three terms in this relation represent atomic physics and transport, whereas the last two ones are more depending on machine performance. For ITER a power flow density in the range of $P_{surf}\approx 0.3$ MW/m^2 is expected, which is not too far from those power flow densities available in present day machines (e.g. TEXTOR, ASDEX-U, JET: 0.14-0.19 MW/m^2). With the neon conditions used before the product $\sqrt{D}\;S$ has a value of about 1500 keVm/s . With an electron density of $n_e=10^{20}$m^{-3} and c_i=1.5% we obtain for

ITER again a value in the order of unity. But any deviation from the flat profiles of impurity densities towards peaking or accumulation in the centre would decrease the maximum γ. Nevertheless, further optimization is possible as is evident from equation 4. With the scalings we found for $c_{i,max}$ and S with respect to (low) Z we obtain the relation

$$\gamma \sim \sqrt{D}\ Z^{0.7}\ n_e / P_{surf} \quad . \tag{5}$$

Thus going to heavier impurities helps to improve the radiation level, but the improvement is rather weak and limited mainly to low Z impurities (Z≈6-18). The counter acting mechanisms of radiation losses and dilution effects in the centre make these improvements even weaker for medium Z and finally negligible for high Z species. It appears to be more important to choose the impurity species consistently with the T_e-range expected at the separatrix. Another improvement of radiation is obtained by increased transport (D) at the plasma boundary. An important example for such an improvement is given by the application of an ergodic magnetic field at the plasma boundary, with the consequence of getting more radiation with less impurities in the plasma [13].

4. Conclusions

A relation is found for the maximum radiation level possible in a burning fusion plasma. It describes the link between energy and particle transport, He-exhaust and line radiation from impurities at the plasma boundary based on an adequate parametrization. The relation provides useful scalings and allows predictions for the next step machines. A cold radiative plasma edge, e.g. in ITER, appears to be feasible, although significant uncertainties still exist. However, there seems to be enough margin to enhance the radiation level without further pollution of the plasma centre with impurites, e.g. by enhanced transport at the boundary (ergodic fields) , a higher Z than neon and operation at the highest $n_e \tau_E T$ possible.

references

[1] Samm U. et al. *Plasma Physics and Controlled Nuclear Fusion Research* **1** 309 (1992)
Samm U. et al., *Plasma Phys. and Control. Fusion* ***35*** *B167 (1993)*

[2] Messiaen A. et al., *Nucl. Fusion* ***34*** ***6*** *825 (1994)*

[3] Kallenbach A. et al., *15th Int. Conf. Plasma Phys. and Contr. Nucl. Fusion Research, Seville (1994)*

[4] Samm U. et al., *Journ. of Nucl. Mater.* ***220*** *25 (1995)*

[5] Tokar' M.Z., *Plasma Phys. and Contr. Fusion* ***36*** *1819 (1994)*

[6] Reiter D., Wolf G.H., Kever H. *Nucl. Fusion* ***30*** ***10*** *2141 (1990)*

[7] Samm U. et al., *Proc. 18th Europ. Conf. on Plasma Physics and Contr. Fusion, Berlin* ***3*** *157 (1991)*

[8] Tokar' M.Z. *this conference (invited paper)*

[9] Becker G., *Nucl. Fusion* ***35*** ***1*** *(1995)*

[10] Engelhardt W. and Feneberg W., *J. Nucl. Mater.* ***111-112*** *337 (1982)*

[11] Tokar M.Z., *Nucl. Fusion* ***34*** *853 (1994)*

[12] Cummings J. et al., *Journ. of Nucl. Mater.* ***176-177*** *916 (1990)*

[13] Grosman A. et al., *Journ. of Nucl. Mater.* ***220-222*** *188 (1995)*

Transport Modelling in Tight Aspect Ratio: Testing against START Ohmic Data and Predictions for MAST

J W Connor, G Counsell, M Gryaznevich, A R Polevoi[1], **C M Roach**, A Sykes, M J Walsh, H R Wilson
UKAEA Government Division, Fusion, Culham, Abingdon, Oxon, OX14 3DB, UK (UKAEA/Euratom Fusion Association)
(1) IV Kurchatov Institute, Moscow, Russia

Introduction

START's detailed and extensive tight aspect ratio (TAR) ohmic data [1] allows a test of transport models in a sparsely populated region of parameter space. Such tests provide confidence in extrapolations to both standard aspect ratio next step devices such as ITER, and to novel tight aspect ratio devices such as the proposed 1 MA spherical tokamak MAST.

Transport Modelling using ASTRA

ASTRA ('Automatic System for TRansport Analysis in a tokamak') [2], is an extremely powerful tool for self-consistent 1.5D transport simulations of tokamaks. It is based on a very fast moments solution of the Grad-Shafranov equation, including elliptical and triangular shaping of the poloidal cross section. Modification of transport coefficients is very simple for the user, and a library of auxiliary routines exists to study stability, neutral beam injection, and many other areas of tokamak physics.

We have chosen four theories of tokamak transport to test against START data: T11 [3] [4], Rebut-Lallia-Watkins [5] (RLW), Lackner-Gottardi as modified by Connor [6] [7] (LG), and Taroni [8] (Tar). All of these models prescribe heat transport, but particle transport is also prescribed by T11 and RLW. With the exception of the T11 model, density transport is neglected in all of our simulations.

Modelling Issues at Tight Aspect Ratio

Equilibrium Quality

The moments method solution to the Grad Shafranov equation is inherently approximate. An ASTRA tight aspect ratio equilibrium has been compared with the solution from a full 2-D tokamak equilibrium solver. Many properties of the equilibria have been compared, and the discrepancies were very small indeed. See Figure 1.

Neoclassical Transport Coefficients

The finite aspect ratio expression for χ_i^{nc} from Chang and Hinton [9] interpolates between χ_i^{nc} at large aspect ratio and the $\epsilon = 1$ value (which is calculated exactly). Additional effects on transport from plasma impurities is also included [10].

$$\chi_i^{nc} = \sqrt{\epsilon}\left(\rho_{i\theta}^2 \nu_{ii}\right)\left\{\frac{\hat{K}_2}{1+1.03\sqrt{\mu_{*i}}+0.31\mu_{*i}} + \frac{1.17\mu_{*i}\epsilon^{1.5}}{1+0.74\mu_{*i}\epsilon^{1.5}} H_P F\right\} \quad (1)$$

We re-evaluate Chang and Hinton's explicit form for χ_i^{nc} to be more consistent with general geometry [11]. In particular we compute numerically from the equilibrium the

flux surface average quantities $\left\langle \frac{B_0^2}{B^2} \right\rangle$ and $\left\langle \frac{B^2}{B_0^2} \right\rangle$ and do not use the approximate aspect ratio expansions given in [10]. We also use the appropriate flux surface averaged quantity for the poloidal ion Larmor radius: ie we take

$$\rho_{i\theta}^2 = \left(\frac{1}{Ze}\right)^2 \frac{m_i T_i}{\langle \nabla \psi^2 \rangle} \frac{I^2}{B_0^2} \tag{2}$$

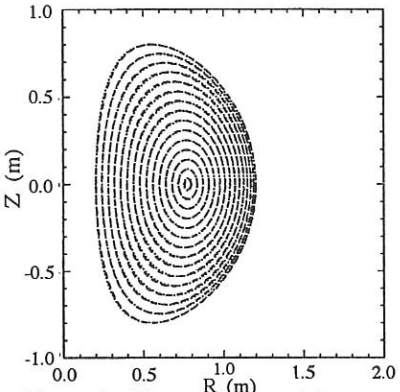


Figure 1: Constant poloidal flux surfaces from ASTRA (dotted) and from a full 2D solver (dashed) for a tight aspect ratio equilibrium.

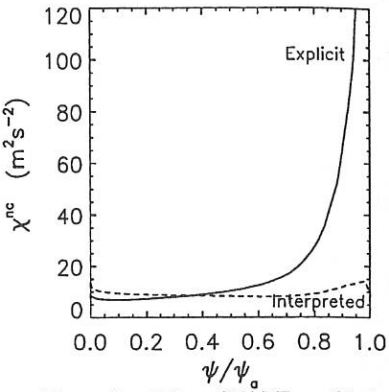


Figure 2: χ_i^{nc} for a START equilibrium: explicitly according to Chang and Hinton (solid), and re-evaluating their expression for TART geometry (dashed).

Model Comparisons with START Experimental Data

Shot Index	κ	I_{pl} (kA)	$\overline{n_e}$ (10^{19} m^{-3})
3	1.45	90	2.55
4	1.50	91	2.38
5	1.45	86	3.6
10	1.45	93	1.38

Table 1: START discharge parameters. $R_0 = .25$ m, $a = .185$ m, $\delta = .3$ and $B_0 = .376$ T in all shots.

Shot	c_1	c_2	c_3	χ_n^2 (dof)
3	3.084	1.941	0.654	20.85 (7)
4	2.709	32.526	1.856	6.835 (4)
5	6.412	7.42	1.25	37.63 (8)
10	1.693	13.441	0.85	6.93 (7)

Table 2: Results of fitting the density profile with: $n_e = c_1 (1 - \rho^2)^{c_2} + c_3$, where ρ is related to the normalised toroidal flux.

Parameters of four START discharges are given in Table 1. We have simulated these discharges using the T11 model in ASTRA and have adjusted a single parameter (in the neutrals model) to fit the experimental chord averaged density $\overline{n_e}$ exactly.

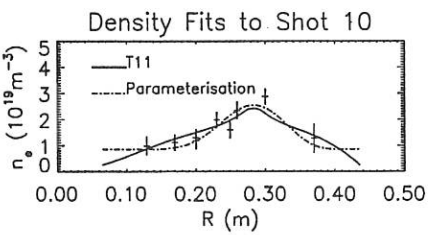


Figure 3: Density fits for shot 10.

In all simulations not using the T11 model we have fixed the density profile using a fit to the experimental measurements.

Shot	$\chi^2_{n_e}$ (dof)	$\chi^2_{T_e}$ (dof)	U : U^{exp} (V)	τ_E (ms)
3	22.9 (8)	8.29 (9)	1.63 : 2.0	1.0
4	9.12 (5)	8.81 (6)	1.53 : 1.9	1.0
5	178 (9)	82.5 (10)	2.12 : 1.8	0.85
10	8.85 (8)	8.08 (9)	1.47 : 1.8	0.79

Table 3: Results from the T11 model.

Shot	Model	$\chi^2_{T_e}$ (dof)	U : U^{exp} (V)	τ_E (ms)
3	RLW	7.31 (9)	1.69 : 2.0	0.96
4	RLW	3.37 (6)	1.76 : 1.9	0.81
5	RLW	15.0 (10)	1.71 : 1.8	1.30
10	RLW	3.25 (9)	1.58 : 1.8	0.64
3	LG	14.9 (9)	1.67 : 2.0	1.00
4	LG	6.33 (6)	1.72 : 1.9	0.85
5	LG	28.6 (10)	1.78 : 1.8	1.20
10	LG	2.70 (9)	1.62 : 1.8	0.65
3	Tar	1980 (9)	0.74 : 2.0	6.10
4	Tar	785 (6)	0.70 : 1.9	5.20
5	Tar	1220 (10)	1.15 : 1.8	3.60
10	Tar	2070 (9)	0.57 : 1.8	4.70

Table 4: Summary of RLW, LG and Tar results.

The fits have the functional form given below Table 2, and were constrained to reproduce the experimental value of $\overline{n_e}$. All density fits are given in Table 2, and Figure 3 shows the fit and T11 prediction for START shot 10. The χ^2_n values and associated degrees of freedom in Table 2 indicate good fits to shots 4 and 10, and poorer fits to shots 3 and 5. Results from the T11 simulations for n_e and T_e are given in Table 3, and Table 4 gives the results from the fixed density simulations. All model electron temperature profiles are compared with the experimental data in Figure 4.

Our results indicate that the Taroni model underestimates electron heat transport in START. The RLW model gives the most accurate predictions, but T11, and Lackner-Gottardi are also consistent with most shots. The simulated loop voltages are generally lower than experiment, but the model predictions are sensitive to the assumed Z_{eff} profile. Taking a larger value for Z_{eff} generally improves the simulated loop voltage.

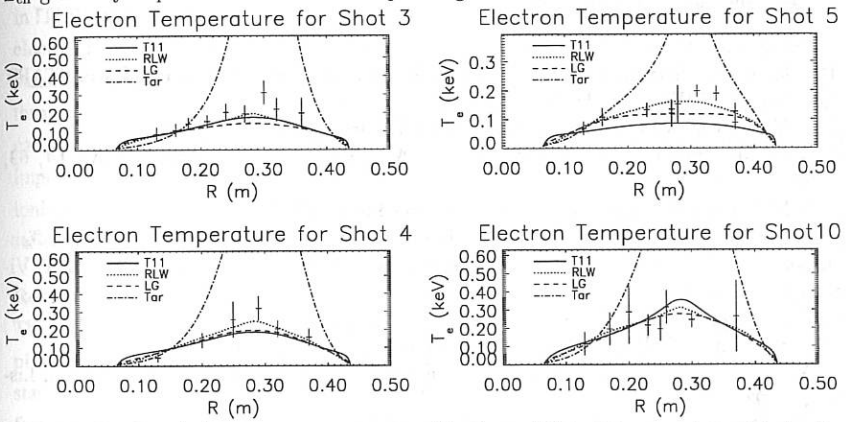


Figure 4: Predicted electron temperature profiles from different transport models for the 4 START discharges, compared directly with the experimental data.

Predictions for a Mega-Amp Spherical Tokamak

The parameters for a 1 MA spherical tokamak proposal (MAST) are: $I_p \sim 1.5$MA, $R_0 \sim .7$m, $a \sim .5$m, $B_0 \sim .57$T, $\kappa \sim 2$, $\delta \sim .25$, $n_{e0} \sim 2 \times 10^{20}$m^{-3}, $Z_{\text{eff}} = 1$ and $P_{\text{aux}} = 5$MW. The transport model which best fits START (RLW) has been used to predict MAST performance, using a crude model for the auxiliary power. The simulated temperature profile for such a device is given in Figure 5, and we obtain the following plasma parameters: $\beta \sim .135$, $g_{T_r} \sim 2.57$, $\tau_E = 24.2$ms, and $\nu_{e*} \sim 0.15$. Similar predictions have been found from the LG model. With a modest confinement enhancement MAST should access the beta limit.

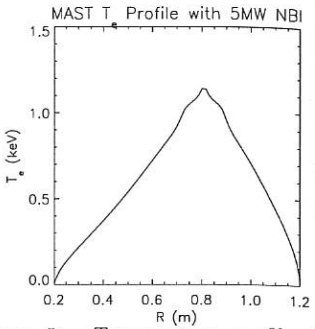


Figure 5: Temperature profile for MAST with 5MW of NBI.

Conclusions

START is indeed a very good testing ground for transport models. It would appear that RLW describes START best, but T11 and LG also perform reasonably well. Taroni's Bohm like model underestimates electron heat transport on START. Improved data, and justification of assumptions (eg the Z_{eff} profile) is needed to discriminate better between the T11, RLW and LG models.

In the future we aim to simulate more START data and study sawteeth. In addition with the addition of NBI to the START experiment, we hope to model auxiliary heated START discharges.

Acknowledgements

It is a pleasure to thank Yu N Dnestrovskij, Jim Hastie and Gregory Pereverzev for useful discussions in the course of this work, which was funded jointly by the UK Department of Trade and Industry and Euratom.

References

[1] 'Global Confinement Properties of the Ohmically Heated Tight Aspect Ratio START Tokamak', M.J.Walsh et al, this conference.

[2] G V Pereverzev et al, Kurchatov Institute Preprint, IAE-5358, 1992.

[3] V.G. Merezhkin, V.S. Mukhovatov, and A.R. Polevoi, Sov J Plasma Phys **14**, 69, (1988).

[4] V.M. Leonov et al, IAEA Conference Proceedings, (1980).

[5] D. Boucher, Proceedings of IAEA Technical Committee Meeting on Advances in Simulations and Modelling of Thermonuclear Plasmas, Montreal Canada, 1992 (IAEA, Vienna,1993), p142.

[6] K. Lackner and N.A.O. Gottardi, Nucl Fus **30**, 767, (1990).

[7] A Sykes et al, ICPP Conference on Plasma Physics, Brazil, (1994).

[8] A. Taroni et al, 20th EPS Conference on Controlled Fusion and Plasma Physics, Lisbon, (1993).

[9] C.S. Chang and F.L. Hinton, Phys Fluids **25**, 1403, (1982).

[10] C.S. Chang and F.L. Hinton, Phys Fluids **29**, 3314, (1986).

[11] F L Hinton, and R D Hazeltine, Rev Mod Phys, **48**, 239, (1976).

ECRH-assisted Start-up in ITER

B. Lloyd, P.G. Carolan and C.D. Warrick
UKAEA Government Division, Fusion, Culham, Abingdon, Oxon OX14 3DB UK
(UKAEA/Euratom Fusion Association)

Introduction

In ITER, the electric field applied for ionisation and to ramp up the plasma current is limited to ~0.3V/m for the reference start-up scenario in which the plasma is initiated close to the outboard wall [1]. In this case, established theories of the avalanche process indicate that ohmic breakdown in ITER is only possible over a narrow range of pressure, p, and error field. Prompt breakdown (i.e. avalanche time $\tau_{bd} \leq 20$ms) requires $p < 2.5 \times 10^{-5}$ torr irrespective of the poloidal magnetic error field level, whereas runaway production is expected for $p < 1.3 \times 10^{-5}$ torr. Low poloidal magnetic error fields broaden the available 'pressure window' but the widening occurs mainly at the low pressure boundary where runaway formation is a concern. Therefore, ECH may be necessary to provide robust and reliable start-up. It has been demonstrated [2] that even at low electric fields, ECH ensures prompt breakdown over a wide range of prefill pressure and error field. ECH can also give control over the initial time and location of breakdown. For ECH-assisted start-up in ITER, the power and pulse length requirements are essentially determined by the need to ensure burnthrough, i.e. complete ionisation of hydrogen and the transition to high ionisation states of impurities. This paper is therefore devoted to the study of the burnthrough phase in ITER.

Theoretical Model

A 0-D code (with inclusion of some 1-D effects) has been developed to analyse burnthrough in ITER and includes the following features:- dynamic fuelling by the ex-plasma volume, electrical circuit model, deuterium recycling, external gas influx, neutral screening, particle balance for electrons, ions and neutrals, separate ion and electron power balance linked through equipartition and a *non-equilibrium* coronal impurity model in which radiation losses can be much higher than for impurities at equilibrium. The impurity model allows for finite impurity confinement (impurity recycling), charge exchange effects on the impurity ionisation balance and radiation and a time-dependent impurity concentration (impurity influx).

Results

The 0-D simulations have revealed the possible important role of dynamic fuelling by the ex-plasma volume, as a result of the small plasma size (compared to the vessel volume) during start-up. Indeed, in many respects, control of the deuterium density appears to be the primary factor in determining whether burnthrough is successful. A pessimistic approach has been adopted by assuming a deuterium recycling coefficient $\psi > 1$ and that the deuterium

inventory is not depleted during the early avalanche. On the other hand, the deuterium is taken to be fully dissociated from the outset, an assumption which will not strongly influence the power balance (since we already take an energy loss of 30eV per ionisation to account for deuterium radiation losses) but which has implications for the assumed neutral temperature, and thus the effectiveness of neutral screening, which can be important for successful start-up. A wide range of deuterium particle (5 - 50ms) and energy (~0.2 - 2 $\times \tau_{INTOR}$) confinement times is assumed but may still overestimate the confinement at low plasma current before magnetic surfaces are fully formed. The initial conditions are taken to be $T_e = T_i = 1eV$ and 1% ionisation. It is found that at modest prefill, i.e. initial neutral density $n_0(0) \sim 2\text{-}3 \times 10^{17}$ m^{-3} the discharge can fail to survive even without impurities (Fig 1) if the discharge is effectively fuelled by the large reservoir of deuterium in the ex-plasma volume ($V_{plasma}/V_{vessel} \sim 0.1$ during start-up). The failure is attributable to large electron equipartition losses to the ions which in turn lose energy primarily through charge exchange. In the case illustrated the resistive voltage, V_{res}, increases rapidly to the applied voltage of

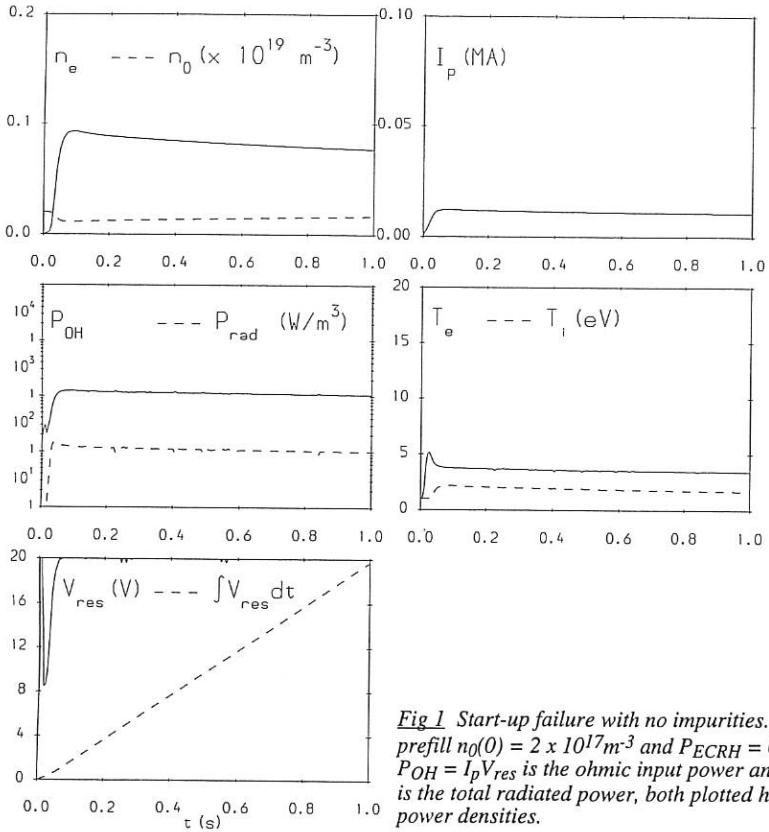


Fig 1 Start-up failure with no impurities. Initial prefill $n_0(0) = 2 \times 10^{17} m^{-3}$ and $P_{ECRH} = 0$. $P_{OH} = I_p V_{res}$ is the ohmic input power and P_{rad} is the total radiated power, both plotted here as power densities.

20V and the plasma current saturates at ~10kA. On the other hand at $n_0(0) \sim 1.5 \times 10^{17}$ m^{-3}, which may result in a post-avalanche electron density ~ 1.5×10^{18} m^{-3} for a deuterium recycling coefficient $\psi \sim 1$, a beryllium impurity level of ~5% may be tolerable without ECH-assist under certain circumstances (e.g. negligible impurity recycling). However, such a discharge is predicted to fail if either a realistic impurity confinement time or a modest decrease in the assumed electron and ion energy confinement times is introduced. Because of the dynamic fuelling effect, even the minimum pressure which allows the avalanche to proceed may result in a post-avalanche density which may be difficult to sustain without ECH. Nevertheless, for the plasma geometry assumed, it appears that post avalanche densities ~ 5×10^{18} m^{-3} with 5% impurity level may be tolerated with 2MW (beryllium) or 5MW (carbon) of *absorbed* power for a wide range of confinement times and impurity recycling times. ECH-assisted start-up (P_{ECRH} = 2MW) with a prefill density $n_0(0) = 5 \times 10^{17}$ m^{-3} and an impurity influx programmed to maintain a constant beryllium concentration (n_{Be}/n_D = 5%) is illustrated in Fig 2. There is no external deuterium influx but a deuterium

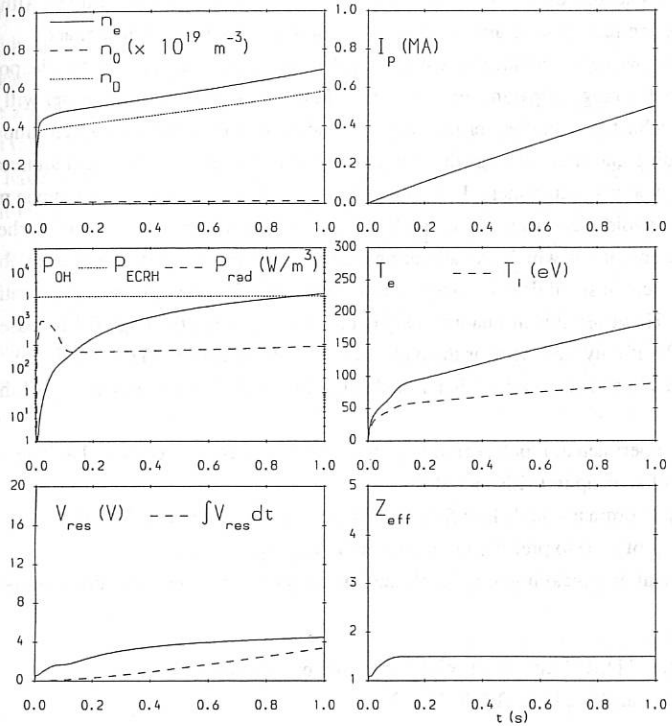


Fig 2 Successful start-up with 5% beryllium and P_{ECRH} = 2MW. Initial prefill $n_0(0) = 5 \times 10^{17}$m^{-3}. No impurity recycling. n_D is the deuterium ion density.

recycling coefficient $\psi = 1.01$ is assumed. In this case the plasma current increases at a rate of ~0.5MA/s for the constant applied voltage of 20V.
The calculations described so far were carried out with a fixed plasma size of a = 1m. Studies of the impact of plasma size have shown that high power ECH (i.e. ~ 5MW absorbed) ensures that start-up remains robust but 2MW is insufficient to guarantee start-up with 5% beryllium. It has been concluded that an *absorbed* power of ~ 3MW is necessary to ensure burnthrough for beryllium over a wide range of conditions with ~ 5MW required for carbon. A pulse length of a few seconds is adequate and a frequency ~130-135GHz is required for start-up on the outboard limiter at full toroidal field.

Summary and Discussion

Control of the deuterium density is the key factor for ensuring successful start-up in ITER, where the role of neutral screening is also crucial. If the effectiveness of screening of neutrals from the plasma volume is reduced, for example because of increased neutral temperature, start-up becomes more problematic, particularly for carbon impurity, but an ECRH power of 3MW remains adequate for a beryllium concentration of 5% for most conditions. Although start-up is a complex process and there must remain some uncertainty over exact requirements, we can conclude that without ECRH, successful start-up will only be possible over a restricted range of parameters but 3MW(5MW) of *absorbed* ECRH power will ensure reasonably robust start-up for a broad range of conditions with beryllium(carbon) impurity. An outstanding question concerns the extrapolation from the *absorbed* power requirement to the *launched* power requirement. If low-field-side launch is used, the ordinary mode must be employed to avoid wave accessibility problems but this mode is weakly damped in the low temperature conditions which prevail during start-up. The mode of launch has been observed not to be critical in small devices; one can rely upon multiple reflections and polarisation scrambling. However, this mechanism may not be so effective in the large ITER vessel. Alternatively, if only start-up near the outboard wall is to be used in ITER, it may be advantageous to consider extraordinary mode high-field-side launch from the top of the vessel.
Additional experimental input, preferably from large tokamaks, which would aid the assessment of start-up in ITER includes:

- efficiency of ordinary mode low-field-side launch for start-up assist,
- relationship of $n_e(t)$ to prefill pressure when $(V_{vessel}/V_{plasma}) \gg 1$,
- measurement of typical impurity levels and impurity confinement time during start-up.

References

[1] A. Portone, ITER Team, Naka Joint Work Site, private communication.
[2] B. Lloyd et al, Nuc. Fus. **31** (1991) 2031.

Acknowledgements

This work was jointly funded by the UK Department of Trade and Industry and Euratom.

PREDICTIVE MODELLING OF ENERGY TRANSPORT IN JET DISCHARGES

M.Erba, A. Cherubini, V. Parail, E. Springmann, A. Taroni.
JET Joint Undertaking Abingdon Oxon OX14 3EA U K

1) INTRODUCTION

Energy transport in the different regimes of confinement observed at JET can be studied using a Bohm-like model for L-mode electron transport [1] as a starting point:

$$\chi_e = \alpha_e \frac{c|\nabla(n_e T_e)|}{eBn_e} aq^2 \quad , \quad \chi_i = \chi_i^{neocl} + \alpha_i \chi_e \qquad (1)$$

where q is the safety factor, χ^{neocl} is the neoclassical ion diffusivity while α_i,α_e are numerical coefficients to be determined empirically. Using model (1) it is possible to simulate a variety of L-mode and ohmic JET discharges with fixed numerical coefficients (sections 2 and 3).
Since at the L-H transition a global sudden reduction of the electron heat diffusivity is observed [2], we have been able to set up a model for the H-mode regime reducing the diffusivities by a constant factor over all the plasma (see section 4). It has not been possible to study the Bohm versus gyro-Bohm aspects of the scaling of heat transport in H-mode due to the restricted variation of plasma parameters in our selected discharges; a gyro-Bohm-like model with a radially increasing shape [3] can be equally successful.
To simulate predictively the formation of the temperature pedestal we assume the existence of a neoclassical transport barrier on a thin layer ($\sim\rho_{pi}$) inside the separatrix, and the H-mode numerical simulations have been repeated using these boundary conditions successfully reproducing the experimental trends (section 5).

2) SIMULATION OF JET L-MODE DISCHARGES

In our approach we start from the observation that the results of TRANSP analysis of ordinary L-mode JET discharges indicate that $\chi_i > \chi_e$ all over the plasma column, so that we use eq. (1) for χ_i with α_i>1. We consider a set of L-mode discharges chosen in the JET data-base where the experimental ion temperature profiles are available with parameters in the range: $0.11 \leq \langle n_e \rangle (10^{20} m^{-3}) \leq 0.55$, I_p (MA) ≈ 3 , B_t (T) ≈ 3 , $4 \leq P_{in}$ (MW) ≤ 18.

The simulations have been carried out in a semi-predictive way using the JETTO transport code: only heat diffusion has been modelled, while experimental density and Z_{eff} profiles have been imposed throughout the time evolution. It is found that a model with $\alpha_e = 2.0 \cdot 10^{-4}, \alpha_i = 3$ gives good results also in cases with predominant electron heating.

3) SIMULATION OF JET OHMIC DISCHARGES

Analysis of ohmic discharges [4] has shown that when the density is too high the confinement time does not rise linearly with density as prescribed by the so-called Neo-Alcator scaling law and saturates. Recent results from ALCATOR C-MOD [5] suggest that this regime might be described using an L-mode-like model. We choose for simulation a set of 5 JET ohmic discharges with parameters in the range: $0.10 \leq \langle n_e \rangle (10^{20} m^{-3}) \leq 0.37$, $1 \leq I_p$ (MA) ≤ 7 , $1.7 \leq B_t$ (T) ≤ 3.3.

In fig. 1 the profiles obtained with a neoalcator-like model [6], with the Bohm model (with the same value of the coefficients given above) and the experimental profiles are shown. Analysis of the corresponding values of thermal energy shows that the linear scaling with density and weak scaling with current, typical of the neoalcator-like model, are not in agreement with experimental results, which are much closer to the L-mode scaling.

4) SIMULATION OF H-MODE ELM-FREE, MHD-FREE DISCHARGES

Following the results presented in [2], we derive a model for H-mode by reducing the numerical coefficient α_e by ~10 times with respect to L-mode down to $0.2 \cdot 10^{-4}$. Due to the non-linearity in the parametric dependencies of χ this results in a reduction of the numerical value of χ by a factor ~ 3. We point out that due to this reduction the neoclassical ion transport becomes important in the central part of the plasma column.

In this way we model the entire ELM-free H-mode phase for shots which have no large scale MHD activity (like roll-over), and we succeed in simulating both the evolution of the thermal energy and the temperature profiles at different times. Some of the selected discharges fall into the category of VH-mode with enhancement factor H>3, while others have 2<H<3.

We can simulate discharges with different values of the H-factor using the same transport model because an important role is played by effects not directly related to heat diffusion, like the shape of the power deposition profile and the temperature pedestal. Edge temperatures of at least 3 keV are in fact characteristic of high performance shots in JET, and roughly half of the total thermal energy is stored in this pedestal.

5) A MODEL FOR BOUNDARY CONDITIONS IN H-MODE DISCHARGES

Assuming that perpendicular transport inside a transport barrier located at the plasma edge is of the order of the neoclassical one in the banana regime we obtain the following condition:

$$\chi_i n_i \nabla T_i + \frac{3}{2} T_i D \nabla n_i \approx -n_i T_i \frac{\rho_{pi}}{\sqrt{\varepsilon}\tau_{ii}} F_T \qquad (2)$$

where ρ_{pi} is the ion poloidal Larmor radius, τ_{ii} is the ion-ion collisional frequency, ε is the inverse aspect ratio near the separatrix, F_T is a coefficient which depends on the geometry, collisionality and radial electric field and $0 \le F_T \le 1$[7]. The boundary condition for electron heat flow is similar to eq. (2) if we assume that the remaining magnetic turbulence near the separatrix keeps the electron particle flux at the level of the ion neoclassical flow. We find that using the above boundary conditions we can reproduce the experimentally observed ion and electron temperature evolution near the separatrix in the best Hot-Ion H-mode discharges, and that in case of relevant volume power losses the edge temperature is significantly decreased (see fig. 2a). An important property of boundary conditions (2) is that in the banana regime the heat flow does not depend on the temperature near the separatrix and $Q_{e\text{-}i} \propto n_i\, n_{e\text{-}i}$. This feature allows us to explain the experimentally observed fact that the global plasma energy confinement time in hot-ion VH-modes, formally defined as $\tau_E = W/(P - dW/dt)$, grows almost linearly with time together with the total energy content W (see fig. 2b). A saturation may occur in collisional regimes, where a temperature dependence is introduced by the plateau expression of the neoclassical diffusivity.

REFERENCES

[1] Taroni A., et al., Plasma Phys. Control. Fusion **36** (1994) 1629.

[2] Balet B., et al., "The Physics of L and H-mode Confinement in JET", 15th Int. Conf. on Plasma Physics and Contr. Nucl. Fus. Res., Seville, Spain (1994).

[3] Erba M., et al., "Simulation of L-mode Tokamak Discharges and ITER Performance with Energy Transport Coefficients of Bohm and gyro-Bohm Type", Proc. Workshop on Local Transport Studies in Fusion Plasmas, Varenna (1993) 39.

[4] Garbet X. , Payan J. , Laviron C. , et al. , Nucl. Fus. **32** (1992) 2147

[5] Porkolab M. , et al. , 'Overview of recent results from Alcator C-MOD', 15th Int. Conf. on Plasma Phys. and Contr. Nucl. Fus. Res. , Seville (1994).

[6] Merezhkin V.G. and Mukhovatov V.S., JETP Lett, **33** (1981) 446.

[7] S.-I. Itoh and K. Itoh, Phys. Rev. Lett. **60** (1988) 2276.

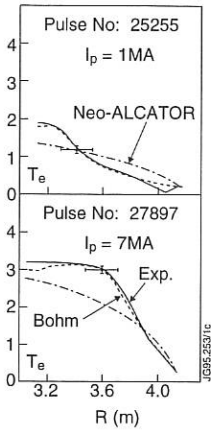


Fig. 1: Experimental temperature profiles (solid lines) and computed temperature profiles with the Neo-alcator-like and Bohm models (dotted lines) for a 1 MA and a 7 MA ohmic JET discharge.

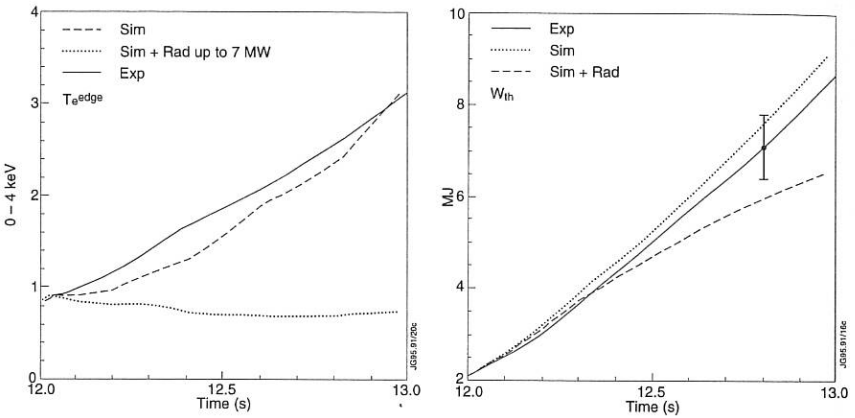


Fig. 2a : Time evolution of the edge electron temperature from experimental measurements (solid line) and from simulations carried out with and without the effect of 7 MW of radiated power (dotted lines).

Fig. 2b : Time evolution of the thermal energy from experimental measurements (solid line) and from simulations carried out with and without the effect of 7 MW of radiated power (dotted lines).

Numerical Studies of the Dynamics of MARFEs for a Deuterium-Carbon Plasma at ASDEX-Upgrade

H. Kastelewicz, R. Schneider and J. Neuhauser

Max-Planck-Institut für Plasmaphysik, EURATOM Association, Germany

1. Introduction

Marfes are poloidally localized, axisymmetric regions in the edge plasma of tokamaks with strongly enhanced plasma density, reduced temperature and high radiative energy losses due to impurities (cf. ,e.g., / 1 /). They occur close to the high density limit and are accompanied by a strong decrease of the power flux to the divertor plates or even by complete plasma detachment. In ASDEX Upgrade marfes are usually formed near the (lower) x-point, they may move upwards at the high field side of the boundary plasma, eventually causing a major disruption / 2 /.

The formation of marfes is based on a thermal instability which may develop in an impure plasma if the radiation characteristic of the plasma has a negative derivative / 3 /. This is preferably the case for low-Z impurities like carbon or oxygen which show strong destabilizing radiation characteristcs in the temperature range around 10eV.

In the present paper, the multifluid B2 plasma code (D-C plasma) has been used to study the formation, the temporal behaviour and possible stabilization of marfes at ASDEX Upgrade. A more extensive treatment of this subject is to be published / 4 /.

2. Numerical Model

The edge and divertor plasma is described in the hydrodynamic approximation by the B2 2d multi-fluid code (for the 7 ions of D and C), which is coupled to simplified models describing deuterium recycling from the target plates and neutral deuterium and carbon influxes from the torus wall region. These influxes (assumed to be homogeneously distributed) are used to control the plasma density and carbon concentration. Each ion species is treated as separate fluid. The essential boundary conditions are:

at the bulk plasma side: total energy input P_{in} = 950kW, zero density gradients $\frac{\partial n}{\partial y}|_{core} = 0$;

at the wall side and private region side: electron and ion temperature $T_e = T_i$ = 2eV, ion density decay length (all ion species) $\lambda_n = 1cm$;

at the targets: Bohm conditions with $v_{\parallel} \geq v_{mach}$ ($v_{\parallel}$ = parallel velocity), recycling factor R_p = 0.8

Physically reasonable variations of these boundary conditions have been proved not to influence the principal results of this study.

For the anomalous radial transport: we assume:

diffusion: $D_i = 1m^2/s$, or alternatively $D_i = (1/16)(T_e/eV)/(B/T)m^2/s$ (Bohm ansatz);

heat conduction: $\kappa_{e,i}/n_{e,i} = 1m^2/s$; viscosity: $\eta_i/m_i n_i = 0.2m^2/s$.

3. Formation and temporal development of MARFEs

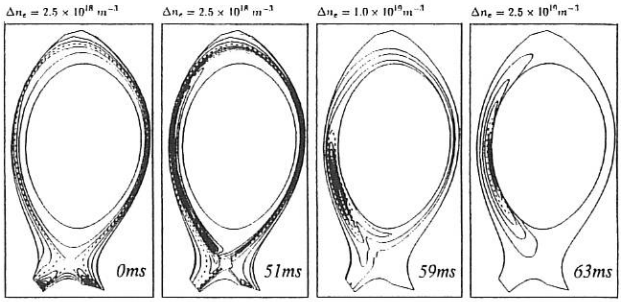


Fig.1: n_e contour plots showing the non—linear development of a marfe

In analogy to the experiment, marfe formation is initiated numerically by starting from a pre-marfe plasma and enhancing the external neutral influxes of deuterium and carbon with time, keeping the impurity concentration about constant ([C]≈3% , $F_{C^0}/F_{D^0} = const$ = 0.035). The development of the marfe is shown by a sequence of ne contour plots at different times in Fig. 1 (const. diff. coefficients).

The neutral influx rate (representing gas puff and recycling) has been linearly increased up to the beginning of the marfe ($\approx 50ms$) and then kept constant. The marfe is formed near the x-point, then - although all discharge parameters are fixed - it moves further upwards at the inner plasma side while increasing in intensity (density, impurity radiation). In the final phase it penetrates to the core plasma (bounded by the calculational grid). During this last stage the radiated energy exceeds temporarily the total input power on account of the inner energy of the boundary plasma which cools down to wall temperature in the whole domain. The time dependence of some parameters are shown in Fig. 2. This scenario corresponds to a typical density limit discharge, where the edge cooling and current channel contraction by the marfe finally causes a major disruption.

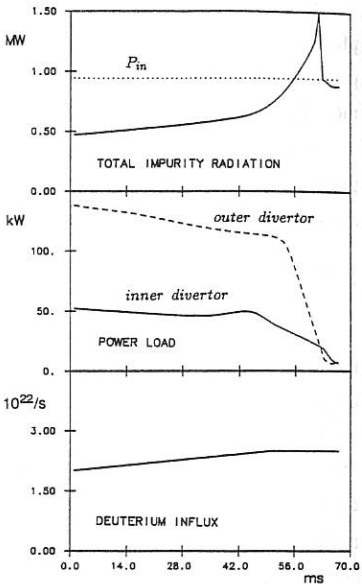


Fig.2: Temporal evolution of the total impurity radiation, the divertor power loads and the gas fuelling rate

Other time dependent scenarios yield in principle the same results as long as a sharply defined critical gas influx rate necessary for marfe formation is exceeded. Thus it seems that marfes, once formed, are principally unstable under such conditions.

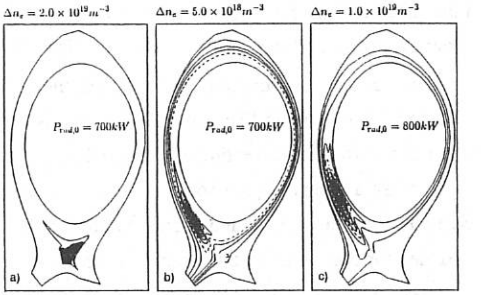
4. Steady state MARFEs

Marfes can readily be stabilized by external feed-back control using the radiated energy as control parameter. We introduce the following feed-back loop into the plasma code which decreases the neutral influx rate F_{D^0} if the radiated energy P_{rad} exceeds a prescribed value $P_{rad,0}$ and vice a verse:

$$\frac{F_{D^0}(t+\Delta t) - F_{D^0}(t)}{F_{D^0}(t)} = -\alpha \frac{P_{rad}(t) - P_{rad,0}}{P_{rad,0}} \quad ,$$

where α is of the order of 10^{-2}.

In this way one obtaines continuously converging (stationary) solutions with $P_{rad} = P_{rad,0}$ and self-adjusted neutral fluxes F_{D^0} and F_{C^0} ($\propto F_{D^0}$). Fig. 3 shows some examples for different radial transport laws and prescribed radiated energies. It should be noted that the small radial diffusivity for Bohm diffusion at the marfe as compared with the case of constant diffusion coefficients is compensated by a higher density peak (and steeper density gradients). Thus in both cases a very effective cross-field transport is provided which is the basic driving mechanism of a marfe. In the following we restrict ourselves therefore to the case of constant diffusion coefficients. The position of the marfe depends in particular on the radial transport law, the neutral particle model and the radiated energy.



a) Bohm-diffusion $F_{D^0} = 1.58 \times 10^{22} s^{-1}$, $n_{e,max} = 5.0 \times 10^{20} m^{-3}$
b) const. diff.-coeff. $F_{D^0} = 1.90 \times 10^{22} s^{-1}$, $n_{e,max} = 8.9 \times 10^{19} m^{-3}$
c) const. diff.-coeff. $F_{D^0} = 1.49 \times 10^{22} s^{-1}$, $n_{e,max} = 1.7 \times 10^{20} m^{-3}$

Fig.3: Steady state marfes for different radial transport laws and radiated energies

In virtue of the feed-back loop which may be considered as an integrated part of the system of plasma equations the complete set of stationary solutions can be represented in an $F_{D^0} - P_{rad}$ diagram of steady states by a double-valued function (Fig. 4) where the lower branch describes marfe-free and the upper branch marfe plasma states.

The upper branch can only be reached after having enhanced F_{D^0} above a critical value $F_{D^0,crit}$. No steady states are possible for $F_{D^0} > F_{D^0,crit}$. In principle, the plasma system may smoothly be moved along this curve and kept stationary at any desired value of P_{rad}.

The local mechanism sustaining a steady state marfe, i.e. a region of enhanced density and lowered temperature relative to the surrounding medium within a basically diffusive system, is provided by a complicated dynamic equilibrium between parallel and radial particle, momentum and energy fluxes. From the equation of continuity one finds that the ions are transported to the density maximum in parallel direction and removed from there radially outward and inward by anomalous diffusion. Thus a marfe like that of Fig.3c causes a strong - poloidally localized - particle sink at the flux surfaces intersecting it, and provides particle sources in the adjacent (more outer and inner) plasma layers. These sources induce poloidal ion fluxes on closed flux surfaces and an asymmetry of the particle and energy outflow to the divertor plates. Actually, the marfe acts as a barrier for the radial particle transport across the intersecting flux surfaces.

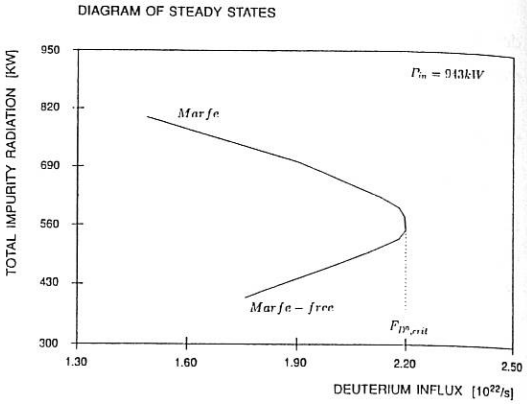


Fig.4: F_{D^0} – P_{rad} diagram of steady states for a deuterium-carbon boundary plasma

From the momentum balance one finds that the basic mechanism responsible for driving the D^+ and C^+ ions into the local density maximum are pressure gradient forces. In addition there is a strong coupling between the different ion species via thermal, frictional and viscosity forces. Higher charged ions are dragged to the density maximum mainly by the strong frictional coupling with the background plasma.

The energy is transported to the marfe by parallel conduction and convection and radiated there. For the marfe of Fig.3c about 35% of the total radiation is emitted by the marfe itself (mostly by C^{3+} and C^{2+} radiation).

Corresponding address: H. Kastelewicz, Max-Planck-Institut für Plasmaphysik, EURATOM Association, Bereich Berlin, Mohrenstr. 40/41, D-10117 Berlin, Germany

References

/ 1 / B. Lipschultz, J. Nucl. Materials 145-147 (1987) 15

/ 2 / V. Mertens, W. Junker, M. Laux et al., Plasma Phys. Control. Fusion 36 (1994) 1307

/ 3 / J. Neuhauser, W. Schneider, R. Wunderlich et al., Nucl. Fusion 26 (1986) 1679

/ 4 / H. Kastelewicz, R. Schneider, J. Neuhauser, Plasma Phys. Control. Fusion (to be published)

Alpha-particle driven TAE instability suppression by the resonant RF field.

V.S. Marchenko and A.Yu. Pan'kin
Institute for Nuclear Research, pr. Nauki, 47, Kiev - 252028, Ukraine

One of the major issues in the α-particle physics of tokamaks is the low n toroidicity-induced Alfven eigenmode (TAE) instability driven by α–particle pressure gradient and the resultant α–particle transport [1-5]. The main results of the previous studies of this problem are that the volume averaged α–particle beta threshold for TAE instability is small and is on the order of 10^{-4}, and that for relatively low fluctuation level with $(\delta B_r/B_0) \geq 10^{-4}$ the α–particle loss time is comparable and even shorter than the α–particle slowing-down time. That is why the problem of efficient suppression of this instability seems to be important.

Several damping mechanisms of TAE modes has been considered in literature. They are: electron Landau damping [1], ion Landau damping [4], continuum damping [6], collisional damping on trapped electrons [7]. The last three mechanisms taken together could increase α–particle beta threshold by more than an order of magnitude. In the present work we consider an alternative damping mechanism which should arise in the stationary tokamak reactor, when the plasma current is driven by lower hybrid (LH) waves, which is the most promising current drive scheme at present. It is well known [8] that α–particles could interact with LH modes via transversal Landau resonance $v_{ph\perp}=v_{\alpha\perp}$, where $v_{ph\perp}$, $v_{\alpha\perp}$ are the perpendicular to the equilibrium magnetic field velocity components of LH wave phase and α–particle respectively. Such interaction have been observed recently during LHCD experiments in JET [9]. The interaction results in the quasilinear diffusion in the resonant part of the α–particles phase space. Quasilinear diffusion operator modifies α–particle response on the Alfven perturbation in a such a way, that TAE mode becomes heavely damped for moderate values of LH power. This damping mechanism has been reported previously [10], where continuum Alfven waves instability on the trapped α–particles was considered. Here we are extending the theory to the TAE instability driven by resonance with passing α–particles.

With the help of Ampere's law and quasineutrality condition one could obtain the following two coupled second-order eigenmode equations for the poloidal electrical field E_θ, which include kinetic instability drive due to Cherenkov resonance with passing particles [1] and dissipation due to quasilinear diffusion in the external RF field (all other damping mechanism are dropped, see for detail [11]):

$$\left\{\frac{d}{dr}r^3\left(\frac{\omega^2}{v_A^2}-k_{\|m}^2-A_{am}-A_{am}^{QL}\right)\frac{d}{dr}-r^2B_{am}^{QL}\frac{d}{dr}-r\left[(m^2-1)\left(\frac{\omega^2}{v_A^2}-k_{\|m}^2-A_{am}\right)-C_{am}^{QL}\right]\right. \tag{1}$$

$$\left.+r^2\left[\left(\frac{\omega^2}{v_A^2}\right)'-A'_{am}-mB'_{am}-(A_{am}^{QL})'-m(D_{am}^{QL})'\right]\right\}E_m+\epsilon_1\frac{d}{dr}\left(\frac{\omega^2}{v_A^2}\frac{r^4}{a}\frac{d}{dr}E_{m+1}\right)=0$$

$$\left\{\frac{d}{dr}r^3\left(\frac{\omega^2}{v_A^2}-k_{\|m+1}^2-A_{am+1}-A_{am+1}^{QL}\right)\frac{d}{dr}-r^2B_{am+1}^{QL}\frac{d}{dr}-r\left[((m+1)^2-1)\left(\frac{\omega^2}{v_A^2}-k_{\|m+1}^2-A_{am+1}\right)-C_{am+1}^{QL}\right]\right. \tag{2}$$

$$\left.+r^2\left[\left(\frac{\omega^2}{v_A^2}\right)'-A'_{am+1}-(m+1)B'_{am+1}-(A_{am+1}^{QL})'-(m+1)(D_{am+1}^{QL})'\right]\right\}E_{m+1}+\epsilon_1\frac{d}{dr}\left(\frac{\omega^2}{v_A^2}\frac{r^4}{a}\frac{d}{dr}E_m\right)=0$$

where $\epsilon_1=3a/2R$, the prime denotes radial differentiation, $k_{\|m}=(m-nq)/qR$ is the parallel wavenumber with a, R the minor and major radii respectively and q the safety factor. The quantities $A_{am}=Q_{m-1}-Q_{m+1}$ and $B_{am}=Q_{m-1}+Q_{m+1}$ are derived in [1], where $Q_{m\pm1}$ is given by

$$Q_{m\pm1}=-i\frac{\beta_\alpha}{2R^2}\frac{\pi\omega}{v_\alpha^4}\int d^3v\left(\frac{v_\perp^2}{2}+v_\|^2\right)^2\left(-T_\alpha\frac{\partial\overline{F}_\alpha}{\partial\varepsilon}-\frac{\omega_{*am}}{\omega}F_\alpha\right)\delta\left(\omega-k_{\|m+1}v_\|\right) \tag{3}$$

Also,

$$A_{am}^{QL}=L_{m-1}+L_{m+1}$$
$$B_{am}^{QL}=S_{m-1}+S_{m+1}-L_{m-1}-L_{m+1}$$
$$C_{am}^{QL}=m^2\left(K_{m-1}+K_{m+1}\right)+m\left(S_{m-1}-S_{m+1}-K_{m-1}+K_{m+1}\right)-S_{m-1}-S_{m+1}$$
$$D_{am}^{QL}=S_{m-1}-S_{m+1}$$

where L, S, K are given by

$$\left\{\begin{matrix}L_{m\pm1}\\S_{m\pm1}\\K_{m\pm1}\end{matrix}\right\}=\left\{\begin{matrix}\left\langle\sin^2\theta\right\rangle^2\\\left\langle\sin^2\theta\right\rangle\left\langle\cos^2\theta\right\rangle\\\left\langle\cos^2\theta\right\rangle^2\end{matrix}\right\}\frac{\beta_\alpha}{2R^2}\frac{1}{v_\alpha^4}\int_u d^3v\frac{\left(v_\perp^2/2+v_\|^2\right)^2}{2+\Delta_+\Delta_-}\left(-T_\alpha\frac{\partial\overline{F}_\alpha}{\partial\varepsilon}-\frac{\omega_{*am}}{\omega}\overline{F}_\alpha\right)$$

$$\times\left\{\left[2\left(1-\frac{1}{\Delta_+^2}\right)+\left(\frac{1}{\Delta_-^2}-\frac{1}{\Delta_+^2}\right)\Delta_-\right]H(\mathrm{v}_{\|})\exp\left\{i(1+i)\left(\frac{\omega}{2\nu_{QL}}\right)^{1/2}\Delta_+(1-\varpi^{-2})\right\}\right. \tag{4}$$

$$\left.+\left[2\left(1-\frac{1}{\Delta_-^2}\right)+\left(\frac{1}{\Delta_+^2}-\frac{1}{\Delta_-^2}\right)\Delta_+\right]H(-\mathrm{v}_{\|})\exp\left\{i(1+i)\left(\frac{\omega}{2\nu_{QL}}\right)^{1/2}\Delta_-(1-\varpi^{-2})\right\}\right\}$$

where $\beta_\alpha = 8\pi n_\alpha T_\alpha/B^2$, $\int d^3\mathrm{v}\overline{\mathrm{F}}_\alpha = 1$, $\mathrm{v}_\alpha^2 = 2T_\alpha/m_\alpha$, $\omega_{*\alpha m} = \dfrac{m}{r}\left(\dfrac{T_\alpha c}{e_\alpha B}\right)\dfrac{d\ln n_\alpha}{dr}$, $\langle A\rangle$ denotes the bounce or transit average of A, $H(\mathrm{v}_{\|})$ is the unit step function and integration carried out over passing particles,

$$\Delta_\pm^{m\pm1}(\varepsilon,r) = \left(1\mp\frac{4\pi(m\pm1-nq(r))}{q(r)R}\ln^{-1}\left(\frac{256\omega}{\nu_{QL}(\varepsilon,r)}\right)\frac{(\varepsilon r/R)^{1/2}}{\omega}\right)^{1/2}$$

$$\nu_{QL}(\varepsilon,r) = \frac{1}{2}\left(\frac{r}{R}\right)^{1/2}\left(\frac{e_\alpha}{m_\alpha}\right)^2|E_\sim|^2\left(\frac{\Omega}{k_{0\perp}}\right)^2\left(\frac{r}{R}\varepsilon\right)^{-2}\left(2k_{0\perp}^2\varepsilon-\Omega^2\right)^{-1/2}$$

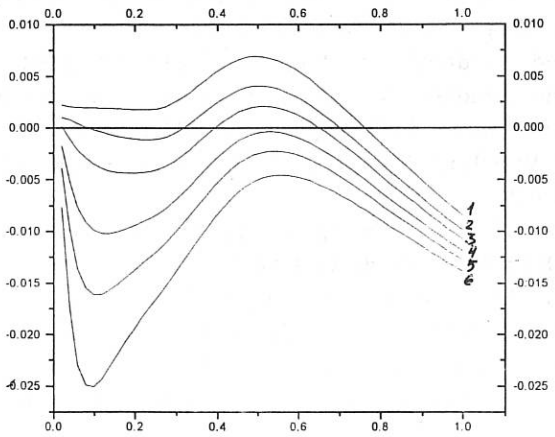


FIG. 1. Growth rate (normalized to the real frequency ω_0) for n=-1 TAE mode as a function of the alpha particle density gradient scale length, for different values of $\upsilon_{QL}^{(0)}/\omega_0$: (1) 0; (2) $9\cdot10^{-4}$; (3) $2\cdot10^{-3}$; (4) $4\cdot10^{-3}$; (5) $6\cdot10^{-3}$; (6) $9\cdot10^{-3}$

It should be noted, that hereafter we ignore the LH power deposition profile and put $|E_-|^2(r) = const$. Treating kinetic terms in (1), (2) perturbatively, we analyze the stability of the TAE mode in the presence of external RF field resonating with α–particles. Figure 1 shows the grows rate (normalized to the real frequency) as a function of the alpha particle density scale length L_α with $\beta_a = \beta_a(0)\exp\left(-r^2/L_\alpha^2\right)$ for the different values of $\nu_{QL}^{(0)}/\omega_0$. The parameters chosen are the following: $a/R=1/4$, $\rho_{\alpha 0}/a=0.05$ with $\rho_{\alpha 0}$ the alpha Larmor radius, $v_{\alpha 0}=2v_A$, $\beta_\alpha(0)=1\%$, $T_e=10\ keV$, $n_e=10^{14}\ cm^{-3}$, $\Omega/k_{0\perp}v_{\alpha 0} = 2^{-1/2}$.

As one can see from Fig. 1, suppression of the instability occurs for the $\nu_{QL}^{(0)}/\omega_0 \approx 5\cdot 10^{-3}$. Corresponding RF field amplitude for the parameters chosen is $E_{thr} \sim 5kV/cm$. This value could be exceeded in future experiments on LH current drive. The key point here is whether the RF power be considerably depleted due to current drive before the $q(r) = (2m+1)/2n = 3/2$ surface, where the TAE mode is localized. Note that the threshold RF power does not depend on the β_α, but only on the fraction of the resonating α–particles, which in turn depends on the value $\Omega/k_{0\perp}v_{\alpha 0}$.

References

[1] Fu G.Y. and Van Dam Y.W., *Phys. Fluids* B1 1949 (1989)

[2] Cheng C.Z., *Phys. Fluids* B3 2463 (1991)

[3] Betti R. and Freidberg Y.P., *Phys. Fluids* B3 538 (1991)

[4] Betti R. and Freidberg Y.P., *Phys. Fluids* B4 1465 (1992)

[5] Hsu C.T. and Sigmar D.Y., *Phys. Fluids* B4 1492 (1992)

[6] Berk H.L., Van Dam Y.W., Guo Z., Lindenberg D.M. *Phys. Fluids* B4 1806 (1992)

[7] Gorenlenkov N.M. and Sharapov S.E., *Phys. Scr.* 45 163 (1992)

[8] Karney C.F.F, *Phys. Fluids* 22 2188 (1979)

[9] de Andrade M.C.R. et al. *Interaction of Lower Hybrid with Fast Ions in JET, Preprint JET-P(93)37*, p.79

[10] Marchenko V.S., *Nucl. Fusion* 33 1871 (1993)

[11] Catto Y. and Rosenbluth M.N., *Phys. Fluids* 24 243 (1981)

Energetic Ion Effects on the Propagation and Absorption of Kinetic Alfvén Wave in Fusion Plasma

L. Huang N. Ding X. M. Qiu and Y.X. Long

Southwestern Institute of Physics, P.O.Box 432, Chengdu 610041, P.R.China

1. Introduction

In recent years, fusion research on tokamaks has made substantial progress on plasma confinement under condition with strong auxiliary heating power. An extensive series of deuterium-tritium (D-T) experiments has been performed successfully utilizing ICRF heating together with NBI heating at the TFTR. With combining LHCD and NBCD, current profile control experiment was proceeded in JT-60U. Both of these motivate one to investigate combining Alfvén wave and NBI heating and current drive. In addition, the recent choice by the ITER of fast wave current drive with $\omega<\omega_{ci}$ increases the importance of demonstrating and understanding low frequency current drive in tokamak. Especially, the Phaedrus-T tokamak has first demonstrated Alfvén wave current drive (AWCD) successfully[1]. Either combining Alfvén wave and NBI to heat plasma/drive current in tokamaks, or AWCD in an ignition tokamak, addresses an important issue concerned in the effects of energetic ions on Alfvén wave.

In the present work, we study the propagation and absorption of kinetic Alfvén wave (KAW) in the presence of fusion alpha particles in a D-T tokamak plasma. We examine the KAW eigenfunction — the wave structure in the cylindrical geometry. We take into account the effects of ion sound and transit time magnetic pumping (TTMP) related to the finite-β value, and discuss the influence of two different antenna structures, (l=2,m=-1) and (-2,1), on Alfvén wave heating (AWH), previous work[2] only considered the single mode (-2,1).

2. Model

The fundamental equation for the AWH with alphas is the three by three Ampère's law:

$$\nabla\times\nabla\times\boldsymbol{E}=\left(\omega^2/c^2\right)\left(\chi_p+\chi_\alpha\right)\cdot\boldsymbol{E}, \tag{1}$$

where $\boldsymbol{E}$ is the perturbed electric field and ω is its frequency. Because a D-T tokamak plasma has two components: the bulk plasma and the fusion alphas, χ_p and χ_α represent the physics of the bulk plasma response and the alphas response, respectively.

From the well-known low-frequency susceptibility tensor for a uniform plasma, a simple self-adjoint χ_p for the nonuniform plasma may be constructed[3], including the various important kinetic effects. It is noteworthy that in this work the effects of ion sound and TTMP are remained in $(\chi_p)_{//}$ and $(\chi_p)_{ii}$ (i=r,⊥). In the D-T tokamak plasma, the finite ω/ω_{ci} effect is

much smaller than the equilibrium current density gradient effect and may be dropped. The form for χ_α, on the other hand, is obtained[4] from the solution of the drift kinetic equation for circulating alpha particles (the effect of trapped particles being neglected). For convenience, the electric field $\boldsymbol{E}$ is decomposed into $\boldsymbol{E} = E_r\hat{r} + E_\perp \hat{b}\times\hat{r} + E_{//}\hat{b}$ where $\hat{b}=\boldsymbol{B}/B$ is the unit vector along the magnetic field $\boldsymbol{B}$ and $\hat{r}$ is the unit vector in the radial direction. Thus, Eq.(1) provides a unified kinetic description of the Alfvén wave heating plasma in the present of the alphas. It is solved numerically under appropriate boundary conditions.

In order to compare with our previous work[2], the geometry system, the equilibrium magnetic field and the equilibrium profiles of the bulk plasma are identical to that used in Ref.[2]. The alpha particle density profile is taken to be $n_\alpha(r)=n_{\alpha 0}(0)exp(-r^2/L_\alpha^2)$, where L_α is the alpha particle density gradient scale length. Both the slowing-down distribution[4] and Maxwellian distribution of the alphas are used in calculations.

3. Results

In cylindrical geometry, a set of three second-order differential equations in r for the perturbed fields E_r, $E_\perp$, and $E_{//}$ is numerically solved by means of a computational physics method developed by Qiu and Ding[5]. The Alfvén wave field structure, the absorption and the plasma impedance in the presence of the alphas for the TFTR parameters are given. Figure 1 shows the Alfvén wave structure of the (-2,1) mode in normalized radial position, with [see Fig.1(a)] and without [see Fig.1(b)] alphas. We find that the wave structures are changed remarkably by the alphas. On the one hand, the wave amplitude of the large rapidly varying parts of E_r and $E_{//}$ are decreased. On the other hand, the wave amplitude of the small rapidly varying parts of E_r and $E_{//}$ near the core are also decreased. These imply that the alphas obstruct the KAW propagating in the plasma interior, which leads to damped more quickly than that without alphas. It is worthwhile to point out that the compressional wave almost is not affected by the alphas. In a word, the influence of the alphas alters the propagation of the Alfvén wave in the D-T tokamak plasma. Furthermore, it decreases the KAW amplitude, which leads to the decrease in the energy deposition of the KAW.

Now let us consider the different mode numbers effect on the KAW heating in the presence of the alphas. Figures 2(a) and 2(b) present the most interesting results of the numerical computation, the real part of the plasma impedance, Z_r, plotted versus frequency normalized to the Alfvén continuum threshold (defined to be the minimum of $k_\parallel v_A$). For the (−2,1) mode [See Fig.2(a)], the alpha terms induce a reduction in the impedance. In particular, for the lower frequency, the effects of alphas on the impedance are remarkable. For the higher frequency, the influences of alphas tend to vanish, as discussed in Ref.2. For the (2,−1) mode [See Fig.2(b)], the Z_r-ω curve with smaller L_α, here $L_\alpha/r_p=0.3$, exhibits two sharp peaks which correspond to the destruction of the condition $\omega>(P_{m\pm1}/R_{m\pm1})^{-1}\omega_{*\alpha m}$, where $\omega_{*\alpha m}$ is the diamagnetic drift

frequency of the alpha particle, the terms $P_{m\pm1}$ and $R_{m\pm1}$ are the alpha particle contribution given in Eqs.(12a) and (12b) of Ref.2. These high peak impedance may be unusable for heating D-T plasmas because of the following two reasons. First, they are so sensitive to frequency that under experimental conditions they are found only with difficulty. Second, the frequency in the peak region is just unstable[4], that is $\omega<(P_{m\pm1}/R_{m\pm1})^{-1}\omega_{*\alpha m}$. However, as ω increases or for larger L_α, here $L_\alpha/r_p=0.4$, the impedance varying tends to smooth, which is corresponding to $\omega>(P_{m\pm1}/R_{m\pm1})^{-1}\omega_{*\alpha m}$.

4. Conclusion

The alphas tend to alter the Alfvén wave structure and energy deposition. We find that the presence of the alphas makes the KAW propagate toward the central region of the tokamak plasmas more difficultly and KAW's amplitude reduce. The absorption of KAW by the bulk plasma depends sensitively on both the velocity-distribution of alphas and the spatial profile of the alpha particle density as well as on the frequency of the injected wave. The calculations using both Maxwellian and slowing-down alpha distributions are performed, showing that, for the same alpha density and energy density, the slowing-down distribution more obviously affects and reduces the energy deposition of the KAW than the Maxwellian distribution. The energy deposition decreases rapidly as the total number of the slowing-down alphas increases and as the number near the resonant layer increases. The influences of the ion sound and TTMP on the KAW are remarkable. In addition, we point out here that for positive poloidal mode number m, $\omega_{*\alpha m}$ is negative and hence $\omega_{*\alpha m}<\omega$, whereas for negative m it is positive and hence $\omega_{*\alpha m}>\omega$ or $\omega_{*\alpha m}<\omega$. Our results indicate that the frequency of the injected wave within the range of KAW's continuum should be larger than the threshold $\omega_{*\alpha m}$ characterized by the alphas.

Reference

[1] N.Hershkowitz *et al.*, Proc.15th IAEA Conference on Plasma Physics and Controlled Fusion, Seville (IAEA, Vienna,1994), p.79.

[2] N. Ding, L. Huang, X.M. Qiu, and Y.X. Long, *Phys. Plasmas* **2**(5), 1529(1995).

[3] D.W. Ross, G.L. Chen, and S.M. Mahajan, *Phys. Fluids* **25**, 625 (1982).

[4] Y.M. Li, S.M. Mahajan and D.W. Ross, *Phys. Fluids* **30**, 1466 (1987).

[5] X.M. Qiu and N. Ding, *Nucl. Fusion Plasma Phys.* **8**,154 (1988). (*in Chinese*).

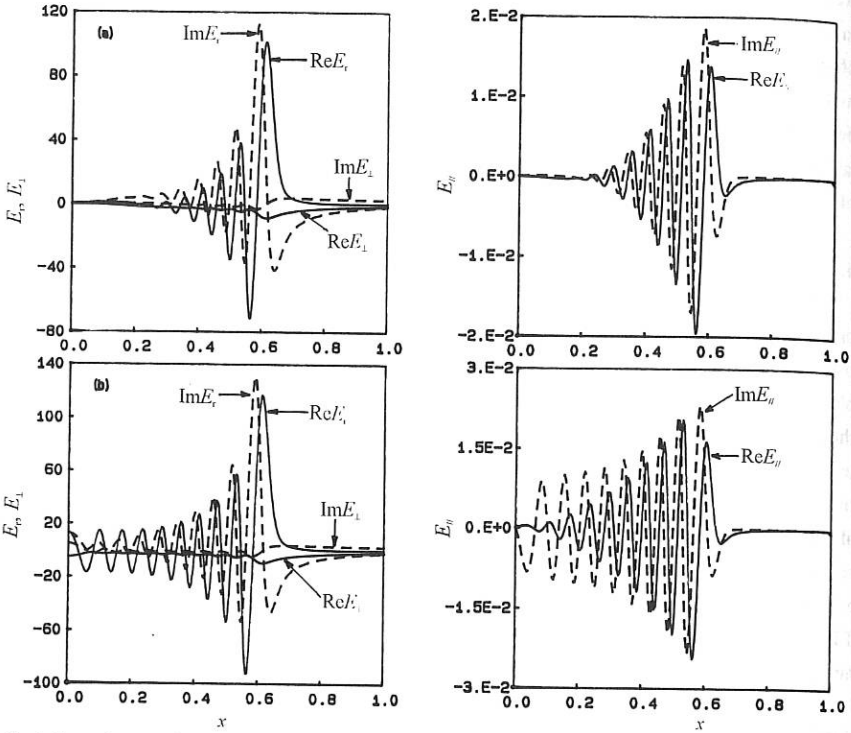


Fig.1. Typical wave electric field components E_r, $E_\perp$, and $E_{//}$ for the TFTR parameters, ω=0.6515 761×10^{-7}, m=1, l=-2. Position of resonant layer x_s=0.62. (a) with alphas; (b) without alphas

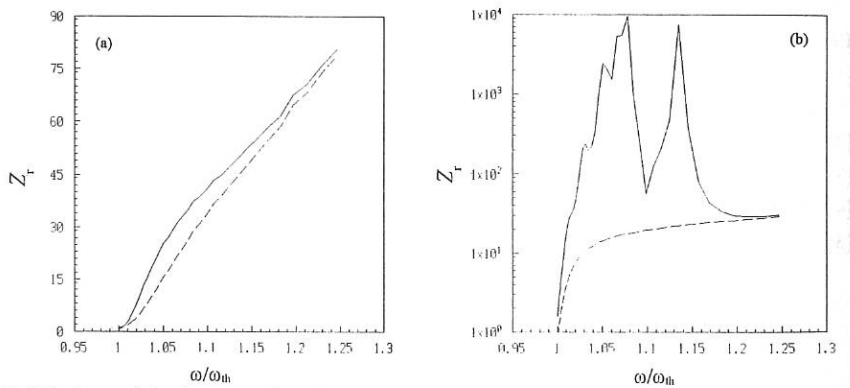


Fig.2 Real part of the plasma impedance Z_r versus normalized frequency ω/ω_{th} for (a) *the* (-2,1) *mode and* (b) *the* (2,-1) *mode. Solid line: L_α/r_p=0.3; dotted line: L_α/r_p=0.4. ω_{th}=0.7644 739×10^9.*

Interpretation of Ion Cyclotron Emission from Sub-Alfvénic Fusion Products in TFTR

R O Dendy, K G McClements, C N Lashmore-Davies, G A Cottrell[1], S Cauffman[2] and R Majeski[2]
UKAEA Government Division, Fusion, Culham, Abingdon, Oxon, OX14 3DB, UK
(UKAEA/Euratom Fusion Association)
[1]JET Joint Undertaking, Abingdon, Oxfordshire, OX14 3EA, UK
[2]Princeton Plasma Physics Laboratory, Princeton University, Princeton, New Jersey 08543, USA

1. Introduction

Ion cyclotron emission (ICE) has been observed during neutral beam-heated supershot discharges in the TFTR deuterium-tritium campaign at sequential cyclotron harmonics of fusion products [1]. The emission originates from the outer midplane edge plasma, where, during the initial phase of the discharge, fusion products are likely to have a drifting ring-type velocity-space distribution which is anisotropic and sharply peaked. The birth velocity of fusion products is smaller than the local Alfvén speed at the outer midplane in the TFTR supershot discharges considered here, in contrast to the situation for JET ICE observations [2]. In this paper it is shown that the magnetoacoustic cyclotron instability [3], which results in the generation of obliquely propagating fast Alfvén waves at low cyclotron harmonics of the fusion ions, can occur under TFTR supershot conditions. Moreover, the time evolution of the maximum growth rate closely follows the observed time evolution of ICE amplitude, averaged over several TFTR supershot discharges.

2. Mechanism for Ion Cyclotron Emission from TFTR

The magnetoacoustic cyclotron instability (MCI) with $k_{\|} \neq 0$ [3] provides the most likely emission mechanism for ICE at fusion alpha-particle harmonics observed in JET [2,3] and TFTR [1,4]. Free energy is provided by the distinctive non-Maxwellian velocity-space structure, localised to the outer midplane, that arises from the drift orbit characteristics of centrally-born fusion products with large Larmor radii [2-6]. In the locally uniform approximation, the MCI can be studied by solving the dispersion relation [3]

$$(\varepsilon_{xx} - k_z^2 c^2/\omega^2)(\varepsilon_{yy} - k^2 c^2/\omega^2) = -\varepsilon_{xy}^2 \qquad (1)$$

Here the dielectric tensor elements ε_{ij} are built up from contributions from thermal ions and electrons, responsible for numerous damping mechanisms, as well as from the fusion products. The drifting ring-type velocity distribution of the latter, appropriate to the outer mid-plane, can be modelled analytically by

$$f_\alpha = n_\alpha (2\pi^2 u v_{r\|} v_{r\perp})^{-1} \exp\{-(v_{\|} - v_d)^2/v_{r\|}^2 - (v_\perp - u)^2/v_{r\perp}^2\} \qquad (2)$$

The use of such models for the super-Alfvénic JET regime has yielded linear growth rates for the MCI that match observed ICE power in terms of spectral structure, spectral splitting, and scaling with fusion product concentration [2,3].

In TFTR supershots, fusion products at their birth energy are sub-Alfvénic at the outer midplane emission region. While the MCI as originally conceived with $k_{\|} = 0$ [7,8]

cannot operate in this regime, we have found that in the new theory with $k_{\|} \neq 0$ [3], Eqs (1) and (2) yield instability in the sub-Alfvénic case with parameters appropriate to TFTR [4]. The MCI is, however, less robust in the sub-Alfvénic regime: its growth rate is typically lower and, importantly, the MCI is more susceptible to termination by spreading of the fusion product population in velocity space (Fig 1). In contrast, the super-Alfvénic fusion products which are present in the outer midplane of JET can drive the magnetoacoustic cyclotron instability even if they are isotropic or have a relatively broad distribution of speeds [3,8,9]. These conclusions may help to explain the observation that fusion product-driven ICE in JET persists for longer than fusion product-driven ICE in TFTR supershot discharges.

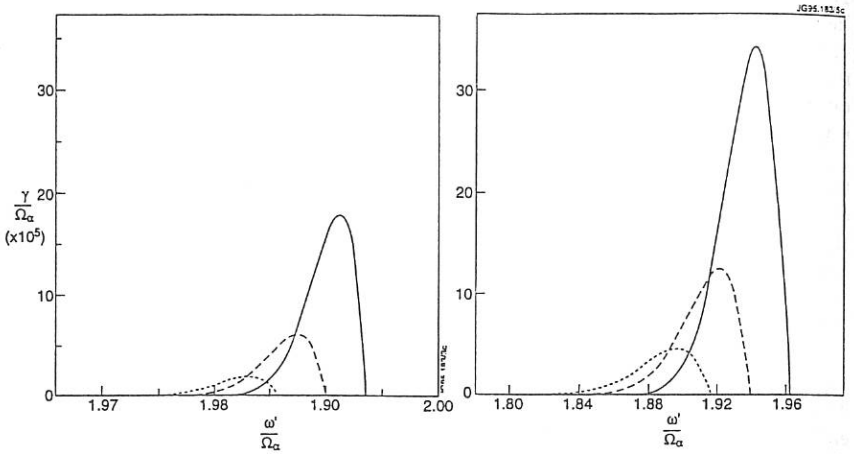


Fig 1: Linear growth rate of the MCI versus $\omega' = \omega - k_{\|} v_d$ for alpha-particles near the second cyclotron harmonic, for sub-Alfvénic $u/c_A = 0.5$ (left) and super-Alfvénic $u/c_A = 1.5$ (right) cases. Wave propagation angle $80°, \beta_i = 10^{-4}, n_\alpha/n_i = 10^{-4}, v_d/u = -0.5$ in both cases. Solid line: $v_{r\|}/u = 0.04$ (left), 0.1 (right); dashed line: $v_{r\|}/u = 0.05$ (left), 0.125 (right); dotted line: $v_{r\|}/u = 0.06$ (left), 0.15 (right) and $v_{r\perp} = v_{r\|}$ in all cases [4].

3. Time Evolution of Ion Cyclotron Emission in TFTR

The time variation of the linear MCI growth rate appropriate to a TFTR discharge can be calculated [4] by introducing time evolution, constrained by experimental data, into Eq (2). Specifically, $n_\alpha(t)$ follows the measured neutron source rate [10] and $v_{r\|}(t) \simeq v_{r\perp}(t)$ follows the velocity-space spreading calculated from Sigmar's model [11]. The latter is dominated by two physical effects: collisional slowing down of the alpha-particles and the

measured evolution of their birth rate. For an idealised isotropic population, Sigmar's model yields [4]

$$f_\alpha(v,t) \sim \frac{\sin^2\{\pi[t - T(v)]/2\tau_o\}}{v^3 + v_c^3} H(v - V(t))H(v_\alpha - v) \qquad (3)$$

Here $\tau_o = 500$ms is inferred from the TFTR neutron rate [10] which happens to fit a $\sin^2$ dependence, v_α is the birth velocity, v_c is the usual critical velocity, and $V(t)$ and $T(v)$ describe retardation [4,11]. Numerical evaluation of Eq (3) yields the time evolution of the full width at half maximum $\Delta v(t)$. Next we identify $\Delta v(t) = v_{r\|}(t) = v_{r\perp}(t)$ in our analytical representation Eq (2) of the fusion product distribution at the outer midplane. This yields time-dependent expressions, obtained by evaluating the standard kinetic integrals, for the dielectric tensor contribution of the fusion products. Inclusion of these in Eq (1), and numerical solution of the latter, gives the time evolution of the linear MCI growth rates. The latter closely matches the observed time evolution of the ICE power in TFTR (Fig 2).

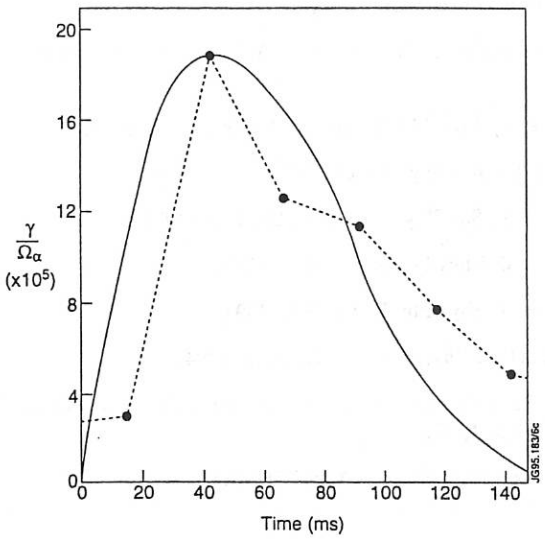


Fig 2: Data points: time evolution of ICE intensity at the ^{3}He cyclotron frequency, averaged over six TFTR discharges. Solid curve: linear growth rate of MCI using data from Ref [10] and the model of Ref [11] for velocity space evolution [4].

4. Conclusions

A single emission mechanism, the magnetoacoustic cyclotron instability [3,4], appears to be responsible for ion cyclotron emission from fusion products in JET [2] and TFTR [1].

Differences in the observed characteristics of ICE between JET and TFTR, including the time evolution of ICE in TFTR, are explicable in terms of the properties of this instability. The mechanism is distinct from that responsible for ICE from injected beam ions in TFTR [12]. Measurements of fusion alpha-particle ICE from TFTR under regimes resembling those on JET are continuing at present [1], and lend further support to the interpretation in terms of the specific collective instability presented here.

5. Acknowledgements

This work was funded jointly by the US Department of Energy (under Contract No DE-AC02-76CH03037), the UK Department of Trade and Industry, and Euratom.

References

[1] S Cauffman, R Majeski, et al, this Conference.

[2] G A Cottrell et al, Nucl Fusion **33**, 1365 (1993).

[3] R O Dendy et al, Phys Plasmas **1**, 1918 (1994).

[4] K G McClements et al, Report UKAEA FUS 280, submitted to Phys Plasmas (1995).

[5] V S Belikov et al, Proc IAEA Conf Innsbruck, **1**, 561 (1978).

[6] T E Stringer, Plasma Phys **16**, 651 (1974).

[7] V S Belikov et al, Sov Phys Tech Phys **20**, 1146 (1976).

[8] R O Dendy et al, Phys Fluids B**4**, 3996 (1992).

[9] R O Dendy et al, Phys Fluids B**5**, 1937 (1993).

[10] J D Strachan et al, Phys Rev Lett **72**, 3526 (1994).

[11] D J Sigmar, Proc Varenna Course on "Physics of Plasmas close to Thermonuclear Conditions" 1979, **1**, 271.

[12] R O Dendy et al, Phys Plasmas **1**, 3407 (1994).

Modelling Collective Losses of Energetic Particles

H L Berk, B N Breizman, J Fitzpatrick,[1] M Pekker, F Porcelli,[2] and H V Wong
Institute for Fusion Studies, The University of Texas, Austin, TX 78712

Instabilities due to shear Alfvén-like modes such as the TAE and fishbones, have been observed in several experiments. A critical question arises, particularly under fusion conditions, as to how such modes can effect containment of the energetic particles that are generating the instability. We have developed a self-consistent nonlinear theory that is based on the principles of weak turbulence theory for a discrete set of modes. The essential aspect of the theory is to accurately follow the dynamics of resonant particles. The critical issue is whether resonance overlap arises due to the growth of unstable waves. If it does not, modes saturate at a rather low level due to local flattening of the distribution function, without otherwise significantly affecting the global energetic particle distribution function. If resonance overlap occurs, the wave energy can explosively amplify to a level that causes global diffusion of the resonant energetic particle, possibly giving rise to significant particle loss.

These processes have been modelled in several computer codes. One code is based on deriving a self-consistent set of mapping equations for both the resonant particles and the waves. This model has verified the theoretical picture for the paradigm problem of the bump-on-tail instability, and is now being run for an Alfvén problem with energetic particles. Results relating of mode saturation with and without resonance overlap are discussed.

A complementary approach is the development of a quasilinear code, that can simulate both overlapping and non-overlapping regimes. This code can also exhibit a pulsating response to the instability.

The simulation results are obtained from a numerical code that follows the interaction of resonant particles with linear waves, based on a self-consistent wave-particle Lagrangian mapping approach. By using action-angle variables for the unperturbed energetic particle and linear Alfvén modes, we reduce the basic Lagrangian to the following form

$$L = \sum_{\text{particles}} \left[p_\theta \dot{\theta} + p_\phi \dot{\phi} - H(p_\theta, p_\phi) \right]$$

$$+ \sum_{\text{modes}} \dot{\alpha} A^2 + 2\,\mathrm{Re} \sum_{\substack{\text{particles} \\ \text{modes}}} A V_\ell(p_\theta, p_\phi) \exp\left[-i\alpha - i\omega t + in\phi + i\ell\theta \right].$$

Here θ and ϕ are the generated poloidal and toroidal angles and p_θ and p_ϕ their canonical momenta; $H(p_\theta, p_\phi)$ is an unperturbed guiding-center Hamiltonian; A and α are the mode

[1]permanent address: University of California, Berkeley, U S A
[2]Politecnico di Torino, Italy

amplitude and phase, ω and n are the mode frequency and toroidal number; and $V_l(p_\theta, p_\phi)$ is the matrix element that describes the wave particle interaction [for a given mode structure $V_l(p_\theta, p_\phi)$ is a known function of p_θ and p_ϕ]. From this Lagrangian, we construct an area-preserving map that allows the energetic particles to be rapidly processed on the time scale of the inverse instability growth rate; this is much more efficient than following the particle dynamics on the inverse mode frequency time scale. Background wave damping, particle sources, and classical relaxation processes are superimposed on this map to allow appropriate simulation of the collective transport of the alphas on an experimental time scale. The particle source is included in the code by modifying the macro-particle weighting, rather than by introducing new particles. A similar approach can be used to simulate the classical relaxation processes.

The simulation results show that either benign or an "explosive" response can arise depending on the parameters that define the problem. In the benign case the distribution flattens locally in phase space. If $\omega_n^*/\omega \gg 1$ (ω_n^* is the hot particle drift frequency) the distribution flattens radially at the resonance position at fixed energy. Figure 1 shows this flattening due to pulsations when there is no mode overlap. With a slight change of parameters, this mode produces overlap, with a larger release of wave momentum. The excess wave momentum is extracted from the canonical momentum stored in the distribution function. We see in Fig. 2 that particle distribution flattens over the three modes present in this simulation. For N modes, the wave-momentum release increases by a factor of N^2 compared with the non-overlap case.

These simulations results suggest how a quasilinear model can be constructed to give realistic self-consistent saturation levels when modes do not overlap, and give self-consistent diffusion when modes do overlap. We now have results of a quasilinear model for a one-dimensional distribution function, where the resonance width of each mode is comparable to the separatrix width of the particle interaction. This model is capable of demonstrating a "domino" effect, where the excess free energy of a few overlapped modes allows more widely spaced neighboring modes to overlap. This case is shown in Figs. 3 and 4. In Fig. 3 we see the mode widths, which is proportional to $A^{1/2}$, where A is the mode amplitude rapidly broaden once mode overlap is achieved. This leads to a loss of particles to the edge. This is seen in Fig. 4, where we plot the distribution as a function of $x \equiv 1 - V/V_{\max}$ and the relative time $\gamma_L\, t$.

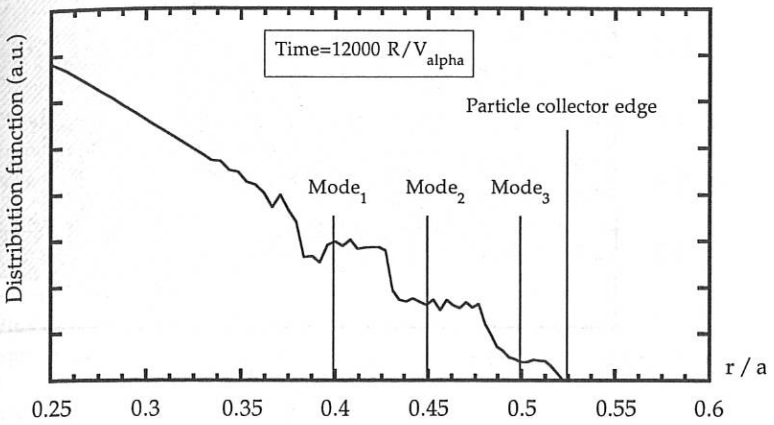


Fig.1. Snapshot of the particle distribution function without mode overlapping.

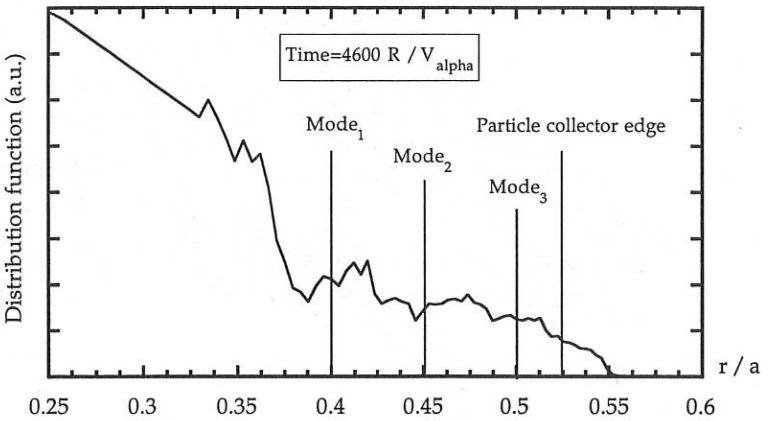


Fig.2. Snapshot of the particle distribution function with mode overlapping.

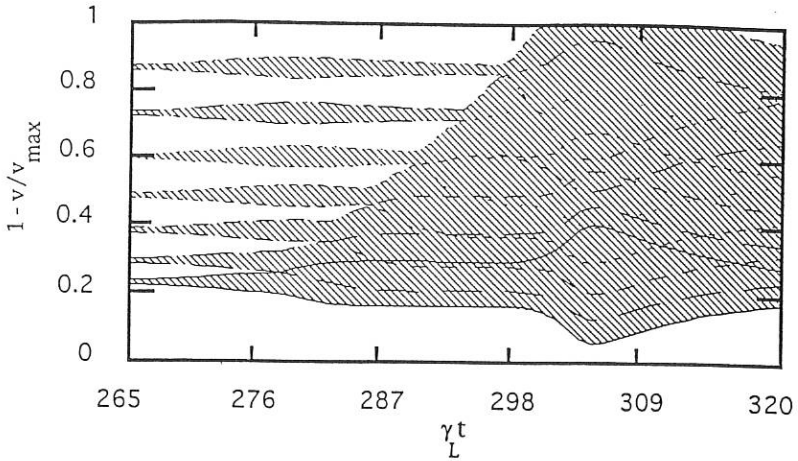


Fig. 3. Time evolution of resonance widths (shaded areas) for a multi-mode system in which mode overlap leads to the domino effect. The curves, in different line styles, show the limits of individual resonances.

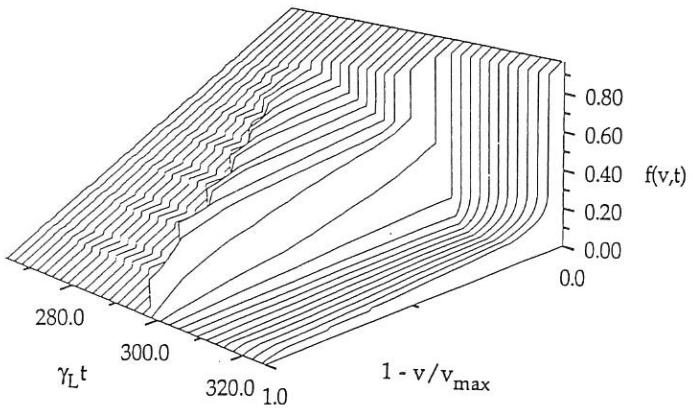


Fig. 4. Time evolution of distribution function during domino effect of Fig. 3.

KINETIC TOROIDICITY INDUCED ALFVÉN EIGENMODES IN TOROIDAL SHAPED PLASMAS

D.Borba, J.Candy, H.A. Holties*, G.T.A. Huysmans, W. Kerner, S. Sharapov**.

Jet Joint Undertaking, Abingdon, Oxfordshire OX14 3EA, UK,
*FOM Institute for Plasma Physics Rijnhuizen, Nieuwegein the Netherlands,
**RRC Kurchatov Institute, Moscow, Russia

ABSTRACT

The MHD model including first order finite Larmor radius effects of core ions and finite longitudinal electric field is used to compute both the radiative damping and the eigenfrequencies of the Kinetic Toroidicity induced Alfvén Eigenmodes in toroidal plasmas.

INTRODUCTION

The physics of weakly-damped Alfvén modes has been long recognised to be crucial for the confinement of fusion born alpha particles in a tokamak reactor. Within the framework of ideal magnetohydrodynamics (MHD) much attention has been given to the Toroidal Alfvén Eigenmode (TAE), whose eigenfrequency lies in the shear-Alfvén continuum gap. As the TAE eigenfrequency does not satisfy the local Alfvén resonance condition, it is more weakly damped than usual cylindrical shear-Alfvén waves, and therefore it can be more easily destabilised by resonant alpha-particles. In hot plasmas, Finite Larmor Radius (FLR) effects[1] convert the TAE mode energy into Kinetic Alfvén waves increasing the outgoing wave energy flux significantly; i.e., the overall damping of the mode via radiative damping. On the other hand for high plasma temperatures, a new branch of Kinetic Toroidal Alfvén Eigenmodes (KTAE) appears and can be driven unstable by energetic particles. Both the radiative damping and the eigenfrequencies of the KTAE spectrum are very sensitive to the plasma parameters. In particular, toroidal and shaping effects in the plasma equilibrium are important.

In this paper the KTAE spectrum is computed for toroidal plasmas with an arbitrary shape including realistic JET scenarios. The FLR kinetic effects and parallel electric field effects are included in the toroidal linear MHD spectral code CASTOR. This model allows one to compute effectively the KTAE spectrum and the radiative damping of TAE and KTAE for arbitrary plasma configurations as a function of the relevant FLR parameter. Included in this spectrum are two types of core localised modes[2], which may be particularly dangerous to plasma confinement as they are peaked near the plasma centre where the drive from fusion alphas or RF ions is strongest. We calculate the radiative damping of the lower frequency mode, and also describe the transition of the upper frequency mode into a KTAE. These results indicate a strategy for a systematic experimental[3] study of the KTAE spectrum.

MHD MODEL INCLUDING FIRST ORDER FINITE LARMOR RADIUS EFECTS

In the outer region away from the resonance surface both KTAE and TAE can be described by the ideal MHD equation, which reduces to a vorticity equation

$$L\phi = b\cdot\nabla\left(\nabla_\perp^2 b\cdot\nabla\right)\phi + \nabla\cdot\left(\frac{\omega^2}{V_A^2}\nabla_\perp\right)\phi = 0\,.$$

Here, ω is the eigenfrequency, v_A the Alfvén velocity, b the equilibrium magnetic field and ϕ is the TAE/KTAE perturbated potential. First order FLR effects of core ions and a finite longitudinal electric field modify the vorticity equation in the boundary layer around the TAE resonance region. These corrections have been calculated in detail by Rosenbluth and Rutherford[4] and lead to the modified current equation:

$$\nabla\cdot j \cong -\frac{3}{4}\frac{i\omega\rho}{B^2}\rho_s^2\nabla_\perp^4\phi - \frac{i}{4\pi\omega}(b\cdot\nabla)\nabla^2 E_{||}\,,\ \text{with}\ E_{||} \cong -i\rho_s^2(1-i\delta)(b\cdot\nabla)\nabla^2\phi\,.$$

The vorticity equation equation takes the form:

$$b\cdot\nabla\left(\nabla_\perp^2 b\cdot\nabla\right)\phi + \nabla\cdot\left(\frac{\omega^2}{V_A^2}\nabla_\perp\right)\phi + \frac{1}{4\pi\omega}\rho_s^2(1-i\delta)(b\cdot\nabla)\nabla_\perp^2(b\cdot\nabla)\nabla^2\phi + \frac{3}{4}\frac{\omega^2}{V_A^2}\rho_i^2\nabla_\perp^4\phi = 0\,.$$

The structure of this equation is analogous to the structure of the resistive MHD equations with a general complex parameter η defined by: $\eta = 4\pi\omega\rho_s^2\delta\left(\upsilon_e\right) + i4\pi\omega\left(\frac{3}{4}+\frac{T_e}{T_i}\right)\rho_s^2$

For typical of JET parameters, e.g. $\mathrm{Im}[\eta] = 4.4\ 10^{-2}\ T_i[Kev]\ n_e^{-0.5}[cm^{-3}]\ B_T^{-1}[T]$, it is convenient to express η in normalized units $\mathrm{Im}[\tilde{\eta}] = \frac{\mathrm{Im}[\eta]}{\mu_0 R_m V_A} \approx 5.3\ 10^{-10}\frac{T_i[eV]}{B^2[T]}$, which gives $\mathrm{Im}[\tilde{\eta}] \approx 10^{-6}$ in JET auxiliary heated discharges.

KTAE SPECTRUM IN TOROIDAL GEOMETRY USING THE CASTOR CODE

The CASTOR code computes dissipative MHD spectra for arbitrary 2D axisymmetric equilibria. Kinetic modifications to MHD can be modelled by CASTOR within reasonable accuracy by introducing the complex parameter η in the induction equation. In this fashion, a correct result is obtained for normal modes localised in the gap region. Furthermore the coupling between the TAE modes and kinetic Alfvén waves yields the conversion of TAE energy into Kinetic Alfvén waves inside the gap region. Although the propagation of kinetic Alfvén waves across the entire plasma cross-section is not accurately described, the energy transfer from the TAE mode to the KAW is reasonably accurate in this model and since these kinetic waves are strongly damped the radiative damping is well described within this approximation. Applying the Castor code to a reconstructed JET equilibrium, the KTAE spectrum was computed for the shot #34188. In this pulse #34188 several modes were observed

during RF heating by the Active Alfvén diagnostic in the passive mode. The modelling shows the existence of two sets of KTAE's with toroidal wave number n=3, one set localized in the central gap and the second set at a minor radius of r=0.5. The central set consists of n=3 KTAEs which are particularly undamped and localized where the RF ion drive is strongest. The frequency of the modes is within 10% of the experimental values and their spacing also agrees with the experimental results using $\mathrm{Im}[\tilde{\eta}] \approx 10^{-6}$ in the modelling. Both branches exhibit equally spaced modes and the damping increases linearly with radial wave number p, for the first branch. For the second branch the damping depends strongly on the mode parity.

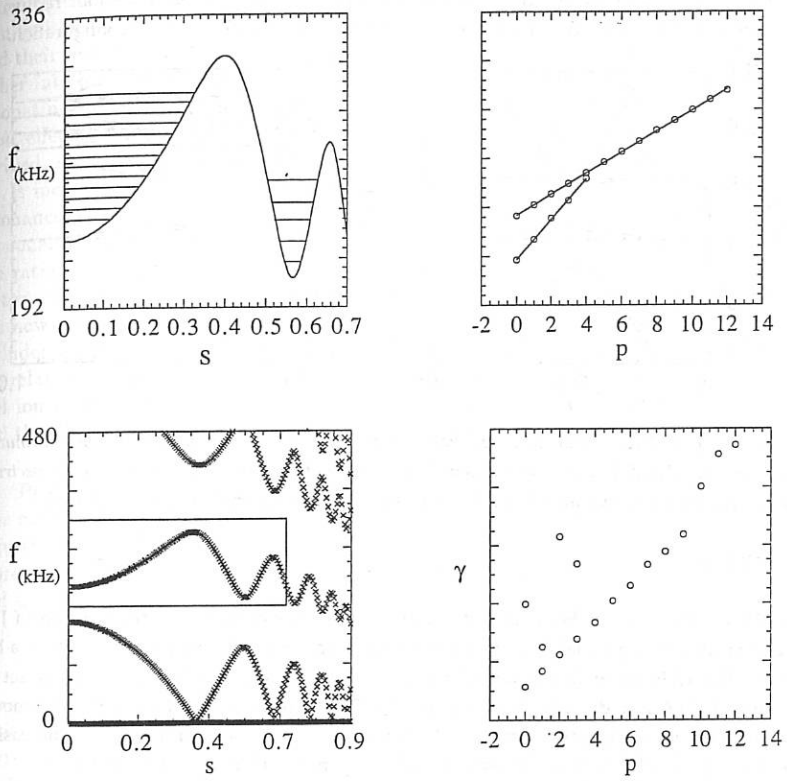


Figure 1 a) KTAE spectrum for the shot #34188 b) frequency of the KTAE modes as function of radial mode number c) continuous spectrum for the shot #34188 d) radiative damping of the KTAE modes as function of radial mode number.

CORE LOCALIZED MODES

Both in TFTR and JET equilibria there exist core localized modes in the low shear and large aspect ratio region. These types of modes can be dangerous to plasma confinement as they are peaked near the plasma center where the drive from alpha particles or radio frequency heated ions is strongest. The FLR effects on the core localized modes can be studied using CASTOR. For this purpose a low shear, large aspect ratio circular equilibrium with a linear q profile varying from q=1 to q=1.25 is introduced, which contains a single gap for n=3 modes. The upper mode does not have significant radiative damping with increasing Larmor radius, in contrast with the lower mode. The KTAE spectrum appears in the hot plasma configuration.

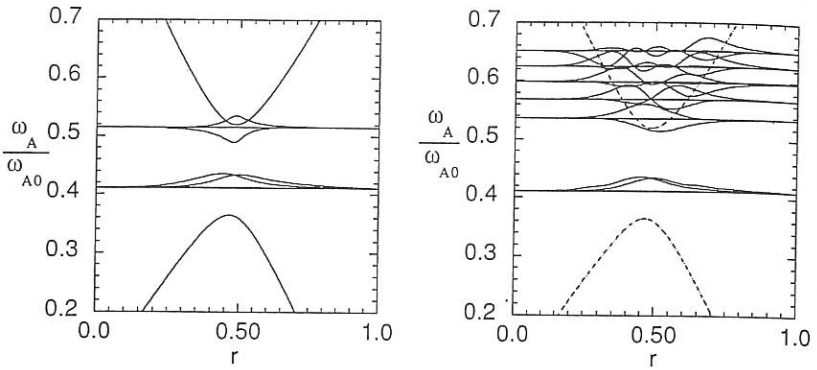


Figure 2 Two n=3 core localized modes that exist in a COLD plasma, In addition the continuous spectrum is displayed, b) the n=3 spectrum for an equivalent HOT plasma, the continuum spectrum (dotted line) is replaced by a discrete KTAE spectrum. The eigenmode structure is also displayed

CONCLUSIONS

The KTAE spectrum has been computed in toroidal geometry using a reconstruction of JET equilibria. In a cold plasma one or possibly two core localized TAE modes exist, while in a hot plasma the TAE mode has increased radiative damping $|\gamma_{TAE}| > 10\ |\gamma_{KTAE}|$, and a set of undamped KTAE modes appear just above the TAE gap. In a JET hot plasma the model predicts the existence of a set of low n KTAE modes with equally spaced frequencies increasing linearly with radial mode number p and with linearly increasing radiative damping

REFERENCES

[1] J.W. Connor, et al, in Controlled Fusion and Plasma Physics Vol 18 B Part II 616 (1994) [2] G.Y. Fu, et al, Submitted to Phys. Plasmas. [3] A Fasoli, et al, I.A.E.A International Conference Seville, September (1994) [4] M.N.Rosenbluth, et al, Phys.Rev. Lett 34 1428,(1975)

Modelling the Expulsion of Helium Ash from Tokamaks at the Precessional Drift Resonance

R O Dendy, C G Gimblett, B M Harvey, R J Hastie, **K F Kam** and T J Martin
UKAEA Government Division, Fusion, Culham, Abingdon, Oxon, OX14 3DB, UK
(UKAEA/Euratom Fusion Association)

1. Introduction

Burning fusion plasmas will rely on collisional heating by confined alpha particles to sustain ignition. Once they have slowed down, however, such particles constitute Helium ash and their removal may be necessary in order to reduce fuel dilution. MHD perturbations, either internally generated or externally applied, could in principle perform this role by resonating with the natural frequencies of trapped alpha particles, giving rise to secular orbit effects. We study this mechanism for the expulsion of Helium ash using equations derived via a Hamiltonian formulation pioneered by Boozer, White and co-workers [1-4]. It includes in principle the potential occurrence of a double resonance: a frequency resonance which occurs when the perturbation frequency matches the local toroidal precessional drift frequency of an alpha-particle; and a spatial resonance which occurs when the ratio of poloidal and toroidal mode numbers matches the local value of the safety factor. This study describes results obtained when these processes are modelled using the new toroidal guiding centre orbit-following code TAROT. The questions addressed include: the width of the region of enhanced diffusion in velocity space and real space; the relative strength of the impact of this pumping mechanism on Helium ash and on the fuel ion population; the dependence on the radial structure of the MHD perturbation; and the distribution of point-of-loss in poloidal angle.

2. Perturbed Guiding Centre Orbits

Our code TAROT solves a system of coupled differential equations derived, with minor adjustments, from the Hamiltonian approach of Refs [1-4]. The magnetic perturbation is represented by $\delta \boldsymbol{B} = \nabla \times \alpha \boldsymbol{B}$ where $\boldsymbol{B}$ is the axisymmetric equilibrium magnetic field and α is a scalar function of position,

$$\alpha = \sum_{m,n} \alpha_{nm}(\psi) \sin(n\phi - m\theta - \omega_{nm} t - \delta_{nm}) \qquad (1)$$

Here $\psi = r^2/2$ for circular flux surfaces where r is the minor radius, ω_{nm} is the perturbation frequency, m and n are the poloidal and toroidal mode numbers, and $\alpha_{nm}(\psi)$ is a perturbation amplitude profile. Incorporation of $\delta \boldsymbol{B}$ and its associated electric potential Φ [1] in the guiding centre Hamiltonian leads to a direct formulation of the resulting perturbation of the equilibrium toroidal orbits. Figure 1 shows the secular rapid expulsion of a trapped 100keV alpha particle with precessional drift frequency ω_p when the exact resonance condition $\omega_{nm} = \omega_p(\psi)$ is achieved. The alpha particle drifts out of the plasma with constant average radial velocity. This strong effect is not restricted to exact frequency resonance and, depending on the size of the perturbations, particles within a range of perpendicular energies (hence, with different ω_p) can also be expelled rapidly from the plasma. Even quite far from exact resonance, with $|(\omega_{nm} - \omega_p)/\omega_p| < 0.2$, the alpha

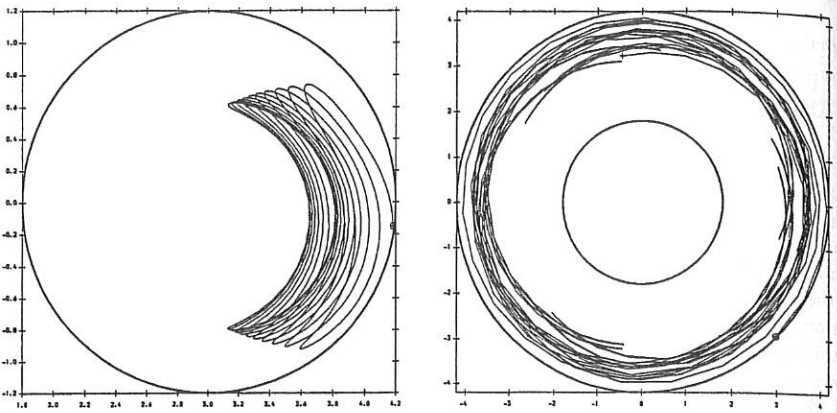


Fig 1: Expulsion of a trapped 100keV Helium ash particle at exact drift precessional frequency resonance with an external magnetic perturbation. Poloidal (left) and toroidal (right) orbit projections.

particle's radial position oscillates sinusoidally (2) at a frequency equal to the difference between the applied and precessional frequencies, and with an amplitude inversely proportional to this frequency difference. Thus, the radial excursion is often significantly enhanced over that of an unperturbed orbit, and this increases the diffusion of the particles substantially when collisions are included.

3. Helium Ash Pumping

The effect of selectively applied external magnetic perturbations on Helium ash transport has been quantified both in terms of the time taken to leave the plasma and as a quasi-diffusive process. Ensemble-averaged results show the following general features. (1) Typical effective loss times are a few milliseconds depending on mode amplitude and other factors. (2) There are two separate pitch angle ranges where 100keV Helium ash particles are lost from the plasma. This is an unexpected result which has not been predicted from previous analytical approaches. (3) Particles with greater pitch angles leave the plasma most rapidly. This occurs because they are more deeply trapped, giving rise to better-defined resonance because of their restricted spatial excursion. This effect is so strong that it can overcome pronounced frequency mis-match. (4) It is easy to select perturbation amplitudes and frequencies such that the impact on fuel ions is negligible. (5) The Helium ash flux is localised in poloidal angle near the outer mid-plane. For deeply trapped particles it peaks at $\pm 10°$, with a small flux at $0°$, whereas for less deeply trapped particles the flux is negligible for $-5° < \theta < 5°$ and peaks in the range $\pm(15° - 20°)$.

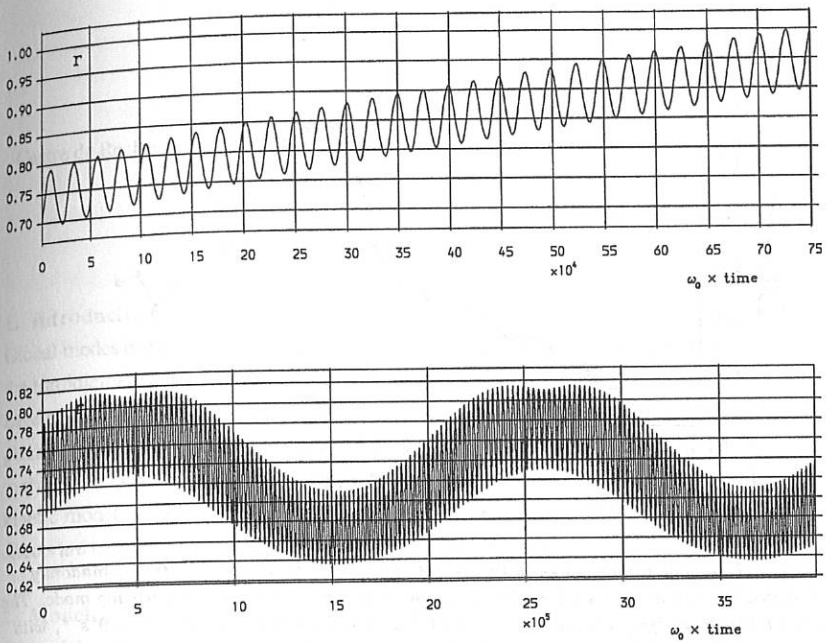


Fig 2: Time evolution of minor radial coordinate of a trapped 100keV Helium ash particle at exact precessional drift frequency resonance (upper) and 15% off-resonance (lower) with an external magnetic perturbation; ω_0 denotes cyclotron frequency.

4. Effect of Tearing Modes on Helium Ash

The diamagnetic frequency ω_* associated with tearing modes can satisfy $\omega_* \simeq \omega_p$: for 10keV bulk deuterons and deeply trapped 100keV Helium ash we find $\omega_*/\omega_{p\alpha} \simeq 0(m/q(r))$ so that frequency resonance is possible. We have used numerical solutions of the linear tearing mode equation [5] to determine the form of α in Eq (1) for use in TAROT. The spatial resonance $q(r_s) = m/n$ is handled using magnetic island flattening [1], $(n - m/q)^{-1} \rightarrow (n - m/q)[(n - m/q)^2 + \Delta_{nm}^2]^{-1}$ where Δ_{nm} matches the standard island width equation [5]. Figure 3 shows the local enhancement of Helium ash diffusivity that can occur near the mode rational surface at frequency resonance.

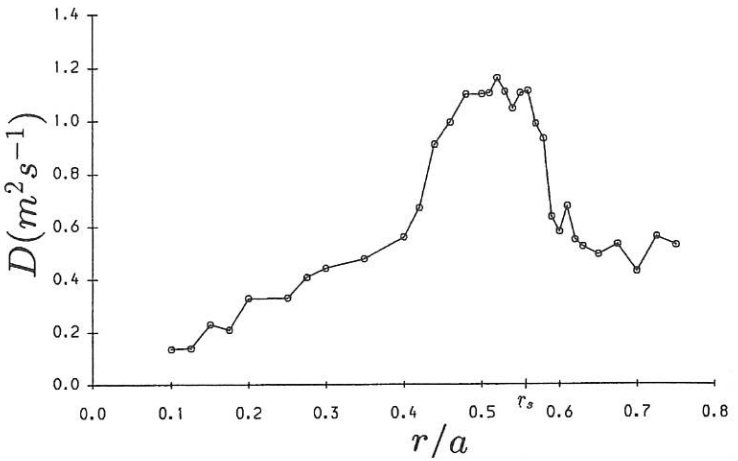


Fig 3: Ensemble-averaged local diffusion rate of 100keV Helium ash particles, randomly distributed in pitch angle, as a function of minor radius in the presence of a tearing mode. The mode has $m/n = 2/1$, maximum $\delta B/B = 10^{-3}$ and toroidal frequency $\omega_{nm} = -10^4 s^{-1}$, with mode rational surface at r_s shown.

5. Conclusions

We have quantified the way in which externally applied and internally generated magnetic perturbations satisfying $\omega_{nm} \sim \omega_p$ affect the transport and confinement of Helium ash in tokamaks. In particular, Helium ash loss can be made selective in velocity-space, fuel ions need not be affected, and the distribution of point-of-loss is poloidally localised. Tearing modes may create significant local enhancements of Helium ash diffusion.

References

[1] R B White, R J Goldston, K McGuire, A H Boozer, D A Monticello and W Park, Phys Fluids **26** 2958 (1983).

[2] A H Boozer and R B White, Phys Rev Lett **49** 786 (1982).

[3] R B White, A H Boozer and R Hay, Phys Fluids **25** 575 (1982).

[4] A H Boozer, Phys Fluids **23** 904 (1980).

[5] J A Wesson, Nucl Fusion **18** 87 (1978).

Non Perturbative Kinetic Effects on Alfvén Eigenmodes in Tokamak Plasmas

A Jaun, **K Appert**, J Vaclavik and L Villard
Centre de Recherches en Physique des Plasmas, Association Euratom - Confédération Suisse
Ecole Polytechnique Fédérale de Lausanne
Av. des Bains 21, 1007 Lausanne, Switzerland

1. Introduction

Global modes of the Alfvén wave exist in tokamaks because of the equilibrium current (GAE), the toroidicity (TAE), the pressure (BAE) and the shaping of the plasma (EAE). These modes have already been studied numerically [1,2,3] using either cylindrical kinetic or toroidal fluid plasma models; comparisons with experiments showed however important limitations and led to the recent development of the toroidal PENN code [4], which includes a resistive fluid and a kinetic model based on a finite Larmor radius (FLR) expansion. Using this new tool, kinetic effects are here studied for a GAE mode in a medium size tokamak.

2. Model

To model the propagation of Alfvén waves in a tokamak, a general MHD equilibrium is first computed using the CHEASE code [5] and the geometry extended further into a vacuum region limited by a perfectly conducting wall. The linear field perturbations expressed in terms of the electromagnetic potentials $(\mathbf{A},\Phi)$ are then obtained for a given model of the dielectric tensor.

The fluid plasma model [6] has been derived in the frame of resistive MHD, assuming that the resonant wave-particle interactions and the Larmor excursion of the particles remain negligible. The more sophisticated kinetic approach [7] is based on a finite Larmor radius (FLR) expansion and takes both of these effects into account: it provides a consistent description of the Landau damping and allows for conversion to either the kinetic Alfvén wave (KAW) or the surface quasi-electrostatic wave (SQEW), depending on whether the ratio between the parallel phase velocity of the wave and the thermal speed of the electrons $\omega/(k_{//}v_{th,e})$ is smaller or bigger than unity.

The oscillating helical antenna current driven inside the vacuum region serves to calculate the response of the cavity and to check the consistency of the numerical solution using the balance between the power absorbed by the plasma, the energy flux and the antenna load.

3. GAE mode in the TCA tokamak

A force-free equilibrium of circular cross-section is defined with the parameters R_0=0.61 m, R_0/a=3.39, R_W/a=1.167, B_0=1.5 T, q_0=1.05, q_a=4.55, $n_e=n_D=5.2\times10^{19}(1-0.98s^2)^{0.7}$ m^{-3}, $T_e=2T_D=T_0(1-0.84s^2)$ eV reminding the TCA experiment [9], except for the rather flat temperature profile which has been chosen to avoid conversion to an SQEW at the plasma edge. A helical antenna current (n=-2, m=-1) is driven in the vacuum region half way between the plasma edge and the perfectly conducting wall .

Using first the fluid model to calculate the plasma response, a generator frequency scan illustrated in fig.1 reveals the presence of a GAE mode at 2.38 MHz and the edge of the continuum at 2.41 MHz. Apart from the global m=-1 structure in the center which is characteristic for this mode, the fluid wavefield in fig.2 shows that several Alfvén resonances are simultaneously present at radial positions s=0.79, 0.88, 0.93, 0.96, 0.97, 0.985 and yield a continuum damping of $|\gamma/\omega| \cong 0.75\%$ via resonant absorption.

The same study is then repeated with the kinetic model for an electron temperature increasing from T_0=400, 600, 800 eV to 1 keV. Fig.1 shows that the GAE mode is first clearly found at 2.32 MHz, but is then up-shifted to 2.33 and 2.37 MHz before it disappears completely for the highest temperature. Although it is difficult to measure the damping rate precisely, approximate values obtained for the three lowest temperatures give $|\gamma/\omega| \cong 1$, 1.5 and 2.6% which are an order of magnitude higher than those predicted by cylindrical FLR models [9]. Combined with a Fourier analysis of the kinetic wavefields, fig.2 suggests how toroidal FLR effects damp the GAE mode via two different mode conversion processes.

At T_0=400 eV, the global GAE wavefield is clearly dominant inside and its radial extension agrees remarkably well with the fluid result. Unlike for the fluid model, short wavelength oscillations appear between s=0.55 and the center, with poloidal Fourier amplitudes m=-1 increasing, and m=0, +1 decreasing towards the center. A comparison with the local dispersion relation indicates that these oscillations correspond to a KAW. The innermost Alfvén resonance is at s=0.79, but no conversion takes place there. Therefore, we interpret the existence of the kinetic wavefield between s=0.55 and the center as a result of the toroidal coupling between the global wavefield and the KAW. This *non-perturbative* interaction (in the sense that it cannot be obtained perturbatively from a toroidal fluid model because the finite-Larmor radius effects are a *singular perturbation*) is strongest at s=0.55 where $R_0/a \cong 6$ is still not very large. The KAW is subsequently damped by electron Landau damping as it propagates towards the center. This whole process has been called *radiative damping* in ref.[10].

Increasing the temperature to T_0=600 eV, brings the ratio $\omega/(k_{//}v_{th,e}) \cong 0.5$ at s=0.9 down to 0.37, so that the conversion begins to be possible at the outer resonances: the KAW does however still not propagate very far and the global mode damping is probably still dominated by the Landau damping of the KAW in the plasma core.

At T_0=800 eV and 1 keV, this ratio is further reduced to 0.32 and 0.29, so that the mode conversion taking place at the resonances becomes strong enough that it drowns the GAE mode character in the center, damping out the peak in the plasma response (fig.1).
Despite the qualitative difference between the fluid and the kinetic results, both predict GAE damping rates which are in good agreement with the experimentally observed $|\gamma/\omega| \cong$ 1-2%. The single fact that this value remained constant during all the years of exploitation of TCA speaks however strongly in favor of the non-perturbative damping process in the plasma core, where the parameters remained much more similar from shot to shot than in the edge region.

4. Conclusion

An analysis has been carried out for the GAE mode observed in the TCA tokamak. Both, the fluid and the kinetic models implemented in the toroidal PENN code predict frequencies and dampings which are in good agreement with the experiment. Using the fluid model, the GAE mode is located in the plasma core and damped via resonance absorption in the plasma exterior. With the kinetic description, two conversion mechanisms lead to the Landau damping of a KAW: one is the counterpart of the fluid models' resonance absorption and occurs in the external parts of the plasma; the other has no such fluid correspondance, and is induced non perturbatively in the plasma core through toroidal coupling between the global GAE wavefield and the KAW.

Acknowledgments

This work was supported in part by the Swiss National Science Foundation.

References

[1] Appert K, Gruber R, Troyon F, Vaclavik J, *Plasma Physics* **24** (1982) 1147
[2] Cheng C Z, Chance M S, *Phys.Fluids* **29** (1986) 3695
[3] Heidbrink W W, Strait E J, Chu M S, Turnbull A, *Phys.Rev.Lett.* **71** (1993) 885
[4] Jaun A, Appert K, Vaclavik J, Villard L, *submitted to Comput.Phys.Commun.*
[5] Lütjens H, Bondeson A, Roy A, *Comput.Phys.Commun.* **69** (1992) 287
[6] Vaclavik J, Appert K, *Nucl.Fusion* **31** (1991) 1945
[7] Brunner S, Vaclavik J, *Phys.Fluids B* **5** (1993) 1695
[8] Collins G, Hofmann F, Joye B, *Phys. Fluids* **29** (1986) 2260 and references cited therein.
[9] Appert K *et all., Plasma Physics (Proc. 7th Int. Conf. Kiev, 1987),* Invited papers Vol.2, World Scientific, Singapore (1987) 1230
[10] Mett R R, Mahajan S M, *Phys.Fluids B* **4** (1992) 2885

Max-Planck-Institut für Plasmaphysik
- Bibliothek -

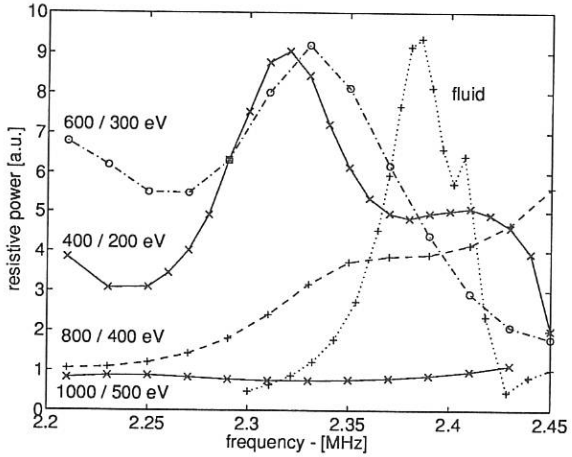


Fig.1: Power absorption as a function of frequency using the fluid and the kinetic model with different temperatures

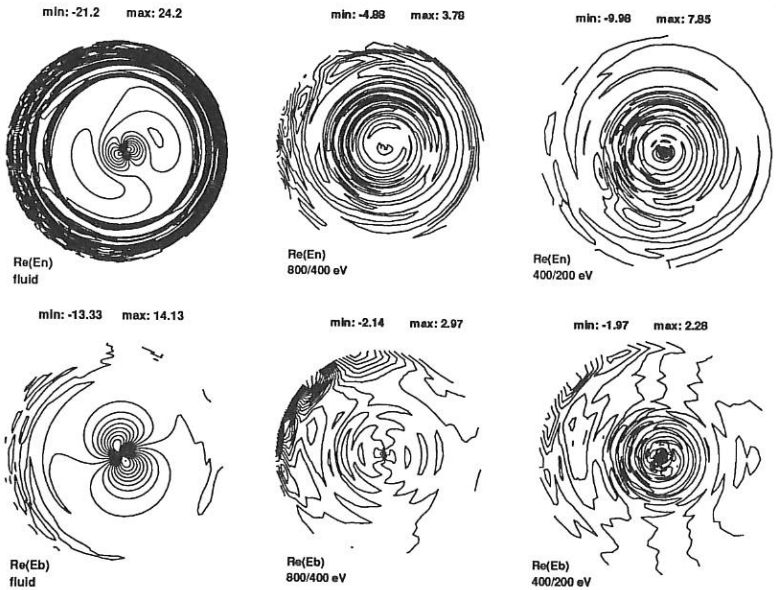


Fig.2: Radial E_n and poloidal E_b electric field for three GAE modes of fig.1

Influence of Alpha Particle Diffusion on Burn Dynamics in Tokamaks

M.J. Mantsinen and R.R.E. Salomaa
Helsinki University of Technology, Department of Technical Physics,
Association Euratom-Tekes, Rakentajanaukio 2C, FIN-02150 Espoo, Finland

1. Introduction

For the operation of a DT-fusion reactor, a good coupling of the α-particle power to the plasma is essential. We have studied the influence of α-particle slowing down and diffusion on fusion reactor dynamics using the volume-averaged (0-D) particle and power balance code FRESCO [1]. The effects considered are: (A) α-particles slow down instantaneously in collisions at the location of the fusion reaction and deposit their energy to bulk electrons and ions in unequal proportions. (B) α-particles diffuse outward radially while slowing down and are lost at the plasma boundary. (C) A part of the α-particle power may be extracted by waves and diverted to fuel ions, which modifies fusion reaction rates and relative heating rates between electrons and ions.

2. Coupling of the α-particle power to the plasma

(A) Instantaneous slowing down in Coulomb collisions. If the slowing down time of α-particles is much shorter than their spatial loss time, the α-particles can be assumed to slow down instantaneously at their birth place and deposit all their energy in the plasma. In this case, the α-particle power absorbed by the plasma, $P_\alpha^{\rm abs}$, is equal to the α-particle power produced by the plasma, $P_\alpha^{\rm tot} = E_\alpha \int S_\alpha^{\rm th} {\rm d}V$, where E_α is the initial kinetic energy of the α-particle, $S_\alpha^{\rm th}$ is the α-particle production rate due to thermonuclear DT-fusion reactions, and V is the plasma volume. The average fraction $\bar{\xi}_{\alpha\to{\rm i}}$ of $P_\alpha^{\rm abs}$ deposited in plasma ions ($\bar{\xi}_{\alpha\to{\rm e}} = 1 - \bar{\xi}_{\alpha\to{\rm i}}$ in electrons) is calculated as $\bar{\xi}_{\alpha\to{\rm i}} = \int \xi_{\alpha\to{\rm i}} S_\alpha^{\rm th} {\rm d}V / \int S_\alpha^{\rm th} {\rm d}V$ where $\xi_{\alpha\to{\rm i}}$ is the local ion heating fraction given by Stix [2]. Typically, $\bar{\xi}_{\alpha\to{\rm i}}$ is 0.2–0.3.

(B) Radial transport while slowing down. Actually, the α-particles diffuse radially while slowing down in collisions. As a consequence, the α-particle power deposition profile broadens and the α-particle power coupling efficiency $\bar{\eta}_\alpha = P_\alpha^{\rm abs}/P_\alpha^{\rm tot}$ decreases below 100%. We calculate $\bar{\eta}_\alpha$ as the volume-average of the α-particle coupling efficiency $\eta_\alpha = [1+\tau_{\rm SD}/(2\tau_\alpha)]^{-1}$ given by Sigmar *et al.* [3]. Here $\tau_{\rm SD} = 1.98\times10^{19} A_\alpha T_{\rm e}^{3/2}/(Z_\alpha^2 n_{\rm e} \ln\Lambda_{{\rm e}\leftrightarrow{\rm e}})$ is the slowing-down time of the α-particles which depends via the plasma parameters on the plasma radius, while the spatial loss time of the α-particles, $\tau_\alpha = a^2/(4D_\alpha)$, is constant for a spatially constant α-particle diffusion coefficient D_α. Moreover, a is the minor radius, A_α and Z_α are the mass and charge number of the α-particles, and $n_{\rm e}$, $T_{\rm e}$ and $\ln\Lambda_{{\rm e}\leftrightarrow{\rm e}}$ are the electron density, temperature and Coulomb logarithm, respectively. SI units are used, except that $T_{\rm e}$ is in keV. For $D_\alpha \le 2$ m^2/s, $\bar{\eta}_\alpha$ may decrease by about 20% at typical DT-fusion reactor densities and temperatures. In existing experiments the diffusion coefficient of fusion product ions has been found to be typically about 0.1 m^2/s [4]. In the next-step devices, where the MHD activity is of greater concern, the value of D_α may, however, be significantly greater. The total α-particle power $P_\alpha^{\rm tot}$, and the fractions $\bar{\xi}_{\alpha\to{\rm i,e}}$ are calculated as in model (A).

(C) Extraction of the α-particle power by waves. Recently, it has been suggested that a part of the α-particle power could be channelled to radio frequency waves [5,6]. This would provide a possibility to control the α-particle power deposition in fusion reactors.

The scheme relies on quasi-linear diffusion of α-particles both in space and energy, and on selective wave damping on plasma particles. To model the extraction of the α-particle power by waves and the damping of these waves on fast fuel ions, we assume that the particle-wave interactions take place typically on shorter timescales than other plasma phenomena. Thus α-particle power is transferred directly to fast ions.

When a fraction θ of the α-particle power is diverted to fast ions, which are here chosen to be deuterium ions, the fast ion density is given by $S_{\rm fast} = \theta P_\alpha^{\rm tot}/(E_{\rm fast} V)$ where $E_{\rm fast}$ is the characteristic energy of fast ions. A spatially homogeneous fast ion distribution is assumed, although the localization of the fast ions in the plasma core would be beneficial due to a higher reactivity. The fast ions either fuse or slow down in collisions. When thermal and beam-thermal DT-fusion reactions are taken into account, the total fusion heating power is $P_\alpha^{\rm tot} = E_\alpha \int (S_\alpha^{\rm th} + S_\alpha^{\rm b-th}) {\rm d}V$. The beam-thermal reactivity is averaged over the slowing down velocity distribution of fast ions, and the energy broadening of the α-particle distribution function due to beam-thermal reactions is neglected. The fast ions that do not fuse are assumed to slow down in Coulomb collisions with the thermal background. Assuming that the fast ions slow down istantaneously, the power $P_{\rm fast}^{\rm abs} = E_{\rm fast} \int (S_{\rm fast} - S_\alpha^{\rm b-th}) {\rm d}V = \theta P_\alpha^{\rm tot} - E_{\rm fast} \int S_\alpha^{\rm b-th} {\rm d}V$ is deposited by them in the plasma. The fractions $\bar{\xi}_{\rm fast \to i,e}$ of $P_{\rm fast}^{\rm abs}$ that are absorbed by thermal ions and electrons are calculated in the same fashion as $\bar{\xi}_{\alpha \to {\rm i,e}}$ above. Because the fast ion energy is typically much lower than E_α, the fast ions slown down predominantly on thermal ions: the value of $\bar{\xi}_{\rm fast \to i}$ for 100-keV deuterons is about 80–90%.

3. Reactor Dynamics Model

The above models for α-particles have been included into the time-dependent particle and power balance code FRESCO (Fusion REactor Simulation COde) [1]. FRESCO solves the system of volume-averaged (0-D) particle and power balance equations

$$\frac{{\rm d}E_{\rm e}}{{\rm d}t} = -\frac{E_{\rm e}}{\tau_{E,{\rm e}}} + \bar{\xi}_{\alpha \to {\rm e}} P_\alpha^{\rm abs} + \bar{\zeta}_{\rm e} P_{\rm ext} - P_{\rm rad} + P_{\rm Ohm} + \bar{\xi}_{\rm fast \to e} P_{\rm fast}^{\rm abs} - P_{\rm e \leftrightarrow i} \qquad (1)$$

$$\frac{{\rm d}E_{\rm i}}{{\rm d}t} = -\frac{E_{\rm i}}{\tau_{E,{\rm i}}} + \bar{\xi}_{\alpha \to {\rm i}} P_\alpha^{\rm abs} + \bar{\zeta}_{\rm i} P_{\rm ext} + \bar{\xi}_{\rm fast \to i} P_{\rm fast}^{\rm abs} + P_{\rm e \leftrightarrow i} \qquad (2)$$

$$\frac{{\rm d}N_{\rm ash}}{{\rm d}t} = -\frac{N_{\rm ash}}{\tau_{\rm part}^*} + S_{\rm ash} \qquad (3)$$

for the thermal background. Density, current density, and temperature profiles of the form $X = X_0[1 - (r/a)^2]^{\alpha X}$ are assumed. $E_{\rm e}$ is the total energy and $\tau_{E,{\rm e}}$ is the energy confinement time of electrons, respectively, and $\bar{\zeta}_{\rm e}$ is the fraction of external heating power $P_{\rm ext}$ absorbed by electrons. Similar notations are used for ions. The formulae used for radiative power $P_{\rm rad}$, which includes both Bremsstrahlung and cyclotron radiation, as well as for Ohmic heating power $P_{\rm Ohm}$ and the temperature relaxation term $P_{\rm e \leftrightarrow i}$ can be found in [7]. The particle balances for thermal deuterium and tritium ions are written similarly as that for helium ash, Eq. (3). The helium ash production rate is given by $S_{\rm ash} = \int S_\alpha^{\rm th} {\rm d}V$ for model (A) and by $S_{\rm ash} = \bar{\eta}_\alpha \int S_\alpha^{\rm th} {\rm d}V$ for model (B). For model (C), either $S_{\rm ash} = \int (S_\alpha^{\rm th} + S_\alpha^{\rm b-th}) {\rm d}V$ or $S_{\rm ash} = \theta \int (S_\alpha^{\rm th} + S_\alpha^{\rm b-th}) {\rm d}V$ is used, the latter taking heuristically into account the possibility that the helium ash production rate decreases when α-particles, while their energy is extracted by waves, are displaced to the plasma periphery [5,6]. Equal ion and electron energy confinement times are assumed and they

are estimated from the ITER89-P scaling law [8] with an H-mode factor of 2. Furthermore, the effective particle confinement time $\tau^*_{\rm part}$ of the thermal background is assumed to be eight times longer than τ_E.

4. Results

Figure 1 shows the fusion power and helium ash concentration during the start-up and burn phase for an ITER-sized reactor with 50:50 DT-fuel mixture for various values of D_α. The start-up of the plasma current and density is similar to that in [9], and the plasma is heated to ignition temperatures within about 100 s. After the ramp-up, the average electron density is 1.2×10^{20} m^{-3}. An increase in D_α (model B) reduces the fusion power and the ash concentration as compared to model (A). The decrease in the fusion power dominates, and therefore the fusion burn may quench after ignition. In the $(n_{\rm e}, T)$-plane this means that the steady state operation contour with $P_{\rm ext} = 0$ shifts to higher plasma densities with increasing D_α.

An important feature in Fig. 1 is the large overshoot in fusion power even when the fusion burn is not extinguished. These overshoots cause severe additional thermal stresses on the reactor structures, in particular on the divertor. To avoid the high divertor and wall loads, more ingenious plasma scenarios should be adopted where, instead of keeping the electron density constant after ignition, the fusion power of the reactor is controlled. With fuelling modulation, the power overshoots can be reduced by 80–90% [7].

Figure 2 shows the evolution of the fusion power and ash concentration after a sudden increase in D_α in steady fusion burn, triggered, for instance, by an instability or increased MHD-activity. Fuelling rates are kept constant. Interestingly, a larger D_α than that in Fig. 1 is possible without quenching of the burn because of the density build-up.

Figure 3 shows the evolution of the fusion power and the fractions $\bar{\xi}_{\alpha\to{\rm i}}$ and $\bar{\xi}_{{\rm fast}\to{\rm i}}$ when a given part of the α-particle power is diverted to deuterium ions at 100 keV. Because of a higher $T_{\rm i}/T_{\rm e}$-ratio as compared to the case where no power is diverted, the channelling of α-particle power to fuel ions increases the fusion power of the reactor. Here $S_{\rm ash} = \int(S^{\rm th}_\alpha + S^{\rm b-th}_\alpha){\rm d}V$ has been used. When $S_{\rm ash} = \theta\int(S^{\rm th}_\alpha + S^{\rm b-th}_\alpha){\rm d}V$ is adopted, a further amplification of the fusion power follows due to a decrease in the ash concentration. To avoid enhanced power overshoots after ignition, it is beneficial to divert α-particle power to fuel ions only after the start-up. For a D^{3}He-reactor, the channeling of the fusion particle power to fuel ions appears to be even more advantageous because the collisional slowing down of fusion products results in a lower value of $\bar{\xi}_{\rm i} \approx 0.15$–$0.2$.

According to FRESCO calculations, the α-particle effects are of a high importance in fusion reactor dynamics, and worth a more detailed modelling.

References

[1] M.J. Mantsinen, Rep. TKK-F-B157 (Helsinki University of Technology, Espoo, 1995)
[2] T.H. Stix, Plasma Phys. **14**, 367 (1972)
[3] D.J. Sigmar, R. Gormley, and G. Kamelander, Nucl. Fusion **33**, 677 (1993)
[4] W.W. Heidbrink and G.J. Sadler, Nucl. Fusion **34**, 535 (1994)
[5] N.J. Fisch and J.-M. Rax, Phys. Rev. Lett. **69**, 612 (1992)
[6] N.J. Fisch and M.C. Herrmann, Nucl. Fusion **34**, 1541 (1994)
[7] M.J. Mantsinen, Rep. TKK-F-B155 (Helsinki University of Technology, Espoo, 1994)
[8] P.N. Yushmanov *et al.*, Nucl. Fusion **30**, 1999 (1990)
[9] D.E. Post *et al.*, ITER Doc. Series No. 21 (IAEA, Vienna, 1991)

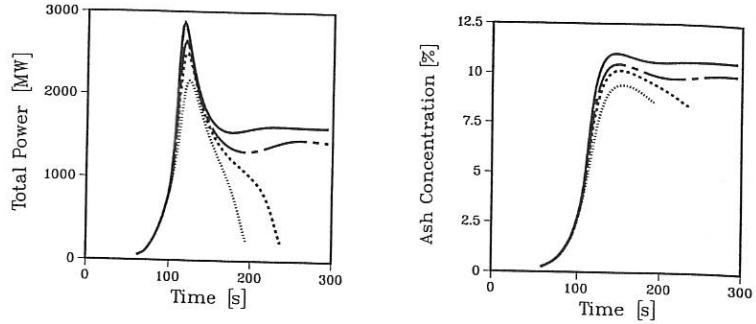


Figure 1: *Fusion power and helium ash concentration for start-up and fusion burn with* $D_\alpha = 0$ *(solid),* 0.3 m^2/s *(chain-dashed),* 0.5 m^2/s *(dashed), and* 1.0 m^2/s *(dotted) in an ITER-sized tokamak.*

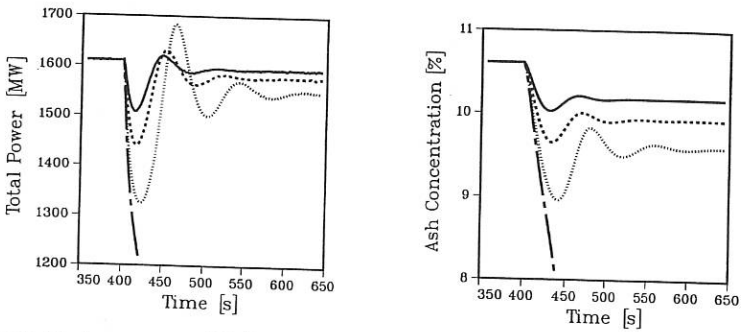


Figure 2: *Fusion power and helium ash concentration after* D_α*:0* $\rightarrow$ 0.25 m^2/s *(solid),* 0 $\rightarrow$ 0.4 m^2/s *(dashed),* 0 $\rightarrow$ 0.6 m^2/s *(dotted), and* 0 $\rightarrow$ 0.75 m^2/s *(chain-dashed).*

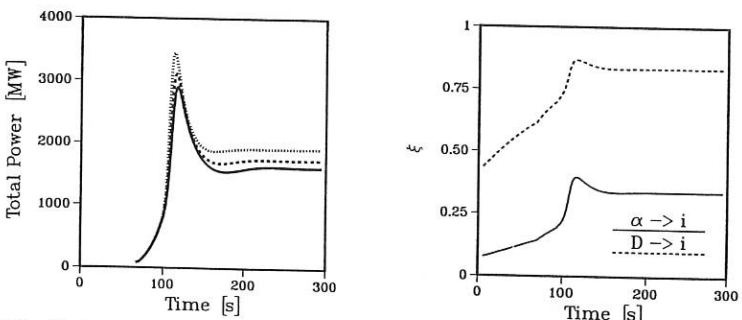


Figure 3: *Fusion power in an ITER-sized tokamak when 10% (solid), 25% (dashed), and 50% (dotted) of the* α*-particle power is diverted to deuterium ions at 100 keV, and ion fractions of* α*-particle and deuterium power for the 50% case.*

TOPOLOGICAL TRANSITIONS OF FAST ION ORBITS

I. Furno, F. Porcelli, Department of Energetics, Politecnico di Torino, ITALY
L. G. Eriksson, JET Joint Undertaking, Abingdon, Oxfordshire, OX14 3EA, U.K.

INTRODUCTION. In a central plasma region of radius $\delta_p = \Delta^{2/3} R$, with $\Delta \equiv 2q\rho / R$, the standard banana orbit width, $\delta_b \equiv \varepsilon^{-1/2} q\rho$, with $\varepsilon = r / R$, exceeds the radial distance from the magnetic axis, r. Within this region the banana orbit is distorted into a potato orbit of width of order δ_p. For example, for a 1MeV hydrogen ion in the JET tokamak, $\delta_p \approx 0.3m$. Most of the ions produced by on-axis ICRF heating on JET have potato orbits, with parallel-to-perpendicular velocity ratio $v_{//} / v_\perp \leq (\delta_p / R)^{1/2}$. A correct description of the high energy ion orbits is important to assess their effects on the energy balance and on MHD stability.

GUIDING CENTRE HAMILTONIAN. Consider a standard low-β tokamak equilibrium, where the flux surface cross sections depart from circles by terms of order ε. The orbit equation for the guiding centre can be obtained from the invariance of the kinetic energy, $E = mv^2 / 2$, magnetic moment, $\mu = mv_\perp^2 / 2B$, and the toroidal canonical momentum, $P_\varphi = (Ze / c)\psi - mRv_{//} B_\varphi / B$, where $\psi \geq 0$ is the poloidal magnetic flux. To leading order in ε, $v_{//} = \sigma_{//} v_{\perp 0} (\lambda + \varepsilon \cos\vartheta)^{1/2}$, where $\sigma_{//} = sign(v_{//})$, $v_{\perp 0} = (2\mu B_0 / m)^{1/2}$, B_0 is the value of B on axis and $\lambda \equiv (E / \mu B_0) - 1$. We introduce the dimensionless variables $\hat{r} \equiv r / \delta_p$, $\hat{\lambda} = (R / \delta_p)\lambda$, $\hat{\psi}_\varphi = (2q_0 / B\delta_p^2)\psi$, where the characteristic potato width, $\delta_p \equiv (2q_0 v_{\perp 0} / \Omega_0 R_0)^{2/3} R_0$, is defined as an invariant of the motion, R_0 is the distance of the magnetic axis from the torus simmetry axis, $\Omega_0 \equiv ZeB_0 / mc$ and $q_0 \equiv q(0)$. For fast ions confined in a region of low magnetic shear, i.e. $(d \ln q / d \ln r) << 1$ for $r << \delta_p$, the orbit equation can be cast in the form

$$\sigma_{//} (\hat{\lambda} + \hat{r} \cos\vartheta)^{1/2} = \hat{r}^2 - \hat{\psi}_\varphi . \qquad (1)$$

The orbit equation (1) is equivalent to the Hamiltonian for the guiding centre motion

$$H(\hat{x}, \hat{y}, \hat{\psi}_\varphi) = (\hat{x}^2 + \hat{y}^2 - \hat{\psi}_\varphi^2)^2 - \hat{x} = \hat{\lambda} \qquad (2)$$

where the cartesian coordinates $\hat{x} = \hat{r} \cos\vartheta, \hat{y} = \hat{r} \sin\vartheta$ are canonically conjugate, with $\hat{x}$ playing the role of the canonical momentum variable and $\hat{\lambda}$ that of the effective energy. The parameter plane $(\hat{\lambda}, \hat{\psi}_\varphi)$ is subdivided into three region by the stationary solutions of Hamilton's equations (Fig. 1): each point in region I corresponds to two orbits nested into each other; one orbit pertains to each point within region II, while no orbits exists within region III. Non-standard orbits satisfy the inequalities $\hat{\psi}_\varphi \leq 1, \hat{\lambda} \leq 1$. The limiting curves $\hat{\lambda} = \hat{\lambda}_0 (\hat{\psi}_\varphi)$, $\hat{\lambda} = \hat{\lambda}_+ (\hat{\psi}_\varphi)$ correspond to the locus of the co- and counter- passing orbits, where $\sigma_{//} = \pm 1$, respectively, while the separatrix curve $\hat{\lambda} = \hat{\lambda}_- (\hat{\psi}_\varphi)$ corresponds to the locus of the pinch orbits. A more detailed orbit classification can be found in Ref.[1].

All the orbits are closed in the $(\hat{x}, \hat{y})$ plane. The bounce time, $\tau_b (\hat{\lambda}, \hat{\psi}_\varphi) = \oint d\tau$, can be evaluated analitically in terms of elliptic integrals; it has a logaritmic singularity on the pinch orbit, while it remains finite for the co- and counter-passing stagnation orbits.

TRANSITION PROBABILITIES. If we now take into account the collisions of the ions with the thermal plasma we are led to consider the drift kinetic Fokker-Planck equation

$$\partial f / \partial t + \mathbf{v}_{gc} \cdot \nabla f = C(f) + S, \qquad (3)$$

where f is the fast ions distribution function, $\mathbf{v}_{gc}$ is the guiding centre velocity , S the fast ion source term, $C(f) = \tau_s^{-1} v^{-2} \partial\left(v^3 f\right)/\partial t$ is the collisional drag term, τ_s the slowing down time. In the high energy limit, $E > E_{crit} \approx \alpha T_e$ with T_e the electron temperature and $\alpha \approx 10$ a mass-dependent factor, only the collisional drag by thermal electrons is important. Since for MeV ions and typical plasma parameters the ratio $\delta \equiv \tau_b / \tau_s$ is very small except in an exponentially thin strip around the pinch locus, we can expand $f = f_0 + (\tau_b / \tau_s) f_1 + \ldots$ To leading order in ε, $\mathbf{v}_{gc} \cdot \nabla f_0 = 0$, thus $f_0 = f_0(v, \lambda, P_\varphi, t)$ is a function of the invariants of the motion. After bounce averaging and performing the variable transformation $(r, \vartheta) \to (P_\varphi, \tau)$, where τ is the time along the orbit, the drag term splits into two parts $\partial f / \partial v \to \partial f / \partial v + [(P_\varphi - Ze\psi / c) / v] \partial f / \partial P_\varphi$. With the further transformation $(v, P_\varphi) \to (\hat{\lambda}, \hat{\psi}_\varphi)$, Eq. (3) takes the form $dF / d\hat{t} = \tau_s v^3 \langle S \rangle$, where $\hat{t} = t / \tau_s$, $F = v^3 f$ and the characteristic equations are

$$\dot{\hat{\psi}} = \langle \hat{r}^2 \rangle + \hat{\psi}_\varphi \qquad \dot{\hat{\lambda}} = 2\hat{\lambda} / 3 \qquad (4)$$

where $\dot{\alpha} = d\alpha / d\hat{t}$ and angle brakets denote bounce averaging. The function $g(\hat{\lambda}, \hat{\psi}_\varphi, \sigma) = \langle \hat{r}^2 \rangle$ is double-valued within region I of Fig. 1, hence we need to introduce an index $\sigma = +1$ for the outer orbit and $\sigma = -1$ for the inner orbit. The support for the function $g(\hat{\lambda}, \hat{\psi}_\varphi, -1)$ coincides with region I, while the function $g(\hat{\lambda}, \hat{\psi}_\varphi, +1)$ is analytic across the curve $\hat{\lambda} = \hat{\lambda}_+$. Note that g is single-valued on the pinch locus, where $g \to \hat{r}_p^2$ reduces to the square of the pinch radius.

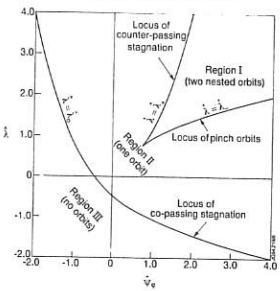


Fig.1.

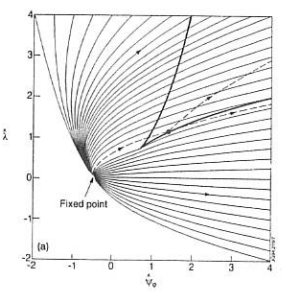


Fig.2

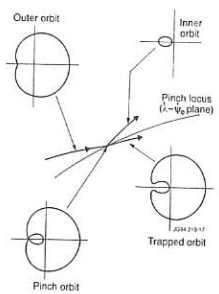


Fig. 3.

As shown in Fig. 2, the characteristic curves in the $(\hat{\lambda}, \hat{\psi}_\varphi)$ plane can be thought of as originating from an unstable fixed point, placed at $\hat{\lambda} = 0$, $\hat{\psi}_\varphi = -3(16)^{-2/3}$, as $\hat{t} \to -\infty$. Some of these curves intersect the pinch locus. At the intersection point a branching of the solutions occurs, as represented by the diagram of Fig. 3. An outer orbit evolves into a pinch orbit, thereafter a small perturbation transforms the orbit either into the adjacent inner orbit in region I, or into the trapped orbit in region II. A third branch, which maps the pinch locus onto itself, is dynamically unstable.

To determine the fast ion distribution function we must decide which of the two branches an orbit will follow. The Hamiltonian (2) describes the guiding centre motion on the time τ_b, where $\hat{\lambda}$ and $\hat{\psi}_\varphi$ can be taken as constant, while the system (4) represents the orbit evolution on the collisional (slow) time scale. Within this description any information of the quickly varying phase is lost. A statistical closure, as described below, leads to the introduction of transition probabilities across the locus of the pinch orbits. The equations of motion are determined by the time dependent Hamiltonian $H[\hat{x},\hat{y},\hat{\psi}_\varphi(\hat{t})]=\hat{\lambda}(\hat{t})$, where $\hat{\psi}_\varphi$ obeys Eqs. (4). With reference to Fig. 4, let us identify the separatrix at a given time $\hat{t}=\hat{t}_0$ and for a given $\hat{\psi}_\varphi(\hat{t}_0)$, $\hat{\lambda}=[\hat{\psi}_\varphi(\hat{t}_0)]$, nested into a higher $\hat{\lambda}=\hat{\lambda}_{out}(\hat{t}_0)$ trajectory and denote by I_i, $i=A,B,C$ the areas enclosed respectively by the two lobes of the separatrix and the higher trajectory.

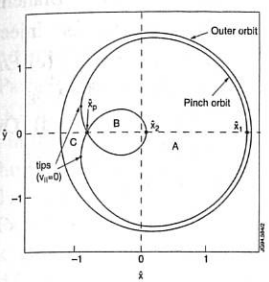


Fig. 4.

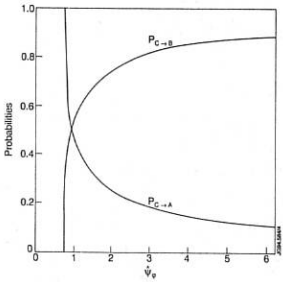


Fig. 5.

At the later time, $\hat{t}=\hat{t}_0+\Delta\hat{t}$, the separatrix and the new trajectory corresponding to $\hat{\lambda}=\hat{\lambda}_{out}(\hat{t}_0+\Delta\hat{t}_0)$ will have modified their shapes and so I_i will have changed. However, owing to Liouville theorem, $\sum_i I_i=\text{const}$, thus, since within a short time $\Delta I_i=\dot{I}_i(\hat{t}_0)\Delta\hat{t}$, it follows that $\sum_i \dot{I}_i=0$. Let, for example, I_C decrease, $\dot{I}_C<0$, so that the phase trajectories leave region C and move into A or B. The probability of transition from C to A or B is determined as the ratio of the measure of all the trajectories moving into A or B to that of all trajectories leaving C:

$$P_{C\to A}=-\dot{I}_A/\dot{I}_C \qquad P_{C\to B}=-\dot{I}_B/\dot{I}_C \tag{5}$$

A proof of this, which is referred to as Kruskal's thorem in Ref. [2], can be found e.g. in Ref. [3]. It should be noted that the adiabatic approximation breaks down in a very narrow strip around the separatrix. However it can be shown that this introduces small correction of order $\delta\ln\delta$ to the transition probabilities in (5). The computation of (5) leads to the following analytic expressions for the transition probability functions:

$$P_{C\to A}=[1-g(\hat{\psi}_\varphi)]/[1+g(\hat{\psi}_\varphi)], \qquad P_{C\to B}=1-P_{C\to A} \tag{6}$$

where $g(\hat{\psi}_\varphi)=(2/\pi)\arcsin[(2z_p-z_2+z_1)/(z_2+z_1)]$, $z_j=(\hat{\lambda}+\hat{x}_j)^{1/2}$ and $\hat{x}_j$, $j=p,1,2$ are the roots of $\hat{y}$ (cf. Fig 3). Graphs of the transition probabilities along the pinch locus are shown in Fig. 5. Note that in the standard orbit limit the transition probability to the inner orbit approaches unity, while $P_{C\to A}\approx 1$ near the cusp point at $\hat{\psi}_\varphi=3/4$.

INWARD PARTICLE DRIFT. To illustrate the effects of slowing down, let us study the co-injection of a mono-energetic neutral beam at an angle $\alpha_{inj} = 56^0$ $(\cos\alpha_{inj} = v_\perp / v)$. We assume a source, $S \approx \delta(\vartheta)\exp\{-[(\hat{r} - \hat{r}_{inj})/\Delta\hat{r}]^2\}\delta(v - v_0)$, with $\hat{r}_{inj} = 1.4$ and $\Delta\hat{r} = 0.2$. The flux surface averaged density profile is $n(r,t) = (m^2 r R_0^{-1})\int f(E,\mu,P_\varphi,t)(d\tau/dr)dEd\mu dP_\varphi$.

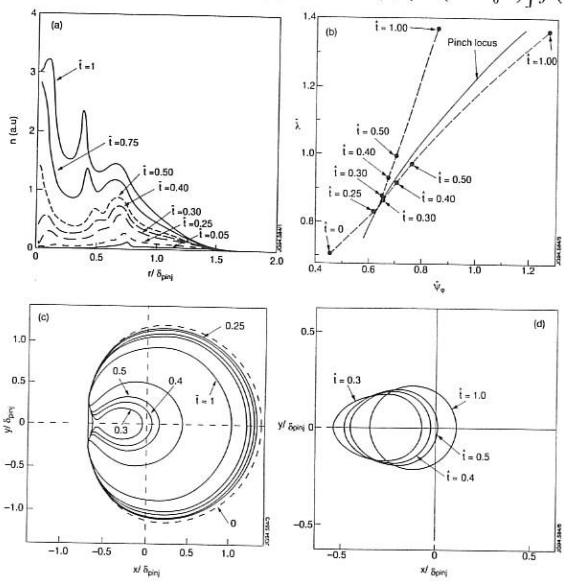


Fig. 6.(a) Density profiles at various normalized times; (b) Branching characteristic for injected ions with $\hat{r} = \hat{r}_{inj}$; (c) Orbit evolution following the trapped branch; (d) Orbit evolution following the inner orbit.

The time evolution of $n(r,t)$ is shown in Fig.6a. Fig. 6b shows the characteristic followed by orbits born at $\hat{r} = \hat{r}_{inj}$,.The transition probability to trapped orbits is about 27%. Figures 6c and 6d show examples of ion orbits at various times along this characteristic. Ions on inner orbits drift inward, encircle the magnetic axis and eventually become standard passing ions. Also, the inner leg of trapped orbits intersects the magnetic axis during slowing down. These two effects produce the build up of the ion density in the centre, as can be seen in Fig. 6a.

CONCLUSIONS. We have discussed the branching of the slowing down characteristic curves associated with the Fokker-Planck equation when the finite radial width of fast ion orbits is taken into account. A statistical method has been proposed to predict the orbit evolution across the branching curve[4]. Our theory is particulary relevant to the dynamics of energetic ions in magnetically confined plasmas. A new significant inward radial transport of the fast ion orbits as they slow down in energy has been found.

REFERENCES. [1] F.Porcelli *et al*, *Proc. 21th EPS Conf. on Contr. Fusion and Plasma Physics* (Montpellier, 1994), Vol II, p. 648. [2] D.Dobrott and J.M. Greene, *Phys. Fluids* **14**, 1525 (1971). [3] A.S. Bakaj, in *Asymptotic Analysis II*, Vol 985 of *Lecture Notes in Math.*, Ed. F. Verhulst (Springer, N.Y, 1983), p.96. [4] F.Porcelli, L.-G.Eriksson and I.Furno, *Topological Transitions of Fast Ions Orbits*, JET-P(94)72, submitted to *Phys. Rev. Lett.*

Particle Simulations of Transport of High Energy Ions in Tokamak Plasmas

Mieko KASHIWAGI
Department of Electrical Engineering
and
Shunji IDO
Department of Functional Material Science
Faculty of Engineering, SAITAMA University
255 Shimo-okubo, Urawa, Saitama 338 **JAPAN**

1.Introducton

Particle flux on the divertor plate is observed in the present tokamak experiments such as JT-60U[1], JET[2] and DIII-D[3]. One of sources of particle flux is ion orbit loss, where the ions in the region near the separatrix escape from the insides of the separatrix to the outer due to the toroidal drift. High energy ions which pass through the separatrix and hit a divertor area and neighborhood.

Particle orbit simulations are carried out to study the ion loss at the plasma edge of a tokamak. By tracing the orbits of high energy ions, the loss conditions and thermal flux are analyzed in the cases with and without the radial electric fields.

2.Model

2-1.Particle orbit simulation

The equation of motion is solved in this study. Compared with the guiding centre model, this method contains the finite Larmor radius effect of an ion which moves over the spatial distribution of a radial electric field. The equation is solved by Runge-Kutta-Gill method.

2-2.Magnetic field and electric field

The magnetic field configuration is refered to that of Doublet III-D. The major radius R=1.67m, the minor radius a=0.668m, the plasma current Ip=1.6m and the toroidal magnetic field Bto=2.1T are applied. The reference tokamak plasma has the double null sepraratrix configuration .

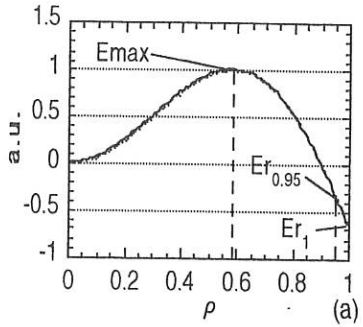
The radial electric field Er is a function of minor radius at the midplane as shown in Fig.1(a) by referring to the profiles obtained in the experiments of Doublet III-D[4]. The corresponding field vector in the poloidal cross sectoin is shown in Fig.1(b). Er is assumed to be zero in the outer region of separatrix. In Fig.1(b), the radial electric fields is reversed at the 0.9 ρ . Ion loss occurs mainly in the region of $0.95< \rho <1.0$, where $Er_{0.95}$ =-0.317 × Emax and Er_1 =-0.588 × Emax. If Emax is positive, Er near the separatrix is negative and vice versa.

3.Results

3-1. Ion loss region and the effect of Er

The theory and the simulation study of ion orbit loss are shown in Refs.5,6,7. Figure 2 shows the orbits of deuterium ions which have the negative velocity component parallel the magnetic fields in the initial points. These ions go across the separatrix and escape through the X-point.

Figure 3 shows the particle fluxes of 5keV ions from the outer region on a midplane in the cases of Er_1=(a)0kV/m, (b)-17.6kV/m and (c) -35.2kV/m, Emax=0,30,60kV/m. Here, the relations between the positions of particle flux in a divertor and the initial points on a midplane are pictured. Particle flux at the inner and outer hit points is due to the losses of Fig.2(a) and (b), respectively. When the negative radial electric field becomes larger, the particle flux at the inner hitpoint decreases. Similar results are also obtained for the particle flux from the inner region which corresponds to the ion loss of Fig.2(c).



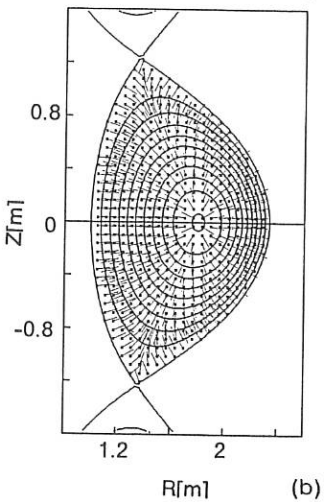
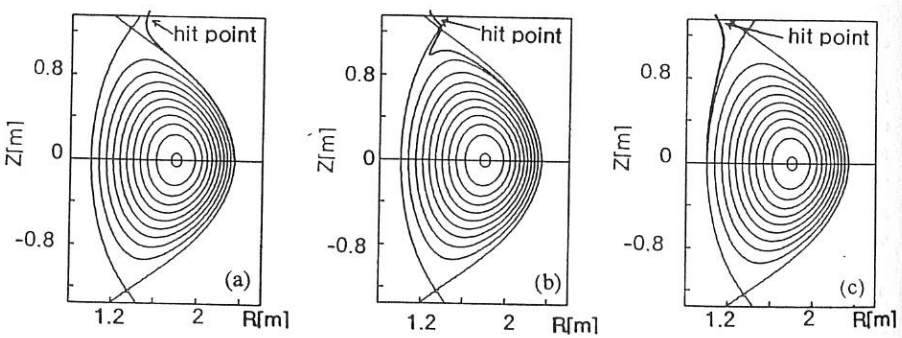


Fig.1 Radial electric field distribution.
(a)In a minor radius,
(b)Two-dimensional distribution on the magnetic surface.

Fig.2 Ion orbit in a poloidal surface.
(a)(b)v//<0 and from outer region,
(c)v//>0 from inner region.



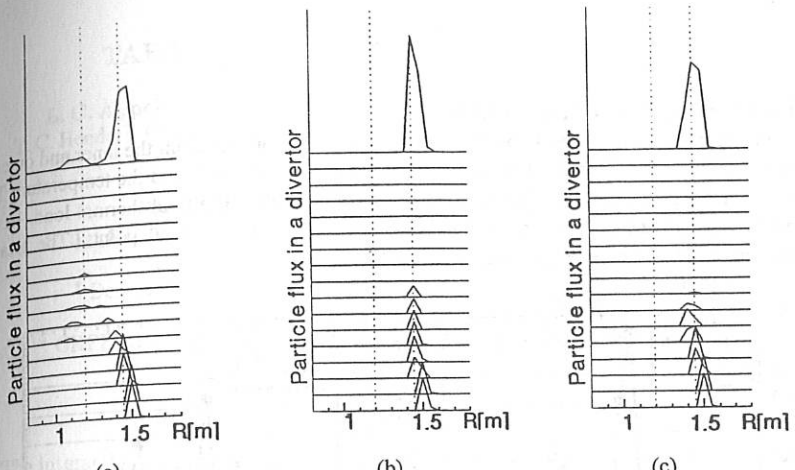


Fig.3 Particle flux in a divertor region. $Er_{\rho=1}$=(a)0, (b)-17.6 (c)-35.2kV/m.

3-2.Thermal load

Figure 4 shows the thermal loads in a divertor when the distributions of the ion density N and the temperature T are assumed in the cases of Er_1=(a)0kV/m, (b)-17.6kV/m and (c) -35.2kV/m, Emax=0,30,60kV/m. The temperature is $T_{\rho=1}$ =1.5keV and $T_{\rho=0.8}$

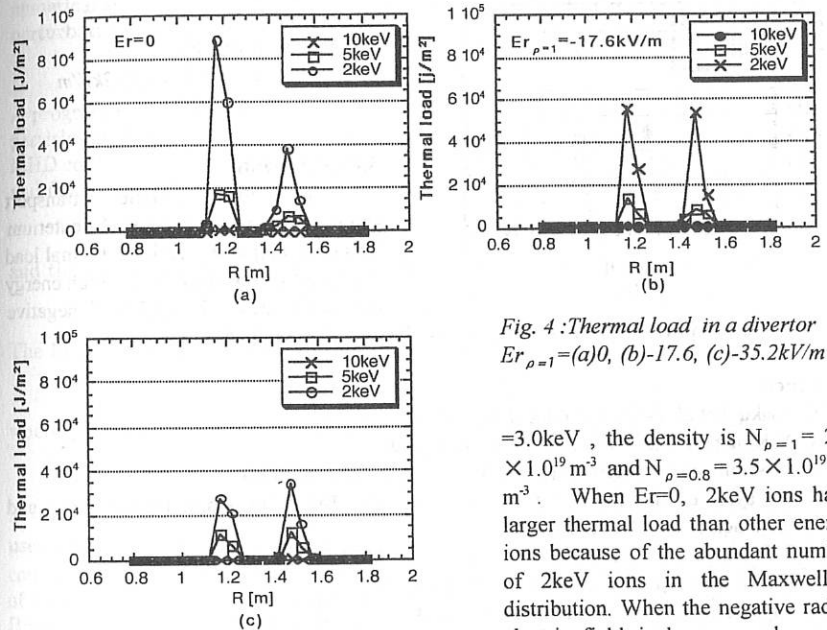


Fig. 4 :Thermal load in a divertor $Er_{\rho=1}$=(a)0, (b)-17.6, (c)-35.2kV/m

=3.0keV , the density is $N_{\rho=1}$= 2.0 $\times 1.0^{19}$ m^{-3} and $N_{\rho=0.8}$= 3.5 $\times 1.0^{19}$ m^{-3}. When Er=0, 2keV ions have larger thermal load than other energy ions because of the abundant number of 2keV ions in the Maxwellian distribution. When the negative radial electric field is larger as shown in Fig.4(b) and (c), the decrease of thermal load is found for the whole ions of 2, 5 and 10keV.

3-3.Total thermal flux in a divedrtor

Figure 5 shows the total thermal load due to the ion orbit loss from the inner and outer regions in the cases of $Er_1 = 0$, -17.6, -35.2kV/m, where the density N and the temperature T is assumed to be constant; N is $2.0 \times 1.0^{19} m^{-3}$ and T is 2keV. The total thermal load has two peaks in a divertor area corresponding to the inner and outer hit points. The total thermal load is decreased in a negative Er.

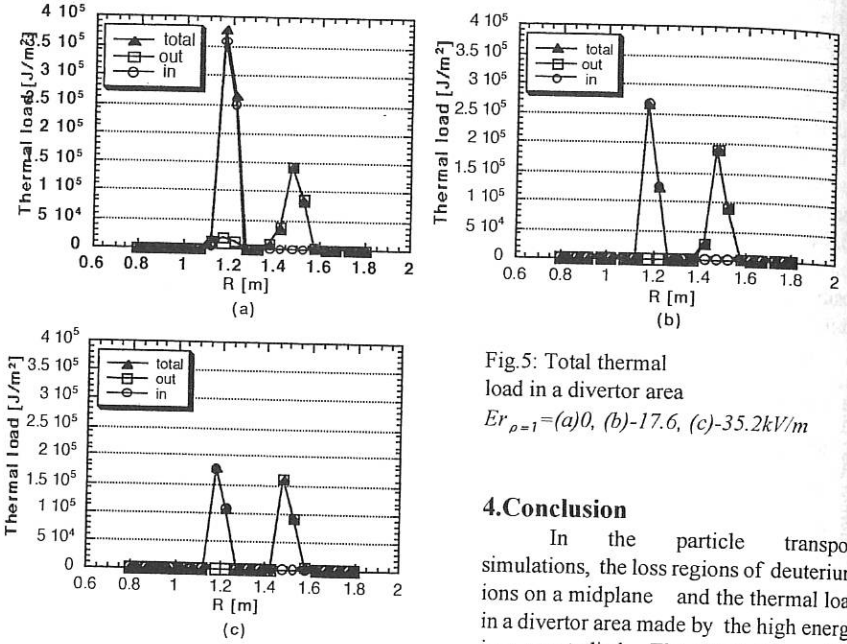


Fig.5: Total thermal load in a divertor area
$Er_{\rho=1}$=(a)0, (b)-17.6, (c)-35.2kV/m

4.Conclusion

In the particle transport simulations, the loss regions of deuterium ions on a midplane and the thermal load in a divertor area made by the high energy ions are studied. The effect of negative electric fields is shown for the ion orbit loss and the total thermal load.

Reference

[1] N. Asakura et al. *IAEA-CN-60/A-4-I-3.*(1994)
[2] N. A. Kouanen et al. *Nuclear Fusion* **32** 5 (1992)
[3] R. D. Stambaogh for DIII-D Team. *IAEA-CN-60/A-1-I-4.*(1994)
[4] T. S. Taylor et al. *IAEA-CN-56/A-3-1, Proc.* 14th IAEA Int. Conf. Plasma Phys. and Controlled Nucl. Fusion Res.(1992).
[5] K. S. Putvinskii; *Plasma Phys. Control Fusion* **35** 219-234 (1993)
[6] A. V. Chankin et al. *Nuclear Fusion* **33** 10 (1993)
[7] K. Miyamoto; *J. Phys. Soc. Jpn.* **63** 4017 (1994)

TAE-induced Diffusion of Fast Particles in JET

L. C. Appel†, H. L. Berk§, D. Borba, B. Breizman§, L - G. Eriksson, A. Fasoli*,
T. C. Hender†, G. T. A. Huysmans, W. Kerner, E. Monticelli, M. Pekker§, S. D. Pinches‡
and S. E. Sharapov

JET Joint Undertaking, Abingdon, Oxon, OX14 3EA, UK.
† UKAEA Government Division, Fusion, Culham, Abingdon, OX14 3DB, UK.
§IFS,University of Texas at Austin,Austin, Texas 78712.
‡ Department of Theoretical Mechanics, The University of Nottingham,
University Park, Nottingham, NG7 2RD, UK.
* CRPP-EPFL, Ass. Euratom-Swiss Confederation, 21 av. des Bains, CH-1007
Lausanne.

Introduction

The interaction between magnetically confined plasmas and fusion generated $\alpha-$particles is one of the key issues to be resolved before the completion of a next step fusion device. Global Alfvén modes such as the toroidicity-induced Alfvén eigenmode (TAE) are of particular concern because the resonant interaction of fusion α-particles may lead to enhanced loss of energetic particles. At high plasma temperatures a spectra of "Kinetic" TAE modes can appear, equally spaced in frequency and occurring above the TAE frequency [1]. In this paper we use the guiding centre code HAGIS [2] to carry out a numerical study of trapped fast particle orbits in JET in the presence of TAE and KTAE perturbations.

The HAGIS code

A programme, HAGIS, has been written that follows the guiding centre drift motion of particles in the presence of general electromagnetic perturbations provided by the resistive MHD code CASTOR. Using the straight field line coordinates ψ_p,θ, ζ introduced by White and Chance [3], the equilibrium magnetic field can be written

$$\mathbf{B} = \delta(\psi_p,\theta)\nabla\psi_p + I(\psi_p)\nabla\theta + g(\psi_p)\nabla\zeta \qquad (1)$$

and the perturbations in terms of magnetic vector and electric scalar potentials,

$$\tilde{\mathbf{A}}(\mathbf{r},t) = \tilde{A_{\psi_p}}\nabla\psi_p + \tilde{A}_\theta\nabla\theta + \tilde{A}_\zeta\nabla\zeta \quad ; \quad \tilde{\Phi} = \tilde{\Phi}(\mathbf{r},t) \qquad (2)$$

The Lagrangian for the guiding centre motion is

$$\mathcal{L} = p_\theta\dot{\theta} + p_\zeta\dot{\zeta} + \mu\dot{\xi} - \mathcal{H} + \rho_c\delta\dot{\psi}_p \qquad (3)$$

where ξ is the gyro-angle, $\mathcal{H}$ the Hamiltonian, and p_θ, p_ζ the canonical momenta given by

$$p_\theta = p_\parallel I + \psi + \tilde{A}_\theta \qquad p_\zeta = p_\parallel g - \psi_p + \tilde{A}_\zeta \qquad (4)$$

in which $\rho_\parallel = v_\parallel/\omega_c$ is the parallel gyroradius and ψ is the toroidal flux. Presently, HAGIS uses a simplified form of perturbation $\tilde{\mathbf{A}} = \alpha(\psi_p,\theta,\zeta)\mathbf{B}$, computed to match the radial component of $\tilde{\mathbf{B}}$ from CASTOR. Substituting the components of $\alpha\mathbf{B}$ into the equations of motion we obtain the same expressions for $\dot{\psi}_p$,$\dot{\theta}$,$\dot{\zeta}$,$\dot{\rho}_\parallel$ as used by White and Chance [3]. Based on this system of equations the HAGIS code has been developed in order to follow particles within an arbitrary plasma geometry and in the presence of time-dependent perturbations.

Interaction of trapped particles with TAE modes

A series of experimental discharges were run in JET using ion cyclotron heating of deuterium plasmas with absorbed power 3-4MW, B_ϕ=1.4T, I_p=1MA, $n_e(r = 0) = 3\times10^{19}\mathrm{m}^3$, $T_e(\mathrm{r} = 0) = 3\mathrm{keV}$. Heating was primarily through the second harmonic heating of minority hydrogen. Three high frequency n=3 modes were observed experimentally and the radial structures were computed by CASTOR. Tail temperatures of 1MeV were assumed, taken from the combined Fokker-Planck and wave propagation code PION [4]. High-energy ions interact with the Alfvén eigenmodes through the trapped particle resonance, which can be written for the simplest case as [5, 6]

$$\omega = n < \omega_{Dh} > + l\omega_{bh}, \qquad l = 0, 1, 2.... \tag{5}$$

where ω_{bh} is the bounce frequency and $< \omega_{Dh} >$ is the toroidal precession frequency. For multiple eigenmodes and for $\omega_{bh} \sim n < \omega_{Dh} >$, the structure of the resonances becomes more complicated, and the resonances require numerical analysis.

Monte-Carlo simulations were carried out using HAGIS with 11200 particles, initial energy between 300keV and 3MeV for 0.3msec in the presence of 3 TAE modes. The results, shown in figure 1a identifies one class of particles for which the toroidal precession frequencies are in fundamental resonance with the wave. A second class of resonant particles with lower precession frequencies can be identified as those particles shown in figure 1b with poloidal bounce frequencies in fundamental resonance with the wave. On average, the energy fluctuations of particles in toroidal precession resonance are twice those of particles in poloidal bounce resonance. This is in qualitative agreement with theory [6]. Calculations have shown that a single particle resonant with the toroidal precession frequency undergoes slow time-varying perturbations of the precession frequency; stochastic behaviour occurs when it comes close to a neighbouring resonance. For the complete distribution, one can consider the temporal evolution of the quantity $<\Delta p_\zeta^2>= \left\langle p_\zeta^2 \right\rangle - \langle p_\zeta \rangle^2$ (<> denotes the ensemble average) [7]. Figure 2 plots the variation of $< \Delta p_\zeta^2 >$ for particles arranged in 8 bins of initial p_ζ. From the figure, stochastic particle motion is evident for particles with initial $p_\zeta \approx -0.06\mathrm{eV}-\mathrm{secs}$. This figure is for $\delta\tilde{B}_r/B_\circ = 3.33 \times 10^{-4}$, just above the stochastic threshold.

Trapped particle behaviour with KTAE modes

In some JET discharges with strong ICRH heating ($P \sim 7\mathrm{MW}$) of the minority hydrogen species and $T_e(\mathrm{r} = 0) = 7\mathrm{keV}$, multiple KTAE modes are excited. The CASTOR code identified seven KTAE modes with frequencies agreeing well with the measured mode frequencies. Using HAGIS, simulations were carried out with 2500 particles, for 1ms in the presence of 7 KTAE modes with amplitude $\delta\tilde{B}_r/B_\circ = 4 \times 10^{-4}$. The initial particle distribution used a tail temperature of 1MeV, obtained from PION, and other details of the initial distribution are similar to those used previously. Figure 3 shows the KTAE-induced energy changes of this trapped-particle distribution. In this case all particles have poloidal bounce and toroidal precession frequencies beneath the perturbation mode frequencies, resulting in a more complex resonance structure. The threshold for stochasticity is calculated as $\delta\tilde{B}_r/B_\circ \geq 10^{-4}$ per mode. The threshold is lower than the other case analyzed, and this can be explained by the closeness of the eigenfrequencies.

Self-consistent particle-wave evolution

A simplifying approximation for the non-linear self-consistent problem, is that the TAE/KTAE eigenmode structure is assumed to be invariant during the wave evolution, with only the wave amplitude and phase varying. Each eigenmode has therefore just two degrees of freedom, namely the amplitude A_s and the phase β_s, so that the perturbation can be represented in the form

$$\tilde{\mathbf{B}} = \sum_s A_s(t)\tilde{\mathbf{B}}_s(\mathbf{r})e^{-i(\beta_s(t)+\omega_s t))} \tag{6}$$

where s is the index of the eigenmode with frequency ω_s and $\tilde{\mathbf{B}}_s(\mathbf{r})$ is the fixed linear TAE/KTAE eigenfunction, as computed by CASTOR. To include the wave evolution in the Hamiltonian equations for energetic particles, the wave Lagrangian is introduced

$$\mathcal{L}_w = \sum_{\substack{\text{core}\\ \text{plasma}}} \left[\frac{1}{2}mv^2 + e\left(\mathbf{A}\cdot\mathbf{v} - \Phi\right)\right] + \frac{1}{2\mu_o}\int\left(\frac{E^2}{c^2} - B^2\right)dx^3 \tag{7}$$

Taking into account equation 6, this wave Lagrangian in the approximation $\dot{\beta}_s \ll \omega$ can be reduced to the form

$$\mathcal{L}_w = \sum_s \frac{A_s^2\dot{\beta}_s}{2\mu_o\omega_s}\int \tilde{\mathbf{B}}_s(\mathbf{r})\tilde{\mathbf{B}}_s^*(\mathbf{r})\mathrm{d}x^3 \tag{8}$$

Lagrange's equations then determine the wave evolution

$$\dot{A}_s = \frac{-i\omega_s}{2A_s\overline{W}_s}\sum_{\text{particles}} \rho_\parallel B^2\tilde{\alpha}_s - \tilde{\phi}_s \tag{9}$$

$$\dot{\beta}_s = \frac{\omega_s}{2A_s^2\overline{W}_s}\sum_{\text{particles}} \rho_\parallel B^2\tilde{\alpha}_s - \tilde{\phi}_s \tag{10}$$

where $\overline{W}_s$ is the normalized eigenmode energy E_s for unit mode amplitude, i.e. $E_s = A_s^2\overline{W}_s$ Given an initial particle distribution and the amplitudes and phases of the TAE/KTAE modes, the HAGIS code can be run to obtain the simultaneous evolution of plasma modes and energetic particles. Conservation of the total system energy with time in the self-consistent HAGIS code is to an accuracy of $\sim 10^{-7}$.

Conclusions

A Hamiltonian guiding centre particle following code HAGIS has been used to simulate particle-wave interaction for two JET discharges with populations of high energy trapped particles which exhibit TAE activity. ICRH-generated fast ion tails in the presence of KTAE-modes were found to display stochastic orbit behaviour for $\delta\tilde{B}_r/B_o \geq 10^{-4}$. This stochasticity threshold is below that for the TAEs due to the finer structure of trapped particle resonances and larger number of KTAE modes considered. The HAGIS code has been generalized to incorporate self-consistent particle-wave evolution.
Diffusion from particle stochasticity will be in addition to that due to neo-classical and other 'anomalous' transport processes. Presently, work is underway to obtain experimental evidence of changes to the particle distribution due to stochasticity. In the future, it is expected that the enhanced diffusion calculated by HAGIS will be incorporated in Fokker-Planck modelling of the fast ion distribution.

Acknowledgements: The UKAEA authors were jointly funded by the UK Department of Trade and Industry and Euratom. The authors thank Mr. M.O'Brien for useful discussions.

References: [1] Breizman B and Sharapov S, IFS-R671 (submitted to Plasma Physics and Controlled Fusion). [2] Appel LC et al., submitted to *Nuclear Fusion*. [3] White RB and Chance MS, *Phys.Fluids* **27** 2455 1984. [4] L-G.Eriksson and T.Hellsten, Physica Scripta **52**, 70 (1995). [5] Fu GY and Cheng CZ,*Phys.Fluids* B **4**, 3772 (1992). [6] Biglari H, Zonca F and Chen L, *Phys.Fluids* B4, 2385-2387 (1992) [7] Hsu CT and Sigmar DJ, Phys.Fluids B **4**, 1492 (1992).

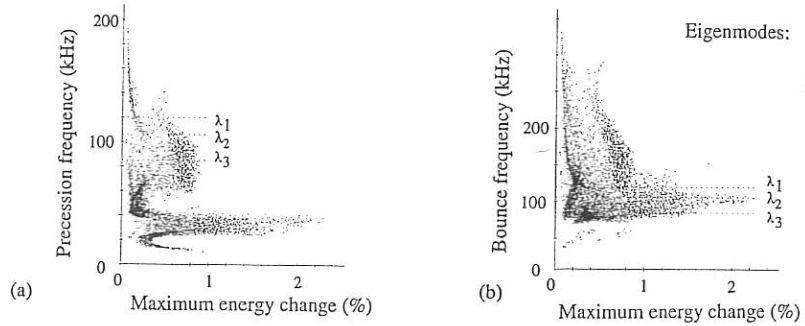


Figure 1. *Maximum change in energy for a population of energetic particles, plotted versus (a) initial toroidal precession frequency, and (b) initial poloidal bounce frequency* ($\delta\tilde{B}_r/B_o = 10^{-3}$).

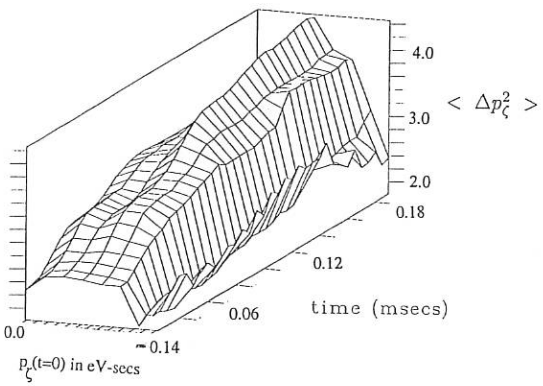


Figure 2. *Time-variation of* $< \Delta p_\zeta^2 >$ *for particles arranged in 8 bins of initial* p_ζ ($\delta\tilde{B}_r/B_o = 3.33 \times 10^{-4}$).

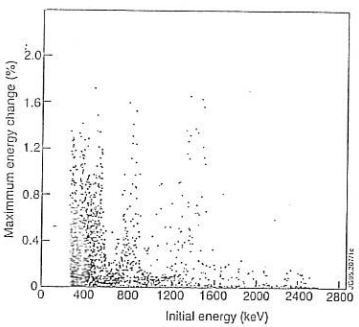


Figure 3. *Trapped particle resonances for ICRH-generated fast ions in the presence of seven (n=3) KTAE modes.*

3D Calculations of Fast Ion Distributions in Tokamaks

M R O'Brien, M Cox, C A Gardner and †F S Zaitsev
UKAEA Government Division Fusion, Culham, Abingdon, UK
(UKAEA/EURATOM Fusion Association)
†Moscow State University, Russian Federation

1. Introduction

In a burning plasma the heating profile and helium ash source profile will be determined by the slowing down and radial transport of the α-particles . It is therefore important to understand the behaviour in tokamak plasmas of fast ions in general and α-particles in particular. Several experiments have shown that the behaviour of fast ions produced by ICRH and NBH is usually consistent with neo-classical theory. The recent D-T campaign on TFTR has confirmed that, to date, in the absence of large scale MHD this also applies to α-particles if orbit width and ripple effects are allowed for [1].

In this paper we use the FPP 3D Fokker-Planck code [2] to calculate f_α the distribution function in velocity and real space for α-particles born in a high power TFTR D-T supershot. The code includes self-consistently the full neoclassical collision operator [3] and can treat orbits which deviate greatly from flux surfaces. Results are compared with those from the TRANSP simulation code [1] which uses a Monte Carlo technique to follow the α-particles. The Monte Carlo approach with relatively small numbers of test particles is suitable for a simulation code like TRANSP but requires very large numbers for smoothness and detail of f_α to be comparable with the Fokker-Planck approach. In addition to the TFTR calculation, the first results from a model ICRH operator in FPP are presented, demonstrating the importance of large orbit width effects.

2. TFTR Simulation

We used the time evolution of plasma profiles from the TRANSP simulation of a high fusion power discharge ($P_{fus} = 7.5$MW, shot 76770 [1]) to calculate the α-particle source profile and the collisions with the background species. The plasma geometry varied little and was kept fixed: $R_o = 2.5$m, $R_{magaxis} = 2.62$m, $a = 0.9$m, circular plasma, $I_p = 2.5$MA, $B_o = 5.1$T. Neutral beam heating of power 33.5MW heated the plasma for 0.8s, and the simulation followed the α-particle evolution for this period.

FPP and TRANSP agree very well for the time dependence of the profiles of alpha density and plasma heating by the slowing-down α-particles. This confirms that modest numbers of Monte Carlo test particles can be used in a code like TRANSP (8000 were used). The evolution of f_α in velocity space and in radius is complicated with a number of effects competing. These include: the different orbits of co- and counter-particles; the more rapid slowing down of particles passing near the edge, since the collision frequency varies as $n_e(r)/T_e^{3/2}(r)$; the change of orbit shape as the particles slow down; the removal, by a loss term, of particles with orbits that leave the plasma; and the time variation of the α-particle source and the electron density and temperature profiles.

Figure 1 shows the time evolution of f_α at the high field side of the flux surface with $r = a/2$. Three times are shown: 0.2s, 0.5s and 0.8s. These distributions are calculated from $f_\alpha(v, \theta, r)$ for those combinations of (v, θ, r) which correspond to orbits which pass through the high field side of the $r = a/2$ surface. At $t = 0.2$s f_α peaks for counter-particles ($\theta = \pi$). This is because these particles have orbits that pass near the plasma centre where the source is greatest. At later times, the imbalance between the number of co- and counter-particles persists, though is less apparent in Figure 1. This is because the plot becomes dominated by its low energy peak. The co-particles have a low source rate as they have orbits near the edge of the plasma, but they also have a high average collision frequency as they pass through regions where the electron temperature is low. They therefore slow down more rapidly than the counter-particles which have a higher source rate and a lower average collision frequency. This effect tends to equalise the distributions of co- and counter-particles at low energies, as does pitch-angle scattering which can be comparable with slowing down at these energies. The imbalance of counter- over co- remains, however, and is confirmed by integration of f_α over energy to give the number of particles as a function of pitch-angle. Plots for the outside of the flux surface (not shown) show similar behaviour in reverse, with co-particles outnumbering counter-particles.

These differences between the distribution function for co- and counter-particles and how they vary in time, energy and around a flux surface show the importance of including orbit width effects in the calculations. The commonly-used analytic approximation for the slowing down distribution ($f_\alpha \sim 1/(v^3 + v_c^3)$) has no such pitch-angle or poloidal angle dependence. It is therefore important to retain these orbit effects, both for comparisons with experimental measurements of f_α and for use as input to other calculations (for example, of the influence of f_α on MHD behaviour such as TAE modes). A Fokker-Planck approach, as described here, is more suitable for this purpose, particularly if details of the distribution function are important, because it gives smoother distributions than the alternative Monte-Carlo method.

3. Ion Cyclotron Heating

A model ICRH operator has been included in FPP to investigate orbit width effects. The operator is diffusive in the local $v_\perp$ and averaged over particle orbits. The diffusion coefficient is taken to be of the form $D = D_o(R, Z)\exp[-(k_\parallel - k_{\parallel o})^2/(\Delta k_\parallel)^2]$ with $k_{\parallel o}$ and $\Delta k_\parallel$ the parallel wave vector and its spread for the spectrum (both taken to be 3m^{-1}), and $k_\parallel = (\omega - \Omega_{ci})/v_\parallel$. The spatial dependence of $D_o(R, Z)$ is in practice a complicated function of the wave propagation, absorption and polarisation but here, for simplicity, is taken to be $D_o = D_N\exp(-(Z/\Delta Z)^2)$ with vertical spread $\Delta Z = 0.3$m. The constant D_N is adjusted to give the desired value for the total absorbed power. The code gives Stix-like distributions in the appropriate limits.

Typical JET-like parameters were used: $\kappa = 1.5$, $a = 1$m, $R_o = 3$m, $R_{magaxis} = 3.2$m, $n_{Do} = 0.8n_{eo} = 4 \times 10^{19}\text{m}^{-3}$ and $T_{Do} = T_{eo} = 10$keV. Fundamental minority hydrogen

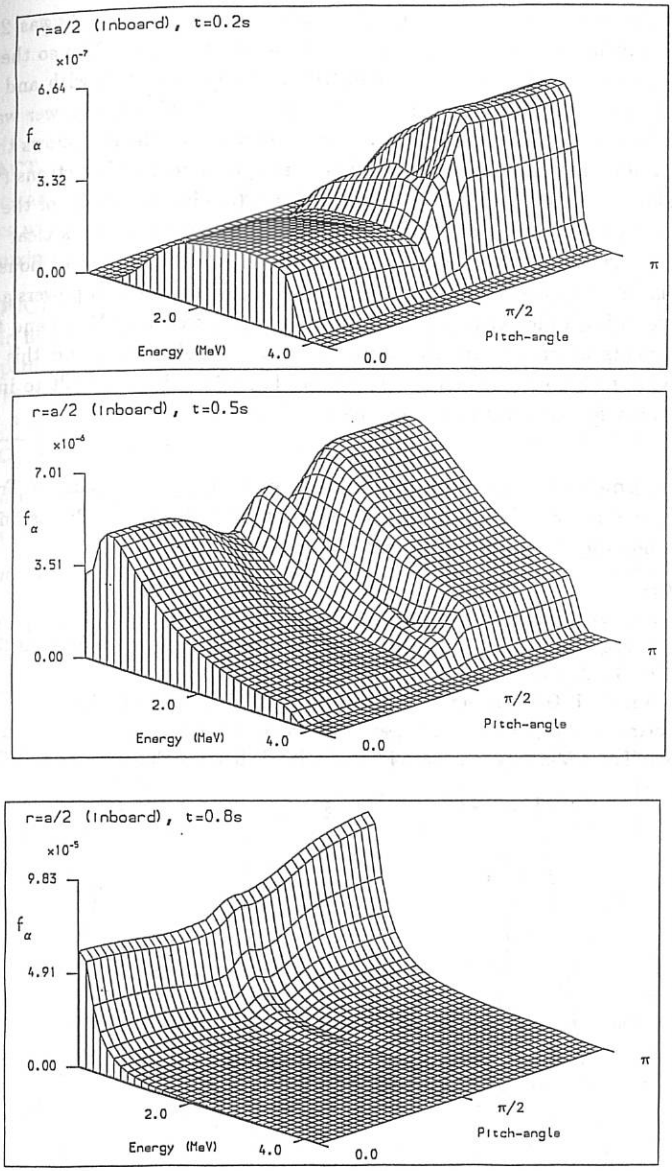


Figure 1 Alpha-particle distribution function in velocity space (arbitrary units) at the high field side of the flux surface with $r = a/2$ at $t = 0.2$s (top), $t = 0.5$s (centre) and $t = 0.8$s (bottom).

heating with $n_H = 0.05 n_D$ was considered. The magnetic field at R_o was 2.5T and the wave frequency was 42MHz, giving cold resonance at $R_{res} = 2.72$m so the heating peaked at $r/a \sim 0.4$. The steady-state distribution was calculated, with and without the excursion of orbits from flux surfaces allowed for. The absorbed power was set at 2.5MW, which gives tail temperatures of a few hundred keV. Figure 2 shows the ICRH power deposition and collisional heating of the background ions and electrons (with the electron heating dominant) for $I_p = 1.5$MA. Figure 2(a) gives the result of the calculation neglecting orbit widths and Figure 2(b) that including them. It is clear that the orbit effects significantly broaden the plasma heating, confirming the previous simpler calculations in references [4] and [5]. This broadening will rise for high powers and lower minority densities (which give higher tail temperatures, exceeding 1MeV) and for lower plasma currents which give increased orbit widths. We plan to extend this work to include radial transport (neglected in these calculations): this is difficult to include in simpler approaches such as those in references [4] and [5].

Acknowledgments: This work was funded by the UK Department of Trade and Industry and Euratom. The authors are very grateful to R Budny, Princeton Plasma Physics Laboratory for providing the data for the TFTR simulation.

References

[1] R V Budny, et al., this meeting.

[2] M R O'Brien, et al., IAEA Technical Committee Meeting on Advances in Modelling Plasmas, Montreal 1992, p527.

[3] F S Zaitsev, M R O'Brien and M Cox, Physics of Fluids B **5** (1993) p509.

[4] G A Cottrell and D F H Start, Nuclear Fusion **31** (1991) p61.

[5] E Righi, "Large Minority Ion Orbit Effects in ICRF Heating Experiments in JET", JET-R(94)08, 1994.

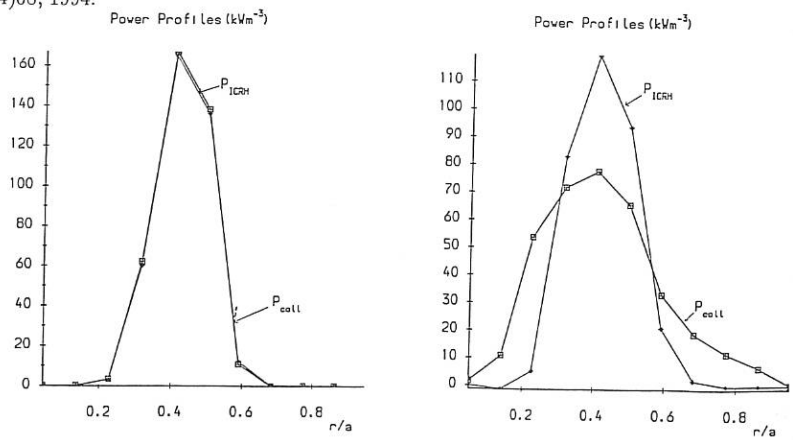


Figure 2 Radial profiles of ICRH power deposition and collisional heating of the bulk electrons and ions for $I_p = 1.5$MA: orbit widths neglected (left) and included (right).

The Distribution Function of Fusion Products at Birth

G.J.Sadler and P.van Belle
JET Joint Undertaking, Abingdon, OX14 3EA, UK

ABSTRACT

It is customary to approximate well established nuclear physics cross-sections and reaction kinematics when diagnosing present day plasmas. Some adverse consequences of applying such approximations to fusion products are presented.

INTRODUCTION

Fusion products not only carry the energy released in the fusion process but also yield information on the distribution function of the reacting particles. The birth energy distribution function of fusion products M_3 from the reaction: $M_1 + M_2 \rightarrow M_3 + M_4$ taking place in a plasma is given by:

$$\frac{\partial^2 N}{\partial\Omega_3 \cdot \partial E_3} = \iiint f_1(\vec{v}_1) \cdot f_2(\vec{v}_2) \cdot \frac{d\sigma}{d\Omega_3 \cdot dE_3 \cdot d\Omega_4 \cdot dE_4} \cdot |\vec{v}_1 - \vec{v}_2| \cdot d\vec{v}_1 \cdot d\vec{v}_2 \cdot d\vec{v}_4 \quad \text{, where}$$

$$\frac{d\sigma}{d\Omega_3 \cdot dE_3 \cdot d\Omega_4 \cdot dE_4} = \frac{d\sigma}{d\Omega_3 \cdot dE_3} \cdot \delta(E_3 - E_3^*) \quad \text{and}$$

$$E_3^* = \tfrac{1}{2} \cdot m_3 \cdot V^2 + \frac{m_4}{m_3 + m_4} \cdot (Q + K) + \cos(\theta) \cdot V \cdot \sqrt{\frac{2 \cdot m_3 \cdot m_4}{m_3 + m_4} \cdot (Q + K)} \quad \text{, with } Q = \text{Energy}$$

release of the reaction, V = CM velocity, K = kinetic energy of reactants in the centre of mass (CM), θ = angle between relative velocity and velocity of fusion product in the CM.

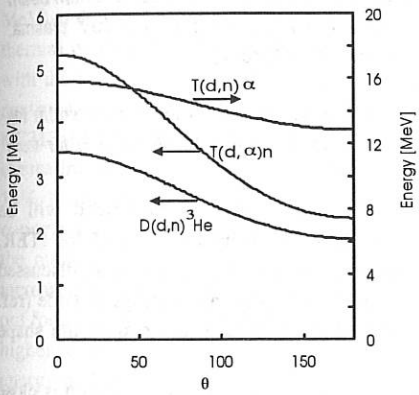


Fig.1: Showing the variation of fusion product energy as a function of θ for: a) neutrons from d->T, b) α-particles from d->T, c) neutrons from d->D for a monoenergetic d beam with E_d = 500 keV in a cold plasma.

For neutrons from thermal D-D and D-T plasmas the dependence of the product energy on the details of the reaction kinematics is well exploited by measurements of the broadening of the neutron peak to deduce the plasma ion temperature. Conservation of momentum dictates a corresponding broadening for the associated charged particles. The FWHM of the α-particle distribution from a 25 keV thermal plasma will be 900 keV and 18% of the particles will have an energy in excess of 4 MeV (2% in excess of 4.5 MeV). How well will these α-particles be confined in a device designed to confine α-particles with a nominal energy of 3.5 MeV? Most, if not all, present day simulation and interpretation codes ignore the spread in energy.

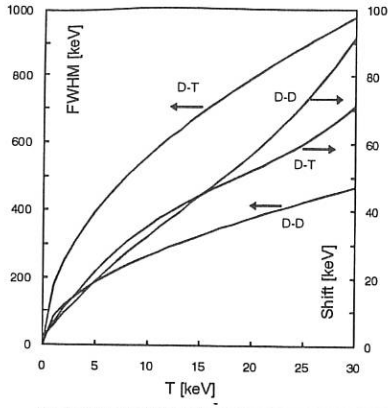


Fig.2.: The full width half maximum (FWHM) and associated energy shift for D-D and D-T neutrons as a function of temperature:

$FWHM = g \cdot \sqrt{T_i}$ (ref.1), where g is weakly dependent on T_i (ref.2). The broadening of the associated charged fusion product spectrum is identical to that of the neutron.

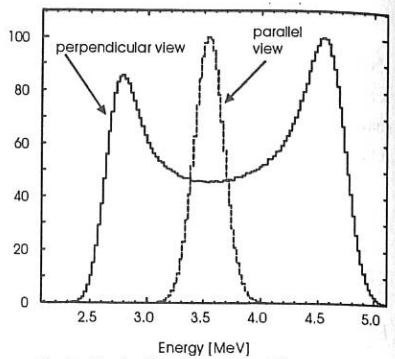


Fig.3: Illustrating the α-particle spectrum at birth for a perpendicular (to the toroidal magnetic field, B_T) monoenergetic deuterium beam of E_d=200 keV circulating in a 5 keV plasma. (Reactivities not to scale)

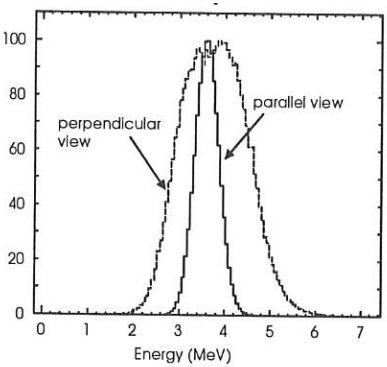


Fig.4: Calculated α-particle birth spectra from a perpendicular RF-driven fast deuterium tail (T_{tail}= 200 keV) in a tritium background plasma (T_i= 12 keV). The distribution function is far from monoenergetic even if viewed parallel to B_T.

DRIVEN SYSTEMS: Doppler Shift For driven systems the spread will be enhanced (the energy range of α-particles from 500 keV D° beams, as proposed for ITER, will range from 2.2 to 5.3 MeV) and, moreover, anisotropy will play a role as discussed below. Results were obtained with a Monte-Carlo relativistic kinematics computer code (ref. 2). The effects on the spectra are illustrated in Figs. 2 and 3. Note that the spectrum shape depends on the angle of emission.

Anisotropy: Due to the relatively low mass of the neutron, neutron emission is close to isotropic in present day machines even for D-D neutrons despite the deviation from isotropy of the D-D cross section in the CM above ~ 100 keV. This is not the case for the 1 MeV tritons released, which are often used for studying fast particle behaviour via their burn-up. The number of 140 keV D° beam generated tritons emitted in a 30° forward cone is more than doubled (X 2.4) as compared to isotropic emission; is this part of the explanation for the extremely flat and sawtooth resistant 14 MeV neutron profiles as observed in JET?

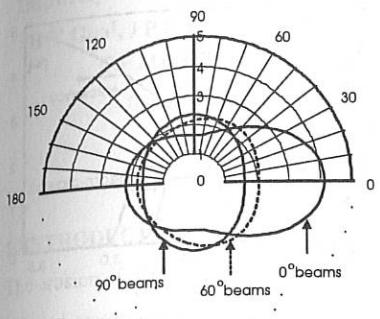


Fig.5: $\int \frac{\partial^2 N}{\partial \Omega_3 \cdot \partial E_3} \cdot dE_3$ *for tritons from 140 keV D beams injected at pitch angles of 0°, 60°, and 90° and slowing down in a 10 keV plasma (0° = parallel to the B_T field lines)*

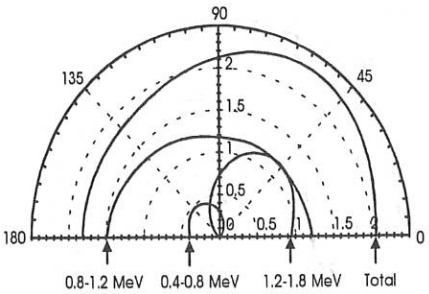


Fig.6.: Differential cross-section for the emission of tritons in 3 energy ranges; beams with E_d=140 keV injected at a pitch angle of 60°.

D-D neutron emission from d beam heating in present day machines The slight anisotropy in the D-D neutron emission on present day machines is normally neglected. However, if the variation in the shape of the energy spectra as a function of emission angle is taken into account and detectors with energy dependent efficiencies (as in the JET neutron profile monitor) are used, this is no longer justified. At JET with 140 keV D^0 beams the NE213 detectors of the profile monitor are used as counters (in an energy window around 2.5 MeV) and their detection efficiency is determined by assuming a gaussian spectrum as from a thermal plasma. This neglect of the variation of the detector efficiency with energy together with the shape of non-gaussian beam spectra lead to a 7 % overestimation of beam-plasma neutrons. Adding the effect from anisotropy (~6%) yields a total of 13%. A 5% error in the NE213 bias setting or an equivalent drift in the photomultiplier gain results in a 17% overestimation. For beam-beam neutrons the enhancement becomes 19% and anisotropy adds 13%, leading to a total of 34%.

α-particles Although the D-T cross section is almost isotropic in the CM frame, the number of α-particles produced in a forward cone of 30° by 140 keV D° beams is increased by 50% due to the CM-laboratory frame transformation. Orbit calculations carried out for a typical high performance JET plasma (I_p=3.8 MA and B_T=3.4 T) indicates a ~9 times higher probability of prompt loss for 4.5 MeV α-particles than for those that are born with an energy of 3 MeV.

D-D neutrons from high energy beams At 500 keV injection energy, as proposed for ITER, even the 2.5 MeV neutron emission will become anisotropic (50% increase in a 30° forward cone) thus rendering the measurement of D-D neutron yields extremely difficult and measuring n_D/n_T ratios within a factor of 2 accuracy, using neutron diagnostics in the presence of beams, can almost certainly be excluded.

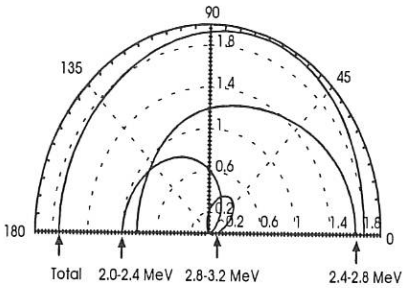


Fig.7: Neutron emission from a 140 keV deuterium beam injected at 60° and slowing down in a 10 keV plasma.

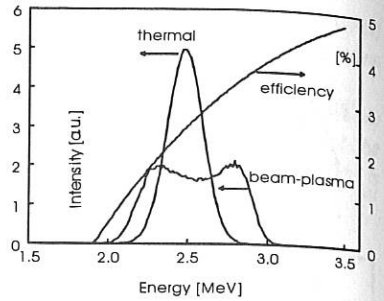


Fig.8: Calculated neutron spectra for perpendicular viewing under conditions of fig.7. Also shown is the detection efficiency of the JET neutron profile monitor detector (NE213 scintillator biased at 1.9 MeV).

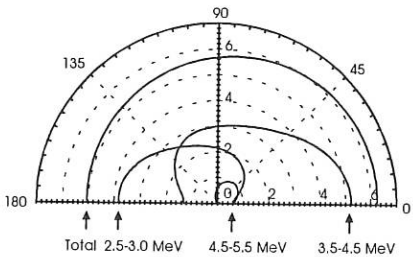


Fig.9: α-particles generated by 500 keV d beams (as proposed for ITER) injected at ~ 60° and slowing down in a 25 keV plasma.

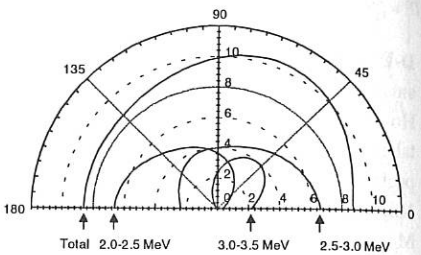


Fig.10: D-D Neutron emission from 500 keV d beams injected at 60° and slowing down in a 25 keV plasma.

CONCLUSIONS Doppler shift of fusion products is significant and should not be ignored in interpretation and prediction codes. Anisotropy of the fusion product emission in (anisotropically) driven systems should not be ignored for: a) tritons and ^{3}He-particles from deuterium beam reactions with $E_{beam} \geq 100$ keV, b) α-particles from beam reactions with $E_{beam} \geq 100$ keV, c) neutrons from beam reactions with $E_{beam} \geq 500$ keV. Broadening and anisotropy needs to be incorporated into triton burn-up interpretation codes. Full α-particle spatial birth profiles (including pitch angle distribution as needed for calculating α-particle densities) cannot be deduced from 2 dimensional neutron profile measurements in driven systems. Accurately diagnosing D-D neutrons generated from 500 keV d-beams in ITER-like plasmas will be extremely difficult and requires additional, non perpendicular viewing, energy sensitive neutron diagnostics.

References: 1. Brysk H, Plasma Physics 15 (1973) 611.

2. Van Belle P, Sadler G, Basic and Advanced Fusion Plasma Diagnostic Techniques (Varenna 1986) Vol III 767 EUR 10797 EN.

Impurity Production and Erosion/Redeposition at the JET MKI Divertor

H Y Guo[1], J P Coad, J D Elder[2], L D Horton, A Hwang, X L Li, J Lingertat, A Loarte, G F Matthews, R D Monk[3], M F Stamp, P C Stangeby[2] and A Tabasso

JET Joint Undertaking, Abingdon, Oxfordshire, OX14 3EA, UK
[1]INRS-Energie et Matériaux, Université du Québec, Canada
[2]and University of Toronto, Institute for Aerospace Studies, Canada
[3]Dept. of Physics, Royal Holloway College, University of London, UK

1. INTRODUCTION

The erosion of plasma facing materials is one of the crucial issues to be faced in the design of a fusion reactor. For most materials the dominant erosion process under ion bombardment is physical sputtering, while chemical sputtering has also proven to be important for graphite [1]. However, the redeposition of the eroded particles created by different erosion mechanisms and their efficiency in plasma contamination are less understood. This paper describes the colorimetric measurements of erosion rates in the JET MKI carbon divertor and the simulation of colorimetric results and divertor carbon profiles using the DIVIMP code. The relative roles of physical and chemical sputtering on the net erosion and impurity influx are also discussed.

2. EROSION / REDEPOSITION OF THE MKI CARBON DIVERTOR

During the 1994/5 JET operations a colour viewing system has been routinely used to measure erosion/redeposition from changes in the complementary colours of redeposited films using the method of Wienhold *et al* [2]. A CCD colour video camera views the outer part (400 x 350 mm) of the divertor floor from the top of the vessel using illumination provided by a halogen lamp with a dichroic reflector. Colour images are taken automatically after each pulse using a frame grabber. With an analysis program, the colour coordinates RGB (red, green, blue) of images are converted to hue values, which are then related to the film thickness.

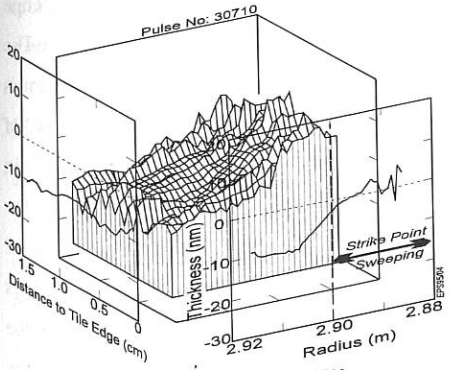


Fig.1. Erosion/Redeposition profile for shot 30710.

Fig.1 shows the erosion profile for shot 30710 as a function of the radial distance to the machine centre, and the toroidal distance to the divertor tile edge. For this pulse, the separatrix swept over the region

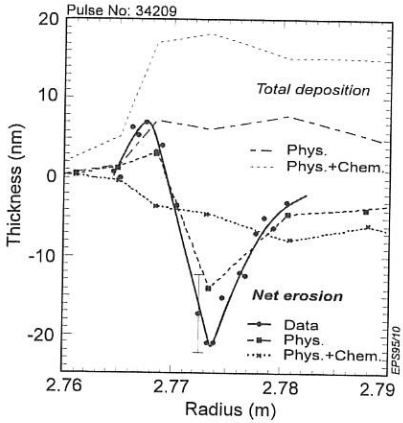


Fig.2. Experimental and simulated erosion/redeposition profiles for a hot ion H-mode: shot 34209.

R=2.8 to 2.9 m, the central plasma density was $5x10^{19}$ m^{-3}, NBI heating power was 12 MW with a duration of 3.5s. As can be seen in the region swept by the plasma, there is little change on the net erosion profile. However, in the SOL near the turning point of the plasma sweeping the erosion is about 10 nm. At high power, much higher erosion rates have been observed. Fig.2 shows the erosion/redeposition profiles for a hot ion H-mode discharge. For this pulse, the total heating power was initially 22 MW, then stepped down to 12 MW, with a duration of about 1 s in total. The strike point was very stable during this period. The plasma parameters at the target plates, as measured by Langmuir probes, also remained constant. As can be seen the profile is peaked and narrow (~ 1 cm) with a net erosion of about 20 nm near the strike point. Eroded atoms are redeposited nearby in the private region.

3. DIVIMP SIMULATIONS

To investigate the effects of different impurity production mechanisms on the net erosion and impurity influx we have simulated measured erosion and divertor carbon profiles, using the DIVIMP code [3,4]. A 2-D background plasma is generated using a one-dimensional quasi-analytic model, based on the measurements of Langmuir probes at the target plates to define boundary conditions, assuming $T_i = 2T_e$.. The cross-field diffusion coefficient is $D_\perp = 1$ m^2/s for impurity ions. Chemical sputtering of graphite has been newly implemented in DIVIMP. Slow C-atoms are launched at the target (600 K) with the yields calculated according to the formulae by Garcia-Rosales and Roth [5]. Fig.3 shows the Langmuir probe data at the inner/outer target plates and the values used as input to the code for shot 34209.

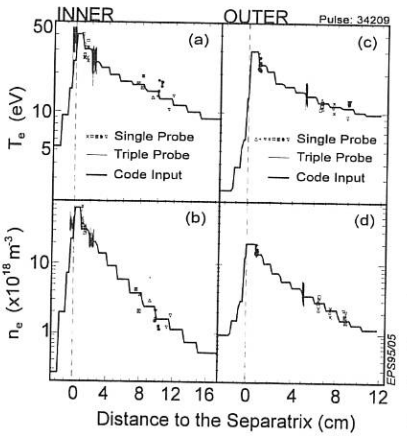


Fig.3. Langmuir probe data and values used as input to the code for shot 34209.

3.1. Erosion/Redeposition

The calculated erosion/redeposition profiles for shot 34209 are also shown in fig.2. The net erosion caused by physical sputtering results in a very peaked profile, in agreement both quantitatively and in shape with the experimental data. With chemical sputtering, yields increase from 1.9% to 4.1% and the net erosion becomes flat. It appears that there is, effectively, no chemical sputtering. The chemically sputtered CD_4 and fragments must redeposit promptly near their point of origin. This has been observed by Lieder *et al* [6].

3.2. CII Intensity Profiles

CII (658 nm) intensity profiles have been recorded with an absolutely calibrated Flux Camera, which views the divertor vertically from the top of the vessel. For shot 34209 (fig.4a), with only physical sputtering, the simulated CII intensities are in good agreement with the flux camera results. However, including chemical sputtering gives higher CII intensity near the outer strike point due to the relatively lower temperature. This effect is much more pronounced for shot 34355 (fig.4b). In this case, the temperature at the target plates are so low (~ 10 eV) that the effective yield is greatly influenced: for physical sputtering, the effective yield is only 0.94%, while with chemical sputtering it is 5.7%. Again, the CII profile at the target shows little contribution due to chemical sputtering. It is estimated (from fig.4b) that chemically sputtered hydrocarbons only contribute 10% of C^+. Shimizu *et al* have also found that only about 10% of target-produced CD_4 reaches C^+ [7], and Kallenbach *et al* estimated only 20% of the CD_4 gets to CD [8].

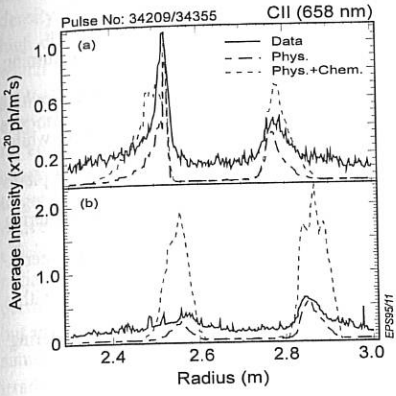


Fig.4. CII profiles for (a) shot 34209, and (b) 34355.

3.3. CIII Intensity Levels

Visible spectroscopy (KS3) has been employed to measure the integrated photon flux of CIII (465 nm) from the inner and outer divertor areas separately. The measurements and DIVIMP results for shots 34209 and 34355 are shown in Table I. Using only physical sputtering, with $T_i = T_e$ or $T_i = 2T_e$, produces a reasonable fit to the data. Including chemical sputtering, the calculated CIII intensity values increase dramatically, by factors of 3 ~ 25 times higher than

the experimental data. Thus, the rate of production of the C^{++} ions following chemical sputtering is low. This is consistent with the analysis of the C^{+} data discussed above.

Table I. CIII spectroscopic data in the inner and outer divertor and DIVIMP results, employing physical sputtering only (Phys), and physical and chemical sputtering (Phys+Chem) for different ion temperatures.

Shot No.	Modelling Details		Outer ($x10^{18}$ ph/s/m^2/sr)	Inner ($x10^{18}$ ph/s/m^2/sr)
34209	*Exp.*	*KS3 data*	*1.6*	*3.4*
(52.3s)	Phys.	$T_i = 2T_e / T_e$	3.1 / 2.3	6.4 /5.8
	Phys.+Chem.	$T_i = 2T_e / T_e$	6.6 / 8.0	10/12
34355	*Exp*	*KS3 data*	*5.0*	*2.2*
(51.2s)	Phys.	$T_i = 2T_e / T_e$	7.0 / 4.8	1.9 /0.8
	Phys.+Chem.	$T_i = 2T_e / T_e$	23 / 23	11/7.4

4. CONCLUSIONS

No net erosion is observed during plasma sweeping, except in the proximity of the turning point. The erosion rate depends on the plasma density and the heating power. At medium power (~ 10 MW), an erosion rate of order of 5 nm/s is observed near the strike point, whilst at high power (~ 20 MW), the erosion rate reaches ~ 20 nm/s. The erosion of the target plates is mainly due to physical sputtering, showing no obvious effect of chemical sputtering evidently due to the prompt and localised redeposition of CD_4 and molecular fragments. Spectroscopic lines of C^{+} and C^{++} are quantitatively reproduced by the DIVIMP code with a dominant physical sputtering source, and also show little effect due to chemical sputtering, suggesting low efficiency of producing carbon ions from CD_4.

5. ACKNOWLEDGEMENTS

HYG acknowledges financial support from the National Fusion Program of Canada.

6. REFERENCES

[1] J. Roth, E.Vietzke and A.A. Haasz, Supplement to Nucl. Fusion **1**, 63 (1991)

[2] P. Wienhold, F. Weschenfelder and J. Winter, to appear in J. Nucl. Mater. **220-222**

[3] P.C. Stangeby, C. Farrell, S. Hoskins and L. Wood, Nucl. Fusion **28**, 1945 (1988)

[4] P.C. Stangeby and J.D. Elder, J. Nul. Mater. **196-198**, 258(1992)

[5] C. Garcia-Rosales and J. Roth, in Proc. of 21st EPS Conference on Controlled Fusion and Plasma Physics, Vol. 18B, Part II, p. 770, Montpellier, 1994

[6] G. Lieder, K. Behringer, A. R. Field, *et al*, *ibid,* p. 722.

[7] K. Shimizu, et al, IAEA-CN-60/D-P-I-2, 15th IAEA Conference, Seville, Spain, 1994

[8] A. Kallenbach, R. Neu, W. Poschenrieder, *et al*, Nucl. Fusion **34**, 1557(1994)

Plasma shield formation and divertor plate erosion for ITER Tokamak plasma disruptions

B Bazylev[1], F Kappler[2], I Landman[3], S Pestchany[3], G Piazza[2], H Wuerz[2]

1. Luikov Institute of Heat and Mass Transfer, Minsk, Belarus
2. Forschungszentrum Karlsruhe, P.O.Box 3640, 76021 Karlsruhe, Germany
3. Troitsk Institute for Innovation and Fusion Research 142092 Troitsk, Russia

1. Introduction

During the thermal quench phase of a tokamak plasma disruption and during ELMs the divertor plates are hit by an intense plasma flow. In ITER this flow is estimated to have the following parameters: impact energy around 10 keV, pulse duration larger than 100 μs, power density W in the direction to the plate up to 10 MW/cm^2 for disruptions and ELMs [1]. This high divertor heat load causes sudden evaporation of a thin layer of divertor plate material which acts as plasma shield and effectively protects the divertor from further excessive evaporation [2]. It was shown numerically that for an impinging plasma flow the vapour shield consists of a rather cold plasma layer at the target and a hot corona at the outside which converts the incoming energy with an efficiency of more than 30% into soft x-ray radiation (SXR) [3]. The plasma shield partially absorbs the energy of the hot plasma but mainly radiates backwards [4]. Disruption simulation experiments with carbon targets irradiated by a hydrogen plasma flow of W ≈ 10 MW/cm^2 have shown that a vapour cloud with temperature up to 80 eV is formed [5].

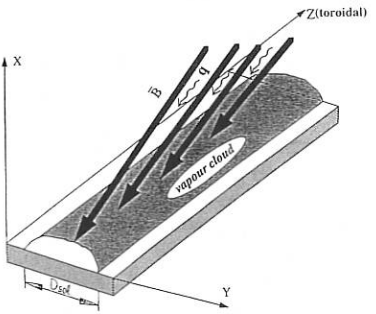


Figure 1. Divertor with inclined magnetic field

Plasma shield formation and target material erosion for carbon, beryllium and tungsten are calculated with the MHD code FOREV for ITER typical disruption conditions. Fig.1 schematically shows the divertor situation. Due to the inclination of the magnetic field **B** and the finite width of the incoming energy flux (D_{sol}) three components of plasma velocity and magnetic field should be taken into account in the MHD modelling of the vapour behaviour. As first step only x and z components of field and velocity have been considered (1½D MHD model). Meanwhile a 2D version of FOREV with symmetry only along the z-axis is available (2½D MHD model).

For low Z materials it is of importance how effectively the intense flash of SXR radiation produced in the high temperature corona is transferred through the dense cold plasma layer to the target. In order to solve this problem adequately a self consistent approach was developed additionally. First results from the self consistent approach are compared with results from multigroup opacity calculations.

2. Features of the MHD code FOREV

In FOREV two discrete spatial grids are used for the solid and the vapour. Heat conduction into the bulk target, surface ion and volumetric electron energy deposition and melt front

propagation are modelled in the solid. Motion of the plasma, its diffusion across magnetic field, Joule heating, electron heat conduction and bound-free electron energy exchange are modelled in the vapour. Energy deposition by monoenergetic and Maxwellian distributed hot electrons and energy deposition and momentum transfer by monoenergetic ions moving along the magnetic force lines is taken into account. The starting velocity of the vaporised material at the target is limited by the sound velocity.

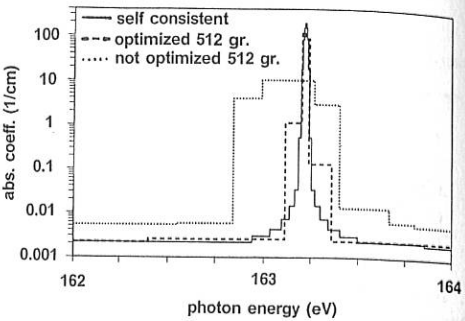


Figure 2. 512 group Planck opacity of absorption for beryllium of density 10^{17} cm^{-3} and temperature 20 eV

For radiation transport the multiray forward reverse method with 6 directions per hemisphere is used. As radiation transport mainly determines the erosion, three radiation transport approaches are available in the code: radiative heat conduction, multi group opacity, and self consistent modes. The last one presently performs calculations with fixed vapour density and temperature profiles as obtained from full 1½D calculations. It uses the TOPATOM atomic data base [6] and produces consistent multi group Planck opacities from actual radiation fluxes.

In the multi group opacity approach the opacities are produced with an optimised frequency mesh which allows to resolve the profiles of important lines (see Fig.2). Another important feature of the 1½D MHD code is spatial mesh optimisation which allows to use a dense mesh in regions of large plasma temperature and density gradients and permanently several cells for describing the energy and momentum deposition of the incoming ion beam.

For the 2½D MHD calculations a rectangular grid is used. To simulate the tilting of the divertor plate in the poloidal plane a special procedure for the boundary conditions was applied.

3. Results of 1½D calculations

Typical temperature and electron density profiles for a carbon plasma at several times up to 200 μs are shown in Fig.3 for W = 10 MW/cm^2. A 5 T magnetic field inclined under an angle

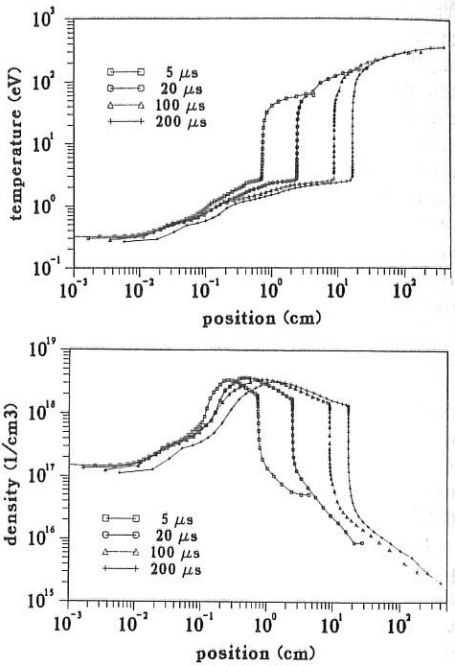


Figure 3. Electron temperature and density of carbon plasma. Symbols indicate the centres of the spatial mesh

of 5° was assumed. The impinging plasma flow consists of 10 keV ions and Maxwellian electrons of temperature 10 keV with equal contributions of both to the power density. At 100 μs the vapour temperature in the corona is up to T_{max} = 300 eV. At the distance L_{max} = 2 m from the target the vapour density N_{min} is $5 \cdot 10^{14}$ cm^{-3}, diffusion across magnetic field plays a minor role. Close to the target the vapour density reaches the value $N_{max} = 5 \cdot 10^{19}$ cm^{-3}, the vapour temperature at the target surface is the carbon sublimation temperature, a neutral layer of thickness of less than 8 mm is obtained adjacent to the target. The magnetic field decreases by less than 15% across the vapour shield because the vapour propagates rather freely along the force lines without distortion of the field. Erosion, backradiated fluxes and fluxes to the target after 100 μs are given in Table 1. For carbon the SXR radiation in the photon energy region 300-600 eV contributes up to η = 27% to the backradiated flux. According to the preliminary results from self consistent calculations for carbon this intense SXR radiation doesn't penetrate to the target and the backradiated intensity is nearly a factor of 2 less. The heat load at the target is due to photons with energies below 10 eV. Direct heating of the target by the high energetic tail of the Maxwellian electrons after 30 μs becomes less than the radiation flux and negligible after 100μs.

For beryllium the results are similar: T_{max} = 350 eV, $N_{min} = 6 \cdot 10^{14}$ cm^{-3}, $N_{max} = 2 \cdot 10^{20}$ cm^{-3}, L_{max} = 2.5 m, η = 27% (SXR in the region 120-300 eV). The thickness of the melt layer is 40 μm, therefore the stability of the melt layer during a disruptive event becomes important. The self consistently calculated radiative heat load to the target is larger. Again the backradiated flux is less. The lower intensity influences the energy balance and would result in even higher temperatures of the plasma corona.

Table 1. Radiation fluxes (MW/cm^2) and erosion in case of corona

target material	carbon		beryllium	
the mode	512 group	self consistent	512 group	self consistent
flux onto target	0.4	0.48	0.15	0.33
backradiated	6.5	3.44	5.9	4.04
erosion *(μm)*	2.7	-	2.1	-

4. First results of 2½D MHD calculations

In the case of a carbon target hit by 10 keV Maxwellian electrons with power density of 10 MW/cm^2 the maximum plasma temperature is 3.7 eV and no hot plasma corona is produced. To investigate how 2 dimensional effects change the results of 1½D modelling a first 2½D calculation was performed for this case. In the modelling the incoming Maxwellian electrons have a Gaussian distribution of power density in y-direction (see Figs.4) with a maximum of 10 MW/cm^2 at y = 10 cm and a half-width of D_{sol} = 5 cm. The target is at x = 0. The vacuum magnetic field is 5 T in z- and 0.5 T in x-direction. 2D distributions of vapour density and temperature at 35 μs are shown in Fig.4. Fig.5 shows erosion profiles at different times. After 35 μs the maximum temperature is 2.4 eV and maximum erosion is 2.8 μm (for the 1½D case 3.5 μm were obtained). The vapour shield converts the incoming power into radiation, a fraction of 16% causes heating and erosion of the divertor plate, about 64% is radiated to the side walls with a maximum radiation intensity at a distance of 15 cm from the target. According to Fig.4 the vapour expansion along the field lines dominates over diffusion across **B**. Thus the main two dimensional effect is radiation to the side walls. Lateral mass losses are less important.

5. Conclusions

1½D and 2½D modelling have been applied to the analysis of ITER tokamak disruptive erosion. For low Z materials the plasma corona effectively converts a significant fraction of the impinging plasma energy into SXR radiation. Because of increase of target heat load, the self consistent approach could become important for an adequate calculation of erosion for beryllium. Preliminary results of 2½D calculations have shown that radiative side losses are more important than lateral mass losses. Further development of the 2½D code is needed for adequate modelling of the tokamak situation including tilting of the target in the poloidal plane and vaporisation of side walls due to intense lateral radiation.

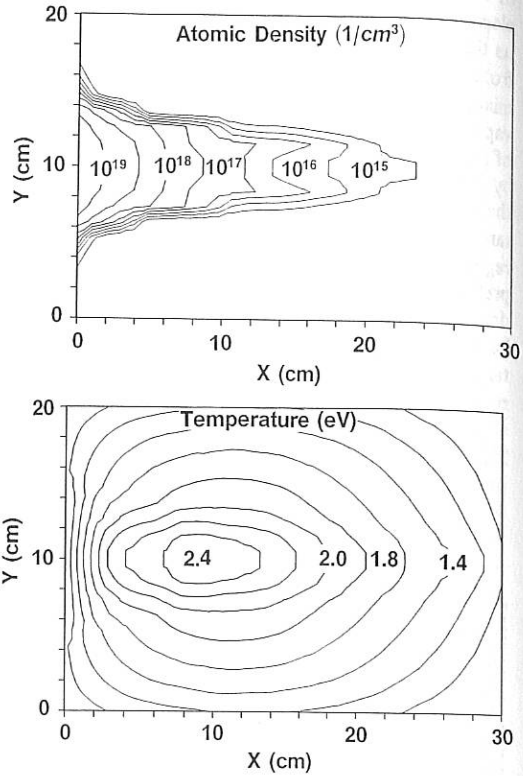


Figure 4. Vapour density and temperature distribution for carbon at 35 μs for 2½D MHD model

References

[1] G Janeschitz et al., 11th Int.Conf. on Plasma Surf.Interac.in Contr.Fus.Dev., Mito 94.

[2] A Sestero, Nucl.Fusion **17**, 1, 1977, p.115.

[3] H Wuerz et al., 21th Conf.on Contr.Fus and Pl.Phys., Monpellier 94, **18B**, II, p.201.

[4] H Wuerz et al., J.Nucl.Mat.,212-215,1994, p.1349.

[5] N.I. Arkhipov et al., 18th SOFT Karlsruhe, 1994.

[6] B Bazylev et al., Phys.Eng.J., **58**, 6, 1990, p.1012 (in Russian)

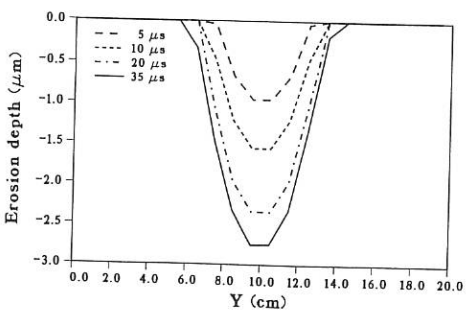


Figure 5. Erosion profile for 2½D MHD calculation

In-situ measurement of erosion/deposition in the DIII-D divertor by colorimetry

F.Weschenfelder[(i)], G.L.Jackson, P.Wienhold[(i)], J.Winter[(i)], N.H.Brooks, W.P.West, R.Lee

[(i)]*Forschungszentrum Jülich GmbH, Institut für Plasmaphysik, Ass. EURATOM-KFA, POB 1913, 52425 Jülich, Germany*

General Atomics, P.O.B. 85608, San Diego, California 92186-9784, USA

Introduction

Erosion of plasma facing materials in both present and future fusion devices such as ITER can seriously degrade plasma performance and limit the lifetime of the device [1]. Net erosion rates are difficult to predict and depend on several complex processes, including chemical erosion, sputtering, transport and redeposition. Accurate erosion measurements in operating tokamaks are needed to improve the understanding of erosion process dynamics and material transport. Since graphite plays a key role as first wall material in most present fusion devices, layers of amorphous hydrogenated carbon (a-C:H) are naturally formed on wall components by codeposition of the eroded carbon and the plasma hydrogen [2]. Changes in the thickness of those carbon films which correspond to growth or erosion can be measured on a shot by shot basis by colorimetry[3]. It observes the shift of interference colors when the film covered surface is illuminated with white light. Colorimetry was introduced in the DIII-D tokamak. The technique and a first erosion measurement will be described.

Three Filter Colorimetry

Colorimetry is used to measure and quantify interference colors of thin transparent layers. In order to infer a film thickness, a set of three color filters and a camera (black and white) is used. The camera signals obtained with each filter when observing an incident white spectrum, $\varphi_i(\lambda)$, reflected from a coated surface can be written as

$$X_R = c_R \cdot \int \varphi_i(\lambda) R(\lambda) P(\lambda) \tau_R(\lambda)\, d\lambda$$
$$Y_G = c_G \cdot \int \varphi_i(\lambda) R(\lambda) P(\lambda) \tau_G(\lambda)\, d\lambda$$
$$Z_B = c_B \cdot \int \varphi_i(\lambda) R(\lambda) P(\lambda) \tau_B(\lambda)\, d\lambda$$

$\tau_R(\lambda)$, $\tau_G(\lambda)$ and $\tau_B(\lambda)$ are the transmissivities of the filters, $P(\lambda)$ the responsivity of the camera, c_R, c_G and $c_B$are calibration constants (white balance) and $R(\lambda)$ is the reflectivity of the coated surface which depends on the film thickness.

Any spectral distribution can then be represented by the two chromaticity coordinates x,y:

$$x = \frac{X_R}{X_R+Y_G+Z_B}\ ,\ y = \frac{Y_G}{X_R+Y_G+Z_B}$$

or the corresponding hue angle h_{xy} which represents the color impression:

$$\tan h_{xy} = \frac{y-y_i}{x-x_i}$$

The so called "no color" point $x_i=y_i=1/3$ determines the calibration of the system for the unchanged "white" illumination spectrum.

The DIII-D tokamak (R=1.67m, a=0.67m) [4] produces a significant flux of fast neutrons ($\leq 5x10^{15}$/discharge) and only radiation hardened black and white cameras can be used near the device. To optimize the light throughput, three filters were chosen with the center wavelengths at 543nm, 643nm and 753nm. Fig.1a shows the development of the calculated color with growing film thickness as a function of the chromaticity coordinates x and y. All detectable colors are located inside a triangle (monochromatic boundary curve). The color trace for a growing film starts at the no color point assuming the film thickness d=0nm, i.e. the spectrum of an halogen lamp is reflected at a blank graphite surface (n_S=2.22, k_S=0.14). As the thickness of the film increases the color follows the curve around the no color point. Every 5nm a point is plotted on the curve. The optical constants of the film are assumed to be n=2.0 and k=0.1. Fig.1b shows the relation between hue and film thickness corresponding to fig.1a. This hue-thickness relation can then be used to determine the film thickness out of a hue measurement.

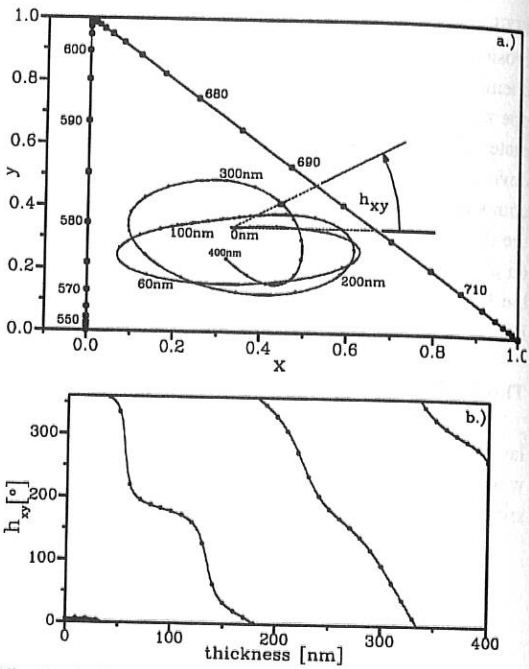


Fig. 1 :a.) Chromaticity coordinates plotted as a function of film thickness (a-C:H film on graphite).
Fig. 1 :b.) Hue - thickness relation corresponding to fig 1a.)

Experimental setup

Fig.2 shows the experimental setup at DIII-D. The light of a 150W halogen lamp with reflector is focused onto the floor of the tokamak in a region of ~15cm diameter. Near the center of this region the Divertor Material Exposure System (DIMES) [5] is located. It is used to insert samples coplanar to the surrounding graphite tiles of the divertor floor. The camera together with a filter wheel is installed at the same toroidal location at a second port. The observation distance between the camera and an exposed DIMES sample is about 3m. Between the discharges the camera signal was recorded with each filter for about 10 seconds. A 5 second sequence of frames was grabbed for each filter from the video tape and the intensities along a poloidal line over the center of DIMES was digitized and averaged. A file with the measured X^M_R, Y^M_G and Z^M_B data is generated and can then be used in a colorimetric program which compares the measured and theoretical hue angles and determines the film thickness.

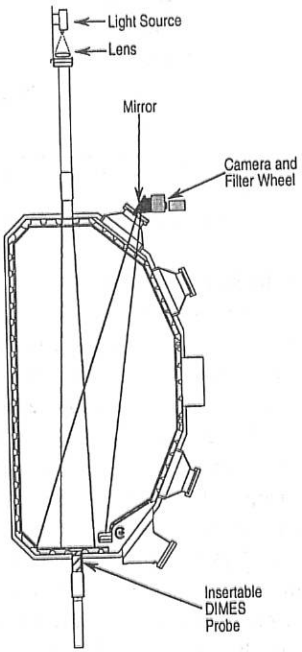


Fig. 2 : Experimental setup at DIII-D

DIMES sample 40 (graphite) was sent to KFA-Jülich, IPP and was coated first with an aluminum layer of several hundred nanometers and then with an a-C:H film during an RF glow discharge in methane. The final thickness of the a-C:H layer was about 300nm. Two small silicon waver pieces were coated during the same discharge showing that the a-C:H film has the optical constants n=2.0 (±0.05) and k=0.275 (±0.01).

The coated DIMES sample was shipped back to GA, San Diego, and was exposed to 9 DIII-D tokamak discharges. During each of these discharges the outer strike point was moved onto the sample for about 1 second. All discharges were ELMing H-mode discharges. The NBI power was varied between 2.5 and 7.1 MW during the second of exposure causing a change in the ELM frequency, heat flux and the outer strike point of the separatrix defined flux surface. The heat flux and the position of maximum heat flux was evaluated out of IR-camera data. The peak heat flux varied between 70 - 125 W/cm^2 with an average peak heat flux of $110W/cm^2$. The average location of the peak heat flux was varying between 146.4cm and 149.5cm, while the outer strike point varied from 146.3cm to 147.7cm. The DIMES sample has a diameter of 4.77cm and the radial position of its center is at 148.5cm. (DIMES: 146.11cm - 150.88cm).

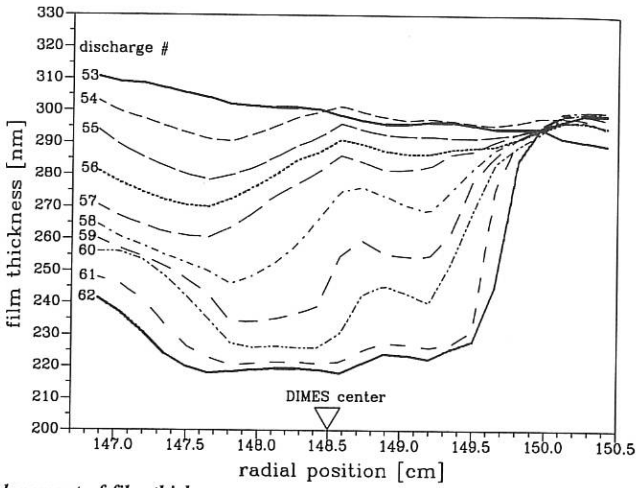


Fig. 3 : Developement of film thickness

Results and discussion

Fig. 3 shows the development of the film thickness discharge by discharge. The thickness is plotted as a function of the radial position. The last two digits of the discharge number after which the thickness was determined is plotted directly left beside each curve. The sample was inserted for the first time after discharge #53 (83653). This curve shows the original film thickness (300 - 310nm). After each discharge the film thickness decreases almost over the entire sample with the position of maximum erosion at 147.7cm. After 9 discharges (9 plasma seconds) the peak erosion is -86nm corresponding to a maximum average erosion rate of 9.56nm/s or 0.3m/year. This rate observed with an average peak heat flux of 1.1MWm^{-2} (averaged over 9 discharges) would result in a very high erosion rate, if extrapolated to ITER conditions (~5MWm^{-2}), making long-term operation questionable. Erosion/deposition mechanisms have to be studied in further detail to form a data base and to benchmark models like ERO, ERO-TEXTOR, WBC and REDEP. For that purpose colorimetry may be a useful instrument since it offers the possibility to measure erosion in situ and over extended areas.

Acknowledgements: This work was made possible with the support of a fellowship by the NATO science committee via the DAAD (Deutscher Akad. Austauschdienst, Kennedyallee 50, D-53175 Bonn).

References

[1] M.F.A.Harrison, E.S.Hotston, G.P.Maddison, NET Report EUR-FU/80/90-97, 1990

[2] P.Wienhold, J.von Seggern, H.G.Esser, J.Winter et al., J.Nuc.Mat. 176&177 (1990) 150

[3] P.Wienhold, F.Weschenfelder, J.Winter, Nucl.Inst. and Meth. in Phy. Res. B 94 (1994) 503

[4] R.D.Stambough and the DIII-D Team, "DIII-D Research Program Progress" in Proc. 13th Conf. on Plasma Physics and Controlled Nuclear Fusion Research, Washington, DC 1990 (IAEA, Vienna, 1991) p.69

[5] C.P.C.Wong, R.Junge, R.D.Phelps, et al., J.Nucl.Mater. 196-198 (1990) 871

DISRUPTION-CAUSED WALL EROSION AND VAPOUR SHIELD FORMATION

P. Lalousis*, L. Lengyel, V. Rozhansky**, P. Spathis*, and I. Veselova**
Max-Planck-Istitut für Plasmaphysik - EURATOM Association
D-85748 Garching bei München, Germany
* IESL.FORTH, Heraklion, GR, ** State Technical University St. Petersburg, RU

During off-normal operational regimes in large-scale tokamaks, as in the case of hard disruptions or giant ELMs, an intense flux of high-energy plasma particles impacts the plasma-facing machine components. According to a set of ITER specifications, the energy flux affecting the divertor plates of ITER during the thermal quench phase of a disruption may be of the order of 10^{10} *to* 10^{12} W/m^2 (10 *to* 150 MJ/m^2 in 0.1 *to* 3.0 ms). The energy flux incident at the divertor plates raises the temperature of the solid until phase transition takes place: a vapour layer forms at the surface which, depending upon the physical properties of the substance used for coating the plates, may deplete the incident particle and energy fluxes and, at the same time, dissipate the energy deposited by radiation to the environment. The physics of this process is described in previous publications [1, 2]. Also the major details of the 1.5-D time-dependent MHD code developed for analyzing this process are outlined there (collisional depletion of the incident particle and energy fluxes with allowance for the self-generated electrostatic shielding field, gasdynamic expansion of the unionized vapour substance, high-beta interaction of the ionized fraction with the skewed magnetic field, phase transition at the solid surface, finite rate ionization and recombination processes, conductive energy transport, radiative energy transport with frequency-averaged Rosseland opacities, etc.). The finite width of the SOL is taken into account by calculating its lateral expansion and the additional radiant losses escaping from its lateral surfaces.

Scenario calculations were made for checking the effect of the parameters of the disrupting plasma and that of the applied magnetic field on the erosion rate. In particular, the effect of the initial energy of the energy carriers and that of the self-generated electrostatic shielding field are considered here in detail. The energy distribution function of the energy carriers together with the electrostatic field generated define the penetration depth of the particles and thus the energy deposition profile. The penetration depths and the associated electric fields are calculated by means of stopping length calculations, and on the basis of the conditions of quasi-neutrality and am-

bipolarity, respectively. In the present model, the currents carried by incident "hot" electrons, thermal "cold" electrons, and cold ions are taken into account, as well as the thermo-electric current contributions associated with the existence of gradients across the vapour layer [2,3]. Also the sheath potential drop forming at the plasma-vapour interface is taken into account. Computations were performed for various magnetic field strengths, thus checking the effect of the magnetic field as well. In particular, the following parameter variations were done:

(a) The mean temperature T_{e0} (Maxwellian energy distribution modelled by a discrete number of energy groups) was varied at a given energy flux value (the density of the disrupting plasma was varied as $n_{e0} \propto {T_{e0}}^{-\frac{3}{2}}$).

(b) The kind of the energy carriers assumed was varied at a given energy flux value. In these calculations, the disrupting thermal plasma (5 $keV/10^{19}$ m^{-3} reference case) was replaced by beams of monoenergetic particles: a 7.5 keV electron beam in one case and an ion beam with a particle energy of 60 keV in the second case; both carrying the same energy flux as the reference disrupting thermal plasma: $q_{e0} \approx 2.2 \times 10^{11}$ W/m^2.

(c) The applied magnetic field strength was varied at given parameters of the disrupting thermal plasma and a given initial angle of incidence.

(d) To assess the relevance of the self-generated electric field, various approximations were used: first, the electric field was completely neglected; second, only the field evolving in the cloud interior was taken into account; third, also the sheath potential drop evolving at the vapour-cloud interface was aken into account.

Results of some scenario calculations

In all scenarios reported herein graphite or graphite-coated divertor plates were considered. An initial SOL width of 3 cm was assumed for all cases. The initial angle of inclination of the skewed magnetic field was 5 degr. The Maxwellian energy distribution function of all disrupting thermal plasmas was modelled by 5 discrete energy groups, each carrying the same initial energy flux.

Effect of the plasma temperature T_{e0}

The following T_{e0} / n_{e0} combinations were considered: 5 keV / 1.6×10^{19} m^{-3}, 7 keV / 1.0×10^{19} m^{-3}, and 9 keV / 0.64×10^{19} m^{-3}, yielding the same thermal energy flux q_{e0}. The assumed magnetic field strength was 4 tesla in all cases, the angle of incidence of the magnetic field 5 degr. The erosion depths corresponding to the three cases and monitored at 100 μs following the moment of plasma - wall contact are as follows: 2.6 μm, 5.8 μm, and 16.0 μm, respectively.

Effect of the kind of energy carriers

The erosion depths monitored at $\approx$ 30 μs following the plasma - wall contact are for the three cases considered as follows: 1.1 μm for the 5 keV thermal plasma case, 0.08 μm for the case of the 7.5 keV monoenergetic electron beam, and 0.06 μm for the case of the monoenergetic ion beam. The depletion of the energy fluxes across the respective vapour layers is shown in Figs. 1 to 3.

Effect of the applied magnetic field B_0

The same disrupting reference plasma as above was assumed (5 $keV/10^{19}$ m^{-3} thermal). The erosion depths monitored at 100 μs for three applied magnetic field strengths $B_0 = 2$, 4, and 6 $tesla$, were found to be 3.7 μm, 1.1 μm, and 0.7 μm, respectively.

Effect of the electrostatic shielding field E

The reference disrupting thermal plasma used in these calculations had a temperature $T_{e0} = 9\ keV$ and a density $n_{e0} = 10^{19}\ m^{-3}$. The applied magnetic field strength was $B_0 = 6\ tesla$. The erosion depths monitored for the three cases considered were: zero electric field approximation: 15 μm; E field only in the cloud interior: 7.6 μm; sheath potential drop also included: 3.6 μm. The sheath potential drop, $\Phi/kT_{ehot} \approx 1.7$ [3], is 15.3 keV in the case considered here.

Conclusions

(1) The erosion rate strongly depends not only on the energy flux carried by the plasma particles but also on the particle energies. The particle energies and/or the form of the respective distribution functions are of primary importance. Particles of the high-energy wing of the distribution function penetrate deep into the vapour layer and determine the intensity and duration of the initial vaporization burst. Monoenergetic beams deposit their energy, as soon as a vapour layer forms, at some distance from the solid surface, causing erosion rates and vapour shield characteristics qualitatively and quantitatively different from those corresponding to thermal plasmas. For comparable total energy fluxes, the fluxes carried by monoenergetic beams to the vaporizing surface are cut off much earlier than those carried by the high-energy particles of thermal plasmas (see Figs. 1 to 3).

(2) Since the vaporized particles, after being ionized, form a high-beta substance, the presence of the magnetic field substantially affects the evolution dynamics of the vapour layer and the resulting erosion rates as well.

(3) The electrostatic field evolving in the vapour layer substantially affects the energy transport to the solid surface and thus the resulting erosion rates. The potential drop across the vapor layer may be, if short-circuiting effects are absent, of the order of tens of kV-s (see Fig. 4), and are of the same order of magnitude as those calculated previously with a simpler model [2].

References

[1] L.L. Lengyel and P. Spathis, Proc. 21st EPS Conf. on Controlled Fusion and Pl. Physics, Montpellier 1994, Vol. 18B, Pt. II, p. 778.

[2] P. Spathis and L.L. Lengyel, Proc. 20th EPS Conf. on Controlled Fusion and Pl. Physics, Lisboa 1993, Vol. 17C, Pt. IV, p.1443.

[3] V.A. Rozhansky and L.L. Lengyel, Calculation of electrostatic fields in vapour shields evolving at ablating surfaces, Rept. 5/53, Max-Planck-Inst. f. Plasmaphysik, Garching, Oct. 1993.

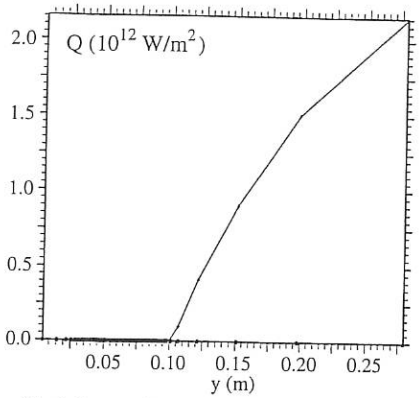


Fig.1 Energy flux depletion, 60 keV ion beam, t = 31.6 μs

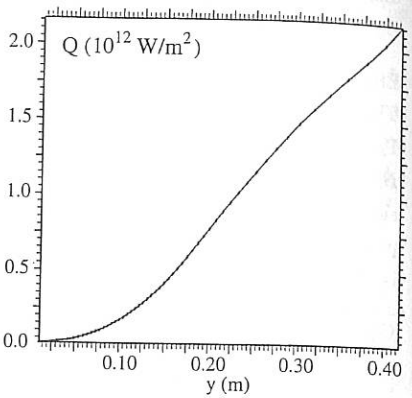


Fig.2 Energy flux depletion, 7.5 keV electron beam, t = 67.8 μs

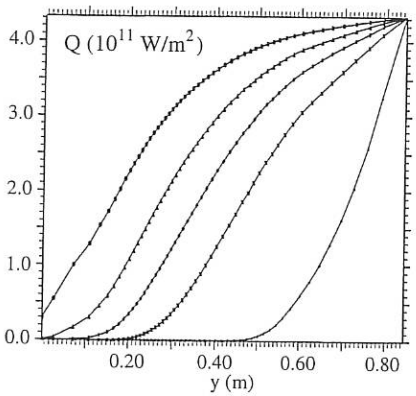


Fig.3 Energy flux depletion, 5 keV thermal plasma (5 energy group approximation), t = 100.0 μs

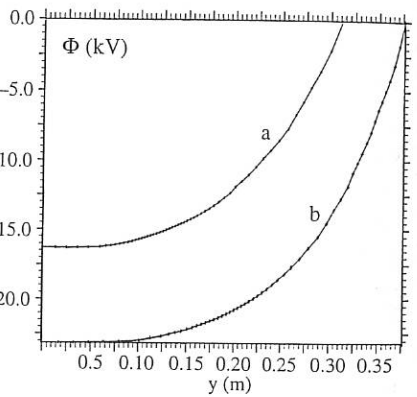


Fig.4 Potential distribution in the vapour layer (a) with sheath effect (the additional -15.3 keV potential drop across the sheath is not shown), (b) without sheath potential.

Boron Erosion and Transport in the ASDEX Upgrade Divertor

K. Krieger, D. Elder[×], A.R. Field, D. Hildebrandt, G. Lieder, B. Napiontek, C.S. Pitcher[†], D. Reiter[‡], P.C. Stangeby[×], W. West[*], ASDEX Upgrade Team, NI Team

IPP – Max-Planck-Institut für Plasmaphysik, EURATOM Assoc., D-85748 Garching

[*]General Atomics, San Diego, USA, [†]CFFTP/[×]UTIAS, Toronto, Canada

[‡]Forschungszentrum Jülich GmbH, EURATOM Assoc., Jülich, Germany

Erosion of divertor target plates and the possible leaking of the eroded particles into the confined plasma is considered as an important problem for the design of a nuclear fusion reactor. Respective laboratory experiments are usually restricted to bombardment with monoenergetic particles at fluxes, which are orders of magnitude lower than the fluxes in a real divertor. Theoretical calculations also assume highly idealized conditions. Therefore, in-situ measurements of material erosion and subsequent transport processes are necessary. To gain a better understanding of the respective processes, it is feasible to start with the investigation of stationary discharge conditions like Ohmic and L-Mode phases.

For such stationary conditions, the erosion and transport of boron in the divertor of ASDEX Upgrade was investigated by means of spectroscopic measurements. In a series of similar discharges, the line emission of neutral boron atoms and of ions in several ionization states (B^+ – B^{3+}) was recorded in the visible spectral range. Two spectrometers were used to view both perpendicularly and tangentially to the outer divertor target plates (Fig. 1). The plasma density and temperature in the divertor region were measured by flush mounted Langmuir probes in the target plates and by a horizontally sweeping Langmuir probe (IVP) some centimetres above the outer target. The heat flux to the target was determined by a thermography system. Data were obtained for plasma densities in the range $\bar{n}_e = 4.7 - 6.7 \times 10^{19}\mathrm{m}^{-3}$ with $I_p = -1\,\mathrm{MA}$, $B_t = +2.1\,\mathrm{T}$ and $P_{\mathrm{NBI}} = 2.6\,\mathrm{MW}$

Right after these experiments, a radial set of the outer target plates was removed and the boron concentration at the surface was determined by Auger-spectroscopy. Since only a few additional discharges had been run before the opening, the so determined radial boron distribution reflects quite accurately the surface conditions during the spectroscopic measurements.

For the interpretation of the measured spectroscopic line intensities, the two-dimensional Monte-Carlo impurity transport code DIVIMP [1] was used in combination with the three-

dimensional neutral gas Monte-Carlo code EIRENE [2].

In a first step, DIVIMP calculates the edge background plasma properties using a so called "onion-skin" plasma model: with radial profiles of electron density and temperature at the target as boundary conditions, n_e, T_e, T_i, $v_\parallel$ and $E_\parallel$ are calculated along the magnetic field assuming particle, momentum and energy balance in the flux tubes, while cross field fluxes are neglected. The so established two-dimensional plasma background is passed to EIRENE to calculate the corresponding ionization source distribution of the neutral particles. This distribution is then passed back to DIVIMP to calculate the background plasma again with the new ionization source entering the particle balance equation. This loop is repeated until there are no more substantial changes between subsequent iterations. The profiles of n_e and T_e at the target plates were set up by mapping the IVP probe measurements to the plates and scaling them to the target probe measurements. Since in the divertor there are no direct measurements of T_i available, $T_i = T_e$ was assumed at the target. With this assumption, measured and calculated power deposition to the target plates are in good agreement. Fig. 2 shows a comparison of the IVP probe measurements with the model results at the IVP location; Fig. 3 shows the evolution of the plasma parameters along a field line just outside the separatrix. Within the experimental error, it is possible to match T_e and n_e at both the target and the IVP location.

Using the finally obtained distribution of the plasma background parameters, the impurity generation and transport processes were modelled assuming physical sputtering at the target plates as the only source of boron. Auger analysis of the target surface (Fig. 4), showed that there is net erosion of boron in the vicinity of the strike points. The resulting radial variation of the boron concentration on the target plates was taken into account by modifying the original erosion yield accordingly. In the DIVIMP model, the sputtered atoms move along straight lines until they become ionized. Then, there motion is determined by friction, electrical and temperature gradient forces along the magnetic field and by anomalous diffusion across the magnetic field until they are deposited again at a wall element. From the resulting distribution of the impurity density in the various ionization states, spectroscopic intensities are calculated for the respective spectrometer viewing chords to allow direct comparison with the experimental results.

The calculated profile as well as the magnitude of the BII line emission is in good agreement with the measurements (Fig. 5). In the measured profiles there are, however, contributions

inside the separatrix position which are not reflected by the model calculations, simply because there is no substantial sputtering source in this region because of the rapid decrease of flux and incident particle energy. On the other hand, an assumed diffuse source of boron from the vessel wall in the model will result in BII radiation further up in the scrape off layer of the outer plasma fan. The respective contributions will show up in the profiles just inside the strike point as a result of the geometric projection to the target plate coordinates [4]. A possible mechanism for a such a diffuse wall source is the formation of boron hydrate molecules by chemical erosion processes similar to the case of carbon [3]. Mass spectroscopic analyis of the neutral gas in the pump ducts shows indeed a small fraction of boron compounds.

The DIVIMP results for the BII radiation in conjunction with the measured radial distribution of boron on the target plates show that physical sputtering is sufficient to explain the observed level of boron influx in the divertor. The corresponding erosion yield is in the range of 1.5–3% in the vicinity of the strikepoint.

While BI and BII emission is determined by the particle influx, the line radiation of the subsequent ionization states will be more and more influenced by the transport of the eroded boron into the divertor plasma. Fig. 6 shows the BIV emission above the target plate as measured by the tangentially viewing DIV spectrometer. In contrast to the modelling result, the maximum of the emission is close to the plate where the temperatures are in the range of 10–20eV. The observed radiation cannot be attributed to direct excitation because the energy difference to the ground state is 203 eV. On the other hand, the excitation energy from the metastable ^{3}S-state is only 4.4 eV. A possible mechanism for the population of this state are CX-processes. The code results, which do not include these effects, therefore reflect only the contributions from direct excitation, which become significant at the higher temperatures further upstream. By the coupling of DIVIMP with EIRENE, the neutral hydrogen distribution needed for the inclusion of CX-recombination and radiation is now available for further analysis.

[1] P.C. Stangeby et al., Nucl. Fusion **28** (1988) 1945.

[2] D. Reiter, *Randschicht Konfiguration von Tokamaks, Entwicklung und Anwendung stochastischer Modelle zur Beschreibung des Neutralgastransports*, Technical Report Jül-1947, KFA Jülich, Germany, 1984.

[3] W. Poschenrieder et al., J. of Nucl. Materials **220–222** (1995) 36.

[4] K. Krieger et. al, J. of Nucl. Materials **220–222** (1995) 548.

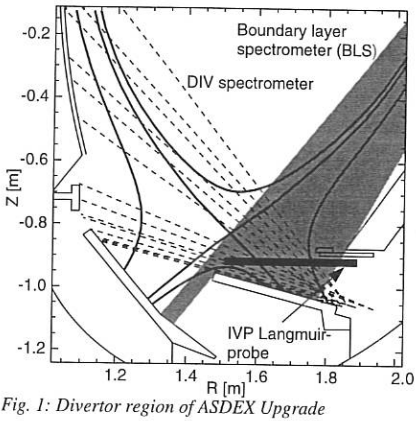


Fig. 1: Divertor region of ASDEX Upgrade

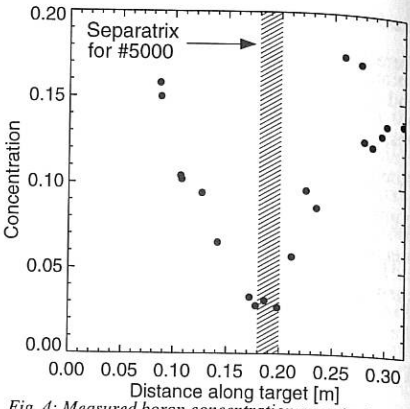


Fig. 4: Measured boron concentration on outer target.

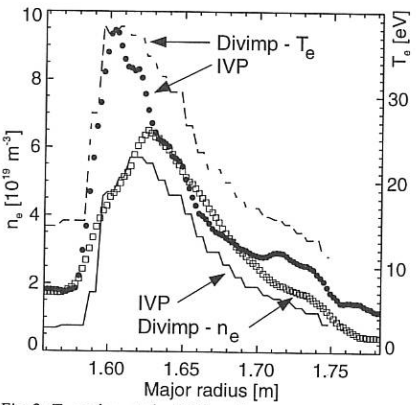


Fig. 2: T_e and n_e at the IVP location

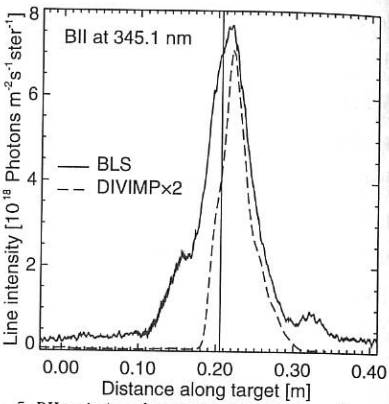


Fig. 5: BII emission above outer target in L-mode.

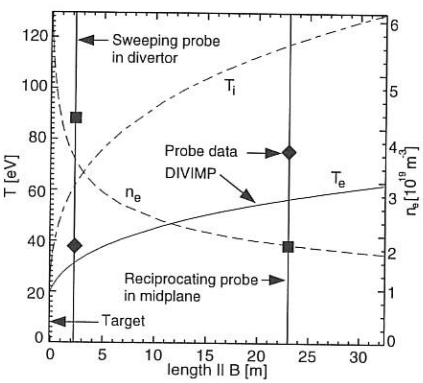


Fig. 3: Evolution of T_e , T_i , n_e along B.

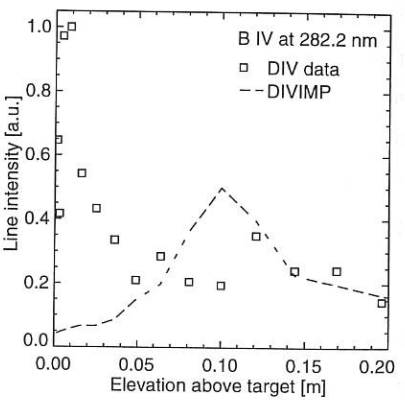


Fig. 6: BIV emission above outer target in L-mode..

Investigation of target plate interaction and impurity radiation from the divertor during high-performance H-mode discharges in ASDEX-Upgrade.

A. R. Field, A. †Herrmann, ‡G. Lieder, †B. Napiontek, M. Weinlich and the ASDEX-Upgrade team.

Max-Planck Institute für Plasmaphysik, Euratom-IPP Association, D-85748 Garching and †D-10117 Berlin, ‡ now at OSRAM GmbH, 81536 München

1. Introduction: High density tokamak operation with controlled enhancement of radiation from the boundary and divertor plasma as a means of reducing the target plate power load is now recognised as being essential for the success of a future reactor. In ASDEX-Upgrade, by means of feedback controlled puffing of deuterium and neon, high performance H-mode discharges with more than 90% radiation of the $\leq$ 10 MW heating power and complete detachment of the divertor plasma from the target plates are achieved (CDH-mode) [1]. Here, we compare the impurity production and emission in the divertor region under varying degrees of detachment by means of fast, multi-channel spectroscopy, thermography and Langmuir probe measurements.

2. Experimental: Line radiation from the divertor region is collected by two arrays of 16 optical fibres, one viewing tangentially and the other almost perpendicularly to the outer target plate (see Fig. 1). By means of interference filters and photomultipliers a narrow spectral band ($\geq$ 1 nm) can be monitored with high time resolution ($\geq$ 11 μs) and moderate spatial resolution (1.5–30 mm tangentially, 20 mm perpendicularly). Here, the perpendicular chords monitor the CII(658.1 nm) line and the tangential chords the CII(514.5 nm) line, which are excited from the ^{2}P ground and ^{4}P metastable states respectively. The IR-thermography system [2] and the arrays of fixed Langmuir triple probes [3] are described elsewhere.

3. Results: Three H-mode discharges with I_p = 1 MA, B_t = −2.5 T (grad-B drift towards x-point), $\overline{n}_e$ = 7.4 to 11.8x10^{19} m^{-3} in deuterium with 8 MW of NBI heating (7.4 MW deposited power, P_H) are compared: #4875 without additional gas puffing; #4906 with deuterium puffing into the main chamber alone; and #4881 with deuterium and neon puffing.

Without gas puffing radiation from the main chamber P_{rad} amounts to 56% of P_H leaving 3.2 MW flowing into the divertor region. Even between ELMs the target power density P_{Dep} near the separatrix is about 2.5 MW/m^2 resulting in local erosion of the graphite as

Shot #	4875	4906	4881
$\overline{n}_e$ [x10^{19} m^{-3}]	7.4	9.4	11.8
Φ_{D2} (Φ_{Ne}) [x10^{21} s^{-1}]	— (—)	6.0 (—)	4.3 (0.14)
P_{rad} [MW]	4.0	4.3	5.8
$P_{SOL} = P_H - P_{rad}$ [MW]	3.2	2.9	1.6
$n_{D2,\,Div}$ [x10^{20} m^{-3}]	0.35	2.5	1.35
$\tau_E/\tau_{E,\,ITERH92\text{-}P}$	1.01	0.81	0.91

Table 1 Discharge parameters at 3.71s.

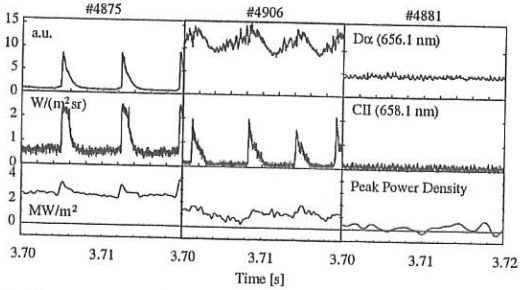


Fig. 1 Dα intensity viewing outer target from above; CII intensity viewing tangentially 1.5 mm above target; and peak target power loading from thermography.

indicated by the peaking of the CII intensity at the target. Here, T_e measured by the triple probes peaks at about 10 eV which is sufficient for the physical sputtering yield to reach 1%. (Assuming $T_i = T_e$, $T_e \geq E_{th}/5 \approx 5$ eV is required for the incident ion energies to exceed the sputtering threshold E_{th}.)

During the type-I ELMs P_{Dep} increases to over 4 MW/m^2 and the deposition profile broadens outside the separatrix. Peak values of T_e just outside the separatrix increase to ≥ 20 eV (the dynamic range of the triple probes is limited to 20 eV) resulting in a further increase in yield. The greatest relative increase of ion flux Γ_i occurs further out resulting in a broadening of the carbon influx profile during the ELMs. Overall, the associated increase in particle flux and electron temperature (and hence incident ion energies) result in at least a factor 4 increase in sputtered carbon influx (ionisations/emitted photon for CII increases with T_e).

During discharge #4906 strong deuterium puffing into the main chamber increases $\overline{n}_e$ by about 30%. Bulk radiation losses are, however, hardly increased because the more frequent ELMs induced by the gas puffing screen the impurities from the bulk plasma more effectively. As a result P_{Div} is hardly changed at 2.8 MW. The increased particle flux to the divertor enhances the neutral deuterium density there by a factor 7. Consequently, the deuterium line radiation from the divertor increases, marginally during the ELMs but by over a factor 10 between, the radiation efficiency of D^0 being higher at lower temperature. That an appreciable fraction of P_{Div} is lost by radiation or charge-exchange processes is manifested by the strong reduction in the peak target power load to ≤ 2 MW/m^2.

Both between and during the ELMs the power deposition profile is broadened and shifted a few cm outside the separatrix. Between the ELMs the reduced ion flux Γ_i measured by

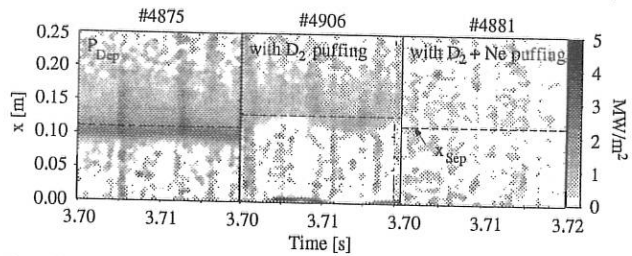


Fig. 2 Power deposition profiles measured by IR-thermography across the outer target plate (x — distance from inner edge).

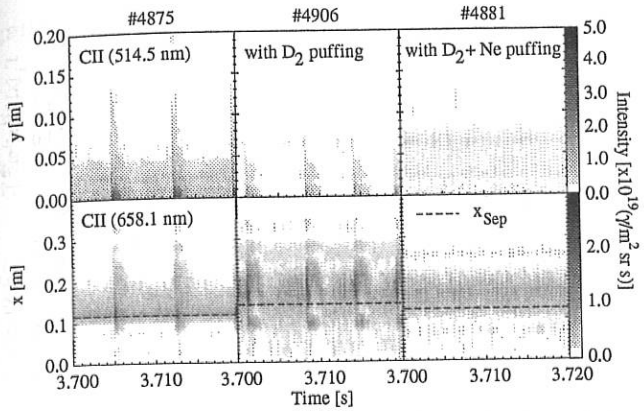


Fig. 3 Intensity distributions of CII lines measured across (x — distance from inner edge) and above (y — elevation) the outer target plate as a function of time.

the Langmuir triple-probe arrays in the vicinity of the separatrix shows that the plasma is detached from the target in this region. The electron temperature is also strongly reduced peaking at about 4 eV just outside (2 cm) the separatrix. Although between the ELMs the temperature is insufficient for physical sputtering to be effective the CII intensity observed viewing normal to the target is enhanced compared to that without gas puffing. This emission is not, however, localised above the target. A distributed carbon influx along the SOL in the form of C_mD_n molecules produced by chemical erosion of the plasma facing structures by the high fluxes of low energy D^0 atoms is probably the source of this emission. The greater path length of the perpendicular chords through this region leads to relatively higher intensities in these chords than observed viewing tangentially.

The D_2 puffing strongly increases the number of particles exhausted by the ELMs as well as their frequency. The ion flux Γ_i is increased by about a factor 2 and the ELM duration exceeds 1 ms. The greatest increases in Γ_i and T_e occur well outside the separatrix (5 cm), T_e increasing there to about 10 eV. This leads to an enhancement of the erosion of the target in this region as seen from the localised CII emission profiles. The ELMs thus burn through to the target temporarily reattaching although well outside the separatrix. The energy confinement time is somewhat degraded by the gas puffing, τ_E being 80% of that from the ITER H-mode scaling.

In order to achieve complete detachment, also during ELMs, the power flow across the separatrix must be reduced. This is achieved by enhancing P_{rad} by controlled puffing of neon into the main chamber. It is found that by simultaneously puffing deuterium the neon is better compressed in and pumped by the divertor thus facilitating the regulation of P_{rad}. During discharge #4881 about 80% of P_H is radiated from the main plasma, the neon producing a radiating mantle at the boundary, with about 75% radiated from inside the separatrix. P_{Div} is consequently reduced to 1.6 MW and smaller, high frequency ($\approx$ 2 kHz) type-III ELMs result. The energy confinement is degraded less than with D_2 puffing only, τ_E being 90% of that from the ITER H-mode scaling.

Because less D_2 is puffed than in #4906 the Dα emission from the divertor is reduced, in proportion to the D^0 pressure. The heat and particle pulses from the ELMs only slightly

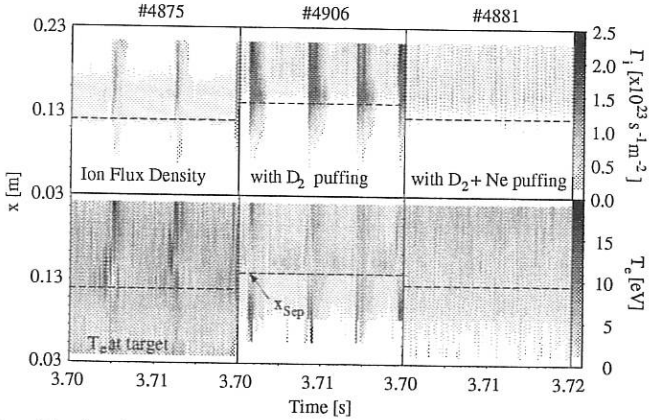


Fig. 4 Profiles of ion flux density Γ_i and electron temperature T_e measured by an array of Langmuir triple probes in the outer target plate. (The high values of T_e shown inside the separatrix for shot #4906 are due to early saturation of the electron branch of the probe characteristic.)

modulate the Dα intensity. The power density at the target is reduced to below the resolution of the thermography system (≤ 1 MW/m^2), T_e near the separatrix being reduced to ≤ 5 eV and the ion flux density Γ_i to a low level indicating permanent detachment in this region. The profiles of T_e and Γ_i peak further outside the separatrix (10 cm) where T_e fluctuates with the ELM activity between about 5 and 10 eV. The CII emission is not localised near the target being emitted mainly from a diffuse zone extending about 5 cm above. The heat pulses from the ELMs increase the CII emission which decays, however, within a short distance from the target. This indicates that the volume energy losses effectively buffer the ELM energy from the target. Between the ELMs in the outer regions of the SOL and a few cm above the target the temperature is sufficiently low that eroded carbon atoms or molecules may penetrate a few cm into the plasma before being excited and further ionised by the ELM heat pulses.

4. Conclusions: The intense target plate loading occurring under normal ELMing H-mode conditions can only be partially alleviated by strong D_2 puffing which enhances recycling and radiation losses from the SOL plasma and thus leads to partial detachment between ELMs. The heat pulses from type-I ELMs, however, still burn through to the target producing intense erosion. Bulk radiation losses can be increased in a controlled manner by puffing neon such that the power flow into the SOL is sufficiently reduced that the plasma remains detached from the target. The energy pulses from the resulting more frequent type-III ELMs are sufficiently small that they are buffered from the target by volume radiation losses. Under such conditions the carbon influx and associated radiation losses are maintained by chemical erosion of the in-vessel graphite structures due to the high fluxes of low energy neutral deuterium atoms.

References:

[1] Gruber O., Kallenbach A. et al., Phys. Rev. Lett., 74 (1995) 4217.

[2] Herrmann, A. et al., Plasma Phys. and Contr. Fus., 37 (1995) 17.

[3] Weinlich M., *Elektrostatische Sonden in starken Magnetfelder*, Ph.D. Thesis, Technischen Universität München, 1995.

Investigation of Chemical Sputtering in the Plasmagenerator PSI-1 First Experimental Results and Modelling

W. Bohmeyer, H. Behrendt, G. Fussmann, H. Grote, P. Kornejew, H. Meyer, D. Naujoks, E. Pasch+, H.D. Reiner

Max-Planck-Institut für Plasmaphysik, Berlin Branch, EURATOM Association, Germany
+ Seconded from KFA Jülich, EURATOM Association, Germany

1. Introduction

For fusion devices using graphite as first wall or target material the erosion of the material by chemical sputtering via hydrocarbon formation is an outstanding problem. There is, however, a saturation of the chemical erosion expected at high ion flux density due to increasing recombination of hydrogen [1]. Especially the erosion yields for high ion flux densities will be decisive for the choice of the material. Extensive investigations have been performed in ion beam experiments [2] where, however, the upper flux limit of $\approx 10^{20}$ $m^{-2}s^{-1}$ is rather low. Substantially higher fluxes can be achieved in high current arc devices where a neutral plasma beam is used. First experiments of this type were performed in PISCES [3]. In this paper we report on similar experiments in the stationary plasma generator PSI-1. We describe the measuring procedures and some preliminary results that concentrate on the comparison of three different graphite materials.

2. Experimental

The plasma in the PSI-1 device (fig. 1) is generated between a heated LaB_6-cathode and an anode made from copper. It expands through the hollow anode along the axial magnetic field into the target chamber onto the floating target. The plasma parameters in the target chamber are determined by the magnetic field configuration, the neutral gas pressure (absolute pressure and pressure ratios between cathode, differential pumping stage and target chamber), and the electrical power input of the discharge. A tungsten diaphragm (ϕ 40 mm) was used to create a homogeneous plasma column at the target location. The target (ϕ 30 mm) was placed concentric to this plasma beam.

In the experiments under discussion the electron temperature was kept constant at $T_e \approx 3.5$ eV. The electron density n_e was varied between 3.5 - $7*10^{16}$ m^{-3} by changing the discharge electrical power input while keeping the neutral gas pressure constant ($1.3*10^{-3}$ mbar in the target chamber), thus varying the ion flux density between 4.4 - $8.3*10^{20}$ $m^{-2}s^{-1}$. Under these conditions the ionization lengths for hydrocarbons are comparable to or larger than the discharge dimensions, hence redeposition is not expected to play a role. Radial profiles of T_e and n_e (fig. 2) were routinely measured 8 mm in front of the target (with and without target) by a fast scanning Langmuir probe. The density of neutral atomic hydrogen in the plasma column was determined from space-resolved H_α-line intensities.

Information about the purity of the plasma was obtained from residual gas analysis and spectroscopy. The residual gas pressure in the vacuum system is $3*10^{-8}$ mbar. Spectroscopic analysis give no indications for any impurities. For a further assessment of the purity of the plasma sputtering experiments with a biased tungsten-target were carried out. The threshold energies for W-sputtering are 447 eV and 209 eV for hydrogen and deuterium, respectively. For all heavier atoms or ions the W-threshold energy is lower. Biasing now the target to -350 V, no tungsten could be detected in hydrogen discharges. In contrast an increasing WI-intensity could be observed in deuterium for bias voltages beyond -300 V. A similar effect would have been expected for traces of any impurity ions.

Samples of different graphite materials - EK 98, CFC N-112, CFC-10% Si - were exposed to

various plasma conditions (table 1). The graphite targets were inserted into the plasma for 240 min each. Their temperature could not be controlled actively but was measured by an attached thermocouple and (in some cases) by a pyrometer. Weight loss measurements and scans with an optical profilometer over the eroded crater area were used to determine the mass loss. Additionally, surface analysis methods (SIMS, AES and SEM) were used to check for possible impurities deposited on the target surface.
The methane formation was monitored permanently with a residual gas analyzer. For calibration of the gas analyzer a known flux of methane was blown through a hole in a molybdenum target into the discharge under identical conditions as for graphite target exposure. The axial dependence of the CH-band intensity at 430 nm was measured in front of the target and is used as input for the ERO-code calculations.

3. Results and Discussion

A comparison of the erosion yields of three different graphite materials was performed. EK 98 graphite was exposed to plasmas with various ion flux densities. The results of the erosion measurements are summarized in table 1.
There is a good agreement between the measured weight loss and the amount of carbon derived from the methane signal of the calibrated gas analyzer. Both values are higher by a factor of ≈ 2 than the mass loss evaluated from the crater depth profile, which was used for the determination of the erosion yields given in table 1. This difference may be due to the fact that the profilometer detects solely the mass loss of the surface facing directly the plasma whereas the two other methods measure the total loss of the target including possible contributions from the mantle surface. Taking the ratio of the corresponding areas into account, the yield-values of all three methods agree fairly well. It should also be noted that measurements of the ion saturation current to the biased target confirmed the particle flux determined by the Langmuir probe.
In general, the erosion yields given in table 1 are higher by about a factor of 2 compared to published data. Since it is well known that oxygen has very high yields for chemical sputtering on carbon the possible influence of this impurity was studied separately. To this end O_2 was blown into the discharge. An addition of 0.2 % of oxygen to the H_2 influx was clearly detected by visible spectroscopy and changed the mass spectrometer signals at m/e = 16 (CH_4^+) and 28 ($C_2H_4^+$ and CO^+) remarkably. It is thus concluded, that the oxygen content in the hydrogen discharge is normally well below 0.1 % and hence of no importance.

4. Modelling

The CH_4 production at the graphite target can be investigated spectroscopically by means of molecular band intensities. For these measurements the CH band around 431 nm is used which is due to the $A^2\Delta$ - $X^2\Pi$ electronic transition of the CH molecule. Fig. 3 shows the density distributions of the CH molecules, as obtained from the measured photon intensity $I\Phi$, for three different electron densities. The CH density was calculated using the electron excitation rate coefficient from ref. [4].
For the interpretation of the CH densities in terms of the methane fluxes the multi-step break-up of the hydrocarbon molecules is to be considered. In the frame of a zero-dimensional model eight rate equations of the type

$$\frac{dn_{CH_x}}{dt} = -\frac{n_{CH_x}}{\tau_{CH_x}} - n_e \cdot n_{CH_x} \cdot \sum \langle \sigma v \rangle_i + n_e \cdot \sum n_{CH_y} \cdot \langle \sigma v \rangle_k$$

for the CH4...CH molecules and their ions were solved, taking into account the dissociation and ionization processes according to [5]. By defining particle confinement times τ_{CH_x} the transport and thus the losses out of the observation volume can be approximated. Using infinite

confinement times a ratio of $n_{CH}/n_{CH4} = 0.7$ is obtained at an electron temperature of 3.5 eV (see fig. 4a).
For a confinement time of $\tau = 2*10^{-4}$ s for all dissociation products, which is an adequate value for the plasma conditions and geometry in the PSI-1, this ratio is reduced by three orders of magnitude (fig. 4b). This drastic change is due to the very large reaction lengths resulting from the low electron density and temperature. The small CH density of about $1*10^{14}$ m^{-3} as measured by spectroscopy (fig. 3) can be explained in this way, because for the methane density a value of about $1*10^{17}$ m^{-3} in the plasma volume is inferred from our other measurements. In principle, the CH density can be calculated by the ERO-code [6], as done for higher plasma densities and temperatures. In the code the real geometry of the PSI-1 and the profiles of the electron density and temperature are included. The code uses the same rate coefficients as mentioned above for the complicated break-up of the released methane molecules. All losses due to transport and redeposition on the target plate are taken into account. In the code it is assumed that the hydrocarbon molecules which leave the plasma volume do not come back into the plasma. The calculated CH density and the particle confinement times are thus much smaller than the measured values. The discrepancy is probably due to elastic reflection of the different molecules. In the future this process will be included into the ERO code.

5. Summary

Various graphites were exposed to ion flux densities up to $8 \cdot 10^{20}$ $m^{-2}s^{-1}$ at low plasma temperatures and densities in hydrogen discharges. Chemical erosion yields in the range of 0.02 - 0.05 were obtained.
The experiments will be continued under improved conditions: biasing of the targets and active control of the target temperature. Also a comparison between hydrogen and deuterium is planned.

material	n_e	T_e	Φ_i	$I_{dis.}$	diaphr.	T_{target}	ΔM	$Y_{ero.}$	Δp_{CH_4}	Δd
	$[10^{16}\ m^{-3}]$	$[eV]$	$[10^{20}\ m^{-2}\ s^{-1}]$	$[A]$		$[^\circ C]$	$[mg]$	$[C/H^+]$	$[10^{-12} A]$	$[\mu m]$
N112	13.0	3.5	18.3	200	no	450	17	0.033	6.5	8.8
N112				200	no	430	18		6.7	9.6
EK98	10.0	3.5	14.7	100	no	360	10	0.024	3.5	5.4
EK98	16.0	3.5	20.2	200	no	420	14	0.030	4.3	9.4
EK98	7.0	3.5	8.3	200	yes	240	5	0.025	2.2	3.2
EK98	5.0	3.5	6.4	140	yes	220	2	0.024	1.3	2.4
EK98	3.5	3.5	4.4	80	yes	170	2	0.021	1.3	1.4
C-Si	7.0	3.5	8.3	200	yes	230	5	0.048	2.2	5.6
N112	7.0	3.5	8.3	200	yes	225	4	0.030	2.5	3.6

Table 1: Summary of experimental data and results

References

[1] C.H. Wu, U. Mszanowski, J. Nucl. Mater., 218, 293, 1995
[2] J. Roth, E. Vietzke, A.A. Haasz in Atomic and Plasma-Material Interaction Data for Fusion, Suppl. to Nucl.Fusion, 63-78, 1991
[3] Y. Hirooka et al., J. Vac. Sci. Technol. A8 (3), 1790, 1990
[4] K. Behringer, J. Nucl. Mater., 176&177, 606, 1990
[5] A.B. Ehrhardt, W.D. Langer, Collisional Processes of Hydrocarbons in Hydrogen Plasmas, PPPL-2477, 1987
[6] D. Naujoks, R. Behrisch, J. Nucl. Mater., 220-222, 227, 1995

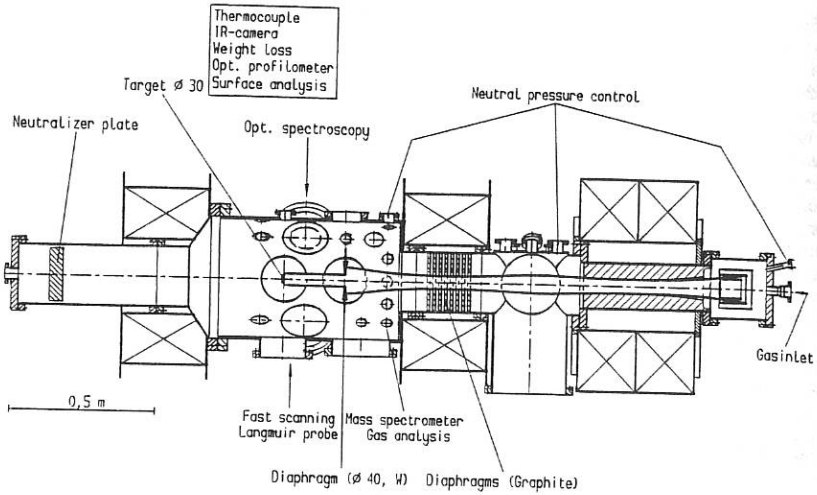


Fig. 1: Experimental arrangement at the PSI-1 plasma generator

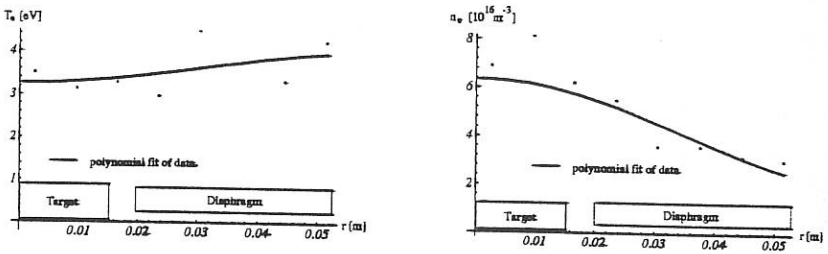


Fig. 2: Radial profiles of the electron temperature and density

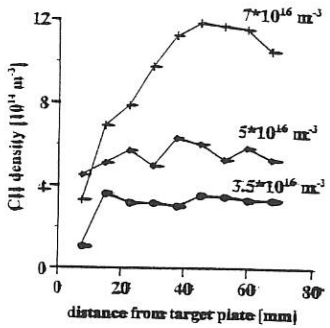


Fig. 3: CH density distribution for different electron densities in PSI-1

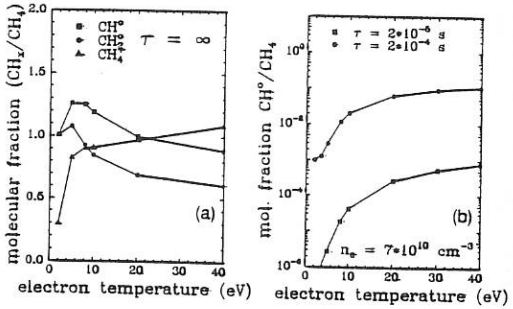


Fig. 4: Densities of different hydrocarbons, normalized to the methane density, as a function of the electron temperature for different confinement times, as indicated in the figure

Surface layer composition of the JET vessel walls, material transport and hydrogen trapping in the vessel walls

M. Mayer [a], R. Behrisch [a], V. Prozesky [b],
P. Andrew [c] and A.T. Peacock [c]

[c] JET Joint Undertaking, Abingdon, United Kingdom
[a] Max Planck Institut für Plasmaphysik, EURATOM Association, Germany
[b] Guest scientist from National Accelerator Laboratory, Faure, South Africa

1 Introduction

The plasma facing vessel walls of todays thermonuclear fusion experiments are bombarded with high fluences of energetic hydrogen ions and neutrals as well as by impurity ions. This bombardment causes an erosion of the vessel walls and introduction of impurity atoms into the plasma. The impurities will impinge back onto the vessel walls together with hydrogen atoms and a surface layer with a new composition is formed. In a future fusion reactor the accumulation of implanted D/T in the surface layers of deposition dominated areas presents a major problem of T inventory.

2 Experimental

In order to get more insight into the actual composition of the JET vessel wall, the hydrogen trapped in the surface layers of the wall, and the problems of erosion, redeposition and material transport, 30 carbon **L**ong **T**erm **S**amples (LTS), partly covered with 800 nm aluminium, were mounted on the JET vessel wall in December 1993 and replaced in September 1994 after about 2500 discharges. 20 LTS were mounted in octant 3 and 4, distributed poloidally (fig. 1), the rest were mounted in the midplane of the torus at the inner and outer walls distributed toroidally. The wall temperature in JET during operation is about 525 K. Beryllium is routinely evaporated over the vessel wall. The JET vessel wall is made of inconel (about 75% Ni, 15% Cr, 10% Fe).

The thickness and composition of the surface layers of the LTS were analysed with MeV ion beam techniques (RBS, NRA, PIXE, ERDA, HERDA).

3 Results

The poloidal distribution of the total amount of all elements deposited on the LTS as well as the erosion of the evaporated Al-layer is shown in fig. 2. All samples mounted on the inner wall of the torus showed erosion of the aluminium layer and only minor deposits. The samples at the outer wall of the torus showed thick deposited layers with thicknesses up to 2.5 μm. The composition of the deposited layers was about 70% Be, 15% C and 15% O (fig. 3 top). The concentration of Ni, Cr and Fe in the deposited layer was about 1 atomic % (fig 3 bottom), other elements such as B, N, Si, S, Cl, K, Ca and Cu were detected as traces.

All LTS mounted on the inner wall of the torus in the midplane showed erosion of the Al-layer. The observed erosion was toroidally uniform within about 10%. The thickness and composition of the deposited layers on the LTS mounted at the outer wall in midplane was uniform within about 30%, if the samples were not shadowed from the Be-evaporators. Samples at the outer wall which were shadowed from the Be-evaporators showed minor deposits and erosion of the Al-layer was observed.

The amount of deuterium was about 1×10^{17} atoms/cm^2 at the inner wall of the torus due to implantation of energetic neutral deuterium atoms created in charge exchange processes. At the outer wall of the torus between 2×10^{17} and 6×10^{17} deuterium atoms/cm^2 were measured. The deuterium was distributed through the whole deposited layer at a concentration of a few percent. The concentration of hydrogen was comparable to the deuterium concentration.

4 Discussion

At the inner wall of the torus, as well as at the outer wall at areas shadowed from the Be-evaporation, erosion of the Al-layer on the LTS was observed, while at the other areas of the outer wall large deposition is measured. This is due to:

- The observed erosion is likely caused by CX-neutrals. The calculated CX-flux to the inner and outer wall is roughly equal, therefore the asymmetry in the erosion behavior at the inner and outer wall cannot be explained by different CX-fluxes.

- The amount of beryllium deposited during evaporation varies greatly over the surface of the vessel. Most of the outer wall LTS positions were close to the evapo-

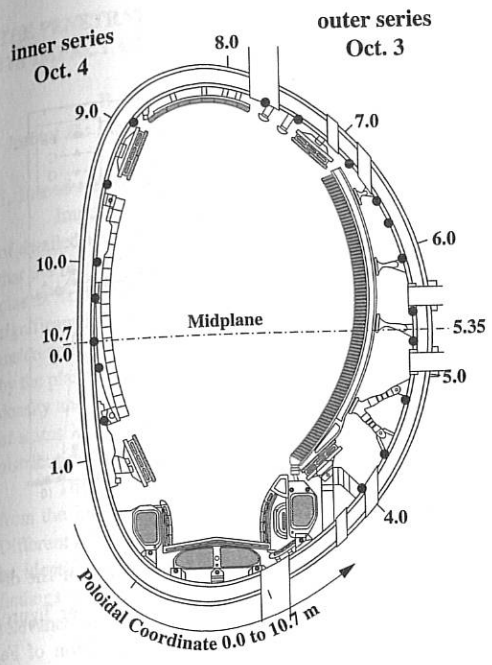


Figure 1: Poloidal positions of the long term samples. The samples are drawn as dots. Samples at the inner wall of the torus were mounted in octant 4, the samples at the outer wall of the torus were mounted in octant 3.

rators, where about 5 times more Be is deposited than at the inner wall. At the outer wall positions, the Be deposition by evaporation is larger than the removal by CX-sputtering. This is supported by net erosion being observed at the outer wall at positions shadowed from the evaporators. At the inner wall the amount of evaporated Be is not sufficient to protect the wall from erosion.

At the inner wall the trapped D is implanted by CX-bombardment. The regular evaporation of Be at the outer wall produces fresh layers of Be which are subsequently implanted with CX-deuterium resulting in higher amounts of D.

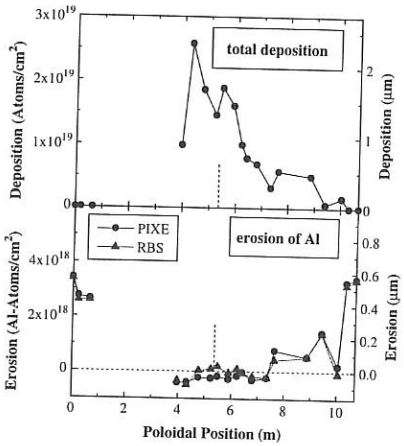


Figure 2: Poloidal distribution of the total deposition (all elements) on the LTS (upper figure) and poloidal distribution of the erosion of the evaporated Al-layer measured with RBS and Pixe (lower figure).

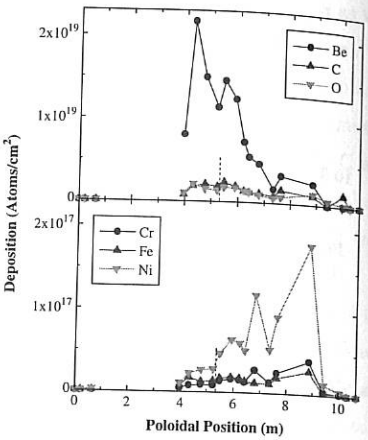


Figure 3: Poloidal distribution of the deposition of Be, C and O (upper figure) and distribution of the deposition of Fe, Cr and Ni (lower figure).

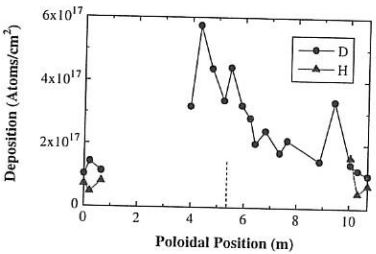


Figure 4: Poloidal distribution of the deposition of hydrogen.

THE PENETRATION OF IMPURITY ATOMS INTO THE PLASMA BOUNDARY AND ITS IMPACT ON THE CENTRAL IMPURITY CONCENTRATION

B. Unterberg, V. Philipps, A. Pospieszczyk, U. Samm, B. Schweer
Institut für Plasmaphysik, Forschungszentrum Jülich GmbH, Association KFA- EURATOM
D- 52425 Jülich, Germany

1. Introduction

Impurity transport is a key issue in controlled fusion research. While there is still a lack of detailed knowledge about the physics of radial anomalous transport, it is widely recognized that the impurity production processes at the targets, the penetration of impurity atoms into the plasma and the ion source distribution resulting from ionization by electron impact have significant influence on the built-up of the central impurity density. The ion source distribution inside and outside the separatrix is depending on the velocity distribution of neutrals (determined by the plasma- wall interaction processes) and the local ionization rate (given by the local electron density and temperature and the ionization potential of the atomic species). The penetration depth of atoms $\lambda_i^0 = \overline{v}_0 / (n_e < \sigma v >_{ion})$ can be used to characterize the radial extension of the ion source distribution inside the LCFS.

The velocity distribution of several impurity species has been determined at TEXTOR from the Doppler broadening of line emission (carbon, oxygen [1], neon [2] and silicon [3]). Different release mechanisms as physical and chemical sputtering, reflection and desorption could be identified. These results are used to interpret the penetration measurements shown. The findings are discussed in context with the central impurity densities observed to point out the relevance of edge processes for the central impurity built-up.

2. Experiment and evaluation of measured data

The experiments have been performed on the tokamak TEXTOR with a major radius R = 1.75 m and a minor radius a = 0.46 m at standard values for the toroidal magnetic field B_T = 2.25 T and the plasma current I_P = 350 kA. The measurements shown below base on optical methods [4] and have been carried out at test limiters made of different materials and introduced into the vacuum vessel with the help of a limiter lock system at the bottom of the torus. The limiters are observed from a tangential side view using a spectrometer equipped with an intensified CCD camera as detector which yields spectra of radially resolved line emission in the wavelength range from 200 - 800 nm. Additionally CCD camera measurements with interference filters are made to analyze the overall 2d spatial distribution of emission in toroidal and radial direction. The spatial resolution of these measurements is about 0.5 mm. More details of the experimental set- up are given in [5].

The measured profiles of line emission from impurity atoms can be transferred to the ionization source distribution by the adequate rate coefficients for ionization and excitation of atoms. The neutral flux and the neutral density can be deduced from the integral of the ion source distribution up to the radius where all neutrals are ionized [6]. The electron temperature (T_e) and density (n_e) profiles necessary for such calculations are obtained by means of a thermal helium beam [7], the velocity distribution of neutrals from Doppler broadening of line emission. Fig.1 shows an example of a 2d normalized ion source distribution of carbon (test limiter at the main limiter radius r=46 cm, $\overline{n}_e = 4.8 \cdot 10^{13} cm^{-3}$, P_{in} = 1.6 MW). The toroidal axis is oriented horizontally (limiter width 10 cm). The vertical axis refers to the radial direction (LCFS at y=0), negative values correspond to the scrape- off layer. The limiter is also curved in the poloidal

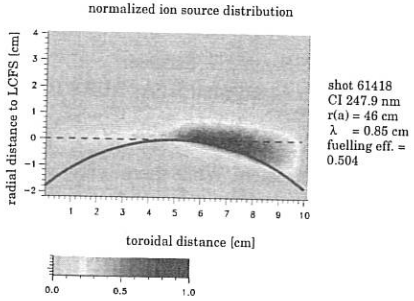


Figure 1 *2d ion source distribution of carbon (y=0 : LCFS, y<0: SOL)*

direction and has a poloidal width of 6 cm. The left (electron drift) side of the limiter is for this limiter radius shaded by the main toroidal ALT II limiter due to a short connection length of 1.5 m. From this measurement a *neutral fuelling efficiency* can be deduced, defined as the ratio of the total neutral flux released from the limiter surface (total integral of the ion source distribution) to the neutral flux entering the confined plasma (integral starting at the LCFS). In a first approximation one can account for the effect of prompt redeposition of ions within the first gyro radius by starting the integration for the neutral flux entering the confined plasma one gyro radius inside the LCFS. The largest uncertainty of the fuelling efficiency in this integration is given by the position of the LCFS ($\mp$ 1 camera pixel $\Leftrightarrow$ 0.5 mm). The resulting error is in the order of 5% of the total ion source rate and can be rather significant regarding species where the neutral fuelling efficiency is small.

3. Results and discussion

To identify different mechanisms of impurity release we compare the measured radial intensity distribution of line emission with calculations based on the velocity distribution and the profiles of n_e and T_e at the plasma edge. The release of carbon is at low densities (high edge temperature) governed by physical sputtering unless the sublimation rate becomes dominant at surface temperatures larger than 2000 °C. Fig. 2a) shows examples for both conditions (carbon test limiter at r= 45 cm, $T_e(r_{lim})$= 60 eV). At a surface temperature of 1600 °C a Thompson velocity distribution of carbon atoms as measured in (dashed line) gives satisfactory agreement with the measured emission profile (boxes). When the limiter is heated to temperatures over 2400 °C, the penetration is considerably shorter (crosses) and can be reproduced by a thermal Maxwellian velocity distribution corresponding to the surface temperature. The penetration depth decreases from 0.75 cm to 0.15 cm in the latter case.

At lower edge temperatures (higher central densities) chemical erosion gets more relevant (s. emission profile (boxes) for $T_e(r_{lim})$ = 20 eV in fig. 2b)., The penetration is shorter than expected from physical sputtering alone (upper dashed curve). The emission profile of carbon atoms originating from molecular dissociation was experimentally determined during CD_4 -puffing through the limiter. This distribution can be reproduced by a gaussian velocity distribution corresponding to a dissociation energy of 1 eV (lower dashed curve) as observed in [1] for the case of detached plasmas (chemical sputtering dominant). If one assumes 80% of the line intensity coming from physically sputtered carbon atoms and 20% from chemically sputtered ones (pointed curve), it is possible find reasonable agreement with the measured intensity distribution (boxes) including both physical and chemical sputtering. As dissociative excitation is less efficient with respect to the population mechanisms of the emission line than collisional excitation of atoms, these values give a lower limit for the fraction of chemically released carbon.

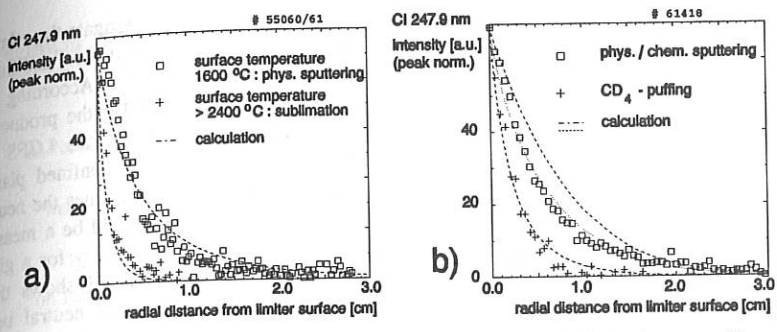


Figure 2 *Radial intensity distribution of CI emission (247.9 nm) for different plasma conditions and release mechanisms of carbon*

Variations of local n_e and T_e have been inferred by changing $\bar{n}_e$. An increase of the central density leads to a decrease of the penetration depth and of the fuelling efficiency for most species as carbon, silicon or molybdenum, where the ionization rate at the limiter increases and the averaged neutral velocity is independent of the local plasma parameters (e.g. for physically sputtered atoms) or decreases (as for carbon). Neon behaves differently as the fraction of fast particles increases with increasing density (decreasing energy of neon ions hitting the limiter) due to an increasing reflection coefficient [2]. Typical numbers are given in the following table at a low density of $\bar{n}_e = 1.5\text{-}2.0 \cdot 10^{13}\text{cm}^{-3}$ and a high density of $\bar{n}_e = 4.5\text{-}5.0 \cdot 10^{13}\text{cm}^{-3}$ ($P_{in} = 1.6$ MW).

impurity species	local n_e [10^{13}cm^{-3}] / local T_e [eV] at r_{lim}		λ_o [cm]		f_0 [%]	
	low $\bar{n}_e$	high $\bar{n}_e$	low $\bar{n}_e$	high $\bar{n}_e$	low $\bar{n}_e$	high $\bar{n}_e$
carbon r_{lim} = 46 cm	0.3 / 55	1.4 / 20	2.1	0.9	82	50
neon r_{lim} = 46 cm	0.4 / 35	0.8 / 15	1.5	2.0	-	70
silicon r_{lim} = 45 cm	0.3 / 70	1.0 / 25	1.0	0.5	65	34
molybdenum r_{lim} = 45 cm	0.45 / 80	1.6 / 27	0.3	0.1	24	<5

Penetration depth and fuelling efficiency decrease with increasing charge and mass number (decreasing ionization energy of neutrals and decreasing neutral velocity). This fact leads to a very efficient screening for molybdenum, especially at high plasma density. Here the effect of prompt redeposition is drastic (reduction of f_0 from 12% to less than 5% when accounting for prompt redeposition) as the gyro radius ($\rho_L \approx 1.5$ mm) is about the same as the penetration depth. A further discussion on this effect is given in [8].

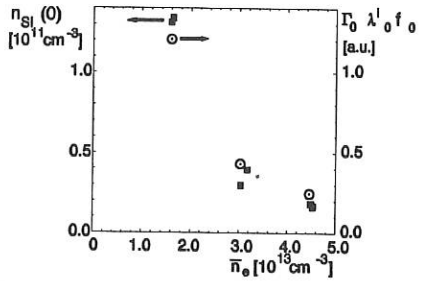


Figure 3 *Impurity screening at the plasma edge and central impurity built-up of silicon*

We will now investigate the relation between central impurity density and impurity penetration at the edge. According to a simple diffusion model [9] the product of penetration depth λ_0^i inside the LCFS and neutral flux entering the confined plasma (the total flux Γ_0 released times the neutral fuelling efficiency f_0) should be a measure of the central impurity density for a given diffusion coefficient. Fig. 3 shows these quantities for silicon under neutral beam heated conditions in a siliconized machine as a function of $\bar{n}_e$. The central silicon density has been deduced from the SXR- pulse height spectrum. If one assumes the variation of edge parameters at the test limiter to be similar to those at the main limiters, it can be concluded that the variation of the central silicon built-up is due to the variation of the silicon release and penetration at the edge. A similar coupling between edge and center can also be observed for carbon and molybdenum in neutral beam heated plasmas. The situation is quite different for molybdenum under ohmic conditions where neoclassical transport leads to molybdenum accumulation in the plasma center at high densities although flux of neutrals at the edge and penetration depth do not change.

4. Summary

The penetration of impurity atoms into the plasma edge has been investigated by optical methods at the tokamak TEXTOR. Different release mechanisms could be identified by comparing the radial intensity distribution of line emission with calculations based on the velocity distributions resulting from characteristic plasma- surface interaction processes and on measured n_e-/ T_e- profiles. Penetration depth and neutral fuelling efficiency are minimal at high densities and with additional heating. The variation of neutral flux, neutral fuelling efficiency and penetration depth inside the LCFS determines the variation of the central impurity density under these conditions, this strong coupling underlines the relevance of edge processes for the central impurity built- up.

References:

[1] P. Bogen and D. Rusbüldt, J. Nucl. Mater. 196-198 (1992) 179

[2] B. Unterberg et al., J. Nucl. Mater. 220-222 (1995) 462

[3] Ph. Mertens et al., Proc. of the 20th Europ. Conf. on Plasma Physics and Controlled Fusion, Lissboa (1993), Vol. III 1123

[4] P. Bogen and E. Hintz, "Plasma Edge Diagnostics Using Optical Methods" in "Physics of Plasma-Wall Interaction in Controlled Fusion", edt. by D.E. Post and R. Behrisch, Plenum N.Y. (1986) 211

[5] V. Philipps et al., Nucl. Fusion 34 (11) (1994) 1417

[6] A. Pospieszczyk, "Diagnostics of Edge Plasmas by Optical Methods", in "Atomic and Plasma- Material Processes in Controlled Thermonuclear Fusion", edt by R.K Janev and H.W. Darwin, Elsevier, Amsterdam (1993) 213

[7] B. Schweer et al., J. Nucl. Mater. 196-198 (1992) 174

[8] V. Philipps et al, these proceedings

[9] W. Engelhardt and W. Feneberg, J. Nucl. Mater. 76-77 (1978) 518

Chemical Erosion Measurements from various Carbon based Limiters and Coatings in TEXTOR

A.Pospieszczyk, V.Philipps, E.Casarotto[1], U.Kögler, B.Schweer, B.Unterberg, F.Weschenfelder, G.Y.Diao[2]

Institut für Plasmaphysik der Forschungszentrum Jülich GmbH, Association EURATOM-KFA, D-52425 Jülich, Germany

[1]on leave from University of Padova, Dep.of Electr.Engineering, Italy

[2]on leave from Southwestern Institute of Physics, Chengdu, Sichuan, P.R.China

1. Introduction

Since the introduction of carbon based materials as wall coatings and limiters in fusion devices, a growing interest has been developed for the examination of chemically sputtered species from these surfaces in erosion experiments. Only very qualitative information about the source function, the transport and the redeposition properties of released hydrocarbons has been obtained during the last decade because both of the lack of molecular data bases and the non sufficient diagnostic access to the locations of their origin. One major subject of these investigations is to find the flux dependence of the chemical hydrocarbon erosion yield, as this knowledge may allow to extrapolate the magnitude of the molecular hydrocarbon sources in a carbon surrounded fusion device.

2. Experiment, methods, and calibrations

The impurity release from the limiter is studied using a 0.5 m spectrometer equipped with a 2D-CCD camera with image intensifier, which was set at a fixed toroidal position conventionally chosen near the location of largest power loading or a hole for gas blow experiments 15 mm from the center. The same line of sight is shared by an intensified CCD-camera with interference filters in front, which allows the simultaneous 2D-observation of the cross section in the light of a specific spectral line or molecular band (CD: 430.7 nm ($\pm$0.75 nm); C I: 247.8 nm, C II: 514.5 nm, C III: 464.7 nm). More experimental details can be found in [1]. The plasma parameters at the radial position of the limiter were measured by means of thermal He- and Li-beams [2],[3].

The limiters (10 cm long, 6 cm wide and 5 cm high) with a toroidal and poloidal curvature of 8.5 and 6 cm, respectively, were introduced into TEXTOR through a limiter lock from the bottom of the torus. Silicon and titanium doped (SiC30, RGTi), B_4C and pure graphite (EK98) testlimiters as well as metal limiters were used for the experiments and had been positioned at the same plasma radius as the toroidal belt limiter ALT-II (r_{Lim} = 46 cm). In order to be independent of the limiter heating by the plasma itself, which strongly depends on the discharge conditions chosen, the graphite limiter could be internally heated up to about 700 °C. The TEXTOR vessel itself was routinely boronized.

Specific care was taken for the conversion of measured photon intensities into molecular CD_4-fluxes. The observed CD transition ($A^2\Delta$-$X^2\Pi$ at about 431 nm) is well known and spectra have been already published in several journals (e.g.[4],[5]). Very near to this band is also a BD-

band (at 432.9 nm) and the D_γ-line (at 433.9 nm), the latter is very convenient to be used for the determination of the deuterium flux and the CD_4- to D-flux ratio. Moreover CD^+-band emission can be identified at 420 nm (fig.1) Experimental [6] and theoretical [5] attempts have been made to determine the value S/XB for the CD-band in order to correlate the measured photon ratios Φ_{CD}/Φ_D to the CD_4/D-flux ratios. These conversion factors are considerably dependent on T_e, n_e, and ratio of molecular/atomic source of deuterium. Within the conventional experimental plasma parameter range all three factors together can lead to a variation of 0.06 - 0.13, with which the measured photon flux ratios have to be multiplied in order to obtain the particle fluxes CD_4/D. Therefore, not only the local plasma parameters have to be known (which they are mostly not) but also the source of the level population for D_γ. In [7] a number of S/XB=100 for CD is adopted and in [5] S/XB=800 for D_γ. We have raised the latter value to 1000 taking into account latest calculations, which also consider molecular sources for the atomic deuterium level population [8]. By CD_4-injection through a hole in the limiter we could verify the measurements of [6] concerning the temperature dependence of S/XB for the CD-band.

3. Results and Discussion

- Experiments with a heated graphite limiter

In [1] experiments have been presented, where parts of a graphite limiter have been heated up to about 1900 °C. There has been found a clear indication that the methane production yield drops continuously by a factor of 4. However, because of the inhomogeneous heating, which smoothes the line integrated optical observations, we performed experiments on homogeneously heated limiters below 1000 °C, where a maximum of the production yield (more or less strongly dependent on the impinging ion energy) was found in laboratory experiments [9]. The CD_4/D-flux ratio was measured for three different discharge conditions (fig.2). Surprisingly no expressed maximum or drop could be detected up to the achievable temperature of about 700 °C and also no expressed dependence on the boundary temperature. By further (however inhomogeneous) heating of the limiter surface by the plasma, a drop in the production yield could actually be detected in the course of the discharge indicated by the black box at some higher temperature (see insert in fig.2).

- Experiments with graphite limiters

Fig.3 shows the dependence of the CD_4/D-flux ratio on the impinging deuterium flux Γ_D. A value of about 1 % was found for the highest fluxes, which increases to lower Γ_D. The error bars shown indicate both the uncertainty in the conversion factor (see above) and in the experimental measurements, which is higher at lower fluxes (i.e. lower intensities). Together with experimental values measured with a sniffer probe in the TEXTOR scrape-off layer, a weak tendency for a decrease with growing deuterium flux can be seen by both laboratory experiments at low ion energies and tokamak experiments as well as plasmasimulators [10].

- Experiments with different C-based limiters and coated metal limiters

Surprisingly the CD_4/D-flux ratio for boron, silicon, and titanium doped graphites does not show a significant deviation from that for pure graphite limiters (fig.4), although in these cases a reduction of about a factor of 5 and more had been expected from laboratory experiments [11]. This behaviour is similar, when pure metal limiters have been exposed to the plasma

in the limiter position. Limiters, which were withdrawn only 0.5 cm behind the main limiter displayed immediately a similar CD_4/D-flux ratio during the first exposure discharge. However, metal limiters 0.5 cm inside the main plasma radius show a significantly lower CD_4/D-flux ratio because their surface is constantly eroded.

- Molecular intensities and penetration depths for different discharge conditions

Under the conditions in TEXTOR the generation of higher hydrocarbons plays a minor role, as the C_2-band at 516.5 nm revealed always a very low intensity except for the case of a detached plasma, when the radiation of this band rose dramatically. This latter condition obviously resembles more those in the throat of the pumped limiter at TORE-S [12] or in the ASDEX-U divertor [7][13], where a considerably larger contribution from higher hydrocarbons has been routinely detected. The measured radial intensity profiles for CD and CD^+ (fig.5) are verified by an interpretation model (ERO-TEXTOR, a derivative of the ERO code [14]), which simulates the many reaction paths by taking the reaction rates of [15] into account. However, in 2D-observation geometry the model calculations show stronger deviations in toroidal direction from the experimental observations, which have been obtained by detecting the light emission with a CCD-camera connected with a filter for the CD-band emission (fig.6). From these measurements fuel efficiencies for CD_4-blow and sputtering can be derived, which are relatively large (about 80%), which means that a major part of the discharge can actually be fueled by molecules. That this fact is not strongly reflected in a major change in the atomic carbon signal (see fig.2 in [1]) can be attributed to different population mechanisms of these lines by electron collisions or dissociative excitation (compare the respective numbers S/XB in [6] with those for atoms!)

4. Summary and Conclusions

- No expressed maximum in the CD_4/D-flux ratio could be found for graphite limiters up to 700 °C.
- For pure graphite limiters the highest values in the flux dependence of the CD_4/D-flux ratio are about 1% at $\Gamma_D = 10^{20} cm^{-2} s^{-1}$.
- No differences could be found for doped graphites and coated metal limiters.
- The ERO-TEXTOR code allows a modelling of the observed molecular 2D-emission pattern, which fits qualitatively well the measured radial, but not the toroidal distribution.

References

[1] V.Philipps, A.Pospieszczyk, B.Schweer et al., J. Nucl.Mater. **220-222** (1995) 467
[2] B.Schweer, G.Mank, A.Pospieszczyk et al., J.Nucl.Mater. **196-198** (1992) 174
[3] A.Pospieszczyk, F.Aumayr, H.L.Bay at al., J Nucl.Mater. **162-164** (1989) 574
[4] A.Pospieszczyk, H.L.Bay, P.Bogen et al., J Nucl.Mater. **145-147** (1987) 547
[5] K.Behringer, J.Nucl.Mater. **176-177** (1990) 606
[6] A.Pospieszczyk, Y.Ra, Y.Hirooka et al., Report UCLA-PPG-1251 Dec.1989
[7] G.Lieder et al., Proc. 21th EPS Conference, Montpellier 1994, Europhysics Conf. Abstr. 18B Part II (1994) 722
W.Poschenrieder, K.Behringer, H.-St.Bosch et al., J.Nucl.Mater. **220-222** (1995) 36
[8] K.Sawada, K.Eriguchi, T.Fujimoto, J.Appl.Phys. **73** (1993) 8122
[9] J.Roth in *Atomic & PMI Processes in Contr.Thermonucl.Fusion* (R.K.Janev & H.W.Drawin), Elsevier 1993, 381
[10] J.Roth, E.Vietzke, A.A.Haasz, Suppl. to Nucl.Fus. **1** (1991) 63
[11] V.Philipps, E.Vietzke, M.Erdweg, Plasma Phys. and Control. Fusion **31** (1989) 1685
[12] C.C.Klepper et al., Proc. 20th EPS Conference, Lisbon 1993, Europhysics Conf. Abstr. 17C Part II (1994) 599
[13] A.Kallenbach et al., Nucl.Fus. **34** (1994) 1557
[14] U.Kögler, J.Winter, G.Esser et al., this conference
[15] A.B.Erhardt and W.D.Langer, Report PPPL-2477, Princeton Univ., 1987

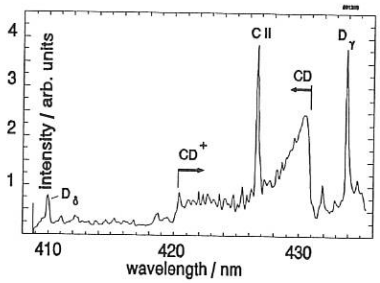


Fig.1: Spectrum showing the transitions for CD: $A^2\Delta - X^2\Pi$ and CD^+: $A^1\Pi - X^1\Sigma^+$ during a CD -gas blow of $1x10^{19}$ molec/s

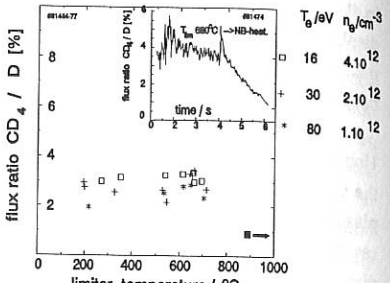


Fig.2: CD_4/ D-flux ratio for a graphite limiter as a function of T_{lim} for different boundary plasmas. For insert and black box see text.

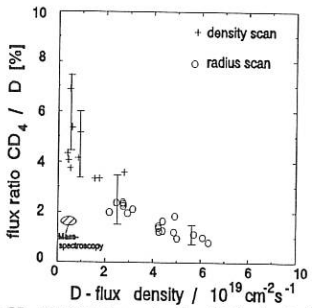


Fig.3: CD_4/ D - flux ratio as a function of D-flux density for a C - limiter (T_{lim} ~ 550°C) by optical and mass spectroscopy

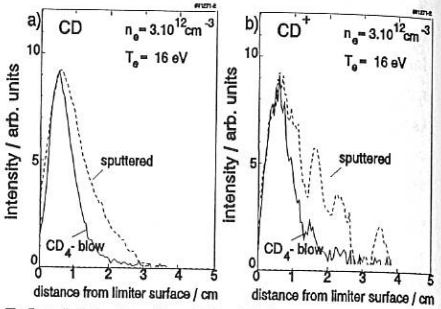


Fig.5.: radial intensity profiles of CD and CD^+ with (a) and without (b) a CD4-gas blow of $1x10^{19}$ mol/s. Separatrix is 1.35mm above surface

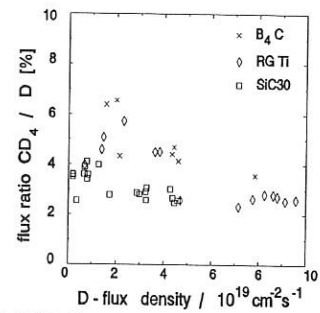


Fig.4: CD_4/ D - flux ratio as a function of D-flux density for different limiter materials

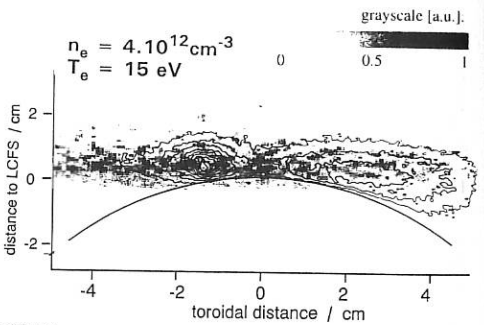


Fig.6.: 2D-intensity distrib. of CD-light - CD_4 -gas blow & ERO-T Code. CD_4 -blow (see fig.5) at -1.5cm: contours; ERO-T: shaded area

Impurity screening in Alcator C-Mod

G M McCracken, B Lipschultz, B LaBombard, F Bombarda*, M Graf,
J A Goetz, R Granetz, D Jablonski, H Ohkawa, J E Rice,
J L Terry , Y Wang and B L Welch.
Plasma Fusion Center
Massachusetts Institute of Technology
Cambridge, MA 02139
*Associazione EURATOM-ENEA sulla Fusione, Frascati, 00044,Italy

1. Introduction

One of the principal roles of the divertor is to prevent impurities produced at the target from returning to the confined plasma. A series of experiments has been carried out to investigate the screening effect of the divertor and SOL by injecting recycling (Ne and Ar) and non-recycling (CH_4 and N_2) gases at different locations in Alcator C-Mod diverted discharges. The use of gaseous impurities has the advantage of giving independent control of the injection rate under a range of operating conditions compared with studying intrinsic impurities. Spectroscopic measurements of impurity densities and detailed profiles of the plasma density and temperature in the divertor have been made.

2. Experiment.

Alcator C-Mod is a high field , high density, divertor tokamak [1,2]. Typical operating conditions for the present experiments are I_p=0.8 MA, $\bar{n}_e$=1.3-2.8x10^{20} m^{-3}, B_T=5 Tesla, $T_e(0)$=1.0-1.8 keV and elongation =1.6, in a single null diverted configuration. The arrangement of the impurity injection systems and the diagnostics is shown in fig 1. One gas injection system consists of an array of capillary tubes connected to poloidal positions, A and C, at the divertor target plates and the inner wall. A second system delivers gas to a point, B, near the outer midplane. The second system has a valve close to the vacuum vessel and is faster acting than the capillary system. Pulses of gas ~ 30 ms can be injected and the subsequent distribution of the impurities followed in space and time.[3]

The impurity radiation in the core plasma is measured with a single spatial channel, absolutely calibrated, VUV spectrograph and, in the case of the argon, also with a crystal spectrometer [4] viewing Ar XVII at up to 5 chords simultaneously. The impurity brightness in the divertor is monitored with a visible spectrometer using a 2-D CCD detector. A wavelength range of up to 45 (70) nm can be scanned in 30 ms with a spectral resolution of 0.1 (0.15) nm. Optical fibers view up to 14 locations at both the inner divertor, P,Q, and outer divertor, R,Q, simultaneously, Fig 1. In addition there are core measurements of the n_e, T_e, total radiation and Z_{eff} profiles and other spectroscopic measurements. The n_e and T_e

profiles in the SOL and along the target plates are measured with a scanning probe and an array of Langmuir probes in the tiles [5]. Typical conditions at the divertor plate which have been used for impurity injection experiments, vary from T_e=20 eV, n_e=1x10^{19} m^{-3} to T_e< 5 eV, n_e=3x$10^{20}$$m^{-3}$.

3. Results

With a short pulse (~40 ms) of neon or argon, typically 1 to 3% of the injected atoms get into the confined plasma and stay there for the duration of the discharge, Fig 2. The MIST code [6] is used to calculate the charge state distribution and hence the total impurity content, calibrating the results to the measured brightness of the Ar XVII or Ne VIII. The fraction of injected impurities entering the confined plasma decreases with density [3]. Gas has also been injected via the capillary tubes into the private flux zone in the divertor , at the inner wall midplane and into the outer SOL. If the impurity flow rate into the divertor is constant, (typically 1x10^{19} s^{-1}), the impurity density in the plasma increases roughly linearly during the length of the diverted phase. These results indicate that neon and argon are recycling impurities, as expected. The fraction getting into the core plasma does not depend strongly on the position of injection .

In the case of a pulse of nitrogen or methane the impurity concentration in the confined plasma decays with a time constant of ~ 30 ms after the injection pulse, Fig 3. This contrasts with the recycling gases. The time constant is comparable to that measured for impurities injected by laser ablation and indicates an impurity recycling coefficient ≤ 0.3. For a long impurity injection pulse the impurity concentration rises to a constant value. The impurity injection rate, obtained from the pressure rise in the vacuum vessel during a calibration pulse, has also been plotted in fig 3. It is observed that the total number of impurities in the plasma is proportional to the *injection rate* over the whole injection cycle, rather than the integrated amount as is the case for the recycling impurities. The total number of impurities in the core plasma can therefore be normalized to a constant influx for a range of different conditions. The results for nitrogen and carbon are shown in fig 4. The impurity number/influx is a time constant which varies from 10^{-5} to 10^{-2} s, depending on species and plasma conditions. Lower impurity core densities are obtained for carbon than for nitrogen and the number of core impurities decreases with increasing core electron density.

Using the measured SOL profiles of n_e and T_e, the ionization rate of both CH_4 and N_2 has been calculated as a function of minor radius. For typical C-Mod conditions the methane is ionized further from the separatrix than the nitrogen. This is consistent with a model in which the ionization occurs in the SOL and the impurity density in the confined plasma is determined by the dynamic flux balance between the injection rate, cross field diffusion to the separatrix and parallel flow in the SOL to the target. Direct observations of the parallel flow towards the divertor have been made by viewing the CII and CIII spatial distribution during CH_4 injection, using CCD cameras and interference filters.

A background nitrogen impurity density is observed which builds up in successive discharges, indicating that nitrogen is accumulating on surfaces, probably the divertor target plates. In the case of carbon there is always significant background both for low and high charge states since carbon is an intrinsic impurity in C-Mod.

A preliminary assessment of the spatial distribution of the impurities in the divertor has been carried out using the multi-channel visible spectrograph with chords spanning the inner and outer divertor. In the case of argon the chordal brightness of Ar II is highest at the inner divertor. This is consistent with the measurements of the Dα and the total radiation. At low to medium density the radiation comes from the region just above the inner divertor nose. The results are also consistent with probe measurements which show the temperature is much lower at the inner than the outer divertor target [5]. In the case of N and C there is little increase observed in the divertor radiation during impurity injection

4. Conclusions

There is a striking difference between the rare gases, Ne and Ar, and the non recycling species, C and N. In both cases there is good screening; this is attributed to the high plasma and power density which leads to high ionization rates in the SOL. The radial location of ionization is, in all cases, in the SOL. This is partly due to the low energy of the injected gas species. Less good screening is observed for laser injected scandium which has a directed energy ~10 eV. For sputtered atoms, with energies $\geq$ 5eV, the peak in the ionization is calculated to be much closer to the separatrix, also implying lower screening. The lower screening of sputtered atoms may account for the high carbon background and the buildup of the nitrogen background. In the case of non-recycling gas injection the effective loss time along the SOL is short compared to impurity transport times in the main plasma. It appears that most of the impurity flux is ionized in the SOL, then flows to the target and sticks there.

Acknowledgements: The authors are grateful to the whole Alcator team and in particular to the operations group, for the excellent operation of the machine. This work is sponsored by the US Department of Energy under contract No DE-AC02-78ET51013

References:

[1] I H Hutchinson, Physics of Plasmas, **1** 1511 (1994).
[2] B Lipschultz, J Goetz, B Labombard et al, J. Nucl. Mater., **220-222** 50 (1995).
[3] G M McCracken, F Bombarda, M Graf et al J. Nucl. Mater. **220-222** 264 (1995).
[4] J E Rice and E S Marmar, Rev Sci Instrum., **61** 2753 (1990)
[5] B Labombard, Phys of Plasmas,**2**, 2242, (1995)
[6] R A Hulse, Nuclear Technology/Fusion, **3** 259 (1983)

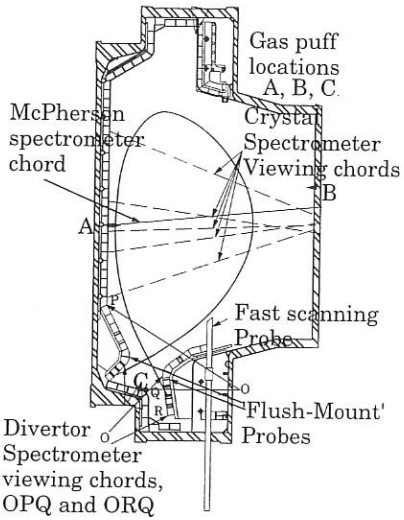


Fig 1. Poloidal cross section of C-Mod showing gas puffing positions and spectroscopic views

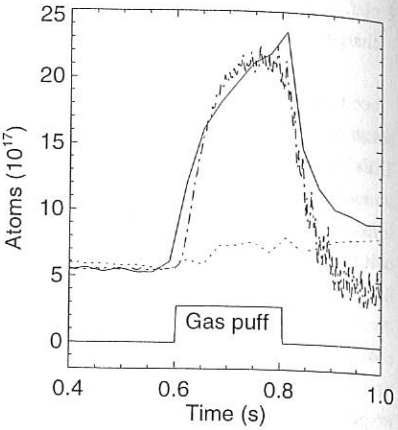


Fig 3. Nitrogen atoms in the plasma with 200 ms gas puff, $\bar{n}_e = 1.6 \times 10^{20}$ m^{-3}

——— N in confined plasma

..... N background, no gas puff

- - - - - - - N *injection rate* x0.005/s

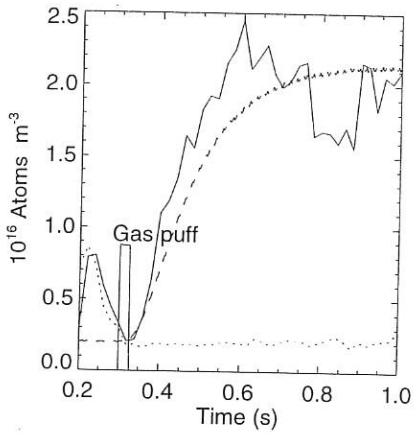


Fig 2. Argon atoms in the plasma with 30 ms gas puff, $\bar{n}_e = 1.6 \times 10^{20}$ m^{-3}

——— Ar in confined plasma

..... Ar background, no gas puff

- - - - - - - Ar atoms injectedx0.02

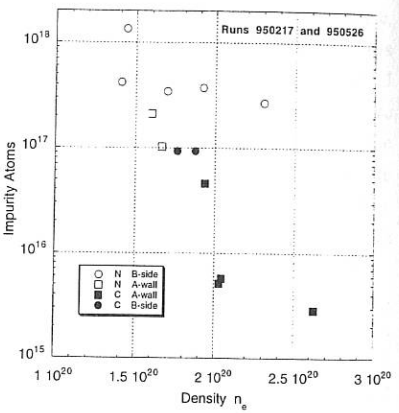


Fig 4. N and C atoms in the plasma for an injection rate of 1×10^{20}/s at inner wall, A and outer midplane, B

Impurity Influxes and Production Mechanisms in RFX.

L.Carraro, E.Casarotto, **M.E.Puiatti**, P.Scarin, M.Valisa
Gruppo di Padova per Ricerche sulla Fusione
ENEA-EURATOM-CNR-Univ. di Padova Association
Corso Stati Uniti, 4 - 35127 Padova (Italy)

Introduction - Impurity and hydrogen influxes into the plasma are routinely monitored in the RFP device RFX (R=2m, a=0.46m) along 5 chords in one poloidal section. The optical set-up allows the simultaneous measurement of CII 6578Å, OII 4415Å and H_α 6561Å emissions from exactly the same position [1]. In this paper the results of the measurements are discussed with reference to the modes locking at the wall, which characterize all the RFX discharges, and carbon blooming phenomena, observed at high plasma current (~800kA). Some observations about the role of hydrogen and oxygen in carbon production are also presented.

Locked modes and carbon blooms - RFX is characterized by strong asymmetries in the plasma-wall interaction, both poloidally (shift of the plasma column)[2] and toroidally (locked modes and toroidal field ripple) [3]. In the regions where modes are locked to the wall an important impurity source is localized. Fig.1 shows a comparison, in terms of CII and OII emissions, of two discharges performed at ~800kA of plasma current, one with mode locking at a toroidal angle near the influx measurement section and the other with mode locking at the opposite side to the diagnostic section . It is difficult to estimate which fraction of highly ionized carbon in the main plasma is due to the influx from the region where modes are locked, because in general the CII emission saturate; an increase by a factor ≥50 has been estimated as lower limit in those cases. In addition, an enhanced emission by a factor of ~10 has been observed for carbon influx with the locking at $\pm 40^0$ from the spectroscopic diagnostic section. Therefore, the effective influx of carbon, responsible for the carbon content in the plasma, is likely to be dominated by the locking region. The effect is less pronounced for oxygen: in fact OII emission in presence of the locking modes increases by a factor ≤10.

Carbon blooming events have been observed in ~50% of the high plasma current discharges (≥750kA). They consist in a sudden increase of the CV and CVI emissions well correlated with an increase in the loop voltage [4], sometimes representing an operational limit. As an example fig.2 shows the time behaviour of CV density together with the plasma current. In the discharges in which carbon blooms occur, the ccd camera show surface temperatures of the graphite tiles covering the vacuum chamber higher than $1800 \div 2000$ °C, namely above the threshold for carbon blooms [5,6,7]. This suggests that radiation enhanced sublimation or

direct thermal sublimation are the physical processes responsible for these phenomena. In addition, though normal fluxes are the primary reason for hot spots, also a very high carbon self-sputtering yield (that approximates to 1 if the incident ions have very high energies or very high grazing incidence angles [7]) may contribute to the sustainment of the carbon blooms . In conclusion, at high plasma current the local carbon influx in the region where modes are locked has a large influence on the carbon content in the plasma. In fact, the CII influx measured in regions unaffected by the locking and CV+CVI densities are not correlated, as shown in fig.3 (where each point represents one discharge), while in discharges performed at lower plasma current (~500kA) carbon blooms phenomena are not observed and the correlation is much better. The density of OVII is correlated with OII influx also at high current (fig.4).

Impurity production mechanisms - From the analysis of the influxes measured outside the toroidal section affected by the locking of the modes, it has been found that a hydrogen unloaded wall is a more favourable condition for a low carbon influx into the plasma. In fact it has been observed that the ratio between oxygen and carbon influxes is strongly dependent on the wall conditioning. Just after a helium glow discharge cleaning session, the carbon influx Γ_C decreases more than the oxygen one (Γ_{OX}), leading to a clear increase of the ratio Γ_{OX}/Γ_C, as shown in fig.5. In coincidence, the electron density and the effective recycling coefficient, defined as the ratio between the number of electrons actually present in the discharge and the number of hydrogen atoms puffed into the vacuum chamber , decrease. Hydrogen influx and efflux (as measured by a neutral particle analyzer) also decrease after an helium glow discharge. Therefore, under the same oxygen influx, an unloaded wall, with low recycling and low hydrogen efflux, corresponds to a lower carbon influx, indicating that hydrogen plays an important role in the carbon production via physical and chemical sputtering. Actually, both at low and high plasma current, carbon and hydrogen influxes are correlated and the ratio Γ_C/Γ_H increases with the effective recycling, i.e. with the degree of wall loading in RFX, as shown in fig.6.

In order to study the role of oxygen in carbon production, the influxes measured before and after the trimethylboron boronizations performed in RFX have been considered. In fact, after a boronization a decrease in the oxygen influx has been observed, by a factor ~2 for discharges at 800kA, and by a factor as high as 6 when the boronization has been performed between discharges at 500kA. However, in both cases, a much lower decrease of Γ_C has been measured. With the hypothesis that for carbon the release mechanisms not connected with oxygen are not influenced by the boronization, the comparison between the experimental influxes before and after the boronization allows us to estimate that for 500kA discharges before boronization ~50% of carbon influx was due to oxygen, and only ~25% for higher current discharges. This is related to the frequent occurence, at high currents, of "hot spots"

phenomena, and to the subsequent increase of carbon emission. For both currents it has been observed that, while before the boronization the ratio Γ_C/Γ_H is well correlated with Γ_{ox}/Γ_H, the correlation is worse after the boronization, indicating that in this condition the carbon influx is less related to oxygen: for the higher current case this is shown in figs.7 and 8, that may be interpreted by a simple carbon production steady state model [8] ($\Gamma_C^{in} = \Gamma_C^{out}$):

$$\frac{\Gamma_c}{\Gamma_H} = \frac{\eta_o Y_o + (1-\eta_o) Y_{cc}}{1-Y_{cc}} \cdot \frac{\Gamma_o}{\Gamma_H} + \frac{Y_H + \eta_H Y_c + (1-\eta_H) Y_c Y_{cc}}{1-Y_{cc}}$$

where: Y_H, Y_C are the physical and chemical sputtering yields due to hydrogen ; Y_O, Y_{CC} are the carbon sputtering yield due to oxygen and the carbon self-sputtering yield(Y_O=1 may be assumed[9]); η_H, η_O are the carbon fraction penetrating into the plasma.

To estimate the penetration efficiency the molecular emission measurements have been used. The hydrocarbon influx deduced from the C_2 5165Å and the CH 4314Å bands results to be about 2-3 times greater than the measured atomic influx [10], and therefore a penetration efficiency of 0.5 has been assumed. With this hypothesis, the linear fit in fig.7 gives Y_{CC}~0.3. After the boronization a linear fit does not show a good regression coefficient (fig.8); however, it would indicate for Y_{CC} a higher value of ~0.5. This is quite a high value; in RFX it can be justified with high energies and/or grazing angles for incident ions.

Conclusions - The impurity production mechanisms in RFX are strongly affected by the mode locking at the wall. At high currents (~800kA), due to the high power density losses at the wall, the formation of hot spots (≥1800 °C) is often observed, with the associated phenomena of carbon blooming ; these may sometimes represent a machine operational limit. The plasma deformation associated to the locking effects is 1/5 to 1/10 of the total surface, but it is responsible for 50-75% of the total carbon content. Therefore the removal of mode locking phenomena would represent a sensible improvement of the cleaning situation and of the effective charge in RFX. Once locking is removed as the main impurity source the plasma performance would benefit from the consideration that both oxygen and hydrogen play a role in carbon production. The former content has been reduced by boronization procedures, while the latter contribution may be reduced operating with unloaded graphite tiles.

REFERENCES
[1]Carraro,L.,et al., Rev.Sci.Instrum.,66(1995)610
[2]Carraro,L.,et al., Jour. of Nucl.Mat., 220-222(1995)646
[3]Antoni,V.,et al., "Analysis of wall locking phenomena and their consequences in RFX", this conference
[4]Carraro,L.,et al.,"Effects of the impurities on the loop voltage in RFX", this conference
[5]Patel,A.,Carolan,P.G., in Physics of Mirrors,Reversed Field Pinch and Compact Tori, Int.School of Plasma Physics,Varenna (Italy)(1987)vol.III,p.1103
[6]Philipps,V.,et al., Nucl. Fusion,33 (1993)953
[7]Ramsey,A.T.,et al., Nucl.Fus. 31 (1991)1811
[8] Antoni,V.,et al., Jour. of Nucl. Mat. (1995)650
[9] Vietzke,E.,et al., Jour. of Nucl. Mat., 145-147 (1987)425
[10]Pospieszczyk,a.,et al.,"Spectroscopic studies of carbon containing molecules and their break-up in PISCES-A", UCLA-PPG-1251, December 1989

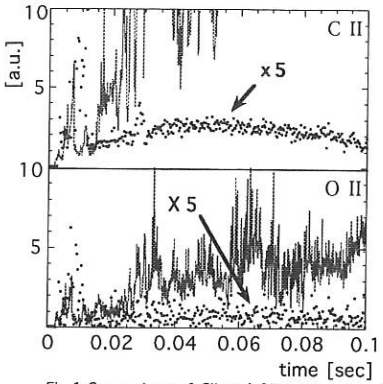


Fig.1-Comparison of CII and OII emissions with modes locking near the diagnostic section(——) or at the opposite side of the torus(·····)

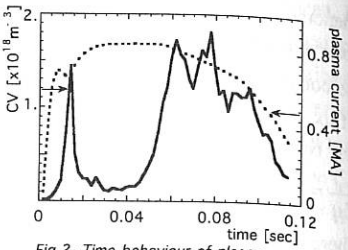


Fig.2- Time behaviour of plasma current and CV density in presence of a carbon bloom

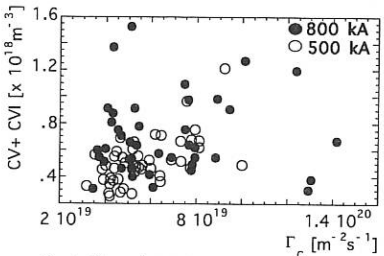


Fig.3-CV and CVI density as a function of carbon influx at high and low plasma current

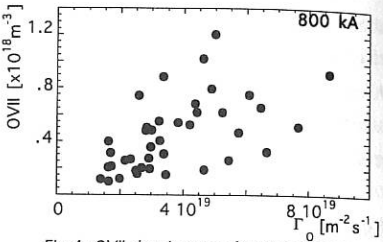


Fig.4- OVII density as a function of oxygen influx in high plasma current discharges

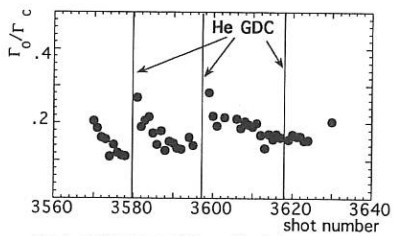


Fig.5- Behaviour of the ratio between oxygen and carbon influxes in correspondence with helium glow discharge cleaning sessions

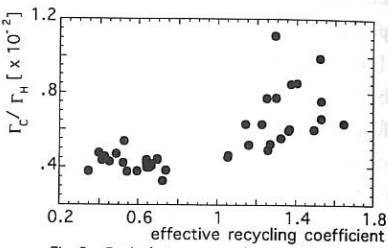


Fig.6 - Ratio between carbon and hydrogen influxes as a function of the effective recycling coefficient

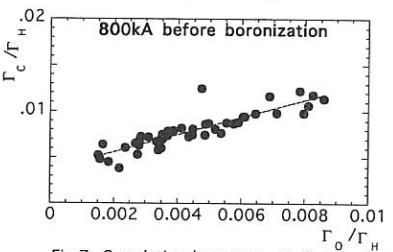


Fig.7- Correlation between Γ_C / Γ_H and Γ_O / Γ_H before the boronization

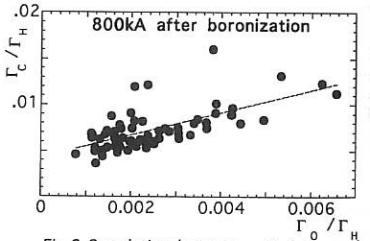


Fig.8-Correlation between Γ_C / Γ_H and Γ_O / Γ_H after the boronization

Studies of high-Z wall components in TEXTOR 94: local impurity release and its impact on the plasma core.

V.Philipps, M.Tokar, A.Pospieszczyk, U.Kögler, R.Koslowski, A.Krämer-Flecken, J.Rapp, U.Samm, B.Schweer, B.Unterberg, J.Winter, D. Naujoks[1], T.Tanabe[2], Y.Ueda[2], M.Wada[3], K.Ohya[4], J.Ongena[5], G.van Oost[5], M. Rubel[6], D.Larsson[6]
Forschungszentrum Jülich, Institut für Plasmaphysik, D-52425 Jülich, Germany, Ass. Euratom-KFA, [1]Max Planck Institut für Plasmaphysik Bereich Berlin, Ass. Euratom, [2]Faculty of Engineering Osaka University, Suita, Osaka 565, Japan, [3]Doshisha University, Kyoto, Japan, [4]University of Tokushima, Japan,
[5]Laboratoire de Physique des Plasmas-Laboratorium voor Plasmafysica-,Ass Euratom-Belgian State Ecole Royale Militaire, Koninklijke Militaire School, B-1040 Brussels, Belgium,
[6]Royal Institute of Technology, Physics Department Frescati, Frescativagen 24, S-104 05 Stockholm, Ass Euratom-NFR, Sweden

1. Introduction

High Z metals offer the option of reduced impurity production if the impact energies of plasma particles are near or below the threshold for physical sputtering [1]. However the possible benefit of low impurity production at low plasma edge temperatures competes with strong radiation and possible accumulation effects if suppression of impurity production is not strong enough. This narrows the operational range of accessible plasma conditions. In order to evaluate these conditions a systematic analysis and understanding of high Z impurity production, local ionization and penetration processes into the near wall plasma and high Z transport into the plasma core is needed. At TEXTOR a research program has been started in the framework of the TEXTOR-IEA cooperation to analyse these conditions using test-limiters made from solid molybdenum and tungsten.

2. Experimental

Movable Mo- and W-limiters with dimensions of 10x6 cm were inserted from the bottom of the vessel through a limiter lock up to 3cm inside the minor plasma radius defined by the toroidal ALT-II pump limiter (r=46 cm). Local limiter diagnostics included IR-thermography, calorimetry and visible spectroscopy by means of a spectrometer and 2D-CCD cameras coupled to interference filters. Observations of high Z impurities in the main plasma were based on VUV-spectroscopy, soft X-ray emission and radial profiles of the radiated power from bolometry. Edge electron temperature and density profiles were measured by means of atomic beam techniques (He and Li beams). Graphite collector probes in the SOL were used to collect Mo,W and other impurities. Some more details are found in [2].

3. Results:

The fraction of the total convective plasma power (heating power minus radiated power) which has been deposited onto the Mo-and W-testlimiters (determined by calorimetry) increased from about 1% at r=46cm up to about 7% at r=44cm which indicates the relative importance of the high-Z components in relation to the entire graphitic wall. At these positions the limiters are always under erosion dominated conditions. The spectroscopically measured carbon and oxygen impurity fluxes remitted from the high Z limiters amount to about 2-4 % and 0.5-1% of the deuterium flux. Sputter erosion modelling shows that high-Z sputtering is dominated by

carbon and oxygen impurity impact and deuterium sputtering can be neglected [2]. Using a fraction of 1-8 % of the overall deuterium flux impinging on the Mo and W-limiters (proportional to the power fraction) and a (C+O)/D flux ratio of 2.5 % the overall Mo/D release rate can be estimated between $6x10^{-5}$ and $5x10^{-4}$ Mo/D (at T_e=40 eV). Since impurity release is dominated by C and O impact these numbers are only a factor of about 2 smaller for the W-limiter.

3.1. High-Z accumulation behaviour in ohmically heated discharges

Under ohmic heating conditions a suddenly starting high Z impurity accumulation in the plasma core has been observed when the central density reached a critical value. This behaviour is similar for both the Mo and W-limiter experiments. We will concentrate on the operation with W-limiters (part of the results with Mo-limiter are published /2/). The general accumulation behaviour is demonstrated in fig1. showing the traces of the line averaged density, the central electron temperature and the total radiation for an ohmic discharge for which the density was ramped in steps. At n_e=3.2 $10^{13}/cm^3$ (t= 3.2 s) accumulation occurs suddenly as can be seen from the drop of the electron temperature and increase of radiation. Fig 2 shows some details of the accumulation process: the W-concentration at the core (determined from central radiated power, ne(0), Te(0) and W-radiation potential from corona equilibrium) rises within about 300ms up to about $8x10^{-5}$. After the W-concentration has somewhat increased, the ne-profiles steepen, the electron temperature drops and sawtooth activity decreases. The drop of the central electron temperature is due to a flattening of the T_e-profiles within the q=1 surface (+-12cm from the magnetic axis). T_e-profile flattening occurs always first on the high field side. The accumulation leads finally to an internal disruption after which the central W-concentration remains high and T_e profiles have flat central regions with somewhat steeper gradients at outer plasma regions. Thermal instabilities due to high-Z accumulation occur then several times during one discharge accompanied by development of m=2 MHD instabilities which are not detectable during the first accumulation process. Fig 3 shows that the critical central density at which accumulation is observed depends only weakly on the limiter position,respectively on the intensity of the W-source.

The accumulation in ohmically heated discharges is well explained by a thermal instability caused by the temperature dependence of the neoclassical impurity flux: growing central W-concentration leads to growing radiation and flattening of the Te-profiles which increases furthermore the impurity flux to the center due to decreasing temperature screening. More details can be found in [3].

3.2 Evidence of local screening under high edge density conditions

By applying NBI and/or ICRH heating with sufficient power, high-Z accumulation is prevented or disappears when it had occurred during the ohmic phase. This behaviour is described in more detail in [4]. We will concentrate here on the strong evidence that sputtered W-and Mo-impurities are locally redeposited onto the limiter surface with an efficiency reaching values well above 90%. This behaviour is seen most clearly on the profiles of radiated power taken at different plasma densities and limiter positions and on collector probe data measuring

the deposition rates of Mo and W in the SOL: both, the additional radiation which must be attributed to high-Z W-and Mo-impurities, and the W-and Mo-deposition rates decrease significantly with increasing plasma density. Fig 4a shows the dependence of the total W-concentration in the plasma evaluated from the radiation profiles under the assumption of coronal equilibrium together with W-deposition rates at collector probes in the SOL on plasma density. Fig 4b shows for the Mo-limiter case the density dependence of Mo-SXR-intensity for L-shell emission (~ 2.3 keV) and Mo-deposition rates. These data show a trend to decrease significantly with increasing local plasma density. Local spectroscopy of MoI(413.4 nm)-and WI-light (400.8 nm) and sputter modelling show that the local source intensities of sputtered Mo and W decrease only slightly (by less than a factor of 1.5) with density and can thus not account for the strong decrease of the plasma pollution by Mo and W. Spatially resolved CCD spectroscopy shows that the penetration depths of the W-neutrals (and W^+) decrease to less than 1-2 mm at high plasma densities. This has to be compared with the gyroradii of 2mm of singly ionized W-atoms having kinetic energies originating from the sputter process of about 4eV. Only slightly larger penetration depths have been found for Mo-neutrals[5]. Local Monte Carlo modelling with the ERO-TEXTOR code has been performed to model the penetration depths of sputtered Mo and W-neutrals and in particular the fraction of ions being redeposited within the first gyroorbit. Fig5 shows the result of these calculations displaying the fraction of sputtered atoms which survive the first gyromotion without intersecting the surface. As can be seen this value decreases from an upper value of about 10 % at low density in ohmic plasmas down to less then 2% at high density NBI conditions. This effect is very effective in screening sputtered Mo and W atoms and opens interesting prospectives in using high-Z wall components.

4. Summary

- Power fractions up to about 7% have been deposited onto the Mo-and W-testlimiters. Mo and W-impurity release is dominated by carbon and oxygen impurity impact.
- Under ohmic heating a suddenly starting high Z impurity accumulation has been observed when the density approached a critical value. The accumulation leads to minor disruptions which can repeat several times during one discharge. The accumulation can be explained by a thermal instability caused by neoclassical impurity transport.
- Under NBI heating accumulation is prevented. At high local densities ($\sim 10^{13}/cm^3$) the penetration depth of Mo and W neutrals decrease down to 1-2 mm. A strong decrease of plasma W-and Mo-pollution with increasing plasma density has been observed. This is attributed to a strong efficiency of prompt redeposition of sputtered W-and Mo-atoms within the first Larmor orbit as (predominantly) singly charged ions.

References:

[1] Tanabe T, Noda N, Nakamura H J, J.Nucl. Mat 196-198 (1992) 11

[2] Philipps V, Tanabe T, Ueda Y et al, Nucl. Fusion Vol 34 No 11 (1994) 1417

[3] Tokar M Z, Baelmanns T, Philipps V et al, this conference

[4] van Oost G, Messiaen A M, Philipps V et al , this conference

[5] Ueda Y, Tanabe T, Philipps V et al J. Nucl. Mat 220-222 (1995),663

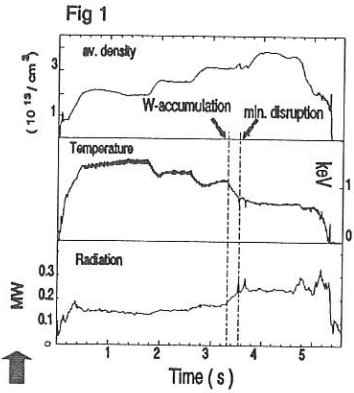


Fig 1 Upper: Evolution of $\bar{n}_e$, $T_e(0)$ and total radiated power for an ohmic discharge with. W-accumulation starts at 3.25 s. At t= 3.6 s an internal disruption occur.

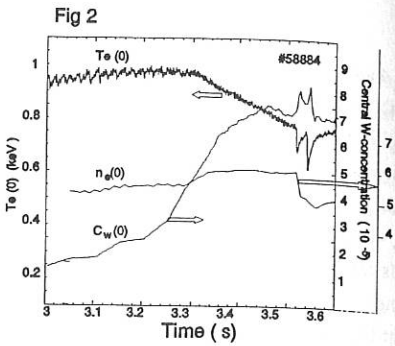


Fig 2 Right upper: Evolution of $T_e(o)$, $n_e(0)$ and W-concentration on axis during the accumulation process.
lower: development of Te profiles during the accumulation process.

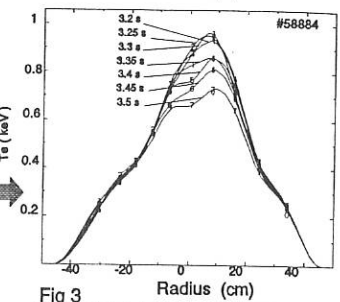
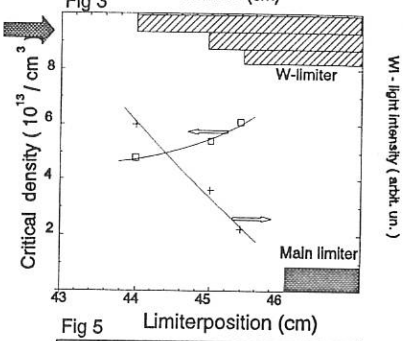


Fig 3 Right: dependence of critical density for W-accumulation on the radial position of the W-limiter. The right scale shows the increase of the local WI-light in front of the limiter.



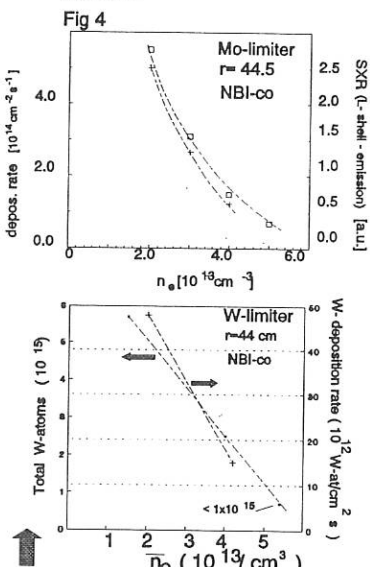


Fig 4 Dependence of Mo- and W- plasma contamination on plasma density (Mo: from SXR at 2.3 keV, W: from bolometrie. Also shown are Mo- and W- deposition rates in the SOL.

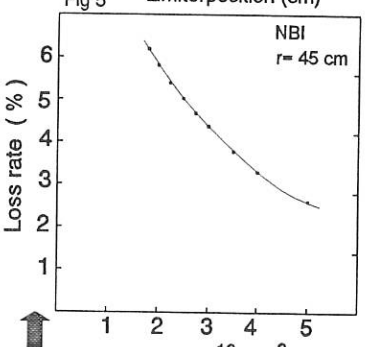


Fig 5 Fraction of sputterd W-atoms not promptly redeposited during first larmororbit (calculated with ERO-TEXTOR)

Fundamental Deuterium, Second Harmonic Tritium and Alpha Particle Heating and Current Drive in Fusion Plasmas*

J.E. Scharer, N.T. Lam, R.S. Sund, and M. Bettenhausen

Department of Electrical and Computer Engineering
University of Wisconsin, Madison, WI, USA 53706

Abstract

We consider the problem of second harmonic tritium heating for TFTR plasmas and fundamental deuterium heating and current drive for ITER in the presence of a population of fast alpha particles. We also consider the influence of alpha particle heating for TFTR $2\omega_{CT}$ supershot experiments utilizing the XWAVE and SEMAL computer codes. We find that a substantial fraction of wave power can be coupled to the alphas for typical fast wave spectra. We consider profile effects and the off-axis heating as well as the on-axis ω_{DT} resonance for fast alpha particle current drive in ITER.

Modelling of Second-Harmonic Tritium Heating on TFTR

We consider D-T supershot experiments with ICRF heating at the second harmonic of tritium in cases where both background and beam ions are present, which produce significant concentrations of alphas. We use the 1D full-wave single pass code XWAVE [1] and the global full wave code SEMAL [2] which includes the alpha effects of high-order ($n \geq 3$) cyclotron harmonics for high fusion yield shots.

We concentrate on shot #74471, which has a 60% tritium density and small concentrations of He^3, carbon , D, and T (background and beam) and electrons. The plasma parameters are obtained directly or inferred from TRANSP calculations of experimental data [3]. For this case, TRANSP calculates an on-axis alpha concentration of only 0.08% n_e and we utilize an absorption equivalent [4] Maxwellian temperature of 1.3 MeV.

All densities and temperatures are assumed to follow parabolic profiles, i.e. $n(T) = n(T)_0(1-r^2/a^2)^c$ with c = 1 for density and 2 for temperature. To simulate the 20 cm Shafranov shift, we take R_{major} = 2.83 m and the minor radius is a = 0.96 m. With the magnetic field set at B = 4.1 T near R = 2.8 m, the $2f_{ct}$ layer coexists with fundamental D and alpha layers on the high field side. To compute the fractional power absorption for each species, we use SEMAL, a global 1-D code with a single parallel wave number k_z. The values used for the parallel wavenumber in the heating simulations are based the antenna coupling spectrum obtained from a simulation run with the WICS computer code

[5,6]. The plasma density model used is based on experimental data from TFTR. We choose representative values of $k_z = 6\ m^{-1}$ corresponding to the edge region and $11\ m^{-1}$ corresponding to the plasma core accounting for toroidal upshift. (Taking into account the evolution of the wave number as the wave propagates towards the center would give more accurate estimates of the fractional absorption.) Figure 1 shows the total absorption profile for $k_z = 6\ m^{-1}$. The modulation in the profile is indicative of standing waves and weak single-pass absorption. Electron absorption accounts for 30% of the total absorbed power for $k_z = 6\ m^{-1}$. The deuterium and tritium ions absorb 45% of the power within the region $r/a < 0.8$, with the remainder going to the He^3 and the alphas. For $k_z = 11\ m^{-1}$, the fractional electron power absorption increases to 45% and the total D and T absorption fraction drops to 31%. For these plasma parameters, the power splits predicted by SEMAL agree closely with those predicted by TRANSP.

For the ion temperatures and densities of TFTR, fusion alphas with concentrations up to 0.4% n_e can be generated in the TFTR D-T plasma. Following TRANSP calculations, we have set the alpha concentration at $n_{a0} = 0.1\%\ n_{e0}$. SEMAL shows that up to 6% of the total absorbed power is coupled to the alphas. Figure 2 depicts the absorption profile of the alphas for $k_z = 11\ m^{-1}$. The estimated value of the alpha absorption coefficient appears consistent with measured experimental data on alpha losses.

ICRF Heating and Applications to ITER

We consider the effects of a small concentration of alpha particles on ICRF wave propagation and absorption for an ITER D-T plasma near the on-axis fundamental deuterium cyclotron resonance.

We assume that the plasma has $n_e = 9 \times 10^{13}/cm^3$, $B = 4.85$ T, $R_0 = 6$ m, $n_D/n_T = 0.5$, $T_e = T_T = 15$ keV and a self-consistent deuterium temperature of 15-25 keV with corresponding fast alpha particle concentrations, including the effects of enhanced reactivity, which we have calculated [4], of $n_{af} = 0.1\text{-}0.8\%\ n_e$. The two-ion-hybrid resonance lies at $x = -0.7$ m towards the high field side from the fundamental resonance on the axis. The corresponding left-hand circularly polarized component peaks in a localized region near the two-ion-hybrid resonance. The Maxwellian equivalent alpha particle distribution is chosen to have the same number of resonant particles in this region as the slowing down distribution. The $|E_{left}|$ peak extends over a comparatively narrow interval near the two-ion hybrid resonance, and most of the power that goes to the alphas is absorbed in that narrow region. Consequently, we choose the number of resonant particles

at x_p, the location of the $|E_{left}|$ peak, to be the basis of equivalency [4] between two distributions.

We find that up to 25% of the ICRF power can be coupled to alphas near the two-ion-hybrid resonance on the high field side. When we reduce the wave frequency so that the two-ion hybrid resonance is on the axis for an advanced ITER scenario, we find that up to 80% of the ICRF power can be coupled to alphas at energies near $E_\alpha = E_c = 1$ MeV. This is an attractive scheme for core seed current for high-bootstrap-fraction confinement scenarios for ITER.

Summary

The influence of alpha particle absorption on ICRF fundamental deuterium and second harmonic tritium heating can be significant and must be considered for TFTR supershot heating and current drive scenarios and ITER. Alpha particle absorption processes are predicted to be 6-10% for current-high-fusion-yield TFTR ICRF experiments. We find that under appropriate advanced confinement ITER conditions, the presence of the two-ion (D-T) hybrid resonance can give rise to a substantial enhancement of the local fast alpha particle absorbed power density (P_a = 60-80% P_{inc}). We are currently examining alpha particle current drive scheme using this absorption process for advanced confinement, high-bootstrap-fraction tokamaks.

Acknowledgments

We would like to thank C. Phillips, R. Majeski and R. Wilson for assistance in collaboration on modelling TFTR ICRF experimental results.

*Research supported by US DOE Grant Nos. DE-FG02-86ER53218 and DE-FG02-93ER54196.

References

1. R.S. Sund and J.E. Scharer, Physics of Fluids B 3, 1326 (1991).
2. O. Sauter, J. Vaclavik, Nucl. Fus. 32, 1455 (1992).
3. C.K. Phillips et al., to be published in Physics of Plasmas (1995).
4. N. Lam, J. Scharer and R. Sund, "Influence of Alpha Particle Absorption on Fundamental Deuterium Heating in a Fusion Plasma," Nuclear Fusion 34, 1161-1167 (1994).
5. M. Bettenhausen, Ph.D. thesis, University of Wisconsin (1995).
6. M. Bettenhausen and J. Scharer, "Simulation of Ion Bernstein Wave Edge Parasitic Coupling During Fast Wave Heating", submitted to Nuclear Fusion (1995).

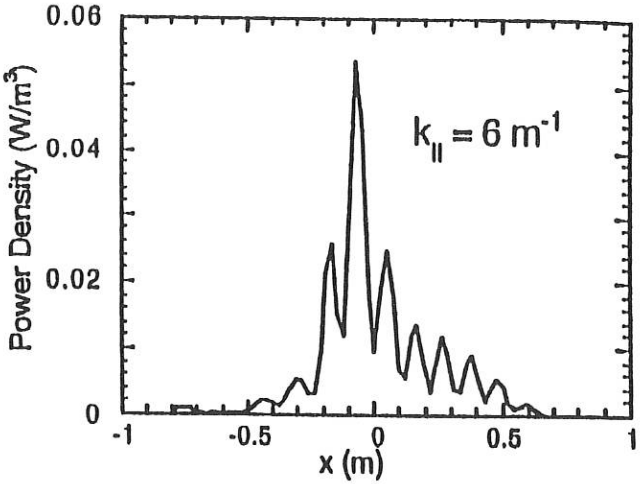


Figure 1. Total absorption profile for $k_z = 6\ m^{-1}$

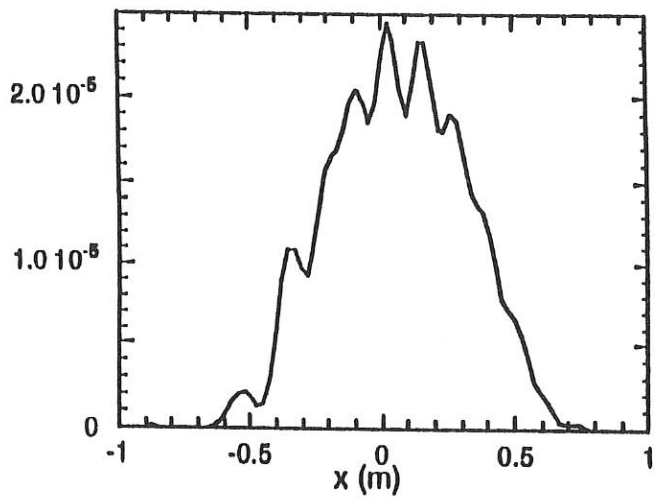


Figure 2. Alpha absorption profile for $k_z = 11\ m^{-1}$

Physics aspects of coupling the ICRF A2 antennae to JET discharges

P U Lamalle, G Bell*, V P Bhatnagar, M Bures, B Fechner, C Gormezano, J Jacquinot, A Kaye, M Lennholm, F Nguyen#, E Righi, A Sibley, D F H Start, M Timms, T J Wade

JET Joint Undertaking, Abingdon, Oxon OX143EA, U.K.

* Oak Ridge National Laboratory, U.S.A. # CEA, Centre d'Études de Cadarache, France

1. Introduction

The four A2 antennae were designed for rf heating and current drive in the JET divertor configurations ([1], Fig.1); they have been active since early 1994. Each antenna is an array of 4 side-by-side straps driven by 4 independent amplifiers (2MW, 25 to 56MHz); this allows operation with arbitrary current phasings, i.e. with various radiated power spectra (dominant parallel wavenumber $k_{//}$ adjustable between 0 and 6.4m^{-1}, Fig.2). Now 12 to 15MW are routinely launched into the plasma (including ELM-free and ELMy H modes) in 0ππ0 phasing. This major improvement since 1994 [2-4] is due to the reliability of the new electronics. The record coupled power is 16.5MW with the same phasing (i.e. a total of 19.5MW at the amplifiers, the available maximum being 32MW); it is mainly limited by the antenna coupling properties, which are the object of this paper.

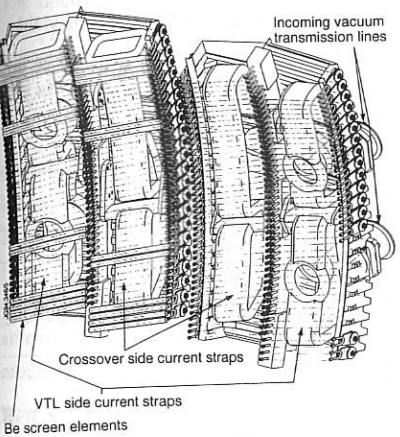


Fig.1 JET ICRF A2 antenna

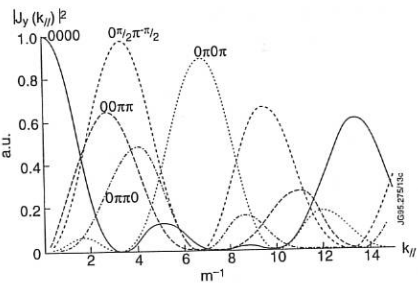


Fig.2 $k_{//}$ spectra ($|J_{rf}|^2$) for the main phasings in use.

2. Analysis of coupling

The coupling resistance R_c is defined for each line+strap system by $P = \frac{V_{max}^2}{2 Z_c^2} R_c$, where P is the generator power, V_{max} the associated maximum voltage on the main transmission line (MTL) and Z_c the line characteristic impedance (30Ω). As the lines share the same admissible

maximum voltage, the R_c's reflect their respective power coupling ability. In terms of the MTL reflection coefficient amplitude r and the VSWR s, $R_c = Z_c\,(1-r)\,/\,(1+r) = Z_c\,/\,s$ (1). R_c critically depends upon plasma conditions (boundary shape, scrape-off layer parameters); it includes a contribution of transmission line losses $R_{loss} \approx 0.0623\,\sqrt{f_{MHz}}$ (0.3 to 0.5Ω), i.e. $R_c = R_{ca}+R_{loss}$, where R_{ca} corresponds to the effective strap radiation (in $0\pi0\pi$ phasing ca.20% of power is lost at 52MHz, up to 30% at 32MHz for typical H mode conditions). Below 50MHz the two inner straps of each array have a lower average R_c than the outer ones. Comprehensive measurements have been carried out on an antenna prototype loaded with absorbing foam, and their analysis is under way. The high characteristic impedance of the 'cross-over' conductors feeding the two inner straps of each array is a source of imbalance; other possible causes are intrinsic dissymmetries between the main conductors, and their enhancement by the tilted Faraday shield elements (Fig.1).

R_c is lowest in dipole ($0\pi0\pi$) and highest in monopole (0000) mode. These variations, inherent to the variable $k_{//}$ spectrum facility, are analyzed below.

2.1 Experimental determination of the antenna scattering matrix S on plasma

S is a 4 by 4 matrix connecting the forward (V_+) and reflected (V_-) complex voltages at the antenna input:

$$V_- = S\,V_+ \qquad (2)$$

It gives a synthetic description of the linear response to arbitrary array excitations (for given plasma and rf frequency). A method has been developed to routinely determine S in a single shot. It relies on programmed phase ramps between the generator voltages, which yield a large number of independent sets of eq.(2) (this only requires a 3 second rf pulse with steady plasma); S results from a linear least-squares fit thereto. The associated impedance matrix is

$$Z = Z_c\,(E+S)\,(E-S)^{-1} \qquad \text{(E: identity matrix)} \quad (3)$$

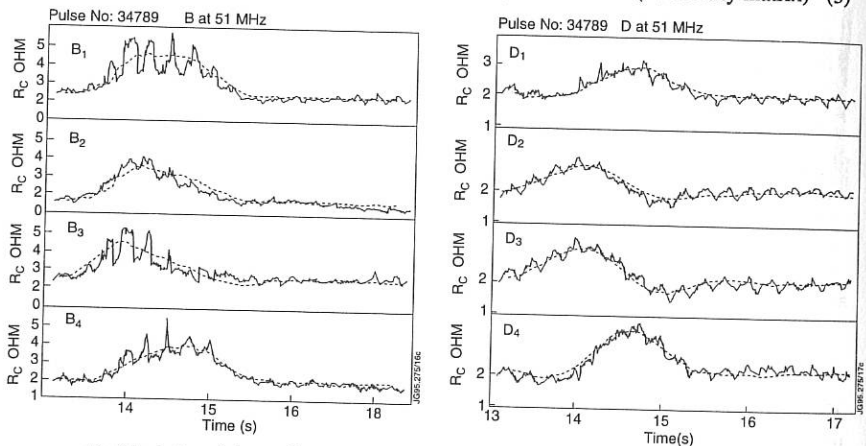


Fig.3 Evolution of the coupling resistances during phase ramps (pulse 34789, antennae B and D at 51MHz). Their estimations based on scattering matrices (dashed lines) show a good fit quality.

two halves of antenna D during the March 1995 shutdown; the following re-assessment of heating efficiency has shown a significant improvement at low $k_{//}$.

4. Spots on a limiter

These spots are observed on a poloidal limiter when the adjacent antenna is active, before and after introduction of the separator, except in $0\pi0\pi$ and $0\pi\pi0$ phasings. Their presence and intensity are correlated with the antenna-plasma distance, and their vertical position with $q_{.95}$. They are possibly linked with radial rf currents.

5. Developing resilience to ELMs

Giant ELMs induce rapid variations in R_c by a factor of 4 or more, hence transient high reflection at the rf generators and frequent trips. Short-term solutions rely on electronic discrimination of ELMs from arcs based on the D_α signal, followed by various actions such as desensitizing the control electronics to suppress generator tripping during the ELM, or restoring the power faster after an ELM-trip than after a normal trip. Long-term rf hardware modifications for broad-band adaptation are also under study; the favourite scenario uses a prematching stub in each line and fast frequency variations to perform adaptation on the ELM timescale. This remedy would also considerably reduce the line losses.

6. Achievements in 1995

The sideband problems linked with the control electronics [4] have been cured by the end of 1994, leading to substantial improvement in the performance and reliability of the ICRF plant (gain of ca.50% in routinely coupled power, routine operation at MTL voltages ~ 30kV). RF-only H modes have been produced under various conditions: at high power (present record 16.5MW in $0\pi\pi0$, 2.5MA/3.5T plasma) with characteristic sawteeth stabilization and production of giant sawteeth; at high plasma current (8MW rf in 4.7MA/3.2T plasma); with a low power threshold (6MW rf in 3MA/2.8T plasma). The record combined auxiliary power of 32MW (15MW RF, 17MW NBI) has been coupled to a divertor plasma during an ELMy H mode. ICRH has also contributed to hot-ion H modes (3MA/3T plasmas). The rf heating efficiency has been improved at low $k_{//}$ after addition of a separator between the two halves of antenna D, but the power is limited by arcs. Newly designed separators will be installed in all modules during the 1995 shutdown.

References

[1] A.Kaye *et al.*, *Fusion Engineering and Design* 24 1 (1994); T.J.Wade *et al.*, *ibid.* p.23.
[2] M.Bures *et al.*, 21st E.P.S. Conference on Controlled Fusion and Plasma Physics (1994)
[3] The JET Team (presented by F.G.Rimini), 15th I.A.E.A. Conf. on Plasma Physics and Controlled Nuclear Fusion Research, Seville (1994)
[4] A.C.C.Sips *et al.*, 36th Ann. Meeting, A.P.S. Div. of Plasma Physics, Minneapolis (1994)
[5] D.F.H.Start *et al.*, 11th Topical Conf. on R.F. Power in Plasmas, Palm Springs (1995)
[6] A.M.Messiaen *et al.*, 3rd Joint Varenna-Grenoble Int. Symp. on Heating in Toroidal Plasmas (1982)

2.2 The main features of the results are summarized as follows

1) Large diagonal elements ($|S_{ii}| > 0.75$), i.e. low average coupling; the coupling imbalance at low frequency is reflected by $|S_{11}|, |S_{44}| < |S_{22}|, |S_{33}|$.

2) The linear regime assumption is adequate at the power levels used in determining S.

3) Models limiting interstrap coupling to first-neighbours $S_{i,i\pm1}$ fairly represent most usual phasings, but give a wrong prediction of R_c in monopole, the only case where wavenumbers $|k_{//}| \leq \omega/c$ have been excited. On the other hand the fits of S using an *a priori* full matrix fairly describe all phasings, with interstrap coupling terms S_{ij} ($i \neq j$) all of the same order of magnitude (consistent with measurements on a foam-loaded antenna in torus). This indicates a peak in the plasma spectral resistance near $k_{//}=0$; moreover the sensitivity of R_c to divertor x-point sweep is strongly enhanced in 0000, 00ππ (Fig.3, $t \approx 14.1$s). These features suggest the presence of global edge or coaxial modes predicted by theory [6].

Table I:
S obtained from pulse 34789 (antenna D at 51MHz, Fig.3) confirms the R_c's observed in neighbour fixed-phased pulses (cf.Fig.4).

$\|S_{ij}\|$				arg S_{ij} (°)			
0.831	0.062	0.049	0.053	-113	81	54	56
0.062	0.842	0.050	0.050	81	-121	58	58
0.049	0.050	0.815	0.084	54	58	-139	72
0.053	0.050	0.084	0.798	56	58	72	-110

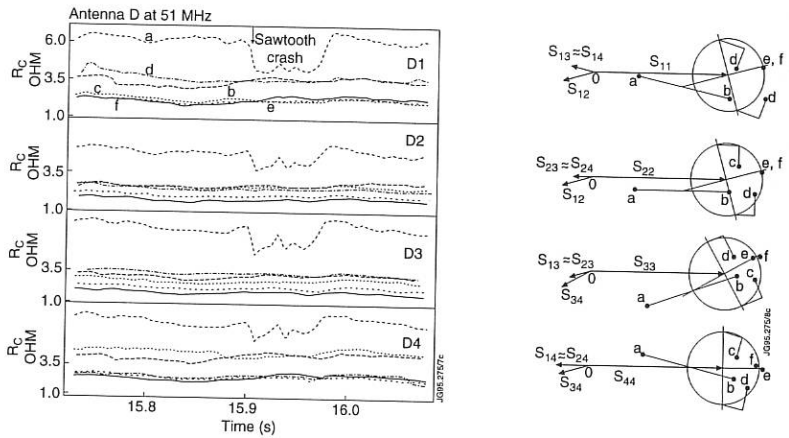


Fig.4 Coupling resistances measured for various excitations of antenna D (left). Complex reflection coefficients obtained from Table I (right, schematic; S_{ii} is taken as phase reference for each strap), showing good agreement (cf.eq.1). The strap phasings are a: 0000; b: 00ππ; c: 0,π/2,π,−π/2; d: 0,-π/2,π,π/2; e: 0π0; f: 0π0π.

3. The heating efficiency is defined as the ratio (change in stored energy) / (change in rf power) at a given phasing. Evaluation on the original A2 antenna using a 1Hz modulation of the rf power shows that this quantity is the highest for large-$k_{//}$ phasings (0ππ0, 0π0π), but at least 5 times smaller in monopole phasing. A vertical separator has been installed between the

Three-Dimensional Antenna Coupling to Core Plasma in Fusion Devices

M.D. Carter, E.F. Jaeger, D.C. Stallings, J.D. Galambos, D.B. Batchelor, C.Y. Wang,
Oak Ridge National Laboratory, Oak Ridge, TN 37831-8071

1. Introduction

A complete understanding of the RF physics from the launcher to the plasma core is required to fully analyze RF experiments and to evaluate the performance of RF antenna designs in ITER. This understanding requires a consistent model for the RF power launching system, propagation and absorption through the edge region, and the response of the core plasma to the RF power. As a first step toward such a model, the three-dimensional (3D) antenna modeling code, RANT3D [1], has been coupled with the reduced order full wave code, PICES [2]. Preliminary results from this model are presented in this paper for parameters similar to those found in the DIII-D [3] experiment.

The RANT3D code solves Maxwell's equations in vacuum for a collection of connected rectangular waveguide sections. The geometry of the antenna box, the septa between straps, and other features of the tokamak first wall are modeled by these waveguide sections. The antenna is driven by a set of prescribed currents [4] on the main current straps. Return currents in the sidewalls and septa are determined by conducting boundary conditions and are calculated self-consistently. The plasma boundary is determined by a generalized impedance matrix [5]. Fig. 1 shows the RANT3D model typically used for the DIII-D antenna.

The PICES code uses a reduced order approximation and a poloidal mode expansion to generate a set of coupled differential equations that are solved by finite differences. The code calculates the current driven by fast waves using the absorbed power in a current drive model by Ehst [6].

Both RANT3D and PICES have been separately benchmarked with experimental data [1,2]. For ICRF current drive experiments, the combined model can be used to generate the launched current drive spectrum in 3D and follow the power into the plasma core. Results from the combined codes are presented for heating and current drive scenarios in the next section.

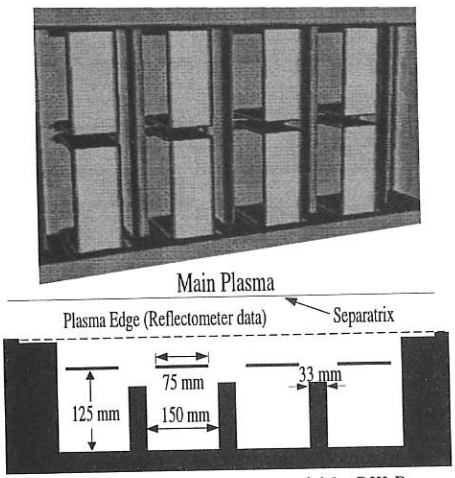


Fig. 1 Typical RANT3D antenna model for DIII-D.

The interface between the two codes is done in two steps. The first step is to perform a RANT3D calculation using a slab code such as PLASMAIMP [7] (cold) or GLOSI [8] (warm) for the plasma response. The second step is to take the tangential electric fields from the RANT3D calculation and use these fields as the outer boundary condition for the PICES code.

In the first step, the PLASMAIMP and GLOSI codes presently assume an outgoing boundary condition near the center of the plasma. This approximation is reasonable if the power reflected directly back to the antenna by the inside wall of the tokamak is small. The coupling of poloidal modes by toroidal effects in the plasma is ignored in the impedance matrix at this point; however, the 3D geometry of the antenna ultimately couples all of the poloidal and toroidal modes in the RANT3D calculation. Both slab codes retain both field polarizations and are periodic in both the toroidal and poloidal directions. The first step produces electric field components tangent to the tokamak first wall that are zero everywhere except in the neighborhood of the antenna opening as shown in Fig. 2.

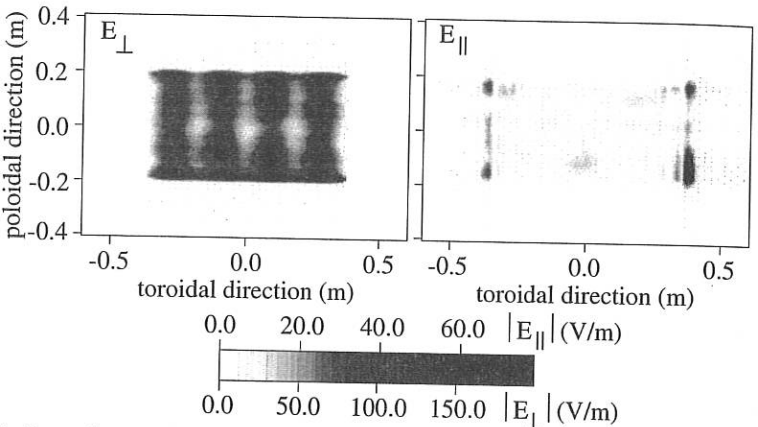


Fig. 2 *Image of tangential electric field components from RANT3D model used as boundary condition for PICES code. 'DIIID-like' parameters were used for this calculation π/2 phase difference between straps. The values marked on the palette correspond to 1 Amp of current driven in each current strap.*

In the second step, the electric field components tangent to the first wall from the RANT3D solution are mapped onto a surface having the same shape as the last closed flux surface given by the VMEC [9] code. The tangential fields on this surface then provide the outer boundary condition for the PICES code.

2. Results

For the model shown in Fig. 1, each of the current strap segments are in phase poloidally and have a phase difference of π/2 toroidally for the current drive modeling. Fig. 2 shows typical values of the modulus of $E_\perp$ and $E_\parallel$ generated by RANT3D for the PICES boundary

using a warm plasma impedance matrix from GLOSI. The tangential electric fields are zero outside the opening of the antenna because of the conducting wall. Thus, only the localized fields in front of the antenna port contribute to the PICES boundary condition. Note the strong localization of the parallel electric field component near the edge and corners of the port.

Fig. 3 shows a poloidal cross-section of the electric fields and absorbed power calculated by PICES using the electric field boundary condition obtained from RANT3D. The localized nature of the electric field boundary condition provided by RANT3D is preserved in PICES.

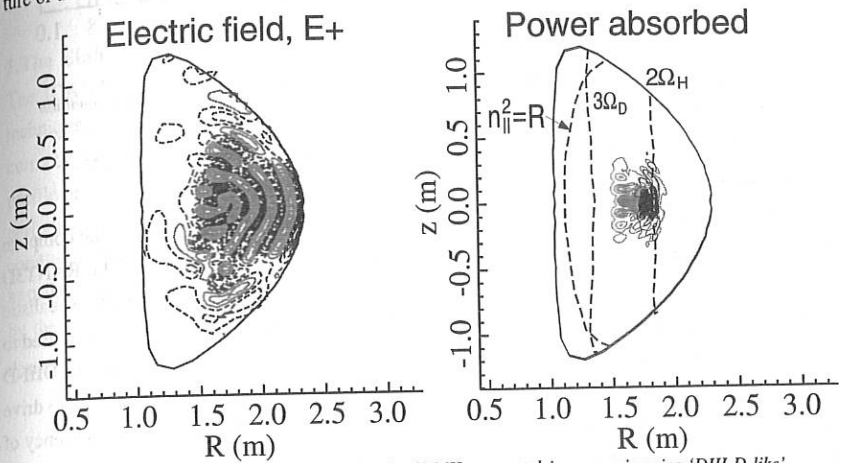


Fig. 3 Electric field and absorbed power for the 60 MHz current drive scenario using 'DIII-D-like' parameters.

A study of the parasitic absorption by the second harmonic hydrogen resonance was made to determine the importance of removing all traces of hydrogen from an experiment. (DIII-D is able to reduce hydrogen concentrations to < 1%.) For the 60 MHz case shown in Fig. 3, the power absorbed by the second harmonic hydrogen resonance is ~50% with 4% hydrogen, but drops to ~30% with 1% hydrogen. Increasing the frequency to 90 MHz reduces the hydrogen absorption to < 10% for a 1% hydrogen concentration.

Fig. 4 shows the driven current caused by fast wave absorption by electrons. A driven current of 60 kA is predicted from the model for 0.8 MW of coupled power at 60 MHz. An additional current of 68 kA is predicted when 0.6 MW of power is added at 90 MHz. The increase in efficiency from γ=0.02 A/(Wm^2) for 60 MHz to γ=0.03 A/(Wm^2) for the 90 MHz scenario is largely due to the reduced cyclotron absorption by the hydrogen impurity. Experimental efforts are underway to determine the accuracy of these modeling results [3].

The first pass absorption for the waves in these scenarios was 14% and 10% for the 60 MHz and 90 MHz cases respectively. The low first pass absorption causes interference patterns that may be responsible for the the depression of the driven current density near the axis in Fig. 4.

Max-Planck-Institut für Plasmaphysik
- Bibliothek -

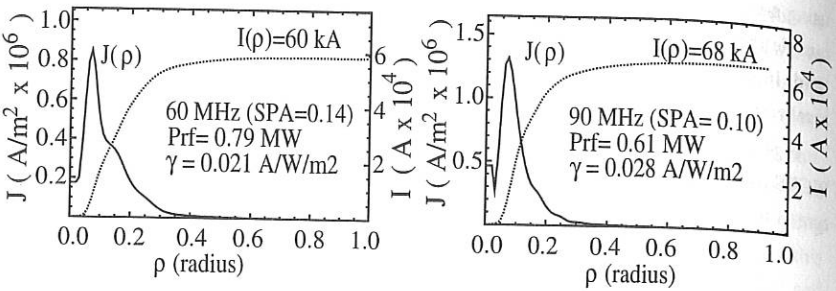


Fig. 4 Deposited current for the 60 MHz and 90 Mhz scenarios from PICES using a boundary condition provided by the RANT3D code.

The reduced current density on axis is caused by a reduced value of $E_{\|}$ near the axis.

3. Summary

The coupling of the RANT3D and PICES codes represents a first step toward the complete modeling of RF power delivery systems from the antenna to the core plasma. The RANT3D code uses a 3D antenna model and information from the plasma edge to provide a realistic 'footprint' of the antenna for input to the full-wave PICES code. The codes have been used to model fast wave current drive for plasma parameters similar to those found in the DIII-D experiment. The results show that both 60 MHz and 90 MHz scenarios should be able to drive current in the 60 to 70 kA range with less that 1 MW of input ICRF power. The efficiency of the 90 MHz current drive scenario can be ~ 50% higher than the 60 MHz scenario because of absorption at the second harmonic resonance of a 1% residual hydrogen species at 60 MHz.

References

[1] Carter, M.D. et al.,'Three-Dimensional Modeling of ICRF Launchers for Fusion Devices,' to be published in *Nucl. Fusion* (1995).

[2] Jaeger, E.F., Batchelor, D.B., Stallings, D.C., *Nucl. Fusion* **33** 179 (1993).

[3] Forest, C.B. et al., 'Experimentally Determined Profiles of Fast Wave Current on DIII-D,' Poster II3, 11th Topical Conference on Radio Frequency Power in Plasmas, AIP Conf. Proc., Palm Springs, CA, May 1995.

[4] Ryan, P.M. et al., 'Integrated Design and Analysis of RF Heating and Current Drive Systems', Invited paper, 11th Topical Conference on Radio Frequency Power in Plasmas, AIP Conf. Proc., Palm Springs, CA, May 1995.

[5] Brambilla, M., *Nucl. Fusion* **28** 549 (1988).

[6] Ehst, D.A., Karney, C.F.F., *Nucl. Fusion* **31** 1933 (1991).

[7] Stallings, et al., Bull. Am. Phys. Soc. **39**(7), 1628 (1994)

[8] Wang, C.Y., Report number ORNL/TM-12923, NTIS, Springfield, VA, http://www.fedworld.gov/ntis/ntishome.html (1995).

[9] Hirshman, S.P., Lee, D.K., Comput. Phys. Commun. **31** 161 (1986).

On a new method to compute RF antenna characteristics

S. Pécoul, S. Heuraux, R. Koch* and G. Leclert.

Laboratoire de Physique des Milieux Ionisés, URA CNRS 835,

Université Henri Poincaré, Nancy I, BP 239, 54506 Vandœuvre Cedex (France)

*Laboratoire de Physique des Plasmas - Laboratorium voor Plasmafysica, Association "Euratom-Etat Belge" - Associatie "Euratom-Belgische Staat",

Ecole Royale Militaire -Koninklijke Militaire School 1040 Brussels (Belgium)

1.The Slab Coupling Model and Implementation of the ICANT code

The ICANT code solves the antenna radiation problem using a finite boundary element technique combined with a spectral solution of the interior problem[1]. That is to say, the current on the antenna is represented as a superposition of finite current elements (with a linear profile or gamma function or Dirac function, for instance) The slab approximation is used and periodicity in y and z directions is introduced to account for toroidal geometry. The boundary conditions between the plasma and the vacuum can be easily related to the spectral surface impedance matrix[1] $\underline{\underline{\xi}}$. That is to say, the Fourier components of the fields at x=-v are related by the expression $(E_y,E_z)= \omega\underline{\underline{\xi}}_s(B_z,B_y)$. The plasma description can, in principle, have any desired degree of sophistication.

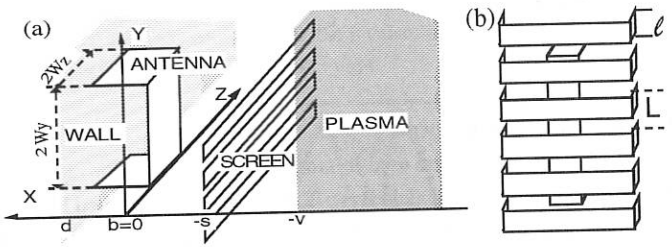


Fig 1: Geometry of the system antenna-plasma (a) and of the discrete screen (b).

We choose a finite element representation of the current $\mathbf{J}=\sum c_i \mathbf{T}_i$ where the finite element current $\mathbf{T}_i$ automatically ensures the current continuity. The current profile is built self consistently by imposing the vanishing of the tangential electric field on the antenna surface as the conditions $\int_{-v}^{d} \mathbf{E}.\mathbf{T}_i \, dx = 0$. This provides the set of equations that determines the unknown c_i's. The i-th equation of this set writes:

$$\sum_j c_j Q_{ij} = \sum_A c_A Q_{iA} \qquad (1)$$

where $Q_{ij} = \sum_{ky,kz} \iint \mathbf{T}_i^* . \mathbb{R} . \mathbf{T}_j \, dx d\rho$ and $\mathbb{R}$ is a tensor defined by Koch et al[1] which combines the contributions of the TE and TM parts of the electric field. $\sum_j$ represents the sum over passive elements (metallic parts of the antenna and surroundings) and $\sum_A$ is the sum over the

active elements (antenna excitation). From the set of c_j which determines the current on the antenna we can obtain the needed parameters to characterise the antenna (radiated power, impedance, electric field,...).

2. Radiation in vacuum of a single antenna facing a metallic wall

The code has been tested[2] for several cases in vacuum for which analytical formulas are available. We present here the additional case of a single antenna facing a metallic wall.

This case is intended to show the effect of spurious coaxial mode resonances which arise when currents profiles are computed self consistently. The radiated power is very small as expected. Furthermore, one notices in figure 1 the occurrence of resonances of the self consistent propagation constant ß. These spurious resonances occur at each zero of $k_y^2+k_z^2-k_0^2$ and are related to the existence of a current J_x perpendicular to the wall. At low-frequency the value of ß is in agreement with the static limit, $ß^2= k_0^2 \frac{s\ (d+v)}{v\ (s+d)}$ as long as the J_x effect is negligible, i.e. d is small .

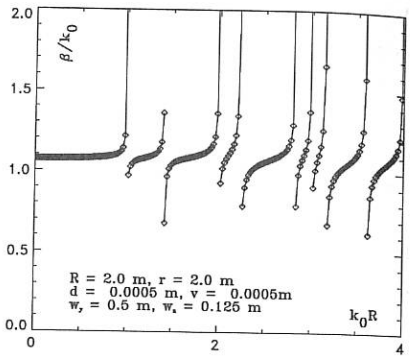


Fig 1 : Self-consistent propagation constant ß(ko)

3. Plasma with magnetosonic wave

In this section, ITER parameters are used in most computations: major radius R= 7.75 m, minor radius r= 2.8 m and magnetic field B_T=6 T. The plasma is modelled by a density step with a surface impedance matrix resulting from the magnetosonic wave dispersion relation, $k_\perp^2 = u(1 - \mu^2)$, $u = \varepsilon_1 - n_z^2$, $\mu = \varepsilon_2/u$, where ε_1 and ε_2 are the xx and xy components of the dielectric tensor. The plasma density n_e ranges from 10^{17} to 2 10^{20} pm^{-3}. The antenna parameters are $2w_y$= 1.12 m, $2w_z$= 0.34 m, d= 0.10 m and v=0.2 m . For the antenna array (2 or 4 straps) the spacing lengths are 0.72 m and 1.20 m, respectively in the z and y directions. The frequency is chosen to avoid the ß resonances. We present results for the following cases:

-1) the single antenna (ß and real power versus n_e, spectral power),

-2) the two-strap case for different phasings (spectral power),

-3) the eigth-strap case with and without septa (spectral power).

In the last case, the strap width, spacing length in the z direction and y direction are respectively 0.16 m, 0.34 m, 1.06 m and the strap length is shorter $2w_y$= 1.0 m .

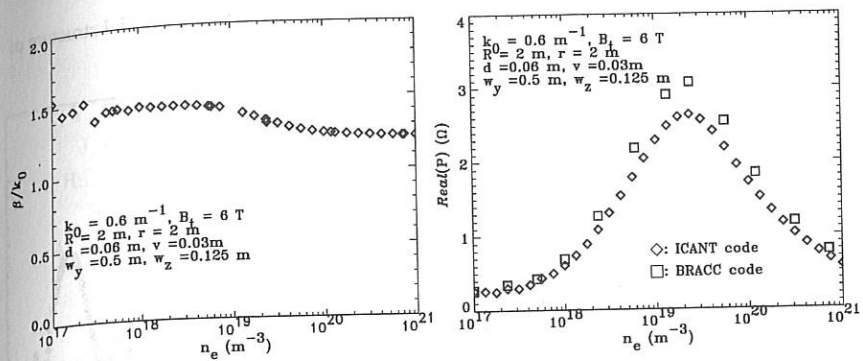


Fig. 2 : Single antenna - a) ß versus density b) Real power versus density

3.1 Single antenna

Figure 2a displays the evolution of the propagation constant ß with the plasma density. As expected, since the impedance matrix for the magnetosonic wave includes an ideal Faraday screen , the low density limit is the vacuum value for this case, $ß^2 = k_0^2 \frac{d+v}{v}$. For the same reason, the above mentioned spurious resonances still occur. In the high density limit, the plasma behaves like a metallic wall, with very little power radiated. Figure 2b gives the real power versus the density, and figure 3 displays the k_z-spectral power for $n_e = 2.\ 10^{20}$ pm^{-3}. Comparison with the BRACC code[3] (with the ß values of ICANT as an input) shows a good agreement within 14%.

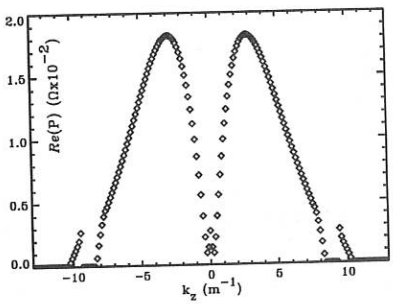


Fig 3 : Single antenna - k_z spectral power for $n_e = 2.\ 10^{20}$ pm^{-3}

3.2 Two-strap antenna

The spectral power radiated by a two-strap antenna is shown in figure 4 for the phasings (0,0) $(0,\pi),(0,\pi/2)$. The k_z spectrum is falling off for those k_z values that are above the cut-off value, $k_z \approx k_o\ \omega_{pi}/\omega_{ci}$. For $\omega \ll \omega_{ci}$, the cut-off is close to the Alfven resonance, $\varepsilon_1 - n_z^2 = 0$. The few propagating modes ($k_x^2 > 0$) lying on the high n_z-side of the resonance produce the small outer

peaks of the spectrum. The main peak positions depend as expected on the spatial structure of the antenna array.

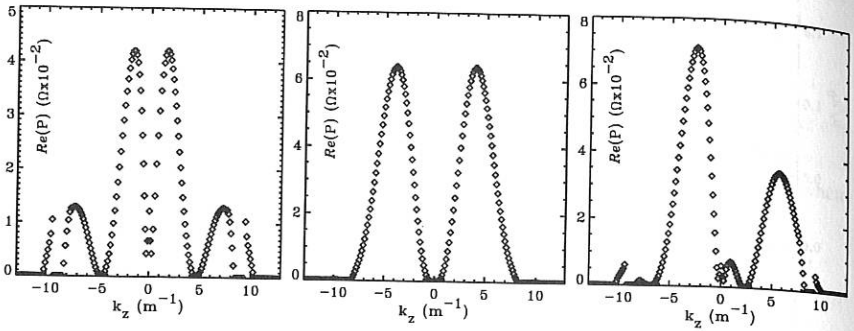


Fig 4 : Two-strap antenna - k_z spectral power for different phasings (0,0) (0,π) and (0,π/2) k_0=0.2 m, B_T=6 T, n_e =2 10^{20}pm^{-3}, R=7.75m, r=2.8m, d=0.35m, s=0.05m, v=0.1m, w_y=0.56m, w_z=0.17m.

3.3 Eight-strap antenna with and without septa.

Figure 5 illustrates the influence of septum bars on the spectral power radiated by an ITER-like 8-strap antenna. For the phasing shown (3π/2, π, π/2, 0) the currents induced in the septa decrease the power by a factor of about 4. For an in-phase antenna, we find a decrease of a factor of 9. This kind of behavior has been found for other antenna systems[4].

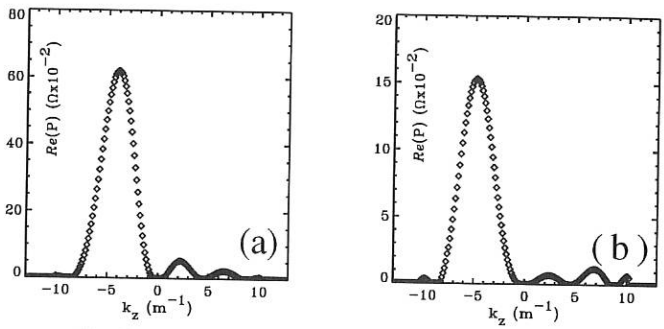


Fig. 5 : 8-strap antenna without (a) and with (b) septa

References

[1] Koch R, Bhatanagar VP, Messiaen AM and van Eeester D,*Comp.Phys.Com.* **40** 1 (1986).

[2] Pécoul S, Heuraux S, Koch R and Leclert G, in *Proc. Heating in toroidal plasmas*, Palm Springs (1995) to be published.

[3] LLP-ERM/KMS Reports n°84 Brussels (1987) "Extension and illustration of ICRH evaluation codes installed at JET".

[4] Saigusa M, Yamamoto T,Petty CC, Yoshioka K, Kazumi H, Kawashima H, Fujii T, Kimura H, Miura Y and Tamai H, *Nucl. Fus.* **33** 421 (1993)

ICRF Heating and Enhanced Confinement Modes in Alcator C-Mod*

Y. Takase, R. Boivin, F. Bombarda,† P. Bonoli, C. Fiore, D. Garnier, J. Goetz, S. Golovato, M. Graf, R. Granetz, M. Greenwald, S. Horne, A. Hubbard, I. Hutchinson, J. Irby, H. Kimura,‡ B. LaBombard, B. Lipschultz, R. Majeski,# E. Marmar, M. May,** A. Mazurenko, G. McCracken, A. Niemczewski, P. O'Shea, R. Pinsker,†† M. Porkolab, J. Reardon, J. Rice, C. Rost, J. Snipes, J. Terry, R. Watterson, B. Welch,‡‡ S. Wolfe

MIT Plasma Fusion Center, Cambridge, MA 02139 U.S.A.

1. Introduction

Alcator C-Mod ($R = 0.67\,\mathrm{m}$, $a = 0.22\,\mathrm{m}$, $\kappa = 1.7$ typical) is a compact high field tokamak with all metallic (mostly molybdenum) plasma facing components. Presently, two transmitters at a frequency of 80 MHz, each capable of 2 MW output, are operational. C-Mod has operated successfully up to a toroidal field of 8.0 T and a plasma current of 1.2 MA, and up to 3.5 MW of RF power has been coupled into the plasma using two dipole antennas (two current straps driven out of phase). The main heating scenario employed thus far has been H minority heating in D majority plasmas at 5.3 T. Other scenarios investigated include ^{3}He minority heating in D majority at 8.0 T, second harmonic H minority heating in D majority at 2.6 T, and mode conversion electron heating in H-^{3}He plasmas at 6.5 T. Second harmonic ^{3}He minority heating in D majority plasmas at 4.0 T was not successful. H-mode is routinely observed, and P-mode is observed in combination with lithium pellet injection.

2. L-Mode

D(H) heating of L-mode plasmas was performed in the parameter range $B_T(0) = 3.5 - 5.5\,\mathrm{T}$, $I_p = 0.4 - 1.2\,\mathrm{MA}$, $\overline{n}_e = (0.5 - 3) \times 10^{20}\,\mathrm{m}^{-3}$ (target), and $n_H/n_{H+D} = 0.01 - 0.2$. At high RF powers it was necessary to reverse the direction of the ion ∇B drift direction (away from the X-point) to prevent the plasma from going into H-mode.

Central temperatures of $T_{e0} = 5.8\,\mathrm{keV}$ (top of sawtooth) and $T_{i0} = 4.0\,\mathrm{keV}$ (sawtooth averaged) were obtained at $\overline{n}_e = 1 \times 10^{20}\,\mathrm{m}^{-3}$ with $P_{RF} = 3.5\,\mathrm{MW}$. Heating is most effective at low H concentrations ($n_H/n_e < 0.05$). Degradation of heating at

* Supported by U.S. D.O.E. Contract No. DE-AC02-78ET51013.

† Associazione EURATOM-ENEA sulla Fusione, Frascati 00044 Italy
‡ Japan Atomic Energy Research Institute, Naka, Ibaraki, Japan
Princeton University Plasma Physics Laboratory, Princeton, NJ, U.S.A.
** Department of Physics, The John Hopkins University, Baltimore, MD, U.S.A.
†† General Atomics, San Diego, CA, U.S.A.
‡‡ Institute for Plasma Research, University of Maryland, College Park, MD, U.S.A.

higher H concentrations is more pronounced at higher electron densities. Heating degrades gradually as the resonance layer is moved off-axis by reducing the toroidal field, with no heating observed when the resonance layer is moved out to $r/a \geq 0.75$.

For on-axis D(H) heating the absorption efficiency, estimated from the discontinuity of slope in the diamagnetic stored energy, was very high (80–100%). The plasma current and input power dependences of energy confinement are roughly consistent with the ITER89-P scaling, as shown in Fig. 1. However, there is an indication of gradual degradation of confinement at higher densities, as well as at very low densities ($\overline{n}_e < 1 \times 10^{20}\,\mathrm{m}^{-3}$).

3. H-Mode

ICRF heated H-mode is routinely observed in C-Mod. Almost all high power ($\gtrsim 2\,\mathrm{MW}$) RF heated discharges make the transition into H-mode, even with the outer gap (separatrix to outboard limiter distance) as small as 1 cm. No special wall conditioning is required to obtain the H-mode.

The H-mode power threshold (with the ion ∇B drift directed toward the lower single-null X-point) scales similarly to the ITER scaling $P/S(\mathrm{MW/m^2}) = 0.044\,\overline{n}_e B_T$ ($10^{20}\,\mathrm{m}^{-3}\,\mathrm{T}$) [1], but H-mode transitions well below this threshold (by up to a factor of 2) are often observed, as shown in Fig. 2. The peaked density profile after Li pellet injection seems to be beneficial for accessing the H-mode. We note here that the values of P/S and $\overline{n}_e B_T$ achieved in C-Mod are an order of magnitude greater than those achieved in ASDEX-UG, DIII-D, and JET, and are comparable to or greater than what is expected for ITER. H-mode was not observed when the ion ∇B drift was away from the X-point, indicating that the H-mode power threshold in this case is higher by at least a factor of 2. H-mode was observed up to a target density of $\overline{n}_e = 2.6 \times 10^{20}\,\mathrm{m}^{-3}$ ($\overline{n}_e = 3.2 \times 10^{20}\,\mathrm{m}^{-3}$ during the density decay after Li pellet injection). However, H-mode has not been observed below a low density limit of $\overline{n}_e \simeq 1 \times 10^{20}\,\mathrm{m}^{-3}$.

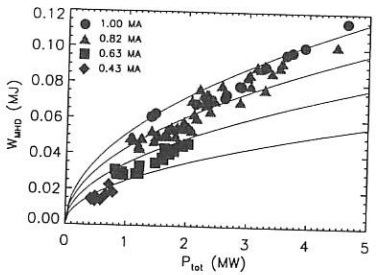


Fig. 1: L-mode confinement. Solid lines represent the ITER89-P scaling.

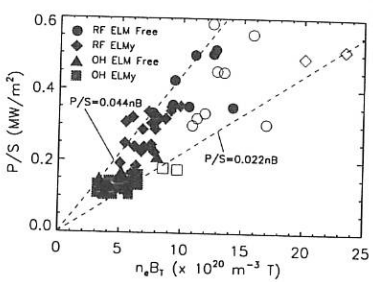


Fig. 2: H-mode threshold. Open symbols indicate plasmas with Li pellet injection.

An H-factor (energy confinement enhancement over the ITER89-P L-mode scaling

[2]) for ICRF heated ELM-free H-modes of up to 1.5 has been observed. For our parameters, ITER94 ELM-free H-mode scaling [3] predicts 1.6 – 1.8 for the H-factor. In ohmic ELM-free H-modes at $B_T = 3.5\,\mathrm{T}$, H-factors of up to 2 have been observed [4].

4. P-Mode (PEP Mode)

Li pellet (1.2×10^{20} electrons) injection followed by central ICRF heating produces the PEP mode [5]. These plasmas are characterized by highly peaked density and ion temperature profiles, resulting in an enhanced fusion rate, typically by an order of magnitude over similar L-mode discharges. The PEP mode is observed over a wide range of target densities ($\overline{n}_e = 1.0 - 2.5\times10^{20}\,\mathrm{m}^{-3}$), but only when the pellet penetrates to the plasma center.

In the 7.9 T, 1 MA discharge (^{3}He minority heating) shown in Fig. 3 a fusion neutron rate of $9\times10^{13}\,\mathrm{sec}^{-1}$, $T_{i0} = 3.7\,\mathrm{keV}$, and $T_{e0} = 3.0\,\mathrm{keV}$ were obtained at $\overline{n}_e = 2.9\times10^{20}\,\mathrm{m}^{-3}$ with $P_{RF} = 2.5\,\mathrm{MW}$. In this example a transition into ELMy H-mode occurred at 0.828 sec and a transition into ELM-free H-mode occurred at 0.845 sec, but the neutron rate starts to decline after 0.830 sec. Simultaneous PEP and H-modes have also been observed. The cause of PEP mode termination is not well understood. It is sometimes, but not always, accompanied by enhanced MHD activity. It appears to be related to the loss of the peaked density profile. The neutron rate starts to decline when the density peak-to-average ratio $n_{e0}/\overline{n}_e$ falls below a critical level of approximately 1.5.

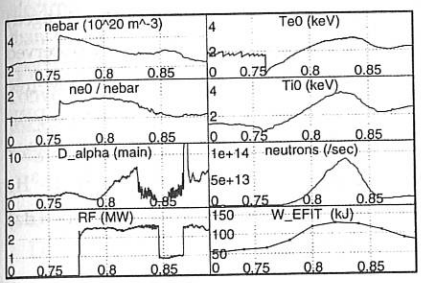


Fig. 3: D(^{3}He) PEP mode at $B_T = 7.9\,\mathrm{T}$ and $I_p = 1\,\mathrm{MA}$.

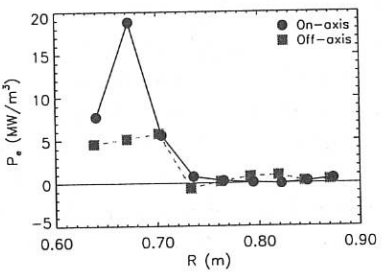


Fig. 4: Power deposition profiles for on-axis and off-axis mode conversion electron heating.

5. Mode Conversion Electron Heating

Highly localized direct electron heating using the mode converted ion Bernstein wave (IBW) [6] was observed in H-^{3}He plasmas at 6.5 T. H-^{3}He plasmas are analogous to D-T plasmas, because $\Omega_H/\Omega_{^3He} = \Omega_D/\Omega_T$. At this field, the H resonance is at $R = 0.82\,\mathrm{m}$ and the ^{3}He resonance is at $R = 0.55\,\mathrm{m}$, both more than half way out radially from the plasma center. Mode conversion to IBW occurs near the ion-ion hybrid layer, which shifts toward the high field side as the ^{3}He concentration is decreased or

the toroidal field is reduced. The IBW is strongly damped near the mode conversion layer. Effective central electron heating is observed with $n_{^3He}/n_e \simeq 0.25$ when the mode conversion occurs near the plasma center.

An electron heating power density (determined from the sawtooth reheat rate) of $25\,\mathrm{MW/m^3}$ was obtained with $P_{RF} = 1.4\,\mathrm{MW}$, an order of magnitude larger than the ohmic value with $P_{OH} = 1.1\,\mathrm{MW}$. The central electron temperature increased to 5.1 keV from an ohmic value of 2.3 keV [7]. The RF power deposition profile can be determined from the break of slope of the electron temperature at RF power steps. When the power deposition is inside the sawtooth inversion radius the RF power deposition can be determined from the difference in the sawtooth reheat rate between RF heated and ohmic phases. When both measurements are available, the two methods yield the same result. The RF power deposition profiles for on-axis and (near center) off-axis heating are shown in Fig. 4. For on-axis heating, the heating profile was highly peaked with a FWHM of 5 cm, compared to a typical FWHM of 13 cm for H minority heating.

6. CONCLUSIONS

Efficient ICRF heating of high density ($\overline{n}_e \lesssim 3 \times 10^{20}\,\mathrm{m^{-3}}$) plasmas was obtained in Alcator C-Mod at ITER relevant power densities ($P/S \lesssim 0.6\,\mathrm{MW/m^2}$). For on-axis D(H) heating at 5.3 T near complete absorption is achieved. The energy confinement in L-mode plasmas was found to be consistent with the ITER89-P scaling. Central temperatures of $T_{e0} = 5.8\,\mathrm{keV}$ (top of sawtooth) and $T_{i0} = 4.0\,\mathrm{keV}$ (sawtooth averaged) were obtained in an L-mode plasma at $\overline{n}_e = 1 \times 10^{20}\,\mathrm{m^{-3}}$. H-mode is routinely observed with ICRF heating. The highest stored energy of 130 kJ was achieved in an ELM-free H-mode plasma. The highest fusion reactivity of $9 \times 10^{13}\,\mathrm{sec^{-1}}$ was obtained in a PEP mode plasma with Li pellet injection and on-axis ICRF heating. At $B_T = 6.5\,\mathrm{T}$ highly localized direct electron heating by the mode converted IBW was observed in H-^{3}He plasmas. The near term plans call for the addition of 4 MW of tunable (40–80 MHz) power and a FWCD antenna in collaboration with PPPL.

REFERENCES

[1] F. Ryter, et al., Proc. 20th EPS Conf. on Cont. Fusion and Plasma Physics, 1993 (Lisboa), Vol. 17C, Part I, I-23.

[2] P.G. Yushmanov, et al., Nucl. Fusion **30**, 1999 (1990).

[3] K. Thomsen, et al., Nucl. Fusion **34**, 131 (1994).

[4] J. Snipes, et al., Nucl. Fusion **34**, 1039 (1994).

[5] B. Tubbing, et al., Nucl. Fusion **31**, 389 (1991).

[6] R. Majeski, et al., Phys. Rev. Lett. **73**, 2204 (1994).

[7] Y. Takase, et al., to be published in Radio Frequency Power in Plasmas (Proc. 11th Top. Conf., Palm Springs, CA, 1995), AIP, New York.

ON THE LOWER HYBRID CURRENT DRIVE IN HL-1 TOKAMAK

Yudong Pan Siwen Xue Xiaodong Li Yunwen Qin and Lin Huang
Southwestern Institute of Physics,P.O.Box 432,Chengdu,610041,P.R.China

1. INTRODUCTION

In the first part, a method has been proposed to describe macroscopic parameters in a tokamak during lower hybrid current drive (LHCD) by a system of two-dimensional Fokker-Planck equation (with electric field) in velocity space and tokamak circuit equations. The two-dimensional F-P equation is solved to obtain RF driven current which is then substituted into the circuit equations, and the circulation condition for solving circuit equations is that the DC electric field in F-P equation is equal to the induced electric field of secondary circuit (plasma).The preliminary simulation results of LHCD experiments in HL-1 are given.

In the second part, a simple simulation model was used to analyze the LHCD experiments and the possible ways of improving LHCD efficiency were put forward. For some small or medium-sized tokamaks, the electron temperature is usually about 1keV and, on this condition, the LHCD efficiency can be enhanced in large quantity with increasing electron temperature because much of LHW power is absorbed by electron-ion collision in the periphery of plasma if the electron temperature is lower than 1keV. Another way of improving LHCD efficiency is to drive current by using a spectrum with large poloidal mode number(m). Such a spectrum can be launched with conventional antenna as long as the grill turns a definite angle about its axis. For HL-1 tokamak with Te(0)=1keV, the calculated LHCD efficiency when m=100 is twice as much as that when m=0.

2. INTERACTION BETWEEN THE PRIMARY AND SECONDARY CIRCUITS DURING LHCD (By Yudong Pan,Yunwen Qin and Lin Huang)

A two-dimensional kinetic equation for the electron distribution function with velocities higher than the thermal velocity is determined by the following equations[1]:

$$\frac{\partial f}{\partial \tau} - E\frac{\partial f}{\partial w} = \frac{\partial}{\partial w} D \frac{\partial f}{\partial w} + C(f) \quad , \tag{1}$$

$$C(f) = \sum_{\beta(e,i)} C_\beta(f) \quad , \quad C_\beta(f) = \frac{z_\beta}{x^2}\left\{\frac{\partial}{\partial x}\left[\frac{\xi_\beta^2 a_\beta}{2x}\frac{\partial f}{\partial x} + \frac{m_e}{m_\beta}a_\beta\right] + \frac{c_\beta}{\xi_\beta \sin\theta}\frac{\partial}{\partial\theta}\sin\theta\frac{\partial f}{\partial\theta}\right\} \quad , \tag{2}$$

$$a_\beta = a_\beta(x) = \frac{4}{\sqrt{\pi}}\int_0^{x/\xi_\beta} e^{-s^2} s^2 ds \quad , \quad c_\beta = \frac{1}{\sqrt{\pi}}\{e^{-x^2/\xi_\beta^2} + (\frac{2\xi_\beta}{x} - \frac{\xi_\beta^3}{x^3})\frac{\sqrt{\pi}}{4}a_\beta\} \quad , \tag{3}$$

where, $C(f)$ is coulomb collisions of electrons with each other and with all species of ions, $x = V/V_T$, $w = V_{//}/V_T$, $\cos\theta = V_{//}/V$, $V_T \equiv \sqrt{2T/m_e}$, $\xi_\beta = V_\beta/V_T$, $\tau = \nu t, \nu$ is

electron coulomb collision frequency, E is the DC electric field in unit of $E_{Dr}/2 = m_e V_T v/e$, D is the diffusion coefficient, assuming

$$D(w) = \begin{cases} D & w_1 \le w \le w_2 \\ 0 & w < w_1, \quad w > w_2 \end{cases} . \tag{4}$$

For a equivalent circuit with LHCD operations(Fig.1),the set of equations is as follows:

$$rI_{OH} + L\,dI_{OH}/dt + NMd\,(I_{OH} - Ip/N)/dt = V_e \quad , \tag{5}$$

$$Rp\,(Ip - I_{rf}) + Lp\,dIp/dt = M\,d(I_{OH} - Ip/N)/dt \quad , \tag{6}$$

$$V_d - R_p(Ip - I_{rf}) = V_{rf} \quad , \tag{7}$$

where, most signs are known besides that V_{rf} is the equivalent LHCD voltage and V_d is the equivalent voltage describing the collisional dissipation of RF driven current[2]. (note that a similar equivalent circuit has been used in Ref.[3]). The circulation condition for solving this set equations is that (R is the plasma major radius),

$$R_p(Ip - I_{rf}) = 2\pi RE \quad . \tag{8}$$

The parameters used for these simulations are listed in Table 1. The simulation results are compared with experimental data of HL-1 LHCD in Table 2 and Fig.2 (The latter is the results for the discharge with a bank of capacitors).

The power flow equations derived from the set of equations (5)-(7) have the form:

$$rI_{OH}^2 + LI_{OH}\frac{dI_{OH}}{dt} + NMI_{OH}\frac{d}{dt}(I_{OH} - Ip/N) = P_e \quad , \tag{9}$$

$$Rp\,(Ip - I_{rf})^2 + LpIp\frac{dIp}{dt} - MIp\frac{d(I_{OH} - Ip/N)}{dt} = P_{el} \quad , \tag{10}$$

where $P_{el} = P_{rf} - V_d I_{rf}$ is the electrical power transformed from a part of RF power P_{rf}. If $MIp\,d(I_{OH} - Ip/N)/dt \cong NMI_{OH}\,d(I_{OH} - Ip/N)/dt \le 0$ and $dIp/dt \ge 0$, we can define the recharge efficiency definitely,

$$\varepsilon = MIp\left|d(I_{OH} - Ip/N)/dt\right| / P_{rf} \tag{11}$$

The expected HL-1 typical recharge efficiency is shown in Fig.3.

3. THE POSSIBLE WAYS OF IMPROVING THE LHCD EFFICIENCY OF SMALL OR MEDIUM-SIZED TOKAMAK(by Siwen Xue and Xiaodong Li)

In the present stage, the LHCD efficiency of large tokamaks is much higher than that of small or medium-sized tokamaks. What is the reason? This part of the paper is to discuss how to improve the LHCD efficiency of small or medium-sized tokamaks.

In current drive phase($n_{//} \leqslant 3$), the power of LHW is absorbed mainly by electron landau damping and electron-ion collision and only the power absorbed by electron landau damping can drive current. The condition for landau damping absorption is that $n_{//}\sqrt{Te}$ is at least larger than 5. Therefore, the power of LHW can be absorbed efficiently only when $n_{//}$ is upshifted to a larger value on condition that the Te is lower. Multi-pass ray tracing is responsible for upshift of $n_{//}$ from its original value. But the lower the Te, the larger value the $n_{//}$ must be upshifted to and thus the number that the

rays need to be reflected at plasma edge increases and more power of LHW is absorbed by electron-ion collision in the perephery of plasma.

The same ray tracing model(including shafranov shift) as Bonoli's[4] is adopted. For avoiding complicated numerical calculation, the well-known current drive efficiency formula:

$$\frac{n_e R \Delta I_{rf}}{\Delta P} = \frac{31}{\log \Lambda} \times \frac{4}{5 + Z_{eff}} \times \frac{1}{< n_{//}^2 >} \tag{12}$$

is used to obtain the RF current profile. The method is that the power Δ P absorbed by electron landau damping at a point of ray tracing is changed into the current through above formula. In calculation, only electron landau damping and electron-ion collision absorption are taken into account and the spectrum is chosen as $P(n_{//}) \propto P_T \exp[-(n_{//} - n_{//P})^2 / \Delta n_{//}^2]$, where the $\Delta n_{//}$ is half width of spectrum and the spectrum is divided into 20 rays with different initial $n_{//}$. For HL-1 tokamak parameters, the change of LHCD efficiency with electron temperature is given in table 3 (where the Pei is the power absorbed by electron-ion collision and P_T is the power absorbed by plasma, $\eta = n_e(10^{13} cm^{-3}) R(m) I_{rf}(kA) / P(kW)$ and assuming $\bar{n}_e = 1.0 \times 10^{13} cm^{-3}$). Computations show that when Te(0)=0.75keV the power of LHW is absorbed completely after the ray takes three time reflection at plasma edge while one time reflection is enough for absorption of LHW when Te(0)=1.75keV. For HL-1 tokamak(Te(0)=0.7-1keV), the experimental LHCD efficiency is about 0.3-0.5 and this is in agreement with calculated LHCD efficiency.

Along with the ray tracing, $n_{//}$ is upshifted by means of increasing the poloidal mode number(m). If the grill can launch a spectrum with a large m, the number of times that the ray needs to be reflected at plasma edge(for upshifting $n_{//}$) decreases. With one(or two at most) time reflection of ray at plasma edge, the power of LHW can be absorbed completely. Therefore, the absorption of election-ion collision decreases and the LHCD efficiency enhances. For HL-1 tokamaks (Te(0)=1keV), the calculated LHCD efficiency when m=100 is twice as much as that when m=0.

For small or medium-sized tokamaks, it is difficult to rise the electron temperature. Therefore, driving current with the spectrum with a large m is a effective way of improving LHCD efficiency. The spectrum with a large m may be launched with conventional grill antenna as long as the grill turns a definite angle about its axis. Thus the electrical field at grill mouth has a quantity of poloidal direction. On this condition, part of the LHW power may be coupled to fast wave. The coupling calculation is underway.

REFERENCES

[1] Yu.N.Dnestrovskij, et al.,Nucl. Fusion **28**(1988) 267.

[2] F.C.Jobs,et al., in Tokamak Start-up, Edited by Heinz Knoepfel, Plenum Press, New York and London,1986, p.203.

[3] O.Mitarai and A.Hirose, Nucl. Fusion **24**(1984) 481.

[4] Bonoli P. T. and Englade R.C., Phys. Fluids **29**(1986) 2937.

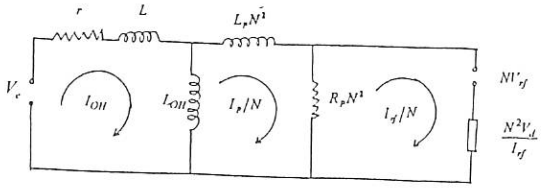


Fig1 Model equivalent circuit for LHCD operations

Table 1 HL-1 Parameters

Plasma major radius R	1.02m
Plasma minor radius a	0.20m
Turn number of the OH coil N	64
Primary external inductance L	80μH
Primary coil inductance L_{OH}	80mH
Primary external resistance r	2.7mΩ
Mutual inductance M	1.25mH
Plasma inductance Lp	1.2μH

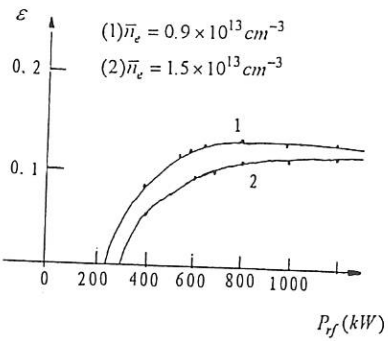


Fig3 The average recharge efficiency ε versus RF power P_{rf} (Ip=90kA, Te=1.3keV, Zeff=1.5).

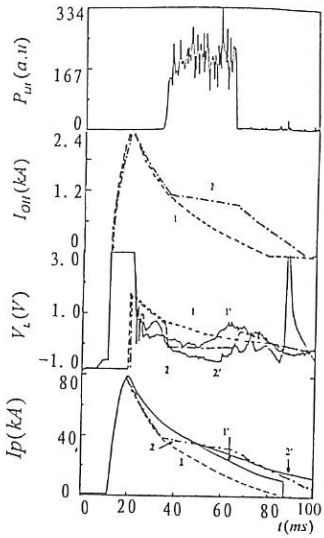


Fig2 Comparison between simulation (dotted line) and experimental data(solide line) of HL-1 LHCD(11547#): 1,1′ without RF current drive; 2,2′ with RF current drive.

Table 2 Comparison Between Simulation Results and Experimental Data of HL-1 LHCD

shot number	$\bar{n}_e$ ($10^{13}cm^{-3}$)	I_P (kA)	Te (ev)	Z_{eff}	D	(w_1, w_2)	P_{rf} (kA)	$(t_{on}, t_{off})^*$ (ms)	I_{rf}^{exp} (kA)	I_{rf}^{th} (kA)
11702	0.90	111	1000	1.5	1.27	(3, 5)	94	(250, 350)	27.8	23.0
11767	1.65	82	1000	1.5	0.87	(3, 5)	112	(300, 400)	8.2	14.1
11801	1.13	88	1000	1.5	1.57	(3, 5)	93	(300, 400)	23.4	29.8

* RF duration

Table 3 The Change of LHCD Efficiency vs. Electron Temperature

Te(0)(keV)	0.75	1.0	1.25	1.5	1.75
P_{ei}/P_T	55%	32%	23%	14%	11%
η	0.33	0.56	0.67	0.83	0.93

Momentum and Energy Exchange between LH Waves and MeV Alpha Particles

J.A. Heikkinen[1] and S.K. Sipilä[2]

[1]VTT Energy, EURATOM–TEKES Association, P.O. Box 1604,
FIN–02044 VTT, Finland
[2]Helsinki University of Technology, FIN–02150 Espoo, Finland

Abstract
The energy and momentum transfer between fusion-born α particles and lower hybrid (LH) waves in a tokamak are studied using a Monte Carlo method. A bipolar current density profile is obtained, arising from the radial diffusion associated with the wave-α interaction. The power transfer behind the obtained current density profile is seen to differ from that related to other bipolar current generation mechanisms, where wave energy is required in momentum generation irrespective of the current polarity.

1. Introduction

In radiofrequency heating and current drive of tokamak plasmas increasing interest has been recently devoted to the interaction of fusion born α particles or other fast ions with the rf waves. The analysis of the wave–α interaction is based on the diffusion equation in one dimension [1], which describes the wave–α interaction by diffusion along the diffusion paths $\epsilon + x =$ constant, where ϵ and x are the perpendicular energy and location of the particle, respectively. In describing the diffusion, a Fokker–Planck diffusion coefficient [2] is valid for sufficiently large wave angular frequency and perpendicular wavenumber.

The large poloidal wavenumber required for an effective power transfer from particles to the wave can accompany a large parallel wavenumber due to the finite poloidal magnetic field of the tokamak. Thus, the wave–α interaction scheme can contain significant momentum generation in the direction of the magnetic field. The momentum generation mechanism presented in Ref. [3] for a homogeneous plasma is combined with the radial and energy diffusion of the particles [1] associated with the wave-α interaction in a toroidal geometry [4], and a Monte Carlo approach [5] is utilized in the study of energy transfer and momentum generation.

It is found that significant current can exist for the established system, and it is shown how the current profile and direction depend on the direction of the poloidal wavenumber. Complete simulations in an ITER–sized tokamak in the presence of a fusion-born α particle source and a diffuse wave intensity distribution are presented.

2. Toroidal Monte Carlo model of the wave–particle interaction

In a toroidal axisymmetric geometry, the relation

$$dv_\phi = (k_\phi/m\omega)dW_\perp + (qB_\theta/m)d\rho \tag{1}$$

is found from the wave–α interaction Hamiltonian [4] by approximating the resonance condition as $\omega = n\Omega_\alpha$ for large wave frequencies $\omega \gg \Omega_\alpha$ and neglecting variations in the gyrofrequency Ω_α and major radius R. Here, ϕ and θ denote the toroidal and poloidal directions, respectively, ρ is the radial coordinate, and $W_\perp = mv_\perp^2/2$ is the perpendicular kinetic energy. The α particle mass and velocity are m and v, respectively, and B is the magnetic field. Assuming $k_\phi = 0$, Eq. (1) yields $dv_\phi = (k_\eta/m\omega)(B_\theta/B)dW$, where $k_\eta = k_\theta B_\phi/B - k_\phi B_\theta/B$ is the perpendicular component of the wavenumber projected on the magnetic surface and $dW = (m\omega\Omega_\alpha/k_\eta)d\rho$. The local coordinate system ρ, η, z has been defined where z is in the direction of the magnetic field vector and η is the coordinate perpendicular to the magnetic field on the magnetic surface. The particle experiences a positive shift in v_ϕ for either negative k_η (for positive B_θ/B_ϕ), when W reduces due to the particle transport to larger ρ, or for positive k_η, when W increases due to the particle transport to smaller ρ. This shift occurs for all particles irrespective of their toroidal velocity. Assuming that r_{gc}/R, $k_\phi v_\parallel/\omega$, and B_θ/B are small quantities, one obtains

$$dv_\parallel = k_\parallel dW_\perp/m\omega \tag{2}$$

with $k_\parallel \equiv k_z = k_\theta B_\theta/B + k_\phi B_\phi/B$, which agrees with the quasilinear model [3] derived in local velocity space for a uniform configuration space in the presence of a wave with finite $k_\parallel$.

The equivalent Monte Carlo operators [5]

$$\Delta W_\perp = (1/s)[\partial/\partial W_\perp - (k_\eta/m\omega\Omega)\beta(\partial/\partial\rho)](sD)\Delta t \pm \sqrt{2D\Delta t}, \tag{3}$$

$$\Delta\rho = -\Delta W_\perp(k_\eta/m\omega\Omega)\beta, \tag{4}$$

$$\Delta v_\parallel = (k_\chi/m\omega)[1 + (B_\theta/B_\phi)(k_\eta/k_\chi)]\Delta W_\perp \tag{5}$$

are obtained for the changes of α particle perpendicular energy, magnetic surface coordinate, and parallel component of the velocity with respect to the magnetic field during the time step Δt. Here, $\beta = (1 + k_\chi v_\parallel/\omega)/[(k_\eta v_\parallel/\omega)(B_\theta/B_\phi) - 1]$ and $k_\chi = k_\phi B_\phi/B$. $s(\rho)$ is the area of the magnetic surface at ρ. The diffusion coefficient D is given in unnormalized units as $(1/2|k_\eta|)(\omega/k_\eta)^2(2eE_\eta)^2/\sqrt{v_\perp^2 - \omega^2/k_\eta^2}$.

As is already clear from Eq. (1), the operators for $\Delta v_\parallel$ and $\Delta\rho$ are directly proportional to $\Delta W_\perp$. In writing Eq. (3), D has been assumed not to depend on $v_\parallel$, which similarly to the other assumptions is valid if $\omega \gg \Omega_\alpha$, $|k_\chi v_\parallel|/\omega \ll 1$, and $|\Delta v_\parallel| \ll |\Delta v_\perp|$. The time step in the operators has to be chosen small enough so that $\sqrt{2D\Delta t}/W_\perp \ll 1$ in order to ensure sufficiently accurate statistics.

In order to properly account for the wave–α interaction close to $\epsilon = \epsilon_w$, all the test particles are made to be reflected along the diffusion path by the wave boundary $v_\perp = \omega/|k_\eta|$, which is the Monte Carlo interpretation of the fact that the particles cannot leave the wave region because of the wave forces acting upon them. It has been shown earlier that special absorbing boundary conditions are required for wave amplification [5,6,7].

3. Reactor Simulations

The parameters $R = 7.75$ m, $a = 2.8$ m, $B = 6.157$ T, $I = 15$ MA, $T_{i,e} = 20$ keV,

$n_e = 0.84 \times 10^{20}$ m^{-3} are chosen for the major radius, minor radius, magnetic field, plasma current, ion (i) and electron (e) temperature, and plasma electron density, respectively. An elongation $\kappa = 1.68$ for the cross section with a parabolic current profile and equal deuterium and tritium concentrations with no impurities are assumed. These parameters yield a fusion α power of 252 MW. The lower hybrid wave is modelled with a single poloidal wavenumber and a frequency of 3.7 GHz. The wave is centered at $\rho_0 = 1.4$ m with $\rho_d = 0.42$ m. We use a wave electric field of $|E_{\|0}| = 3$ kV/m, which with $k_{\chi 0} = -220$ m^{-1} corresponds to an LH input power of about 100 MW and a $|k_\eta|$ value of 4553 m^{-1}.

In the calculations utilizing the ASCOT code [8], the 3.5 MeV α particles are initially distributed uniformly in pitch $v_\|/v$, and in ρ and θ according to the local fusion reactivity. They are followed until they either are thermalized or escape from the plasma.

The cumulative energy transfer to the wave, the power deposition profile and the α current density profile for this case are shown in Fig. 1. The cumulative energy transfer (Fig. 1a) saturates in about 3.5 seconds to a fraction of about 0.4 of the α birth energy, indicating a power transfer of about 100 MW. The radial profile of the power transfer is shown in Fig. 1b. Figure 1c depicts the radial distribution of the α current density caused by the wave–α interaction. In the presence of the reflective boundary at $\epsilon = \epsilon_w$, the net current obtained varies in sign according to the sign of k_η, a positive k_η yielding a positive current (in the direction of the plasma current) and vice versa. The total α current is about +0.64/–0.29 MA for positive and negative k_η, respectively. The positive current peak obtained in the case of positive k_η represents a total current of about +0.66 MA, while in the case of negative k_η the negative and positive current peaks represent total currents of about –0.50 MA and +0.23 MA, respectively. It of interest to note that the currents obtained from the wave-α interaction approach the currents in the range of 0.7 MA required for MHD stabilization of the plasma in ITER.

The polarity of the current profile remains unchanged regardless of the sign of k_η. This follows from the fact that since $k_\| \propto k_\theta \approx k_\eta$, particles escaping (due to collisions with the background) from the spatial wave region along the diffusion paths of Eq. (4)

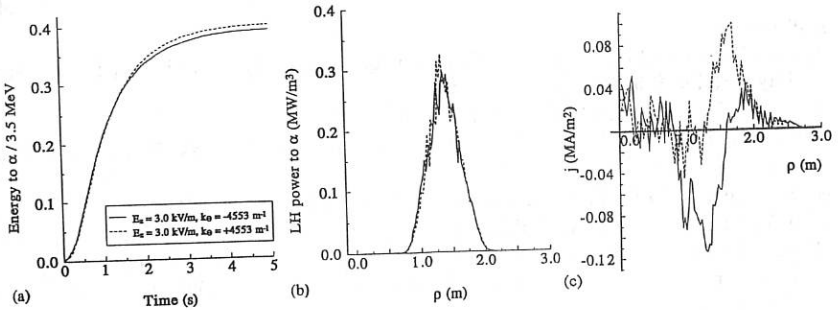


Fig. 1: (a) The average fraction of the α particle birth energy transferred to the wave as a function of time for $|E_z| \equiv |E_{\|0}| = 3$ kV/m and poloidal wavenumbers $k_\eta = \pm 4553$ m^{-1}. (b) The power deposition profiles for the cases in Fig. 1a. (c) The α current density profiles for the cases of Fig. 1a.

always contribute to the current in one specific direction at a specific spatial boundary in accordance with Eq. (2), since the direction of the diffusion paths changes with the sign of k_η.

In both cases of Fig. 1, the obtained currents exceed and are much more localized than the bootstrap current of the α particles. Simulations with a much larger number of α particles ($\sim 40000 - 80000$) indicate a fairly broad bootstrap current profile being finite also at the axis but with a maximum current density less than 30000 A/m^2. In the results of Fig. 1, this current is overwhelmed by the statistical noise, and can not be resolved.

4. Conclusions

In practical situations of smooth wave diffusion profiles, with no absorbing boundaries or mechanisms which can remove fast ions approaching the outer edge or the lower velocity limit of the wave regime, the net power transfer from the ions to the wave calculated with the present Monte Carlo method has been shown to be negative indicating wave damping.

On the other hand, a fast ion current enhanced by the finite B_θ effect is found irrespective of power transfer direction. Thus a significant α particle current may accompany the wave Landau damping, and can clearly exceed the bootstrap current of α particles by neoclassical diffusion. In ITER–relevant conditions, we obtain α current profiles which represent total currents approaching the 0.7 MA range required for MHD stabilization.

The α particle current is affected by the choice of the signs of k_ϕ and k_θ, and by the boundary conditions applied at the boundary $v_\perp = \omega/|k_\eta|$. The choice in the sign of k_η affects the direction of the current but has no impact in practical situations on the direction of the power transfer. On the other hand, boundary conditions can determine the net power transfer direction, and thus affect also the direction of the current. The current profile depends strongly on the radial diffusion of the α particles. With intense waves, a bipolar shape of the current profile specified by the sign of ΔW and by the direction of the diffusion paths is found.

References

[1] N.J. Fisch and J.-M. Rax, Phys. Rev. Lett. **69**, 612 (1992); N.J. Fisch and J.-M. Rax, Phys. Fluids B **5**, 1754 (1993).

[2] C.F.F. Karney, Phys. Fluids **22**, 2188 (1979).

[3] D. Anderson, V.S. Belikov, Ya. I. Kolesnichenko, and M. Lisak, Phys. Fluids B **3**, 3125 (1991).

[4] Z. Gášek, L. Krlín, Z. Tlučhoř, Czech. J. Phys. B **37**, 571 (1987).

[5] J.A. Heikkinen and S.K. Sipilä, Phys. Rev. E. **51**, 1655 (1995).

[6] J.A. Heikkinen and S.K. Sipilä, in the 11th Topical Conference on Radio Frequency Power in Plasmas, Palm Springs, California, May 17–19, 1995; to appear in the Proceedings.

[7] J.M. Rax, N.J. Fisch, and L. Laurent, Plasma Phys. Control. Fusion **35**, B129 (1993).

[8] J.A. Heikkinen, S.K. Sipilä, and T.J.H. Pättikangas, Comp. Phys. Comm. **76** (1993) 215; J.A. Heikkinen and S.K. Sipilä, EPS Conference Abstracts **18B**, pp. 1158–1161, European Physical Society 1994.

Fast Wave Current Drive experiments in JET divertor plasmas

F. Nguyen[1], L.-G. Eriksson, B. Fischer, C. Gormezano,
E. Righi, F. Rimini, G. Sadler, A. Sips, D. Start
JET Joint Undertaking, Abingdon, Oxon, OX14 3EA, UK.
[1] Permanent address: CEA, Centre d'Etudes de Cadarache, France.

Abstract:

As part of the JET experimental campaign in the pumped divertor configuration with the new ICRF A2 antennae [1], studies of Fast Wave Heating and Current Drive scenarii have been carried out [2]. For the experiments described in this paper, the scenario with 3rd harmonic D cyclotron layer at centre and both fundamental and 2nd harmonic H cyclotron layers at the edge has been chosen. The experiments have been carried out in 2 MA D plasmas and 2.2 T on axis with f_{ICRF}=51.4 MHz and a target temperature of T_e (0)~1.5-2 keV. Significant Fast Wave Heating has been observed and studied for varying plasma parameters (B_T, ICRF power, antenna phasing, density). There is evidence of both Fast Wave Direct Electron Heating and heating through 3rd harmonic D cyclotron absorption. These two effects disappear when the 2nd harmonic H cyclotron layer enters in the plasma on the high field side. The power partition between these two heating channels is difficult to assess experimentally. The results are compared with numerical simulations of the power deposition (PION, SINGLE). Furthermore, a prediction of the current drive efficiency is given (ALCYON). This scenario provides efficient heating, since elmy H-mode is triggered when the electron density and the ICRF power in $0\pi\pi0$ phasing are increased and a RF only record DD reaction rate of 1.8 10^{16} s^{-1} has been achieved. $0\pi0\pi$ phasing gives similar results.

Fast Wave Electron Heating and Current Drive scenario:

The target plasma parameters are B_T=2.2 T, I=2 MA and T_e(0)~1.5-2 keV in Deuterium. At ICRF frequency of 51.4 MHz, 3rd harmonic D cyclotron layer is at centre while both fundamental H cyclotron resonance (also 2D and 2 ^{4}He) and 2nd harmonic H (also 4D and 4 ^{4}He) cyclotron layers are marginally present at the edge (e.g. # 35320, fig. 1). Unless otherwise specified, the phasing is $0\pi\pi0$. A similar scenario has been experimented on Tore Supra [3].

Experiment:

A heating with sawteeth is observed but is sensitive to H resonance layer position. A scan of the magnetic toroidal field has been done (# 35520). When the H cyclotron 2nd

harmonic layer enters plasma on the low field side (fig. 1), the density, the radiated power and neutral H flux (Neutral Particle Analyser horizontal line) increase while the DD reaction rate, high energy neutral D flux (NPA horizontal line) and T_e drop. There is evidence of Fast Wave Electron Heating. The analysis of the fast switch off of P_{ICRF} and of the sawteeth slope [4] yields peaked deposition profiles (# 35319, fig. 2a, b). One finds P_{FWEH}=0.9 MW for an ICRF launched power of 6.5 MW which means 14% of damping on electrons in $0\pi\pi0$ phasing (fig. 2b). The power directly coupled to electrons in + 90° and - 90° phasing is estimated to be less than 50% of $0\pi\pi0$ heating [5]. The pre-heating with LH power produces no visible difference. Two pulses in ^{4}He have been performed. The second one (# 35328) is approximately 50% ^{4}He and 50% D and the results are similar to D plasma (# 35325). In particular, the T_e profiles are identical. Part of the ICRF power is clearly absorbed at the 3rd harmonic D cyclotron resonance as indicated by a high DD rate and γ emission from the plasma centre (3.1 MeV from $^{12}C(d, p)^{13}C$ with E_d>1.8 MeV). Fast D is detected with the vertical high energy NPA up to the highest energy channel available (E=1.1 MeV) (fig. 3). This contrasts with Tore Supra results that show dominant electron heating and no fast ions in ^{4}He plasma [3]. This is likely to be due to the better ion confinement in JET that allows the build up of a hot ion tail but models have to be developed. A power and density scans have been done. When the density and ICRF power increase, the plasma evolves towards better performance (fig. 4): the diamagnetic energy content and the DD reaction rate increase and one finally obtains an elmy H-mode. The H factor was 1.6 (ITER89-P) and 0.8 for H93 (H-mode scaling with subtraction of the energy of fast particles) for pulse # 35525 with $0\pi\pi0$ phasing (fig. 3) (similar results were obtained for # 35526 with $0\pi0\pi$ phasing). For this pulse, the record DD reaction rate for ICRF only ($1.8\ 10^{16}\ s^{-1}$) was achieved with P_{ICRF}=12.9 MW. The other parameters are W_{DIA}=3.2 MJ (with $W_{fast\ particles}$=0.6 MJ), $\langle n_e \rangle = 3.9.10^{19}\ m^3$, $T_e(0)$=5.7 keV, P_{total}=13.5 MW. This performance is comparable to hot ion mode (DD reaction rate of $2.10^{16}\ s^{-1}$ for P_{NBI}~14.6 MW at 1.75 MA, # 34489).

Numerical simulations (based on the ICRF and plasma parameters of pulse # 35320):

The power partition between Fast Wave Direct Electrons Heating and heating through D cyclotron absorption at the 3rd harmonic is difficult to estimate. Single Pass Absorption (SPA) estimate (SINGLE code [6], (fig. 5)) is larger for electron (4.5 keV) compared to D absorption of the bulk (2.7 keV) but the SPA for a population of fast D (1% of the D bulk) becomes predominant above 300 keV at the most favourable $k_{//}$ for electron damping (N=33, $k_{//}$=11 m^{-1} on axis). The PION code simulation (self consistent treatment of the D tail formation and the Fast Wave absorption [7]) with hot D confined up to an energy of 2.5 MeV indicates equipartition of the coupled ICRF power between electron and deuterium. The ALCYON (2D full wave code [8]) simulation provides almost identical power deposition profile on electrons

for 90°, 0ππ0 and 0π0π phasing and predicts a current drive efficiency of 0.018 10^{20} A/W/m^2 in 90° phasing.

Conclusion:

Significant Fast Wave Direct Electron heating (~14%) and heating through D absorption at cyclotron 3rd harmonic have been observed. This contrasts with the Tore Supra results that show dominant electron heating and no fast ions with the same scenario [3]. The power partition is difficult to assess. The competition with lower cyclotron harmonic (H or D) should be avoided (edge absorption). The Fast Wave Current Drive efficiency is estimated to be 0.018 10^{20} A/W/m^2 for 90° phasing with the plasma parameters of pulse # 35320 which is comparable to the Tore Supra results [3]. Elmy H-mode is triggered when density and ICRF power in 0ππ0 phasing are increased and a RF only record DD rate of 1.8 10^{16} s^{-1} has been achieved. Similar effect is observed in 0π0π phasing. An efficient heating scenario at 2 MA, 2.2 T with no minority ion population has been found, which can start on low T_e (1-2 keV) target plasma and might provide suitable conditions for very long pulse (60 s) operation for advanced tokamak scenarii on JET.

Acknowledgements:

The work on Fast Wave Current Drive is carried out in collaboration with CEA. Part of the ALCYON computation has been performed at Cadarache. The authors are very grateful to Dr A. Becoulet for his active participation and to Drs J. Jacquinot, B. Saoutic, A. Gondhalekar and W. Zwingmann for many fruitful discussions. We gratefully acknowledge the JET team for the accomplishment of this experiment.

References:

[1] A. Kaye *et al.*, Fusion Engineering and Design, **24** 1 (1994).

[2] The JET team, 15th IAEA Conf. (1994). IAEA-CN-60/A3/5-P-7.

[3] Equipe Tore Supra, 15th IAEA Conf. (1994). IAEA-CN-60/A-3-I-6.

[4] D.H. Start *et al.*, Nuclear Fusion **30**(10) 2170 (1990).

[5] D. Start *et al.*, 11th topical Conf. on RF power in plasmas, Palm Springs, CA, 1995.

[6] D. Fraboulet *et al.*, 21st EPS Conference, Montpellier (France), 1994.

[7] L.-G. Eriksson *et al.*, Nucl. Fusion **33** (7) 1037 (1993).

[8] A. Becoulet *et al.*, Physics of Plasmas, **1** 2908 (1994).

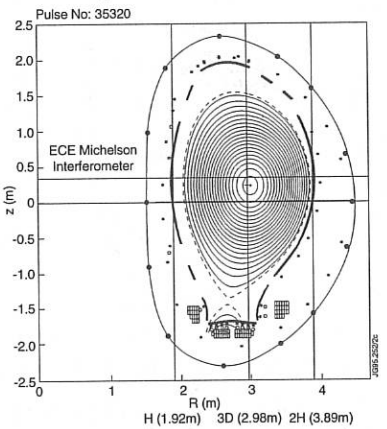


fig. 1: location of the different ion cyclotron layers on a poloidal view of the plasma.

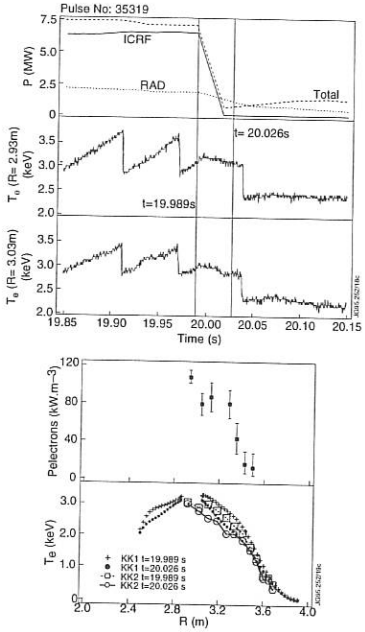


Fig. 2: pulse nº 35319, 0ππ0 phasing, 51.4 MHz, 2.18 T, Deuterium, 1.8 MA, a: P_{ICRF} sharp switch off, effect on the sawteeth, ECE Grating Polychromator (z=25cm), b: direct electron heating profile c: ECE T_e, profiles in the plane z=z(axe).

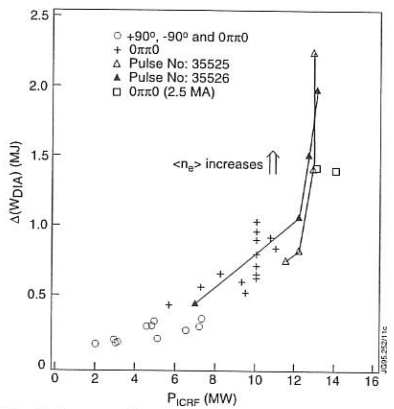


Fig. 4 diamagnetic energy increase in function of the ICRF power, 51.4 MHz, 2 MA, 2.18 T.

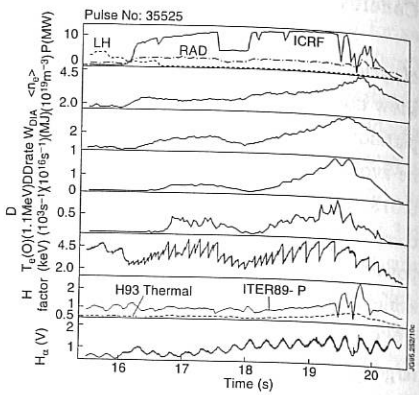


Fig. 3: pulse nº 35525 0 π π 0 phasing, 51.4 MHz, 2 MA, 2.18 T, Deuterium.

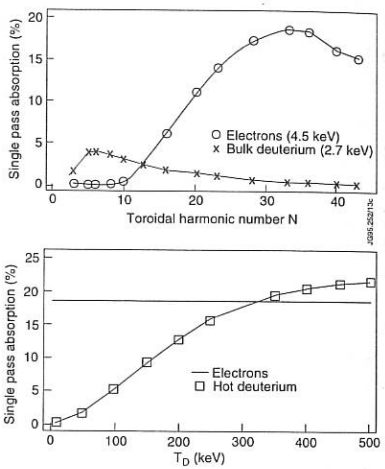


Fig. 5: SINGLE simulation of the pulse nº 35320 at t=16.2 s, a: SPA on electrons (TTMP and ELD) and on bulk D (3rd harmonic) in function of the toroidal harmonic number N, b: SPA for the toroidal harmonic number N=33 ($k_{//}$=11 m^{-1} on axis)on electrons and hot D (1% of the bulk in density) in function of T_D.

Role of MHD activity in LH-assisted discharges in the PBX-M tokamak

M. Talvard†, R. E. Bell, S. Bernabei, S. Kaye, M. Okabayashi,
S. Sesnic, S. von Goeler

Princeton Plasma Physics Laboratory, Princeton University, P.O. Box 451, Princeton, NJ 08543

† Association Euratom-CEA sur la Fusion, Centre d'Etude de Cadarache, 13108 Saint Paul-lez-Durance, France

I INTRODUCTION

The main objective of the PBX-M (Plasma Beta Exp't - Modification) tokamak experiment is to use current and profile control techniques to explore advanced tokamak regimes. In this machine, Lower Hybrid Current Drive (LHCD) with a 2 MW source power at 4.6 GHz has been chosen to shape the current density profile. Wave-induced MHD oscillations are expected to affect the confinement of the suprathermal electrons created by the LH waves degrading both the performance and the control of the discharges. We analyze here the role of MHD activity in those discharges so as to optimize the plasma performance. This work is supported by a data base of about 200 shots selected in the 1993 run period of PBX-M. The tools used for this study are i), a soft X-ray (SXR) diode array with a frequency bandwidth of [0-300] kHz and a detectivity in the energy range of [1.2-12] keV ii), a 2D hard X-rays (HXR) pinhole camera /1/ working in the energy range of [45-150] keV with a temporal resolution of 5 ms and iii), a magnetic probe array with sampling rates up to 100 kHz.

II OBSERVATIONS BEFORE THE MHD ONSET

In the data base, the average line density just before the application of the LH power (up to 480 kW) is in the range 1-3 10^{19} m^{-3}, the plasma current ranges between 145 and 250 kA and the toroidal magnetic field between 1.25 and 1.9 T. In most of the cases, the filling gas is D_2 and the plasma bean shaped.

The HXR images are often characterized by a bright ring that is supposed to roughly localize the LH power deposition in the poloidal plane. The radius of this bright ring is plotted in Fig. 1 versus $\frac{B^2}{n_e} \approx \frac{\omega_c^2}{\omega_p^2}$, a parameter relevant of the accessibility of the LH waves. The linear dependence observed indicates that the wave absorption (Landau damping of the wave launched at $N_{//} = 2.1$ on a 1 keV Maxwellian distribution requiring $N_{//} > 5$) seems to occur at a radial position determined by the wave accessibility condition. If the HXR bright ring were related to the power absorption radius, this would imply that there is no $N_{//}$ upshift for the waves absorbed in PBX-M. Another possibility is that the bright ring corresponds to the emission of a few energetic electrons only (which also corresponds to most of the RF current deposition since the current drive efficiency is higher for high energy electrons). As a consequence, the HXR bright ring will be supposed to represent the deposition of the RF

current. It appears on Fig. 1 that the localization of the RF current is not the parameter able to separate MHD active and quiescent discharges before the MHD onset.

A way to separate those discharges is to plot the internal inductance l_i (taken in most of the cases 50 ms after turning on the LH power) as a function of the parameter $P\frac{B^2}{n_e}$ where P is the LH power (Fig. 2). High power combined with on-axis coupling of the LH waves is most likely MHD unstable. The fact that l_i may be a determining parameter confirms the role played by the current profile on MHD stability. Within the error bars in the determination of the internal inductance, it is reasonable to define two separate domains on the figure. The separation curve is attributed to the local contribution of LHCD to the total plasma current. This representation then combines local effects associated with the RF current deposition ($\frac{B^2}{n_e}$) and the global property of the ohmic target plasma (l_i).

In the horizontal mid-plane, a direct Abel inversion of the HXR integrated image can be achieved. An inverted profile calculated for a typical off-axis coupling of the LH power namely, a "hollow" discharge, is shown on Fig. 3a. An asymmetry such as the one visible on Fig.3b appears sometimes on several successive profiles prior to the MHD onset for all the hollow-type discharges analyzed. This corresponds in all the cases (7 available in the data base) to LH pulses starting with hollow images, characterized by a bright ring that suddenly becomes rather uniform, with an intensity averaged with respect to the previous images. The good correlation with the MHD activity may exclude any instrumental problem. A resonance between the population of fast trapped electrons and turbulent waves present in the background plasma has been proposed elsewhere to support the observations /2/.

III NATURE AND EFFECTS OF MHD

The onset of a 1/1, 2/1, 3/1 rotating mode is frequently observed a few tens of ms after turning on the LH power. The three components are coupled (same frequency) but the SXR normalized fluctuation amplitude is maximum for 2/1 and 3/1, which turn out to be the driving modes (Fig. 4a). After saturation of the mode, we observe a minor disruption with an inversion radius of 20 cm. The minor disruption associated with the collapse of the 2/1, 3/1 components, triggers a very fast growth of the pre-existing 1/1 component (Fig. 4b). The radius of the HXR bright ring (< 16 cm) is consistent with a RF current driven within the $q = 2$ surface ($\approx$ 20 cm). It has been observed that the $m = 2$ and $m = 3$ components are more destabilized at deposition radii closer to the $q = 2$ radius, which is consistent with a steepening of the current density gradient inside this resonant surface. The destabilized 2/1 mode then drives the 3/1 and 1/1 components by toroidal coupling since the frequencies are the same for the three modes. The minor disruption probably involves a reconnection between the $q = 2$ and $q = 3$ surfaces.

MHD instabilities induce SXR intensity losses of about 50% mainly localized around 10 cm, between the $q = 1$ and the $q = 2$ surfaces. This is consistent with HXR measurements except that intensity losses are smaller by a factor 2 for energetic electrons. On the other hand, global modes reduce by a few centimeters only the deposition radius of the RF current . MHD reduces slightly the HXR profile hollowness (enhanced diffusion of fast

electrons) and tends to smooth the asymmetries if any. The increase of peakedness of the HXR images usually observed during MHD activity is the effect of the associated minor disrruptions that trigger runaway electrons. Hot spots appear often on the HXR images as soon as global MHD develops. These generally do not induce a catastrophic end of the discharge. Mode locking is a particular evolution of a growing magnetic activity. HXR intensities do not behave differently in that case in other words, whether island chains rotate or not (in the range 1-5 kHz) does not affect substantially the behaviour of energetic electrons.

REFERENCES

/1/ *S. von Goeler et al., Rev. Sci. Instrum.* ***65****, 1621, (1994).*

/2/ *M. Talvard et al., PPPL Report 3036, (1995).*

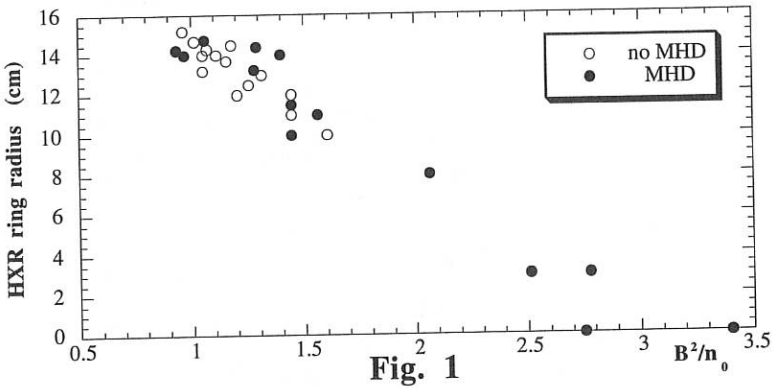


Fig. 1

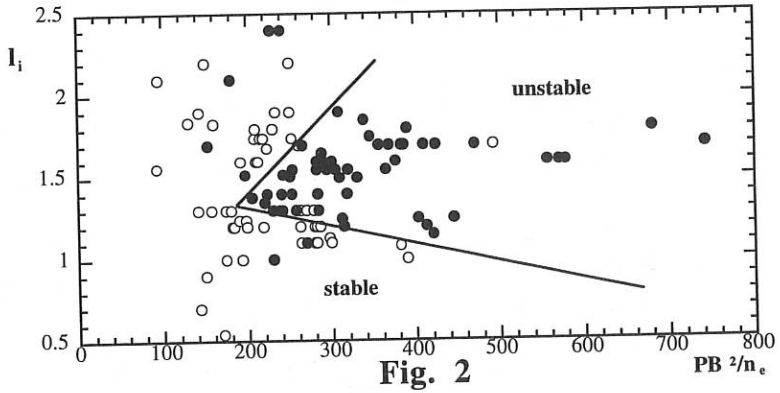


Fig. 2

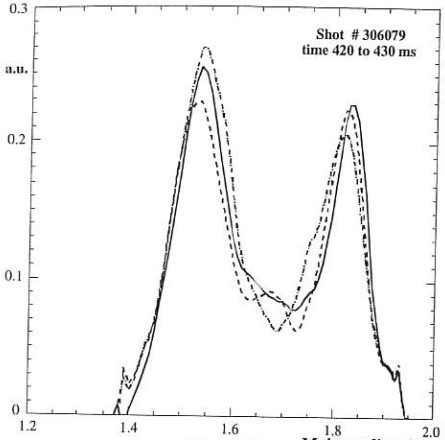


Fig. 3(a)

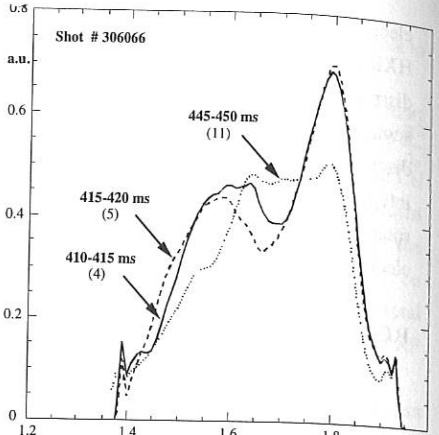


Fig. 3(b)

Fig. 4(a)

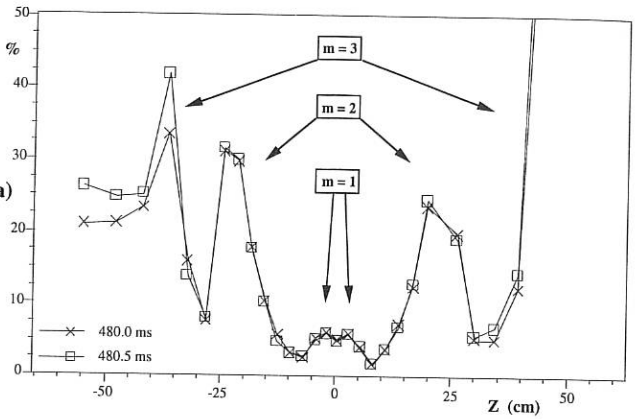
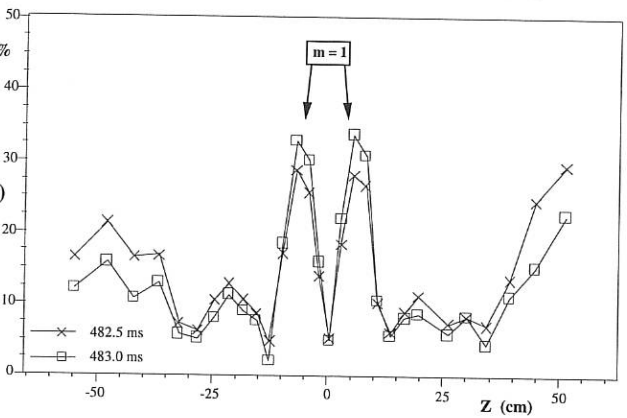


Fig. 4(b)



LOWER HYBRID CURRENT DRIVE EXPERIMENTS ON THE TdeV TOKAMAK*

A Côté, Y Demers, X Litaudon[1], C Côté, R Décoste, V Fuchs, D Michaud, M St-Onge, G Abel, D Boyd[2], P Brooker, E Haddad, P Jacquet, J-L Lachambre, HH Mai, F Martin, GW Pacher, B Quirion, N Richard, IP Shkarofsky, MM Shoucri, F Skiff[2] and W Zuzak.

Centre canadien de fusion magnétique
1804 Montée Ste-Julie, Varennes, Québec, J3X 1S1, Canada

I. Introduction

The lower hybrid current drive (LHCD) system installed on TdeV (R/a= 0.86/0.25 m; B_T <1.8T; I_p < 250 kA) operates routinely and has already delivered 1.3 MW of RF power at the generator[1]. No significant arcing has been observed even at the maximum power density reached at the grill mouth (5 kW/cm^2). The peak of the launched $N_{//}$ spectrum can be adjusted within the limits $2.0 \leq N_{//} \leq 3.3$. Completely RF driven discharges of 190 kA were sustained over half a second at moderate densities ($\bar{n}_e = 1.9 \times 10^{19}$ m^{-3}) [2]. The duration of the LH current driven plasma is limited only by the power handling capabilities of the divertor plates (maximum 4 s). The system is used mainly for current drive experiments and as an electron heating system for divertor biasing studies with auxiliary heating. In this paper, we focus on a comparison of global energy confinement with scaling laws as well as current profile modification experiments with LHCD leading to enhanced electron energy confinement.

II. Global Energy Confinement Scaling

The global energy confinement of combined ohmic and lower hybrid driven plasmas has been analyzed at various plasma densities and plasma currents. All plasma discharges are in deuterium with good isotopic ratio ($n_D/(n_H+n_D) > 0.8$) due to the boronized vessel. Only plasmas with low radiated power have been selected for the present analysis ($P_{RAD}/P_{TOT} < 0.4$).

In TdeV, the energy content of the plasma is inferred using three different methods. First, the diamagnetic energy is measured by the diamagnetic loop with proper error fields correction.Secondly, the kinetic energy is obtained by integrating over the plasma cross-section the electronic and ionic pressure which are measured respectively by Thomson scattering and charge exchange combined with interferometric data. Finally, the "equilibrium energy" is determined by subtracting half the internal inductance (l_i) obtained by polarimetry from the ($\beta_p+l_i/2$) calculated with the Lackner equilibrium code.

Figure 1 shows the global energy confinement time (τ_E) measured using these methods versus the total power for two different line average densities ($\bar{n}_e$ = 3 and 5 x 10^{19} m^{-3}). The plasma current is 190 kA, B_T = 1.8 T (q_{95}=3.8) and the RF power varies from 0 to 0.8 MW at a $N_{//}$ of 3.3. The total power (P_{TOT}) is defined as the ohmic power plus the injected RF power minus the radiated power from the main plasma. No correction for the fraction of absorbed power has been included. Overall, there is good agreement among the three

---

[1]Association Euratom-CEA, Cadarache, France [2]Univ. of Maryland, USA.

* Supported by the *Centre canadien de fusion magnétique* with funds from AECL, Hydro-Québec and INRS.

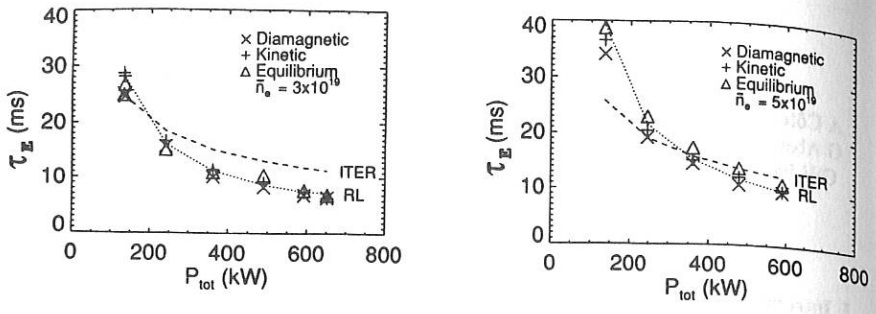


Figure 1: Comparison of τ_E with ITER-89P(dash) and Rebut-Lallia(dot) scaling laws.

independent methods, which gives confidence in the various measurements. The τ_E values predicted by the ITER-89P[3] and Rebut-Lallia[4] scalings are also plotted on the same graphs. For the latter case, the total energy content is obtained by dividing by 0.7 (kinetic measurement of $W_e/(W_e + W_i)$) the following expression for the electron energy content:

$$W_e^{RL} = 0.026\ \bar{n}_e^{3/4} Z_{eff}^{1/4} (B_T I_P)^{1/2} (\kappa a^2 R)^{11/12} + 0.012\ I_P P_{TOT} (\kappa a^2 R / Z_{eff})^{1/2}$$

(in units of MJ, 10^{19} m^{-3}, Tesla, MA, m, MW, Z_{eff} is the effective charge number, κ is the plasma elongation). The power dependence of the energy content follows more closely the Rebut-Lallia scaling. Also, the global confinement shows a significant dependence on plasma density, a behaviour which is inconsistent with ITER-89P scaling($\propto \bar{n}_e^{0.1}$). The ITER scaling was mainly derived from experiments using NBI which principally heats the ions. Experiments performed with electron heating systems such as ECRH (T-10[3]) and LHCD (Tore-Supra[5]) also show a strong dependence of the energy content on density. This supports arguments (Petty *et al.* .[6]) that it is important to uncouple the ion and electron energy loss channels instead of considering the global confinement as a whole.

The kinetic electron energy content is compared with the Rebut-Lallia scaling in figure 2 for a broader scan in plasma parameters (I_P=150, 190 and 230 kA; $\bar{n}_e$= 1.5-8 x 10^{19} m^{-3}; B_T = 1.8 T and P_{HF} =0, 250 and 500 kW @ $N_{//}$ = 3.3). There is close agreement between the two except for two features. First, the energy content seems to saturate at larger density and the saturation value depends on the plasma current as indicated on the figure. This has been observed on many tokamaks. Secondly, there are some points which indicate better confinement than the scaling predictions. This enhancement is similar to the Lower Hybrid Enhanced Performance (LHEP) mode as observed on Tore-supra[5,7] and will be discussed in the next section.

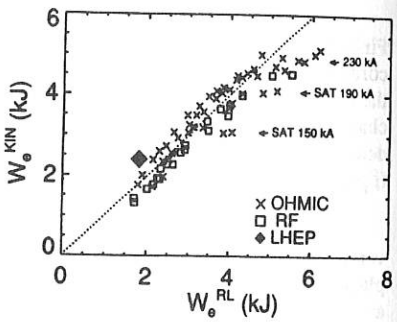


Figure 2: Kinetic electron energy versus Rebut-Lallia showing the saturation and the LHEP regions.

III. LH Current Profile Modification

The aim of LH current profile experiments is to explore the confinement and stability of various current density shapes (hollow or peaked) under stationary conditions. The LHCD system of TdeV is an efficient tool to produce current profile modifications. Due to the low magnetic field and low plasma temperature (weak electron damping), the LH wave propagates many times around the torus before being absorbed[8]. In this multi-pass regime, the LH rays wander within the phase-space domain ($N_{//}$, r) whose boundaries are defined by the slow wave dispersion relation (caustic and accessibility). The upper limit (caustic) which defines the location of the absorbed power depends mainly on the current and density profiles[9]. Therefore the power deposition in TdeV can be tuned by a proper selection of $N_{//}$, q_{95} and $N_{//}^{acc}$(accessibility$\propto \bar{n}_e/B_T^2$).

Figure 3 illustrates the large changes in internal inductance ($\Delta l_i = l_i^{RF} - l_i^{OH}$) that can be induced with LHCD for discharges with q_{95} between 4 and 6.5. For smaller q_{95}, which corresponds to broader current profile, only a small decrease of l_i has been observed. Peaking of the current profile at large q_{95} is obtained by launching LH waves with large $N_{//}$, for which the plasma centre is accessible ($N_{//} > N_{//}^{acc}$). Inversely, broadening of the current profile is obtained with small $N_{//}$ and/or LH waves for which the plasma centre is inaccessible. Occasionally, an MHD event which increases suprathermal electron losses occurs[2], preventing these changes in l_i from occurring .

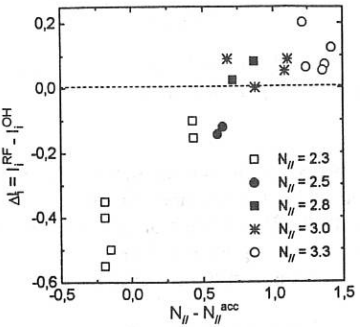


Figure 3: Variation of l_i with $N_{//}$ - $N_{//}^{acc}$ for plasmas with $4<q_{95}<6.5$.

Increases in l_i are accompanied by peaking of temperature, current density and soft x-ray emission(2-20 keV) profiles. Hard x-rays (30-80 keV) which are mainly bremsstrahlung emission from LH induced suprathermal electrons, also exhibit this peaking behaviour. In contrast, a decrease of l_i is associated with broadening of all the previous profiles. An electron cyclotron absorption diagnostic[9] which measures the electron distribution function at two radial positions, also sees the broadening and even a hollow profile when low $N_{//}$ waves are injected. The density profile always broadens with LHCD, possibly an indication of increase in edge recycling [10] and/or radial changes in the particle diffusivity ($D_\perp$).

The time evolution of a LHEP shot (25198) is shown in fig. 4 (I_p =140 kA, B_T= 1.4T, $\bar{n}_e = 1.9 \times 10^{19}$ m^{-3}) for which 500 kW of RF power at a $N_{//}$ value of 3.3 were injected. In the ohmic phase, sawteeth are observed (T_{ST} = 2.5 ms). Their inversion radius inferred from the soft x-ray camera ($r_{inv}/a \approx 0.4$) agrees with the radius of the q=1 surface measured from polarimetry or calculated with neo-classical theory. During the RF pulse, the loop voltage drops by 75% of its ohmic value (dotted line) and the central electron temperature nearly doubles. The internal inductance increases from 1.6 to 1.7 and q_0 decreases from 0.8 to 0.7. However, the sawteeth are stabilised within 10 msec during the RF ramp up with less than 150 kW of power. CRONOS[7] simulation of current diffusion shows that a time of 100 ms will be necessary to increase q_0 from 0.8 to 1, further indicating that the sawtooth stabilisation is

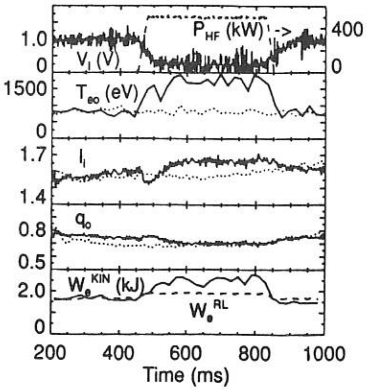


Figure 4: Time evolution of shot 25198 exhibiting LHEP behaviour.

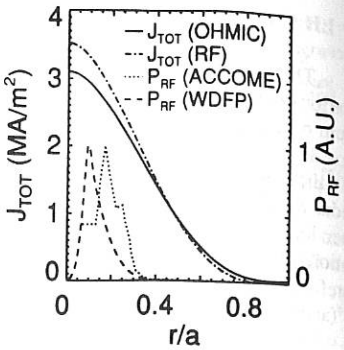


Figure 5: Current density profile before and during the RF for LHEP shot with predicted power deposition profiles.

not caused by current modification. The electron kinetic energy is about 40% larger than the Rebut-Lallia (dashed line) predicted value (H_{RL}=1.4) at $\beta_p = 0.35$. The experimental current density profile steepens at half-radius during the RF as shown in figure 5. The improved confinement regime could be explained by sawtooth stabilisation and/or an increase of the magnetic shear in the confinement zone.

Complete analysis of the non-inductive current profile has been performed with the ACCOME[8] ray tracing code and WDFP[11] which uses a statistical approach. Both codes yield central power deposition within $r/a \approx 0.3$, as illustrated in figure 5. As a final validation of the calculated J_{RF}, a dynamic analysis of the resistive current diffusion was carried out using CRONOS. Good agreement is observed between the time evolution of the measured Faraday rotation signal and its simulated behaviour.

References:

1. Y. Demers, A. Côté, R. Décoste et al., Proc. of 21st EPS Conf. on Controlled Fusion and Plasma Physics, Montpellier, France, Vol. 18B(1994), p.1086.
2. Y. Demers, A. Côté, C. Côté et al., Proc. of 11th Topical Conf. on RF power in Plasmas, Palm springs, California 1995, to be published.
3. P.N. Yushmanov, T. Takizuka, K.S. Riedel et al., *Nucl. Fusion*, **30** (1990) 1999.
4. P.H. Rebut, P.P. Lallia, M.L. Watkins, Plasma physics and controlled nuclear fusion, Proc. 12th Int. Conf. Nice, 1988, (IAEA, Vienna, 1989) Vol **2**, p 191.
5. G.T. Hoang, C. Gil, E. Joffrin, D. Moreau et al., *Nucl. Fusion*, **34** (1994) 75.
6. C.C. Petty, T.C. Luce, R.I. Pinsker et al., *Phys. Rev. Lett.*, **74** (1995) 1763.
7. Équipe Tore Supra (presented by X. Litaudon) , in ref. 2, to be published.
8. V. Fuchs, P.T. Bonoli, I.P. Shkarofski et al., *Nucl. Fusion*, **35** (1995) 1.
9. D. Boyd, F. Skiff and S. Gulick, Proc. of 9th Joint Workshop on Electron Cyclotron Emission and ECRH, Borrego Springs, California 1995, to be published.
10. B. Stansfield, N. Richard, R. Marchand et al., this conference.
11. K. Kupfer, D. Moreau and X. Litaudon, *Phys. Fluids B*, **5** (1993) B253.

Absorption of finite-size LH wave beams in tokamak plasmas

G.V.Pereverzev
Max-Planck-Institut für Plasmaphysik, D-85748 Garching, Germany

1. Introduction

The method commonly used for describing lower hybrid (LH) heating and current drive in tokamak plasmas is ray tracing (RT). In this technique a wave front is split into small pieces, which are then assumed to be fully independent and treated separately from one another. Each of them has its own space trajectory, a wave number and a group velocity. This approach has proved to be highly useful and efficient in conventional optics. However, direct transfer of the technique to LH waves is not justified [1]. The problem is that the RT technique can only be used over a ray length ℓ satisfying the well-known Fresnel condition $\ell \leq (\Delta a)^2/\lambda$, where Δa is the linear size of each piece of the phase front and λ is the wavelength in the medium. Otherwise, i.e. at remote points of a trajectory the interference pattern is created by the whole wave field distribution and so the individual pieces cannot be treated as independent any longer. As the absorption in plasmas is usually very small, the ray path before complete decay is very long and the Fresnel condition can hardly be met in most plasma applications. As a result of this violation the RT technique fails to describe the spectral and space broadening of the LH wave packet which takes place during LH wave propagation in tokamaks [2].

For the same physical reason RT does not properly describe LH wave absorption either. An advanced beam tracing (BT) technique was recently developed [3] which allows one to deal with a wave packet as a whole. It is shown in the present report that successive implementation of the technique results in a modified expression for the wave absorption in which the convolution of the two Fourier harmonics (δ-function) appearing in the well-known formula for Landau damping is replaced by a convolution of two Gaussian functions of finite spectral width. The conventional expression for Landau damping is then obtained as a particular limiting case of a monochromatic wave.

2. General formulation

Consider high-frequency ($\omega \gg \omega_{ci}, \omega_{pi}$) electrostatic oscillations of the electron component of an inhomogeneous plasma. These oscillations are described with a set of kinetic and Poisson equations which in conventional notation reads

$$\frac{\partial f_e}{\partial t} + \mathbf{v} \cdot \nabla f_e + \frac{e}{m} \nabla \varphi \cdot \frac{\partial f_e}{\partial \mathbf{v}} - \frac{e}{m} \frac{\mathbf{v} \times \mathbf{B}_0}{c} \cdot \frac{\partial f_e}{\partial \mathbf{v}} = 0, \tag{1}$$

$$\Delta \varphi = 4\pi e \left(n_i - \int f_e d^3 v \right). \tag{2}$$

The usual procedure [4] for solving the kinetic equation Eq. (1) can be applied, which

comprises (i) linearization of Eq. (1) assuming that the electron distribution function f_e takes the form $f_e = f_{0e} + \delta f_e$ and that its perturbed part $\delta f_e = \delta f_e(t, \mathbf{r}, \mathbf{v})$ is small with respect to the steady-state distribution function $f_{0e} = f_{0e}(\mathbf{r}, \mathbf{v})$, (ii) solving the linearized equation in the Fourier space and transition back to the configurational space. As a result, an expression for the perturbed distribution function δf_e in terms of the electrostatic potential φ is obtained. The expression is strongly simplified if the additional assumption $v_{Te} k_\perp / \omega_{ce} \ll 1$ is adopted so that the approximation of a cold plasma is implied. On substituting the resulting expression for δf_e into the Poisson equation (2) one obtains

$$\mathcal{P}[\varphi] = \operatorname{div} \hat{\varepsilon} \nabla \varphi = -i \frac{4\pi^2 e^2}{m_e} \mathcal{F}^{-1} \left\{ D_f(k_\parallel) \mathcal{F}[\varphi] \right\}. \tag{3}$$

Here $\hat{\varepsilon}$ is the Hermitian dielectric tensor for a cold plasma [4], $D_f(k_\parallel) = -\partial f_{0e}/\partial v_\parallel \big|_{v_\parallel = \omega/k_\parallel}$ and the notations $\varphi_{\mathbf{k}} = \mathcal{F}[\varphi] = \int \varphi(\mathbf{r}) e^{-i\mathbf{k}\mathbf{r}} d^3x$, $\varphi = \varphi(\mathbf{r}) = \mathcal{F}^{-1}[\varphi_{\mathbf{k}}] = (2\pi)^{-3} \int \varphi_{\mathbf{k}} e^{i\mathbf{k}\mathbf{r}} d^3k$ are used for the Fourier transform. The time dependence of the electrostatic wave potential φ and δf_e is assumed to have the form $e^{-i\omega t}$ and is omitted here and in what follows. Using Eq. (3), one can form the combination $\int_V \{\varphi^* \mathcal{P}[\varphi] - \varphi \mathcal{P}^*[\varphi^*]\} d^3x$, where V denotes some space domain bounded by a surface S. The domain will be specified later. So far we assume only that its linear size is large in comparison with the wavelength $\operatorname{diam}(V) \gg \lambda$, and then after standard transformations we obtain the equation

$$\oint_S (\varphi^* \hat{\varepsilon} \nabla \varphi - \varphi \hat{\varepsilon}^* \nabla \varphi^*) \cdot d\mathbf{S} = -2i \frac{4\pi^2 e^2}{m_e} \int \frac{d^3k}{8\pi^3} D_f(k_\parallel) |\varphi_{\mathbf{k}}|^2 \tag{4}$$

describing the energy conservation law.

3. Wave absorption in the beam tracing approach

Before proceeding further we emphasize that no assumptions were imposed on the potential φ during the derivation of Eqs. (3)-(4). Starting from this point, we assume that the wavelength λ is small in comparison with the characteristic length L of the inhomogeneity of the medium so that the problem involves a large parameter $\kappa = L/\lambda \gg 1$. Then, as shown in [3], the homogeneous equation $\mathcal{P}[\varphi^{(0)}] = 0$ has a general solution $\varphi^{(0)}(\mathbf{r}) = \sum_n C_n^{(0)} \Phi_n(\mathbf{r}) = \rho(\mathbf{r}) \sum_n C_n^{(0)} \varphi_n(\mathbf{r})$, where $C_n^{(0)}$ are constants and the functions $\Phi_n(\mathbf{r}) = \rho(\mathbf{r}) \varphi_n(\mathbf{r})$ are so-called Gaussian or beam modes. Each of them satisfies the homogeneous equation $\mathcal{P}[\Phi_n] = 0$. The most rapid and therefore the most significant variation of the solution is described by the common factor

$$\rho(\mathbf{r}) = \exp\Big\{ i\kappa \Psi(\mathbf{r}) - \frac{\kappa}{2} \left[u^2(\mathbf{r}) + v^2(\mathbf{r}) \right] \Big\}, \tag{5}$$

where $\Psi(\mathbf{r})$ is the eikonal and the two real functions $u(\mathbf{r})$ and $v(\mathbf{r})$ describe the field amplitude decay. These functions are determined by a set of ordinary differential equations

formulated in [3]. Here we assume that all three of them are known functions. Formula (5) shows that a propagating wave packet can be imagined as a tube or beam extending along the spatial curve $u(\mathbf{r})=v(\mathbf{r})=0$, which can be viewed as a beam axis. It can be shown that the curve is tangential to the direction of the group velocity $\mathbf{v}_g$, that is $\mathbf{v}_g\cdot\nabla u=\mathbf{v}_g\cdot\nabla v=0$. The amplitude $|\varphi|$ of the wave packet varies only slightly along the beam axis. In contrast, in the perpendicular cross-section the amplitude decays rapidly so that the beam is strongly localized with the characteristic size $\Lambda=[\sqrt{\kappa}\max(|\nabla u|,|\nabla v|)]^{-1}\approx L\kappa^{-1/2}\ll L$. It is also seen that the RT solution is included in Eq. (5) as a particular case, namely the limiting case of a very wide wave packet $u(\mathbf{r})\approx v(\mathbf{r})\approx 0$ or $\Lambda\to L$.

We could now use the full system of functions Φ_n as a basis of expansion and, making use of the Galerkin method, seek a solution φ of the full problem Eq. (3) in the form $\varphi(\mathbf{r})=\sum_n C_n(\mathbf{r})\Phi_n(\mathbf{r})$. In this case, no special assumption about the right-hand side of Eq. (3) is needed. However, to avoid unreasonable complications we take advantage of the smallness of the right-hand side of Eq. (3). Physically, this means that the energy absorption is very small and the energy exchange between the different eigenmodes in the expansion for φ is neglected. This allows us to keep in the expansion one harmonic $\varphi=C_l\Phi_l$ only and substitute it directly into Eq. (4) instead of Eq. (3). For tokamak applications it is convenient to choose the integration domain in Eq. (4) as a thin layer enclosing a magnetic surface S. This means that the domain V is taken as a torus bounded by the magnetic surface S with subsequent passage to the limit $\lim\limits_{\Delta V\to 0}\dfrac{1}{\Delta V}\int_V d^3x$. Introducing the notations for the carrying wave vector $\overline{\mathbf{k}}$ of the wave packet, its effective group velocity v_g^a and the wave energy density W averaged over a magnetic surface,

$$\overline{\mathbf{k}}=\kappa\nabla\Psi\Big|_{u=v=0},\quad v_g^a=\frac{\omega}{2\overline{k}^2}\left[\nabla a\,(\hat{\varepsilon}+\hat{\varepsilon}^*)\,\overline{\mathbf{k}}\right]\Big|_{u=v=0},\quad W=\frac{d}{dV}\int_V\frac{|\nabla\varphi|^2}{16\pi}d^3x=\frac{\omega|C_l|^2}{32\pi v_g^a}\frac{da}{dV},$$

we obtain

$$\frac{d}{dV}\left(Wv_g^a\frac{dV}{da}\right)=-\pi\frac{\omega}{\overline{k}^2}\frac{4\pi e^2}{m_e}W\int\frac{dk_\parallel}{2\pi}D_f(k_\parallel)F(a,k_\parallel).\qquad(6)$$

Here the variable V denotes the volume of the torus, a is an arbitrary magnetic surface label, $\Phi_{l,\parallel}=\Phi_{l,\parallel}(x,y,k_\parallel)=\int\Phi_l(\mathbf{r})e^{-ik_\parallel z}dz$ is the longitudinal with respect to the direction of the external magnetic field Fourier transform of the eigenfunction $\Phi_l(\mathbf{r})$ and $F(a,k_\parallel)=\left(\int|\Phi_{l,\parallel}|^2\,dS\right)\Big/\left(\int dk_\parallel\int|\Phi_{l,\parallel}|^2\,dS\right)$ is normalized to the unity spectral distribution of the wave energy density averaged over the magnetic surface a. Only the leading-order terms with respect to the large parameter $\kappa=L/\lambda$ are retained in Eq. (6). This means that all spatially dependent functions except for $\Phi_l(\mathbf{r})$ are considered as slowly varying over the space size Λ and are taken out of the integrals. The error introduced by this procedure is of the order $O(\kappa^{-1/2})$.

4. Discussion and comparison with ray tracing

Equation (6) represents the energy conservation law in the beam tracing (BT) approach. If the wave packet $\varphi(\mathbf{r})$ is sufficiently extended in the real space, then it can be strongly localized in the spectral space so that the distribution function F in Eq. (6) is reduced to $F(a, k_\parallel) = 2\pi\delta(k_\parallel - \overline{k_\parallel}(a))$. Then the factor in front of W on the right-hand side of Eq. (6) arrives at the usual expression for the Landau damping $\left.\frac{\pi\omega\omega_{0e}^2}{\overline{k}^2 n_e}\frac{\partial f_{0e}}{\partial v_\parallel}\right|_{v_\parallel=\omega/\overline{k_\parallel}}$ and Eq. (6) coincides in outward appearance with the correspondent equation of RT. This coincidence, though, is no more than a formal one. The difference is that BT deals with the total energy flux $W v_g^a \frac{dV}{da}$ through a magnetic surface and shows that it is absorbed at the rate described by the right-hand side of Eq. (6) which in turn is determined by the whole spectrum of the wave packet. The absorption is manifested as a decrease of the pre-factor $|C_l|$ or W in Eq. (6) without any change in the structure of the function $\Phi_l(\mathbf{r})$. In contrast, the analogous equation for RT is concerned with only a small fraction of the total energy flux and its absorption is determined by an average value of the wave vector $\overline{k}_\parallel$. If this fraction of the whole packet is absorbed, the others further propagate fully independently.

Along with this clear difference, there is a basic similarity between the two approaches. If we consider a partial plane wave treated by RT and the function Φ_l of the BT solution as approximate eigenfunctions of the problem (3), then the two approaches describe propagation and absorption of an eigenfunction as a whole. From this point of view the two approaches describe the same physical process and supplement one another. For a wide wave packet the diffraction can be neglected and then RT gives the appropriate description. In the opposite case, the BT approach has to be used. Unfortunately, a criterion for the applicability of RT cannot be obtained within its framework. The Fresnel condition [1] or the BT solution [3] should be used to prove the applicability of RT. For the particular case of LH current drive in present-day tokamaks, the wave beam spectra undergo essential diffractional broadening [2]. As a result, the RT technique may underestimate the absorption by orders of magnitude and therefore the BT description should be used.

References

[1] G. V. Pereverzev, 20th EPS Conference on Contr. Fusion and Plasma Phys., Lisboa, 26-30 July 1993, Contributed Papers, Vol.17C, Part III, p.885

[2] G. V. Pereverzev, *Nuclear Fusion*, **32(7)** 1091 (1992)

[3] G. V. Pereverzev, in *Reviews of Plasma Physics*, ed. by B. B. Kadomtsev, Vol. 19, Consultants Bureau, New York, 1995

[4] V. D. Shafranov, in *Reviews of Plasma Physics*, ed. by M. A. Leontovich, Vol. 3, Consultants Bureau, New York, 1967

A Photoelectron Spectrometer with Magnetic Analyzer (Measurements on the T-10 Tokamak)

Yu.V. Gott and **V.A. Shurygin**

RRC "Kurchatov Institute", Moscow, Russia

1. Introduction

The basic principles of the photoelectron diagnostics are the conversion of the plasma x-ray flux to the photoelectrons and the energy analysis of these photoelectrons in the electric or magnetic fields. Although the quantum efficiency of this conversion is rather low (about 10^{-2} - 10^{-3} electrons/quantum), the large intensity of the plasma x-ray emission allows the effective analysis of the x-ray spectra even at low electron temperatures and modest sizes of plasmas both in the tokamaks and in the mirror traps [1-5]. Recently the temporal evolution of the X-ray spectrum in the energy range of 0.1 - 1.5 keV was measured by a differential photoelectron spectrometer (PES) with resolution of about 50 μs in the startup phase of a discharge and during a major disruption in a small tokamak TVD [5]. It is evident that in the larger tokamaks with higher temperatures the efficiency of the photoelectron technique increases in proportion to the plasma x-ray flux. In this paper, we report the first series of measurements with the compact PES, which is intended for the x-ray studies in a wide energy range (0.1 -100 keV) in the T-10 tokamak.

2. PES design and calibration

The high sensitivity of the photoelectron measurements with PES is provided by its analyzer with high transmission (~ 2 %) and by its target with large area (~1.5 cm^2), since the PES energy resolution (~ 30 - 40 %) is dominated by the equilibrium energy distribution of the photoelectrons emitted from the thick target under effect of the monoenergetic photons [2]. The design of this spectrometer seems to be rather simple, as shown in Fig. 1, since the energy resolution of the PES analyzer can be as low as 10-20 %. The photoelectrons emitted from the target 1 are analyzed in energy in longitudinal magnetic field produced by the coils 4 and then registered by the microchannel electron multiplier 3. It is important that calibration of the PES analyzer can be made *in situ* using the plasma x-ray emission as follows. The plasma x-rays pass through the carbon filter (with thickness of about 500 Å), which is placed before the PES enter and intended to protect the detector 3 from ultraviolet radiation and neutrals coming from the plasma. The incident x-rays are converted by the PES target 1 to the flux of slow secondary electrons (besides the photoelectrons) with energies E_S < 50 eV with efficiency which is more than two orders of magnitude higher than that for the photoelectrons. Hence, the intensity of this flux appears to be enough high and to be proportional to the intensity of the x-ray emission in the region E_γ > 100 eV. The energy distribution of these slow secondary electrons is independent of the spectrum of the exciting radiation and has a maximum in the region E_S < 10 eV. The negative voltage U of about 0.1 - 5.0 kV is applied between the metal target and the PES walls. Therefore, the secondary electrons are accelerated transverse to the target surface up to the energy $eU >> E_S$. The energy analysis of these accelerated electrons with PES analyzer provides the shape of the analyzer response function and the relation between their energies (given by U) and the current in the analyzer coils. Hence, there is no need in special x-ray calibration of such

instruments, as the equilibrium photoelectron energy distribution is known [2] and the PES analyzer can be calibrated *in situ* in such a way. The emission of slow secondary electrons under effect of the plasma x-rays gives a good opportunity to measure the integral x-ray flux emitted by the plasma and passing through the changeable filters (see, for example [6]). The temporal evolution of the sawtooth oscillations in the x-ray flux with E_γ > 100 eV and their inversion after the gyrotron launching in T-10 is shown in Fig.2.

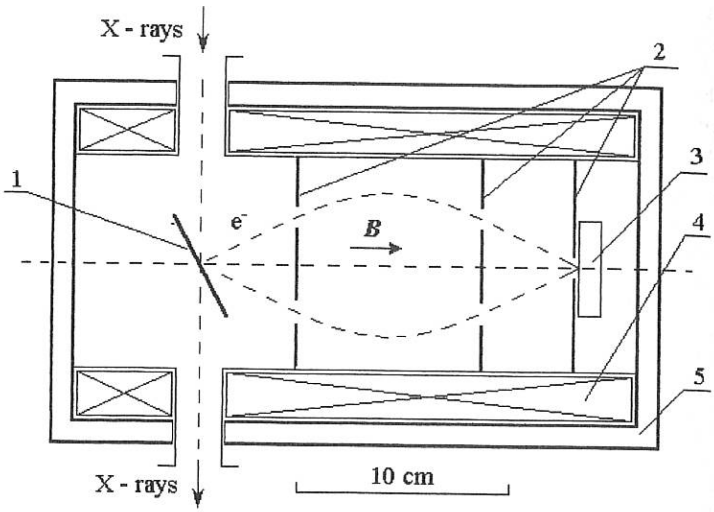


Fig. 1. PES with magnetic analyzer: 1 - target, 2 - diaphragms, 3 - detector, 4 - coils, 5 - magnetic shielding.

3. Efficiency of the target

The transformation of the plasma x-ray spectrum into the corresponding components of the photoelectron spectrum: lines and continuum is performed in the PES target [2]. The efficiency of this transformation is determined by the photoionization cross-sections μ_n of the atomic shells of a target and by the effective range R of the photoelectrons escaping from the target. Moreover, the relative contribution of different atomic subshells to the photoelectron spectrum depends on the x-ray spectrum $I_\gamma(E_\gamma)$. In the case of the continuum of a Maxwellian plasma, when $I_\gamma \propto \exp(-E_\gamma / T_e)$, the photoelectron spectrum is found to be determined by T_e [2]

$$I_e \propto F(E_e, T_e) \cdot \exp(-E_e / T_e), \tag{1}$$

where the function

$$F(E_e, T_e) = \sum_n \mu_n R \cdot \exp(-E_n / T_e), \tag{2}$$

describes the efficiency of the x-ray spectrum transformation into the photoelectron continuum, E_n is the electron binding energy in the n-th subshell. Using the function (2)

the efficiency of the targets with different Z can be calculated. A comparison of these efficiencies computed with T_e=1.0 keV for carbon, aluminum, titanium and silver targets is shown in Fig.3. The contributions of all atomic shells from K- to N- were taken into account in these calculations. From (2) it follows that the photoelectron spectrum is produced mainly by the subshells with $E_n / T_e < 1$, for example, by the M_I - M_V subshells in the case of silver target and T_e=1.0 keV. It is important to note that the efficiency of the PES target not only increases with increasing Z, but also it becomes more weaker function of the energy in a wide energy range. In the present experiments several target materials were tested in PES. It was found that the silver target provides the most intense photoelectron signal.

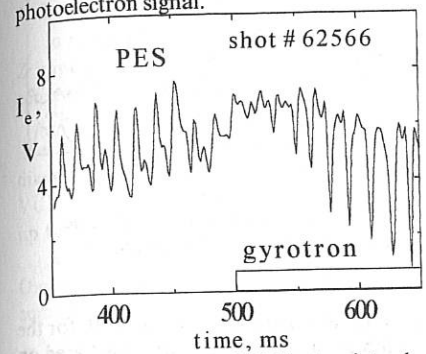


Fig.2. Time trace of PES signal in the integral regime (with Ti target).

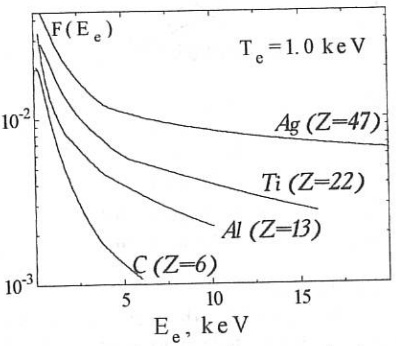


Fig. 3. Efficiency for several target materials calculated from (2).

4. Observations in T-10

The spectral signals produced by PES can be recorded in two main regimes. The first allows one to measure the photoelectron spectrum excited by the plasma x-ray emission. The second regime can be used to record the time traces for different x-ray energies with high temporal resolution. A photoelectron spectrum and an example of T_e determination are shown in Fig.4. This spectrum was recorded in the time interval of about 200 ms. This time was limited due to low intensity of the x-rays incident on the PES target from the plasma. Unfortunately, in these first experiments the x-ray flux coming to the PES target was strongly restricted by the small size collimator with the spatial resolution in the plasma centre of about 1.5 cm. It is evident that the increase of this size up to 5-8 cm leads to significant (squared) increasing of the measured signal. It is expected that in the next experimental series the temporal resolution for the spectrum recording will be of the order of several milliseconds at least. The x-ray energy range of PES was restricted also by the collimator size, as the spectral intensity of the x-ray emission towards the higher energies falls very rapidly. The upper limit of this range was about 8 keV. The lowest one was about 100-200 eV due to carbon filter before PES.

The recording of the time traces for the spectral signals are of special interest, since the correlation of these traces with ECE signals reveals the valuable information about interaction processes between the plasma electrons and impurities. The correlation between the PES signals ($E_\gamma \approx 1$ keV) and the ECE signals recorded just after the disruption in T-10 is shown in Fig. 5. From Fig. 5 it is seen that the PES signals are shifted in time compared with the ECE signals and the delay time is about 1.9 ms. It is

clear that the high temporal resolution of the PES spectral signals and their scanning in a wide energy range give the new approach to study the nonstationary processes, particularly, for the edge plasma study with proper analysis [5].

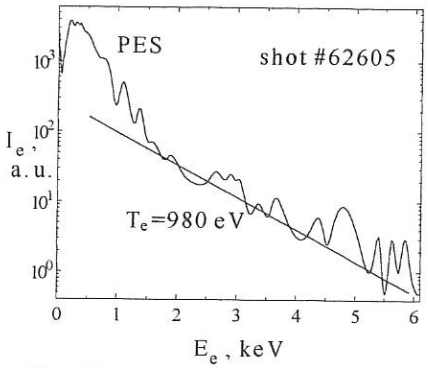


Fig.4 Photoelectron spectrum (Ag-target) measured for a one shot.

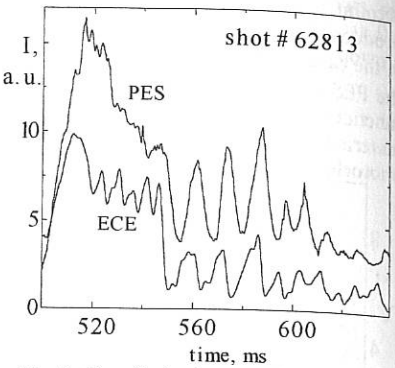


Fig. 5. Correlation between PES and ECE signals just after disruption.

5. Conclusions

Compact PES with magnetic analyzer was constructed and installed on T-10 for the x-ray studies in a wide energy ranges. The PES calibration technique *in situ* was based on the emission of secondary electrons using directly the plasma x-ray emission as an exciting source. The experiments and calculations show the high registration efficiency of the targets with higher Z . Moreover, they have also the weaker energy dependence of their efficiencies in comparison with lower Z targets. It is shown that PES has three main regimes which are 1) the integral x-ray flux measuring (the regime of the x-ray detector), 2) the differential regime to measure the x-ray spectra for a one shot of plasma device, 3) the recording of time traces of spectral intensities in different x-ray energy regions. The results were compared with those of the traditional diagnostics (PHA system and ECE).

It should be noted that the developed spectrometer is supposed to have the low sensitivity to the hard x-ray and neutron radiation, as its detector located far from the diagnostic channel axis and does not see the plasma directly. Since the corresponding radiation background in the instrument is known to decrease rapidly with increasing distance from the axis channel, the needed rearrangement can readily be performed for PES. Hence, this diagnostics is very promising and can be suitable for the large tokamak devices with D-T plasmas. It should be tested on existing large tokamaks.

References

[1] Afrosimov V.V., et al., *Sov.J.Plasma Phys.* **5**, 551 (1979).
[2] Gott Yu.V., Shurygin V.A. *Plasma Phys. Rep.* **19**, 559 (1993).
[3] Dimov G.I., et al. *Plasma Phys.Rep.***19** (1993).
[4] Takahashi E., et al., *Rev.Sci.Instrum.* **66(2)**, 565 (1995).
[5] Shurygin V.A. Preprint IAE-5887/7, Moscow (1995) and this conference.
[6] Lee P., et al., *Rev.Sci.Instrum.* **59**, 883 (1988).

Measurement of Line Radiance of Low-Z Impurity by USX and VUV Spectroscopy on CASTOR Tokamak

J Badalec, J Moravec, V Piffl

Institute of Plasma Physics, Czech Academy of Sciences,
Za Slovankou 3, P.O.Box 17, CZ-182 11 Prague 8, Czech Republic

1. Introduction

In most tokamak experiments Carbon and Oxygen are identified as the dominant low-Z impurities. Moreover, a remarkable dependence of the density limit on the Oxygen concentration has been reported [1].

The present work aims to evaluate absolute intensities of Carbon and Oxygen spectral lines using the vacuum-ultraviolet (VUV) spectroscopy and the ultra-soft x-ray (USX) diagnostic based on the multilayer mirror (MLM). An improved diagnostic technique of VUV and USX spectroscopy enables to measure the line radiance of high ionized stage up to the H-like ions even in a small-scale tokamak.

A simple radiative model had to be developed to allow an estimation of Carbon and Oxygen concentration, because a space resolved measurement, which would give more complex experimental data, was not available.

2. Model

The measured line radiance B_{pq} can be compared with an intensity calculated using an appropriate model in order to determine the concentration of the impurity.

The line radiance, which corresponds to the transition $p \rightarrow q$, is

$$B_{pq} = \frac{1}{4\pi} \int_0^a n_z(r)\, n_e(r)\, V_{pq}(T_e)\, \mathrm{d}r \quad , \tag{1}$$

where $n_z(r)$ is a density of the ion of the z-th stage and the excitation rate coefficient $V_{pq}(T_e(r))$ is calculated after Van Regemorter formula.

The density of the individual ions can be determined using the coronal model [2] for calculation of the fractional abundances $f(z, T_e(r))$ of the ions

$$n_z(r) = n_{imp}(r) \cdot f(z, T_e(r)) \quad . \tag{2}$$

In the present model, we have supposed a parabolic profile both of the temperature and plasma density and also a parabolic distribution of impurity atoms $n_{imp}(r)$

$$n_{imp}(r) = \sum_z n_z(r) = C \cdot n_e(r) \quad , \tag{3}$$

where C is the concentration.

Using (2),(3) the line radiance B_{pq} can be expressed as

$$\begin{aligned} B_{pq} &= \frac{2a}{4\pi} \cdot C \cdot n_e(0)^2 \int_0^1 \left(1 - x^2\right)^2 V_{pq}(T_e)\, \mathrm{d}x = \\ &= \frac{1}{2\pi} \cdot a \cdot C \cdot n_e(0)^2 \cdot Q_M \quad , \end{aligned} \tag{4}$$

where Q_M substitutes for the integral and the central electron density $n_e(0)$ is derived from measured line average value $\bar{n}_e$. Thus, the impurity concentration is

$$C = \frac{2\pi B_{pq}}{a \cdot n_e(0)^2 \cdot Q_M} \quad , \tag{5}$$

where the line radiance B_{pq} is measured by USX or VUV spectroscopy.

3. Experiment

The experiment was performed on the small-size CASTOR tokamak (major radius $R = 0.4$ m, minor radius $a = 0.083$ m, toroidal magnetic field $B_T = 1$ T) with plasma current $I_P = 6 - 16$ kA, central electron temperature $T_e = 150 - 300$ eV and plasma density $\bar{n}_e \leq 1.2 \cdot 10^{19} \mathrm{m}^{-3}$.

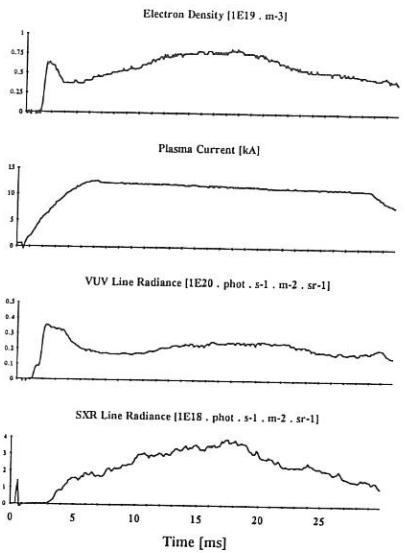


Figure 1: *Tokamak discharge parameters.*

Spectral line radiation of the dominant low-Z impurities (Oxygen and Carbon) are measured in the CASTOR simultaneously in the ultra-soft x-ray (USX) and vacuum-ultraviolet (VUV) ranges. The line-of-sight both of the spectrometers are crossing the plasma in the tokamak midplane.

The USX spectroscopy used in this experiment is a combination of filter method and dispersive spectroscopy. The radiation is first filtered by suitable metallic submicron films to stop visible and VUV light and then diffracted by a flat multilayer mirror (MLM) according to the Bragg rule and detected by a channeltron.

A two-channel MLM spectrometer of classic scheme has been designed in IPP Prague [3]. A clock-like mechanism allows the mirror and the detector to be turned separately at the angle Θ and 2Θ, respectively, without a vacuum break. Both the channels are placed in common housing with an autonomous pumping, which can be easily disconnected from tokamak vacuum. All that allows a quick modification of the set-up (exchange of mirrors or filters) and makes the diagnostic flexible.

The MLM spectrometer covers the wavelength ranges 14 - 24 Å (500-880 eV) and 31-45 Å (270-400 eV), depending on the used mirror, what allows the He-like and H-like ions radiation to be measured with spectral resolution power $\lambda/\Delta\lambda \approx 30$. A relatively high throughput of the MLM spectrometer due to the high reflectivity of the multilayer mirror, high transmittance of the metal filter and high gain of channeltron, which is used as detector in photon counting mode, allows the resonant line radiance of the high ions to be measured with a good time resolution (≈ 0.1 ms) even in a low-size and low-density plasma such as is in the CASTOR tokamak ($2 \cdot a \cdot \bar{n}_e \leq 10^{18} m^{-2}$). ·

A Seya-Namioka type grating VUV monochromator covers a wavelength range 500-6000 Å with spectral resolution about 3 Å in the VUV range [5]. That allows the radiance of resonant line of the lower-stage ions to be measured up to the Li-like C^{3+} (C IV) and O^{5+} (O VI) ions. Moreover, the transition 2s ^{3}S-2p ^{3}P of the He-like ions C^{4+} (C V) and O^{6+} (O VII), which are linked with the intercombination lines, can be measured by the VUV monochromator as well.

The time evolution of line-of-sight integral radiance B_{pq} of the ions mentioned above was measured in Ohmic discharges of the CASTOR tokamak in several regimes, which differs in plasma current. The main discharge parameters were kept as possible the same during every set of measurements.

Absolute data of the main component of the MLM spectrometer, namely the filter transmissivity, mirror reflexivity and efficiency of the detector were available. The calibration coefficient was available also for the VUV monochromator. Consequently, the line radiance B_{pq} could be measured in absolute units (photon $\cdot$ cm^{-2} $\cdot$ s^{-1} $\cdot$ sr^{-1}).

4. Results

The concentration of Carbon and Oxygen were calculated using the model described above. A designed computer code uses the plasma density and signals of the MLM or VUV spectrometers from the tokamak database as input data and the electron temperature as a parameter. Since a direct measurement of the electron temperature was not available in this experiment, the temperature was evaluated from the experimental data of plasma current and loop voltage after Spitzer. The Spitzer temperature has varied from 150 eV to 300 eV, depending on the plasma current. The concentration of Carbon was derived

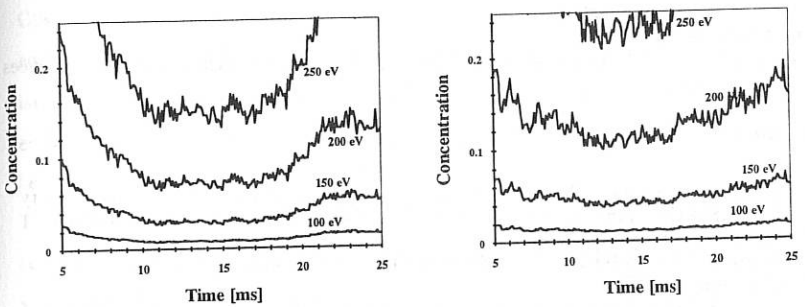


Figure 2: *Concentration of Carbon derived from VUV line C IV (left) and USX line C V (right).*

independently from the simultaneously measured radiances of resonant USX line C V (40.7 Å) and two resonant VUV lines of C IV (1549 Å) and C III (977 Å). An other VUV line C V (2271 Å) was measured, which doesn't origin from a resonant transition, but from the the transition 2s ^{3}S-2p ^{3}P.

In Fig.1a, the concentration of Carbon is shown which is derived from the USX line C V (40. 7 Å) radiance measurement. In Fig.1b, the Carbon concentration derived from the VUV line C IV (1549 Å) radiance is presented.

Comparing time evolution of the concentration in Fig.1a and Fig.1b, it seems that the best fit of the concentration comes for T_e= 150-200 eV. The best fitted value of Carbon concentration is 3-5% of electron density. The concentration derived from C III line (not shown) is higher by a factor 1.2 for all electron temperatures.

The concentration of Oxygen was derived from the USX line O VII (21.6 Å) and the VUV line O VI (1032 Å) radiances. The concentration of Oxygen, estimated in this experiment, was generally in one order less than the Carbon concentration. The Oxygen concentration of 0.5-1% is best fitted for electron temperature $T_e \leq$ 150 eV, while the Spitzer temperature was evaluated to be 230-300 eV.[1]

5. Conclusion

The line radiance of the Carbon and Oxygen ions was measured simultaneously in VUV and USX wavelength ranges.

The modelling of impurity ions radiation in coronal equilibrium enables the concentration of Carbon and Oxygen to be estimated (as a macroscopic quantity) from the measurement of line radiance, supposing parabolic profile of plasma density and temperature.

The evaluated concentration is in relatively good co-incidence although they are derived independently from line radiance of different ions and even for transitions with different atomic constant. The central electron temperature fitted in our computer code seems to be lower than is the temperature of thermal electrons.

A more sophisticated model including the impurity transport and supported by space resolved measurement of impurity radiation seems to be a way how to explain discrepancies in temperature dependence of the impurity concentration for different ions.

Acknowledgements
The work was partially supported by the Grant Agency of the Czech Academy of Sciences under No. A1043501.

References:

[1] R.Neu et al.: Influence of the Carbon and the Oxygen concentration on the density limit in ASDEX Upgrade, Proc. 21st Conf. on Contr. Fusion and Plasma Phys., Montpellier 1994, part 1, p.6
[2] TFR group: Line radiation in visible and ultraviolet in TFR tokamak plasma, Nucl.Fusion 15(1975)
[3] V.Piffl, J.Badalec et al.: Absolute measurements of light impurities line radiation using MLM-based spectrometer on CASTOR tokamak, Preprint IPPCZ-340, IPP Prague, June 1994

[1] It has to be noted that the temperature of thermal electrons can be substantially less than the Spitzer temperature, if the plasma current is partially driven by overthermal electrons.

High Resolution Spectroscopic Measurements of Impurity Radiation Distributions and Neutral Deuterium Profiles in the JET Scrape-off Layer.

P Breger, R W T König, C F Maggi, Z A Pietrzyk*, D D R Summers, H P Summers, M G von Hellermann

JET Joint Undertaking, Abingdon,Oxon,OX143EA,United Kingdom

* CRPP Lausanne, Switzerland

1. Introduction

A periscope has been installed to image visible radiation from the plasma scrape-off layer at the top of JET on 49 fibres with 0.45cm spatial resolution. 44 fibres are imaged on the entrance slit of an astigmatism-corrected low- resolution spectrometer to yield a line integrated spatial emission profile, 5 fibres are passed to a high resolution spectrometer. Abel inversion of CIII and CVI line intensity profiles identifies emission layer positions. Passive charge-exchange radiation of CVI (n=8-7) is used to determine the fast neutral deuterium density in the edge.

2. Emission Layer Determination

Observed line intensity profiles are linked to local emissivity layers by a set of 44 coupled equations. For the Abel inversion the flux range ψ=0.5 to 1.2 is subdivided into 25 equidistant layers in ψ-space. The numerical inversion is obtained by a) a best fit solution for 25 emissivities and b) by a fit of two gaussian emission distributions. The average agreement between measured and simulated profile is ~15%.

The Doppler shift from the Li I emission of a 60 keV Li-beam yields accurate vertical position coordinates. The full EFIT equilibrium is used to provide a pathlength distribution along the viewing lines in flux space.

3. The Location of the Edge : CIII Emission Profiles

CIII profile measurements were taken on a sequence of pulses from an elm-free H-mode campaign with 5MA plasma current, 3 T field with new Be-tiles in the JET divertor. Both EFIT equilibrium and XLOC boundary determination give magnetic separatrix heights at major radius R=3.252m within $\pm$ 2cm. This position of the magnetic boundary agrees with thermal Li emission (vertical injection at R=3.252). The CIII intensity profile (λ=465.0nm) for two viewing mirror positions has a max. in channels intercepting the beam trajectory at height

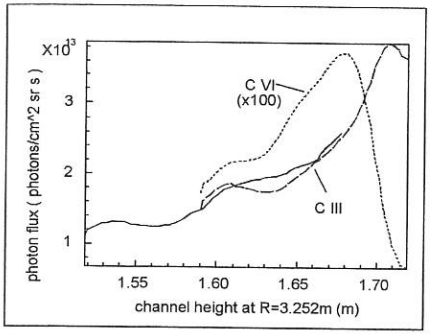


Fig. 1: Measured CIII intensity profile for two mirror positions. A CVI intensity profile is also shown.

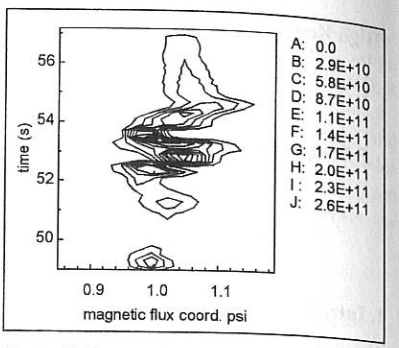


Fig. 2: Abel-inverted CIII emissivity distribution in photons/cm³ sr s

1.7m (Fig.1), corresponding to the viewing line with maximum pathlength in the separatrix layer. Abel-inversion results for the CIII emission are shown in Figs.2-3. The position of the CIII emission layer is at ψ=1.0. The observed movement is correlated to errors in the magnetic data. During onset of the heating phase, the width of the CIII shell drops, and increases with the onset of giant elms, when the total shell emission also increases. At the end of the ICRH heating phase, the width of the shell decreases by factor 4 .

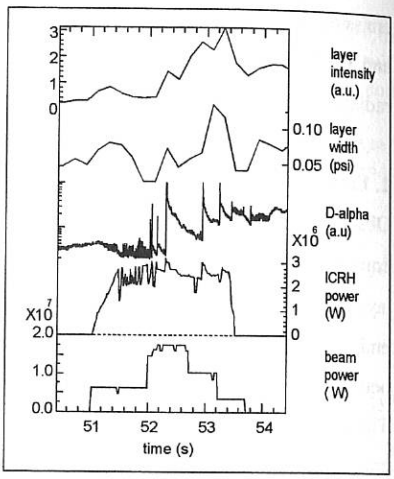


Fig.3: Time evolution of emission layer width and integrated layer intensity.

4. The "luke-warm" charge-exchange layer : CVI emission profiles

Plasma induced emission from CVI (λ=529.05nm) originates from two different emission layers : a "cold" feature (T_i~480 eV), corresponding to emission induced by electron collisions in the CVI ion shell, and a "luke-warm" feature (T_i~4keV) corresponding to cx-emission (see section 5). During high-performance hot-ion mode plasmas with 3.8 MA plasma current at 3.3T field, the passive cx feature is found by spectral line shape analysis to be 6 times more intense than the electron induced radiation. Because of errors in the magnetic data, the Abel inversion was done using an EFIT equilibrium shifted upwards by ~8.5cm (Figs. 4-5). The

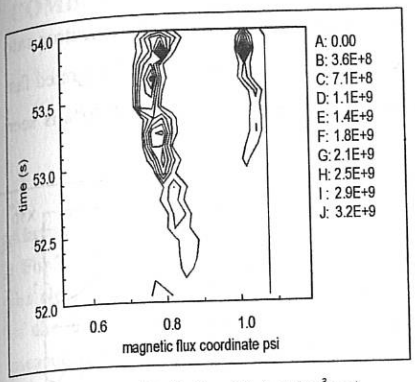


Fig.4: Emissivity distribution (photons/cm^{3}sr s)

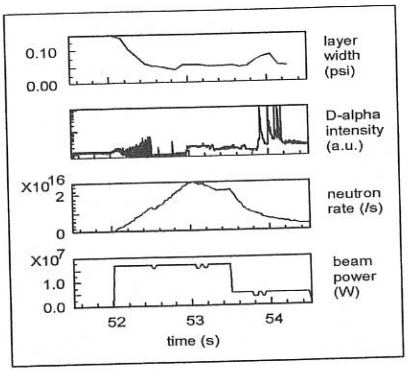


Fig 5: Time evolution of cx-emission layer width

relative spacing of layers was found to be insensitive to vertical shifts. The outside emissivity layer is placed at the separatrix and is interpreted as the electron induced component. The layer at ψ~0.8 is attributed to the charge-exchange induced feature.The motion of the outer layer is seen to correlate exactly with the difference in magnetic prediction of plasma separatrix position at R=3.252m. This is also the case when comparing the motion of thermal Li-beam emission regions with that of the magnetic boundary. Comparing the width of the emission layer with the heating beam power and the vertical D_α-signal, a decrease during the development of the H-mode, and increase during the giant elm phase is seen (Fig. 5).

5. The fast Neutral Deuterium Distribution

Fast deuterons near the plasma edge region collide with cold recycling neutral deuterium. Resonant charge-exchange occurs with some of this recycling deuterium before it is ionised. The D population fraction in the n=2 level will charge-exchange resonantly with C^{6+} to give rise to the hot CVI (n=8) radiating shell :

$$\varepsilon_{CX}(R) = n_C^{6+}(R) \cdot n_D^{n=2}(R) \cdot Q_{eff}^{CX}(CVI, n = 8-7)$$

The effective emission coefficient Q has been calculated for the range of electron temperatures and densities as measured by LIDAR. Ion-temperature and C^{6+} concentration profiles are obtained from the heating-beam cx-diagnostics. The fast deuterium temperature is taken to be the same as the local plasma temperature inside the confined plasma, outside it has been fixed at 5 eV. For the inner cx-layer, electron excitation processes can be neglected as a source of N=8-7 radiation. Using a collisional radiative population model (ADAS) the total fast neutral

deuterium is estimated. A particular point of interest in this shot is the premature neutron rate roll-over at 53s, which is accompanied by increased levels of D_α emission. The integrated fast deuterium density rises by 25% during the roll-over at 53s, and another rise of 40% is seen during the power step-down at 53.5s.

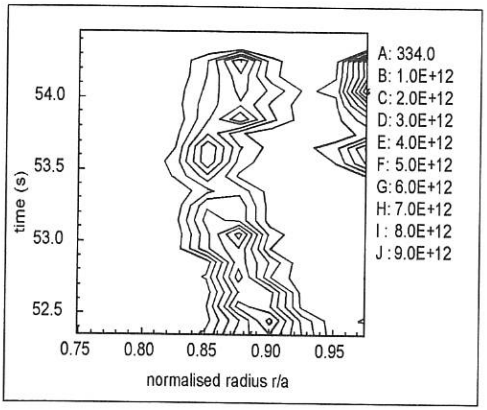


Fig. 6: Fast neutral deuterium density distribution in m^{-3}.

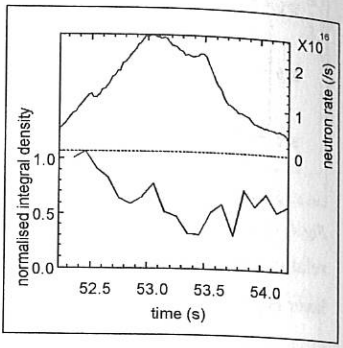


Fig. 7: Integrated deuterium density between r/a=0.8 and 0.94 compared to neutron rate

Although the neutral deuterium densities calculated at a depth of r/a=0.9 are rather small, the recycling cold deuterium which resonantly charge-exchanged with deuterons will have a much higher density, since the charge-exchange process has to compete with rapid ionisation.

7. Conclusions

- Passive intensity profiles may be used to identify the location plasma boundary location, and provide an independent means to verify positions from magnetic coil measurements.
- The existence of a hot charge-exchange induced layer interior to the plasma boundary was verified, and previous crude estimates of position and width could be substantiated.
- From the cx-emission layer a hot neutral deuterium density distribution could be calculated.
- Evidence for a neutral deuterium enhancement was found during the neutron rate roll-over phase.

We should like to thank the Swiss National Science Foundation for partially funding this work.

COMBINED MEASUREMENT OF THE ELECTRIC AND POLOIDAL MAGNETIC FIELD IN A TOKAMAK DEVICE

G. Bertschinger

Forschungszentrum Jülich, Ass. EURATOM-KFA 52425 Jülich, FRG

Abstract

For TEXTOR an active diagnostic is proposed to measure simultaneously the magnetic and the electric field. The method uses a molecular beam injected into the plasma. By analysis of the dissociation products the direction of the magnetic field and the electric field are measured. Using asymmetric molecules increases the resolution and allows to optimize the experiment for both measurements at the same time. In the plasma center it is expected to get a space resolution of 2.5 to 4.5 cm and a temporal resolution of .1 to 1 ms. The accuracy is 1.5% for the magnetic field and 36 V/cm for the electric field.

Introduction

In a hot plasma, the losses for electrons and ions are different. Even though originally quasi neutral, the different losses lead to a static plasma potential until the electrical field equalizes the confinement times of electrons and ions. So the plasma potential indirectly influences the confinement. It was shown that even the total confinement time can be changed by biasing the plasma edge. As the local transport coefficients depend on a variety of plasma parameters, the plasma potential or correspondingly the electric field has to be measured separately. In addition, changes in the magnetic structure of the tokamak induce transient electric fields. During the sawtooth crash, the transport is strongly enhanced and is expected to produce strong electric fields. Measurement of these electric fields with time resolution high enough to follow the dynamics of the sawtooth crash will give additional information on the process of reconnection of magnetic islands. The crash time is in the order of some 10^{-4} s and the width of the magnetic islands is some cm, therefore a time resolution well below 1 ms and a spatial resolution of a few cm is required.

Description of the method

The method was originally proposed by Jobes [1] to measure the magnetic field and was extended by W. Herrmann to measure the electric field [4].

A beam of diatomic molecules is injected into the plasma. In the plasma, the molecules are ionized. The ion gyrates around the guiding center of the local magnetic field. By collisions with the plasma electrons or ions, the molecular ion dissociates into a neutral and an ionized atom. After dissociation, the velocities of the ion and the atom are equal to the velocity of the molecular ion. The remaining neutral will follow the tangent to the Larmor cycle at the position of dissociation and can leave the plasma, the ion will be confined in the plasma. The

neutral is then detected in a neutral particle analyser. The analyser measures both the direction and the energy of the escaping neutrals.

If there is a potential difference along the gyration path, the molecular ion will change its energy. So the energy of the neutral depends on the difference of the electric potential between ionization and dissociation. For a symmetric molecule, e. g. hydrogen or deuterium, the energy of the escaping particle is half the beam energy. In an experiment where the molecular beam and the line of sight of the analyzer are perpendicular, the potential difference is measured over one gyro radius. For a hydrogen beam with an energy of 30 keV the Larmor radius is 1.6 cm in a magnetic field of 2.25 T. To measure potential differences in the range of a few tens of V, the resolution of the analyser has to be about 50 eV at an energy of 15 keV.

Accuracy of the measurement

In order to investigate the accuracy and the spatial and temporal resolution, we use a neutral beam of 1 mA and a diameter of 25 mm. The beam energy is between 20 keV and 35 keV, corresponding to the data of the Rutherford Scattering Experiment RUSC, until recently operated at TEXTOR by the FOM-Instituut voor Plasmafysica 'Rijnhuizen'.

For symmetric molecules the accuracy of the measurement of the magnetic field were analyzed by Herrmann [2] and by Afanasiev et. al. [3], of the electric field by Herrmann [4]. It was shown that the accuracy of the magnetic field measurement is independent of the mass, but increases with the beam energy, for the electric field measurement the accuracy is independent of energy but it is higher for higher mass. The Larmor radius increases with increasing mass and energy and the space resolution decreases. In a real experiment in a medium size tokamak the spatial resolution is mainly determined by the width of the neutral beam however.

The calculations of Herrmann [2,4] are extended to asymmetric molecules, e. g. HD, what can easily be produced in a ion source operated with a mixture of H_2 and D_2 gas. It is shown that for asymmetric molecules the resolution of both the magnetic and the electric field measurement is higher compared to symmetric H_2 or D_2 molecules. Using HD instead of H_2, D_2 is favorable for both measurements, whereas for symmetric molecules H_2 has to be used for the magnetic field measurement and D_2 for the electric field measurement. At the very edge, highly asymmetric molecules as CH or HCl can probably be used, further increasing the resolution.

Apart from spatial resolution, which depends on the width of the beam and the Larmor radius, the resolution is determined by molecular and atomic processes.
In the ion source, molecular ions are produced by electron collisions in a discharge. By properly choosing the discharge conditions, the fraction of molecular ions is maximized. The ions are then accelerated in an electrostatic gap and pass a neutralizer, filled with hydrogen or deuterium gas where they undergo charge exchange. In the plasma the fast neutral molecules are reionized, mainly by electron collisions or by charge exchange with plasma

ions. About 10 % of the molecules are ionized by collisions with protons. The dissociation of the molecular ion is mainly by electron and proton collisions. Finally the escaping neutral atom is ionized in a gas stripper, its energy is measured and it is detected by a channelplate detector.

On the way between the ion source and the detector, there are 4 conversions between ions and neutrals, and a dissociation process. Each conversion may change the energy and the direction of the particle. For the determination of the magnetic field, changes in the direction will decrease the accuracy of the experiment, changes in the energy will influence the measurement of the electric field.

The energy width of the ion source is about 10 eV, the energy loss by charge exchange and collisions by electrons is negligible. The main energy loss is due to stripping in the analyser and is measured to be below 50 eV. The energy loss is taken into account by a suitable calibration process, either by injecting the neutral beam into the discharge vessel filled with hydrogen gas and with applied toroidal field or by measurements in the plasma center where no electric field is expected.

Kinematic effects

The main broadening is due to kinematic effects in the dissociation process of the molecular ion. After ionization, the H_2^+ ion is in the ground state, higher states are unstable. The average excitation energy of the H_2^+ molecule in the dissociation process is about 8.6 eV which occurs in the frame of center of gravity. In the lab frame, the velocities of the particles in the center of gravity frame add to the velocity of the molecule in the center of gravity.

For a molecule with the masses m_1 and m_2 of its components, a kinetic energy E_0 of the molecule and a Franck-Condon energy Q, the energy change is maximum, if the velocity of the center of gravity and the dissociation are parallel. The full energy width of mass m_2 is then

$$\Delta E_{2FC} = \sqrt{\frac{4 E_0 Q m_1}{m_2}} = \sqrt{\frac{4 E_0 Q \mu_1}{\mu_2}} \quad \text{with } \mu_i = \frac{m_i}{m_p} \text{ the mass number of the particle i.}$$

The resolution of the electric field measurement depends on the ratio between the energy broadening due to Franck-Condon effect and the energy the particle gains by acceleration of the molecular ion in the electric field F over a Larmor radius ρ_l. The fraction α is the measurable shift of the maximum compared to the total energy width $\Delta E_{2\,FC}$ and is supposed to be 5% full width (10% FWHM). The detectable field is

$$F = \frac{\alpha}{e} \frac{\Delta E_{2FC}}{\rho_l} = \alpha B \sqrt{2 \frac{Q}{m_p}} * \sqrt{\frac{\mu_1}{\mu_2} \frac{1}{(\mu_1 + \mu_2)}} \,.$$

The ratio between broadening and Larmor radius is independent of the injection energy. Both

kinematic broadening and Larmor radius increase with the square root of injection energy. So the injection energy can be used for adjusting the spatial resolution. The kinematic broadening can be reduced by proper choice of the masses μ_i.

For the magnetic field measurement, the width is maximum if the directions of the molecule and the dissociation products are perpendicular. The maximum angular width is

$\delta = \sqrt{\frac{Q}{E_0}\frac{\mu_1}{\mu_2}}$ and decreases with increasing beam energy E_0 and asymmetry $\frac{\mu_2}{\mu_1}$ of the molecule.

Optimization using symmetric molecules requires H_2 for magnetic field measurement and D_2 for electric field measurement. With asymmetric molecules, the light particle will get more momentum than the heavy one reducing the energy width of the detected particle and allowing simultaneous optimization.

Expected data for the experiment at TEXTOR :

B_t	1.6	2.8 T
a	0.46 m	
$n_e(0)$	$1.*10^1$	$1.*10^{14}$ cm^{-3}
beam energy	30 keV	
beam current	1 mA	
count rate at detector (r=0)	10^7	10^6 s^{-1}
time resolution	10^{-4}	10^{-3} s
space resolution	2.5	4.5 cm

resolution of the electric field measurement (2.25 T)

H_2	D_2	HD
65 V/cm	46 V/cm	37 V/cm

resolution of the pitch angle measurement

H_2, D_2	HD
2 mrad (1.5 %)	1.5 mrad (1 %)

References

[1] F. C. Jobes 2nd Top. Conf. High Temp. Diagn. Santa Fe 1978

[2] W. Herrmann, Plasma Physics and Contr. Fusion 32, 8, (1990)

[3] Afanasiev V. I. et. al. Proposal to applying the active neutral particle diagnostic for current density measurement on tokamak TEXTOR Ioffe Physical-Technical Institute St. Petersburg(1992).

[4] W. Herrmann, 17th EPS Conference on Controlled Fusion and Plasma Heating, Amsterdam (1990), p. 1672

Determination of absolute metal impurity densities in Tore Supra

P.Platz , M.Mattioli and F.Sattin *

Association EURATOM-CEA, CE Cadarache
13108 St.Paul-lez-Durance, France
* Dipartimento di Ingegneria Elettrica, Università di Padova
35131 Padova, Italy

Introduction. On Tore Supra, high-resolution X-ray spectroscopy of the n=2-n=1 transitions in He- and Li-like ions of intrinsic impurities (Cr, Mn, Fe, Ni, Cu) is a standard diagnostic for electron and ion temperatures, and for the toroidal rotation velocity [1]. In this paper, we present a technique for the absolute calibration of our crystal spectrometer [2] which enables us to determine also the absolute densities of these impurity elements.

Basic relations. For any spectral feature, i.e. a line or an interval of the continuum , the count rate, r, of the detector is linked to the brightness, ε, of the source, by :

$$r\ [\text{counts/s}] = \eta\ [\text{counts/photon}] * C\ [\text{cm}^2\ \text{sr}] * \varepsilon\ [\text{photons/cm}^2\ \text{sr s}]$$

where $C = \tau_{Be} * \tau_{He} * hc * lc * Ri * hd / (R * \sin\Theta)$

Here η is the quantum efficiency of the detector, and C is the effective throughput. τ_{Be} and τ_{He} are the transmission factors of two Beryllium foils (each 0.027cm thick) and of the Helium in the spectrometer (total path length 590cm; pressure 1 atm), respectively. hc and lc are the height and length of the crystal, respectively. Ri is the integrated reflectivity of the crystal, and R the bending radius; hd is the height of the position-encoding proportionnal counter and Θ is the Bragg angle.
In principle, the η*C product may be calculated (Ccalc, in the following) with the data given in table I, probably with considerable uncertainty (transmission of Be at $\lambda \geq 3$Å, Ri, ...). It is the purpose of this paper to present, and to make the use of, an experimental procedure to determine η*C (Cexp, in the following).

Experiments. As will be explained in the following paragraph, Cexp is obtained from the continuum radiation (which is dominated by the filling gas and the light impurities). The line spectra from the metal impurities discussed here are superposed on this continuum, together with a parasitic background from neutrons, gammas and stray light. In order to get the true "spectral" continuum (ff + fb), we have placed a metal strip on the focussing circle (on the source side) producing an "absorption dip" which indicates the true continuum level we need. This is shown in Fig.1 and 2 for highly ionized Cr and Mn , respectively. The data we take from the spectra are the intensities of the (ff + fb)-continuum (counts/Å s) and of the n=2-n=1 transition, w, of the helium-like ion (counts/s). The Mn spectrum demonstrates the situation for an extremely low-density impurity.

Finally we notice that the measured continuum level is not affected by contributions from higher orders of diffraction, because both ε and Ri decrease with the photon energy.

Determination of Cexp (or r/ε) At any wavelength (visible or X), the brightness of the continuum is dominated by the ions from the working gas and from light impurities (carbon, oxygen). On Tore Supra, we have a Zeff - diagnostic based on an absolute measurement of the continuum in the visible, and an XUV spectrometer for the lines emitted by the C and O ions. Data from these two diagnostics are the input of an atomic physics and particle transport code [3,4], which calculates the radiation properties (lines and continuum) of the plasma. We therefore know the spectral brightness of the continuum at the wavelengths of the lines w of Cr22+, Mn23+ and Fe24+. The values of Cexp (=r/ε) thus obtained are given in the last column of Table I. For Cr and Fe, we have been able to apply the procedure to several discharges and time slices with ohmic and additional heating, and have found very little scatter for Cexp (5 % for Cr, 14% for Fe). Several factors may be responsible for the differences between Ccalc and Cexp (see table I). For Ccalc, for exemple, a possible candidate is the value of the integrated reflectivity, Ri, (calculated here following Hirsch and Ramachandran) which is not necessarily valid for a real, curved crystal. τ_{Be} has been calculated from the physical data and chemical composition of " typical" Be foils, and η from the photo-electric cross-section of the gas used for the proportional counter (80% Xe, 20% CO2; 1.5atm.).

Determination of absolute metal impurity densities. The code mentioned above also contains "test densities" for the metal impurities (at a level too low to affect the continuum) and calculates the corresponding brightnesses of the principal lines of the X-ray spectra (w, q, j). From the experiment we have got the absolute brightness of the line w (= r/Cexp), and thus obtained the absolute density of the impurity element by adjusting the test density.

In Fig.3 we show the results from two similar discharges with four pulses of LH additional heating (Bt=3.8T, Ip=0.6MA, nl=3 $10^{19}m^{-2}$) in which we have studied the densities of Fe and Cr. Notice the strong modulation of Te (between 2 and 4keV) and of the brightnesses of the continuum at 2.173Å and of the resonance line w of Cr22+ (similar modulations are seen on the features recorded for Fe, i.e. the continuum at 1.844Å and the line w of Fe24+). For the absolute density (in units of $10^{14}m^{-3}$) we have obtained values as low as 0.8 for Fe and 0.4 for Cr during the ohmic time slices, and up to 2.7 for Fe and 1.0 for Cr during the time slices with the LH additional heating.

In another type of discharges (Bt=3.7T, Ip=1.5MA, nl=6.6 $10^{19}m^{-2}$, ICRF at 1MW) we have studied Mn. With the data obtained from Fig.2, we have obtained a density of 0.25 $10^{14}m^{-3}$ during ICRF.

Minimum detectable impurity densities. The threshold for detection is given by the photon noise of the spectrum. If we consider a time resolution of a few seconds,

the spectrum shown in Fig.2, with 5000 + - 200 counts in the line w of Mn23+, may illustrate the minimum quality required. Inspecting Fig.1, with an excellent signal-to -noise ratio for the line w of Cr22+, we estimate that a much lower count rate for the line (say, 5 times lower) would also be quite acceptable. We conclude that for Cr and Mn the minimum detectable density in Tore-Supra plasmas with $T_e \geq 2$keV is of the order of $2\ 10^{13} m^{-3}$. For Fe, the same threshold needs a slightly higher temperature (≥ 2.5 keV).

Impurity transport and fractional ion densities. For the deduction of the total densities of Cr and Fe (nCr, nFe in the following) from the measured absolute brightnesses of the lines w (from the 2-electron ions), the fractional ion densities, i.e. the nature of the ionization equilibrium, must be known. It is interesting to check the impact of the latter on nCr and nFe. This approach is also suggested by the observed line intensity ratio Iq/Iw, always higher than expected (a similar discrepancy for Ni is discussed in [5]). For example, for Cr with LH additional heating (see Fig.1) we observe 0.2, rather than 0.1, indicating that the plasma is less ionized than expected from the standard transport model (diffusion coefficient D and inward convection velocity $v=r/a*V_A$).The origin of this "under -ionization" is not well understood, but it can be recovered by an appropriate modification of the coefficients D and V_A [4], or by adding charge exchange recombination (CX). In Table II we show the results from six runs with different coefficients, including standard or near standard (No 2,3,5) and unlikely (No 1,4, 6) ones. Obviously, the value of nCr is very little affected.

Conclusion We have measured absolute densities of Cr, Mn, and Fe with an absolutely calibrated crystal spectrometer. Minimum detectable densities are of the order of $2\ 10^{13} m^{-3}$.

References

[1] P.Platz, V.Basiuk , B.Saoutic, R.Arslanbekov, J.Carrasco, this conference
[2] P.Platz et al.; 20th EPS Conference, Lisbon 1993, Vol 17C, Part III,p.1083
[3] R.Guirlet et al.; 21st EPS Conf., Montpellier 1994, Vol.18B,Part III,p.1280
[4] M.Mattioli, C.DeMichelis, P.Monier-Garbet, Nucl.Fus., 1995, in press
[5] M.Bitter et al.; Phys.Rev. A; Vol.44, No 3, p.1796 (1991)

ion	λw [Å]	hkl	2d[Å]	τBe	τHe	Ri [rad]	η	Ccalc[*]	Cexp[*]
Cr 22+	2.1814	223	2.3604	0.56	0.92	1.24 e-5	0.95	8.5 e-7	10.8 e-7
Mn 23+	2.0061	312	2.1632	0.65	0.93	0.59 e-5	0.91	4.5 e-7	7.4 e-7
Fe 24+	1.8498	115	1.9792	0.55	0.96	0.65 e-5	0.82	3.9 e-7	2.80 e-7
hc = 2.3cm, lc = 4.5cm, hd = 4cm, RsinΘ = 295cm, * counts/(photon/cm^2 sr)									

Table I

Run	D	V_A	comment	Iq/Iw	nCr
	m^2/s	m/s			$10^{14} m^{-3}$
1	0.15	0.4	corona equilibrium	0.06	0.82
2	1.5	4	Tore Supra standard conditions	0.1	0.80
3	1.5	4	D and V_A divided by 10 for $r \leq 0.3*a$	0.07	0.90
4	1.5	4	with CX; central D° density = $5\ 10^{13} m^{-3}$	0.18	0.81
5	1.5	8	V_A = 2 times standard value	0.09	0.76
6	4.5	12	very fast inflow and diffusion	0.18	0.82

Table II

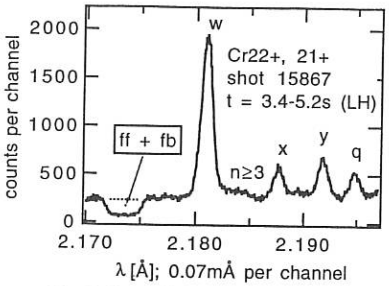


Fig.1 Partial Spectrum of Chromium

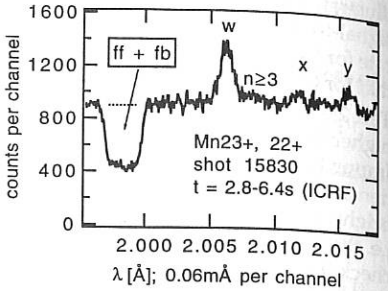
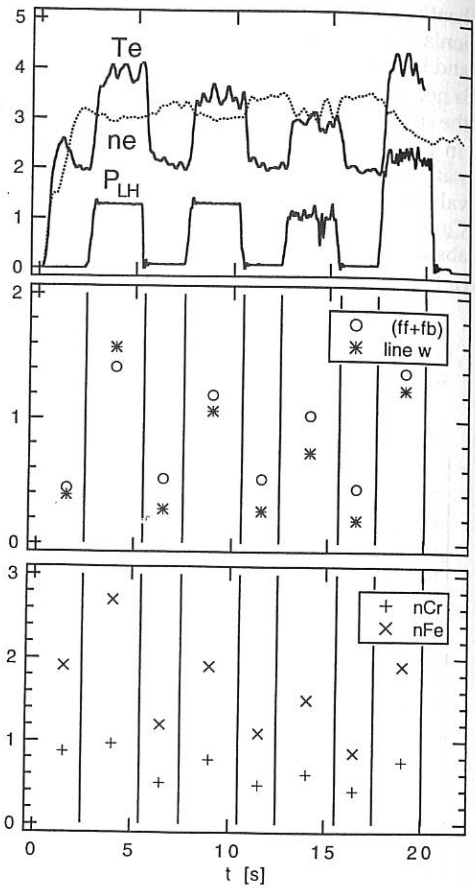


Fig.2 Partial Spectrum of Manganese

Fig.3a
Central Te [keV] , ne [10^{19} m^{-3}] and P_{LH} [MW] for shots 15865 and 15867

Fig.3b
Spectral brightness of the continuum [10^{6}counts/Ås] at 2.173Å, and brightness of line w [10^{4}counts/s] of Cr22+

Fig.3c
Absolute central densities [10^{14} m^{-3}], of Fe (shot 15865) and Cr (shot 15867)



Spectral and Angular Dependence of Photodiode Response to Soft X-Rays

M. Anton, M. J. Dutch and H. Weisen

Centre de Recherches en Physique des Plasmas, Association EURATOM - Confédération Suisse

École Polytechnique Fédérale de Lausanne, CH-1015 Lausanne, Switzerland

Introduction

Planar arrays of photodiode detectors for soft X-ray tomography on magnetic fusion devices have become very popular. They are economic and allow very compact camera designs. Unlike X-ray cameras based on single element detectors placed on a semicircle around the pinhole, the angle of incidence is different for each diode of such an array. Since uniformity of response is crucial for tomography we have investigated the effect and ways to compensate for it.

Modeling of pn-Photodiode Response

We adopt a simplified model [1, 2] to calculate the efficiency of n-type Si pn photodiodes[1]. Below the Si_3N_4–passivated surface the substrate of thickness D is strongly doped. Passivation and p+-zone form a dead layer of thickness d with a transmission $\tau = exp(-\alpha_d d)$. The probability $p(x)$ of detecting a charge generated within the depletion zone of thickness V is unity, whereas for charges generated at a distance x from the junction $p(x) = exp(-x/L_p)$. L_p is the diffusion length of the minority carriers. The responsivity equals $r = r_0 \times \tau \int \alpha \ \exp(-\alpha x)\ p(x)\ dx$. $r = r_0\eta$ where $r_0 = e_0/E_{e^- - hole} = 1/3.63\ AW^{-1}$. The efficiency η then is

$$\eta(\nu,\theta) = \tau[1 - \frac{\exp(-\alpha V)}{1+\alpha L_p}(1 + \alpha L_p \exp[-(\alpha + 1/L_p)(D-V)])], \quad \alpha = \frac{\alpha(\nu)}{\cos(\theta)}. \qquad (1)$$

Values of the absorption coefficients α were taken from [3]. For radiation with a spectral power distribution $w(\nu)$ (units $AW^{-1}Hz^{-1}$), we define a spectrum averaged efficiency $<\eta>$ as

$$<\eta> = \int \eta(\nu) w(\nu) d\nu / \int w(\nu) d\nu, \qquad (2)$$

$<\eta>$ multiplied by r_0 equals the photocurrent induced by $1W$ of radiation with a spectral distribution $w(\nu)$.

[1] In the following we always refer to CENTRONIC LD20-5T arrays in photoamperic mode, $D = 380\mu m$, $V = 3\mu m$ [4]

Determination of Diode Efficiencies from Angular Dependences

The spectral efficiency $\eta(\nu)$ can be determined from measurements of angular dependences of the diode signal using monochromatic light [5]. We have applied a similar approach using a commercial X-ray source. With the help of PHA-spectra of our X-ray source for $10kV$ and $30kV$ we were able to calculate $< \eta >$ as a function of the unknown parameters L_p and d, *i.e.* $< \eta >=< \eta(\theta, L_p, d) >$. Comparison of theoretical and experimental photodiode current densities j following

$$\frac{j_{diode}(50^o)}{j_{diode}(0^o)} = \frac{< \eta(50^o, L_p, d) >}{< \eta(0^o, L_p, d) >}. \qquad (3)$$

yielded approximate values of L_p and d. $\eta(\nu)$ is then determined by (1). Note that *only relative measurements* are required.

We have applied the method to CENTRONIC LD20-5T arrays which equip the soft X-ray cameras of the TCV tokamak. Typical diffusion lengths are $\approx 200\mu m$, the dead layer thickness varies between $0.5 - 0.8\mu m$. Details may be found in [6].

Angular Dependence of $< \eta >$ for Radiation from a Plasma

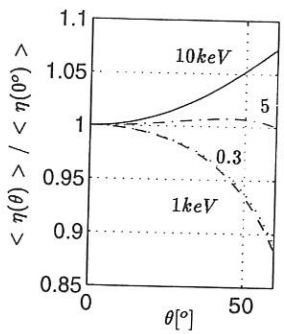


Figure 1: $< \eta(\theta) > / < \eta(0^o) >$ for $47\mu m$ curved Be, $L = 200\mu m$, $d = 0.5\mu m$

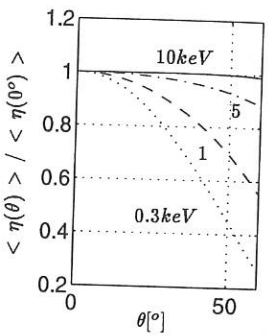


Figure 2: $< \eta(\theta) > / < \eta(0^o) >$ for $47\mu m$ flat Be, $L = 200\mu m$, $d = 0.5\mu m$

We have calculated $< \eta >$ as a function of the angle of incidence θ for soft X-rays from a thermal plasma using [7]

$$w(\nu) = \int_0^1 \frac{\exp(-h\nu/kT_e(\rho))}{\sqrt{kT_e(\rho)}}\, d\rho \quad \text{with} \quad T_e(\rho) = T_e(0) \times (1 - \rho^2) \qquad (4)$$

which is a reasonable fit to spectral distributions seen in many fusion devices. Figures 1 and 2 display $< \eta(\theta) > / < \eta(0^o) >$ for $kT_e(0) = 0.3, 1, 5, 10keV$. To obtain fig. 1, $w(\nu)$ was multiplied by the transmission factors of $47\mu m$ thick Be independent of θ. This corresponds to the soft x-ray cameras on TCV and ALCATOR C-mod which are equipped with curved Be foils. For fig. 2, the Be foil was assumed to be flat, *i.e.* the effective thickness varies like $1/\cos(\theta)$.

As a result, we see that the actual angle of incidence has to be taken into account for the calibration. Otherwise errors of up to 10% at $\theta = 60^o$ may result, even if the Be foil thickness is θ-independent. For a flat foil, errors may exceed 40%.

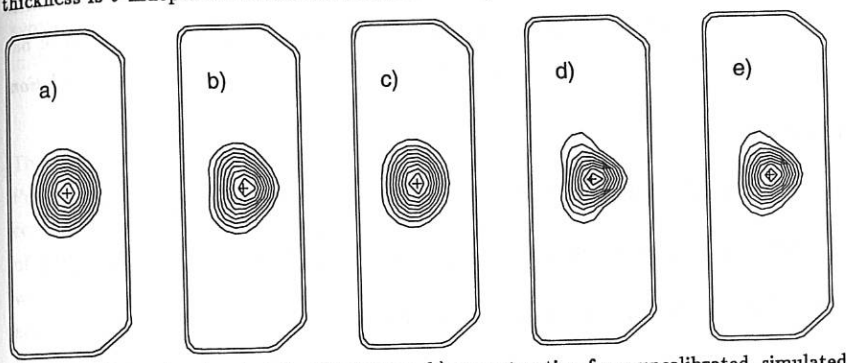


Figure 3: a) simulated emissivity distribution, b) reconstruction from uncalibrated, simulated data, c) from simulated, calibrated data, d)from experimental, uncalibrated data, e)from experimental, calibrated data. Calibration with $< \eta(\theta) >$. Granetz method, $\ell_{max} = 8, m_{max} = 3$

A more sophisticated approximation of the spectral distribution than (4) can be obtained using actual results from other diagnostics such as magnetics or Thomson scattering. We have simulated the spectral plasma emissivity of TCV discharge # 7067 at $t = 0.497s$, using the flux contours ψ from magnetic reconstruction, assuming a flat density profile and $T_e = 0.6keV \cdot \psi_{norm}^{0.8}$,where $\psi_{norm} = \psi/\psi_{axis}$. Fig 3 shows some examples of tomographic inversions using the Cormack-Granetz method [8] with $\ell_{max} = 8$ and $m_{max} = 3$. Part a) shows the simulated emissivity profile, b) is a reconstruction based on the simulated, uncalibrated detector signals, making use of the actual parameters D, d, V and L_p of the 180 diodes installed on TCV. Part c) shows a reconstruction using the same artificial dataset, calibrated with $< \eta >$, where $w(\nu)$ is taken from the simulation. Part

d) represents a reconstruction of uncalibrated, *experimental* data, for e) the experimental data were calibrated with the same factors as c).

Although this correction is possibly not yet sufficient (n-type Si photodiodes may become unstable, see [9]), the results displayed in fig. 3 clearly show that a calibration using $< \eta(\theta) >$ improves the accuracy of the tomographic reconstruction.

Acknowledgements

We gratefully acknowledge fruitful discussions with *Roland Payne* from CENTRONIC as well as the communication of LD20-5T specifications. We also thank *Thierry Buchillier* and the 'Institut de Radiophysique Appliquée', Lausanne, for providing spectra of our X-ray source. This work was partly supported by the *Swiss National Science Foundation*.

References

[1] *KINGSTON, R H:* 'Detection of Optical & Infrared Radiation' Springer (1978)

[2] *SZE, S M:* 'Physics of Semiconductor Devices', 2nd ed. Wiley, New York (1981)

[3] *VEIGELE, W M J:* Atomic Data **5**, No. 1 (1973)

[4] *CENTRONIC:* main catalogue and private communication

[5] *KRUMREY, M and TEGELER, E:* Rev. Sci. Inst. **63** (1) (1992)

[6] *ANTON, M, DUTCH, M J and WEISEN, H:* Rev. Sci. Inst., probably July (1995)

[7] *MIYAMOTO, K:* 'Plasma Physics for Nuclear Fusion', MIT Press (1976)

[8] *GRANETZ, R S and SMEULDERS, P:* Nuclear Fusion **28** 3 (1989)

[9] *TEGELER, E and KRUMREY, M:* Nucl. Inst. Meth. **A 282** 701 (1989)

Ultra-soft X-ray Spectroscopy using multilayer mirrors on TCV

H. Weisen*, V. Piffl+, A. Krejci+, J. Moravec+, J. Raus+, M. Dutch* and P. Paris*
*Centre de Recherches en Physique des Plasmas, Association EURATOM-Suisse
Ecole Polytechnique Fédérale de Lausanne, 1015 Lausanne, Switzerland
+Institute of Plasma Physics, Czech Academy, Prague, Czech Republic

The TCV tokamak has recently been equipped with an ultrasoft X-ray multichromator allowing low resolution ($\lambda/\Delta\lambda \approx 30$) measurements in the energy range 200-800 eV. Its purpose is to monitor emission from the main resonance lines of highly ionized light impurities such as Boron, Carbon and Oxygen. Wavelength selectivity is achieved by synthetic multilayer mirrors (MLM) [1,2] having 30-40 alternate layers with layer periods in the range 30 to 70Å depending on the wavelength range to be investigated.

1. Spectrometer design

The spectrometer developed at the IPP Prague is of the θ-2θ design (fig. 1). The centre wavelength of each of the 4 channels of the device can be independently adjusted while maintaining alignement. This is achieved by mechanically coupling the mirror incidence angle and position, as well as the detector orientation. The channeltron dectectors are housed in a cylindrical soft iron magnetic shield with a total thickness of 4 cm to guard them from the poloidal fields (~0.1 T) at its location 1.5 m above the TCV vacuum vessel. Russian type VEU-6 channeltrons with a gain of 10^7 and a maximum count rate of 0.5 MHz are used with tungsten photon-electron converters biased to -400 V at the channeltron input. Although this leads to a approximately four-fold reduction in overall sensitivity as compared to an open channeltron, it has the advantage of a uniform response accross the detector surface.

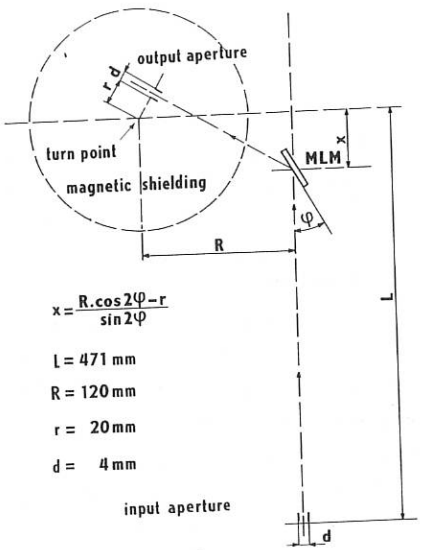


Fig. 1. Geometry of ultra-soft X-ray multichromator. Detectors are inside the magnetic shielding outlined by the broken circle. Separation from the TCV vacuum is achieved by polymer foils placed below the input aperture.

Pulse shaping electronics are included in the channeltron package. The flat multilayer

mirrors were fabricated at the Institute of Applied Physics, Nizhnij Novgorod, Russia. The four channels of the device use different mirrors optimized for the ranges 200-300, 300-400, 400-500 and 500-800 eV respectively.

The vacuum of the apparatus is separated from the TCV vacuum by 0.3 μm thick polymer foils supported by silicon grids[3] which withstand pressures in excess of 1 bar and have acceptable absorption in the energy range of interest. We found that transmission of undesirable VUV radiation through the polymer window was still significant, as indicated by radiation spikes at breakdown and during plasma termination. Thin (0.2μm) film metal filters have therefore been inserted between the polymer vacuum window and the entrance aperture of the instrument. The characteristics of the components were measured at the IOFFE Institute in St. Petersburg, Russia and are summarized in table 1 for the energies corresponding to the strongest lines from hydrogen-like stages of B,C,N and O.

Table 1. Characteristics of spectrometer components at 4 typical photon energies

E (eV)	ΔE (eV)	R_{MLM}	T_{window}	Filter	T_{filter}	η_{chan}
255	15	0.23	0.45	Ag	0.062	$3.3 \cdot 10^{-3}$
367	13	0.12	0.26	Ag	0.125	$5.7 \cdot 10^{-3}$
501	32	0.13	0.46	Sn	0.12	$6.7 \cdot 10^{-3}$
654	22	0.10	0.53	Ni/C	0.38	$6.3 \cdot 10^{-3}$

The throughput defined as $\xi = A\Omega \cdot T_{filter} \cdot T_{window} \cdot R_{MLM} \cdot \eta_{chan} \Delta E$, is shown as a function of photon energy in fig. 2, where $A\Omega$ is the étendue of the instrument, T stands for transmission, R_{MLM} is the mirror peak reflectivity, η_{chan} the channeltron quantum efficiency and ΔE the energy resolution.

2) Results

The vertically viewing instrument is placed slightly outside the magnetic axis position, with viewing lines crossing the plasma midplane at r/a~0.4. This is not a limitation since most of the line radiation investigated originates from the plasma periphery. Normally the instrument is left to monitor a selected set of lines. Typical count rates for Carbon are 50 kHz in L-modes and 200 kHz in H-modes. In a demonstration experiment a spectrum over the full range was built up in a series of reproducible discharges in L-mode with the following parameters: B_T=1.43 T, Ip = 400 kA, $\langle n_e \rangle \approx 5 \cdot 10^{19} m^{-3}$, R=0.89m, a = 0.24 cm, κ=1.5, Te(0) ≈ 600 eV. The discharges were limited on carbon tiles covering the inner wall. The results in fig. 3 are averages over the ~1 s flat-top of the discharges and show clear peaks at the energies of the main lines of BIV (206 eV), BV (255 eV), CV(308 eV), CVI (367 eV), OVII (574 eV) and OVIII (654 eV). The vessel had not been boronized since the last shut-down when approximately half of the carbon tiles had been replaced. The Boron detected was a remnant from the inner wall tiles which had not been replaced. No Nitrogen or Iron lines were positively identified.

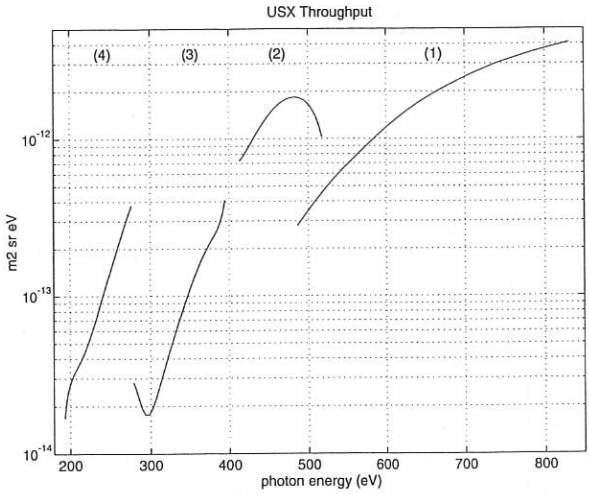


Fig.2. Throughput of the 4 channels of MLM based multichromator

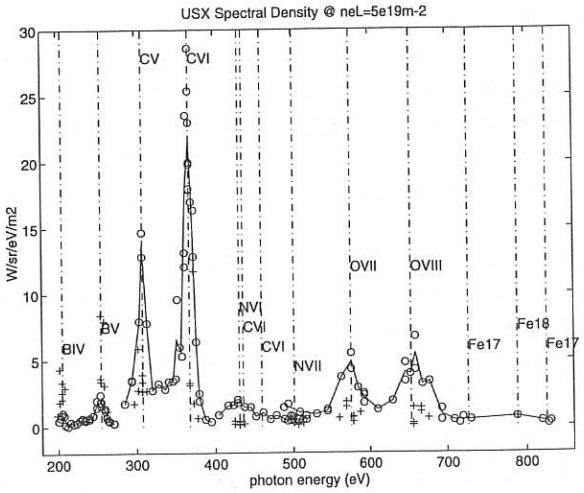


Fig.3 Ultra-soft X-ray spectrum obtained by a shot-to-shot scan of photon energy.

The main lines were revisited a few days (70 discharges) after a fresh boronization ('+' symbols on fig.3). Unfortunately these discharges were not very reproducible and not identical to those of the spectral scan. Oxygen signals were reduced by a factor of 5, Carbon signals by a factor of 2-4, Boron was enhanced by a factor of 2-4.

For the first 50 discharges following the boronisation the Boron signals remained one order-of magnitude above their pre-boronization levels. During the first few shots the impurity concentration estimated from X-rays emitted from the plasma core[4] was nearly a factor of 2 above its pre-boronization level despite a five-fold reduction in Oxygen and Carbon. This is attributed to Boron being substituted to Carbon as the main light impurity immediately following a boronization. An exact evaluation of the effect of boronization is not possible with the presently available data, because impurity signals are also observed to be sensitive to the very variable operating conditions in TCV, with different wall areas being exposed to the plasma at different times.

Since absolute transmission and sensitivity data are available for all of the components a determination of absolute impurity levels is possible if coronal equilibrium can be assumed. For the discharges use in fig. 3 (before boronization) the absolute line emission from hydrogen like impurity ions is consistent with coronal equilibrium modelled using the IONEQ[5] code for $n_C/n_e \sim 2\%$, $n_B/n_e \sim 1\%$ and $n_O/n_e \sim 0.1\%$. However the ratio of intensity from the helium-like lines (such as CV at 308 eV) to the hydrogen like lines (such as CVI at 367 eV) is several times larger than expected from coronal equilibrium. This observation may be explained by inward transport of ions where the higher electron temperature leads to strongly enhanced excitation rates before ionisation to the next stage takes place. Preliminary IONEQ calculations using diffusion coefficients of a few m^2/s are in qualitative agreement with our observations. The above concentrations, which together add up to $Z_{eff} \sim 1.9$ are therefore likely to be overestimates. This is corroborated by the above mentionned X-ray (E>1.5 keV) measurements which are mainly sensitive to fully ionized impurities in the core and are consistent with $Z_{eff} \leq 1.2$.

To conclude, the use of multilayer mirrors for spectroscopic measurements in the ultra-soft X-ray region allows the measurement of line emission from highly ionised light impurities in a way which is similar to the popular filter methods in the visible wavelength range for lower ionisation stages. Present results indicate that even helium-like and hydrogen-like ionization stages of light impurities are not in coronal equilibrium in TCV. It may be worth investigating the neutron resistance of MLMs since they may open up new diagnostics possibilities for the next generation of large fusion research devices.

Acknowledgements: This work was partly supported by the Fonds National Suisse de la Recherche Scientifique. The help of many colleages is gratefully acknowledged.

References:

[1] A P Zwicker, M Regan, M Finkenthal & H W Moss, Rev.Sci.Instrum 61 (1990) 2786
[2] V Piffl, J Badalec, AV Golubev, SV Bobashev, report IPPCZ-340, IPP Prague (1994)
[3] MOXTEK Inc. Orem 452W 1260N,Utah 84057, USA
[4] H Weisen, D Pasini, A Weller & AW Edwards, Rev. Sci. Instrum 62 (1991), 1531.
[5] Courtesy of A. Weller, IPP Garching, Germany

INTERPRETATION OF CHARGE EXCHANGE SPECTRA EMITTED BY FAST ^{3}HE DURING EXPERIMENTS ON TRANSPORT CONTROL BY ICRH ON TEXTOR.

G. Van Wassenhove[1], R. Koch[1], H. Euringer[2], K.H. Finken[2], D. Van Eester[1]

(1) Laboratoire de Physique des Plasmas -Laboratorium voor Plasmafysica,
Association "Euratom-Belgian State",
Ecole Royale Militaire-Koninklijke Militaire School
B-1040 Brussels, Belgium

(2) Institut für Plasmaphysik, Forschungszentrum Jülich,
GmbH Association "Euratom-KFA",
D-5170 Jülich, FRG.

1. Introduction

A method has been proposed by Chang [1,2] to expel the lower energy part of the fast α particle population in a reactor using off-axis RF heating. This method was tested on TEXTOR with RF heating at the second harmonic of fast $^3He^{++}$ ions produced by beam injection [3,4]. The experimental situation is presented in fig. 1. The co-injector injects 0.8 MW of 40 keV ^{3}He, the counter-injector injects 0.8 MW of 50 keV D. Two RF antennae are coupling a power up to 1 MW into the plasma. The toroidal magnetic field is varied between 1.7 and 2.1 T to move the RF heating layer from high to low field side. According to theory, for the experimental situation of fig. 1, 0.5 to 1 MW of RF power coupled to ^{3}He at high field side produces an outward flux of fast ^{3}He comparable to the NBI fuelling rate. Conversely, low field side heating produces an inward flux while central heating produces no net flux. Fast $^3He^{++}$ ion population is measured using charge exchange spectroscopy with injected D atoms and spectra are compared to a theoretical modelling of He II (n=4→3) light emission .

2. The spectroscopic measurements

The light emitted by He II (n=4→3) is observed using a ten lines of sight spectrometer. The 10 chords are located in the equatorial plane at 30 (outboard), 26, 20,16,11,8,4,0,-2,-6 cm (inboard) from the machine axis. The light is focused on ten quartz fibres and transmitted to a spectrometer with Lithrow mounting used in conjunction with a 2D camera. The spectral resolution is 0.15 Å/pixel at this wavelength and the time resolution of the measurement is 100 ms. The spectra measured along the 10 chords are presented in fig.2 and 3. The former series of spectra is measured with only helium beam (without D beam) . A significant level of signal is observed which can be explained by an important fraction of injected $^3He^0$ ionised to $^3He^+$ which survives in this state for more than one toroidal revolution. During its survival time, it undergoes collisional excitation and emits P_α light. We call this signal spontaneous emission (SE) signal. The second series is obtained when the deuterium beam is switched on and provides D neutrals for charge exchange with He^{++} in the observation region.

2. Modelling of the spontaneous emission (SE)

We evaluate the signal intensity linked to spontaneous emission by the He^+ ions starting from the NBI deposition profile computed using the exact TEXTOR plasma geometry including the Shafranov shift and the spatial distribution of the injected neutrals (code DEPON). This deposition profile is used as initial conditions for a drift-orbit tracing code that follows the trajectory of sets of injected $^3He^+$ ions. Along each orbit we take into account the attenuation of the intensity of the $^3He^+$ due to ionisation by the electrons and charge exchange with D^+ and He^{++}. We followed the trajectories during 4 turns around the torus, the excitation probability of each set of ions in the viewing lines giving the rate of light emission . To calculate the Doppler shift of the emission we estimate the projection of the velocity of the $^3He^{+*}$ ion in the observation line, knowing the component of the velocity parallel to the magnetic field and averaging over all possible directions of the perpendicular velocity. All contributions of the individual sample ions are summed. The deformation of the spectrum due to the instrumental width of the spectrometer is also included. Examples of simulated spectra are given in fig. 2. Maximum Doppler shift of the line for an energy of the $^3He^0$ of 40 keV is 24.9 Å. The Doppler shift is due to the velocity v_l in observation line which is related to the parameters of the trajectory via:

$$\frac{v_l}{v_i} = \cos \chi_i \cos (\beta)$$

where v_i is the velocity and χ_i the pitch angle of injected He^0 at the position of the first ionisation and β is the angle between magnetic field and direction of observation at the position of light emission.The average value of χ_i is of the order of 15°. The value of β depends on the observation channel and his average value is increasing when we go from the outer to the inner part of the torus. In this simulation, we neglect the impact of Stark and Zeeman effects. The enlargement of the line due to these effects would be respectively of the order of 1 Å for the Stark effect and of the order of 0.5 Å for the Zeeman effect. We also neglect the scattering of the He^+. When comparing the experimental spectra with the calculated one (without any adjustable parameter in the model) we observe that the evolution of the spectra from one line of sight to the other one is well reproduced. The peaks on the central channels are broader than outboard. The relative maximum intensity from channel to channel is also well described. To simulate the time evolution of the spectra during a discharge, we will suppose that the unavoidable density increase during the shot in presence of helium injection is due to helium. The charge exchange between He^+ and He^{++} contributes strongly to the attenuation of the He^+ beam and the model reproduce quite well the reduction of the intensity observed [3] experimentally . The presence of a tail at low wavelength in the experimental spectra is not well explained by the model. The attenuation of this tail with increasing density is exactly proportional to the attenuation of the main peak, which may suggest that this tail is also due to the light emitted by He^+ due to the neutrals ionised only once. A possible explanation is the presence in the beam of metastable component ionised very easily, deposited at large χ_i.

3. The charge exchange spectra

To simulate the CX signal we must estimate the radial dependence of the velocity distribution function of the beam ions. To evaluate the slowing down distribution function in absence of ICRH we develop it in Legendre polynomials [5],the coefficients of the development being a function of χ_i at the position of first ionisation. Using the power deposition profile calculated with the DEPON code we add, for a given r, the contributions coming from the different χ_i. With this velocity distribution function, following the method described by von Hellermann [6] we evaluate the expected slowing down charge exchange spectrum. The results are presented in fig. 4 for the two different plasma conditions. The mean radius of the charge exchange signal is varying from 44 cm to -8cm.The maximum of CX signal at low wavelength is due to the maximum in the effective emission rate at 37 keV/amu .

Before comparing theoretical predictions and experiment, we must subtract the SE component from the measured spectrum. Due to the well-understood density dependence of this component, we correct the spectrum taking into account the density dependence of the spontaneous emission. The profiles before and after correction are compared in fig. 3. The evolution of the spectra with wavelength and the ratio of intensity from one line of sight to the other one is rather well described by the model in the central region. A theoretical underestimation of the emission is observed on the outer channel which may be explained since we neglect diffusion but also by an underestimation of the power deposited at high radius. The presence of ICRH does not strongly modify the shape of observed spectra but modifies quite strongly the intensity of the light emitted. We also present in fig. 5 the ratio of the spectra obtained when the heating layer is moved from the centre to the high field side. Plasma conditions for the two situations are not completely similar. Taking into account this change in the conditions we find that, out of the ≈35% change in light intensity in the most central channel, 20% are explained by the change in plasma conditions (reflected by the differences between the two simulations presented in fig 4) while the remaining 15 per cent is the true effect of ICRH. This corroborates the earlier analysis of the intensity changes in the innermost channels [3].

4. Conclusions

To interpret the charge exchange signal measured during RF control experiment it is necessary to correct the measured spectra to take into account of the light emitted by the not yet completely ionised ions of the beam. A modelling of that signal and of the CX signal was performed. The new analysis of the experimental results confirms the role played by off-axis ICRH heating in the control of the helium beam slowing down population.

Aknowledgement

We want to thanks Dr J.D. Hey for helpfull discussions about the importance of Zeeman effect.

References

[1] C.S. Chang, Phys. Fluids B3, 259-261 (1991).
[2] C.S. Chang, J.-Y. Lee and H. Weitzner, Phys. Fluids B3, 3429-3447 (1991).
[3] K. H. Finken et al, Phys. Rev. Letters 73 (3),436-439 (1994).
[4] R. Koch et al, 15th Int. Conf. on Plasma Physics and Contr. Nuclear Fusion Research, Seville, IAEA-CN-60/A3/5-P-8,1994.
[5] J.D. Gaffey Jr, J. Plasma Physics, 16(2),149-169(1976).
[6] M. G. von Hellermann et al, Plasma Phys. and Contr. Fusion 35(7),799(1993).

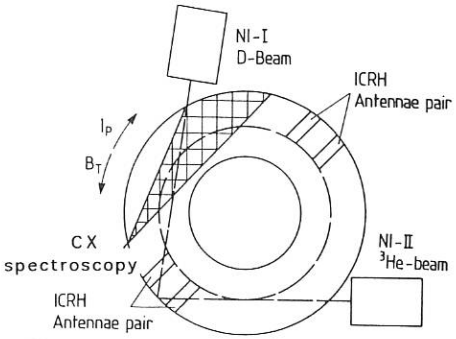


Fig. 1 Configuration of the ^{3}He flux control experiment on TEXTOR.

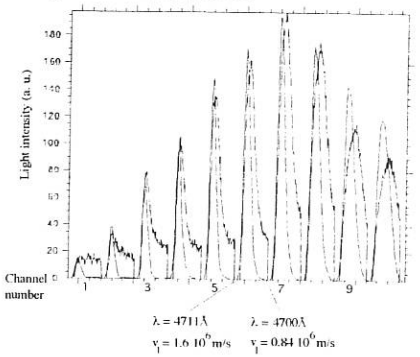
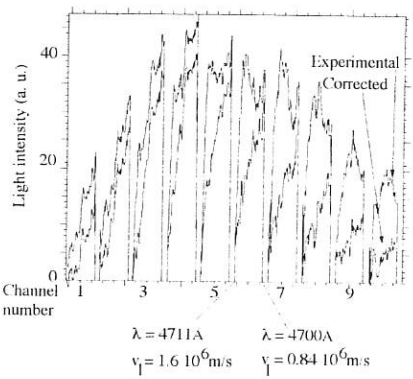


Fig. 2 Experimental and modelled wavelength spectra along the 10 chords from 30 cm outboard (channel 1) of the magnetic axis to -6cm inboard (channel 10) with the ^{3}He beam only (no D beam).



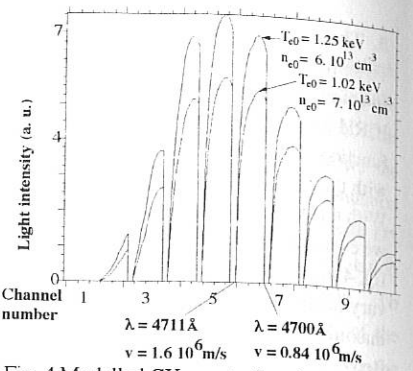


Fig. 4 Modelled CX spectra for channel 1 to 10 (positions: see fig. 3) for 2 plasma conditions

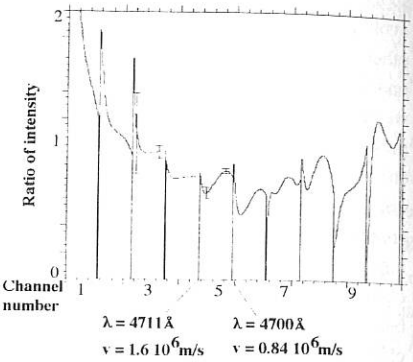


Fig. 5 Ratio of experimental CX spectra with the RF layer displaced to the inner side of the machine to the spectra taken with the layer in the centre.

Fig. 3 Experimental wavelength spectra along the same 10 chords, with the ^{3}He and D beam. The plasma radius of intersection of the viewing line with the center of the beam for channel 1 through 10 is r=44.5 cm (outboard), 30, 21.5, 14 , 8, 3, -1, -4, -6, -8cm (inboard).
The same spectra corrected for SE signal.

Use of Heated, Diagnostic Optical Fiber for the Suppression of Transmission Loss during D-T TFTR Discharges

W Tighe, A T Ramsey, P D Morgan[1)], H G Adler[2)], D L Griscom[3)], and **D W Johnson**

Princeton University, Plasma Physics Laboratory,

P O Box 451, Princeton N J 08543.

1) JET Joint Undertaking, UK. 2) Osram/Sylv. Labs, MA, USA. 3) NRL, Wash., D.C., USA.

1. Introduction and Motivation

There have been many studies characterizing the behavior of optical fiber in nuclear environments[1]. Increased absorption and induced luminescence occur when the fiber is exposed to ionizing radiation[2]. Similar effects are seen in tokamak discharges[3,4]. Increased neutron flux during D-T discharges (with tritium injected by the neutral beams) strongly enhances the absorption and luminescence. On devices using tritium, TFTR (Tokamak Fusion Test Reactor) and JET (Joint European Torus), there are indications that data may be compromised. For future devices such as TPX and ITER, there is a need to address these issues, their avoidance or compensation, so that fiber based systems can operate[5].

Transmission loss can be transient and permanent. Transient loss shows recovery, often described by a "stretched exponential" [6], to pre-irradiation levels on short time scales. Mechanisms for transmission loss have been suggested[7] and involve impurity or defect related arrays of short-lived color centers. Annealing has been found to remove some or all of the incurred damage [8]. It has been shown that some defects may be permanently removed through radiation hardening[9]. We present results from a study evaluating the use of elevated temperature to reduce transmission loss in optical fiber during D-T discharges on TFTR.

2. Experimental Setup.

Details of the experimental arrangement have been given elsewhere [10]. To enhance the effects of neutron irradiation, long lengths of fiber (155 m), were coiled into loops ~30 cm in diameter. All silica, aluminum jacketed, 600 μm core diameter fibers were wrapped in heating tape and placed in insulating ovens in proximity to the TFTR device. Source and detectors were located in experimental areas neighboring the tokamak test cell and light carried to and from the test fiber loop using lead-in/lead-out fiber. Source light was passed through a chopper wheel rotating at 1200 rpm, consisting of two segments; one being variably filtered (400 - 700 nm), the other blocking the source for luminescence measurements. The detector consisted of either an array of photomultiplier tubes (PMTs) or a 1/4 m spectrometer with a CCD detector. The contribution of the lead fibers was determined by connecting a set without a test loop. The source intensity was constantly monitored and the data were corrected for any variations.

3. Results.

3.1. Transient Transmission Loss and Luminescence

Fig. 1 shows the transmission through three optical fibers loops measured simultaneously on a single discharge. While there is some variation in the response to the neutron event, both

unheated fibers (from different preforms) show a precipitous drop as the event starts, following the integrated neutron flux closely. Over the range available in this study, the transmission loss was found to be linear with the neutron yield, allowing normalization to this as well as the fiber length. The neutron yield ranged from 5. x 10^{16} to 2.2 x 10^{18}, with a corresponding flux at the fiber loop location of 1.0 x 10^{8} to 4.4 x 10^{9} n/cm^2.

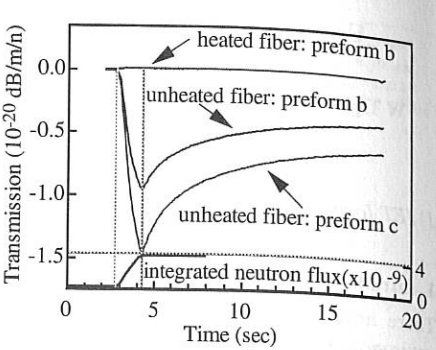


Fig. 1. Time history of transmission during a D-T discharge (#76504). The data are integrated spectrally. The neutron flux reached 4x10^9 n/cm^2.

A careful accounting of the contribution of the lead fibers and interpolation of the luminescence data allowed these factors to be removed from the transmission signal. Over 10 discharges, the peak loss in the heated fiber was $(-0.0013 \pm 0.010)\ x10^{-20}$ dB/m/n while the unheated fiber from an identical preform suffered $(1.00 \pm 0.05)\ x10^{-20}$ dB/m/n loss. The observed loss in the heated fiber is, therefore, determined by the error bar. This implies an improvement of >100x by heating the optical fiber. Recovery begins immediately after the irradiation. It is well described by a "stretched" exponential, $\exp[-(t/\tau)^{\alpha}]$, where $\tau = 0.26\ s \pm 0.06$ and $\alpha = 0.21 \pm 0.01$.

The spectral dependence of the transmission loss was investigated. Stray light and the strong absorption of the test fiber limited the useful spectral range to 500 - 700 nm. A logarithmic ratio of the spectra was taken with the background, but not the lead fiber contributions, removed. Results of this ratio, $10 \cdot \log(T_1/T_2)$, where $T_1(\lambda)$ is the spectral transmission taken before exposure and $T_2(\lambda)$ is the transmission taken immediately after, are shown in Fig. 2. The very strong wavelength dependence was consistent throughout the data set.

The data fit a $1/\lambda^4$ dependence very well which is what one might expect from enhanced Rayleigh scattering [11] from point source defects. The fit is over a limited spectral range and the data may instead be described by the tail of a gaussian from an impurity band centered near 3500 Å and ~200 nm wide. This fit, not shown, is also very good. There is little reason to expect Rayleigh scattering to change dramatically with temperature and an impurity mechanism would more readily explain the observed

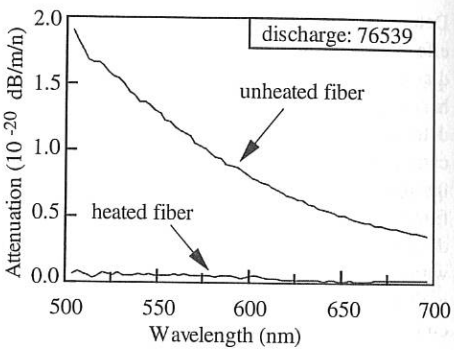


Fig. 2. The ratio of transmission spectra taken before and after the neutron event for both the heated and unheated fibers. The data are averaged over 1 second windows.

decrease in attenuation with heating. There is, furthermore, evidence that a chlorine impurity [12] exists in this region. More data are required at shorter wavelengths to positively identify the loss mechanism.

The time history of the luminescence, corrected for transmission loss [13], clearly followed the neutron rate during the D-T discharge. With the heated fiber, the luminescence spectra had a distinct $1/\lambda^2$ dependence. This, along with the observed time history, provides strong evidence that Cerenkov radiation is the primary source of luminescence. Fig. 4 shows the total luminescence level as the fiber coil was heated from room temperature to 400° C. There is a small, systematic drop with temperature indicating a weak, additional radioluminescent component. Also there is a slightly weaker wavelength dependence seen with the unheated fiber.

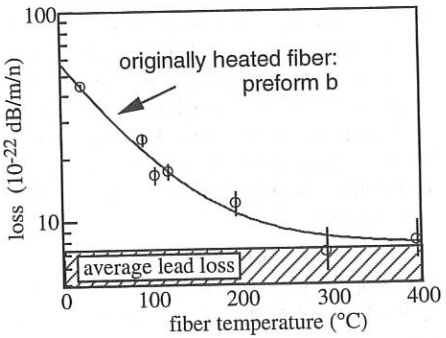


Fig. 3. The temperature dependence of the transmission loss for one of the fibers used in the heated fiber study.

While it is a clear that transient loss can be significantly suppressed by maintaining the fiber at an elevated temperature, the required temperature may depend on the fiber type and the exposure history. Fig. 3 shows the dependence of the susceptibility of one of the test fibers on operating temperature. The largest improvement in transmission occurs as the ambient temperature was raised from room temperature to 250° C. Variation in this dependence was found even among fibers of the same type, from differing preforms.

Two sources of luminescence were examined: radioluminescence[14] from recombination radiation in neutron-induced damage centers and Cerenkov radiation [15] due to high energy electrons propagating through the fiber faster than the speed of light. Cerenkov radiation should display a distinct spectral signature ($1/\lambda^2$), follow the radiation time history, and be insensitive to operating temperature. Radioluminescence from damage centers should be reduced and possibly eliminated in the heated fiber.

3.2 Long Term Loss and Annealing

Following some 30 D-T discharges a comparison of the transmission spectra with that taken before any exposure was made. This long-term loss was predominantly in the red spectral region reaching ~4.0 dB near 700 nm. There was no detectable long-term loss in the fiber that was kept at 400° C throughout the exposure.

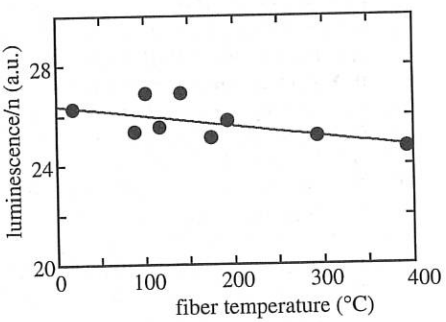


Fig. 4. The luminescence level (spectrally integrated) as a function of temperature

The previously unheated fiber loops were then annealed. Transmission measurements were made as the temperature was raised in 50° C steps to a maximum of 400° C. They were kept at this temperature for 2 hours and then allowed to cool to room temperature. Final transmission measurements were then made. Virtually complete recovery of the long-term loss was observed in the region of maximum loss, from 600 - 700 nm. In the blue region (500 to 550 nm) of the spectrum, however, significant loss was incurred while the fibers were heated. While most of this loss was recovered when the fiber was cooled to room temperature, the damaged fiber retains a reduced transmission of ~0.5 dB at 525 nm at room temperature.

4. Discussion and Conclusions

We have obtained data that characterizes the transmission and luminescence in diagnostic optical fiber during transient neutron bombardment associated with TFTR D-T discharges. By placing the fiber in an environment heated to 400° C, suppression of the transmission loss by at least 100x was attained. Variation with fiber type was significant and individual testing is required for proper characterization. Luminescence was predominantly Cerenkov radiation with a small radioluminescent component and was largely unaffected by operation at high temperature. Shielding, compensation fiber loops, or a modulation of the light source could be used to remove luminescence. No long-term loss was observed in the heated fiber during this study. Results were not significantly altered when the light level (~$5x10^{12}$ photons/cm^2/s/sr) was reduced by ~10x, indicating that photobleaching was not important.

Acknowledgements

We acknowledge the support of the TFTR and JET teams. The assistance of J. Bartolick, B. Bergin, M. Diesso, G. Drodz, L. Guttadora, M. Vocaturo and J. Wright of Wright Instruments was greatly appreciated. Neutron foil activation measurements used to determine the fiber exposure was the work of C. Barnes (LANL) and his colleagues at PPPL. The Al-coated fibres (from Oxford Electronics), the spectrometer and CCD camera were provided by JET. This work was supported by the US. DoE Contract No. DE-AC02-76-CH0307

References

1. see e.g.:J.K. Partin, *SPIE Proc. Fiber Optics in Adverse Environ. II,* **506**, 42. (1984) or A. Robinson, *SPIE Proc. Fiber Optics in Adverse Environ.III.* **721**, 63 (1986).
2. E.J. Friebele et al., *Nucl. Instrum. Methods Phys. Rev. B,* **1**, 335 (1984).
3. A.T. Ramsey and K.W.Hill, *Rev. Sci. Instrum.*, **63** - 10 4735 (1992).
4. P.D. Morgan, *Proc.of the Symposium on Fusion Technology*, Sept. 14-18, 169 (1992)
5. A.T. Ramsey, *Rev. Sci. Instrum.*, **66**, 871, (1995)
6. D.L. Griscom, M.E. Gingerich, and E.J. Friebele, *Phys. Rev. Lett.*, **71**, 1019, (1993).
7. D.L. Griscom, *The Cent. Memorial Issue of The Ceramic Soci.of Japan,* 923 (1991).
8. D.L. Griscom, *J. Non-Cryst. Solids,* **68**, 301 (1984).
9. D.L. Griscom, *J. Appl. Phys.,* **77**, 5008, (1995).
10. W. Tighe et al., *Rev. Sci. Instrum.*, **66**, 907, (1995).
11. D.A. Pinnow et al., *Appl. Phys. Lett.,* **22**, 527, (1973).
12. H. Nishikawa et al., *Phys. Rev. B*, **46**, 8073 (1992).
13. H. Adler et al., *Rev. Sci. Instrum.*, **66**, 904, (1995)
14. M.J. Marrone, *Appl. Phys. Lett.* **38** 115, (1981).
15. J. Golob, P. Lyons, and L. Looney, *IEEE Trans. Nucl. Sci.*, **NS-24, No. 6,** 2164 (1977)

Observations of Ion Cyclotron Emission from Charged Fusion Products in TFTR

S. Cauffman, R. Majeski, and the TFTR Group
Princeton Plasma Physics Laboratory, P. O. Box 451, Princeton NJ 08543, USA.

G. A. Cottrell
JET Joint Undertaking, Abingdon, Oxon, OX14 3EA, United Kingdom.

R. O. Dendy, C. N. Lashmore-Davies, and K. G. McClements
UKAEA Fusion, Culham, Abingdon, Oxon, OX14 3DB, United Kingdom.
(Euratom/UKAEA Fusion Association)

INTRODUCTION

Ion cyclotron emission (ICE) has been observed in TFTR during both deuterium and deuterium-tritium (DT) discharges, using a system of radio-frequency probes located near the top and bottom of the vacuum vessel. In deuterium discharges, emission is observed at harmonics of the ^{3}He fusion product cyclotron frequency evaluated at the outer midplane edge, while in DT discharges, emission is seen at harmonics of the alpha particle cyclotron frequency (Ω_α), again evaluated at the outer midplane edge. A similar origin for charged fusion product ICE has been observed in JET [1]. In typical TFTR supershot discharges, however, emission from fusion products is observed only during the first 100 to 250 ms following the start of neutral beam injection (NBI), and the temporal evolution of fusion product ICE does not, in general, follow that of the neutron emission [2,3]. This is in contrast to the JET observations [1], in which fusion product ICE evolved with the predicted alpha particle population in the outer midplane plasma edge. Recent experiments indicate that these differences may be due to the low edge density in TFTR supershot discharges. In TFTR supershots, the birth alpha particle velocity is below the Alfvén speed in the edge plasma, while in JET, newly born alpha particles are super-Alfvénic, even near the plasma edge. Helium gas puffing has been used to produce discharges in TFTR with edge densities high enough that alpha particles are super-Alfvénic. When this is the case, alpha particle ICE persists.

THE MAGNETOACOUSTIC CYCLOTRON INSTABILITY

The Magnetoacoustic (or Alfvén) Cyclotron Instability (MCI) has been identified as the probable mechanism behind fusion product driven ICE in both JET and TFTR [4,5,6]. While ICE can be modeled with varying degrees of

sophistication, much of the relevant physics is captured by simply solving the local dispersion relation for a uniform plasma with conditions comparable to those in the plasma edge. At the onset of NBI, the alpha particle population in the plasma edge is dominated by barely trapped particles born near the core on very wide banana orbits. (In the plasma edge, only orbits with a very narrow range of pitch angles will sample a significant fraction of the plasma core.) Figure 1 depicts such an orbit in TFTR. A simple model for the distribution of birth alpha particles at the plasma edge is thus $f_\alpha \propto \exp\{-(v_\parallel - v_d)^2/v_{r_\parallel}^2 - (v_\perp - u)^2/v_{r_\perp}^2\}$, where $v_d^2 + u^2 = v_{\alpha o}^2$ ($v_{\alpha o}$ is the alpha particle birth velocity) and $u/v_d = \tan(\theta_o)$ (θ_o is a pitch angle lying close to the trapped/passing boundary). When local dispersion relations for such distributions are solved numerically, modes near harmonics of Ω_α are found to be unstable, depending on the width of the distribution ($\sigma \equiv v_r/u$), the fractional density of alpha particles ($\xi \equiv n_\alpha/n_i$), and the ratio of the alpha particle velocity to the local Alfvén speed ($\zeta \equiv v_{\alpha o}/v_A$). In particular, while growth rates are proportional to ξ, the value of σ required for instability is a strong function of ζ, with instability being possible for much wider distributions if the Alfvén speed is lower [5,7]. One would expect, therefore, that while the initial edge alpha particle population is narrow enough, ICE would be observed as ξ increases, but that as the distribution widens, the ICE would eventually be stabilized for sub-Alfvénic alpha particles. If the alpha particles are super-Alfvénic, however, the instability will be more easily excited, even after the distribution function has widened significantly. To better understand the evolution of sub-Alfvénic ICE, one can allow the distribution function to widen due to collisions while it grows due to the birth of additional fusion products. As shown in reference 5, for parameters appropriate to the outer midplane edge of a TFTR deuterium supershot plasma (T_e = 3 keV, $n_e = 2\times10^{19}$ m^{-3}), the growth rate for the ^{3}He cyclotron fundamental is predicted to evolve as in figure 2. The duration of the instability is consistent with the duration of ICE empirically observed.

ICE IN TFTR L-MODES

Recently, ICE data were obtained during several TFTR discharges with edge densities high enough that 3.5 MeV fusion alpha particles were super-Alfvénic even in the edge plasma. MCI theory suggests that, under such conditions, alpha particle driven ICE should be more easily excited. Figures 3, 4, and 5 provide a comparison of data from three different discharges. The first (figure 3) is a supershot in which edge alpha particles are sub-Alfvénic. In this

case, alpha particle driven ICE is observed only at the start of NBI, when the alpha particle distribution function is a narrow drifting ring. The second discharge (figure 4) is a supershot in which a large He puff causes an L-mode transition. In this case, alpha particle driven ICE is again observed briefly at the onset of beams, but also *reappears* after the He puff, when the density is high enough that $\zeta > 1$. The final case (figure 5) is an L-mode discharge in which the alpha particle birth speed is greater than the edge Alfvén speed throughout NBI. In this case, alpha particle driven ICE is observed immediately after the onset of beams, but persists until the beams are turned off. In all three cases, alpha particle driven ICE is observed only when alpha particles in the edge plasma have a very narrow distribution function, or when they are super-Alfvénic.

CONCLUSION

The data described above provide valuable support for the MCI theory of ion cyclotron emission. While the theoretical treatment presented is simplistic by construction, it nevertheless is qualitatively consistent with empirical observation. More elaborate models (such as the global eigenmode calculation presented in reference 6) should lead to further improvements in our understanding. While the rapidity with which the alpha particle ICE stabilizes as the beams are turned off (see figure 5) remains poorly understood, additional measurements of ICE during L-mode plasmas are planned.

ACKNOWLEDGEMENTS

This work was supported by US DOE contract number DE-AC02-76-CH03073, the United Kingdom Department of Trade and Industry, and Euratom.

REFERENCES

[1] Cottrell, G.A., et al., *Nucl. Fusion* **33** 1365 (1993).

[2] Cauffman, S., Majeski, R., *Rev. Sci. Instrum.* **66** 817 (1995).

[3] Cauffman, S., Majeski, R., *Bull. Am. Phys. Soc.* **39** 1675 (1994).

[4] Dendy, R.O., et al., *Phys. Plasmas* **1** 1918 (1994).

[5] McClements, K.G., et al., "An interpretation of ion cyclotron emission from sub-Alfvénic fusion products in the Tokamak Fusion Test Reactor," submitted to *Phys. Plasmas*.

[6] Gorelenkov, N., Cheng, C.Z., *Phys. Plasmas* **2** 1961 (1995).

[7] Cauffman, S., et al., "Alfvénic Behavior of Alpha Particle Driven Ion Cyclotron Emission in TFTR," to appear in *Nucl. Fusion* (Dec. 1995).

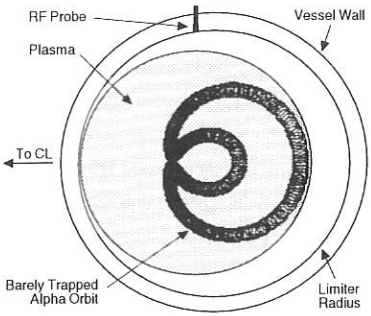


FIG. 1. Barely trapped alpha orbit passing through the plasma edge.

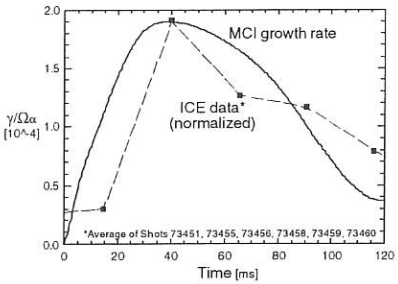


FIG. 2. Evolution of MCI growth rates and measured ICE signals.

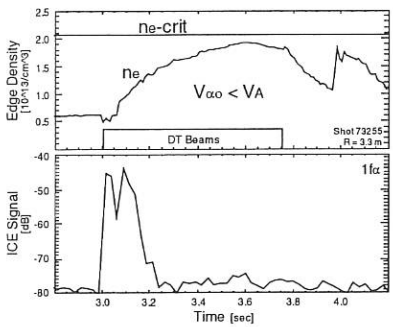


FIG. 3. Alpha-driven ICE during a typical supershot.

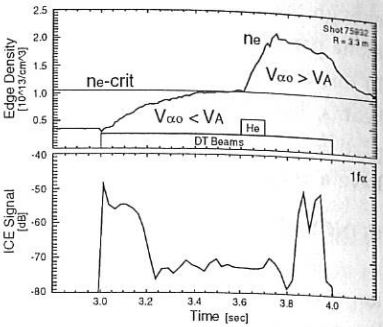


FIG. 4. Alpha-driven ICE during a supershot-to-L-mode transition.

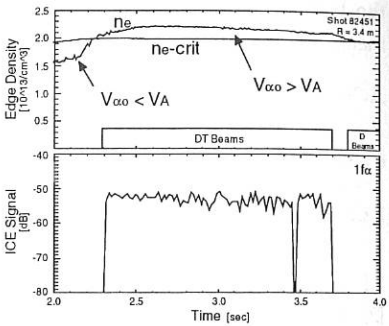


FIG. 5. Alpha-driven ICE during an L-mode.

Time and Space Resolved Soft X–Ray Spectroscopy on RTP

F. G. Meijer*, L. A. Shmaenok, Cao L. and the RTP–team
FOM–Instituut voor Plasmafysica "Rijnhuizen", Association Euratom–FOM,
P.B.1207, 3430 BE Nieuwegein, The Netherlands
and
V.P. Belik, A.A. Sorokin and Y. Shpenik,
A.F. Ioffe Physico–Technical Institute, St. Petersburg, Russia,
* also Physics Faculty, University of Amsterdam, Amsterdam, The Netherlands

1. Introduction

To study the behaviour of multiply ionised impurities in a tokamak plasma we used a five channel soft x–ray polychromator of a new design developed at the Ioffe Institute The instrument as installed at the RTP–tokamak in Rijnhuizen covers the wavelength range from 2 to 5 nm. Due to its high sensitivity and a time resolution of 0.25 ms several phenomena in the plasma could be easily observed as a function of time. Absolute intensity calibration, combined with a good knowledge of the geometry of the setup and its position relative to the plasma allows absolute measurement of several quantities.

2. Experimental setup.

The Multi–Layer–Mirror polychromator has five channels of similar construction. The wavelength selective element of this type of polychromator is a mirror consisting of layers of alternating higher and lower refractive index (see fig.1).

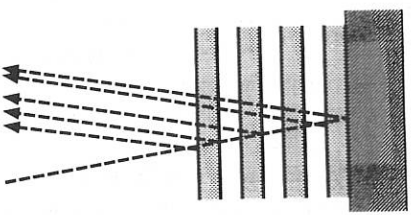


Fig.1a: A multi layer stack

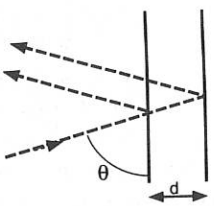


Fig.1b: Requirement for constructive interference

The thickness of these layers is chosen such that all refracted rays are interfering in a constructive way. The path difference, Δ, which for maximum intensity has to be an integral

number of wavelengths, is given by the Bragg–condition :

$$\Delta = 2nd \sin\theta \qquad [1]$$

with d the thickness of the layer, n its refractive index and θ the angle of incidence. It is clear from this formula that the optimally reflected wavelength can be tuned by rotating the mirror. One channel is schematically depicted in fig. 2.

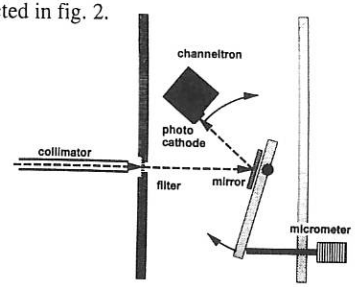


Fig.2: Single polychromator channel; tuning is done by adjusting the micrometer

A filter in front of the mirror excludes longer wavelengths which otherwise could be reflected to the detector by the front layer of the mirror. The photons are detected by a channeltron with a photocathode. The resolving power of this system is of the order of 40, but its real strength is that it can be absolutely calibrated for intensity. As is shown in fig. 3, both the transmission of the filter and the sensitivity of the channeltron as a function of wavelength are well known.

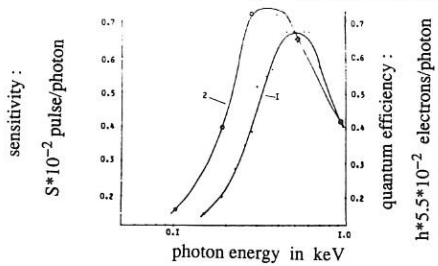


Fig.3a: Sensitivity of the channeltrons
curve 1: absolute sensitivity of the channeltron
curve 2 : literature data for tungsten [1]

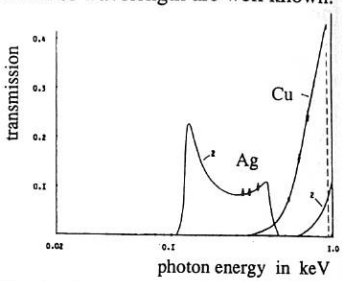


Fig.3b: Filter transmission
solid curve : calculated transmission
crosses : measured data

Also the reflectivity of the mirrors can be calibrated absolutely in the Ioffe Institute. The field of view is determined by a long tube, so the geometry of the part of the plasma which is observed is also well known. Another advantage of the use of multi–layer systems in the wavelength region under consideration is the avoidance of grazing incidence optics, the only alternative with reasonable reflectivity, but suffering from severe optical aberrations. All

together this makes this instrument an excellent device for absolute intensity measurements in the soft x–ray region as long as the spectrum is not too dense. The complete instrument consists of five channels with different orientation respective to the plasma as depicted in fig. 4. In this way also spatial resolution can be obtained.

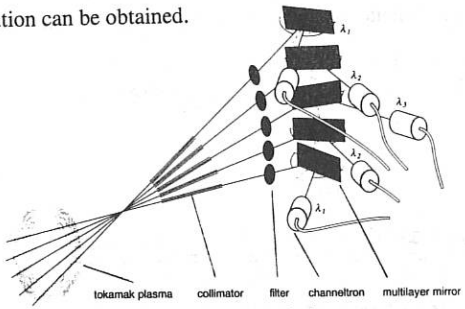


Fig.4: The five channel polychromator

3. Experimental results.

The instrument has been used until now in the following configuration: the outermost channels are tuned to the 4.86 nm line of B V, the central one to O VII (2.164 nm) and the remaining two to C VI at 3.37 nm. A systematic exploration of the parameter space for discharges in the RTP tokamak related to the MLM polychromator signals has not yet been made. However some first results show already some interesting phenomena. During a few discharges a sudden increase in the C VI signal from the upper part of the plasma was observed, coinciding with a comparable decrease in the carbon signal from the lower part (see fig. 5). No other diagnostics showed any related change in signal, except a few channels of the 80–channel soft x–ray tomography system, indicating that this effect happened near the inner wall of the vessel.

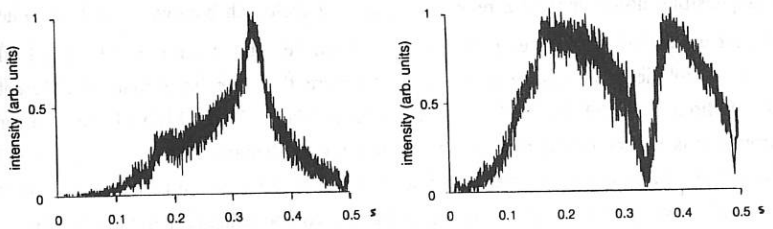


Fig.5: The intensity of the C VI line at 3.37 nm as a function of time; on the left the upper part of the plasma, on the right the lower part.

Often we see a fairly large signal on all channels at the end of the discharge, but this is not always the case (see fig. 6) as could be concluded from a survey with 39 shots of higher and 86

shots with lower densities. It only appears for densities below $5*10^{18}$. No exceptions were found. An explanation could be that after the end of the discharge impurities released from the wall are penetrating the plasma and are ionised. At higher densities it is more difficult for these atoms to reach hotter parts in a short enough time to emit light.

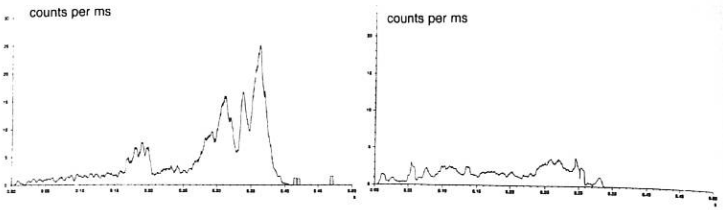


Fig.6: The time development of the O VII line at 2.164 nm;

Left a plasma shot with integrated density of $3.8*10^{18}$; right a shot with a density of $14*10^{18}$

The irradiation of the plasma with 110 GHz radiation can also trigger the emission of the above mentioned lines as is also clear from fig. 6 left, where ECRH radiation was injected from 165–205 ms. During experiments where Ne was mixed into the tokamak we observed changes in the soft x–ray signals coinciding with small changes in the integrated density. Again it seems that particles, released from the wall, are responsible for the observed emission and the slight increase in density.

4. Concluding remarks.

A complete mirror set is now available for the C VI line we studied. By equipping all channels with the same mirrors and filters a crude kind of tomography in the soft x–ray region is possible, however with a relatively narrow wavelength bandwidth and accurate intensity measurement. In this setup the system should be rotated through 90° to get all viewing lines in the same equitorial plane to compare the time behaviour of different species without interference of spatial dependencies. The Multi–Layer–Mirror polychromator is a very useful new device to monitor the behaviour of multiply ionized light impurities as a function of time. Absolute numbers on density can be obtained thanks to our good knowledge of the individual instrumental components. Either information on different species or on the spatial behaviour of one impurity can be obtained by the present setup. This work was performed with financial support from N.W.O. and Euratom.

References

J.J. Grodski and B.W. Schumacher, *Rev. Sci. Instr.* **39** 702 (1968)

SPECTROSCOPIC VECTOR TOMOGRAPHY AT RTP

John Howard
Plasma Research Laboratory, Research School of Physical Sciences and Engineering
Australian National University, Canberra, ACT, 0200 Australia
Frans G. Meijer *
FOM-Instituut voor Plasmafysica 'Rijnhuizen', Association Euratom- F.O.M.,
P.O. Box 1207, 3430 BE Nieuwegein, The Netherlands.
* Also at Physics Faculty, University of Amsterdam, Amsterdam

1 INTRODUCTION

The application of tomographic techniques to the study of vector fields has been demonstrated only in the last few years. Various applications in plasma diagnostics are discussed at length elsewhere [1]. In this paper we consider the possibility for time-resolved tomographic reconstruction of ion flow velocity fields from line-integrated spectroscopic measurements.

The method relies on directly measuring the low order spectral moments of the transition radiation from a given ionic species. The zeroth moment is the spectrally-integrated brightness of the chord-averaged emission. The second moment is proportional to the ionic temperature weighted by the emission intensity and integrated over the viewing chord. Both these quantities can be tomographically inverted to obtain the spatial distribution of the plasma emission and emission-weighted temperature. The first moment (Doppler shift) is proportional to the emission- weighted component of the ion velocity in the direction of, and integrated over the line-of-sight. From a sufficient number of measurements it is possible, using principles of vector tomography, to recover the 2-d structure of the emission weighted flow field [1]. The three low order moments can be simultaneously measured using a path-modulated Michelson interferometer and a single detector. In this paper we discuss the spectroscopic instrument and present some preliminary experimental results obtained for discharges in RTP.

2 VECTOR TOMOGRAPHIC SPECTROSCOPY

We assume a locally Gaussian, isotropic emission profile:

$$I(\boldsymbol{r}, \hat{l}; \nu) = \frac{I_0(\boldsymbol{r})}{\sqrt{\pi} w(\boldsymbol{r})} \exp\left[-\frac{(\nu - \bar{\nu})^2}{2\nu_0^2 \sigma(\boldsymbol{r})^2}\right] \quad (1)$$

where $\boldsymbol{r}$ is a position in the plasma, and $I_0(\boldsymbol{r})$ is the local emission intensity. The species temperature is given by $kT_s/(m_s c^2) = \sigma^2(\boldsymbol{r})$ where m_s is the atomic weight. The Doppler-shifted line centre frequency is $\bar{\nu}(\boldsymbol{r}, \hat{l}) = \nu_0 + \Delta\nu_D(\boldsymbol{r}, \hat{l})$ where ν_0 is the rest frame frequency and $\Delta\nu_D(\boldsymbol{r}, \hat{l})/\nu_0 = \boldsymbol{v}_D(\boldsymbol{r}).\hat{l}/c \equiv \boldsymbol{\beta}_D(\boldsymbol{r}).\hat{l}$ where $\boldsymbol{v}_D$ is the gross flow velocity of the emitting species. The measurement is approximated by an integral $g(p, \phi; \nu)$ of the emission I over the line $L(p, \phi)$ with impact parameter p and direction ϕ in a planar cross-section of the plasma (the x–y plane). The spectral information is carried by the low order spectral moments of the line-integrated emission:

$$\mu^{(m)}(p, \phi) = \int_{-\infty}^{\infty} g(p, \phi; \nu) \, \frac{(\nu - \nu_0)^m}{\nu_0^m} \, \mathrm{d}\nu. \tag{2}$$

It is straightforward to show that

$$\mu_D^{(1)} = \int_{L(p,\phi)} I_0(\boldsymbol{r}) \boldsymbol{\beta}_D(\boldsymbol{r})).\mathrm{d}l \qquad \mu_D^{(2)} = \int_{L(p,\phi)} I_0(\boldsymbol{r}) \, \left[\sigma^2(\boldsymbol{r}) + \beta_D^2(\boldsymbol{r})\right] \, \mathrm{d}l \tag{3}$$

The three low order spectral moments can be measured experimentally by exploiting the frequency response of the dispersing instrument. One means to control and/or increase the sensitivity to the first moment is to use a Michelson interferometer, or Fourier transform spectrometer (FTS). An interferometer offers high optical throughput and can be adapted easily for multiple spatial channels. Moreover, because the line is not spectrally resolved, time resolution is not compromised by having to flush a multi- element CCD array. The intensity at the output port is proportional to

$$S_{\pm} = \int_0^{\infty} g(p, \phi; \nu)[1 \pm \zeta \cos(2\pi\nu\Delta/c)] \, \mathrm{d}\nu \tag{4}$$

where Δ is the path length difference and $\zeta \leq 1$ is the fringe contrast. By sinusoidally modulating Δ the kernel non-linearity gives rise to harmonic components whose amplitudes convey the spectral moment information. For modulation $\varphi = \varphi_0 + \varphi_1 \sin \Omega t$ where $\varphi_0 \gg \varphi_1$, the resulting signal is

$$S_{\pm} = \mu^{(0)} \pm \zeta \int_{L(p,\phi)} I_0(\boldsymbol{r}) \, K(\boldsymbol{r}) \, \mathrm{d}l \tag{5}$$

with

$$\begin{aligned} K(\boldsymbol{r}) \;&=\; {\sum_{n=0}^{\infty}}' 2J_{2n}(\varphi_1) \exp\left[-\gamma(\boldsymbol{r})\right] \cos\left[\varphi_0(1 + \beta_D(\boldsymbol{r}))\right] \cos(2n\Omega t) \\ &-\; \sum_{n=0}^{\infty} 2J_{2n+1}(\varphi_1) \exp\left[-\gamma(\boldsymbol{r})\right] \sin\left[\varphi_0(1 + \beta_D(\boldsymbol{r}))\right] \sin\left[(2n+1)\Omega t\right] \end{aligned} \tag{6}$$

and where the primed sum means that the $n = 0$ terms are to be halved, $\gamma = \sigma^2(\boldsymbol{r})\varphi_0^2/2$ and terms of order φ_1/φ_0 have been ignored. The moments are directly obtained when $\gamma^2 \ll 1$ and $\varphi_0 = (2m + 1)\pi/2$.

We have constructed a proof-of-principle dual channel Michelson interferometer to test these ideas for Hα emission in the RTP tokamak. Two lens coupled optical fibres are installed, one viewing in the poloidal plane, and the other viewing toroidally at the horizontal midplane. The fibres conduct the light via an interference filter to the interferometer. A mirror driven by a loudspeaker at 2 kHz generates the path length modulation. The photomultiplier signals are low pass filtered (10 kHz) prior to digitization at 25 kHz. Light from a hydrogen lamp and He-Ne laser are simultaneously analyzed, the former can be used to estimate the position at which $\Delta = 0$ while the latter is used to monitor fringe visibility and time variations in the dc phase φ_0.

In these experiments, we compare the amplitudes of the odd and even harmonics (normalized to dc) to obtain intensity weighted estimates of β_D and $\exp(-\gamma)$. Since maximum sensitivity to β_D is obtained for $\gamma = 0.5$, the minimum measureable weighted average flow velocity is limited to $\bar{\beta}_D = \bar{v}_D/c \gtrsim (\rho/\zeta)(kT_s/m_s c^2)^{1/2}$ where $\rho = \zeta\varphi_0\mu^{(1)}/\mu^{(0)}$ is the detectable ratio of the second harmonic and dc amplitudes (determined by the noise level). Taking hydrogen at $T_s = 10$ eV, $\zeta = 0.5$ and $\rho = .01$ gives $\bar{v}_D \gtrsim 600$ m/s. The fundamental resolution of the method thus looks promising,

The left and right columns of Fig. 1 show respectively the processed data for sequential, similar ohmic dicharges in RTP. The top trace in each case shows the modulated emission for $\Delta = 0.5$ mm. The corresponding power spectra (below) show carriers at harmonics of the modulation frequency and the isolating bandpass filters used for the calculations. The dc and two lowest harmonics are shown in the centre traces while the bottom two graphs show the inferred temperatures and flow velocities respectively. In these preliminary experiments, the phase noise was dominated by acoustic noise from a mearby cooling system at 50Hz (and its harmonics) at a level $\rho \lesssim 1$. Small alignment inaccuracies caused this to be not completely compensated by the He-Ne laser signal so that the computed drift velocities presented below were required to be low-pass filtered at 50 Hz. These uncertainties, also resulted in some error in estimation of the fringe visibility (which varies with Δ) so that the atom temperatures are not calibrated. Nevertheless, note that the changes in measured toroidal velocities agree approximately (within a sign change) and that the temperature behaviour is reproducible. These variations disappear when $\Delta = 0$. Measurement of the absolute velocity (absolute phase change) requires a measurement of φ_0 using an atomic lamp source just prior to the discharge. It is hoped to build in future a more robust solid-state polarizing interferometer that uses piezo-elastic birefringence modulation, in order to eliminate some of the difficulties encountered in this prototype instrument.

John Howard is grateful to the Australian Research Council and NWO in the Nether-

lands for financial support during this research.

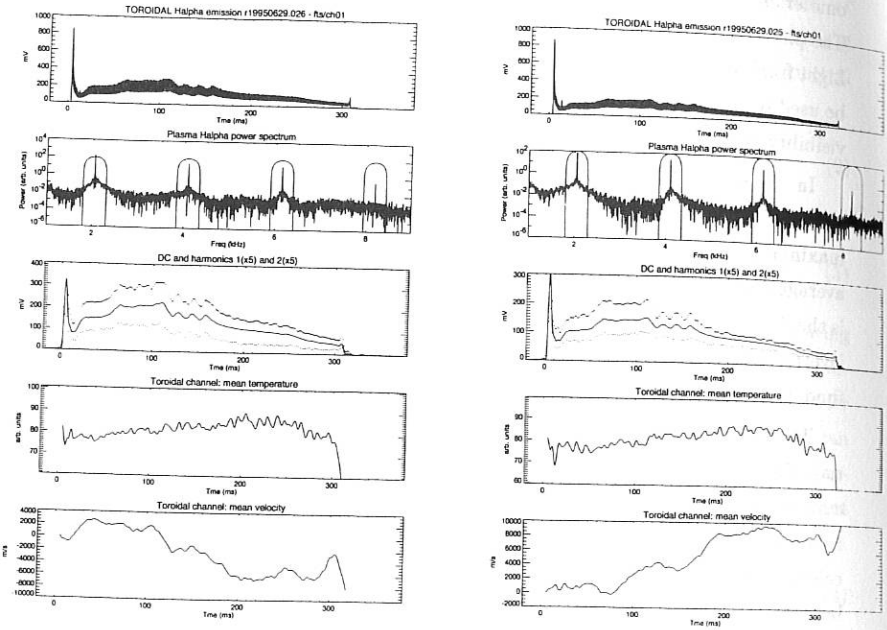


Figure 1: Raw and processed Michelson interferometer signals for two similar ohmic discharges in RTP. See text.

References

[1] J. HOWARD, Plasma Phys. Control Fusion Submitted for publication (1995).

AN INVESTIGATION OF A C V LINE RATIO VARIATION IN THE TJ-I TOKAMAK AND ITS SENSITIVITY TO NEUTRAL CONCENTRATION

K.J. McCarthy and B. Zurro

Asociación EURATOM/CIEMAT para Fusión, Av. Complutense 22, Madrid, E-28040, Spain.

1. Introduction

In recent line of sight measurements across the TJ-I tokamak variations have been seen in the intensity ratios of the He-like carbon (C V) triplet lines $1s2s^3S_1$-$1s2p^3P_2$ (2271.59 Å) and $1s2s^3S_1$-$1s2p^3P_{0,1}$ (2277.97 Å and 2278.63 Å). The ratio of these closely spaced and widely studied lines deviates here from their upper level statistical weights. In order to explain this anomaly, which has not been reported previously in similar fusion plasmas several candidates were investigated. The first, line blending can be dismissed since there are no other low Z lines within +/- 0.5 Å, while TJ-I electron temperatures and densities are several magnitudes too low for changes to occur in the upper level spontaneous emission coefficients [1] or for competition between the decay rates of the 2^3P_1 level to the metastable state 2^3S_1 and that to the ground state 1^1S_0 to alter the line ratio [2]. The only viable explanation found is charge exchange (*CX*) [3], where electrons are selectively captured by high n-states of C V during slow collisions between H-like carbon (C VI) and those neutral hydrogen atoms which exist in the hot plasma centre. We give equations which include *CX* and the subsequent decay of the captured electrons to estimate the population distribution among the 2^3P levels and use them to reproduce, through a model of the TJ-I plasma, the line intensity ratios seen. Furthermore, we suggest that these and similar variations in other low Z He-like ions may provide a means of monitoring neutral hydrogen atoms in plasmas.

2. Experimental Approach

In our experiment series of line of sight UV measurements were made through ohmically heated discharges in the TJ-I tokamak. This machine, which has major radius 30 cm and minor radius 10 cm, was operated here with plasma currents ≈ 40 kA, a toroidal field of 1 T and line averaged electron densities between 2 and 2.5×10^{13} cm^{-3}. Optical access to the entire plasma was possible using a quartz window on the machine. Light from the plasma was rotated through 90 degrees by a set of three mirrors located close to the window before being focused by a lens onto the slit of a 1 m focal length monochromator which had both spatial and temporal resolution capabilities. Spectra were recorded using a commercial multichannel intensified detector with 700 active pixels mounted at the focal plane. With the detector operating in gated mode, line emissions were integrated for 4 - 6 ms, this period being centred

about the peak of the discharge. Rotation of the mirror closest to the window allowed the optical line of sight through the plasma to be varied on a shot to shot basis. This mirror was replaced by a fast rotating polygonal prism to obtain line-integrated emission profiles. A PC was used to control the detector and to store data.

3. Results

Fig. 1 shows that the C v emission lines, centred at 2271.59 Å and at 2278.41 Å, are clear of contamination lines except for the Be-like carbon (C III) line at 2296.9 Å and that despite the use of a high resolution monochromator the lines at 2277.97 Å (from 2^3P_0) and at 2278.63 Å (from 2^3P_1) were not resolved. Using the 2271.59 Å line intensities of such spectra the C v distribution across the TJ-I was determined. See Fig. 2a. In Fig. 2b a sharp rise is seen in the ratio of the two lines, R=I(2271.59 Å) /I(2278.41 Å), when moving inwards from the plasma edge followed by a slow drop which continues to the centre. The changes are greater than experimental error while R is significantly larger, except at the edge, than R=1.9 predicted by extrapolating to the TJ-I conditions the formulae developed by Engelhardt *et al.* [2]. It is these and similar variations seen in the sets of discharges that are the basis for our investigations.

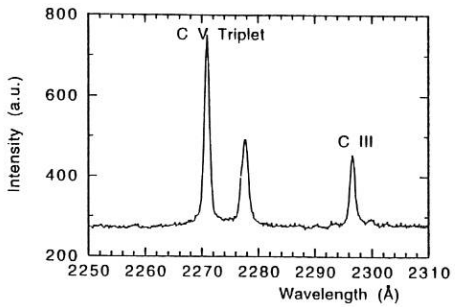


Fig. 1: One of a series of line of sight raw spectra collected during one of several sets of TJ-I discharges.

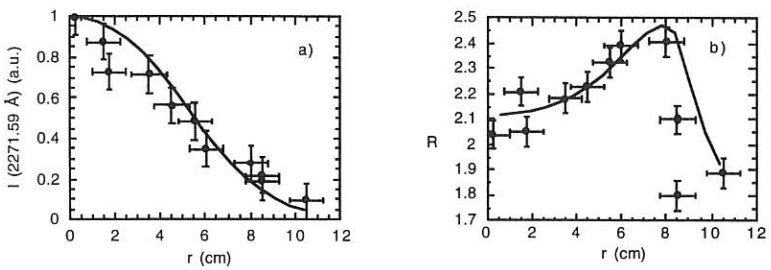


Fig. 2: a) Measured 2271.59 Å line intensity with background subtracted and b) R=I(2271.59Å) /I(2277.75 Å) across a plasma radius. Model results are also shown.

4. Discussion

As the plasma is optically transparent the ratios of the 2^3S-$2^3P_{2,0,1}$ line intensities can be expressed in terms of the ratios of the $2^3P_{2,0,1}$ levels steady state populations n_k, since $I_{km}=A_{km}n_k$ (cm^3 s^{-1}), where A_{km}, the level k transition decay rate to the metastable level 2^3S is similar for each transition. To estimate n_k we have developed equations which include contributions from both electronic collisions, $N_e[n_gC_{gk}+n_mC_{mk}]$ and CX processes, $N_oN_h\sigma_kV_a$. Cascades to these levels which originate as electron excitations into states n = 3 & 4 or as dielectric and radiative recombination of C VI are considered minimal and are neglected [4]. Thus the equations for n_k, which can also be applied to other low Z He-like ions, are

$$\text{for } k=2; \qquad n_2 = \frac{\frac{5}{9}\left[N_e\left[n_gC_{g2}+n_mC_{m2}\right]\right]+N_oN_h\sigma_2V_a}{\left[A_{2m}+N_e\sum_{j=1}^{n}C_{2j}\right]} \qquad (1)$$

$$\text{for } k=1; \qquad n_1 = \frac{\frac{3}{9}\left[N_e\left[n_gC_{g1}+n_mC_{m1}\right]\right]+N_oN_h\sigma_1V_a}{\left[A_{1m}+A_{1g}+N_e\sum_{j=1}^{n}C_{1j}\right]} \qquad (2)$$

$$\text{for } k=0; \qquad n_0 = \frac{\frac{1}{9}\left[N_e\left[n_gC_{g0}+n_mC_{m0}\right]\right]+N_oN_h\sigma_0V_a}{\left[A_{0m}+N_e\sum_{j=1}^{n}C_{0j}\right]} \qquad (3)$$

Here the values $^5/_9$, $^3/_9$ and $^1/_9$ are the statistical weights for 2^3P_2, 2^3P_1 and 2^3P_0, N_e, N_o and N_h are the electron, neutral and H-like ion densities (cm^{-3}), A_{km} and A_{1g} refer to transition probabilities from 2^3P_k to 2^3S_1 and from 2^3P_1 to the ground state, C_{gk} and C_{mk} are rate coefficients for excitations from the ground g and metastable m states to 2^3P, C_{kj} refers to all electron excitation and de-excitations out of the 2^3P levels and n_g and n_m are the absolute He-like ion ground and metastable populations (cm^{-3}). For the latter their relative values are estimated by considering all rates into and out of the triplet states [5]. Although n_m is everywhere less than 10^{-4} n_g it is included as excitation rates from this level are several orders of magnitude larger than those from the ground state. Since practically all CX collisions lead to excited ions, which decay to the ground or metastable levels through photon emission, the cascade corrected emission cross sections σ_k for the C V 2^3P levels (cm^2) can be estimated by

$$\sigma_2 = \sigma(3s) + 0.55\sigma(3d) + 0.55\sigma(4s) + 0.21\sigma(4p) + 0.43\sigma(4d) + 0.55\sigma(4f) \qquad (4)$$

$$\sigma_1 = 0.33\sigma(3d) + 0.023\sigma(4p) + 0.26\sigma(4d) + 0.33\sigma(4f) \qquad (5)$$

$$\sigma_0 = 0.11\sigma(3d) + 0.008\sigma(4p) + 0.09\sigma(4d) + 0.11\sigma(4f) \qquad (6)$$

where the branching ratios are by Suraud *et al.* [6] and the partial cross-sections for the triplet manifold, $\sigma(3s)$ etc., are from Shimakura *et al.* [7]. Here direct capture cross sections for states n=2, 3 and >5 are negligible and neglected. In slow collisions of C VI with neutral hydrogen the $4s^3S$, $4p^3P$ and $4d^3$D levels have the largest cross sections, typically a few times 10^{15} cm^2, thus the σ_2 cross sections can be 10 or more times larger than those of σ_1 and σ_0.

Finally, V_a the relative ion-neutral collision velocity (cm s^{-1}) is determined using the standard ion-thermal velocity formula with fixed H-like ion (150 eV) and neutral (25 eV) temperatures.

In our model the plasma is partitioned into discrete shells described by established TJ-I electron and temperature distributions, n_g and n_m distributions based on 2271.59 Å line measurements and best guess N_o and N_h values. To simulate line of sight measurements the n_k level populations are summed along representative paths. Since N_o and N_h could not be determined directly from measured data best guesses were made for their combined distribution. Several iterations were needed to establish these best guesses and to achieve good fits with the measured data. See Figs. 2 & 3. If it is assumed that the C V and C VI densities are similar then we estimate that the central neutral concentration is a few 10^8 cm^{-3}. In converse, if N_e, n_g and n_m, and N_h are well known then this method should provide a sensitive means to determine neutral hydrogen concentrations. We predict that the line variations should be sensitive to neutral concentrations $>10^8$ cm^{-3} for C V in the TJ-I. Finally, while CX partial cross-sections are not currently available for slow collisions between neutral hydrogen and all low Z H-like ions, we can deduce from total cross-section values and from the classical model $n=q^{0.75}$ where q is the charge on the target [8], that variations may be also seen in the triplet line intensities for the He-like ions between nitrogen and neon, albeit for different plasma temperature ranges. This in turn leads to the possibility of measuring neutral distributions over a wide range of electron temperatures.

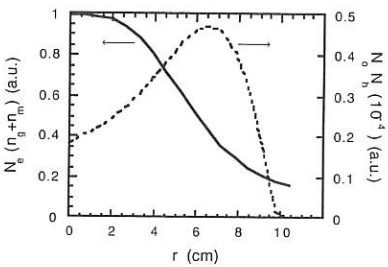


Fig.3. TJ-I radial distribution of $N_e(n_g+n_m)$ and N_oN_h (a.u.). Here $N_e=N_e(0)[1-[r/10\ ]^{3.5}]^5$.

References

[1] Chung Y, Lemaire P and Suckewer S, *Phys. Rev. Lett.* **60** 1122 (1988).

[2] Engelhardt W, Köppendörfer W and Sommer S, *Phys. Rev. A* **6** 1908 (1972).

[3] Isler R.C, *Phys. Scr.* **35** 650 (1987).

[4] Bliman S, Cornille M and Katsonis K, *Phys. Rev. A* **50** 3134 (1994).

[5] Brenning N, *J. Phys. D: Appl. Phys.* **13** 1459 (1980).

[6] Suraud M.G et al., *J. Phys. B: At. Mol. Opt. Phys.* **24** 2543 (1991).

[7] Shimakura N, Koizumi S, Suzuki S and Kimura M, *Phys. Rev A* **45** 7876 (1992).

[8] Olson R.E, *Phys. Rev. A* **24** 1726 (1981)

The vacuum ultra violet spectrum of W VIII

G.Veres, **J.S.Bakos** and B.Kardon
Department of Plasma Physics
KFKI Research Institute for Particle and Nuclear Physics
H-1525 Budapest, POB 49, Hungary

1. Introduction

Because of the intolerable large erosion of low Z materials in case of high wall loading, tungsten has recently got a renewed interest as construction material of tokamak reactors. Therefore its tokamak relevant properties are investigated by various authors [1,2]. Among these properties the transport behaviour is also a key issue. For such an investigation tungsten is injected, for instance, by laser blow-off injection method into the tokamak plasma. In order to investigate the transport of the injected material, its spectrum has to be known. Tungsten is ionised relatively easily to as high ionisation degree as seven at minor radius 2 cm even in the plasma of the MT-1M tokamak of as moderate temperature as 200 eV at plasma centre since the ionisation potential of W^{6+} is 119.7 eV.

The spectrum of seven times ionised tungsten (W VIII) has been measured in the wavelength range from 130 to 300 Å with a spectral resolution of 5 Å. Tungsten was injected by the blow-off method [3] as impurity in the plasma of the MT-1M tokamak. For explaining the spectrum, an empirical method for extrapolating the unknown excitation energy levels of complex ions based on known levels of less complex ones was developed and is presented.

The parameters of our plasma were as follows: major radius 40 cm, limiter radius: 9 cm, plasma current: 20 kA, line averaged electron density through a central chord $2 \cdot 10^{13}$ cm^{-3} and discharge duration 8 ms.

2. Experimental set-up and observations

A layer of 1μm thick tungsten was evaporated on a glass disk. The opposite side of the disk was irradiated by a 30 ns long 700 mJ energy Nd-Glass laser pulse focused to a spot of 1.5 mm diameter. A beam of tungsten atoms, ions and layer fragments (pellets) was formed and flew towards the tokamak with a velocity of 250 m/s. Only the pellets reached the central

regions of the plasma because the ionic component of the beam (due to the magnetic field of the tokamak) did not penetrate the plasma at all and the atoms (due to the rapid ionisation) were deposited at the outer regions.

The spectroscopic instrument used was a 0.3 m Seya-Namioka type vacuum ultra violet monochromator with a holographic grating of 20 Å/mm dispersion and 0.25 mm wide entrance and exit slits. For the detection of photons a VEU-7 type microchannel plate operated at 1.75 kV supply voltage was used. The measured spectrum of tungsten can be seen on Fig.1. It was recorded on a shot-by-shot basis. Several shots were done at each wavelength setting and the average of the measured values was calculated.

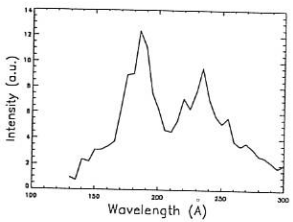


Figure 1: VUV spectrum of W VIII with 5 Å spectral resolution

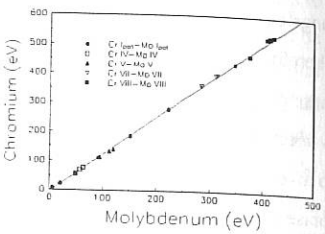


Figure 2: Energy levels of molybdenum as a function of the energy levels of chromium

At three selected wavelengths (185 Å, 215 Å and 235 Å) the line averaged radial distribution of the radiation was also recorded by swinging the monochromator around a suitable axis. Discrimination between the ionisation stages of tungsten was carried out by comparing the measured time histories and radial distributions of the signals with the result of a Monte Carlo simulation [4] that computes the radial movement and successive ionisation of tungsten atoms and ions.

3. Data evaluation

The method described below for estimating the unknown energy levels of complex ions was developed in a purely empirical way by studying large amount of energy level data. The electron configuration of the valence shell of W^{7+} is $5s^25p^5$, i.e. it is isoelectronic with the fluorine's outermost shell. The same valence shell configuration and ionic charge as W^{7+} have

the Cr^{7+} and Mo^{7+} ions. But the principal quantum number of the valence electrons is 3 and 4, respectively, for the latter two ions and 5 for tungsten. As the energy of the excited levels of these ions is taken the sum of the ionisation potentials of all the ions of ionisation degree less than that of the ion plus the excitation energy. One can compare corresponding energy levels of the different ions (i.e. the levels with the same core~ and excited electron configuration and same atomic L, S and J quantum numbers) and look for some special relationship between them.

On Fig. 2 we plotted some term energies of chromium as a function of the corresponding term energies of molybdenum. The solid circles represent the ground states (i.e. the ionisation potentials) of the ions of the different charge. The line on the figure is fitted to these points. The triangles and squares are energy level values from *[5,6]* and lie with a satisfactory agreement on the line fitted to the ionisation potentials. With the help of such a type of linear relationship one can calculate the levels of one element, if the levels of the other one is known. Detailed numerical calculations show, that utilising this method and the known values of the energy levels of molybdenum the calculated values for the excited states of chromium differ from the values in *[5]* by only less than one percent.

For the calculations of W VIII levels we used the level schemes of Cr^{7+} and Mo^{7+}. Fig. 3 demonstrates the procedure in case of molybdenum. The term energies of W VII are also plotted as a function of the same term energies of Mo VII (filled quadrangles).

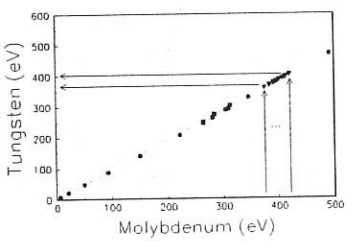


Figure 3: The ionisation and term energies of W VIII as a function of ionisation and term energies of Mo VIII.

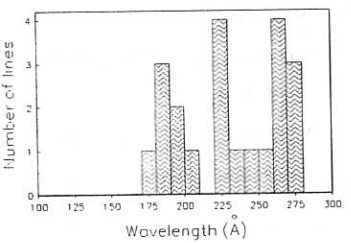


Figure 4: Calculated VUV spectrum of W VIII. The number of radiative transitions in 10 Å intervals is shown.

We calculated the wavelengths of some possible radiative transitions for W^{7+} that have the ground state as their final state. Since no theoretical intensity data are available for these

transitions, as a first approach, Fig. 4 shows the number of calculated transitions in each 10 Å interval as a function of the wavelength in the 130-300 Å range. The similarity between the measured spectrum (Fig. 1) and calculated number of transition (Fig. 4) is remarkable.

4. Conclusion

Tungsten pellets have been injected into the MT-1M tokamak plasma by using the laser blow-off technique and the W VIII spectrum is recorded in the 130 - 300 Å wavelength range. In order to explain the spectrum a method of extrapolation is used for the calculation of excitation energy levels of W^{7+} ions knowing the levels of Cr^{7+} and Mo^{7+} ions. The method is applicable in all cases where the knowledge of the levels or radiative transitions of an ion with a limited (about 10 percent) accuracy is satisfactory.

5. Acknowledgement

This work was sponsored by the Hungarian OTKA foundation (contract No:4087) and by the US-Hungarian Joint Fund contract JF No.099/91.

6. References

[1] Tetsuo Tanabe, Nabuaki Noda and Hiroo Nakamura, *J. Nucl Mat.*, **196-198,** 11, (1992)

[2] S. Hirsch, K. Asmussen et al., 21th EPS Conf. on Contr. Fusion and Plas. Phys., Europhysics Conf. Abstracts, **Vol. 18B**, EPS Geneve, (1994)

[3] Kocsis G., Bürger G., Ignácz P.N. et al., *Plasma Phys. Contr. Fusion* **34,** 1423. (1992)

[4] Veres G., Ignácz P.N., Kardon B. and Kocsis G., *Plasma Phys. Contr.Fusion* **35,** 1085. (1993)

[5] Moore Ch.E., *Atomic Energy Levels* **vol II,** NBS publication, Washington, D.C. (1952)

[6] Moore Ch.E., *Atomic Energy Levels* **vol III,** NSRDS-NBS 35, Washington, D.C. (1971)

Modulational Interaction of Short–Wavelength Ion Acoustic Oscillations in Dusty Plasmas

Sergey I. Popel[a] and Ming Y. Yu[b]
(a) Institute for Dynamics of Geospheres, Leninsky pr. 38, Building 6, 117979 Moscow, Russia
(b) Institut für Theoretische Physik, Ruhr–Universität Bochum, D–44780 Bochum, Germany

Investigation of plasmas containing heavy impurity ions or dust particles is important for the understanding of space and astrophysical phenomena (planetary rings, cometary tails, interstellar clouds, etc.), the Earth's environment (noctilucent clouds, auroras, etc.), many laboratory and technological plasmas (low–temperature rf and dc glow discharges, rf plasma etching, the wall region fusion plasmas, etc.), as well as many materials (semiconductors, dusty crystals, etc.). The impurity ions or dust particles often have large mass, are charged negatively with large charge numbers ($|Z_d|$ up to 10^3), and are of average sizes usually much less than the Debye length (see, *e.g.*, [1]). Such charged impurity particles can significantly modify the properties of the normal modes and their evolution. Moreover, their presence results in the appearance of new normal modes, such as the dust–acoustic waves [2,3], which involve oscillations at such low frequency that the electrons and ions remain in equilibrium and the dynamics is mainly due to the dust particles. The presence in dusty plasmas of the dust–acoustic oscillations results in the possiblility of modulational instabilities associated with the latter. Here we investigate the modulational instability of short–wavelength ion–acoustic waves in a dusty plasma.

Consider a uniform unmagnetized collisionless hydrogen plasma containing massive impurity particles or dust grains with an average negative charge $Z_d e$, where e is the electron charge. When dust grains are involved, the size of the latter is assumed to be much smaller than the Debye length, the wavelength of the perturbations, as well as the distance between the plasma particles. Thus we can treat the dust grains as negatively charged point masses. We also assume that the following conditions are fulfilled:

$$T_e \gg T_i \gg T_d/Z_d, \quad m_e \ll m_i \ll m_d/Z_d, \quad n_{0e} \sim n_{0i} \sim n_{0d} Z_d, \tag{1}$$

where m_α, $n_{0\alpha}$, and T_α ($\alpha = e, i, d$) are the mass, the unperturbed density, and the temperature of the electrons, ions, and dust particles, respectively. Thus both ion–acoustic and dust–acoustic oscillations can exist in the plasma.

In the short–wavelengths limit ($|\mathbf{k}| r_{Di} \ll 1 \ll |\mathbf{k}| r_{De} \ll \sqrt{m_i/m_e}$, the last inequality being needed in order to avoid strong electron Landau damping), the dispersion relation of the ion–acoustic oscillations can be written as

$$\omega_{\mathbf{k}} = \omega_{pi} \left(1 - \frac{1}{2|\mathbf{k}|^2 r_{De}^2} \right), \tag{2}$$

where ω_{pi} is the ion plasma frequency, $r_{De(i)}$ is the electron (ion) Debye length. The dispersion relation (2) for short-wavelength ion-acoustic waves (sometimes called ion Langmuir waves) is typical for media with inverse dispersion [4].

To investigate the modulational instability of the oscillations with linear dispersion (2) we introduce the slowly varying wave envelope of the ion Langmuir pump wave $\mathbf{E}_{iL}(\mathbf{r},t)$, where

$$\mathbf{E} = \frac{1}{2}\left[\mathbf{E}_{iL}\exp(-i\omega_{pi}t) + c.c.\right]. \tag{3}$$

The evolution of $\mathbf{E}_{iL}(\mathbf{r},t)$ is governed by the following equation [4]

$$\nabla\cdot\left(i\frac{\partial}{\partial t}\Delta\mathbf{E}_{iL}\right) - \frac{\omega_{pi}}{2r_{De}^2}\nabla\cdot\mathbf{E}_{iL} = \frac{\omega_{pi}}{2}\nabla\cdot\left(\Delta\left[\frac{\delta n_i}{n_{0i}}\mathbf{E}_{iL}\right]\right), \tag{4}$$

where Δ is the Laplacian and we have introduced the effective density modulation δn_i.

The evolution of the effective density modulation δn_i depends on the regime considered. First, if the modulation frequency Ω satisfies $|\Omega| \ll \omega_{pi}$ and $|\mathbf{K}|v_{Ti} \ll |\Omega| \ll |\mathbf{K}|v_{Te}$, where $\mathbf{K}$ is the wave vector of the modulations and $v_{Te(i)} = \sqrt{T_{e(i)}/m_{e(i)}}$ is the electron (ion) thermal speed, the dust particles do not contribute. For this case the treatment [4] of the ion Langmuir wave modualtional instability in a dust-free *two-component* plasma is applicable. Here the slow density perturbations are also associated with the ion modes. We note [5] that for the situation $|\mathbf{K}|v_{Ti} \ll |\Omega| \ll |\mathbf{K}|v_{Te}$, modulation is possible only when $|\mathbf{K}| \ll |\mathbf{k}_0|$, where $\mathbf{k}_0$ is the wave vector of the ion Langmuir pump wave.

A more important case is one that satisfies $|\mathbf{K}|v_{Td} \ll |\Omega| \ll |\mathbf{K}|v_{Ti}$ and $|\mathbf{K}|r_{Di} \ll 1$, where $v_{Td} = \sqrt{T_d/m_d}$ is the thermal speed of the impurity particles. Under these conditions, the low-frequency motion is described by [5]

$$\left[\frac{\partial^2}{\partial t^2} - v_{sd}^2\Delta\right]\frac{\delta n_i}{n_{0i}} = \frac{Z_d^2 n_{0d}}{16\pi n_{0i}^2 m_d}\Delta|\mathbf{E}_{iL}|^2, \tag{5}$$

where

$$v_{sd} = \left(\frac{n_{0d}Z_d}{n_{0i}}\right)^{\frac{1}{2}}\left(\frac{Z_d T_i}{m_d}\right)^{\frac{1}{2}} \tag{6}$$

is the dust-acoustic speed. In this case the slowly varying density perturbations are associated with the dust-acousic mode (which has the linear dispersion $\omega_{\mathbf{k}} = |\mathbf{k}|v_{sd}$). We emphasize that here the magnitude ($|\mathbf{K}|$) of the perturbation wave vector can be both larger and smaller than that ($|\mathbf{k}_0|$) of the pump.

To find the growth regimes and rates of the modulational instability described by the system (4) and (5), we shall follow standard procedure [6] and present only the essential steps and formulas. We assume that unperturbed (monochromatic pump) wave has an amplitude $\mathbf{E}_0$ given by $\mathbf{E}_{iL} = \mathbf{E}_0\delta(\mathbf{k}-\mathbf{k}_0)$. In the lowest approximation, we have the homogeneous and stationary solution δn_{0i} for any $|\mathbf{E}_0|^2$. By renormalizing the background density $n_{0i} \to n_{0i} + \delta n_{0i}$ we can remove the static density perturbation δn_{0i}. Thus, by combining (4) and (5) in the Fourier space, we obtain the dispersion relation for the modulational instability. It has unstable solutions [5] for the cases of both "short-scale" (when $|\mathbf{K}| \gg |\mathbf{k}_0|$) and "long-scale" (when $|\mathbf{K}| \ll |\mathbf{k}_0|$) modulational instabilities.

Here we consider the case of short–wavelength ($|\mathbf{K}| \gg |\mathbf{k}_0|$) modulations. In this case, the dispersion relation takes the form [5]

$$1 = \left[8\frac{\Omega}{\omega_{pi}}\frac{|\mathbf{k}_0|}{|\mathbf{K}|}\cos\Theta\sin^2\Theta + \frac{2\cos^2\Theta}{|\mathbf{k}_0|^2 r_{De}^2}\right]$$

$$\times\left[4\left(\frac{\Omega}{\omega_{pi}}\right)^2 - 8\frac{\Omega}{\omega_{pi}}\frac{|\mathbf{k}_0|\cos\Theta}{|\mathbf{K}|^3 r_{De}^2} - \frac{1}{|\mathbf{k}_0|^4 r_{De}^4}\right]^{-1}\Sigma|\mathbf{E}_0|^2, \tag{7}$$

where Θ is the angle between $\mathbf{K}$ and $\mathbf{k}_0$, Ω is the frequency of the density modulation, the parameter Σ is defined by

$$\Sigma = \frac{1}{32\pi n_{0i}T_i}\frac{|\mathbf{K}|^2 v_{sd}^2}{(\Omega^2 - |\mathbf{K}|^2 v_{sd}^2)}. \tag{8}$$

We let $|\cos\Theta| \sim |\sin\Theta| \sim 1$, so that interactions with the largest growth rates are represented. Interactions corresponding to $\mathbf{K} \parallel \mathbf{k}_0$ and $\mathbf{K} \perp \mathbf{k}_0$ are not so important since for these the growth rates are much smaller. We also assume

$$\frac{\Omega}{\omega_{pi}} \gg \frac{1}{|\mathbf{k}_0|^2 r_{De}^2}\frac{|\mathbf{K}|}{|\mathbf{k}_0|}, \tag{9}$$

so that (7) reduces to

$$1 = 2\frac{\omega_{pi}}{\Omega}\frac{|\mathbf{k}_0|}{|\mathbf{K}|}\cos\Theta\sin^2\Theta\Sigma|\mathbf{E}_0|^2, \tag{10}$$

which corresponds to the case with the maximum growth rate for $|\mathbf{K}| \gg |\mathbf{k}_0|$. Here, only supersonic ($\gamma \gg |\mathbf{K}|v_{sd}$) development of the modulational instability is possible. The growth rate of the instability is

$$\gamma \sim \left(|\mathbf{K}||\mathbf{k}_0|v_{sd}^2\omega_{pi}W\right)^{\frac{1}{3}}, \tag{11}$$

where $W = |\mathbf{E}_0|^2/16\pi n_{0i}T_i$. The growth rate can have the maximum value given by

$$\frac{\gamma_{\max}}{\omega_{pi}} \sim \min\left\{|\mathbf{k}_0|^2 r_{De}^2\left(\frac{\alpha T_i W}{T_e}\right)^{\frac{1}{2}}, (|\mathbf{k}_0|r_{De})^{\frac{5}{6}}\left(\alpha\frac{T_i}{T_e}\right)^{\frac{1}{4}}W^{\frac{1}{2}}, \left(\frac{T_i}{T_e}\right)^{\frac{1}{6}}(|\mathbf{k}_0|r_{De}\alpha W)^{\frac{1}{3}}\right\}, \tag{12}$$

where $\alpha = m_i Z_d/m_d$. Equation (12) follows from the conditions (9), $\gamma \gg |\mathbf{K}|v_{sd}$, as well as the inequality $|\mathbf{K}|r_{Di} \ll 1$. The maximum growth rate can be realized if

$$W \gg \max\left\{\frac{1}{|\mathbf{k}_0|^8 r_{De}^8}\frac{T_e}{\alpha T_i},\ |\mathbf{k}_0|r_{De}\left(\frac{\alpha T_i}{T_e}\right)^{\frac{1}{2}}\frac{|\mathbf{K}|^2}{|\mathbf{k}_0|^2}\right\}. \tag{13}$$

Thus we see that as a result of the modulational instability, the ion Langmuir waves with wavelengths larger than those of the pump wave can appear in a dusty plasma. Since these waves can interact with the thermal ions, energy transfer to the latter becomes possible. It follows that in a dusty plasma the bulk plasma ions can be heated by the ion

Max-Planck-Institut für Plasmaphysik
- Bibliothek -

Langmuir waves. The corresponding rate of ion heating depends on the parameters of the plasma as well as the pump wave. For example, if

$$\left(\frac{T_i}{T_e}\right)^{\frac{1}{6}} (|\mathbf{k}_0| r_{De} \alpha W)^{\frac{1}{3}} \leq \min\left\{ |\mathbf{k}_0|^2 r_{De}^2 \left(\frac{\alpha T_i}{T_e} W\right)^{\frac{1}{2}},\ (|\mathbf{k}_0| r_{De})^{\frac{5}{6}} \left(\frac{\alpha T_i}{T_e}\right)^{\frac{1}{4}} W^{\frac{1}{2}} \right\}, \qquad (14)$$

then ion Langmuir wave modulations with $|\mathbf{K}| r_{Di} \sim 1$ (i.e., those which are resonant with the thermal ions) grow at the rate (11). The rate of bulk ions heating can be estimated to be

$$\frac{1}{T_i}\frac{dT_i}{dt} \sim \omega_{pi} \left(\frac{\alpha |\mathbf{k}_0| r_{De} |\mathbf{E}_0|^8}{n_{0i}^4 T_i^{7/2} T_e^{1/2}} \right)^{\frac{1}{3}}. \qquad (15)$$

We emphasize that the possibility of heating the bulk plasma ions is the result of nonlinear coupling between finite–amplitude ion Langmuir waves and the dust–acoustic perturbations. Modulational processes in which the low–frequency perturbations are associated with the ordinary ion–sound perturbations do not result in such ion heating because the limit $|\mathbf{K}| \gg |\mathbf{k}_0|$ does not occur.

The nonlinear evolution of the modulational instability can result in a formation of coherent objects such as solitons, phase–space holes, and collapsing cavities. One–dimensional ion Langmuir solitary waves are described [5] by the nonlinear equation for the slowly varying wave envelope $\mathbf{E}_{iL}$. This equation is typical for media with inverse, or negative, dispersion, and has solutions in the form of spiky envelope solitons [5]. Similar solitons were found for other media with inverse dispersion [7]. A physically important feature of the ion Langmuir soliton is the presence in its Fourier spectrum of harmonics with large wave vectors. These short–wavelength harmonics can strongly interact with the thermal ions and are thus heavily damped. Since all the harmonics in the soliton are correlated in amplitude and phase, the entire soliton will also be damped, leading to the heating of the bulk plasma ions. Thus, for plasmas containing heavy impurity or dust particles, the modulational instability of finite–amplitude short–wavelength ion–acoustic waves can lead to the heating of the bulk plasma ions at both the initial and final stages of its evolution.

Acknowledgements

This work is partially supported by the Russian Foundation for Fundamental Research (grant no. 93-02-3357) and by the Sonderforschungsbereich 191 Niedertemperaturplasmen.

References

[1] Tsytovich V.N. and Havnes O., *Comments Plasma Phys. Contr. Fusion* **15** 267 (1993).

[2] Rao N.N., Shukla P.K., and Yu M.Y., *Planet. Space Sci.* **38** 543 (1990).

[3] Salimullah M. and Sen A., *Phys. Fluids B* **4** 1441 (1992).

[4] Rudakov L.I. and Tsytovich V.N., *JETP Lett.* **25** 489 (1977).

[5] Popel S.I. and Yu M.Y., *Phys. Rev. E* **50** 3060 (1994).

[6] Rudakov L.I. and Tsytovich V.N., *Phys. Rep. C* **40** 1 (1978).

[7] Porkolab M. and Goldman M.V., *Phys. Fluids* **19** 872 (1976).

Vlasov Eulerian Simulation in two Dimensions
Phase Space Hole Deflation by a Static Magnetic Field

E. Fijalkow, MAPMO-CNRS, Université d'Orléans
Bâtiment de Mathématiques, BP 6759,
45067 Orléans CEDEX 2, France.

In the absence of magnetic field, two dimensional simulations shown the generation of phase space holes, as the response of the plasma to initial perturbations. Introduction of an increasing static magnetic field induced the deflation of the holes and their total disappearing.

The simulation code.

An Eulerian code [1] based on time splitting and phase space invariance properties of the splitted equations is used to solved the 2D, normalized to plasma frequency, Debye length and thermal velocity, Vlasov equation

$$\frac{\partial f}{\partial t} + v_x \frac{\partial f}{\partial y} + v_y \frac{\partial f}{\partial y} + (E_x - v_y B_z)\frac{\partial f}{\partial v_x} + (E_x - v_x B_z)\frac{\partial f}{\partial v_y} = 0 \qquad (1)$$

coupled to Poisson equation for the electric field. Every time step is symmetric, and at least of order two. For the actual simulation, the system is periodic in space variables. The initial conditions are the same for all simulations, only the value of B_z varies:

$$f(x, y, v_x, v_y, t = 0) = \exp(-(v_x^2 + v_y^2)/2)\,\{1 + .3(\cos k_0 x + \cos 2k_0 y)\} \qquad (2)$$

Numerical results.

As in the one dimensional case [2], holes are created in phase space, as response of the plasma to initial perturbations. Fig. 1 present projections of the distribution function f in two subspaces: (x, v_x) (y, v_y) at initial time. Fig.2 shows the phase space holes at $T = 16$ and $T = 100$. As in the one dimensional case the holes remain as long as the simulation.

It is interesting to note that in spite the fact that the electric field changes direction and amplitude during the evolution, $E_x(x, y)$ averaged on y is more than ten order of magnitude lower than $E_x(x, y)$ averaged on x (respectively averaged on x for E_y).

Fig. 3 presents four snapshots of the time evolution for a small magnetic field: $\omega_c = 0.1$. The begining of the time evolution looks like the preceding case one, but is slower in its evolution. At $T = 24$ we see that the remaining hole is very small, but density

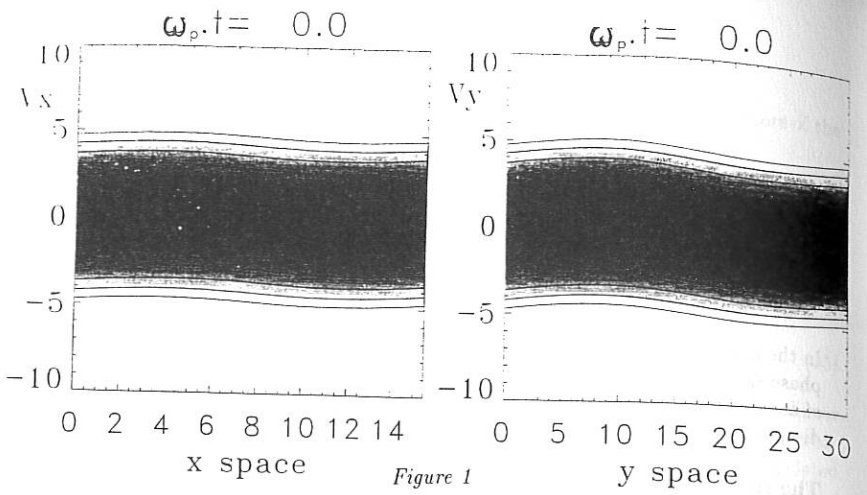


Figure 1

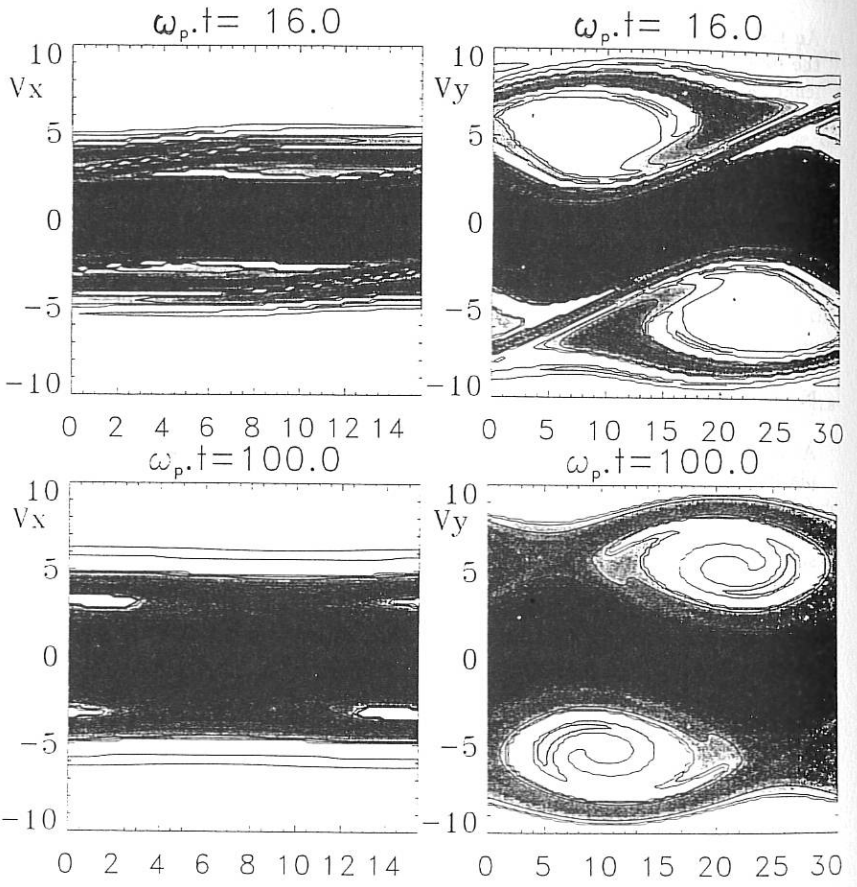


Figure 2

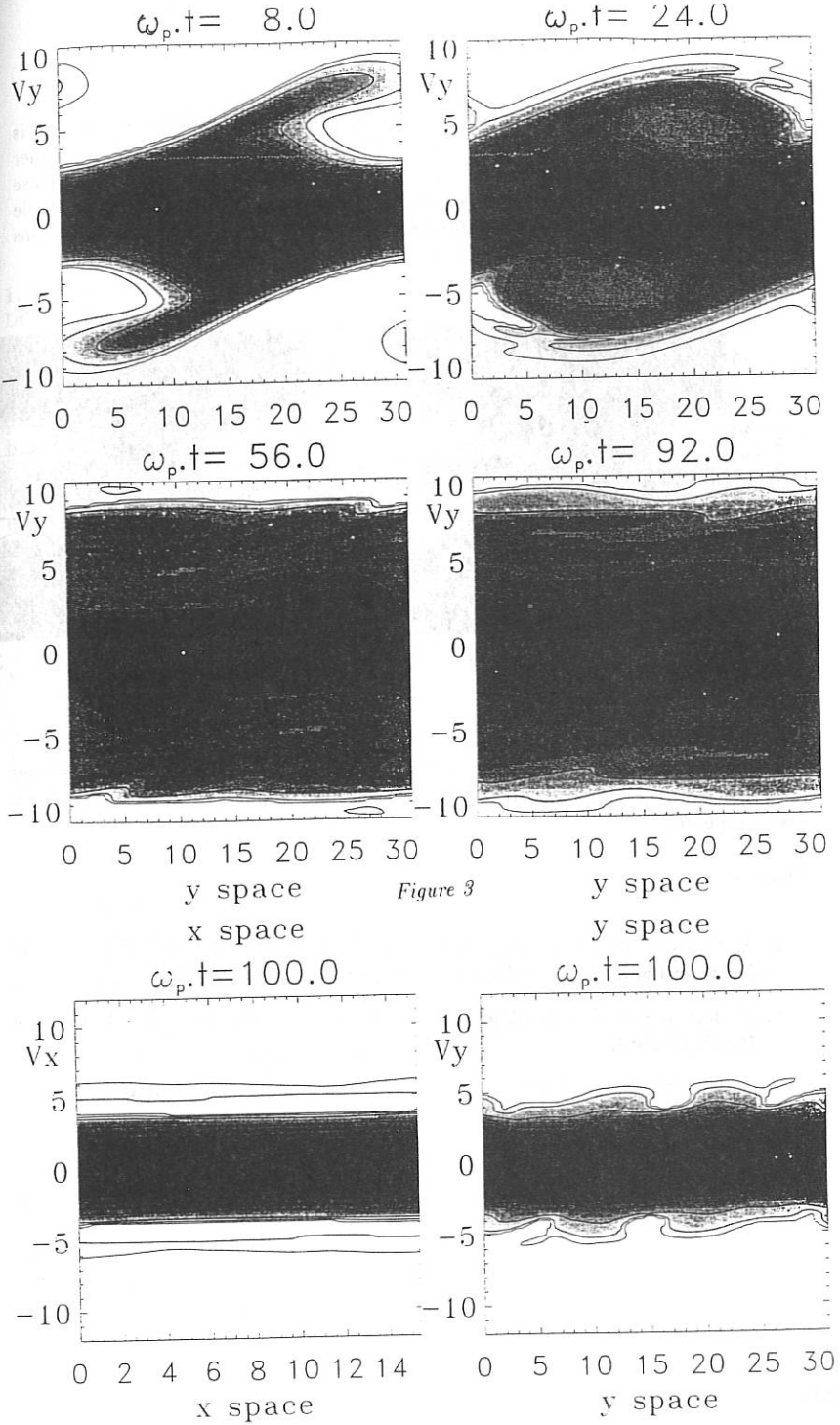

ω_p.t= 8.0
ω_p.t= 24.0
ω_p.t= 56.0
ω_p.t= 92.0
ω_p.t=100.0
ω_p.t=100.0
Vy
Vx
10
5
0
−5
−10
0 5 10 15 20 25 30
0 2 4 6 8 10 12 14
y space
x space

Figure 3

deflation remains. At $T = 56$ the hole disappears but the phase space structure is strongly perturbed and remains like that at longer times ($T = 92$). With an higher magnetic field ($\omega_c = .9$) no holes are created from the begining of evolution. The phase space structure takes forms like that of fig. 4. For strong magnetic field new stable structures appear in the density, structures that do not vary with plasmas oscillations - fig. 5 gives an exemple for $\omega_c = .9, T = 96$ and 100.

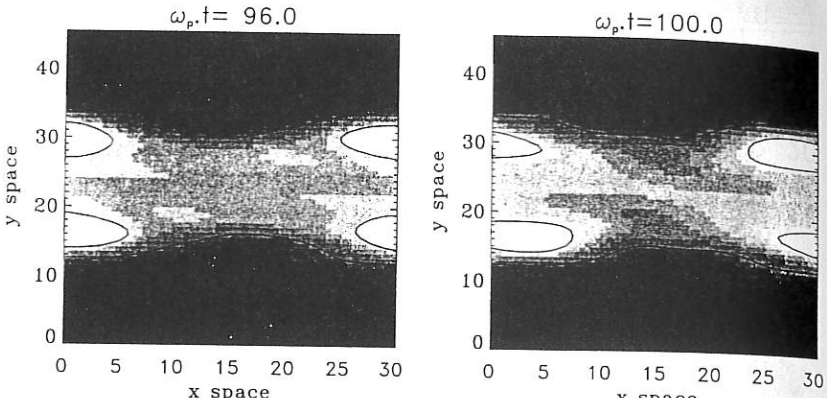


Figure 5

Acknowledgment:
The author undebted to IDRIS (Institut du Développement et des Ressources pour l'Informatique Scientifique, CNRS, Orsay, France) for computer time allocation on the C98 computer.

References:

1) E. Fijalkow et al: A Fully Parallel 2D Vlasov code, 14th Int. Conf. on the Numerical Simulation of Plasmas, Annapolis USA, 3-6 sept.1991

2) P. Bertrand et al in Nonlinear Vlasov Plasmas. F. Doveil/ed: Les Editions de Physique, 1988.

A New Drift Wave Soliton in an Inhomogeneous Plasma

Y Nejoh
Hachinohe Institute of Technology,
Myo-Obiraki, Hachinohe, 031, Japan.

1. Introduction

Drift waves in inhomogeneous magnetized plasmas have been studied experimentally and theoretically in the context of vortices and solitary waves[1]. The drift wave equations take an important place in theories of a magnetized plasma. Recently, the low frequency drift solitary wave is studied theoretically[2]. In the situation where the nonlinear drift wave propagates in interplanetary space, it may be possible that the spiky solitary waves are detected by satellites[3]. Although the lowest-order nonlinearity has been considered in conventional research, the new nonlinear wave mode in the drift wave has not been taken into account. Zakharov stresses the importance of the higher-order nonlinearity with regard to the collapse of Langmuir waves[4]. However, the drift wave is not taken into account and the profilre of the nonlinear wave is not shown.

We consider a nonlinear drift wave equation in an inhomogeneous magnetized plasma as a model equation, that is H-M equation. The purpose of this study is to demonstrate a new type of spiky solitary wave of the nonlinear drift wave equation. It will be expected that this investigation may be applied to explaining the behavior of larger amplitude nonlinear drift waves propagating in plasmas.

2. Derivation of A Nonlinear Evolution Equation

We begin by considering a nonlinear drift wave equation as a model:

$$\frac{\partial}{\partial t}\left(\nabla^2\phi-\phi\right)-\left(\nabla\phi\times\vec{i}_z\right)\nabla\left(\nabla^2\phi-\log n_0\right)=0\,. \tag{1}$$

We take the following assumptions:

1.the magnetic field $B=B_0\vec{i}_z$ is assumed to be constant and homogeneous.

2.the density n_0 is inhomogeneous in the x-direction and depends strongly on the spatial variation.

3.the drift wave is not connected with the temperature gradient.

4.the nonlinearity competes with the dispersion effect.

When the density $n_0=n_0(x)$ varying in a direction perpendicular to the magnetic field in the z-direction, eq (1) is reduced to

$$\frac{\partial}{\partial t}\left(\nabla^2\phi-\phi-\log n_0\right)+\left[\phi,\ \nabla^2\phi-\phi-\log n_0\right]=0\,, \tag{2}$$

where

$$[a,b]=\frac{\partial a}{\partial x}\frac{\partial b}{\partial y}-\frac{\partial a}{\partial y}\frac{\partial b}{\partial x}\quad.$$

In order to obtain stationary wave solution, we put $\phi = \phi(x, \eta)$, $\eta = y - ut$. (3)
Then eq.(2) becomes

$$\left[\phi - ux,\ \nabla^2\phi - \phi - \log n_0\right] = 0. \tag{4}$$

Equation (4) has the integral $F(\phi - ux) = \nabla^2\phi - \phi - \log n_0$
where the function F is an arbitrary function of the argument. Such solutions travel with the velocity u in the y direction. In the case of localized solitary solutions, F is determined from the condition that $\phi = 0$ at $y \to \pm\infty$. Then we obtain

$$\nabla^2\phi - \phi + \log\left[n_0(x - \phi/u)\right] - \log n_0(x) = 0. \tag{5}$$

Expanding $\log[n_0(x-\phi/u)]$ in the power series of ϕ, substituting it into (5), one obtains

$$\nabla^2\phi = c_1\phi + c_2\phi^2 + c_3\phi^3 + c_4\phi^4, \tag{6}$$

where the coefficients are determined to be

$$c_1 = 1 + \frac{1}{u}\left(\left[\frac{\partial}{\partial x}\log n_0\right]_{x=0} + x\left[\frac{\partial^2}{\partial x^2}\log n_0\right]_{x=0} + \frac{1}{2}x^2\left[\frac{\partial^3}{\partial x^3}\log n_0\right]_{x=0} + \frac{1}{6}x^3\left[\frac{\partial^3}{\partial x^3}\log n_0\right]_{x=0}\right),$$

$$c_2 = -\frac{1}{2u^2}\left(\left[\frac{\partial^2}{\partial x^2}\log n_0\right]_{x=0} + x\left[\frac{\partial^3}{\partial x^3}\log n_0\right]_{x=0} + \frac{1}{2}x^2\left[\frac{\partial^4}{\partial x^4}\log n_0\right]_{x=0}\right),$$

$$c_3 = \frac{1}{6u^3}\left(\left[\frac{\partial^3}{\partial x^3}\log n_0\right]_{x=0} + x\left[\frac{\partial^4}{\partial x^4}\log n_0\right]_{x=0}\right),$$

$$c_4 = -\frac{1}{24u^4}\left(\left[\frac{\partial^4}{\partial x^4}\log n_0\right]_{x=0}\right),$$

where $c_1>0$, $c_2<0$, $c_3>0$, $c_4<0$. Since the behavior of stationary wave solutions is determined largely by the spatial dependence of the density $n_0=n_0(x)$, we assume a simple exponential density profile, $n_0(x)=\exp(-fx)$, and constant temperature. Here f is the usual expansion parameter $f = r/L$, where $r = c_s/\omega_i$ is the drift wave dispersion scale length, and L is the density gradient scale length. As is seen in the observation, c_s and ω_i are the sound velocity and the ion cyclotron frequency, respectively.

Since eq. (6) heavily depends on x, we can approximate $d\phi/d\eta << d\phi/dx$. Then the left-hand side of (6) is reduced to $\nabla^2\phi \simeq \partial^2\phi/\partial x^2$. Using these approximations and integrating (6), we obtain

$$\left(\frac{\partial \phi}{\partial x}\right)^2 = c_1\phi^2 + \frac{2}{3}c_2\phi^3 + \frac{1}{2}c_3\phi^4 + \frac{2}{5}c_4\phi^5 = -\mathcal{U}(\phi)$$
$$= \phi^2\left(a_1 - a_2\phi - a_3\phi^2 - a_4\phi^3\right) \qquad (7)$$

where

$a_1=c_1$, $a_2=-(2/3)c_2$, $a_3=-(1/2)c_3$ and $a_4=-(2/5)c_4$.

3. A Spiky Solitary Wave

In order to obtain stationary wave solution, we transform (7) to

$$\left(\frac{\partial \phi}{\partial x}\right)^2 = A\phi^2(\varphi_0 - \phi)^3, \qquad (8)$$

because the solution exist only in the region of $-\mathcal{U}(\phi)>0$, where we determine that $A=a_4$, $\varphi_0=-a_3/3a_4$. A relationship between the potential function $-\mathcal{U}(\phi)$ and ϕ is shown in Fig.1. One can understand that the proper localized solution is obtained in the upper region of the horizontal axis. As a result of this, we have to integrate (8) independently in the above region.

Imposing the boundary conditions ϕ, $d\phi/dx \to 0$ at $x \to \pm\infty$, we have, from (8),

$$\pm\sqrt{A}\,(x - x_0) = \int_{\phi}^{\phi_0} \frac{d\phi}{\phi(\varphi_0 - \phi)^{3/2}} \qquad \text{in the region of } 0<\phi<\varphi_0 \qquad (9)$$

where ϕ_0 denotes the maximum amplitude of the drift wave at $x \to x_0$. We should note the sign of the coefficients of (7). If the coefficients $a_1>0$, $a_2>0$, $a_3<0$, $a_4>0$, then $u>0$ and $\varphi_0>0$.

Integrating (9) and using the boundary conditions, we have

$$\phi_s(x) = \varphi_0 \operatorname{sech}^2\left[\sqrt{\frac{\varphi_0}{\varphi_0 - \phi_s(x)}} \pm \frac{\sqrt{A}}{2}\varphi_0^{3/2}(x - x_0) - \mathcal{H}_1\right], \qquad (10)$$

where $\mathcal{H}_1 = \sqrt{\dfrac{\varphi_0}{\varphi_0 - \phi_0}} - \operatorname{arctanh}\sqrt{\dfrac{\varphi_0 - \phi_0}{\varphi_0}}$.

The wave profile of $\phi_s(x)$ is continuous and finite at $x \to x_0$. A new spiky solitary wave is

formed by (10). We illustrate the wave profile in Fig.2.

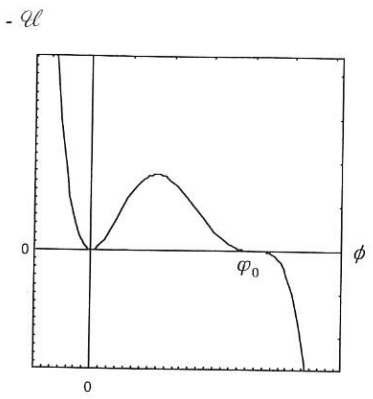


Fig.1: The potential function - $\mathscr{U}$ vs. potential ϕ.

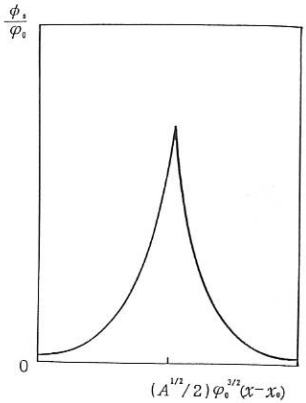


Fig.2: The profile of a spiky solitary wave.

4. Concluding Discussion

We have presented a new type of nonlinear wave mode which occur in nonlinear drift waves, assuming the spatial dependence of the density and using a quasi-one dimensional approximation. The stationary wave solution of the derived nonlinear equation are obtained due to the fifth-order nonlinearity, and bear a spiky solitary wave. The new spiky solitary wave solution appear to make a step forward in the general scheme of nonlinear normal modes for plasma waves.

In actual situations, spiky solitary waves are frequently observed in interplanetary space. Hence, referring to the present spiky solitary waves, we can understand the properties concerning the new nonlinear wave mode of nonlinear drift waves in space. Although the author has not examined the application of these results to a specific observational result, this study is important in discussing the nonlinear wave modes which occur in plasmas.

Acknowledgement

The author wish to thank Aomori Foundation for Promotion of Technological Educations.

References

[1]Hasegawa A and Mima K, *Phys. Fluids* **21** 87 (1978)
[2]Lakhin V P et al, *Plasma Phys. Controlled Fus.* **30** 457 (1988)
[3]Hasegawa A, *Adv. Phys.* **34** 1 (1985)
[4]Zakharov V E, *Sov. Phys. Usp.* **31** 672 (1988)

The effects of sub-Alfvénic shear flow on the resistive G-mode

RB Paris, L Hou
Department of Mathematical and Computer Sciences, University of Abertay Dundee,
Dundee DD1 1HG, United Kingdom
and
AD Wood
School of Mathematical Sciences, Dublin City University, Dublin 9, Ireland

1. Introduction

Since equilibrium mass flows observed in laboratory plasmas are typically much slower than the Alfvén speed, initial studies [1,2] on the effects of shear flow on the resistive tearing mode restricted their attention to the sub-Alfvénic regime. It was shown that the inviscid tearing mode is destabilised by a parallel shear flow and, moreover, that the well-known stability threshold, $\Delta' = 0$ can be modified to result in the possibility of an unstable mode when $\Delta' \leq 0$. More recent work on both the linear and nonlinear regimes has considered flows along the magnetic field comparable to the Alfvén speed [3,4]. In the external ideal region, the parallel shear flow can now dramatically modify the value of the external matching parameter Δ' to produce a strong stabilisation of the tearing mode.

Here the investigation of the effects of a parallel equilibrium shear flow and viscosity is extended to the linear resistive gravitational interchange (or G-mode) by including a gravitational acceleration acting normal to the plane current layer. The equilibrium flow we consider is again supposed to be in the sub-Alfvénic regime. Such flows result in a simplification of the problem since, in the high conductivity limit, the flow is thereby confined to the resistive boundary layer and is too slow to excite the ideal Kelvin-Helmholtz instability.

In contrast to the pure tearing mode where sub-Alfvénic flow exerts a destabilising influence, it is found that the effect of flow on the G-mode is a stabilising one. Such a stabilising tendency is supported by previous work on the influence of mass flows on the ideal, pressure-driven interchange instability in cylindrical geometry [5] and in recent work on the ideal ballooning mode [6].

2. The model

We consider the standard plane slab model of an incompressible plasma specified by the magnetic field $\mathbf{B}_0 = \{B_{0x}(y), 0, B_{0z}(y)\}$ with a diffuse density profile $\rho_0(y)$ and acted upon by a gravitational acceleration $\mathbf{g} = \{0, g, 0\}$ in the positive y direction. In the high conductivity limit, we assume that the equilibrium velocity consists only of a shear flow $\mathbf{V}_0(y)$ directed along $\mathbf{B}_0$. Linearisation of the dissipative MHD equations for a plasma with a uniform resistivity η and perpendicular coefficient of viscosity $\mu_\perp$ yields two coupled equations describing the y-components of the first-order velocity v_{y1} and magnetic field B_{y1}.

Taking all first-order quantities to vary like $\exp[i(k_x x + k_z z) + \omega t]$, where $\mathbf{k} = \{k_x, 0, k_z\}$ is the wave vector and ω is the growth rate, we obtain the system of equations describing the resistive tearing and gravitational interchange modes in the presence of an equilibrium

shear flow as

$$(p+iR_0)\left\{(\rho W')' - \alpha^2\rho W\right\} - i(\rho R_0')'W + \frac{\alpha^2 S^2 G_0 W}{p+iR_0} - N_0\left(\frac{d^2}{d\mu^2} - \alpha^2\right)^2 W =$$

$$\alpha^2 S^2 F\left\{\psi'' - \psi(\alpha^2 + F''/F)\right\} \tag{1}$$

$$(p+iR_0)\psi + FW = \psi'' - \alpha^2\psi, \tag{2}$$

where the primes denotes differentiation with respect to μ and we have introduced the standard dimensionless variables [7] $\psi = B_{y1}/B, W = -i|\mathbf{k}|\tau_R v_{y1}, F(\mu) = (\mathbf{k}.\mathbf{B}_0)/|\mathbf{k}|B$, $\alpha = |\mathbf{k}|a, p = \omega\tau_R, \rho = \rho_0/\langle\rho\rangle, \mu = y/a, S = \tau_R/\tau_H, R_0(\mu) = (\mathbf{k}.\mathbf{V}_0)\tau_R, G_0 = -g(\rho_0'/\rho_0)\tau_H^2$, $N_0 = 4\pi\mu_\perp/\eta$, and $\tau_R = 4\pi a^2/\eta$, $\tau_H = a(4\pi\langle\rho\rangle)^{1/2}/B$ are the resistive and hydromagnetic time scales, $\langle\rho\rangle$, B are measures of the density and magnetic field strength and a is the characteristic dimension of the current layer.

We consider the equilibrium mass flow along the field to be significantly sub-Alfvénic [1,2] characterised by the ordering $|\mathbf{V}_0| \sim S^{-1/5}v_A$, where v_A is the Alfvén speed in the layer, which is typical of the range of observed toroidal rotation speeds in tokamaks. In the ideal outer region the behaviour of ψ is then the same as in the flowless case [7], so that the familiar matching parameter, $\Delta' = [d\ \ln\ \psi/d\mu]_{0-}^{0+}$, is independent of the equilibrium shear flow in this ordering and can consequently be considered as a given parameter dependent on the global structure of the equilibrium magnetic field and the wavenumber α.

Assuming the "weak" viscous ordering $N_0 \sim S^{-2/5}$ and a Suydam stable layer, we now put $F \sim F'\mu$, $R_0 \sim R_0'\mu$, $\tilde{H} = W + iR_0'/F'$ in the boundary layer and rescale all the variables based on the boundary-layer thickness δ. This yields the boundary-layer equations in the "constant-ψ" approximation given by

$$(P+iR\theta)\frac{d^2H}{d\theta^2} - \theta^2 H + \frac{G(H-iR)}{P+iR\theta} - N\frac{d^4H}{d\theta^4} = P\theta + \frac{\sin\chi}{\pi} \tag{3}$$

$$\Delta'/\Delta = \cos\chi = \int_{-\infty}^{\infty}(P+\theta H)\,d\theta, \tag{4}$$

where $\theta = \mu/\delta$, $P = p\Delta^{-4/5}(\alpha SF')^{-2/5}, H = F'\tilde{H}\Delta^{-3/5}(\alpha SF')^{-4/5}, \delta = \Delta^{1/5}(\alpha SF')^{-2/5}$, $R = R_0'\Delta^{-3/5}(\alpha SF')^{-4/5}, G = (G_0/(F')^2)\Delta^{-6/5}(\alpha SF')^{2/5}, N = N_0\Delta^{-6/5}(\alpha SF')^{2/5}$ and [2]

$$\Delta e^{i\chi} \equiv \Delta' - \pi i(F''/F'), \quad \Delta > 0, \quad -\pi < \chi \leq \pi. \tag{5}$$

Introduction of the complex Fourier transform $h(k) = \int_{-\infty}^{\infty} H(\theta)e^{-ik\theta}\,d\theta$, then shows that Eqs.(3) and (4) can be expressed as a pair of third-order boundary value problems on $(-\infty, 0)$ and $(0,\infty)$ given by

$$(R\frac{d}{dk} - P)L[h] - Gh = 0, \quad -\infty < k < 0, \ \ 0 < k < \infty, \tag{6}$$

where L denotes the viscous-tearing mode operator

$$L[h] \equiv \frac{d^2h}{dk^2} + R\frac{d(k^2h)}{dk} - (k^2P + k^4N)h,$$

subject to the boundary conditions

$$h'(0\pm) = -ie^{\pm i\chi}, \quad h''(0-) = h''(0+) + 2\pi iG, \quad h(\pm\infty) = 0.$$

The eigenvalue relation is then expressed in terms of the discontinuity in $h(k)$ across $k = 0$ by

$$2\pi i P = h(0+) - h(0-). \tag{7}$$

3. Results and discussion

We present the results as eigenvalue loci in the complex P-plane as the flow parameter R increases from zero. For the inviscid tearing mode ($G = 0$), it has been previously found [8] that part of the spectrum exhibits a discontinuous behaviour when $R \neq 0$. The eigenvalue loci corresponding to $0 \leq \chi \leq \frac{1}{2}\pi$ emanate from their no-flow values in a continuous manner, while those that eventually form part of the unstable spectrum when $\frac{1}{2}\pi < \chi < \pi$ originate not from the corresponding stable eigenvalues situated on $\arg P = \pm\frac{4}{5}\pi$ (except when $\chi = \pi$), but emerge from the accumulation point of the spectrum at the origin $P = 0$. The loci which emanate from the rays $\arg P = \pm\frac{4}{5}\pi$ remain in $\mathrm{Re}(P) < 0$, eventually moving towards and out along the negative real axis with increasing flow R and consequently have not been shown.

When $G > 0$, there is an abrupt change in the inviscid spectrum. The no-flow eigenvalues with the largest $\mathrm{Re}(P)$ are now all situated on the positive axis. The eigenvalue loci corresponding to $0 \leq \chi \leq \frac{1}{2}\pi$ emanate in a continuous manner from their no-flow locations as R is increased. The loci corresponding to $\frac{1}{2}\pi < \chi \leq \pi$ again consist of two distinct branches: the first branch emerges from the accumulation point (which was at the origin when $G = 0$) situated at the point corresponding to the no-flow eigenvalue with $\chi = \frac{1}{2}\pi$. The second branch emanates continuously from the no-flow positions on the real axis and corresponds to loci with steadily decreasing $\mathrm{Re}(P)$ as R increases [this branch is not shown].

In Fig. 1 we show the eigenvalue loci for different values of G when $N = 0$. The case $G = 0$ corresponds to the pure tearing mode, which is seen to be destabilised by the presence of a shear flow. Modes which are stable in the standard no-flow case (corresponding to $\frac{1}{2}\pi < \chi < \pi$) can be driven unstable by sufficiently large flow in the sub-Alfvénic regime [1,2].

The inclusion of the effects of a gravitational term is complicated by the fact that it is not possible to separate the resistive G-mode from the tearing mode, so that a certain degree of mode mixing is unavoidable. As G progressively increases, the loci pattern moves to the right without topological change. For small R, it is seen that there is a stabilising effect for an increasing range of values of χ, which includes $\chi = 0$ (where the tearing mode is most active) once G exceeds approximately 0.5. For larger values of R, however, all the loci (except that corresponding to $\chi = \pi$) do eventually bend back in the direction of increasing $\mathrm{Re}(P)$ due to the destabilisation effects of the tearing mode.

We have carried out an asymptotic calculation to determine the dependence of P for large values of the flow parameter R (but still such that the ordering of the equilibrium flow $|\mathbf{V}_0| \sim S^{-1/5} v_A$ remains valid). From [9], it is found that

$$P \simeq e^{i\chi/2}\left(\frac{R}{2\pi}\right)^{\frac{1}{2}} + \frac{\cos\chi\,\Gamma(1/3)}{2\pi\, 3^{2/3} R^{1/3}} + \frac{G\Gamma(2/3)}{3^{1/3} R^{2/3}} \quad (R \gg 1). \tag{8}$$

The first two terms are the familiar contribution to the tearing mode [1,2], which scales like $R^{1/2}$ for large R, while the leading-order contribution to the G-mode is independent

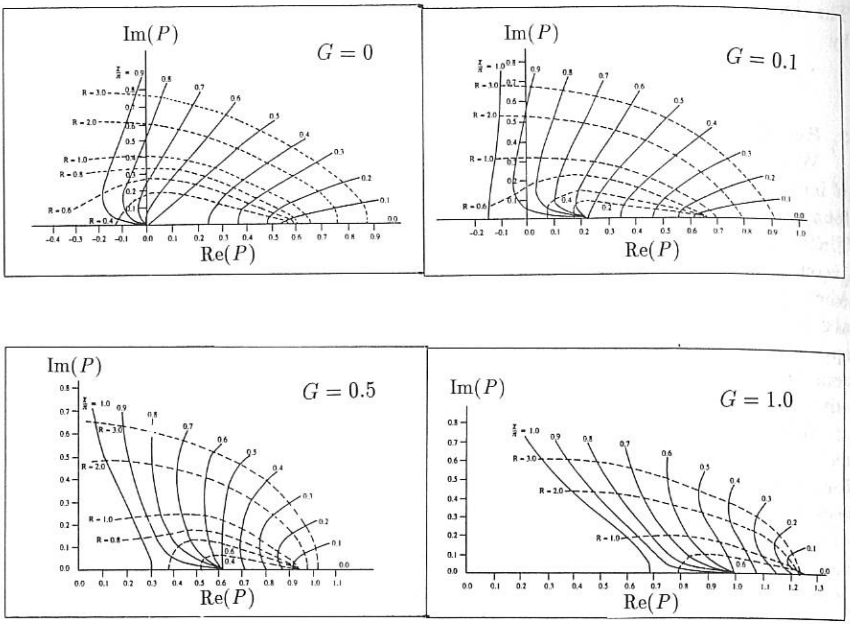


Fig.1: The eigenvalue loci in the complex plane for different values of R and G when $N = 0$. The case $G = 0$ corresponds to the pure tearing mode.

of χ and scales like $R^{-2/3}$. Consequently, in contrast to the tearing mode where increasing the flow results in an increased growth rate (when $|\chi| < \pi$), the gravitational contribution to P is seen to *decrease* as R increases. The approximation in Eq.(8) is found to agree well with the numerical results in Fig. 1 when $R \gg 1$. The effects of viscosity ($N \neq 0$) on the eigenvalue loci is discussed in [9].

This work was supported by European Commission Fusion Contract No. 401-89-11 FUA IRL.

References

[1] RB Paris and WN-C Sy, Phys. Fluids **26**, 2966 (1983).
[2] A Bondeson and M Persson, Phys. Fluids **29**, 2997 (1986).
[3] XL Chen and PJ Morrison, Phys. Fluids B **2**, 495, 2575 (1990); B **4**, 845 (1992).
[4] G Einaudi and F Rubini, Phys. Fluids **29**, 2563 (1986); B **1**, 2224 (1989).
[5] A Bondeson, R Iacono and A Bhattacharjee, Phys. Fluids **30**, 2167 (1987).
[6] RL Miller, FL Waelbroeck, AB Hassam and RE Waltz. Submitted to Physics of Plasmas (1994).
[7] HP Furth, J Killeen and MN Rosenbluth, Phys. Fluids **6**, 459 (1963).
[8] RB Paris, AD Wood and S Stewart, Phys. Fluids B **5**, 102 (1993).
[9] L Hou, RB Paris and AD Wood. Submitted to Phys Fluids B (1995).

Construction and Validation of a Dynamical L-/H- and ELM-model from Experimental data.

P. E. Bak
JET Joint Undertaking, Abingdon, Oxon, OX14 3EA, England

July 28, 1995

1 Introduction

The experimentally observed dynamics of L-/H- and ELMy mode during operation of JET shows a variety of different scenarios of plasma recycling whose qualitative behaviour has been identified through the D_α-radiation. This includes qualitative different so-called dithering cycles, i.e. H-L-H transitions, which are identified after the initial L-H transition. Further qualitative different scenarios of ELMy H-modes including intermittency like characteristics and highly irregular periods of grassy ELMs. Compound ELMs, which are Giant ELMs followed by series of grassy ELMs are described. The analyses to be described are limited to the temporal dynamics. However verification and construction of models with the observed dynamics has to be done accordingly. This work outlines a minimal framework for as simple a model as possible including the complex experimentally observed dynamics.

2 Experimentally observed ELM scenarios

The dynamical behaviour that is observed is based on the recycling of particles in the edge of the plasma which is proportional to the intensity of the emitted D_α radiation. The sampling rate is normally between $20 - 40kHz$ and obtained from the lines of sight as seen in figure 1. The measurement is relatively localised to the edge of the plasma since most of the neutrals are ionised around the last closed surface. Various scenarios of H-L-H transitions and ELM dynamics measured during the recent experimental campaign at JET are identified and qualitatively described in the following. The ELM prolonged High confinement regime is of special interest for steady state operation and a detailed understanding of the on- and offset of ELMs are essential for impurity control as well as power load on the target plates. The advantage of ELM controlled impurity control to the loss of confinement is due to the more steep density profile than temperature profile.

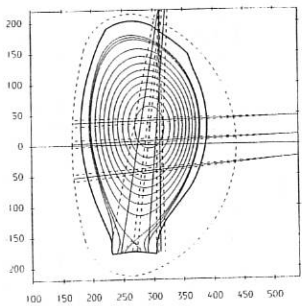


Figure 1: *Cross section of the JET vessel showing the flux surfaces and the lines of sight of the D_α measurements.*

As an example of the experimentally observed scenarios of the particle outflux the D_α-signal during JET pulse 24745 is examined. The pulse was a $I_p = 3MA$ and $B_T = 2.8T$ discharge with additional Neutral Beam Heating (NBI) applied as follows: $8MW$ between $t = 54.0 - 56.0s$, $4MW$ between $t = 56.0 - 57.0s$ and finally $2MW$ between $t = 57.0 - 58.0s$. The dithering cycles and the ELMy H-mode during the $8MA$ NBI $t = 54.0 - 55.0s$ is the scenarios that will be described in the following using the horizontal D_α-trace S3-AD36. The plasma enters the H-mode between $t = 54.1 - 54.15$, figure 2, which is seen as steep decrease in the D_α as a result of the higher confinement and decreased outflux from the plasma edge. A few teens of milliseconds after the steep drop in the D_α-signal the particle outflux starts oscillating, $t = 54.24 - 54.38s$, which essentially is two unstable states one of which is characterised by a higher level in the D_α-signal with small random fluctuations and a second state which has a base line well below the first state and is characterised by a repetitive sequence of outflux starting with a sharp peak, followed by a smooter and longer lasting rise and finally before the back-transition to the first state comes a series of smaller spikes. The total sequence is repeated with a constant frequency of $\sim 52Hz$. The plasma then enters another regime, $t = 54.4 - 54.5s$, which again can be described as

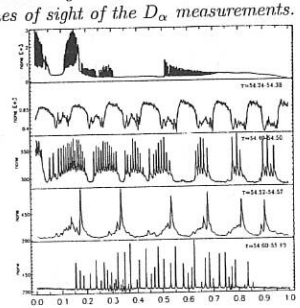


Figure 2: *Different scenarioes of dithering and ELMy H-mode for pulse 24745.*

a mode competition. One state with a generally higher D_α-level overlaid with series of large sharp transitions where each event has the characteristic of an ELM. A second state with a lower quiescent D_α-level. Between $t = 54.52 - 54.57s$, a series of similar events is identified. The D_α-level starts rising and a smaller peak in the trace is followed by a larger peak before the level falls back, which is repeated with a frequency around $26Hz$. At $t = 54.6s$ the plasma is in ELM free H-mode for approximately $50ms$ and then a series of ELMs appears for one third of a second. The ELMs varies in size as well as duration and the on- and offset of the ELMs happens instantaneous.

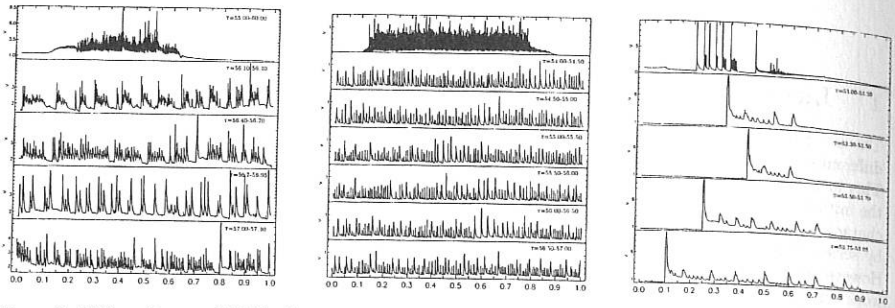


Figure 3: *Different types of ELMy characteristics of H-mode JET plasmas 29677, 33075 and 34207 respectievly. The time axes are normalised with the actual time window given in each sub-figure.*

A different type of ELMy H-mode behaviour is seen in pulse no 29677, which was a $I_p = 2MA$ and $B_T = 2.8T$ pulse with additional heating using NBI. The dynamics is shown illustrated in figure 3 where the following traces show different qualitative behaviour of the ELMs. $t = 56.10 - 56.40$ is characterised by its burst like nature, which starts with a sharp rise in the D_α-signal from the quiescent H-mode level and then a flat burst like level lasting for teens of milliseconds after which the D_α-level returns to the quiescent H-mode level. After this the characteristic of the D_α-signal changes to a more regular behaviour, $t = 56.40 - 56.70$, with periods of $10 - 100ms$ with ELMs occurring regularly with a repetition frequency at about $370Hz$. Between these periods the D_α-level shows the quiescent H-mode level. This is followed by a sequence, $t = 56.70 - 56.95$, which has larger ELMs and the occurrence of ELMs is now only a few events at the time. Finally the ELM characteristic, $t = 57.00 - 57.40$, is of the same qualitative type as seen between $t = 56.40 - 56.70$. In pulse 33075 with $I_p = 2.5MA$ and $B_T = 2.8MA$ a so-called sub H-mode is achieved, where the D_α-signal over a "long" time period exhibit a steady but highly irregular temporal behaviour. There are no burst-like behaviour and the size of the ELMs and the time interval between consecutive ELMs varies over a wide rage. Transient type of events from no 34207are observed. This was a $I_p = 4.0MA$ and $B_T = 4.0MA$ H-mode pulse with a long ELM-free period ended by a series of giant ELMs, some of which are of the compound type. Apart from the duration the compound ELMs has the same characteristic: A giant ELM followed by periods of a few small events and a larger event. Eventually the D_α-level is back at the quiescent H-mode level.

3 Modelling and Data analysis

The most suitable mathematical that allows complex dynamics, which is relatively easy to handle analytical and numerical and holds the possibility of an explicit or at least implicit comparison with experimental data is within the framework of dynamical systems. In general a dynamical system is described by a N-dimensional state vector, $\mathbf{x}$, whose temporal evolution is defined by a set of ordinary differential equations given by the vector field, $\mathbf{F}$, or mapping, $\mathbf{M}$,

$$\dot{\mathbf{x}} = \mathbf{F}[\mathbf{x}(\mathbf{t});t] \quad \mathbf{x}_{i+1} = \mathbf{M}[\mathbf{x}_i;t] \tag{1}$$

where the vector field generally has an explicit time dependency and in which case the system is termed non-autonomous otherwise autonomous. The time evolution of the system is referred to as the trajectory or orbit and takes place in the phase space $(x^{(1)}, x^{(2)}, ..., x^{(N)})$. Representations such as 1 either occurs directly from first principle or as a result of a truncation of partial differential equations. To reconstruct the phase space of an experiment with non linearity it is not necessary to measure all the state variables simultaneously but only one observable under the hypothesis of Takens Theorem[1], which states the existence of a mapping which is a diffemorphis between the evolution of the dynamics in the phase space and the asymptotic dynamics of an experimental system. The reconstruction is performed by use of the method of delays and a practical favourable implementation of the method proposed by Broomhead[2]. The time series is obtained as a compression of the state vector into one observable

$$\mathbf{x}_i = \Phi_{\mathbf{F},v}(\phi_i(\mathbf{y})) = (v_i, v_{i+J}, \ldots, v_{i+(n-1)J})^T \tag{2}$$

and the trajectory matrix is composed as

$$\mathbf{X} = N^{-\frac{1}{2}} \begin{bmatrix} \mathbf{x}_1^T \\ \mathbf{x}_2^T \\ . \\ . \end{bmatrix} = N^{-\frac{1}{2}} \begin{bmatrix} v_1 & v_2 & v_3 & . & . \\ v_2 & v_3 & v_4 & . & . \\ . & . & . & . & . \\ . & . & . & . & . \end{bmatrix} = \mathbf{S} \cdot \sigma \cdot \mathbf{C} \tag{3}$$

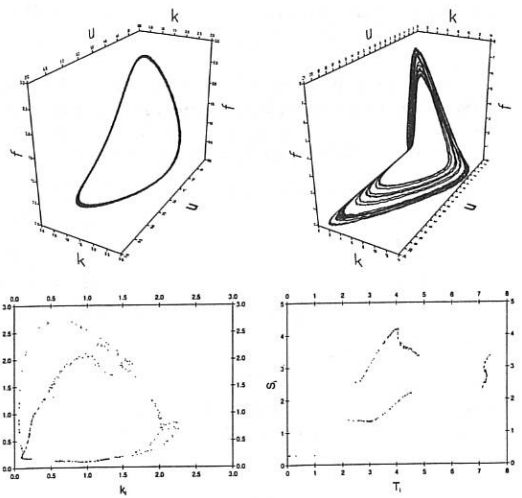
Event like or discrete phenomena, such as the ELMs, can be studied in an equivalent manner by defining a time series by the time interval between two consecutive event and their size such as

$$\mathbf{T} = (t_2^{ELM} - t_1^{ELM}, ..., t_{i+1}^{ELM} - t_i^{ELM}, ..., t_N^{ELM} - t_{N-1}^{ELM}) \quad \mathbf{S} = (s_1^{ELM}, ..., s_i^{ELM}, ..., s_{N-1}^{ELM}) \tag{4}$$

The size of each ELM can then be determined by estimating the area "under" each ELM. The time series $\mathbf{T}$ and $\mathbf{S}$ can the be studied separately or together

$$T_{i+1} = \mathbf{M}^T[T_i] \quad S_{i+1} = \mathbf{M}^S[S_i] \quad (T_{i+1}, S_{i+1}) = \mathbf{M}^{TS}[T_i, S_i] \tag{5}$$

To illustrate this a dynamical model of the L-H transition consisting of three nonlinear ordinary differential equations in which the stationary H-mode in a part of parameter space becomes unstable and shows oscillations which can be understood as ELMs[3] is studied. The model describes the temporal evolution of the three characteristic variables: The turbulent kinetic energy K, the background shear flow kinetic energy F, and the potential energy related to the profile U, which all are defined as:



$$K = \frac{1}{\delta}\int_{-\delta}^{0} \frac{1}{2}\langle \tilde{v}^2 \rangle \, dx, \tag{6}$$

$$F = \frac{1}{\delta}\int_{-\delta}^{0} \frac{1}{2} v_0^2 dx, \tag{7}$$

$$U = \frac{1}{\delta}\int_{-\delta}^{0} \frac{P_0}{n_0 m_i} \frac{(-x)}{L_c} dx. \tag{8}$$

Figure 4: *Dynamics obtained from the Sugama/Horton. Limit cycle oscillation in the H-mode, ELM-like sequence with a sharp transition characteristic, Poincare map for an externally applied time dependent perturbation and the corresponding TS-map.*

And from the reduced resistive MHD equations and appropriate normalization the following closed set of the equations for energy transfer between u, k and f has been derived

$$\dot{u} = q - u^{1/2}k, \tag{9}$$

$$\dot{k} = u^{1/2}k - cu^{-1/2}fk - d^{-1}(u)k^2, \tag{10}$$

$$\dot{f} = cu^{-1/2}fk - cm(u)f. \tag{11}$$

where q is the normalized potential energy input, which is externally controllable parameter, c is a non-dimensional numerical constant. $d(u)$ is the L-mode anomalous diffusivity and a function of u through it's background temperature dependency. And $m(u)$ is related to the ion collisional viscosity. The stationary solutions corresponds to the L and H mode given by (u_L, k_L, f_L) and (u_H, k_H, f_H) respectively. Both u_L and u_H are functions of the control parameter q.

The qualitative reconstruction of phase space has been applied to different periods of dynamics in pulse no 24745. The embedding dimension was chosen to be 80 with a unit lag time, $J = 1$. The singular spectrum generally has the form as seen in figure 5, which is from data between $t = 54.4 - 54.5s$ and from which it is seen that the most significant dynamics can be described by a projection onto the three - possibly four - most significant singular vectors. Further it is concluded that the system evolves in a low dimensional space. The projection onto the most significant vectors to perform the qualitative reconstruction is seen in figure 5, where the H-L mode competition between $t = 54.4 - 54.45s$ shows that the evolution in the 3 dimensional

phase space takes place on a geometrical object whose topology is torus like. Reconstruction of the ELMy H-mode, $t = 54.6 - 55.1s$ shows indications of attractions in terms of the trajectory following bands in the phase space, however the data set is not very large and any conclusive statements cannot be made. To compare the experimentally observed dynamics the topology of the evolution in the phase space has to be evaluated using measures such as Lyaponov exponents.

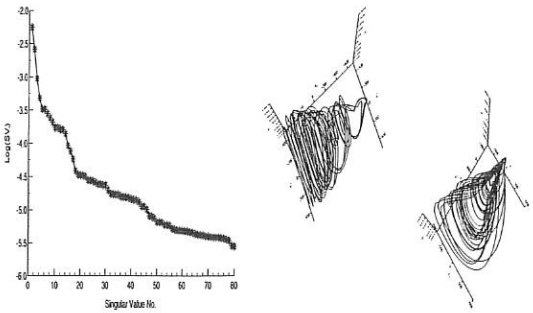


Figure 5: *Singular Value spectrum from the reconstruction performed on the time series obtained from and Qualitative reconstruction of dynamics observed during the H-L-H transitions as well as during the ELMy H-mode in pulse 24745*

Correlation between the size of an ELM and the time-difference of consecutive ELMs is mapped in figure 6 showing the image of the map $\mathbf{M}^{TS}$ as well as a return map representation of the time difference between consecutive ELMs, $\mathbf{M}^{T}$. With the small number of ELMs used no clear picture is seen however there is a clear indication of more favourable sequences of ELMs than others. Using these techniques an indirect comparison between existing models or truncations of PDEs to ODEs, as required for the Itoh-model[4], and identification of the qualitative requirements of the models from the observed dynamics has been formalised. Naturally a more detailed treatment is required, which is beyond the scope of this paper, but not impossible.

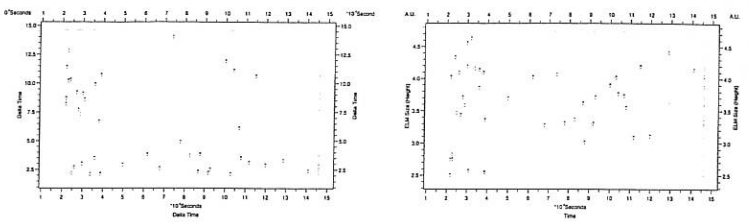


Figure 6: *Correlation and Return map analysis of ELMy sequence obtained during the High confinement mode of JET-pulse 29677 $t = 56.7 - 56.95s$. Time and Size map $[T_i, S_i]$ and Return map $[T_i, T_{i+1}]$.*

4 Conclusion

It is concluded that on the basis of the complex dynamics observed during L-/H- dithering cycles and the different scenarios of ELMs a comprehensive model must in principle exhibit the same qualitative behaviour, and that dynamical systems in terms of a set of three, or finite low-dimensional, non-linear coupled ordinary differential equations is the minimal mathematical framework in which this can be achieved and still holds a relatively easy way to compare with the experimentally observed. Further qualitative phase space reconstruction is introduced as a method to identify elements of dynamics as well as a tool to validate a model against experimental results. Discrete mappings are introduced to identify long term correlation of ELMy scenarios and again the images of these mappings can be used to validate the models. It is believed that with the effects of transient phenomena and truncations of partial differential equations in mind that the proposed framework is essential and sufficient to build the bridge between observed L-/H- and ELMy dynamics and models.

5 References[1]

[1] F. Takens, "Detecting Strange Attrac...", Lecture Notes in Mat., Springer 1980, p366.
[2] D. Broomhead, "Extracting Qualitative ...", Physica 20D (1986) p217-236.
[3] H. Sugama and W. Horton, "L-H confinement...", Plasma Phys. Cont. Fusion, 37 (1995) p345-362
[4] S. Itoh and K. Itoh, Phys. Rev. Lett. 60, 2276 (1988)

[1]The author gratefully acknowledge the JET-team for providing the data and Prof. M. Haines, Drs P. Stott, T. Mullin, D. Broomhead, N. Deliyanakis and G. Vayakis for stimulating discussions.

First Observations of Collective Thomson Scattering from JET Plasmas

J A Hoekzema, H Bindslev, J Egedal, J A Fessey, C P Gatcombe, N P Hammond, T P Hughes[1], J S Machuzak[2], J W Oosterbeek, P J Roberts, A L Stevens, P E Stott
JET Joint Undertaking, Abingdon, Oxfordshire, OX14 3EA, UK.
[1] University of Essex, Colchester, Essex , CO4 3SQ, UK.
[2] Plasma Fusion Centre, MIT, Cambridge, Mass 02139, USA.

1. Introduction

The main aim of the JET fast ion and alpha particle diagnostic is to measure the velocity distribution of the fast alpha particles in JET during the DT phase from collective scattering of high power 140 GHz radiation [1]-[3]. Successful experiments at similar frequencies have recently been reported on the Wendelstein W7-AS stellarator [4]. We report the first observations of collective scattering from JET plasmas. They indicate that the diagnostic will give the predicted performance for observations of alpha particles in JET.

2. The diagnostic system

The gyrotron source can generate 500 kW RF at 140 GHz for 0.5 s, with > 90 % in a Gaussian beam. For these first measurements up to 15 pulses of 1 to 5 ms duration were used. Access to the central plasma is possible at high magnetic fields ($B > 3$ T). The steerable injected and received beams are focused to waists of 30 mm radius near the plasma centre.

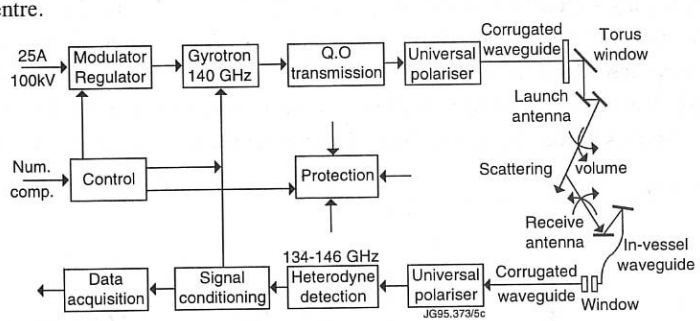


Fig. 1: Schematic overview of the KE4 diagnostic

The gyrotron was operated at ~ 90 % of maximum power to give a stable, spectrally clean output. After filtering and polarization the power was 370 kW, of which almost 100 % reached the torus via ~ 60 m of 88.9 mm ID corrugated waveguide. During transmission the 190 mm diameter water-free fused silica torus window was heated at 100° C/s in the

centre. The beam profile at the torus, determined from the pattern on thermosensitive paper, appeared to be closely Gaussian. The effective reflectivity of the vessel was low: even with no plasma the power injected into the torus caused no damage to any of the diagnostic detectors sensitive to this frequency.

On the receiver side, stray gyrotron radiation reaching the receiver antenna (~ 10 mW) was removed by two notch filters in series, with at least 80 dB attenuation and a full width of 200 MHz at -3 dB. Frequencies outside the notch filter, generated briefly during switch-on and switch-off of the gyrotron, caused temporary saturation of the receiver and negative spikes in the raw data. The receiver bandwidth (134 to 146 GHz) is divided into 32 channels, 21 in the lower sideband and 10 in the upper, and one monitoring stray 140 GHz.

3. Results

O to O mode scattering was selected to minimise the effects of refraction. Intersection was required at R = 3.0 m, 20 cm above the torus centre, with $|\mathbf{k}| = |\mathbf{k}^s - \mathbf{k}^i| = 1520\ \mathrm{m}^{-1}$. To set up the system the incident and scattered rays satisfying the required scattering geometry were found for an actual plasma similar to those expected, with $B_o = 3.4$ T, $n_{eo} = 3.4 \times 10^{19}\ \mathrm{m}^{-3}$. From this the necessary settings of the antenna mirrors and of the universal polarizers were computed. The resulting angle between B and k was 122° and the scattering angle 32°. In operation, one beam was adjusted slightly to optimise the overlap.

Clear scattering signals were seen from plasmas with $B_o > 3$ T. Fig. 2[a] is a sample of the raw data. At lower fields (between ~ 2 and ~ 3 T) absorption of a pulse by EC resonances causes local heating and increased ECE around a flux surface. This is seen in Fig. 2[b]. The linear rise during the pulse and subsequent cooling time constant of a few ms clearly identifies the heating signal. No significant local heating was seen for $B_o > 3$ T.

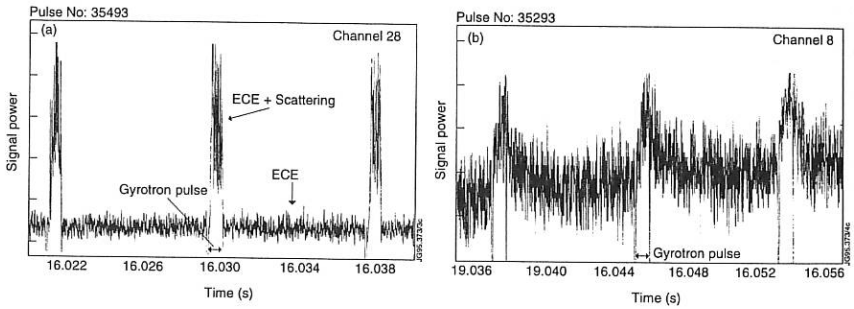


Fig. 2: Raw data from plasmas with [a] B = 3.1 T and [b] B = 2.9 T

In the absence of plasma virtually no signals were observed except in the channel at the gyrotron frequency. Relative calibration was obtained from detected ECE, assumed to be constant over the ranges of interest, and taking into account the measured transmission of the notch filters. System nonliniarity varying between channels was compensated for by using differences between two ECE levels near those observed. Calibration and system nonlinearity are the most important sources of uncertainty in present spectra. In particular the channel at -100 MHz (see Fig. 3a) is unreliable. A rough absolute calibration was obtained by comparing the detected ECE level with that measured by a calibrated ECE diagnostic with a different viewing direction.

Clear scattered signals were obtained for shots with moderate ICRH power coupling to 2nd harmonic of the bulk deuterium. Significant amounts of nitrogen were present (injected for divertor studies). The spectra obtained for these plasmas were all qualitatively similar to Fig. 3a. Spectra were also obtained for a wide variety of other plasma conditions, but the overlap of the injected and detected beams was not always optimised.

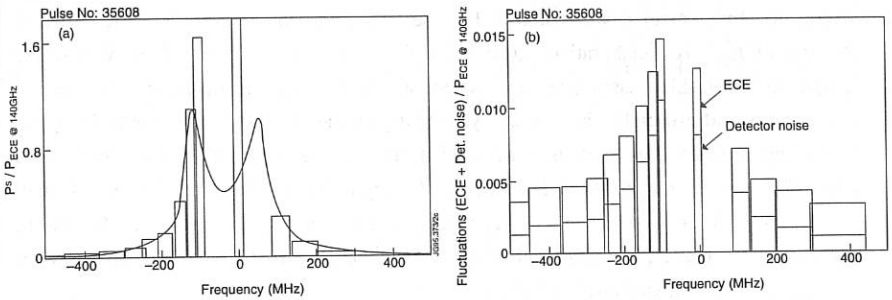


Fig. 3: Shot no. 35608 at 57.5 sec.: 5 MW ICRH, T_{ECE} at 140 GHz = 325 eV.
[a] Spectral intensity of scattered light normalized to spectral intensity of ECE at 140 GHz.
***Histogram:** . Measured scattered signal integrated over 2 gyrotron pulses (1.6 ms).*
***Curve:** theoretical fit. Given: B = 3.1 T, n_e = 4.1 × 10^{19} m^{-3}, T_e = 3.0 keV, angle (k_i,k_s) = 32°, angle(k,B) =122°. Fitted: n_{D1} = 1.2 × 10^{19} m^{-3}, T_{D1}= 3 keV, n_{D2} = 0.8 × 10^{19} m^{-3}, T_{D2} = 20 keV, n_N = 0.3 × 10^{19} m^{-3}, T_N = 3 keV.*
[b] Spectral intensity of fluctuations in ECE and detector noise normalized to spectral intensity of ECE at 140 GHz. Integration time: 1.6 ms.

The histogram represents the measured spectral intensity in each channel normalized to that of ECE at 140 GHz. The curve is theoretical (Bindslev [3]) based on B, n_e and T_e obtained from other diagnostics: the ion parameters were fitted. The fit is only illustrative. It

assumes that scattering in the wings is due mainly to a hot D ion population while the sharp central peak is due to N. The shift of ~ 30 MHz suggests a toroidal drift velocity of $\sim 1.6 \times 10^5$ m/s. The absolute level of the measured spectral intensity is ~ 70 % of that predicted by theory for perfect beam overlap. The discrepancies are well within the uncertainties of the data.

From Fig.3 (a) and (b) the post-detection S/N, *i.e.*

Scattered signal / Fluctuations on integrated (signal + ECE + detector noise),

is in the range from 10 to 100. Similar values are found for other spectra.

4. Conclusions

The diagnostic behaved as expected, and the observed signal-to-noise ratios were in satisfactory agreement with theory. When the full pulse length of the gyrotron can be used with fast modulation, the diagnostic should give the expected performance for observations of fast ions and alpha particles.

Acknowledgements

We are greatly indebted to many people who have contributed to the development of the diagnostic. In particular we acknowledge the unfailing support of Dr M.Keilhacker, Director of JET. A collaborative agreement with the US Department of Energy provided equipment, valuable assistance and encouragement. The involvement of several Associations and especially the University of Stuttgart and the Institute of Applied Physics in Nizhny Novgorod is gratefully acknowledged. Among many individuals we would especially like to thank D V Bartlett, D A Boyd, M P Comiskey, A E Costley, G G Denisov, I H Hutchinson, W Kasparek, C Laviron, A G Litvak, D Markevich, O Menicot, C Moeller, F P Orsitto, L Porte, S D Richards, S R P Smith, W B Suverkropp, M Thumm, M L Watkins and P Woskow.

References

[1]. P P Woskoboinikow, D R Cohn and R J Temkin, Int. J. Infrared & Millimeter Waves **4**, 205 (1983)

[2]. A E Costley, J A Hoekzema, T P Hughes, P E Stott and M L Watkins, JET Report R(88) 08 (1988)

[3]. H Bindslev, Proc. ESGAP Meeting, Aussois (1994), to be published in J Atm. and Terr. Phys.

[4]. E V Suvorov et al., Proc. 9th Joint Workshop on ECE and ECRH, Borrego Springs (1994)

Pellet Refuelling of ELM´y H-Mode Discharges beyond the Greenwald Limit in ASDEX Upgrade

P.T.Lang, K.Büchl, J.C.Fuchs, O.Gehre, O.Gruber, R.S.Lang, M.Maraschek, V.Mertens, H.Salzmann, H.Zohm, ASDEX Upgrade Team, NBI Team

Max-Planck-Institut für Plasmaphysik, EURATOM Association, Boltzmannstr. 2, 85748 Garching, Germany

Introduction

Normally, when refuelling the plasma with gas puffing, the line averaged density clamps to the plasma current I_P and stays below the empirical Greenwald limit. This limitation would result in a density limit of about $0.8 * 10^{20}$ m^{-3} for ITER (EDA), causing problems both to reach detached divertor plasmas and for burn control at the accordingly higher temperatures. One main intention of our current work is therefore to develop scenarios allowing for a more flexible plasma density control and densities beyond the Greenwald limit during the H-mode phases by means of injection of cryogenic solid hydrogen pellets. In a first step, we investigated pellet particle fuelling efficiencies attainable using various deposition depths, finding shallow deposition to be unfavourable for refuelling. Than, applying optimized injection parameters our effords concentrated on the increase of the plasma density beyond the Greenwald limit. Applying pellet fuelling without additional gas puffing into ELM´y H-modes does, in contrast to the ohmic case, not enhance the density operating space. The combination of repetitive pellet fuelling and moderate gas puffing however achieved line averaged densities well beyond the Greenwald limit.

Experimental setup

Several pellet fuelling experiments are executed on ASDEX Upgrade plasmas with lower single null configuration, I_P = 0.8 - 1.0 MA, B_t = 2.1 - 2.5 T, q_{95} = 3.5 - 4 and P_{NBI} up to 7.5 MW. For pellet injection experiments, a centrifuge pellet injector /1/ is available capable to deliver series containing more than 100 pellets at repetition rates up to 80 Hz. By changing the pellet velocity in the range of 240 to 1200 m/s and its particle content from 1.5 to 4 x 10^{20} per pellet, a gradually transition from shallow to deep material deposition can be performed.

Affect of ELM´s on the pellet refuelling efficiency

To get the relation between pellet injection parameters and fuelling efficiency ε_f (plasma particle inventory rise divided by pellet particle content), ε_f was determined for a series of discharges where the pellet penetration depths Δ as well as the heating power was varied. The

maximum ε_f values show a strong degradation of the fuelling efficiency with increasing heating power like in other tokamaks /2/, they decreased from almost unity without additional heating power to about 0.3 for P_{NBI} = 7.5 MW. Besides the ε_f degradation with P_{NBI}, a strong dependence of ε_f on the penetration depths was observed. It turned out that a significant persistent density increase was achieved in ELM´y H-mode discharges only for sufficient penetration depths. In Fig. 1 ε_f values are plotted versus Δ for discharges with identical heating power (P_{NBI} = 5 MW). Whereas almost a vanishing fuelling efficiency is found for shallow penetration, an increasing penetration depth causes an increase in ε_f for the type-I ELM´ing H-mode discharges (circles). For sufficiently deep particle deposition finally a maximum fuelling efficiency (about 0.3) is reached as observed for L-mode discharges. For L-mode discharges, the fuelling efficiency is almost unaffected by the pellet penetration depths (triangles).

We attribute ε_f degradation for shallow deposition in ELM´y H-mode discharges to particle losses correlated with the ELM which is induced by each injected pellet in an H-mode plasma. To get more insight into the behaviour of ε_f we modelled energy and particle transport on a fast timescale following the pellet particle deposition. The code used originally has been developed for modelling the dynamic behaviour of the L-H transition /3/. Code runs confirmed the release of an ELM by each pellet injected into the H-mode phase. The ELM results from a pressure blob occurring near the location of maximum pellet particle deposition, moving outside to the transport barrier layer causing a local exceed of a critical pressure gradient. Deeper penetration of the pellet leads to an increasing delay between injection and ELM release since the diffusion of the pressure blob to the transport layer lasts longer. Thus, particle diffusion yields a broader distribution of the original pellet deposition profile when the ELM occurs. Results obtained when modelling pellets of different masses and penetration depths are shown in Fig. 2. Qualitatively, these results agree well with our experimental findings, showing a strong decrease in fuelling efficiency with reduced penetration depths. From the transport analysis however, no explanation is yielded for the reduction of the maximum fuelling efficiency to about 0.3 at P_{NBI} = 5 MW. A reason for this migth be a rapid radial transport out of the plama due to the local ß-enhancement in the pellet ablation zone. The investigation of this phenomena is still going on.

High density ELM´y H-mode discharges

With the above knowledge, an attempt was made to optimize density enhancement for discharges refuelled using pellets of maximum size and velocity. It turned out replacing the gas puffing by pellet injection

does not enhance the accessible density range whereas a combination of gas puffing and pellet refuelling can lead to plasma densities far beyond the Greenwald limit. This is demonstrated in Fig. 3, where the temporal evolution for a pair of discharges is shown. During this discharges (P_{NBI} = 5 MW) a pellet sequence was injected at a repetition rate of 30 Hz for a duration of 1.3 s. While pellet injection completely replaces gas puffing to the plasma for the one discharge (#6522), gas puffing was maintained during the pellet sequence for the other one (#6523). For the case pellets replacing the gas puff at t = 2.25 s, only a slight increase in density takes place during the pellet sequence despite a particle flux delivered by the pellets is more than three times that of the previous gas puff. In this discharge, $\overline{n_e}$ only approaches to the Greenwald limit ($1.3 * 10^{20}$ m^{-3}, dashed line in Fig. 3). With the combination of gas puff and pellet injection, much stronger influence on the discharge can be caused. First, pellet injection doubles the line averaged electron density while the density profile keeps its shape. For a duration of about 0.3 s, the discharge shows a plateau in the line averaged density while the density profile ondergoes moderate peaking. While the plasma stored energy still stays almost constant, finally pellets successively cool down the plasma and therefore increase their penetration depths. During the last part of the sequence pellets already advance to the plama center, causing a strong peaking of the density profile and a strong further increase of the line averaged density. At the end of the pellet sequence, the density rapidly decreases until the discharge is terminated by accidental switching-off of the NBI heating.

Conclusions

For effective refuelling of ELM´y H-mode discharges by pellets penetration depths well beyond the ELM affected region must be applied. The obviously favourable refuelling scenario for such discharges is to use pellet injection combined with additional gas puffing. Such, a maximum value of $\overline{n_e} \approx 2.6 * 10^{20}$ m^{-3} was reached transiently, exceeding the Greenwald limit by a factor of two. For further improving the refuelling scenario in order to achieve stable operation conditions, too strong cooling of the plama by the pellets must be avoided. Therefore, it is necessary to adjust the heating power and/or the pellet injection rate to the actual plasma conditions. The new ASDEX Upgrade control system, already taken successfully into operation, will allow for this purpose in our next experimental campaign.

References

/1/ C.Andelfinger et al., Rev. Sci. Instrum. 64, 983 (1993)
/2/ L.R. Baylor et al., Nuc. Fus. 32, 2177 (1992)
/3/ H.Zohm et al., Phys. Rev. Lett. 72, 222 (1994)

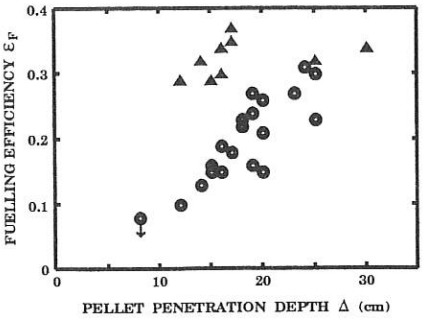


Fig. 1: Fuelling efficiency achieved for discharges with P_{NBI} = 5 MW and I_P = 0.8 - 1.0 MA, plotted versus the pellet penetration depths into the plasma. Circles: pellets injected during H-phases; triangles: L-mode conditions.

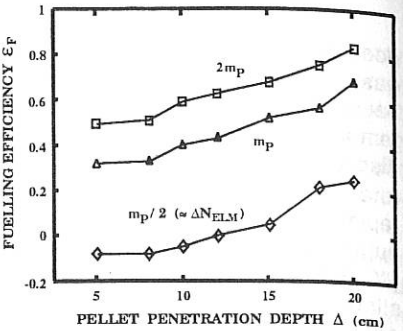


Fig. 2: Fuelling efficiencies versus pellet penetration depths in the case of three different pellet masses calculated using the transport analysis code.

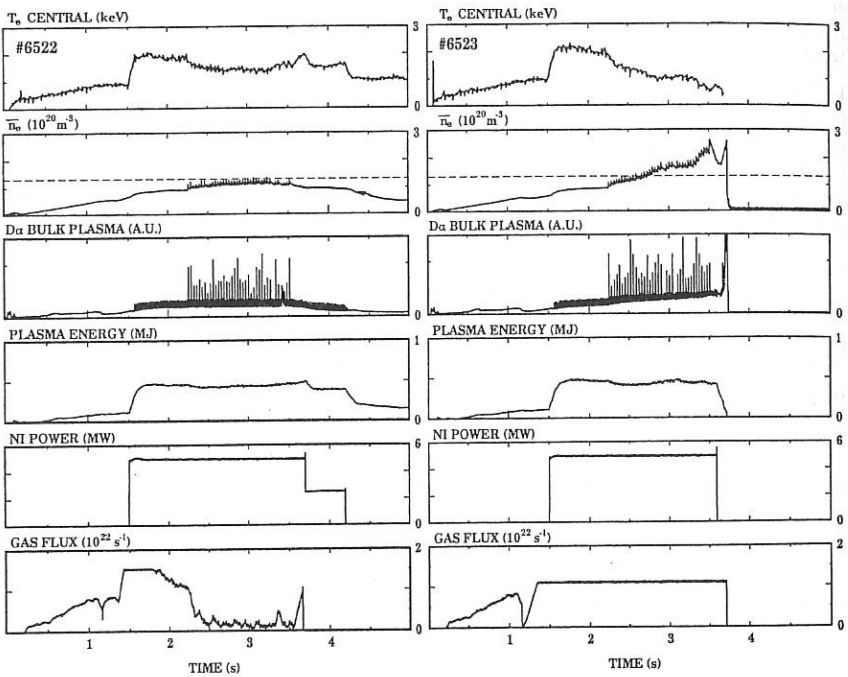


Fig. 3: Temporal evolution of a pair of discharges with either gas puff or pellet refuelling (#6522) or combined refuelling (#6523). An enhancement of the line averaged density beyond the empirical Greenwald density limit (indicated by broken lines) was only achieved for the case of combined refuelling by gas puff and pellet injection.

Toroidal momentum slowing down and replacement times in JET divertor discharges

K-D Zastrow, J C M de Haas, M G von Hellermann, A C Howman and R W T König

JET Joint Undertaking, Abingdon OX14 3EA, Great-Britain

Introduction and summary Several observations of correlated ion energy and toroidal angular momentum confinement during neutral beam injection (NBI) have been reported. For example, it was found on ASDEX that toroidal momentum and energy replacement times were similar [1] with τ_L approaching τ_E for values above 60 msec. On TFTR it was found that ion and momentum diffusivities are equal in L-Mode discharges [2]. At JET, correlation between central rotation frequency and ion temperature has been observed [3]. It was also found that combined neutral beam and radio frequency (RF) heating resulted in a reduced central angular frequency [3,4], whilst slightly improving the energy confinement [5].

In this paper we study the decay of the toroidal angular momentum after NBI in JET and compare the results with the behaviour of the replacement time during NBI. During NBI, when the global energy content is dominated by the ions, we find that the energy replacement time is equal to that of the angular momentum. The angular momentum decay time after NBI, when the global energy content is dominated by electrons, is up to 30% larger than the energy replacement time. In contrast to combined heating we find no evidence for stronger deterioration of momentum than energy confinement in discharges with RF heating only.

Toroidal angular frequency and toroidal angular momentum density The toroidal angular frequency, ω, is derived from Doppler shift measurements using a high resolution X-ray crystal spectrometer and active visible charge exchange spectroscopy. The charge exchange recombination spectrum of $C^{+6}+D \rightarrow C^{+5}$ $(8\rightarrow 7)$ is observed at 10 positions along the upsteered neutral beams in Octant 8. Radial profiles, expressed in terms of the normalised minor radius, $\rho=r/a$, are constructed assuming the angular frequency to be constant on a flux surface by projecting the intersection points of the lines of sight with the neutral beams along the corresponding flux surfaces into the outer half of the magnetic midplane. The resonance line *w* of helium-like nickel (Ni^{+26}) is observed along a line of sight in the geometric midplane of the torus, i.e. 20-30 cm below the magnetic axis. The corresponding effective normalised minor radius of the helium-like nickel emission shell, $\langle\rho\rangle$, and its width, are calculated from

the projected radial profiles of electron temperature and density using a coronal equilibrium model for the fraction of helium-like nickel and for the emissivity of the resonance line.

The relative accuracy, due to photon statistics, of the derived angular frequency, is $\Delta\omega$=1-2 krad/sec for both diagnostics. The reference wavelength for the Doppler shift of the visible spectrum is provided by a diode pumped Nd-YAG Laser (λ= 532 nm). The achieved accuracy of the absolute level is about 5 krad/sec. The time resolution of the visible spectra is typically 50 msec. The reference wavelength of the X-ray spectrometer was determined from a comparison of the derived angular frequencies from both diagnostics under steady-state conditions. The uncertainty of the absolute level is about 10 krad/sec. The time resolution of the X-ray spectra varies in the range 30-120 msec.

The toroidal angular momentum density is calculated using the local electron density as $\ell = m_D\, n_e\, \omega\, (R^2 + r^2/2)$, where R is the major and r is the minor radius of the flux surface on which ω is measured. The mass contributed to the plasma by each electron is the mass of deuterium, m_D, independent of Z_{eff}, since the major plasma constituents, i.e. ^{2}H, ^{4}He and ^{12}C, have nuclei with equal number of neutrons and protons.

Angular momentum slowing down time Directly after the neutral beam power is turned off, the toroidal angular momentum density measured with the X-ray crystal spectrometer is first observed to decay in an irregular manner (typically for about 0.2-0.5 sec). For most discharges, this is followed by a phase of exponential decay. The first phase reflects the change of the radial profile from driven steady state to source free profile. We assume that after this phase the profile decays exponentially as a whole, and that the decay time constant, τ_ℓ, measured at $\rho=\langle\rho\rangle$ is representative of the global toroidal slowing down time. We analyse this decay by performing a least squares fit of the data to an exponential function. We require good time resolution (better than $\tau_\ell/3$) and statistical accuracy for at least three decay times. Discharges where the decay appears not to be exponential are not included.

Angular momentum and energy replacement time During NBI we integrate the angular momentum density profile to obtain the total angular momentum, L, of the plasma. The torque, M, exerted by the neutral beams on the plasma, is calculated from an analytical beam deposition code, that takes the measured local impurity densities into account. Thus we obtain the global angular momentum replacement time as $\tau_L = L/(M - dL/dt)$. During NBI we integrate measured electron and ion energy densities to obtain the total thermal energy, $W_e + W_i$. From

the beam deposition code, we also calculate the fast energy content, W_{fast}. Thus we obtain the global energy replacement time as $\tau_E=(W_e+W_i+W_{fast})/(P-d(W_e+W_i+W_{fast})/dt)$. In this paper we restrict ourselves to quasi steady state conditions, $dL/dt < 0.1M$ and $dW_{tot}/dt < 0.1P$. Outside the NBI phase only the electron energy density profile is available. We therefore approximate W_i as $W_e\ T_i(Ni^{+26})/T_e(\langle\rho\rangle)$.

Results and discussion A comparison of τ_ℓ with τ_E is shown in Fig. 1 for discharges with and without radio frequency heating. Fig. 2 shows the corresponding comparison of τ_L with τ_E. It can be seen that $\tau_\ell > \tau_E$, i.e. without neutral beam heating. There are no data with τ_E significantly larger than τ_ℓ. During NBI we find $\tau_L = \tau_E$ within the errors of the measurement. The dominant driving terms, i.e. neutral beam heating and toroidal torque, have similar radial profiles. Energy and toroidal momentum are however subject to different internal and edge losses, i.e. energy transfer between ions and electrons, radiation, ripple damping, and momentum transfer by charge exchange. Nevertheless both replacement times come out the same, in agreement with the result obtained on ASDEX [1]. In Fig. 3 we present the scaling of τ_E/τ_L and τ_E/τ_ℓ with $(W_i+W_{fast}-W_e)/W_{tot}$. This quantity is negative if the plasma energy is mostly in electrons, and positive if it is mostly in ions. From this figure we conclude that τ_E can at best approach τ_L (and τ_ℓ) when the plasma energy (and thus the energy confinement) is dominated by ions, and that it is smaller if the plasma energy is dominated by electrons.

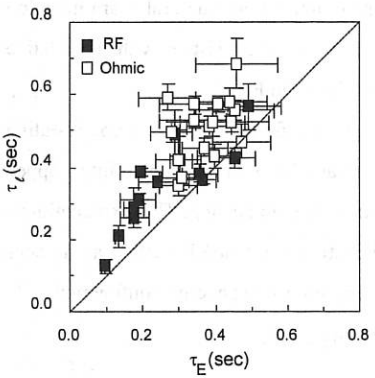


Fig. 1: Time constant for exponential decay of the angular momentum density after neutral beam injection vs. energy replacement time.

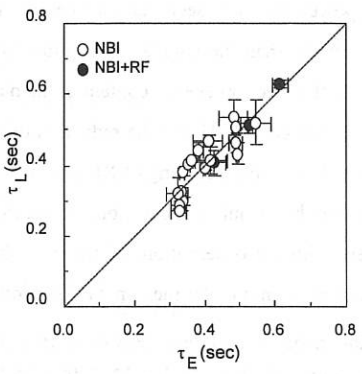


Fig. 2: Angular momentum replacement time during neutral beam injection vs. simultaneously measured energy replacement time.

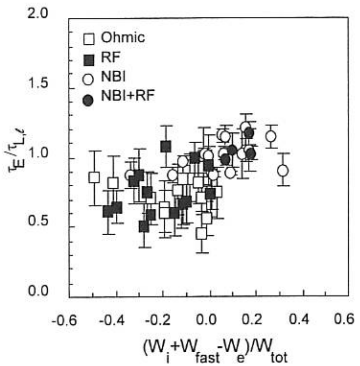


Fig. 3: Scaling of the ratio of energy replacement time to angular momentum replacement time and slowing down time, with relative contribution of ions or electrons to the energy content.

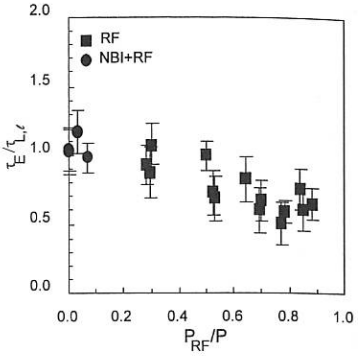


Fig. 4: Dependence on the fraction of RF heating power to total heating power

There is no evidence of stronger deterioration of the confinement of angular momentum compared to energy with combined neutral beam and RF heating within our data base, probably since the RF heating power during NBI accounts for less than 10% of the total heating power (see Fig. 4). Note, however, that the example shown in [5] was obtained at 1.8 MW of RF power, compared to 15 MW of NBI power. When RF heating is the dominant heating power, it can be seen that the energy replacement time without neutral beam injection degrades faster than the angular momentum decay time. This is consistent with the relative increase of the electron energy content of the plasma as shown in Fig. 3.

It has been suggested [4] that the reduction of central angular frequency in combined heating discharges is due to a coupling of RF power to the fast particles, scattering them into trapped orbits where they would not contribute to the torque but instead to heating. This explanation is consistent with our observations after neutral beam injection, i.e. that RF heating alone does not reduce momentum confinement whilst simultaneously improving energy confinement.

[1] A Kallenbach et al, Plasma Phys. Contr. Fusion **33**, 595(1991)
[2] S D Scott et al, Phys. Fluids **B2**, 1300 (1990)
[3] H P L deEsch et al, 17th EPS Conf. Contr. Fusion, Amsterdam 1990, Part I, 89
[4] D Stork et al, 14th EPS Conf. Contr. Fusion, Madrid 1987, Part I, 306
[5] D O'Brien et al, 21st EPS Conf. Contr. Fusion, Montepellier 1994, Part I, 125

Index

Abramova KB II-165
Adams JM II-037, II-053, III-057,
Adler HG II-401
Afanassiev VI II-057
Agostini E III-441
Aizawa M II-137
Akhmetov TD II-181
Akiyama R I-153, III-413, IV-149, IV-153
Albrecht M III-249, IV-413
Alejaldre C II-149, II-157
Alekseev AG III-385
Alexander A IV-089
Alexander M III-001, III-237
Alexeev IS I-049
Ali-Arshad S III-281, IV-021, IV-141
Aliaga-Rossel R II-173
Alladio F I-237
Allen SL III-105
Alonso J II-157
Alper B IV-061
Amemiya H I-397
Amery G I-449
Amosov VN III-385
Anabitarte E I-405
Anderson D I-093
Ando A I-153, III-413, IV-149
Andrejko MV I-033
Andrew P II-301
Ane JM IV-069
Anikeev AV IV-193
Anton M II-389, III-113, IV-081
Antoni V IV-181
Antozzi P III-381
Apicella ML II-121
Appel LC II-261
Appert K II-245, IV-233
Arber T I-257
Arslanbekov R III-373, IV-065, IV-393
Ascasibar E II-149, II-153, II-157, IV-157
Ashall JD IV-213
Askinazi LG I-033
Asmussen K I-065
Axon KB IV-213
Azumi M III-029, IV-237
Babich I III-437
Badalec J II-373
Baelmans M IV-309, IV-321, IV-329
Bagdasarov AA I-049

Bagryansky PA IV-193
Baity FW I-381
Bak PE I-013, II-441, IV-061, IV-405
Bakos JS II-421
Balbin R I-301, I-305, II-157, IV-157
Baldzuhn J III-141, III-145
Balet B I-009, I-013, II-069, IV-061, IV-141
Ballabio L III-381
Baloui T III-201
Bamford RA II-133, III-033
Barabaschi P IV-009
Baranov Y III-361, IV-393
Barnes CW III-013
Barnsley R I-081, I-097, III-121, IV-465
Barsilio ZA I-289
Barth CJ II-129
Barth K II-009, II-121
Bartlett DV III-085, III-261, IV-021, IV-425
Basiuk V III-337, IV-125
Bastasz R IV-049
Batchelor DB II-333, III-365, IV-121
Batha S II-113, III-365
Bayley JM II-173
Baylor L I-113
Bazylev B II-277
Beaumont B IV-397
Becker G I-025, II-193, IV-285
Becoulet A IV-353
Beg F II-169
Behrendt H II-297
Behringer K I-069, III-409
Behrisch R II-301
Beidler CD III-129, III-149
Beikert G III-201
Bell MG II-109, II-329, III-397
Bell RE II-113, II-357, III-013
Belov AM I-421
Bengtson RD I-001, I-281, III-265, IV-097
Bergmann A I-425
Bergsaker H I-173, III-157, IV-277
Berk HL II-233
Bernabei S II-357
Bers A IV-353
Bertrand P III-209, III-357, IV-197
Bertschinger G II-381
Bessenrodt-Weberpals M I-065, IV-133
Besshou S I-137, I-145, I-149, I-157, I-161, III-405
Bettenhausen M II-325
Bettini P IV-185
Beurskens MNA II-129

Bhatnagar VP II-069, II-329, IV-001
Bibet P III-373
Bickley AJ II-009, II-125
Birk G T I-441
Biskamp D IV-205
Blackwell BD II-141
Blow G IV-213
Boedo JA I-057, I-293
Bogomolov LM I-277, III-329
Bohmeyer W II-297
Boivin R II-341
Bolzonella T IV-177, IV-181
Bombarda F II-313, II-341, III-017
Bond DS II-053, III-057
Bondarenko IS II-117
Bondeson A I-213, I-241, III-165, IV-209
Bonnin X III-265
Bonoli P II-341, IV-121
Borba D II-237, II-261, III-081
Borg G II-141
Bornatici M III-185
Borner P IV-321
Borovsci BV I-277
Borrass K I-341
Bosch HS I-321, III-093, III-097, IV-041
Boucher C III-101
Boucher D III-169
Boucher I IV-409
Box FMA II-129
Braams BJ IV-285, IV-305
Bracco G III-021
Brañas B ..... II-157, III-141, IV-157, IV-161, IV-165, IV-429, ... IV-433
Bravenec RV I-001, III-265, IV-097
Breger P II-377, IV-001
Breizman BN II-233, II-261
Bretz NL III-013, III-397
Breun R IV-381
Brooks JN IV-305
Brooks NH II-281, IV-049
Brouchous D IV-381
Brower DL I-001, IV-097, IV-129
Brunner S IV-241
Brunsell P III-157, IV-277
Bruschi A I-361, IV-369
Brzozowski JH I-173, I-177, III-157, III-153
Buchl K I-349, III-097
Budaev VP I-277, III-329
Budnikov VN II-085, IV-385
Budny RV I-409, II-105, II-109, III-013

Buhlmann F I-417
Bulanin V II-089
Buratti P I-361, III-021
Bures B IV-141
Bures M II-329, II-353
Burgos C II-153
Burhenn R III-145
Burmasov V I-445
Burrell KH IV-137
Bush CE II-113, III-013
Bustamante EG I-405
Buttery RJ III-233, III-273, IV-213
Caldas IL I-289
Callis RW I-381
Campbell DJ I-309, II-009, II-073, II-121, II-125, III-081, III-085,
..... III-289, III-293, III-305, IV-001, IV-009, IV-465
Candy J II-237
Cantu P I-453
Cao L II-409
Cappello S IV-181
Carlson A I-425, III-097, III-245
Carolan PG II-025, II-133, II-209, III-033
Carraro L II-317, III-161, IV-177
Carreras B IV-165
Carter M II-333
Cary WP I-381
Casarotto E II-309, II-317
Castejon F II-157, III-041, III-225, IV-269
Castro RM I-289
Cauffman S II-405
Cecil E II-037
Challis CD II-069, III-005
Chamouard C III-109, IV-349
Chan V I-377
Chance M I-193
Chang Z II-113, III-013, III-045
Chankin A III-289, III-309, IV-021
Chashchina GI II-085
Chatelier M I-317, II-041
Chen H I-081
Cheredarchuk A III-437
Cherepanov KV III-205
Chernyatjev Yu V III-285
Cherubini A I-013
Cherubini C II-213
Chistiakov VV I-049, I-369
Chitarin G IV-181, IV-185
Chittenden JP II-173
Chiu SC I-109, I-377, I-381
Chodura R I-425

Choe W II-093
Chrien RE II-061
Christensen C II-341
Christiansen JP I-009, IV-061, IV-141
Christou C I-137, I-145, I-157, I-161
Chu CC I-129, II-013, II-129
Chu MS I-241, IV-137
Chutov Yul IV-453
Cima G I-001, I-005, IV-097
Cirant S I-361, IV-369
Claassen HA IV-293
Clairet F IV-101, IV-409
Clement D III-133
Clement S ..... I-309, II-125, III-281, III-289, III-293, III-305, ... III-309
Coad JP II-273, III-309
Coda S I-297
Coffey IH I-081, III-121
Colas L I-041, IV-101
Collarin P IV-181
Colton A II-025, III-273
Condrea I IV-289
Connor JW I-089, I-261, II-205, III-189, IV-201
Connor K I-001
Conroy S III-381
Conway NJ II-133
Cooper WA II-145, III-133
Coppi B I-461, III-017, IV-025
Corboz M III-113
Cordey JG I-013, II-073, III-229, III-277
Correa-Restrepo D II-189
Corrigan G IV-297
Coster DP III-093, III-249, IV-285, IV-329
Costley A III-377
Cote A II-361, III-101
Cote C II-361
Cottrell GA II-229, II-405
Counsell GC II-205, III-233, IV-365
Cox M II-265, IV-365
Crowley TP I-001, III-265
Cupido L IV-413, IV-425
da Cruz DF I-129, II-013
Da Silva R I-289
Dalla S II-033
Dangor AE II-169, II-173
Darrow D II-105, III-365
Das J IV-313
Daughton W III-017
Davies SJ II-125, III-257, III-293, III-297, III-305, IV-465
Davydova TA I-437

de Angelis R I-053
de Baar M I-385
de Blank HJ I-233, II-029, III-273, IV-133
de Esch H IV-001, IV-061, IV-141
de Haas JCM I-009, II-009, II-069, II-073, II-453
de Kock L III-377
de Kloe J I-129
de la Cal E II-157
de la Luna E II-157, III-141, IV-161, IV-429, IV-433
De Lorenzi A IV-185
De Luca F I-053, II-013, III-009
de Michelis C I-085, III-109
de Peña S III-409
de Pena Hempel S II-005
De Ploey A I-221
de Rover M IV-261
de Vries PC III-053, IV-029
Decoste R III-101
Degrassie JS I-381
Degtyarev L I-217
Deichuli PP IV-193
Deksnis E I-309
Deliyanakis N ..... I-013, I-029, I-053, III-009, III-081, III-121, III-261, ... IV-061, IV-141, IV-405
Demchenko V IV-377
Dementjev GN I-277
Demers Y II-361
De Michelis C II-385, IV-345
Dendy RO I-185, II-229, II-241, II-405, IV-201
Denne-Hinnov B I-085
Denner T I-057
De Ridder G I-241
Deschenaux Ch IV-081
Detragiache P IV-025
Devynck P IV-101
Di Marco JN IV-181
Diebold DA IV-381
DIII-D Team III-105
Ding N II-225
D'Angelo F I-265
Dobbing JA III-081
Doczy M IV-381
Doloc C II-041
Dong JF III-073
Donne AJH III-421, III-425, IV-029, IV-337
Dorn Ch III-409
Doyle EJ I-105, I-109
Drabbe M III-421
Drake JF IV-205
Drake JR I-169, I-173, I-177, III-157

Dreher J I-441
Dreval VV IV-401
Dryagin Yu A I-429
Dubois MA IV-249
Dudok de Wit T I-085
Dumbrajs O III-181
Duong HH I-409
Durodie F III-341
Duroua A IV-097
Durst RD I-001, IV-097
Dutch MJ II-097, II-101, II-389, III-113, IV-077, IV-081
Duval BP II-097, III-113, IV-081
Dux R I-065, I-069, II-005, IV-285
Dyachenko VV II-085, IV-385
ECRH Group III-129
Edenstrasser J I-269
Edery D I-249, IV-065, IV-073
Edlington TE IV-425
Edmonds P I-001, III-397
Edwards AM II-021, IV-061
Edwards ME IV-117
Efthimion PC I-373, III-013
Ehrenberg J I-309, II-121, III-085, III-281
Ejiri A I-153, III-413, IV-149, IV-153
Ekedahl A III-361
Elfimov A IV-381
Emmoth B III-137
Endler M I-301
England A III-365
Erba M I-013, II-213, IV-061
Erckmann V I-353, I-357, I-389, I-429, III-037
Erents SK II-125, III-117, III-257, III-297, III-305
Eriksson L-G I-009, I-093, II-033, II-069, I-209, II-253, II-353,
..... III-381, IV-001
Ermolaev AM III-389
Ernst D III-013
Esipov LA II-085, IV-385
Esposito B II-037
Esser HG IV-281
Esterkin AR IV-389
Estrada T II-149, II-153, II-157, IV-157, IV-161, IV-165,
..... IV-429, IV-433
Euringer H I-057, I-061, II-397
Euripides P IV-045
Evans TE IV-049
Fahrbach H I-025, III-249
Fall T III-157, IV-277
Fanack C IV-409
Fasoli A III-081, IV-085
Fechner B II-329, II-353

Federici G IV-333
Feix MR III-209
Feng Y IV-325
Fenstermacher ME III-105, IV-305
Fernandes J IV-417
Feron S III-317
Ferreira JG III-033
Fiedler S III-253, III-269
Field AR I-069, II-289, II-293, III-097, III-409
Fielding SJ I-097, I-345, II-001, II-025, III-125, III-273,
..... III-369, IV-213
Fijalkow E II-429, III-209
Filippas AV I-281
Filippov AN IV-169
Filippov NV IV-169
Finken KH I-057, I-061, I-133, I-293, II-397, IV-093, IV-341
Fiore C II-341, III-017
Fiorentin P IV-181, IV-185
Fisch N III-365
Fischer B II-037, II-353, III-361, IV-113
Fisher RK I-409
Fishpool G IV-141
Fitzpatrick J II-233
Fivaz M IV-233
Fonck RJ I-001, III-013, IV-097
Fontanesi M I-453, III-441
Forest CB I-381, IV-125
Fraiman AA I-429
Framer-Flecken A II-321
Frances M II-157, IV-429, IV-433
Franzoni G IV-289
Fredrickson E III-045
Frenje J III-381
Froissard P II-037, III-373, IV-397
FTU Team IV-289
Fu BZ III-073
Fuchs CH I-025, III-097, IV-037, IV-285
Fuchs G III-053, IV-341
Fuchs JC I-065, I-069, II-005, III-085, III-401
Fuchs V IV-353, IV-361
Fujii T II-057
Fujisawa A I-001
Fujisawa N IV-009
Fujita J III-417
Fujiwara M III-413, IV-149
Fukuyama A I-205, IV-229, IV-237
Funaba H I-157, I-161, I-285
Furno I II-253
Fussmann G II-297
Gabellieri L I-077, IV-289

Gadeberg M II-069, IV-021
Galambos JD II-333
Galechyan GA II-165
Gandini F IV-369
Gandy R I-001
Gao QD III-073
Garbet X IV-101, IV-253
Garcia L IV-165
Garcia-Cortes I I-305, II-157, III-281
Garcia-Rosales C III-241
Gardner CA II-265, III-233
Gardner HJ II-141, II-145
Gardner MR III-233
Garnier D II-341
Garribba M II-125, IV-009
Garzotti L IV-177
Gasquet H IV-129
Gates DA I-345, II-001, II-025, III-273, III-369, IV-117
Gauthier E I-413
Gehre O I-021, I-025, III-253
Geist T I-429, IV-161, IV-433
Gentle KW I-001, I-005, I-021, III-265
Gerhauser H IV-293
Gernhardt J I-025
Gerstel U II-009
Geruzzi G I-001
Gervais F III-061, IV-101
Gettelfinger G III-397
Ghendrih Ph III-109, III-317, IV-349
Ghizzo A III-209, III-357, IV-197
Giannella R I-053, I-081, I-085, I-089, II-073
Giannone L I-301, IV-265
Giesen B III-341, IV-341
Gill RD IV-061
Gimblett CG II-241
Girka IA IV-357
Giruzzi G I-101, IV-189
Gnesotto F IV-181
Goedbloed JP I-221, IV-085, IV-113
Goetz JA II-313, II-341, III-325
Golant VE I-033
Goldston R III-397
Golovato S II-341
Gondhalekar A II-033
Goniche M III-373, IV-397
Goodall DJH II-017, III-033, III-117
Goossens M I-221
Gordeev OA II-117
Gorini G I-053, II-013, III-009
Gormezano C I-009, II-069, II-329, II-353, III-005, III-081, III-361,

..... IV-001, IV-113
Gott Yu V II-369, IV-221
Gottardi NAC III-085
Gowers CW I-009, II-069, III-005
Graf M II-313, II-341, III-017
Granata G IV-301
Granetz R II-341
Granucci G I-361, IV-369
Gray DS I-057, I-293
Green JM I-241
Greenwald M II-341, III-017
Gregory BC III-101
Grek B III-013
Gresillon D IV-101
Grigull P IV-325
Griscom DL II-401
Grisolia C III-109, IV-349
Grosman A III-109, III-317
Grossman S IV-105
Grote H II-297
Gruber O II-185, III-001, III-093, III-097, III-241, IV-037,
..... IV-089
Gryaznevich M II-017, II-205, III-033, III-117
Guarnieri M IV-181
Guasp J II-157
Guilhem D I-317, III-317, IV-345, IV-397, IV-473
Guirlet R II-385, III-109, IV-345
Guiziou L I-037, I-041, IV-101, IV-253
Gunn JP III-101
Gunther K I-433, II-077
Guo GC III-073
Guo HY I-309, II-273, III-257, III-297, III-305
Gusakov E IV-389
Haas FA III-173
Haas G I-309, I-321, I-325, II-005, III-097, III-241,
..... III-245
Hacker H III-145
Haddad E III-101
Haines MG II-169, II-173, III-213, III-217
Hallock G I-001
Hamada T I-137, I-157, I-161
Hamada Y I-125
Hamamatsu K II-057
Hanatani K I-137, I-161
Harano H II-061
Harbour PJ I-309, II-073, II-121, III-305, IV-465
Harmeyer E III-129, III-149
Harris JH IV-397
Hartfuss HJ I-353, I-357, III-037, IV-161, IV-265, IV-433
Harvey BM II-241

Harvey RW I-381
Hastie RJ I-185, II-241, III-217, III-233
Hawkes NC I-097, II-073, II-125, III-085, III-121, III-261
Haynes PS III-393
Heard JW I-001, I-005, III-265, IV-097
Hedin G I-177, III-157
Hedqvist A III-157
Hegna CC I-261
Heijnen SH IV-441
Heikkinen JA II-349, III-181
Heinrich O III-249
Heliotron-E Group I-141
Hellberg M I-449
Hellblom G I-173, III-157
Heller MVAP I-289
Hender TC I-029, II-017, II-021, II-261, III-233, III-273,
..... IV-061, IV-117, IV-213
Hennequin P III-061, IV-101
Herranz J II-149, II-157
Herre G IV-313
Herrmann A II-005, II-293, III-097, III-241, IV-037
Herrmann MC III-365
Herrmann W I-333, I-349, III-097, III-249
Hershkowitz N IV-381
Hess WR II-385, III-109, IV-345
Hesse M II-385
Heuraux S II-337, IV-409
Hicks JB III-117
Hidalgo C I-301, I-305, I-405, II-117, II-157, IV-157, IV-165
Hidekuma S I-161
Hildebrandt D II-289, IV-325
Hill DN III-105, IV-305
Hillis DL I-061, II-009
Hirano Y I-181
Hirsch K III-409
Hirsch M III-141, IV-161, IV-165, IV-433
Hirsch S II-005, III-097, III-409
Hirt A III-113
HL-1 Team I-273
Hoang GT I-037, I-041, III-373, IV-065, IV-073, IV-101, IV-393
Hoek M II-061
Hoekzema J A II-445
Hoenen F IV-041
Hoffmann C I-349
Hofmann F I-417, II-097, II-101, III-113, IV-077, IV-081
Hofmann JV IV-313
Hogan JT I-325, IV-345, IV-397, IV-473
Hogeweij GMD II-013, III-037
Hokin S I-181
Holakovsky J I-329

Holties HA II-237, III-081, IV-085, IV-113
Holtrop KL IV-049
Holzhauer E I-429
Hone MA II-053, III-057
Hong B IV-469
Horling P I-177, III-157, IV-277
Horne S II-341
Horton L I-309, II-009, II-077, II-121, II-125, II-273, III-085,
..... III-301, III-305, IV-297, IV-465
Hosea JC III-365
Hou L II-437
Houlberg WA I-113
Howard J II-141, II-413, III-421
Howarth PJA III-057
Howe H III-225
Howell DF I-257
Howman AC II-009, II-125, II-453
Huang L II-225
Hubbard A II-341, III-017, IV-121
Hubner K III-201
Hugenholtz CAJ IV-441
Hugill J II-017, II-025, III-033, III-125
Humphreys DA IV-049
Hurwitz PD I-001, III-265
Hutchinson IH II-341, III-313
Huttemann P III-341
Hutter T IV-125, IV-397
Huysmans GTA I-029, I-201, I-341, I-221, II-069, II-237, II-261,
..... III-005, IV-061, IV-085, IV-113
Hwang YS II-093
Hyatt AW IV-049
Ida K I-125, I-161, III-413, III-417, IV-149, IV-153
Idei H I-153, IV-149, IV-153
Ido S II-257, III-449
Igitkhanov Yu IV-317, IV-333
Ignacz P I-065
Ignat D III-365
Iguchi H I-153, III-413, IV-149, IV-153
Ijiri S I-137
Ijiri Y I-145
Ikamura S I-153
Ikezi H I-109, I-381
Imre K II-065
Ingesson LC IV-337
Innocente P IV-177
Intrator T IV-381
Ioffe AF II-081
Irby J II-341, III-017
Irzak MA II-085, IV-385, IV-389
Isayama A I-141, I-157, I-161

Isei N III-029
Ishida S I-017, IV-033
Ishida SI II-069, III-005
Isler RC IV-345
Isobe IV-153
Itoh K I-205, IV-237
Itoh S I-205, IV-229, IV-237
Its ER II-085, IV-385
Ivanov A IV-193
Ivanov N III-077, IV-017
Jablonski D II-341
Jacchia A I-053, II-013, III-009
Jackel HJF I-053, II-069
Jackson GL I-325, II-281
Jacquinot J II-329, III-081
Jaeckel HJ III-085, IV-465
Jaeger EF II-333, III-365
Jagger J I-001
Jakubka K IV-373
Jakubowski L II-161
Janeschitz G IV-317, IV-329, IV-333
Janjua S III-189
Janos A III-045
Jarmen A I-253
Jaroshevich SP I-033
Jarvis ON II-037, II-053, III-057, IV-141
Jasegawa IV-153
Jaspers R IV-093
Jauch Z III-201
Jaun A II-245, III-081
Jenkins I II-017, III-033, III-117
Jernigan TC I-113
Jiang Y I-001, IV-129
Jimenez JA II-149, II-157
Joffrin E III-373, IV-073, IV-125
Johner J IV-069
Johnson DW II-401, III-013, III-397
Johnson LC III-013
Johnson M IV-009
Jones I IV-045
Jones TG II-093
Jones TTC I-029, II-053, II-077, IV-061, IV-141
Joye B IV-081
Junker W III-097
Kabantsev A I-393
Kado S I-161, III-405
Kakurin AM III-077, IV-017
Kallenbach A I-025, I-069, I-321, II-005, III-097, III-409, IV-285,
..... IV-413
Kallstenius T III-157

Kalmykov SG II-081, IV-057
Kam K II-241
Kamada Y I-017, III-029, IV-033
Kamelander G II-185, IV-377
Kammash T IV-345
Kamo Y I-125
Kanaev BI IV-017
Kandaurov IV I-445
Kappler F II-277
Kapralov VG I-117
Karakin MA IV-169
Kardon B II-421
Karelse FA III-421
Karpushov AN IV-193
Kartsev Yu A IV-401
Karttunen SJ III-357
Karzhavin Y I-001, IV-097
Kashiwagi M II-257
Kasilov SV III-341, III-349
Kasparek W I-429
Kass T IV-041
Kassab MM I-269
Kastelewicz H II-217
Kaufmann M III-093
Kawabe T II-177, IV-173
Kawachi T III-417
Kawakami I II-137
Kawashima H I-073
Kawasumi Y I-125
Kaye A II-329
Kaye SM I-373, II-357
Kazarian-Vibert F III-373, IV-065, IV-073, IV-393
Kellman AG IV-049
Kerner W I-201, I-221, II-069, II-237, II-261, III-081, III-229,
..... III-277, IV-001, IV-085
Kessel C IV-121
Khlopenkov KV I-117
Khrebtov SM II-117
Kick M III-137
Kikuchi M I-017
Kim JS IV-097
Kim YB IV-137
Kimura H II-057
Kinoshita T I-157, I-161
Kirneva NA I-369
Kirnev GS III-285
Kishinevsky M IV-381
Kislov D I-369
Kisslinger J III-129, III-149
Klepper CC I-325, IV-345

Kletecka P IV-373
Klima R IV-373
Knight PJ III-049, III-233
Knoll DA IV-305
Knorr G III-209, IV-197
Kobayashi S I-137, I-145
Koch R II-337, II-397, III-341, III-345, IV-341
Koenen L III-345
Koenig R II-053, IV-061
Kogler U II-281, II-321, IV-281
Koide Y I-017, III-029
Komori A I-153
Kondo K I-137, I-145, I-149, I-157, I-161, I-285, III-405
Kondoh T II-057
Konen L III-341
Konig RWT I-029, II-009, II-077, II-125, II-377, II-453, IV-141
Korneev DO II-089
Kornejew P II-297
Kornev VA I-033
Korotkov A III-389
Koslowski HR I-133, II-321, III-053, III-065, III-341
Kostrukov AYu I-121
Kotelnikov IA II-181
Kovrov PE III-077, IV-017
Kozlovskij SS II-057
Kramer-Flecken A III-345
Krasai I-073
Krasilnikov A III-385
Kraux VI IV-169
Kravchenko AYu IV-453
Krejci A II-393
Krieger K II-289
Krikunov SV I-033
Krlin L I-329, IV-373
Krämer-Flecken A I-045
Kruglyakov EP I-445
Krupnik L II-117
Kryska L IV-373
Källne J III-381
Kubo S I-153, III-413, IV-149, IV-153
Kubota T IV-229
Kujanov A I-365
Kukushkin A III-205, IV-317, IV-329
Kumazawa R III-413, IV-149, IV-153
Kupfer K I-381, IV-393
Kupschus P IV-021
Kurimoto Y I-149, I-157, I-161
Kurnaev V III-285
Kurz C II-341
Kurzan B III-069

Kusama Y II-057, II-061
Kuteev BV I-121, IV-057
Kuvshinov BN III-221
La Haye RJ IV-053, IV-137
LaBombard B II-313, II-341, III-017, III-325
Lachambre JL III-101
Lackner K III-093
Lalousis P II-285
Lam N II-325
Lamalle PU II-329, II-353
Landman L II-277
Lang PT I-021, II-449
Lao LL IV-137
Lapshi VI IV-357
Laqua H I-353, I-357, I-389
Larsson D III-157, IV-277
Lashkin VM I-437
Lashkul S II-085, II-085, IV-385
Lashmore-Davies CN II-229, II-405, IV-361
Lasnier CJ III-105
Lauro-Taroni L I-081, I-089, II-009, III-121, IV-465
Laux M III-097, III-241
Lavanchy P III-081
Laviron C IV-101
Lawson KD I-081, II-077, III-121, IV-061, IV-141
Lazarus A IV-137
Lazzaro E IV-449
Lebas J IV-197
Lebedev AD II-085, IV-385
Lebedev S I-033
LeBlanc B III-013
Leclert G II-337, IV-409
Ledl L III-145
Ledyankin AI IV-345
Lee JH I-109
Lee P II-169
Lee RL II-281, IV-049
Lengyel L II-285
Lennholm M II-329, III-361
Leonard AW III-105
Lev ML II-165
Levin LS I-033
Levinton FM II-113, III-365, III-397
Lewandowski JLV II-141
Li GX I-173, I-177, III-157
Li XL II-273, II-345
Liang R I-125
Lieder G I-425, II-289, II-293, III-097, III-409
Lierzer J IV-129
Lin-Liu YR I-381, IV-137

Lingertat H II-125, IV-465
Lingertat J I-309, II-273, III-281, III-305, III-309, IV-297
Liniers M II-157
Lipin BM I-033
Lipschultz B II-313, II-341, III-325
Lister JB II-097, III-081, III-113, IV-081
Litaudon X III-373, IV-065, IV-073, IV-125, IV-393, IV-397
Litwin C IV-381
Liu Y III-073
Llobet X IV-081
Lloyd B I-345, II-001, II-021, II-209, III-369, IV-117
Lo D II-341
Lo E II-093
Loarer T I-317, III-317
Loarte A I-309, I-313, II-121, II-125, II-273, III-257, III-305, IV-297, IV-465
Lok J I-129, I-385
Lomas PJ I-029, I-313, II-077, IV-061, IV-141
Long YX II-225
Lopes Cardozo NJ I-129, II-013, II-129, III-037, IV-093, IV-261
Lopez-Fraguas A II-149, II-157
Lopez-Sanchez A II-157
Lorenz A II-173
Loughlin MJ II-053, II-069, III-057
Lovegrove T III-301
Lowry CG I-309, II-121, III-305
Luce TC III-025
Luciani JF I-189
Luetjens H I-241
Luhmann NC I-109
Lutz T I-317
Lyadina E IV-061
Lysoivan A III-341
Lütjens H I-189
Maas AC II-077, IV-141
Maassberg H I-353, I-357, I-389
Mace RL I-449
Maddison G III-117, IV-309
Maggi CF II-377
Magyar G I-085
Mahdavi MA I-317, I-325
Mai HH III-101
Mailloux J III-101
Maingi R I-113, I-325
Majeski R II-405, III-365
Makashin IN I-421
Maksimov Yu S IV-017
Malinova P I-253
Mancuso A I-237
Manfredi G III-209, IV-197, IV-201

Manhood SJ III-049, III-033
Mank G I-057, I-061, I-133, I-293, IV-341
Mansfield DK I-409, II-109
Manso ME IV-413, IV-417
Mantica P I-053, II-013, III-009
Mantsinen M II-249
Marakami M I-381
Maraschek M III-125, III-273, IV-041
Marchand R III-101
Marchenko VS II-221
Marchiori G IV-185
Marcus FB I-029, II-037, II-053, II-077, III-057, IV-061, IV-141
Marmar E II-109, II-341
Marrelli L IV-185, IV-437
Martin G II-041, II-045, IV-349
Martin P I-181, IV-185, IV-437
Martin R II-017, II-157, III-033, III-117
Martin TJ I-185, II-241
Martin Y II-097, III-113, IV-081
Martines E IV-181
Martini S IV-177, IV-181
Martynov AA I-217, I-369
Martynov DA III-077, IV-017
Masiello A IV-181
Mast KF I-069, II-005, III-097, III-401, IV-285
Masuda S IV-149, IV-153
Matoba T III-377
Matsuoka K I-153, III-413, IV-149, IV-153
Matsuura H I-137
Matthews GF ..... I-309, II-273, III-085, III-257, III-297, III-305, ... IV-297, IV-465
Mattioli M I-085, II-385, III-109
Mau TK I-109
Mauel ME IV-137
Maximov VV IV-193
May M II-341
Mayaux C II-009, II-121
Mayer M II-301
Mazur S I-169, I-173, I-177, III-157, III-457
Mazurenko A II-341
Mazzitelli G I-077
Mazzucato E III-013, III-365, IV-109
McArdle G I-345, II-021, III-369
McCarthy KJ II-153, II-417
McCarthy P IV-133
McChesney JM I-409
McClements KG I-185, II-229, II-405
McCool S I-001
McCormick K ..... I-309, I-313, II-077, II-125, III-257, III-269, III-297, ... III-305

McCracken GM II-313, II-341, III-325
McCune D II-105
McGinnity P I-081, III-121
McGuire KM III-045
Medina F II-149, II-157, III-041
Medley SS I-409, III-397
Medvedev S I-217
Meigs A IV-465
Meijer FG II-409
Meisel D I-321
Melnick IM I-097, II-133
Melnikov AV II-117
Menard J II-093
Mendonca JT IV-217
Meo F III-101
Mertens V II-005, III-097
Meshkov OI I-445
Meslin B III-317
Messiaen A I-133, III-341, III-345
Meyer W III-105, IV-137
Michaud D III-101
Micozzi P I-237
Migliuolo S IV-025
Mikhailov MI III-193
Miller RL I-241, I-377, IV-137
Minami T I-153, III-413, IV-149, IV-153
Minardi E IV-449
Miner W I-001
Mioduszewski PK I-317, I-325
Mirnov S I-421
Mishizawa A I-125
Mitchell IH II-173
Miura Y I-073
Mizuno N IV-173
Mizuuchi T I-137, I-145, I-149, I-157, I-161, I-285, III-405
Moiseenko VE III-341
Moller A I-173, III-153, III-157
Monier-Garbet P III-109, IV-345
Monk RD I-309, I-313, II-121, II-125, II-273, III-085, III-257,
..... III-281, III-293, III-297, III-305, IV-465
Montvai A IV-261
Moravec J II-373
Moreau D III-373, IV-065, IV-393
Moreau P IV-101
Morera JP IV-065
Moret JM I-417, II-097, II-101, III-081, III-113
Moret RA IV-081
Morgan PD II-401, IV-465
Mori M I-017
Morioka A II-057

Morisaki T I-153, III-413, IV-149
Morita S I-153, III-413, IV-149, IV-153
Moriyama S II-057
Moroz PE II-049, III-333
Morris AW ..... I-345, II-001, II-021, II-025, III-049, III-125, III-273, ... III-369, IV-117
Morris R III-217
Mukhovatov V III-377
Murakami M III-365
Muraoka K I-161, III-405
Murari A IV-437
Murmann H III-245
Muto S IV-153
Mutoh S IV-149
Mutoh T IV-149
Myrnas R I-085
Nagasaki K ..... I-137, I-141, I-145, I-149, I-157, I-161, I-285, ... III-405
Nakajima N IV-143
Nakamura Y I-225, IV-143
Nakasuga M I-137, I-161, I-285
Nakayama T I-285
Nanobashvili S IV-373
Napiontek B II-293, III-097, III-409
Narihara K I-125, I-153, III-413, IV-149, IV-153
Nascimento IC I-289
Naujoks D II-297, II-321
Navarro AP III-225
Nave MFF I-013, I-029, II-053, IV-061
Navratil GA IV-137
Nazikian R III-013, III-365, IV-109
Nedzelskij IS II-117
Neilson GH III-397
Nejoh Y II-433, III-445
Nemoto M II-057
Neu R I-065
Neubauer O III-341
Neudatchin S III-029
Neuhauser J II-217, III-093, III-097, IV-285
Nevins WM IV-121
Neyatani Y I-017, I-225, IV-033
Nguyen F II-329, II-353, III-317
Nicolai A IV-341
Niedermeyer H I-301
Nielsen P II-009, II-073
Nielson GH IV-305
Niemezewski A II-341
Nieswand Ch II-097, III-113, IV-081
Niethammer M III-409
Niffikeer SL II-169

Nikitin AN IV-097
Nishimura K I-153, III-413, IV-149, IV-153
Nishitani T II-061
Noll P IV-009
Nonn P IV-381
Nordlund P I-169, I-173, I-177, I-181, III-157, III-457
Noterdaeme JM I-349
Notkin GE IV-057
Novikov A Yu III-077, IV-017
Nowak S IV-369
Nygren RE I-317
Obert W II-009, II-121
Obiki T I-137, I-145, I-157, I-161, I-285, III-405
Ochando MA II-149, III-041, III-225
Odblom A I-093
Ogata K I-149
Ogawa H I-073, III-417
Ohdachi S I-153, III-413, IV-149
Ohya K II-321, III-345
Okabayashi M II-357
Okada H I-137, I-145, I-149, I-157, I-161, I-285, III-405
Okamoto M IV-143
Okamoto T I-285
Okamura S III-413, IV-149, IV-153
Ongena J I-133, II-321, II-397, III-345
Ono M II-093
O'Brien D I-029, I-309, III-297, III-305, IV-465
O'Brien MR I-345, II-265, III-233, III-369, IV-117
O'Connell R II-133
Oomens AAM I-129, II-013
O'Mullane MG I-097, III-121
O'Shea P II-341
Orefice A IV-369
Orlinski D III-377
Orsitto F I-401
Ortolani S IV-009
Osanai Y I-165
Osborne TH IV-137
Ottaviani M I-245
Ouroua A I-001, III-265
Ouroua H I-005
Ozaki T I-017, I-153, III-413, IV-033, IV-149, IV-153
Paccagnella R I-265
Pacher HD IV-317, IV-333
Pakyari A IV-245
Pan YD II-345
Pan'kin A Yu II-221
Parail VV I-013, I-053, II-213, III-361, IV-061, IV-113, IV-257
Paris P II-393
Paris RB II-437

Park H III-013
Parks PB I-409
Parlange F II-045
Pasch E II-297
Pasqualotto R IV-177, IV-181
Pastor I II-149
Patel A I-097
Pattikangas T III-357
Paul SF III-013, IV-105
Paume M IV-101
Pautasso G IV-037
Pavlenko VP IV-209, IV-245
Pavlo P IV-373
Pavlosky D I-001
Pavlov YuD IV-057
Peacock AT II-301
Peacock NJ I-081, I-097, III-121, III-261
Pecoul S II-337
Pecquet AL I-249, IV-073
Pedrosa MA I-305, II-149, IV-157
Peebles WA I-105, I-109
Pegoraro F III-221
Pegourie B IV-301
Pekker M II-233
Penningsfeld FP III-137
Penso A III-441
Pereverzev G II-365, III-001
Pericoli-Ridolfini V III-361
Peruzzo S IV-181
Pestchanyi S II-277
Peters M II-013, III-037
Peterson BJ I-137, I-145, I-157, I-161, I-285
Petrie TW III-105
Petrov SY II-057
Petty CC I-109, I-381, III-025
Peysson Y III-361, III-373, IV-065, IV-393
Pfirsch D II-189
Phelps DA I-381
Philipps V II-305, II-309, II-321, III-345, IV-473
Phillips CK III-365
Phillips PE I-001, I-005, III-265, IV-129
Piazza G II-277
Pickalov VV IV-337
Pieroni L IV-289
Pietrzyk ZA II-097, II-377, III-313
Piffi V II-373, II-393
Pijper FJ I-129, II-013, II-129
Pinches SD II-261
Pinsker RI I-109, I-381
Piovan R IV-181, IV-185

Pitcher CS II-289, III-097, III-241, III-245
Pitts RA II-097, III-113, IV-081
Platz P II-385, III-337
Plyusnin VV III-341
Pochelon A II-097, III-113, IV-081
Pod'minogin AA IV-193
Podushnikova KA II-085, IV-385
Pogutse O III-229, III-277
Polevoi AR II-205
Polman RW I-385
Pomaro N IV-181, IV-185
Popel SI II-425, III-433, IV-445
Porcelli F I-245, II-233, II-253, III-169
Porkolab M I-297, II-341, IV-121
Porte L I-013, I-029, I-053, II-073, III-009, III-081, III-085,
..... III-261, III-281, IV-001, IV-021, IV-061
Porter G III-321
Portnov DV III-385
Pospieszczyk A II-305, II-309, II-321, III-345
Post Zwicker AP I-061
Powers EJ I-001, I-281
Prater R I-381
Preinhaelter J IV-373
Preische S I-373
Prentice R III-281, IV-425, IV-465
Price M II-017, III-117
Probert P IV-381
Prozesky V II-301
Prut VV IV-017
Puiatti ME II-317, II-317, III-161, IV-177
Puri S I-457, II-197
Pyatak AI III-349
Qin J II-149, II-153
Qin YW II-345
Qiu M II-225
Quemeneur A III-061, IV-101
Rachlew-Kallne E III-157
Radford GJ III-305, IV-297
Radobarin GT I-033
Ram A IV-353
Ramsey AT II-401
Ramström E III-381
Ran Li Bo I-273, III-073
Rantsev-Kartinov VA III-205, IV-221
Rapp J I-057, II-321, III-345
Rasmussen D III-365
Ratel G III-101
Rau F III-129, III-149
Raus J II-393
Razumova KA I-369

Reardon J II-341
Redi M II-105
Reichle R I-309, II-125, III-085, III-401, IV-297, IV-465
Reimer H III-341
Reiner HD II-297
Reiter D III-249, IV-285, IV-321, IV-329
Rem J IV-457
Renberg PU III-381
Renda G III-397
Renner H III-149
Rensink M III-321, IV-305
Resendes DG IV-217
Rettig CL I-105, I-109
Rey G III-373, IV-397
Rhodes TL I-105, I-109
Ribeiro C II-017, III-033
Riccardi C I-453, III-441
Rice BW IV-049, IV-129, IV-137
Rice JE II-313, II-341, III-017
Richard N III-101
Richards B I-001, III-265
Riedel KS II-065
Righi E II-073, II-125, II-329, II-353, III-229, IV-001
Rimini FG I-009, II-069, II-353, III-005, III-361
Roach CM II-205, III-189
Roberts DR I-001, I-101, IV-097, IV-129
Robinson DC III-233, IV-117
Rodriguez-Rodrigo L III-041, IV-269
Rogers JH III-365
Rogister A IV-341
Rognlien TD III-321, IV-305
Rogozin AI IV-193
Rohde V III-097, III-241, III-245
Romanelli F I-089
Romanelli M III-221
Rome M I-353, I-357, I-389
Rommers JH III-421
Rookes A III-121, III-261, IV-061, IV-465
Roquemore AL I-409
Rosenbluth MN III-169, IV-009
Ross DW I-001, IV-129
Rossi A II-121
Rost C II-341
Rowan W I-001, I-005, III-265
Rozhansky V I-117, I-337, II-285
Rozhdestvensky VV I-033
Rubel M III-345
Rudakov DA II-141
Rudyj A I-301
Ruffina U III-185

Rust N III-137
Ruzic DN IV-305
Ryter F II-005, III-097, III-125, IV-089
Sabbagh SA II-113
Sabot R IV-249
Sadler G II-037, II-053, II-069, II-269, III-057, IV-001
Sadowski M II-161
Safonova MB IV-017
Sagara A IV-153
Saibene G I-309, II-009, II-121, II-125, III-305, IV-465
Saigusa M II-057
Saito K I-165
Saito KH II-137
Saito KN II-137
Sakakibara S I-153, III-413, IV-149
Sakakita H I-125
Sakamoto K I-137, I-145
Sakamoto M I-125
Salisbury MW IV-425
Sallander J III-157
Salomaa RRE II-249, III-357
Samain A I-249
Samm U I-057, II-201, II-305, II-321, III-345, IV-321
San Jose MAG I-405
Sanchez E IV-157, IV-165
Sanchez J II-149, IV-157, IV-161, IV-429, IV-433
Sander M I-133
Sanin AL I-445
Sannazaro G IV-141
Sano F I-137, I-145, I-157, I-161, I-285, III-405
Santagiustina A IV-461
Saoutic B I-037, III-337, IV-125, IV-353, IV-397
Sardei F IV-325
Sarichev DV III-285
Sarkissian AH III-101
Sartori R II-077, II-121, IV-141
Satherblom H-E I-169, III-457
Sato KN I-125
Sato M III-029
Satoh M II-057
Sattin F II-317
Sauter O I-241, IV-077
Scarin P II-317, III-161, IV-177
Schachter J II-341
Schaffer MJ I-325
Scharer J II-325
Scheffel J I-169
Schep TJ III-221, IV-457
Schild P III-361
Schilling G III-365

Schissel DP II-065
Schittenhelm M III-273
Schivell J II-105, III-013
Schmidt GL II-113, IV-021
Schneider R II-217, III-093, III-249, IV-285, IV-329
Schneider W III-125, IV-037
Schoch PM I-001, III-265
Schonmann K I-065, I-069, III-237
Schoon N III-345
Schram DC IV-337
Schram PJJM IV-453
Schroder KA III-265
Schuller FC IV-029, IV-093, IV-261, IV-441
Schultz SD IV-353
Schumacher U III-409
Schunke B I-029, II-053, II-065, II-077, IV-061, IV-141
Schweer B II-305, II-309, II-321, III-345
Schweinzer J I-233, III-237, III-245, III-249, III-253, III-269
Schwelberger J I-293
Scott B I-229
Scott SD II-109,, III-013, IV-105, IV-109
Scoville JT IV-053
Seidel U IV-037
Semenets AM I-421
Semenov AA II-165
Semenov IB I-421
Senju T I-137, I-145
Senties JM I-405
Sergeev V Yu I-049, II-081, IV-057
Serianni G IV-181
Serra FM IV-413, IV-417
Sesnic S II-357
Shafranov VD III-193
Sharapov S II-237, II-261, III-081
Sharp LE II-141
Shats MG II-141
Shcherbinin ON II-085, IV-385
Shevchenko V IV-421
Shiina S I-165, II-137
Shikhovt'sev IV IV-193
Shirai H I-017, III-029
Shkarofsky IP III-353, III-357, IV-393
Shmaenok LA II-409
Shoji T I-073
Shoucri M ..... III-209, III-357, III-353, III-361, IV-197, IV-201, ... IV-393
Shukla PK I-441, III-429, IV-217
Shurygin VA II-369, IV-013
Shybaev SA IV-017
Sibley II-329

Silva A IV-413, IV-417
Silva F IV-417
Simonetto A I-361, IV-369
Simonini R I-309, III-305, IV-297
Simpson PR I-345, III-369
Sing DS I-001, IV-129
Singleton MA I-097
Sipila S II-349
Sips ACC II-069, III-005, IV-001, IV-113
Sitenko AG III-177, IV-273
Sklyarova EM II-165
Skovoroda AA I-365
Smeulders P I-029, II-053, IV-061, IV-141
Smirnov AI I-033
Smith MEU III-393
Smith RJ IV-425
Smits F III-361
Snipes J II-109, II-341
Sokoll M IV-133
Solano E I-001
Solari G I-361, IV-369
Soldatov SV IV-401
Soldner FX III-361, IV-001, IV-113
Solis RM II-037
Soltwisch H III-065
Sonato P IV-181, IV-185
Spathis P II-285
Spence J I-313, IV-297
Springmann E I-013, I-053, II-213, III-361, IV-113
Stabler A I-349, IV-089
Stallings DC II-333
Stamp MF I-309, I-313, II-009, II-077, II-121, II-273, III-089, IV-021, IV-465
Stangeby PC II-273, IV-465
Stansfield BL III-101
Start DFH II-073, II-329, II-353, IV-001
Steenbakkers MFM II-129
Steimle RF I-001, I-101
Stek P II-341
Stepanov AYu II-085
Stepanov KN III-349, IV-357
Steuer KH I-069, I-349, III-069
Stober J III-249
Stockel J I-329, IV-373
Stodiek W III-065
Storek DJ III-265
Storey P III-301
Stork D I-309, II-009, II-121, II-125
Stott PE III-377
Strachan JD II-109, III-013

Strait EJ IV-137
Streibl B III-093
Stroth U I-389, III-037, III-137, IV-265
Stuart A II-033
Stubberfield P I-009
Stupishin NV IV-193
Stutman D II-093
Subbotin A III-193
Sudo S I-161
Sugihara M IV-317
Sugiyama LE I-461, III-017, IV-121
Summers DDR II-377
Summers HP II-377
Sund R II-325
Sushkov AV I-049, I-369
Suttrop W I-233, III-069, III-237, III-245, III-249, III-273
Suvorov E I-429
Suzuki Y I-161
Svoboda V I-329
Sychev VN I-277, III-329
Sykes A II-017, II-205, III-033, III-117
Synakowski EJ III-013
Tabares F II-149, II-153
Tafalla D II-153
Takahashi C I-153, III-413, IV-149, IV-153
Takase Y II-341
Takeji S IV-033
Takizuka T I-017, III-029
Talvard M I-249, II-357
Tamai H I-073
Tanabe T II-321, III-345
Tanaka K I-153, III-413, IV-149, IV-153
Tanga A IV-009, IV-021
Tanzi C II-029
Taroni A I-013, I-053, I-309, I-313, II-213, III-009, III-305, IV-113, IV-141, IV-297, IV-465
Tatarakis M II-169
Taylor G III-013, III-045, III-365
Taylor P IV-049
Taylor TS IV-137
Tebaldi C I-245
Telesca G III-345, IV-293
Terentiev AR III-205
Terreault B III-101
Terry D I-001
Terry JL II-109, II-313, III-325, II-341
Tessarotto M I-193, IV-225
Teubel A I-349, IV-089
TEXTOR and ERM/KMS Teams I-057
Theimer G I-301

Thomas PRT I-029, II-077, IV-061, IV-141
Thompson E II-121
Thompson SJ IV-137
Thomsen K II-073, IV-061, IV-141
Thyagaraja A III-173
Tighe W II-401
Timms M II-329
Tobin S IV-345
Toda S I-205
Todd TN II-001, III-393
Tohrisawa K II-177
Tohshi K I-137, I-145
Toi K I-125, I-153, IV-149, IV-153
Tokar M II-201, II-321, III-345, IV-321, IV-341
Tokman MD I-365
Tokuda S IV-033
Tolkach V II-277
Tomas J III-033
Tonetti G I-417, II-097, III-113, IV-081
Tramontin L IV-277
Traneus E III-381
Trevisan F IV-181, IV-185
Trofimenko YuV II-117
Trostell B III-381
Trotman DL III-393
Truc A III-061, IV-101
Tsaun SV IV-401
Tsitrone E IV-301
Tsuji S I-017
Tsukahara Y II-057
Tubbing BJD II-069, III-005, III-453, IV-001,
..... IV-113
Tudisco O I-361, III-021
Tukachinsky AS I-033, IV-385
Turlur S I-249, IV-065, IV-073
Turnbull AD I-377, IV-137
Tykshaev VP IV-169
Uckan T I-317
Ueda Y II-321, III-345
Uehara K I-397
Uglum J I-001
Ulrich M IV-037
Umansky M II-341
Unger E III-145
Unterberg B I-057, II-201, II-305, II-321, III-345
Ushakov AA I-337
Vaclavik J II-245, IV-233, IV-241
Valeo E III-365
Valisa M II-317, III-161, IV-181, IV-177, IV-185
Vallet JC IV-073

Valovic M ..... I-097, I-345, II-001, II-025, III-049, III-125, III-273, ... III-393, IV-117
van Belle P II-037, II-269, III-057
Van der Linden RAM I-221
Van Eester D II-397
van Gelder JFM III-425
Van Houtte D II-045, IV-349
van Milligen B Ph II-153, III-225, IV-157, IV-165
Van Nieuwenhove R III-341
van Oost G I-133, III-341, III-345, IV-431
Van Wassenhove G II-397, III-345
Varela P IV-413, IV-417
Vavovic M III-369
Vayakis G I-013, IV-405
Vega J II-153
Veklich A III-437
Verbeek H III-249
Veres G II-421
Verplancke P I-425
Vershkov VA I-049, IV-005, IV-401
Vervier M III-341
Veseleva I II-285
Vikhrev VV III-197
Villar Colome J IV-069
Villard L II-245
Viola R III-309
Vizgalov IV III-285
Vladimirov SV III-429, IV-445
Vlases G I-313, III-305, III-313, IV-297
Voitsekhovitch IA IV-257
Volkov VV III-077, IV-017
Vollmer O IV-089
von Goeler S II-357
von Hellerman M ..... II-009, II-073, II-125, II-377, II-453, III-085, III-089, ... IV-465
Voronin AV II-165
Voskoboynikov SP I-337
Vukovic M IV-381
Vyacheslavov LN I-445
Vyas P III-049
Wada M II-321, III-345
Wade MR I-113, I-325, II-009
Wade TJ II-329
Wahlberg C I-213
Waidmann G I-045, III-053, III-341, IV-029
Wakatani M I-161, I-285
Walsh MJ II-017, II-205, III-033, III-117
Walter H III-137
Wang CY II-333
Wang EY III-073

Wang ZH III-073
Ward DJ II-069, III-005, IV-077
Warr G II-141
Warren R III-273
Warrick CD I-345, II-209, III-369, IV-117
Watanabe K I-161, IV-143
Watari T III-413, IV-149, IV-153
Watkins JG III-105
Watkins N II-037, II-053, III-057
Watterson R II-341
Watts C I-001, I-005, IV-097
Weinlich M I-425, III-097, III-241, III-245
Weisen H II-097, II-389, II-393, III-113, IV-081
Welander A I-173, III-153, III-157
Welch BL II-313, II-341
Weller A I-357, III-145
Wenzel U I-069, III-097
Werley KA IV-305
Weschenfelder F II-281
Wesley J IV-009
West WP II-281
Westerhof E I-385, II-129, III-425
White RB I-193, II-105
Whitehurst GA I-345, IV-117
Whyte D III-101
Wienhold P II-281
Wijnands TJ II-045
Wilson HR I-089, I-261, II-205, III-033, III-233
Wilson JR III-365
Wilson KM II-173
Windsor CG III-393
Winslow D I-001, III-265
Winter Hp III-253
Winter J II-281, II-321, III-341, III-345, IV-281
Winz G IV-381
Wobig H III-129, III-149
Wolfe S II-341, III-017
Wolle BKR III-137, III-201
Woloch F II-185
Wong HV II-233
Wood AD II-437
Wood RD III-105
Wootton AJ I-001, I-005, IV-097, IV-129
Worley JF II-173
Wright JC III-365
Wukitch S IV-381
Wunderlich R IV-285
Wurden GA II-061
Wurz H II-277
Wutte D III-253

Xie H X III-165
Xu DM I-273
Xu J I-125, I-153, III-417, IV-149, IV-153
Xue SW II-345
Yagi M I-205, IV-229, IV-237
Yaguchi K I-137, I-145
Yamada H I-153, IV-149, IV-153
Yamada I I-153, III-413, IV-149, IV-153
Yamaguchi Y II-177
Yamamoto S III-377
Yamauchi K III-413
Yamauchi T I-073
Yamazaki K IV-143
Yan LW III-073
Yang G III-073
Yankov VV IV-209
Yevdokimov DV IV-017
Yoshino R I-225
Young KM III-377, III-397
Yu MY II-425
Yu Q I-197
Yurchenko EI IV-221
Zabajdullin OZ III-197
Zacek F IV-373
Zagorodny AG IV-273
Zaitsev FS II-265
Zarnstorff MC II-105, II-113, III-013
Zastrow KD II-009, II-453
Zehrfeld H IV-133
Zeiler A IV-205
Zeng L IV-129
Zerbini M III-021
Zhang BC I-001, II-141
Zhang W III-101
Zheng LJ I-193, IV-225
Zheng S-B I-001
Zhong GW I-273
Zhong YZ III-073, III-073
Zhovtyansky V III-437
Zhuravlev V IV-161, IV-429, IV-433
Zimeleva A II-117
Zinchenko VF IV-169
Zohm H I-233, II-005, III-097, III-125, III-237, III-273, IV-041
Zoletnik S III-269, III-269
Zou XL I-041, IV-101, IV-409
Zurro B II-149, II-153, II-417
Zushi H I-137, I-141, I-145, I-157, I-161, I-285
Zuzak W III-101
Zweben SJ II-105, III-365, III-397
Zwingmann W IV-085